STATE OF THE CLIMATE IN 2008

T. C. Peterson and M. O. Baringer, Eds.

Associate Eds.: H. J. Diamond, R. L. Fogt, J. M. Levy, J. Richter-Menge, P. W. Thorne, L. A. Vincent, and A. B. Watkins

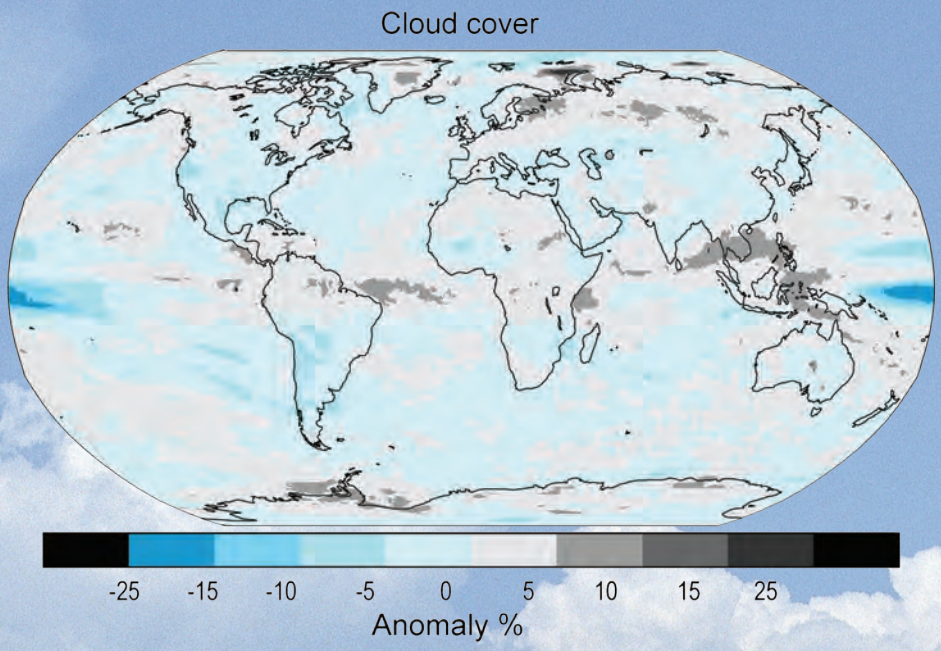

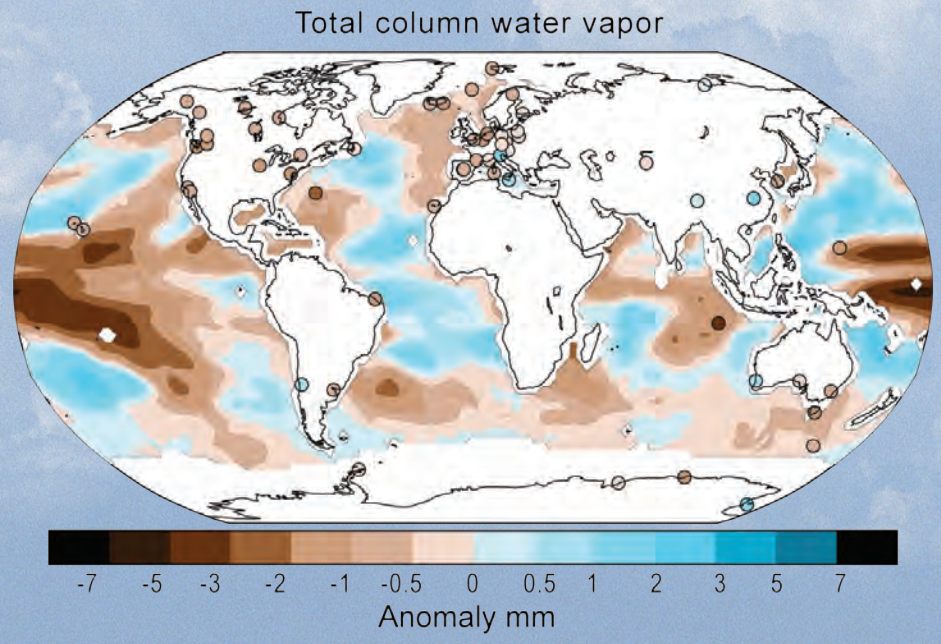

Special Supplement to the *Bulletin of the American Meteorological Society*
Vol. 90, No. 8, August 2009

STATE of the CLIMATE in 2008

HOW TO CITE THIS DOCUMENT

Citing the complete report:

Peterson, T. C., and M. O. Baringer, Eds., 2009: State of the Climate in 2008. *Bull. Amer. Meteor. Soc.*, **90,** S1–S196.

Citing a chapter (example):

Levy, J. M., Ed., 2009: Global oceans [in "State of the Climate in 2008"]. *Bull. Amer. Meteor. Soc.*, **90** (8), S1–S196.

Citing a section (example):

L'Heureux, M., G. Bell, and M. Halpert, 2009: ENSO and the tropical Pacific [in "State of the Climate in 2008"]. *Bull. Amer. Meteor. Soc.*, **90** (8)**,** S1–S196.

AFFILIATIONS (ALPHABETICAL BY AUTHOR)

Aceituno, Patricio, Universidad de Chile, Santiago, Chile

Achard, Frédéric, Institute for Environment and Sustainability, Joint Research Centre, Ispra, Italy

Acheberger, Christine, Earth Sciences Centre, University of Gothenburg, Gothenburg, Sweden

Ackerman, Steven A., CIMSS University of Wisconsin—Madison, Madison, Wisconsin

Alfaro, Eric J., Center for Geophysical Research, University of Costa Rica, San José, Costa Rica

Allan, Rob, Met Office Hadley Centre, Exeter, Devon, United Kingdom

Amador, Jorge A., Center for Geophysical Research, University of Costa Rica, San José, Costa Rica

Antonov, John I., NOAA/NESDIS National Ocean Data Center, Silver Spring, Maryland

Ashik, I., Arctic and Antarctic Research Institute, St. Petersburg, Russia

Attaher, Samar M., Ministry of Agriculture and Land Reclamation, Cairo, Egypt

Baez, Julian, DMH-DINAC/CTA-UCA, Asunción, Paraguay

Bai, L.-S., Byrd Polar Research Center and Department of Geography, The Ohio State University, Columbus, Ohio

Ballard, Robert A., NOAA/NWS, Honolulu, Hawaii

Baringer, Molly O., NOAA/Atlantic Oceanographic and Meteorological Laboratory, Physical Oceanography Division, Miami, Florida

Barreira, Sandra, Argentine Naval Hydrographic Service, Buenos Aires, Argentina

Barriopedro, David, Centro de Geofísica da Universidade de Lisboa, Lisbon, Portugal

Bartholomé, Etienne, Institute for Environment and Sustainability, Joint Research Centre, Ispra, Italy

Beal, Lisa M., Rosenstiel School of Marine and Atmospheric Science, Division of Meteorology and Physical Oceanography, Miami, Florida

Behrenfeld, Michael J., Oregon State University, Corvallis, Oregon

Bell, Gerald D., NOAA/NWS/NCEP Climate Prediction Center, Camp Springs, Maryland

Bell, Michael A., International Institute for Climate and Society, New York

Bellouin, Nicolas, Met Office Hadley Centre, Exeter, Devon, United Kingdom

Belward, Alan S., Institute for Environment and Sustainability, Joint Research Centre, Ispra, Italy

Bennartz, Ralf, Department of Atmospheric and Oceanic Sciences, University of Wisconsin—Madison, Madison, Wisconsin

Benson, R., Byrd Polar Research Center and Department of Geography, The Ohio State University, Columbus, Ohio

Bhatt, U. S., Geophysical Institute, University of Alaska–Fairbanks, Fairbanks, Alaska

Bhattacharya, I., Byrd Polar Research Center and Department of Geography, The Ohio State University, Columbus, Ohio

Bidegain, Mario, Instituto de Fisica, Montevideo, Uruguay

Bissolli, Peter, German Meteorological Service, Offenbach, Germany

Blake, Eric, NOAA/NWS/NCEP National Hurricane Center, Miami, Florida

Boudet, Dagne, Institute of Meteorology of Cuba, La Habana, Cuba

Bowling, Laura C., Department of Agronomy, Purdue University, West Lafayette, Indiana

Box, J. E., Byrd Polar Research Center and Department of Geography, The Ohio State University, Columbus, Ohio

Boyer, Timothy P., NOAA/NESDIS National Ocean Data Center, Silver Spring, Maryland

Brink, Andreas B., Institute for Environment and Sustainability, Joint Research Centre, Ispra, Italy

Bromwich, David H., Byrd Polar Research Center and Department of Geography, The Ohio State University, Columbus, Ohio

Brown, R., Climate Research Division, Environment Canada, Downsview, Ontario, Canada

Bryden, Harry L., Ocean Observing and Climate Research Group, National Oceanography Centre, Southampton, United Kingdom

Bulygina, Olga N., All-Russian Research Institute of Hydrological Information, Obninsk, Russia

Calderon, Blanca, Center for Geophysical Research, University of Costa Rica, San José, Costa Rica

Camargo, Suzana J., Lamont–Doherty Earth Observatory, The Earth Institute at Columbia University, Palisades, New York

Cappelen, J., Danish Meteorological Institute, Copenhagen, Denmark

Carmack, E., Institute of Ocean Sciences, Sidney, British Columbia, Canada

Chen, Deliang, Earth Sciences Centre, University of Gothenburg, Gothenburg, Sweden

Christy, John R., Earth System Science Center, University of Alabama in Huntsville, Huntsville, Alabama

Coelho, Caio A. S., CPTEC/INPE, Center for Weather Forecasts and Climate Studies, Cachoeira Paulista, Brazil

Colwell, Steve, British Antarctic Survey, Cambridge, United Kingdom

Comiso, J. E., NASA Goddard Space Flight Center, Greenbelt, Maryland

Cunningham, Stuart. A., Ocean Observing and Climate Research Group, National Oceanography Centre, Southampton, United Kingdom

Cupo, J. P, National Weather Service, San Juan, Puerto Rico

Cutié, Virgen, Institute of Meteorology of Cuba, La Habana, Cuba

Davydova-Belitskaya, Valentina, National Meteorological Service of Mexico, Mexico City, Mexico

Decker, D., Byrd Polar Research Center and Department of Geography, The Ohio State University, Columbus, Ohio

Derksen, C., Climate Research Division, Environment Canada, Downsview, Ontario, Canada

Diamond, Howard J., NOAA/NESDIS National Climatic Data Center, Silver Spring, Maryland

Dickson, Andrew G., Scripps Institution of Oceanography, University of California, San Diego, La Jolla, California

DiGirolamo, N., Science Systems Applications Inc. and NASA Goddard Space Flight Center, Greenbelt, Maryland

Dlugokencky, Ed, NOAA Global Monitoring Division, Earth System Research Laboratory, Boulder, Colorado

Dohan, Kathleen, Earth and Space Research, Seattle, Washington

Drozdov, D., Earth Cryosphere Institute, Tumen, Russia

Dutton, Geoffrey S., NOAA Earth Science Research Laboratory/ Cooperative Institute for Research in Environmental Sciences (CIRES), Boulder, Colorado

Elkins, James W., NOAA Earth System Research Laboratory, Boulder, Colorado

Epstein, H. E., University of Virginia, Charlottesville, Virginia

Feely, Richard A., NOAA/OAR Pacific Marine Environmental Laboratory, Seattle, Washington

Fekete, Balázs M., NOAA CREST Center, The City College of New York, New York, New York

Fenimore, Chris, NOAA/NESDIS/National Climatic Data Center, Asheville, North Carolina

Fettweis, X., Department of Geography, University of Liège, Liège, Belgium

Fogt, Ryan L., NOAA Earth System Research Laboratory, Boulder, Colorado

Folland, Chris K., Met Office Hadley Centre, Exeter, Devon, United Kingdom

Fonseca-Rivera, Cecilia, Institute of Meteorology of Cuba, La Habana, Cuba

Foster, Michael J., AOS/CIMSS University of Wisconsin—Madison, Madison, Wisconsin

Frolov, I., Arctic and Antarctic Research Institute, St. Petersburg, Russia

Gamedze, Mduduzi S., Swaziland Meteorological Service, Mbabane, Swaziland

Gill, Stephen, NOAA/NOS Center for Operational Oceanographic Products and Services, Silver Spring, Maryland

Gleason, Karin L., NOAA/NESDIS National Climatic Data Center, Asheville, North Carolina

Gobron, Nadine, Institute for Environment and Sustainability, Joint Research Centre, Ispra, Italy

Goldenberg, Stanley B., NOAA/OAR Atlantic Oceanographic and Meteorological Laboratory, Miami, Florida

Goni, Gustavo J., NOAA/OAR Atlantic Oceanographic and Meteorological Laboratory, Physical Oceanography Division, Miami, Florida

González, Idelmis, Institute of Meteorology of Cuba, La Habana, Cuba

Gottschalck, Jonathan, NOAA/NWS/NCEP Climate Prediction Center, Camp Springs, Maryland

Gouveia, Célia C., Centro de Geofísica da Universidade de Lisboa, Lisbon, Portugal

Guard, Charles P., NOAA National Weather Service, Barrigada, Guam

Guo, Yanjun, National Climate Center, Beijing, China

Haimberger, Leopold, University of Vienna, Vienna, Austria

Hall, D., NASA Goddard Space Flight Center, Greenbelt, Maryland

Halpert, Michael S., NOAA/NWS/NCEP Climate Prediction Center, Camp Springs, Maryland

Hanna, E., Department of Geography, University of Sheffield, England

Harris, Glen, Met Office Hadley Centre, Exeter, Devon, United Kingdom

Haywood, Jim, Met Office Hadley Centre, Exeter, Devon, United Kingdom

Heidinger, Andrew K., NOAA/NESDIS University of Wisconsin—Madison, Madison, Wisconsin

Heim, Richard R., Jr., NOAA/NESDIS/ National Climatic Data Center, Asheville, North Carolina

Hernandez, Marieta, Institute of Meteorology of Cuba, La Habana, Cuba

Hilburn, Kyle A., Remote Sensing Systems, Santa Rosa, California

Hirschi, Joel, Ocean Observing and Climate Research Group, National Oceanography Centre, Southampton, United Kingdom

Jaimes, Ena, Servicio Nacional de Meteorología e Hidrología de Perú, Lima, Perú

Jia, G. J., Chinese Academy of Sciences, Institute for Atmospheric Physics, Beijing, China

Johns, William E., Rosenstiel School of Marine and Atmospheric Science, Division of Meteorology and Physical Oceanography, Miami, Florida

Johnson, Gregory C., NOAA/OAR Pacific Marine Environmental Laboratory, Seattle, Washington

Jones, Andy, Met Office Hadley Centre, Exeter, Devon, United Kingdom

Jones, Gareth S., Met Office Hadley Centre, Exeter, Devon, United Kingdom

Kabidi, Khadija, Direction de la Météorologie Nationale, Rabat, Morocco

Kanzow, Torsten O., Ocean Observing and Climate Research Group, National Oceanography Centre, Southampton, United Kingdom

Kennedy, John J., Met Office Hadley Centre, Exeter, Devon, United Kingdom

Khalil, Alaa A., Ministry of Agriculture and Land Reclamation, Cairo, Egypt

Kholodov, A., Geophysical Institute, University of Alaska Fairbanks, Fairbanks, Alaska

Khoshkam, Mahbobeh, Islamic Republic of Iran Meteorological Organization, Tehran, Iran

Kimberlain, Todd, NOAA/NWS/NCEP National Hurricane Center, Miami, Florida

Knaff, John A., NOAA/NWS Regional and Mesoscale Meteorology Branch, Fort Collins, Colorado

Knight, Jeff, Met Office Hadley Centre, Exeter, Devon, United Kingdom

Korshunova, Natalia N., All-Russian Research Institute of Hydrological Information, Obninsk, Russia

Kratz, David P., NASA Langley Research Center, Hampton, Virginia

Krishfield, R., Woods Hole Oceanographic Institution, Woods Hole, Massachusetts

Kruger, Andries, South African Weather Service, Pretoria, South Africa

Kruk, Michael C., STG, Inc., Asheville, North Carolina

L'Heureux, Michelle, NOAA/NWS/NCEP Climate Prediction Center, Camp Springs, Maryland

Lammers, Richard B., WSAG/CSRC Institute for the Study of Earth, Oceans, and Space, University of New Hampshire, Durham, New Hampshire

Lander, Mark A., Water and Environmental Research Institute, University of Guam, Mangilao, Guam

Landsea, Chris W., NOAA/NWS/NCEP National Hurricane Center, Miami, Florida

Lapinel, Braulio, Institute of Meteorology of Cuba, La Habana, Cuba

Lawford, Richard, Hydrological and Biospheric Sciences, NASA GSFC, Greenbelt, Maryland

Lee, Hyun-Soo, Climate Prediction Division, Korea Meteorological Administration, Seoul, Republic of Korea

León, Gloria, Instituto de Hidrología de Meteorología y Estudios Ambientales, Columbia

Leuliette, Eric, NOAA/NESDIS, Laboratory for Satellite Altimetry, Silver Spring, Maryland

Levinson, David H., NOAA/NESDIS National Climatic Data Center, Asheville, North Carolina

Levitus, Sydney, NOAA/NESDIS National Ocean Data Center, Silver Spring, Maryland

Levy, Joel M., NOAA/OAR Climate Program Office, Silver Spring, Maryland

Liu, Hongxing, Department of Geography, Texas A&M University, College Station, Texas

Long, Di, Department of Geography, Texas A&M University, College Station, Texas

Longworth, Hannah R., Ocean Observing and Climate Research Group, National Oceanography Centre, Southampton, United Kingdom

Lumpkin, Rick, NOAA/OAR Atlantic Oceanographic and Meteorological Laboratory, Physical Oceanography Division, Miami, Florida

Luo, Jing-Jia, Frontier Research Center for Global Change, JAMSTEC, Yokohama, Japan

Lyman, John M., NOAA/OAR Pacific Marine Environmental Laboratory, Seattle, Washington, and Joint Institute for Marine and Atmospheric Research, University of Hawaii, Honolulu, Hawaii

Macdonald, Alison M., Woods Hole Oceanographic Institution, Woods Hole, Massachusetts

Maddux, Brent C., AOS/CIMSS University of Wisconsin—Madison, Madison, Wisconsin

Malkova, G., Earth Cryosphere Institute, Tumen, Russia

Marchenko, S., Geophysical Institute, University of Alaska Fairbanks, Fairbanks, Alaska

Marengo, Jose A., Centro de Ciências do Sistema Terrestre (CCST), Instituto Nacional de Pesquisas Espaciais (INPE), Cachoeira Paulista, Sao Paulo, Brazil

Maritorena, Stephane, University of California at Santa Barbara, Santa Barbara, California

Marotzke, Jochem, Max-Planck-Institut für Meteorologie, Hamburg, Germany

Martinez, Rodney, Centro Internacional para la Investigación del Fenómeno de El Niño (CIIFEN), Guayaquil, Ecuador

Mascarenhas, Affonso, Centro Internacional para la Investigación del Fenómeno de El Niño (CIIFEN), Guayaquil, Ecuador

Massom, Robert A., Australian Antarctic Division and Antarctic Climate and Ecosystems Cooperative Research Center (ACE CRC), University of Tasmania, Hobart, Tasmania, Australia

McBride, Charlotte, Climate Service, South African Weather Service, Pretoria, South Africa

McGree, Simon, Fiji Meteorological Service, Nadi, Fiji

McLaughlin, F., Institute of Ocean Sciences, Sidney, British Columbia, Canada

McPhee, M., McPhee Research Company, Naches, Washington

Mears, Carl A., Remote Sensing Systems, Santa Rosa, California

Medany, Mahmoud A., Ministry of Agriculture and Land Reclamation, Cairo, Egypt

Meier, W., CIRES/NSIDC, University of Colorado, Boulder, Colorado

Meinen, Christopher S., NOAA/Atlantic Oceanographic and Meteorological Laboratory, Physical Oceanography Division, Miami, Florida

Menne, Matthew J., NOAA/NESDIS National Climatic Data Center, Asheville, North Carolina

Merrifield, Mark A., University of Hawaii at Manoa, Honolulu, Hawaii

Mhanda, Albert S., Climate Change Office, Harare, Zimbabwe

Miller, Laury, NOAA/NESDIS, Laboratory for Satellite Altimetry, Silver Spring, Maryland

Mitchum, Gary T., College of Marine Science, University of South Florida, St. Petersburg, Florida

Monaghan, Andrew J., National Center for Atmospheric Research, Boulder, Colorado

Montzka, Steve, NOAA Global Monitoring Division, Earth System Research Laboratory, Boulder, Colorado

Morison, J., Polar Science Center, University of Washington, Seattle, Washington

Mote, T., Department of Geography, University of Georgia, Atlanta, Georgia

Mullan, A. Brett, National Institute of Water and Atmospheric Research, Ltd., Wellington, New Zealand

Mutasa, Colin, Meteorological Service Department, Harare, Zimbabwe

Nerem, R. Steven, University of Colorado, Boulder, Colorado

Newman, Paul A., Laboratory for Atmospheres, NASA Goddard Space Flight Center, Greenbelt, Maryland

Nghiem, S. V., Jet Propulsion Laboratory, Pasadena, California

Njau, Leonard, African Centre of Meteorological Applications for Development, Niamey, Niger

O'Malley, Robert T., Oregon State University, Corvallis, Oregon

Oberman, N., MIREKO, Syktivkar, Russia

Obregón, André, Laboratory for Climatology and Remote Sensing (LCRS), University of Marburg, Marburg, Germany

Ogallo, Laban, IGAD Climate Prediction and Applications Centre, Nairobi, Kenya

Oludhe, Christopher, Department of Meteorology, University of Nairobi, Nairobi, Kenya

Osman-Elasha, Balgis, Higher Council for Environmental and Natural Resources, Khartoum, Sudan

Overland, J., NOAA, Pacific Marine Environmental Laboratory, Seattle, Washington

Pabón, Daniel, Universidad Nacional de Colombia, Bogotá, Columbia

Palmer, Matthew, Met Office Hadley Centre, Exeter, Devon, United Kingdom

Parker, David E., Met Office Hadley Centre, Exeter, Devon, United Kingdom

Pasch, Richard, NOAA/NWS/NCEP National Hurricane Center, Miami, Florida

Pelto, Mauri S., Nichols College, Dudley, Massachusetts

Pérez-Suarez, Ramón, Institute of Meteorology of Cuba, La Habana, Cuba

Perovich, D.K., ERDC-Cold Regions Research and Engineering Laboratory, Hanover, New Hampshire

Peterson, Thomas C., NOAA/NESDIS National Climatic Data Center, Asheville, North Carolina

Pezza, Alexandre B., The University of Melbourne, Melbourne, Victoria, Australia

Phillips, David, Environment Canada, Toronto, Ontario, Canada

Polyakov, I., International Arctic Research Center, Fairbanks, Alaska

Proshutinsky, A., Woods Hole Oceanographic Institution, Woods Hole, Massachusetts

Quintana, Juan, National Weather Service, Santiago, Chile

Quintero, Alexander, Servicio de Meteorología de l'Aviación, Maracay, Aragua, Venezuela

Rahimzadeh, Fatemeh, Atmospheric Science and Meteorological Research Center, Tehran, Iran

Rajeevan, Madhavan, National Climate Centre, India Meteorological Department, Pune, India

Rayner, Darren, Ocean Observing and Climate Research Group, National Oceanography Centre, Southampton, United Kingdom

Raynolds, M. K., Institute of Arctic Biology, University of Alaska Fairbanks, Fairbanks, Alaska

Razuvaev, Vyacheslav N., All-Russian Research Institute of Hydrological Information, Obninsk, Russia

Reid, Phillip, Australian Bureau of Meteorology and ACE CRC, University of Tasmania, Hobart, Tasmania, Australia

Revadekar, Jayashree, Indian Institute of Tropical Meteorology, Pune, India

Reynolds, Richard W., NOAA/NESDIS National Climatic Data Center, Asheville, North Carolina

Richter-Menge, J., ERDC-Cold Regions Research and Engineering Laboratory, Hanover, New Hampshire

Rivera, Erick R., Center for Geophysical Research, University of Costa Rica, San José, Costa Rica

Robinson, David A., Rutgers University, Piscataway, New Jersey

Rogers, Mark, Joint Operational Meteorology and Oceanography Centre, Met Office, Exeter, Devon, United Kingdom

Romanovsky, V., Geophysical Institute, University of Alaska Fairbanks, Fairbanks, Alaska

Romero-Cruz, Fernando, National Meteorological Service of Mexico, Mexico City, Mexico

Ronchail, Josyane, Université of Paris, Paris, France

Rossi, S., National Weather Service, San Juan, Puerto Rico

Rossow, William B., NOAA Cooperative Remote Sensing Science and Technology Center, City College of New York, New York, New York

Rusticucci, Matilde, Universidad de Buenos Aires, Buenos Aries, Argentina

Sabine, Christopher L., NOAA/OAR Pacific Marine Environmental Laboratory, Seattle, Washington

Sakai, Yoshitoshi, Climate Prediction Division, Japan Meteorological Agency, Tokyo, Japan

Salinger, M. James, The University of Auckland, Auckland, New Zealand

Sayouri, Amal, Direction de la Météorologie Nationale, Rabat, Morocco

Scaife, Adam A., Met Office Hadley Centre, Exeter, Devon, United Kingdom

Scambos, Ted A., National Snow and Ice Data Center, University of Colorado, Boulder, Colorado

Schemm, Jae, NOAA/NWS/NCEP Climate Prediction Center, Camp Springs, Maryland

Schmid, Claudia, NOAA/OAR Atlantic Oceanographic and Meteorological Laboratory, Physical Oceanography Division, Miami, Florida

Schnell, Russ C., NOAA Global Monitoring Division, Earth System Research Laboratory, Boulder, Colorado

Sebbari, Rachid, Direction de la Météorologie Nationale, Rabat, Morocco

Seidel, Dian J., NOAA Air Resources Laboratory, Silver Spring, Maryland

Sensoy, Serhat, Turkish State Meteorological Service, Ankara, Turkey

Sharp, M., University of Alberta, Department of Earth and Atmospheric Sciences, Edmonton, Alberta, Canada

Shiklomanov, A., University of New Hampshire, Durham, New Hampshire

Shimada, K., Institute of Observational Research for Global Change, Japan Agency for Marine-Earth Science and Technology, Yokosuka, Japan

Shulski, Martha, Alaska Climate Research Center, Fairbanks, Alaska

Siegel, David A., University of California at Santa Barbara, Santa Barbara, California

Skansi, Maria, National Weather Service, Buenos Aires, Argentina

Sokolov, V., Arctic and Antarctic Research Institute, St. Petersburg, Russia

Spence, Jacqueline M., University of the West Indies, Mona, Jamaica

Stackhouse, Paul W., Jr., NASA Langley Research Center, Hampton, Virginia

Stammerjohn, Sharon, University of California, Santa Cruz, Santa Cruz, California

Steele, M., Polar Science Center, University of Washington, Seattle, Washington

Stephens, Scott E., NOAA/NESDIS/National Climatic Data Center, Asheville, North Carolina

Stephenson, Tannecia S., University of the West Indies, Mona, Jamaica

Stott, Peter A., Met Office Hadley Centre, Exeter, Devon, United Kingdom

Takahashi, Taro, Lamont–Doherty Earth Observatory, Columbia University, Palisades, New York

Taylor, Michael A., University of the West Indies, Mona, Jamaica

Tedesco, M., Department of Earth and Atmospheric Sciences, City College of New York, New York, New York

Thiaw, Wassila M., NOAA/NWS/NCEP Climate Prediction Center, Camp Springs, Maryland

Thorne, Peter W., Met Office Hadley Centre, Exeter, Devon, United Kingdom

Timmermans, M.-L., Woods Hole Oceanographic Institution, Woods Hole, Massachusetts

Toole, J., Woods Hole Oceanographic Institution, Woods Hole, Massachusetts

Trewin, Blair C., National Climate Centre, Australian Bureau of Meteorology, Melbourne, Victoria, Australia

Trigo, Ricardo M., Centro de Geofísica da Universidade de Lisboa, Lisbon, Portugal

Turner, John, British Antarctic Survey, Cambridge, United Kingdom

van de Wal, R., Institute for Marine and Atmospheric Research Utrecht, Utrecht University, Utrecht, The Netherlands

van den Broeke, M., Institute for Marine and Atmospheric Research Utrecht, Utrecht University, Utrecht, The Netherlands

Vincent, Lucie, Environment Canada, Toronto, Ontario, Canada

Walker, D. A., Institute of Arctic Biology, University of Alaska Fairbanks, Fairbanks, Alaska

Walsh, J., International Arctic Research Center, Fairbanks, Alaska

Walther, Alexander, Department of Earth Sciences, University of Gothenburg, Gothenburg, Sweden

Wang, Junhong, Earth Observation Laboratory, National Center for Atmospheric Research, Boulder, Colorado

Wang, L., Climate Research Division, Environment Canada, Downsview, Ontario, Canada

Wang, Lei, Department of Geography and Anthropology, Louisiana State University, Baton Rouge, Louisiana

Wang, M., JISAO, University of Washington, Seattle, Washington

Wang, Sheng-Hung, Byrd Polar Research Center, The Ohio State University, Columbus, Ohio

Wang, Xiaoling, National Climate Center, China Meteorological Administration, Beijing, China

Wanninkhof, Rik, NOAA/OAR Atlantic Oceanographic and Meteorological Laboratory, Ocean Chemistry Division, Miami, Florida

Ward, Bill, NOAA/NWS/Pacific Region Headquarters, Honolulu, Hawaii

Watkins, Andrew B., National Climate Centre, Australian Bureau of Meteorology, Melbourne, Victoria, Australia

Weber, Mark, University of Bremen, Bremen, Germany

Weingartner, T., Institute of Marine Science, University of Alaska Fairbanks, Fairbanks, Alaska

Weller, Robert A., Woods Hole Oceanographic Institution, Woods Hole, Massachusetts

Weyman, James, NOAA/NWS/Central Pacific Hurricane Center, Honolulu, Hawaii

Whitewood, Robert, Environment Canada, Toronto, Ontario, Canada

Wilber, Anne C., Science Systems Applications, Inc., Hampton, Virginia

Willis, Joshua K., NASA/Jet Propulsion Laboratory, Pasadena, California

Wolken, G., Department of Earth and Atmospheric Sciences, University of Alberta, Edmonton, Alberta, Canada

Wong, Takmeng, NASA Langley Research Center, Hampton, Virginia

Woodgate, R., Polar Science Center, University of Washington, Seattle, Washington

Woodworth, Philip L., Proudman Oceanographic Laboratory, Liverpool, United Kingdom

Xue, Yan, NOAA/NWS, Climate Prediction Center, National Centers for Environmental Prediction, Camp Springs, Maryland

Yu, Lisan, Woods Hole Oceanographic Institution, Woods Hole, Massachusetts

Zhakata, Washington, Ministry of Environment and Tourism, Harare, Zimbabwe

Zhang, Liangying, Earth Observation Laboratory, National Center for Atmospheric Research, Boulder, Colorado

Zhao, Sansan, National Climate Center, China Meteorological Administration, Beijing, China

TABLE OF CONTENTS

ABSTRACT—M. O. BARINGER AND T. C. PETERSON

The global mean temperature in 2008 was slightly cooler than that in 2007; however, it still ranks within the 10 warmest years on record. Annual mean temperatures were generally well above average in South America, northern and southern Africa, Iceland, Europe, Russia, South Asia, and Australia. In contrast, an exceptional cold outbreak occurred during January across Eurasia and over southern European Russia and southern western Siberia. There has been a general increase in land-surface temperatures and in permafrost temperatures during the last several decades throughout the Arctic region, including increases of 1° to 2°C in the last 30 to 35 years in Russia. Record setting warm summer (JJA) air temperatures were observed throughout Greenland.

The year 2008 was also characterized by heavy precipitation in a number of regions of northern South America, Africa, and South Asia. In contrast, a prolonged and intense drought occurred during most of 2008 in northern Argentina, Paraguay, Uruguay, and southern Brazil, causing severe impacts to agriculture and affecting many communities.

The year began with a strong La Niña episode that ended in June. Eastward surface current anomalies in the tropical Pacific Ocean in early 2008 played a major role in adjusting the basin from strong La Niña conditions to ENSO-neutral conditions by July–August, followed by a return to La Niña conditions late in December. The La Niña conditions resulted in far-reaching anomalies such as a cooling in the central tropical Pacific, Arctic Ocean, and the regions extending from the Gulf of Alaska to the west coast of North America; changes in the sea surface salinity and heat content anomalies in the tropics; and total column water vapor, cloud cover, tropospheric temperature, and precipitation patterns typical of a La Niña. Anomalously salty ocean surface salinity values in climatologically drier locations and anomalously fresh values in rainier locations observed in recent years generally persisted in 2008, suggesting an increase in the hydrological cycle.

The 2008 Atlantic hurricane season was the 14th busiest on record and the only season ever recorded with major hurricanes each month from July through November. Conversely, activity in the northwest Pacific was considerably below normal during 2008. While activity in the north Indian Ocean was only slightly above average, the season was punctuated by Cyclone Nargis, which killed over 145,000 people; in addition, it was the seventh-strongest cyclone ever in the basin and the most devastating to hit Asia since 1991.

Greenhouse gas concentrations continued to rise, with CO_2 increasing by more than expected based on the 1979 to 2007 trend. In the oceans, the global mean CO_2 uptake for 2007 is estimated to be 1.67 Pg-C, about 0.07 Pg-C lower than the long-term average, making it the third-largest anomaly determined with this method since 1983, with the largest uptake of carbon over the past decade coming from the eastern Indian Ocean. Global phytoplankton chlorophyll concentrations were slightly elevated in 2008 relative to 2007, but regional changes were substantial (ranging to about 50%) and followed long-term patterns of net decreases in chlorophyll with increasing sea surface temperature. Ozone-depleting gas concentrations continued to fall globally to about 4% below the peak levels of the 2000–02 period. Total column ozone concentrations remain well below pre-1980, levels and the 2008 ozone hole was unusually large (sixth worst on record) and persistent, with low ozone values extending into the late December period. In fact the polar vortex in 2008 persisted longer than for any previous year since 1979.

Northern Hemisphere snow cover extent for the year was well below average due in large part to the record-low ice extent in March and despite the record-maximum coverage in January and the shortest snow cover duration on record (which started in 1966) in the North American Arctic. Limited preliminary data imply that in 2008 glaciers continued to lose mass, and full data for 2007 show it was the 17th consecutive year of loss. The northern region of Greenland and adjacent areas of Arctic Canada experienced a particularly intense melt season, even though there was an abnormally cold winter across Greenland's southern half. One of the most dramatic signals of the general warming trend was the continued significant reduction in the extent of the summer sea-ice cover and, importantly, the decrease in the amount of relatively older, thicker ice. The extent of the 2008 summer sea-ice cover was the second-lowest value of the satellite record (which started in 1979) and 36% below the 1979–2000 average. Significant losses in the mass of ice sheets and the area of ice shelves continued, with several fjords on the northern coast of Ellesmere Island being ice free for the first time in 3,000–5,500 years.

In Antarctica, the positive phase of the SAM led to record-high total sea ice extent for much of early 2008 through enhanced equatorward Ekman transport. With colder continental temperatures at this time, the 2007–08 austral summer snowmelt season was dramatically weakened, making it the second shortest melt season since 1978 (when the record began). There was strong warming and increased precipitation along the Antarctic Peninsula and west Antarctica in 2008, and also pockets of warming along coastal east Antarctica, in concert with continued declines in sea-ice concentration in the Amundsen/Bellingshausen Seas. One significant event indicative of this warming was the disintegration and retreat of the Wilkins Ice Shelf in the southwest peninsula area of Antarctica.

I. INTRODUCTION—T. C. Peterson and M. O. Baringer

The primary goal of the annual *State of the Climate* collection of articles is to document the year's current weather and climate events from around the world, such as those shown in Fig. 1.1, and put them into accurate historical perspective, with a particular focus on unusual or anomalous events from the past year. This year the *State of the Climate* brings together more than 280 authors from every continent and from numerous different research groups to collaborate, to share data and insights, and to describe the observed changes in climate from different perspectives. Indeed, this year's report has gained an even wider international perspective with the addition of chapter editors from the Met Office, Environment Canada, and Australia's National Climate Centre, as well as an expanding list of international authors. One of the lessons learned from addressing apparent inconsistencies in observations is that one dataset is great but multiple datasets are better because they confirm results and/or help provide estimates of uncertainty (Karl et al. 2001). With this in mind, the authors and editors seek to provide an inclusive synthesis of diverse sources of weather and climate data to describe what took place across our planet last year.

As a guiding principle behind the inclusion of certain climatic variabiles into this report, the Global Climate Observing System has identified Essential Climate Variables (GCOS 2003) (see the appendix for a full list of abbreviations) that are necessary to support the United Nations Framework Convention on Climate Change and the Intergovernmental Panel on Climate Change. These variables are defined as those required for international exchange and should be economically and technically feasible to acquire (Table 1). Some other variables important for research purposes are not included as ECVs; however, the GCOS list of ECVs as well as the other variables presented in this report are continually being reassessed as improved observing technologies emerge. The *State of the Climate* report has strived to include an increasing number of these climatically important variables as the data availability increases and the analysis techniques and attributions improve.

The degree to which each of these ECVs can be assessed and reported depends largely on the level of data availability both currently and within the homogeneous historical record; hence the variables can be divided into categories: being monitored, partially monitored, and not yet monitored. To be listed as monitored, the ECV not only has to be observed across much of the world but there also needs to be a moderately long-term dataset with accompanying analysis. For example, some ECVs, such as water vapor, have been observed across the world for over a century. But in that time, the observing instrumentation has changed, imparting artificial biases to the data. Therefore, to be effectively monitored requires not only observations but also adjustments to the historical data to remove or at least greatly diminish artificial biases. Also, the dataset needs to be updated in near-real time and be included in a peer-reviewed article documenting the reliability of all of these steps. It can be hard work, but progress is being made on many fronts. For example, surface water vapor is expected to be fully included in the report next year. In total, 34 GCOS Essential Climate Variables are reported in the 19th annual *State of the Climate* report.

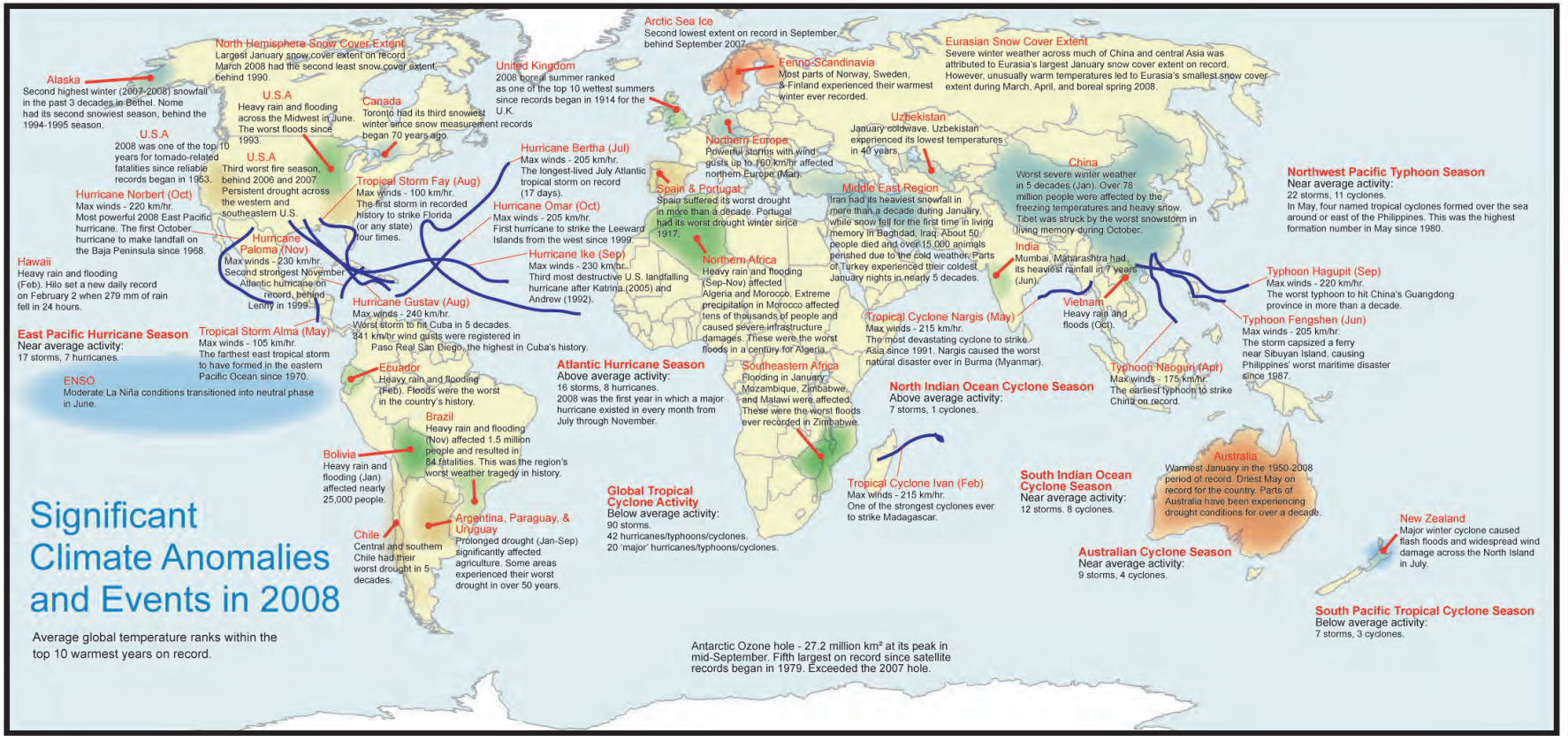

Fig. 1.1. Geographical distribution of notable climate anomalies and events occurring around the planet in 2008.

Table 1.1. The GCOS ECVs and soil moisture (an emerging ECV) and their monitoring status. Like traffic stop lights, green indicates yes, that this ECV is being monitored on a global or near-global scale and that this report includes a section that describes the ECV's changes over time. Amber indicates that the ECV is explicitly discussed in this year's *State of the Climate*, but the data are not updated through 2008 or the coverage is not global. Red indicates more work needs to be done to monitor and document this ECV.

Atmospheric	Ocean	Terrestrial
Surface	**Surface**	Soil moisture (Emerging ECV)
Air temperature	Sea surface temperature	Snow cover
Precipitation	Sea surface salinity	Permafrost and seasonally-frozen ground
Air pressure	Sea level	Glaciers and ice caps
Surface radiation budget	Sea state	River discharge
Wind speed and direction	Sea ice	Water use
Water vapor	Current	Ground water
Upper Air	Ocean color	Lake levels
Earth radiation budget	Carbon dioxide partial pressure	Albedo
Upper-air temperature	**Subsurface**	Land cover
Wind speed and direction	Temperature	Fraction of absorbed photosynthetically active radiation
Water vapor	Salinity	Leaf area index
Cloud properties	Current	Biomass
Composition	Nutrients	Fire disturbance
Carbon dioxide	Carbon	
Methane	Ocean tracers	
Ozone	Phytoplankton	
Nitrous oxide		
Chlorofluorocarbons		
Hydrochlorofluorocarbons		
Hydrofluorocarbons		
Sulphur hexaflurorides		
Perfluorocarbons		
Aerosol properties.		

2. GLOBAL CLIMATE—P. W. Thorne, Ed.

a. *Summary*—P. W. Thorne

2008 was cool, but only in the context of the last few very warm years. It still ranks within the 10 warmest years on record. The primary cause was a moderate to strong La Niña event. 1999, the last year with a similarly large La Niña, was 0.1°C colder. Surface cooling straddled 2007/08. Because the tropospheric response lags the surface, 2008 ranked outside the top 10 warmest tropospheric years regardless of choice of dataset. This difference in rankings does not reflect, as has been variously posited, a fundamental issue for surface record homogeneity.

This year's global chapter incorporates many more climate variables than previous vintages. Where possible, anomalies for those variables in Plate 2.1 and in the individual section diagrams have been plotted in a consistent format to aid comparisons. We have also used more independently derived datasets. The spread provides guidance on how well we can characterize the climate system's evolution. There are substantial questions about how well we understand, particularly, the long-term trends in many variables. However, it is clear that over the 30-yr period of truly global monitoring from satellites, the world has overall become warmer, moister, and probably stormier.

Plate 2.1 shows that the dominant factor for almost all climate variables in 2008 was the La Niña event. total column water vapor, cloud cover, and precipitation provide a consistent picture of areas of drying and moistening typical of a La Niña. The sea level pressure signature of La Niña is also readily apparent, as are the surface and tropospheric temperature signals. Northern Hemispheric snow cover extent for the year was well below average despite record maximum coverage in January. Top-of-atmosphere radiation data imply that 2008 saw a net receipt of radiation into the climate system, but further work on these data is required so this should be treated as provisional. Greenhouse gas concentrations continued to rise, with CO_2 increasing by more than expected based on the 1979 to 2007 trend. Ozone-depleting gas concentrations continued to fall. Total-column ozone concentrations remained well below pre-1980 levels, and the Antarctic ozone hole was particularly large and long-lived. Limited preliminary data imply that in 2008 glaciers continued to lose mass, and full data for 2007 show it was the 17th consecutive year of loss. New land-use and vegetation-state products highlight how we are both directly and indirectly systematically altering the land-surface characteristics. Datasets used in this chapter that are publicly available are referenced in Table 2.5 at the chapter's end.

b. *Temperatures*

1) Global surface temperatures in 2008—M. J. Menne and J. J. Kennedy

2008 was the coolest year since 2000, but still within the 10 warmest on record according to all three datasets [GISS, Hansen et al. 2001; HadCRUT3, Brohan et al. 2006; NCDC, Smith and Reynolds 2005]. Each analysis is based on air temperature data over land and sea-surface temperatures observed from ships and buoys (and satellites in the case of NCDC and GISS) with adjustments to account for changes in observing system bias. Differences in techniques

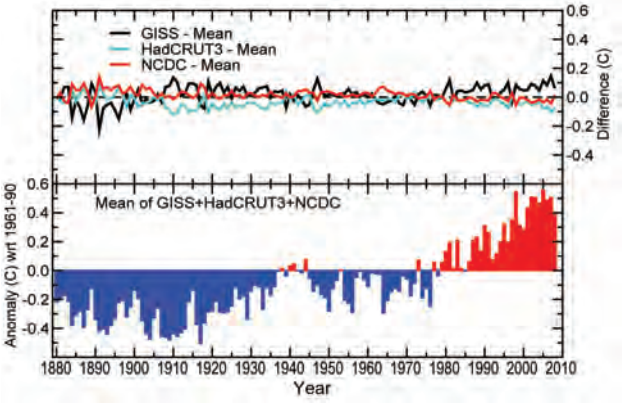

Fig. 2.1. Global surface temperature anomalies with respect to the 1961 to 1990 average. (bottom) Mean of GISS, HadCRUT3 and NCDC; upper panel: difference between GISS, HadCRUT3, NCDC and the mean.

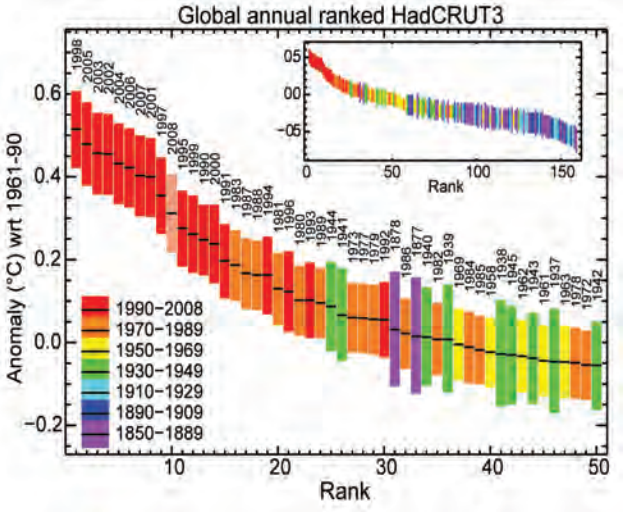

Fig. 2.2. Year-by-year temperature rankings and 95% confidence limits for the HadCRUT3 temperature analysis. The main panel shows the 50 warmest years and the inset shows the full 159-yr record.

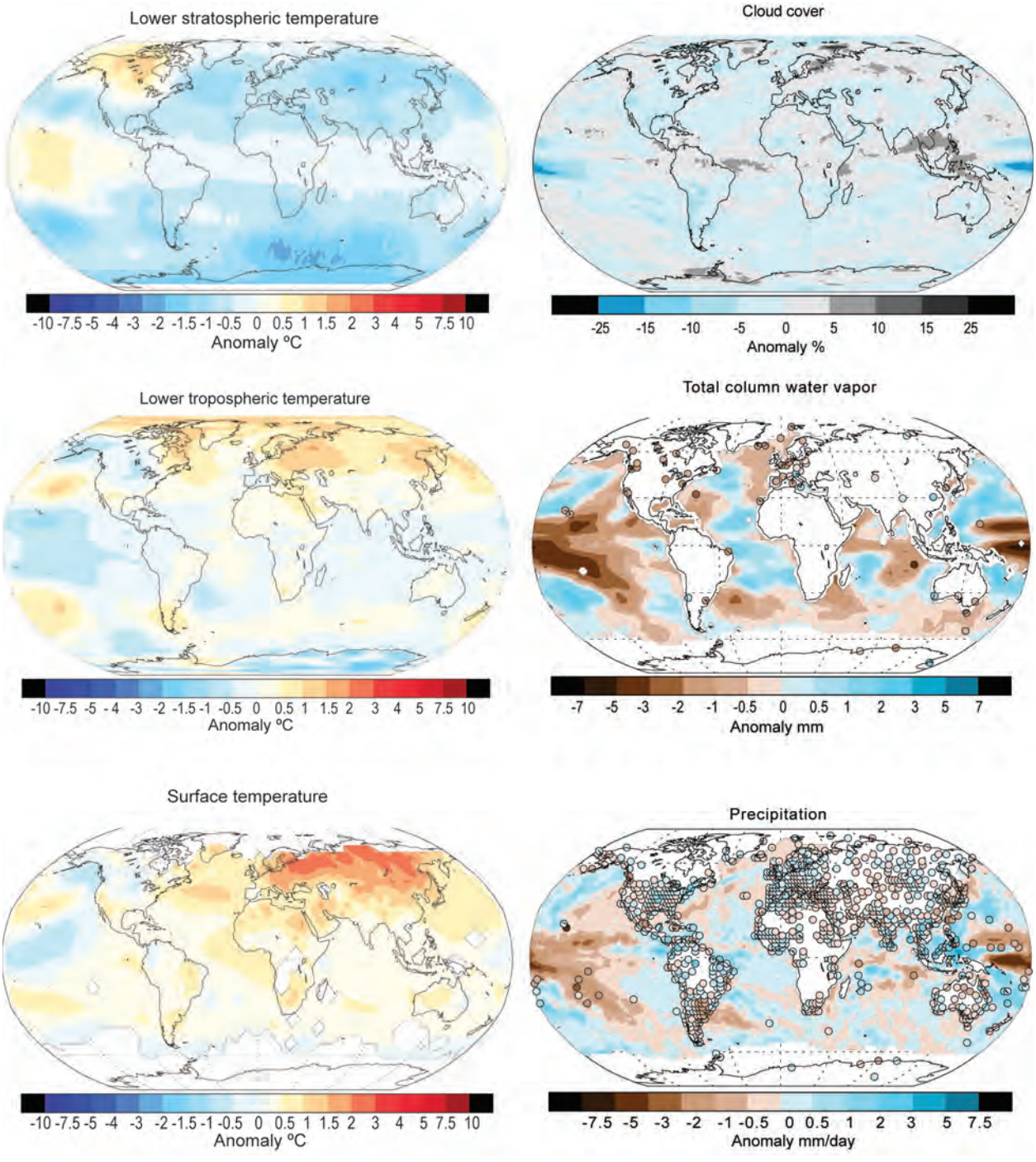

lead to differences in detail especially in regions with sparse data and in the specifics of yearly rankings. However, they are in strong agreement regarding the low-frequency variations in the surface temperature signal (Fig. 2.1, top). Differences rarely exceed 0.1°C and are much smaller than the increase in global mean temperature since the 1970s. Moreover, the uncertainties imply that 2008 is effectively indistinguishable from several of the other high-ranking years (Fig. 2.2). Notably, the 20 warmest years have all occurred since 1981, and the 10 warmest have all occurred in the past 12 years.

2008 was cooler than recent years in part because of the moderate to strong La Niña that developed in the latter half of 2007. La Niña peaked in early 2008 as indicated by the negative anomalies at equatorial latitudes (Fig. 2.3). Evidence of the impact of the ENSO cycle on tropical temperatures can be seen

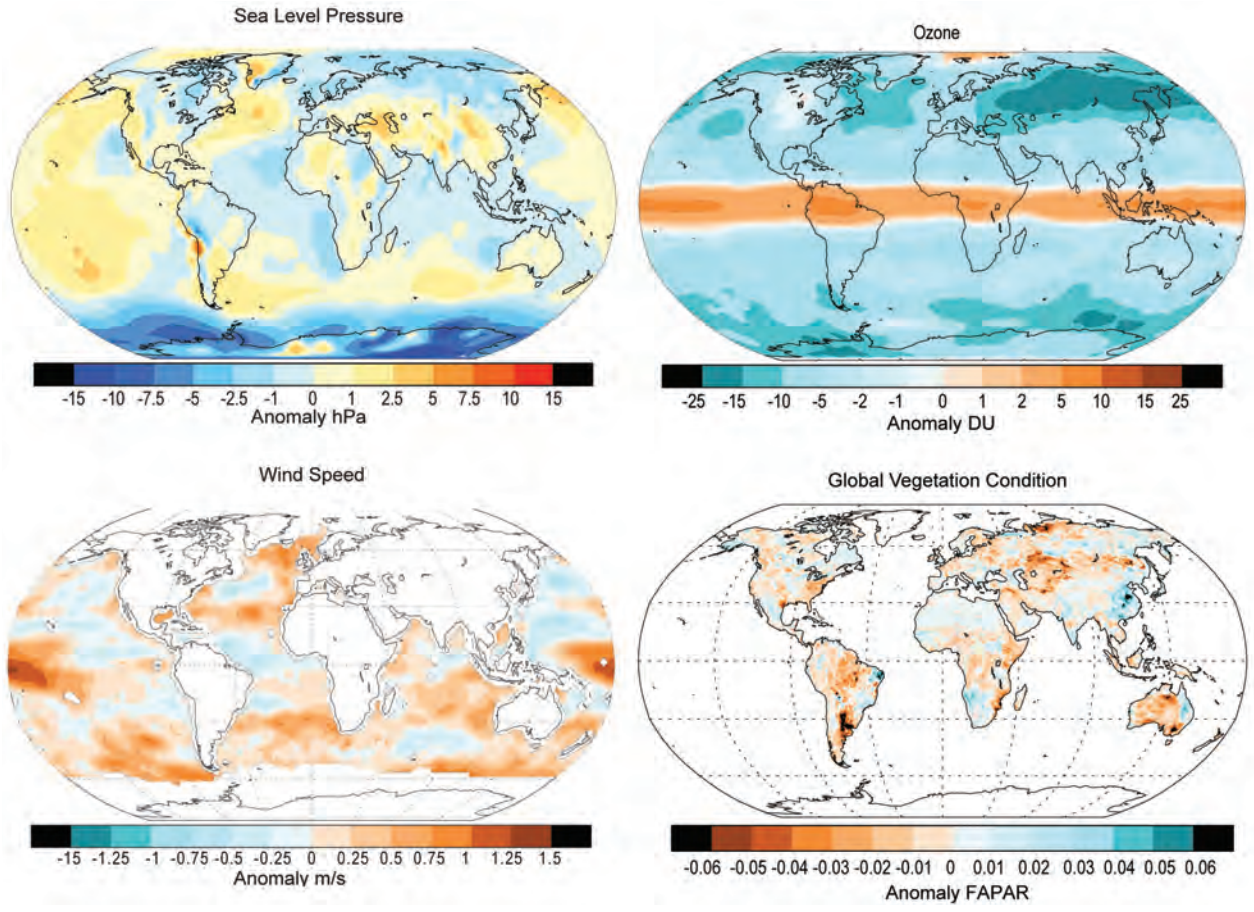

Plate 2.1. Global annual anomaly maps for those variables for which it was possible to create a meaningful anomaly estimate. Climatologies differ among variables, but spatial patterns should largely dominate over choices of climatology period. Dataset sources and climatologies are given in the form (dataset name/data source, start year–end year) for each variable. See relevant section text and figures for more details. Lower stratospheric temperature (RSS MSU 1981–90); lower tropospheric temperature (UAH MSU 1981–90); surface temperature (NCDC 1961–90); cloud cover (PATMOS-x 1982–2008); total column water vapor (SSM/I/GPS 1997–2008); precipitation (RSS/GHCN 1989–2008); mean sea level pressure (HadSLP2r 1961–90); wind speed (SSM/I 1988–2007); total column ozone (annual mean global total ozone anomaly for 2008 from SCIAMACHY. The annual mean anomalies were calculated from 1° × 1.25° gridded monthly data after removing the seasonal mean calculated from GOME (1996–2003) and SCIAMACHY (2003–07)]; vegetation condition [annual FAPAR anomalies relative to Jan 1998 to Dec 2008 from monthly FAPAR products at 0.5° × 0.5° [derived from SeaWiFS (NASA) and MERIS (ESA) data].

throughout the record. Figure 2.3 also illustrates the increase in temperatures at high latitudes of the Northern Hemisphere in recent decades. As shown in Plate 2.1, panel 3, this trend continued into 2008 when above-average temperatures were recorded across all of northern Eurasia and much of the Arctic.

2) Lower tropospheric temperatures—J. Christy, D. Seidel, C. Mears, and L. Haimberger

The 2008 global average temperature of the lower tropospheric layer (TLT, surface to ~8km) was cooler than in recent years due to the La Niña. When the surface cools, the troposphere responds with similar temperature changes, which for the global average lag the surface fluctuations by 2 to 4 months (Christy and McNider 1994). The surface was coolest in January 2008, and consequently the troposphere was coolest in May (~0.4°K below the 2007 average). Overall, 2008 was cooler than 2007 by about 0.25°K. The 51-yr time series of globally averaged TLT (Fig. 2.4) indicate this recent dip. 2008 was the 15th warmest of the mean of the datasets (individual rankings by dataset: 12th to 18th).

Datasets in Fig. 2.4 were constructed by different teams using either balloon-based radiosondes or satellite-based microwave sensors. Continuing

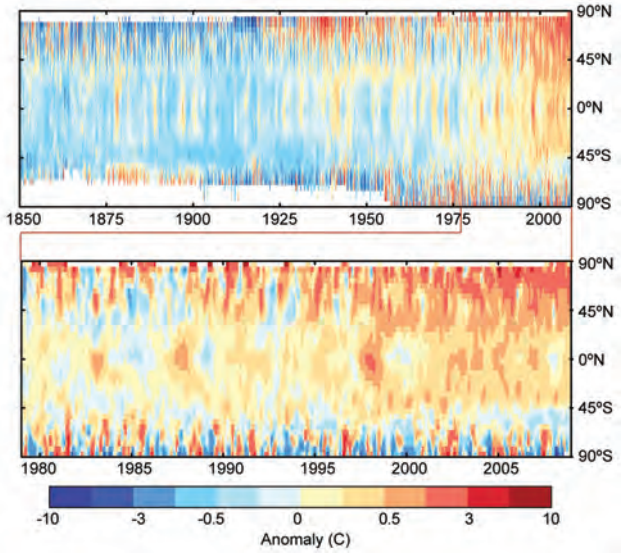

Fig. 2.3. HadCRUT3 monthly average temperature anomalies by latitude for the period 1850 to 2008. The data have been smoothed in space and time using a 1:2:1 filter. White areas indicate missing data.

research has developed procedures to account for inhomogeneities in these systems to provide the most confident estimates of the temperature evolution. Reanalyses have the potential to provide a physically consistent synthesis of all data sources, but inhomogeneities in their data inputs and the intrusion of model biases give reason to discount current reanalysis-based trends (e.g., Karl et al. 2006, Sakamoto and Christy 2009).

The La Niña signal of the cool tropics is clear in the first half of 2008 (Fig. 2.5). Similar but longer-lived cool tropical events occurred around 1985, 1989, and 2000. The cooling in 1992 is related to the volcanic eruption of Mt. Pinatubo. During the last decade or so there has been a general shift to warmer temperatures in the northern latitudes and tropics.

The estimated trend for both the entire time series beginning in 1958 (radiosonde era) and since 1979 (satellite era) is +0.145 ±0.02°C decade^{-1} with the range of the trends calculated from the various datasets. There is no indication of acceleration of the trend, though the relatively large excursions from the trend line make possible other interpretations than a simple trend. Decadal variations and shifts tend to limit the meaning of linear trend estimates (Seidel and Lanzante 2004).

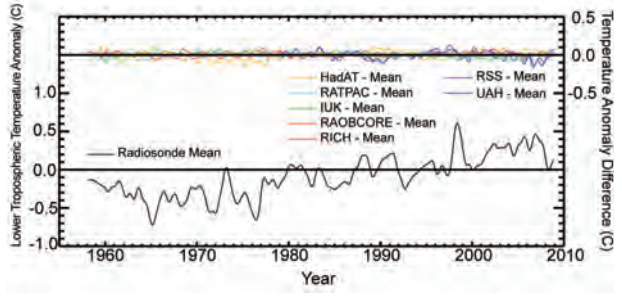

Fig. 2.4. Global mean lower tropospheric temperature (1958–2008) from multiple datasets, including five radiosonde datasets (HadAT, IUK, RAOBCORE, RATPAC, and RICH) and two satellite MSU datasets (RSS, UAH). All time series are for the layer sampled by MSU retrieval 2LT, spanning 0–8 km in altitude. Black curve is the average of all available radiosonde datasets, and the colored curves show differences between individual datasets and this average. References for the radiosonde datasets are Thorne et al. 2005b, Sherwood et al. 2008, Haimberger 2007, Free et al. 2005, and Haimberger et al. 2008; and for the MSU datasets are Mears and Wentz 2009a and Christy et al. 2003.

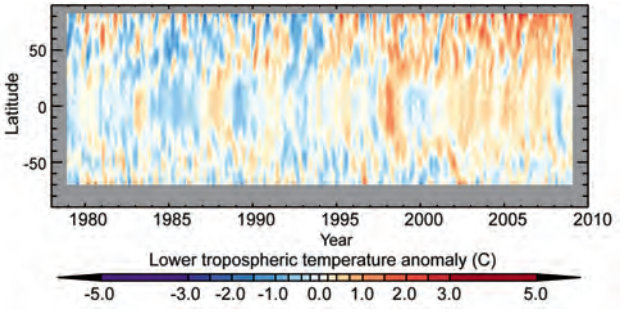

Fig. 2.5. Zonal mean lower tropospheric temperature anomalies (1979–2008) with respect to the 1979–88 mean. Anomalies based on MSU Channel 2LT data, as processed by RSS (Mears and Wentz 2009a).

The atmosphere responded to the equatorial Pacific influence in 2008 in a common "teleconnection" pattern (Plate 2.1, panel 2) with cold equatorial Pacific anomalies, warm regions in the north and south Pacific, and cold regions farther east of these, including into North America (Wallace et al. 2005). Other regions of warm anomalies in 2008 include Arctic Canada and most of Russia. Aside from the broad, cool anomalies in the tropics, the Southern Hemisphere was mostly below average.

3) Stratospheric temperatures—D. Seidel, J. Christy, and C. Mears

The 2008 annual average temperature of the lower stratosphere was similar to that of the last dozen years (Fig. 2.6). Globally, the lower stratosphere has been about 1.5°C cooler over the past decade than

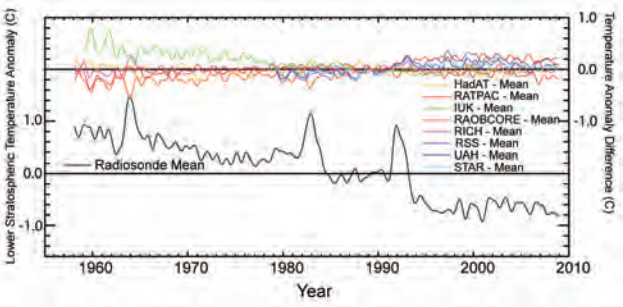

Fig. 2.6. As Fig. 2.4. but all time series are for the layer sampled by MSU channel 4, spanning 10–25 km in altitude, with a peak near 18 km. Additional dataset is STAR (Zou et al. 2008) and RSS Channel 4 is described in Mears and Wentz (2009b).

in the 1960s when the radiosonde network began to offer reasonably global monitoring. The cooling occurred in steps (Ramaswamy et al. 2006; Seidel and Lanzante 2004). Major volcanic eruptions (Agung 1963; El Chichon 1982; Pinatubo 1991) warmed the lower stratosphere for about two years (Free and Lanzante 2009), followed by cooler mean states than before (Fig. 2.6). Volcanic warming events are most notable in the tropics (Fig. 2.7). Other influences on stratospheric temperature changes include greenhouse gas and stratospheric ozone changes and solar variations.

This general evolution of global lower stratospheric temperature is robustly captured in all available radiosonde (1958–present) and satellite (1979–present) datasets (Fig. 2.6). However, the datasets differ in detail. Of those that cover 1979–2008, 2008 ranks as the coldest year in three, the second coldest in one, and the eighth coldest in another. Trends estimated from the average of the radiosonde datasets are −0.35 ± 0.07 °C decade^{-1} for 1958–2008, and −0.50 ± 0.16°C decade^{-1} for 1979–2008; however, there are statistically significant differences

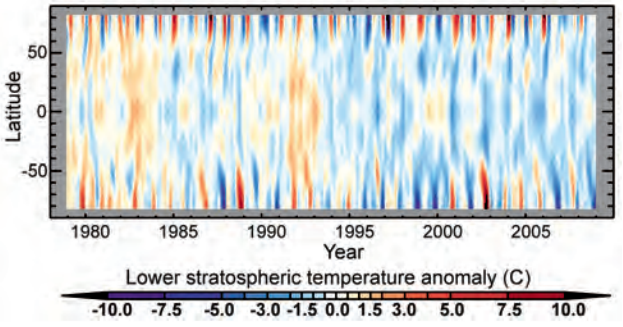

Fig. 2.7. As Fig. 2.5 but for the lower stratospheric channel (Mears and Wentz 2009b).

(of about 0.1°C decade^{-1}) between datasets, with all satellite-based datasets showing less cooling (–0.33° to 0.42°C decade^{-1}) since 1979 than the radiosondes, and even greater disagreement among the radiosonde datasets before that. This uncertainty in the magnitude, and therefore cause, of the long-term trend (Thorne et al. 2005a) is due to the lack of reference quality observations. However, 2008 saw the implementation of a new GCOS Reference Upper-Air Network to provide much higher-quality data, in both the troposphere and stratosphere (Seidel et al. 2009).

The tropical stratospheric QBO in wind direction (Baldwin et al. 2001) imposes a signature on tropical temperatures (Fig. 2.7), also apparent in the global average (Fig. 2.6). The QBO shifted from easterly to westerly in the lower stratosphere during 2008, bringing a change from cold to warm tropical anomalies. Sudden stratospheric warming events in northern high latitudes in January and February brought temperature increases of 10° to 30°K at the 10-hPa level (NOAA CPC 2009a). Their impact is seen in the annual anomaly map for the lower stratosphere (Plate 2.1, panel 1) as warm anomalies over the Canadian Arctic. Over Antarctica, the wintertime stratospheric vortex was the longest-lived since 1979, contributing to 2008 being one of the coldest winters on record in the Antarctic stratosphere and to a long-lived Antarctic ozone hole (NOAA CPC 2009b).

The preceding analysis focused on the lower stratosphere. The state of the global stratosphere at higher levels is more difficult to describe because few long-term datasets are available. The recent comprehensive analysis by the Stratospheric Processes and their Role in Climate program (Randel et al. 2009) included revised and updated data for the middle and upper stratosphere from the satellite-borne SSU for 1979–2005 (Shine et al. 2008). SSU data require homogeneity adjustments for instrument change and drift and for changing atmospheric composition, but they have not yet benefitted from analysis by multiple groups, which tends to facilitate the identification and correction of errors. The revised SSU data indicate long-term cooling of ~0.5° to 1.5°K decade^{-1} of the middle and upper stratosphere (about twice as large as lower stratospheric trends), but relatively constant temperatures during 1995–2005 like both MSU and radiosonde data for the lower stratosphere. However, the SSU channel that samples the lower stratosphere indicates a gradual temperature increase during that period, so there remain unreconciled differences with other datasets and uncertainty in middle and upper stratospheric temperature changes.

DO GLOBAL TEMPERATURE TRENDS OVER THE LAST DECADE FALSIFY CLIMATE PREDICTIONS?—J. KNIGHT, J. J. KENNEDY, C. FOLLAND, G. HARRIS, G. S. JONES, M. PALMER, D. PARKER, A. SCAIFE, AND P. STOTT

Observations indicate that global temperature rise has slowed in the last decade (Fig. 2.8a). The least squares trend for January 1999 to December 2008 calculated from the HadCRUT3 dataset (Brohan et al. 2006) is +0.07±0.07°C decade^{-1}—much less than the 0.18°C decade^{-1} recorded between 1979 and

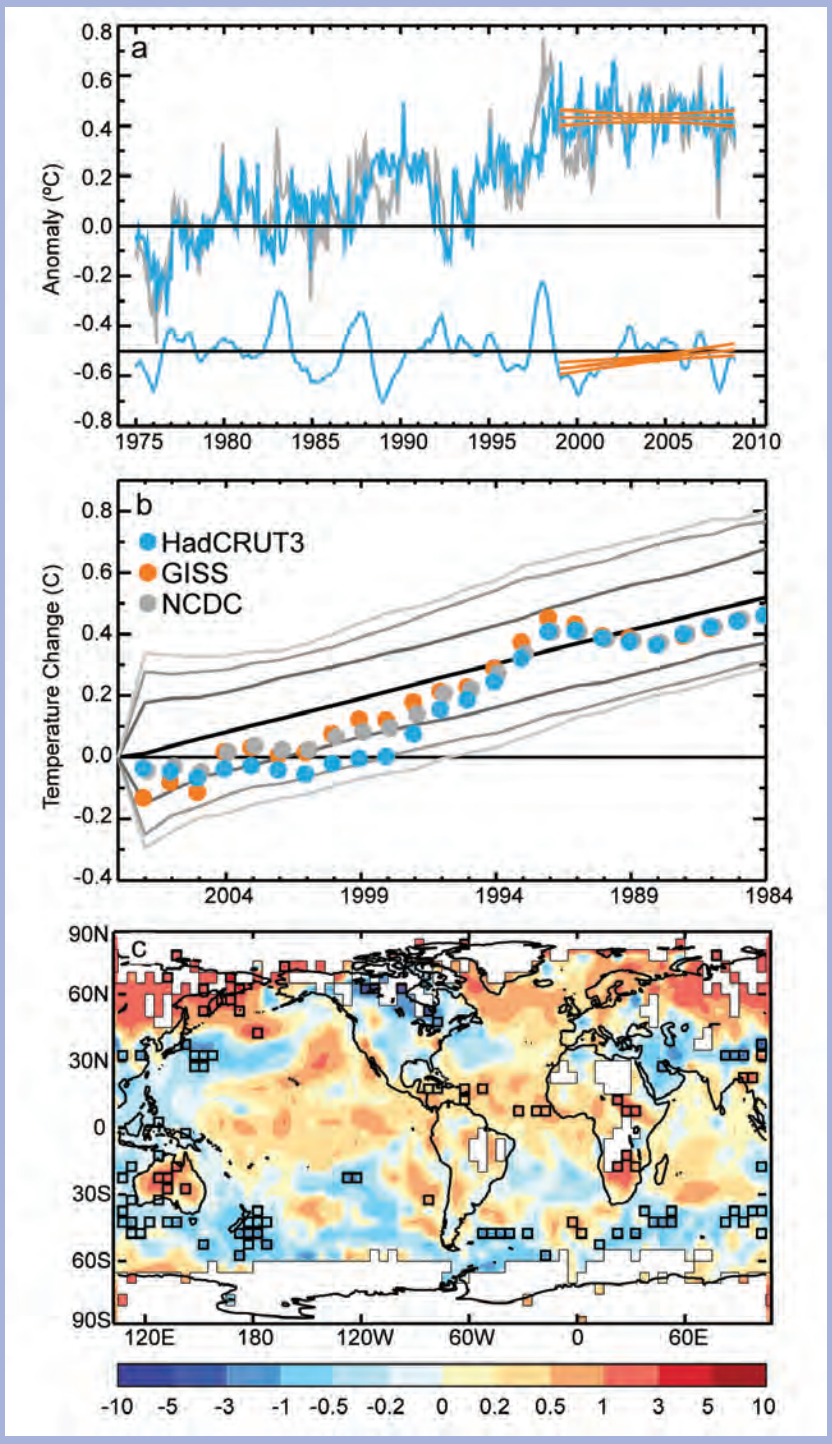

FIG. 2.8. Global mean temperature changes over the last decade in context. (a) Monthly global mean temperature anomalies (with respect to 1961–90 climatology) since 1975, derived from the combined land and ocean temperature dataset HadCRUT3 (gray curve). (top blue curve) The global mean after the effect of ENSO that has been subtracted is also shown, along with (bottom blue curve, offset by 0.5°C) the ENSO contribution itself. Least squares linear trends in the ENSO and ENSO-removed components for 1999–2008 and their two std dev uncertainties are shown in orange. (b) ENSO-adjusted global mean temperature changes to 2008 as a function of starting year for HadCRUT3, GISS dataset (Hansen et al. 2001) and the NCDC dataset (Smith et al. 2008) (dots). Mean changes over all similar-length periods in the twenty-first century climate model simulations are shown in black, bracketed by the 70%, 90%, and 95% intervals of the range of trends (gray curves). (c) Distribution of 1999–2008 trends in HadCRUT3 (°C decade^{-1}). Black squares indicate where the trends are inconsistent at the two std dev level with trends in 17 simulated decades (see text).

2005 and the 0.2°C decade^{-1} expected in the next decade (IPCC; Solomon et al. 2007). This is despite a steady increase in radiative forcing as a result of human activities and has led some to question climate predictions of substantial twenty-first century warming (Lawson 2008; Carter 2008).

El Niño–Southern Oscillation is a strong driver of interannual global mean temperature variations. ENSO and non-ENSO contributions can be separated by the method of Thompson et al. (2008) (Fig. 2.8a). The trend in the ENSO-related component for 1999–2008 is +0.08±0.07°C decade^{-1}, fully accounting for the overall observed trend. The trend after removing ENSO (the "ENSO-adjusted" trend) is 0.00°±0.05°C decade^{-1}, implying much greater disagreement with anticipated global temperature rise.

We can place this apparent lack of warming in the context of natural climate fluctuations other than ENSO using twenty-first century simulations with the HadCM3 climate model (Gordon et al. 2000), which is typical of those used in the recent IPCC report (AR4; Solomon et al. 2007). Ensembles with different modifications to the physical parameters of the model (within known uncertainties) (Collins et al. 2006) are performed for several of the IPCC SRES emissions scenarios (Solomon et al. 2007). Ten of these simulations have a steady long-term rate of warming between 0.15° and 0.25°C decade^{-1}, close to the expected rate of 0.2°C decade^{-1}. ENSO-adjusted warming in the three surface temperature datasets over the last 2–25 yr continually lies within the 90% range of all similar-length ENSO-adjusted temperature changes in these simulations (Fig. 2.8b). Near-zero and even negative trends are common for intervals of a decade or less in the simulations, due to the model's internal climate variability. The simulations rule out (at the 95% level) zero trends for intervals of 15 yr or more, suggesting that an observed absence of warming of this duration is needed to create a discrepancy with the expected present-day warming rate.

The 10 model simulations (a total of 700 years of simulation) possess 17 nonoverlapping decades with trends in ENSO-adjusted global mean temperature within the uncertainty range of the observed 1999–2008 trend (−0.05° to 0.05°C decade^{-1}). Over most of the globe, local surface temperature trends for 1999–2008 are statistically consistent with those in the 17 simulated decades (Fig. 2.8c). Field significance (Livezey and Chen 1983) is assessed by comparing the total area of inconsistent grid boxes with the range of similar area values derived by testing the consistency of trends in each simulated decade with those in the remaining simulated decades. The 5.5% of the data area that is inconsistent in the observed case is close to the median of this range of area values, indicating the differences are not field significant. Inconsistent trends in the midlatitude Southern Hemisphere strongly resemble the surface temperature pattern of the negative phase of the SAM (Ciasto and Thompson 2008), which did indeed show a negative trend in the last decade.

These results show that climate models possess internal mechanisms of variability capable of reproducing the current slowdown in global temperature rise. Other factors, such as data biases and the effect of the solar cycle (Haigh 2003), may also have contributed, although these results show that it is not essential to invoke these explanations. The simulations also produce an average increase of 2.0°C in twenty-first century global temperature, demonstrating that recent observational trends are not sufficient to discount predictions of substantial climate change and its significant and widespread impacts. Given the likelihood that internal variability contributed to the slowing of global temperature rise in the last decade, we expect that warming will resume in the next few years, consistent with predictions from near-term climate forecasts (Smith et al. 2007; Haines et al. 2009). Improvements in such forecasts will give greater forewarning of future instances of temporary slowing and acceleration of global temperature rise, as predicted to occur in IPCC AR4 projections (Easterling and Wehner 2009).

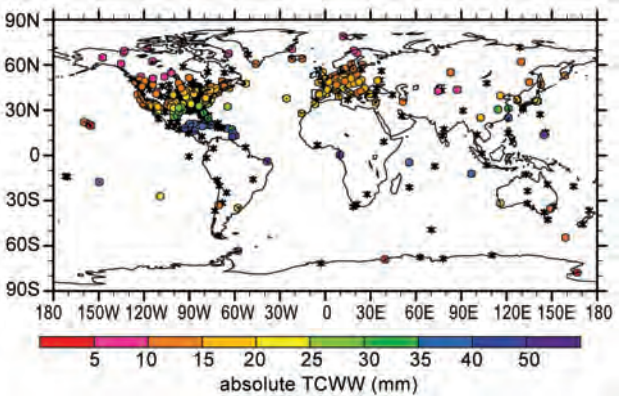

Fig. 2.9. 2008 annual mean TCWV (mm) at 252 stations (colored circles) and 308 stations (denoted by an asterisk) that have data in 2008, but not enough to calculate an annual mean.

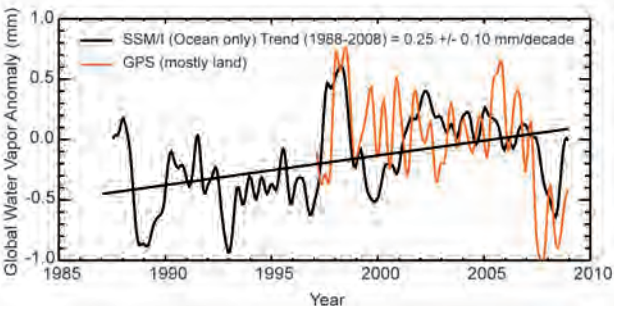

Fig. 2.10. Anomaly time series of TCWV both from SSM/I and from an average of GPS stations. The time series have been smoothed to remove variability on time scales shorter than 6 months. A linear fit to the SSM/I data is also shown, indicating an increasing trend in water vapor over the 1988–2008 period.

c. Hydrological cycle

1) Total column water vapor—C. Mears, J. Wang, and L. Zhang

Total column water vapor over the world's oceans has been monitored continuously since the launch of the first SSM/I satellite in late 1987 (Wentz 1997). These data have been independently evaluated and found to be accurate enough for climate studies (Trenberth et al. 2005). Beginning in the late 1990s, ground-based GPS measurements have provided a second accurate estimate of TCWV over land (Wang et al. 2007); they are an important complement to the ocean-only SSM/I measurements.

Plate 2.1, panel 5 includes data from SSM/I and from a subset of 71 GPS stations with continuous data from 1997 to 2008, allowing meaningful anomaly estimates. The network is expanding rapidly. In 2008 a total of 560 GPS stations had data, and annual means could be calculated at 252 stations (Fig. 2.9). There is generally agreement within 0.5 mm between the SSM/I and GPS measurements where they overlap. The most striking feature is the large dry anomaly centered on the central tropical Pacific, associated with La Niña. The dry region extends poleward and eastward from this source, resulting in dry anomalies over much of the continental United States.

The global ocean average SSM/I TCWV shows dramatic maxima in 1988–89 and 1997–98 associated with ENSO events (Fig. 2.10). Minima associated with La Niña events occur in 1988–89, 1993, 1999, and 2008. The GPS data averaged over the 71 stations in Plate 2.1 show similar features despite the substantially different geographical sampling. The SSM/I data show a 0.25 mm decade^{-1} trend in TCWV. In the tropics this is consistent with increases in lower tropospheric temperature (Mears et al. 2007) and has been formally attributed to anthropogenic change over the 1988–2006 period (Santer et al. 2007). Variability in zonally averaged TCWV is dominated by variability in the tropics caused by ENSO events (Fig. 2.11). The tropics dominate because of the larger changes in TCWV per degree change in temperature at higher temperatures as described by the Clausius–Clapeyron relationship.

2) Global precipitation—D. H. Levinson, K. A. Hilburn, and M. C. Kruk

Land-based data are primarily analyzed from monthly totals of in situ gauge measurements using the GHCN dataset (Peterson and Vose 1997), which for most regions extends back to the beginning of the twentieth century. Several alternative land-based datasets are also considered. Over ocean basins, three satellite datasets are considered:

- Remote Sensing Systems intercalibrated passive microwave rain retrievals (Hilburn and Wentz

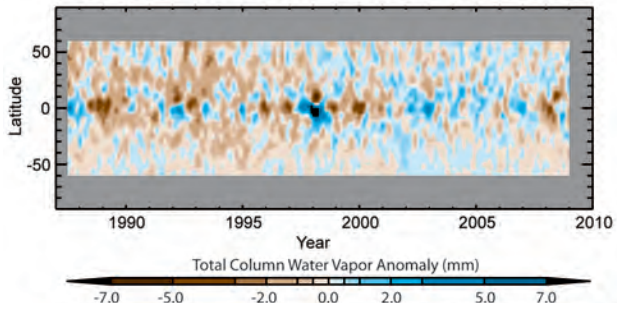

Fig. 2.11. Time–latitude plot of TCWV anomaly calculated using a reference period of 1988–2007. The data have been smoothed in the time direction to remove variability on time scales shorter than 4 months.

2008) that closely match gauges on tropical buoys (Bowman et al. 2009) and are not sensitive to snow, which may account for an apparent low global bias (Wentz et al. 2007)
- The Global Precipitation Climatology Project Version 2, Combined Precipitation Data Set (Adler et al. 2003), a combination of data from microwave and infrared satellite sensors and rain gauges
- NOAA CMAP (Xie and Arkin 1997), combining data from microwave and infrared satellite sensors, rain gauges, and numerical model predictions.

Despite obvious differences among datasets, global land precipitation has clearly varied on interdecadal time scales, and the above-average anomaly in 2008 is part of a longer-term wet period that began in the late 1990s (Fig. 2.12). The 2008 anomaly was dominated by an extremely wet Southern Hemisphere summer (DJF). There is substantial disagreement among the ocean precipitation time series, especially in the first half of the period (Fig. 2.12c). Despite this, RSS and GPCP have similar overall linear trends, both of which are significant at the 95% confidence level. The trend for CMAP is negative but not significant. Significance is estimated from deviations from the linear fit, accounting for autocorrelation (Santer et al. 2000). For RSS, the 95% confidence interval is about 60% larger than that estimated by Wentz et al. (2007), who estimated the uncertainty in RSS by using deviations from hydrological balance.

Spatial trends in GHCN annual precipitation were determined for 1901–2008 and for 1989–2008 (Fig. 2.13). On the century time scale, most of the globe has trended toward wetter conditions, but with notable exceptions, including parts of southern Europe, most of Africa, southwestern Australia, and the west coast of South America. Drying trends were most prominent in the African Sahel, where drought dominated from the 1970s through the 1990s. Since 1989, however, the Sahel has trended wetter (Fig. 2.13b). Two regions that have become significantly drier over

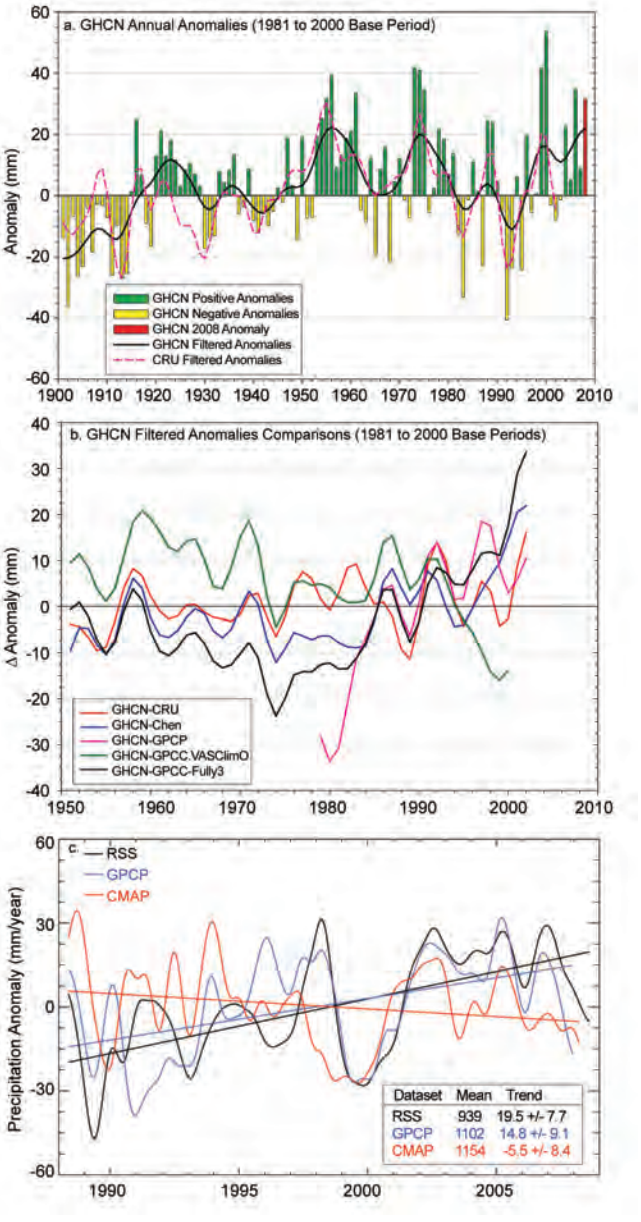

Fig. 2.12. (a) Annual global land surface precipitation anomalies (mm) over the period 1901–2008 from the GHCN dataset (Vose et al. 1992). Precipitation anomalies were calculated with respect to 1981–2000 (Trenberth et al. 2007): green bars are positive anomalies, yellow bars are negative anomalies, and red bar is 2008 anomaly. Smoothed GHCN and CRU (v.3) annual values were created using a 13-point binomial filter. (b) Time series of the difference between the smoothed GHCN annual anomalies and annual anomalies over global land areas from five different global precipitation datasets for the period 1951–2008: CRU v.3, Chen et al. (2002), GPCP, and two from the GPCC (VasClimO and Full v.3). (c) Ocean precipitation anomalies relative to the period 1988–2008. Averages are for the global ocean between 60°S and 60°N latitude using a common definition of "ocean." The annual cycle has been removed and the time series have been low-pass filtered by convolution using a Gaussian distribution, with 4-month width at half-peak power. Note that the RSS data are available through all of 2008, while GPCP and CMAP data are available through Apr and Jul 2008, respectively. The inset gives the 1988–2008 mean (mm yr^{-1}) and the linear trend (mm yr^{-1} $decade^{-1}$) with the 95% confidence interval. Straight lines denote the linear trends, and the confidence interval is estimated based on deviations from the linear fit and does not incorporate a particular dataset's "error."

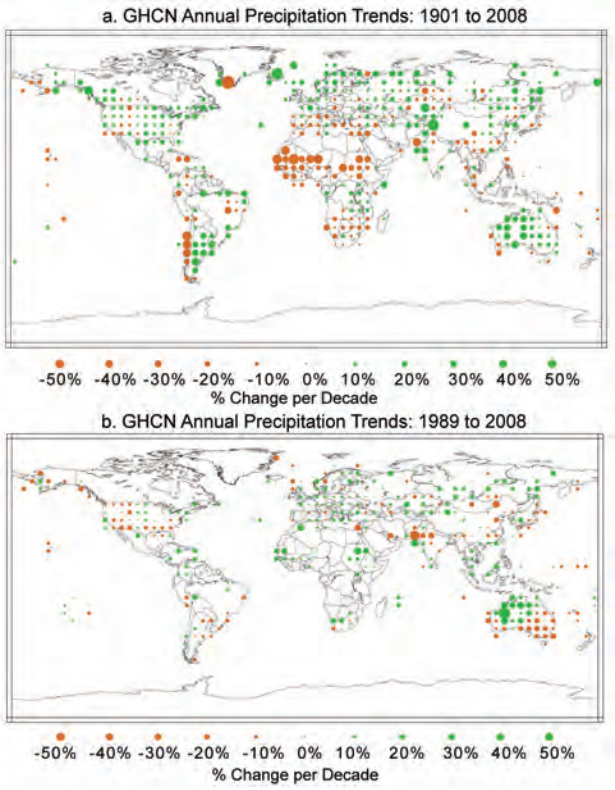

Fig. 2.13. Trends in annual precipitation calculated from the GHCN monthly dataset for two different time periods: (a) 1901–2008 (% change century^{-1}) and (b) 1989–2008 (% change decade^{-1}). Calculation of grid cell trends required at least two-thirds (66%) of the years without missing data during each of the two periods analyzed.

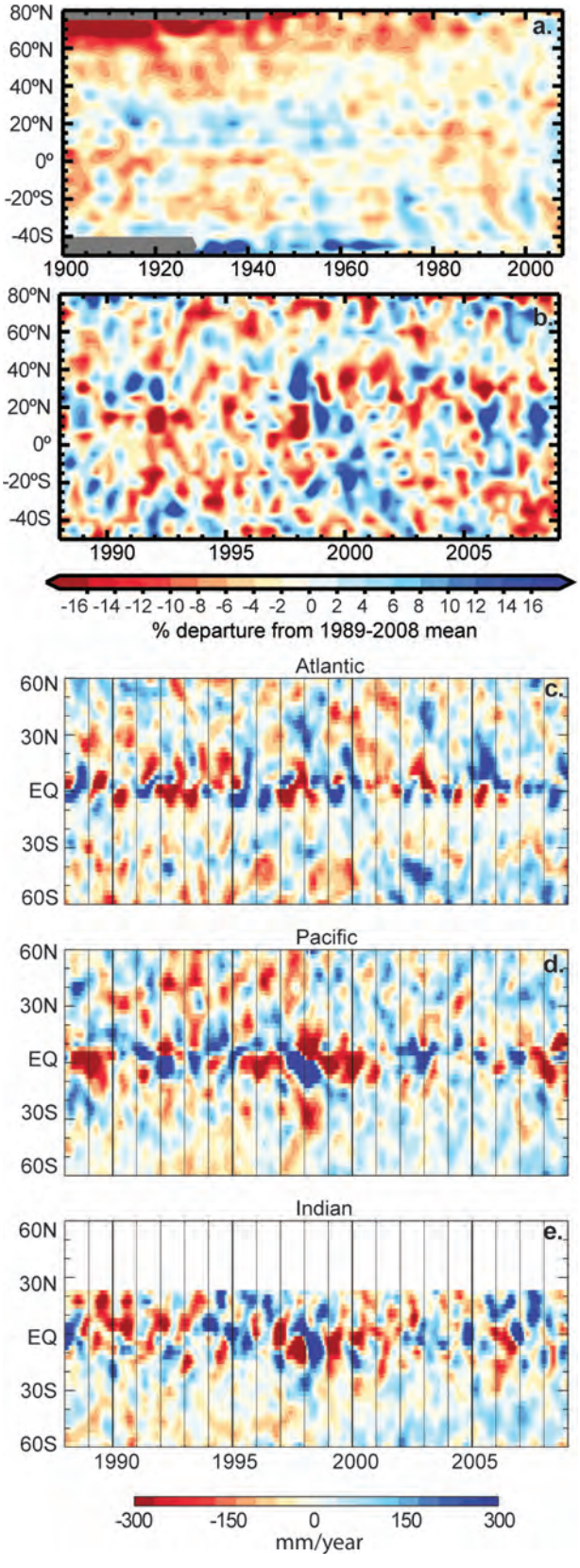

Fig. 2.14. (a) Time–latitude plot of GHCN annual land precipitation in terms of the % departure from 1989 to 2000 base-period means, with zonal means determined over 5°-latitude bands covering the period 1901–2008. Gray shading at higher latitudes in the early twentieth century is due to a lack of data south of 40°S and north of 75°N. (b) Same as (a) but for the RSS satellite record era. (c–e) Time–latitude section of precipitation anomalies (mm yr^{-1}) averaged over the (c) Atlantic, (d) Pacific, and (e) Indian Ocean basins as observed by the RSS monthly averaged dataset. Anomalies were calculated using the 1988–2008 base period by removing the latitude-dependent annual cycle.

the past two decades are the southwestern United States and southeastern Australia.

These regional trends are also apparent in the GHCN zonal mean precipitation (Figs. 2.14a,b). A trend toward drier tropical conditions since the 1950s is clearly evident. There has been a steady increase in precipitation over northern high latitudes during the twentieth century, which has accelerated over the past 5 yr. Figures 2.14c–e show time–latitude sections of precipitation anomalies over the Atlantic, Pacific,

Fig. 2.15. Time–longitude section of precipitation anomaly averaged over the tropical ocean (5°S to 5°N) as observed by the RSS monthly averaged dataset. Anomalies were determined using the 1988–2008 base period by removing the longitude-dependent annual cycle. Missing areas are the results of land masks: between 10° and 40°E are due to Africa, the areas near 100° and 115°E are due to Sumatra and Borneo, and the areas between 280° and 310°E are due to South America.

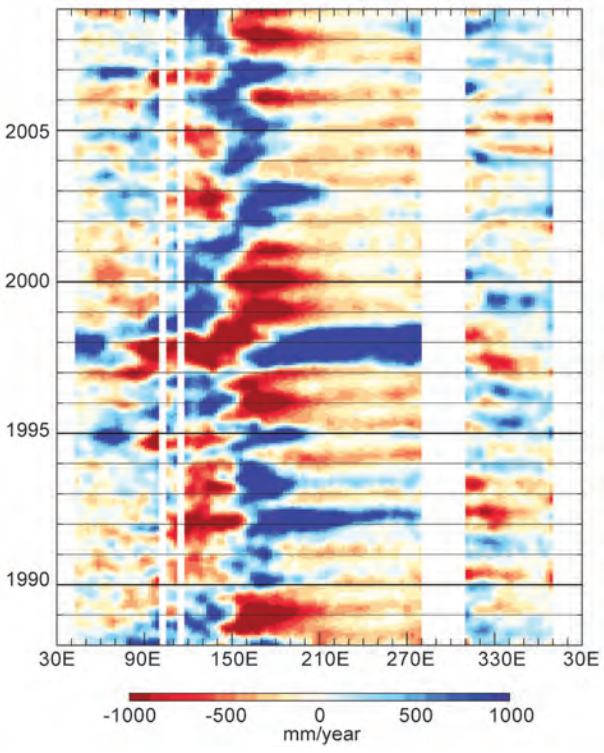

and Indian Ocean basins over the shorter satellite era. Wetter-than-average conditions over the Atlantic basin in 2008 were focused south of the equator in the first half of 2008, and north of the equator for the second half. With the break in the dry conditions over the equatorial Pacific in the middle of 2008, the drier areas shifted northward.

The western equatorial Pacific was wetter than normal in 2008, while it was drier than normal across much of the tropical eastern and central Pacific (Plate 2.1, panel 6), an expected consequence of the 2008 La Niña (Ropelewski and Halpert 1987). The dry anomalies across the central Pacific began in late 2007 (Fig. 2.15) and strengthened in the beginning of 2008 before weakening around June. Dry conditions redeveloped later in 2008 but were not as strong.

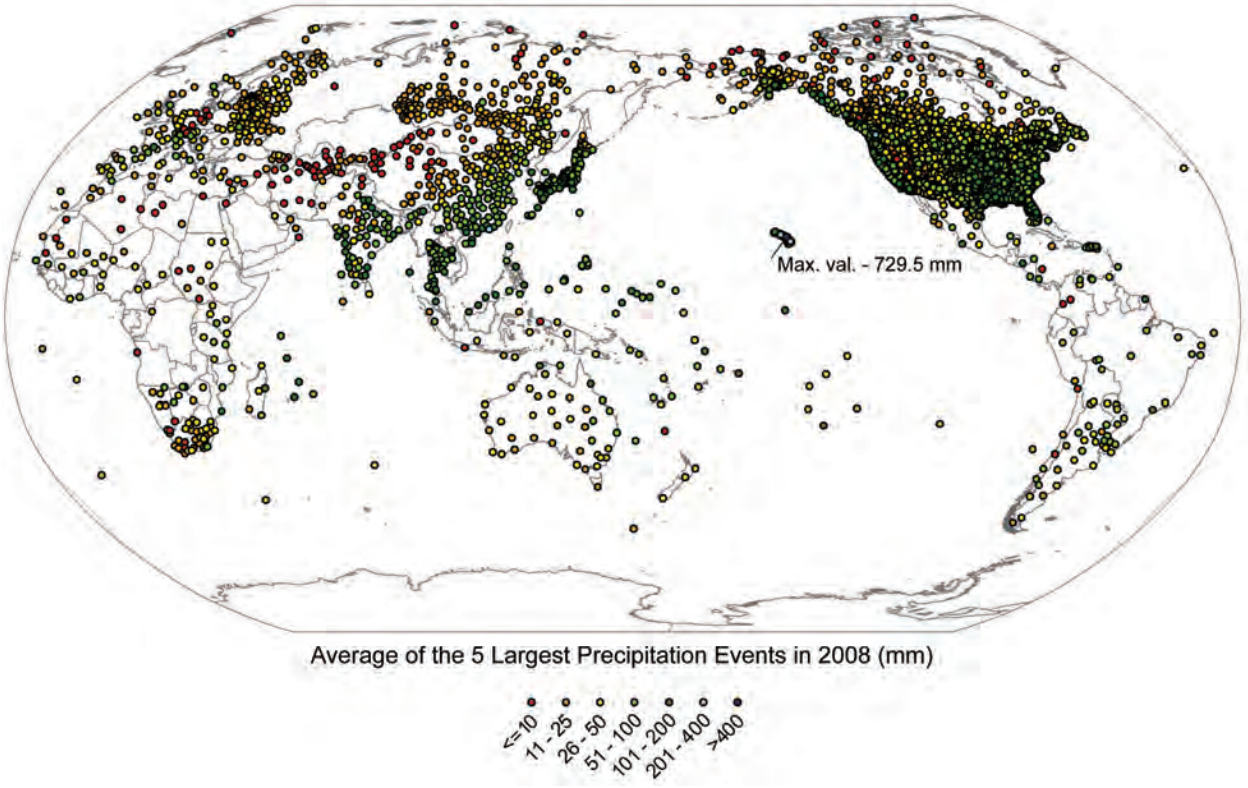

Fig. 2.16. Global map of daily precipitation extremes observed in 2008 from the GHCN dataset. The plotted values are the average of the top five largest daily precipitation events (mm) at each station.

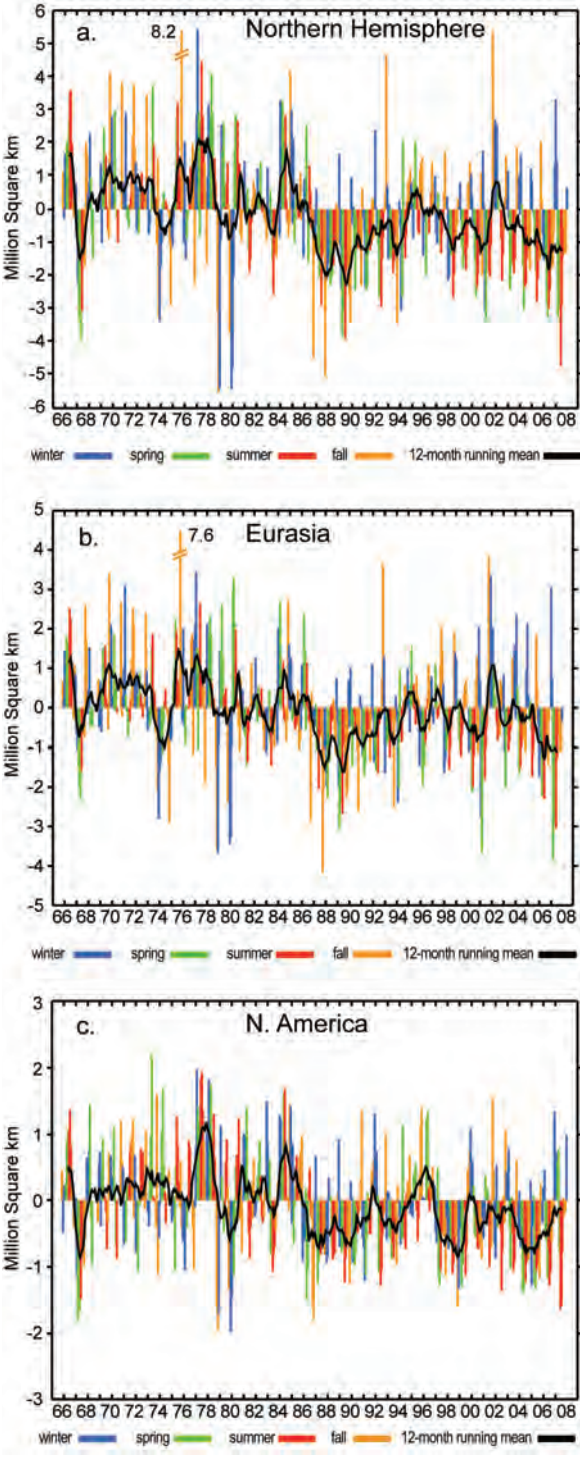

Fig. 2.17. Anomalies of monthly snow cover extent over Northern Hemisphere lands (including Greenland) between Nov 1966 and Dec 2008. Anomalies are calculated from NOAA snow maps. Mean hemispheric snow extent is 25.5 million km^2 for the full period of record. Monthly means for the period of record are used for nine missing months between 1968 and 1971 to create a continuous series of running means. Missing months fall between Jun and Oct; no winter months are missing.

The most extreme land precipitation events observed in 2008 were determined by averaging the five wettest days using GHCN data. The largest extremes affected Japan, Southeast Asia, and numerous locations across the United States (Fig. 2.16). The maximum of 716 mm occurred in the Hawaiian Islands.

3) Northern Hemisphere continental snow cover extent—D. A. Robinson

Annual snow cover extent over the Northern Hemisphere was 1.1 million km^2 less than the 39-yr average; 2008 had the fourth least extensive cover on record (Table 2.1). This includes the Greenland ice sheet. The 12-month running means of SCE were below the long-term average throughout 2008. They were consistently the lowest values since the notable minimum in the late 1980s and early 1990s (Fig. 2.17).

The year commenced with record maximum hemispheric SCE, due to record Eurasian cover (Fig. 2.17b; see also box in regional chapter on the impacts). February SCE remained anomalously large over both continents. Combined with an upper-quartile ranking in December 2007, the winter of 2007/08 had the fourth most extensive hemispheric SCE of the past 42 years (Fig. 2.18). Eurasian snow melted quickly in March, leading to a record low SCE over the continent and the fourth lowest over the hemisphere. In May, North American SCE joined Eurasia and the hemisphere as a whole in the lowest quartile. Record-low June coverage occurred over both continents. Spring coverage was the third lowest on record, and summer SCE was a record low.

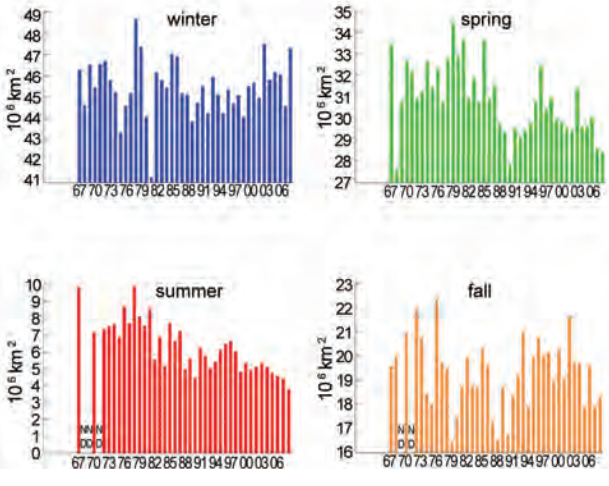

Fig. 2.18. Seasonal snow cover extent over Northern Hemisphere lands (including Greenland) between winter (Dec–Feb) 1966/67 and fall (Sep–Nov) 2008. Calculated from NOAA snow maps.

Table 2.1. Monthly and annual climatological information on Northern Hemisphere and continental snow extent between Nov 1966 and Dec 2008. Included are the numbers of years with data used in the calculations, means, std dev, 2008 values, and rankings. Areas are in millions of square kilometers. 1968, 1969, and 1971 have 1, 5, and 3 missing months, respectively, and thus are not included in the annual (Ann) calculations. North America (N. Am.) includes Greenland. Ranks are from most extensive (1) to least (ranges from 39 to 43 depending on the month).

	Years	Mean	Std dev	2008	2008 Northern Hemisphere rank	Eurasia rank	N. Am. rank
Jan	42	47.0	1.6	50.1	1	1	13
Feb	42	45.9	1.8	47.4	11	13	10
Mar	42	40.9	1.9	37.9	39	42	7
Apr	42	31.3	1.7	29.4	36	42	9
May	42	20.3	1.9	17.7	38	38	34
Jun	41	10.8	2.2	6.6	41	41	41
Jul	39	4.7	1.5	2.4	39	39	39
Aug	40	3.4	1.0	2.4	35	38	34
Sep	40	5.6	1.0	5.1	26	30	17
Oct	41	18.3	2.6	16.8	33	31	26
Nov	43	34.1	2.0	32.8	32	32	25
Dec	43	43.5	1.8	43.9	22	32	7
Ann	39	25.5	1.0	24.4	36	36	25

Eurasian cover consistently ranked near the 25th percentile throughout the fall and into December. North American SCE was slightly above average in September, somewhat below average in October and November, and seventh most extensive in December. This resulted in hemisphere-wide cover between the 20th and 50th percentile during the last four months of 2008, and a fall cover ranking as 10th lowest.

4) Global cloudiness—M. J. Foster, S. A. Ackerman, R. Bennartz, A. K. Heidinger, B. C. Maddux, and W. B. Rossow

Global cloudiness in 2008 was dominated by La Niña, a return of Arctic summer cloudiness due to a weakening of the anticyclonic atmospheric circulation pattern seen in 2007, and an increase in the amount of equatorial Atlantic high cloud in the boreal spring. The primary dataset used for this analysis is the 27-yr record of cloud retrievals in NOAA's AVHRR PATMOS-x dataset.

The La Niña, along with enhanced low-level easterly winds, strengthened large-scale convection in the western Pacific near Indonesia and suppressed it in the central Pacific. Plate 2.1, panel 4 shows below-normal cloudiness in the central equatorial Pacific, and above-normal cloudiness around Indonesia. The magnitude of the central Pacific negative anomaly is approximately 20%–25%. The positive anomaly around Indonesia is between 10% and 15%. Only small portions of the central Pacific negative anomaly are statistically significant at the 95% confidence level, and none of the positive anomaly around Indonesia is statistically significant.

Both MODIS and PATMOS-x capture a positive equatorial anomaly in boreal spring and summer 2008 (Fig. 2.19). This is consistent with an anomalous shift of the ITCZ over the equatorial Atlantic, which may have been influenced by ENSO effects on the Walker circulation (Saravanan and Chang 2000; Chiang et al. 2002). NCEP–NCAR reanalysis data show higher-than-normal SSTs, easterly wind strength, and tropospheric humidity, yielding increased convective activity and a positive high cloud anomaly over 30% relative to the long-term mean for March through May. The magnitude of the anomaly is reduced in Fig. 2.19 by an ENSO-induced negative high cloud anomaly in the equatorial central Pacific, but portions of the annual anomaly are statistically significant at the 95% confidence level.

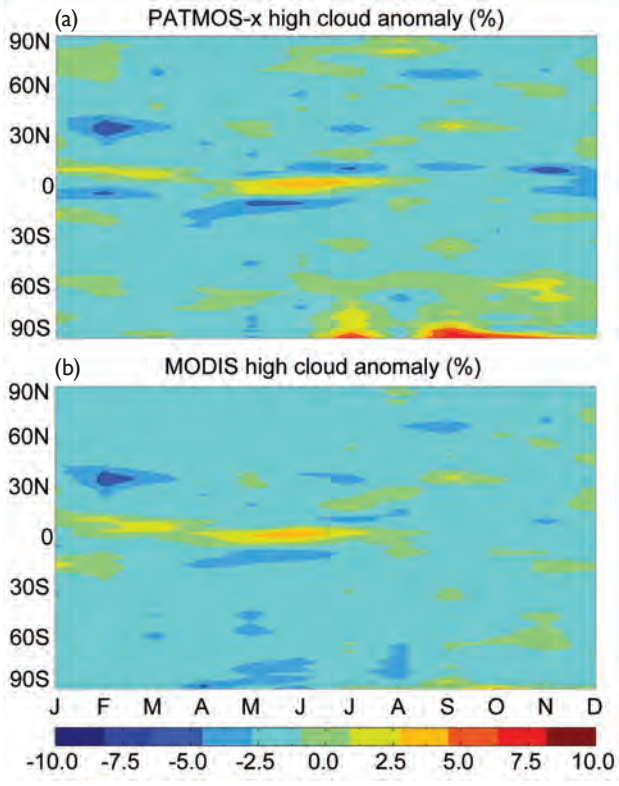

Fig. 2.19. (a) Monthly zonal average PATMOS-x anomalies of high cloud cover (cloud top pressure < 440 hPa) in 2008, relative to 2003–08 climatology based on retrievals from the NOAA-16 and NOAA-18 satellites. The 2003–08 reference period is chosen to match that of MODIS (b) to facilitate comparison. (b) Same as (a) but for MODIS (cloud top pressure < 440 hPa) based on retrievals from the *Aqua* and *Terra* satellites.

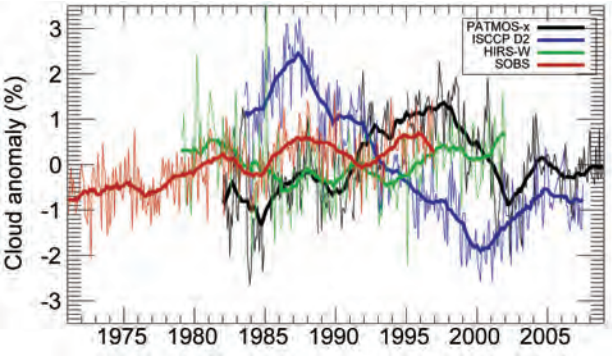

Fig. 2.20. Anomalies of monthly cloud amount between Jan 1971 and Dec 2008 taken from four datasets. The thick solid lines represent smoothing with a boxcar filter with a 2-yr window. There are 6 months missing from the PATMOS-x time series between Jan 1985 and Feb 1991, as well as a gap from Jan 1994 to Feb 1995.

In 2007 increased temperatures and decreased tropospheric humidity associated with an anticyclonic atmospheric circulation pattern caused noticeable decreases in Arctic summer cloudiness (Kay et al. 2008). In 2008 this anticyclonic atmospheric circulation pattern persisted through boreal spring but weakened during the Arctic summer, resulting in an increase in cloudiness over northern Greenland and much of the Arctic Ocean of 15% to 20%. None of these increases is statistically significant.

Figure 2.20 shows global mean monthly cloud amount anomalies since January 1971 from four sources: SOBS for 1971–96, infrared sounder instruments on the NOAA polar orbiting weather satellites (HIRS-W) for 1979–2002, imaging radiometers on operational weather satellites (ISCCP) for 1983–2007 (and continuing), and the PATMOS-x data. The records appear to disagree on the long-term variation of cloudiness, but the variations and their differences are smaller than the estimated uncertainties and are much smaller than the annual cycle. We conclude that the global monthly mean cloud cover did not vary by more than a few percent over more than two decades. This upper limit is significant in light of other, simultaneous variations of the climate: the lack of change needs to be explained as much as would a significant change.

PATMOS-x is the only record shown that currently extends throughout 2008. Its 2008 annual mean globally averaged cloud amount is 65%, very close to its 27-yr mean of 65.2; all months were within 1% of the long-term mean cloudiness.

5) River discharge—A. M. Macdonald, B. M. Fekete, L. C. Bowling, R. B. Lammers, R. Lawford

Discharge is a uniquely useful climate indicator among water cycle components as hydrograph observations integrate both in space and time. Runoff varies in response to natural and anthropogenic forcing (e.g., land-use change, reservoirs, dams) (Milliman et al. 2008; IPCC 2007; Gedney et al. 2006). Variations that affect the water available in local watersheds contribute to changes in ocean freshwater budgets (Talley 2008; Peterson et al. 2006), and play a significant role in the temporal variability and trends of the global water cycle (Oki and Kanae 2006). Modern estimates of global runoff vary by less than 10% (Table 2.2). Regional year-to-year discharge is dominated by variations in precipitation but is also nonlinearly dependent on groundwater contributions, regional runoff fractions, and surface water withdrawals.

Most discharge records have temporal gaps and/or infrequent or spatially inhomogeneous sampling. Divergent methods of data collection and apparent political disincentives to report accurately com-

Table 2.2. Estimates of long-term mean annual global runoff ($km^3 yr^{-1}$) into major ocean basins. Percent variation is a measure of the variation among the different estimates and is equal to the std dev divided by the mean times 100. Rows 1–3, 5, and 7 are adapted from Dai and Trenberth's (2002) Table 4, which states that the values exclude the Antarctic runoff into the Southern Ocean that they estimate at ~2614 $km^3 yr^{-1}$ after Jacobs et al. (1992) (see their references). Rows 4, 6, and 8 are estimated from GRDC (2004). Including only those estimates made in the last decade reduces the percent variation among the estimates to 16%, 6%, 8%, 42%, 10%, and 4% for columns 1 to 6, respectively

	Arctic	*Atlantic*	*Indian*	*Mediterranean & Black Seas*	*Pacific*	*Total*
Baumgartner and Reichel (1975)	2,600	19,300	5,600	0	12,000	37,713
Korzun et al. (1977)	5,220	20,760	6,150	0	14,800	46,930
Oki (1999)	4,500	21,500	4,000	0	10,000	40,000
Shiklomanov (1999)	4,281	19,799	4,858	0	12,211	41,149
Fekete et al. (2000)	2,947	18,357	4,802	1,169	11,127	38,402
Fekete et al. (2002)	3,268	18,506	4,858	475	10,476	37,583
Dai and Trenberth (2002)	3,658	19,168	4,532	838	9,092	37,288 ±662
GRDC (2004)	3,863	20,373	5,051	0	11,245	40,533
Average, Std Dev and % Variation of above Values	3,792 ±863 23%	19,720 ±1,102 6%	4,981 ±653 13%	827 ±347 42%	11,369 ±1724 15%	39,950 ±3176 8%

pound the issue. Although satellite measurements may improve global coverage, orbit tracks present issues for spatial and temporal resolution (Alsdorf et al. 2007).

The primary archive for global in-situ river discharge data is the GRDC. As of December 2007, it held 3.3 million monthly discharge estimates from 7,332 stations in 156 countries worldwide, representing some 276,000 station years of data. The shortest records are for a single year, the longest 197 years. However, the most recent data available (GRDC 2009) are for 2004.

Planned discharge data products will combine discharge observations with rainfall runoff simulation based on meteorological observations to provide spatially distributed estimates (Fekete et al. 2001). Alsdorf and Lettenmeier (2003) also recommend incorporation of satellite estimates. As a precursor to such merged products, the Global Terrestrial Network for Hydrology publishes runoff and river discharge estimates based on climate and precipitation data forcing. There is strong spatial variability of 2007 runoff and anomalies (Fig. 2.21), reflecting the integral quality of discharge. Such products offer the potential for global monitoring, even where primary data are not readily accessible.

d. Atmospheric circulation

1) Mean sea level pressure—R. Allan

The major feature of the 2008 annual global MSLP field was the influence of the moderate La Niña event. Annual MSLP anomalies were 1 to 2.5 hPa above average across the bulk of the Pacific Ocean and up to 1 hPa below average across the Indian Ocean and the "maritime continent" of Indonesia (Plate 2.1, panel 7). El Niño and La Niña events can be monitored by the SOI, the normalized MSLP difference between Tahiti and Darwin (Allan et al. 1996). El Niños (negative SOI) and La Niñas (positive SOI) vary in magnitude, duration, and evolution, and no two events or episodes are exactly the same. Major events can be near global in their influence on weather patterns, due

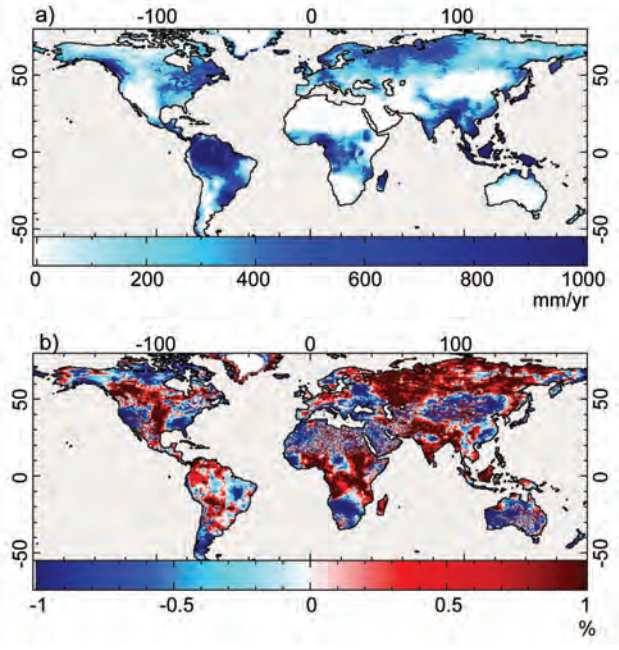

Fig. 2.21. Estimates for 2007 of (a) runoff and (b) its anomaly based on outputs from a hydrometeorological model utilizing GPCP precipitation measurements.

to dynamical teleconnections from the Indo-Pacific region to higher latitudes in both hemispheres. There are also protracted El Niño and La Niña episodes, such as the protracted El Niño in the first half of the 1990s and the protracted La Niña from 1998 to 2000 (Allan and D'Arrigo 1999; D'Arrigo et al. 2008). Such episodes are characterized by periods with weak–moderate anomalies, but their persistence over several years has substantial impacts. They also tend to show within-episode fluctuations, with measures such as the SOI suggesting that an episode can show signs of waning but then be reestablished. The SOI

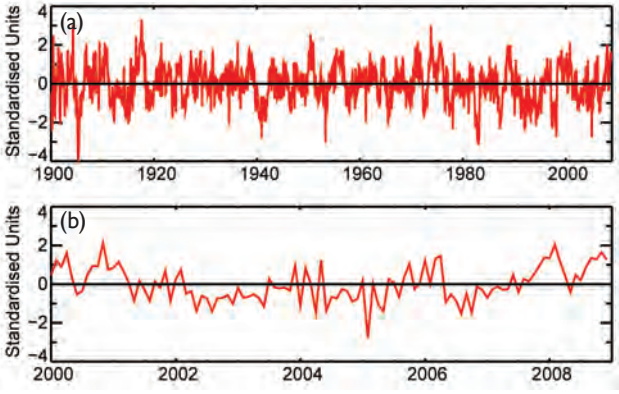

Fig. 2.22. The SOI for (a) 1900 to present and (b) from 2000 to 2008 relative to the 1876 to 2008 base period.

since 1900 is dominated by interannual to multidecadal vacillations, but very-long-term trends are not evident (Fig. 2.22). Figure 2.22b indicates that the weak–moderate La Niña in 2008 is part of a longer, persistent episode that started in 2007.

In the Southern Hemisphere in 2008, high latitudes were dominated by negative MSLP anomalies, with positive MSLP anomalies at middle latitudes, particularly across the southern Atlantic and Indian Ocean sectors (Plate 2.1, panel 7). This indicates a strong positive phase of the Southern annular mode (Fig. 2.23b) which plays an important role in modulating climatic patterns across the Southern Hemisphere continents. The 2008 annual MSLP anomalies in the North Atlantic region, being negative at higher latitudes and positive at midlatitudes, reflect a positive winter NAO (Fig. 2.23a). The instrumental NAO record is dominated by interannual to multidecadal fluctuations. The negative MSLP anomalies over the United Kingdom and Scandinavia in 2008 also reflect the circulation pattern underlying the wet 2008 summer in the United Kingdom.

2) Surface wind speed—C. Mears

Surface wind speed over the oceans began to be monitored continuously with the first SSM/I satellite in late 1987. This uses measurements of upwelling microwave radiation to infer the surface roughness of the world's oceans, and thus surface wind speed (Wentz 1997). Here we use Version 6 of the SSM/I dataset produced by RSS. The average winds over the global ocean exhibited a maximum in 1988–89, followed by an increasing trend since 1990 (Fig. 2.24). The sharp peak in mid-2008 may be an artifact of missing data in the SSM/I dataset, because the sharp peak is not seen in wind speeds derived from the QuikSCAT microwave scatterometer (Lungu and Callahan 2006).

Zonal mean surface wind speed is dominated by short-term variability that makes it difficult to discern interannual and decadal scale changes (Fig. 2.25). The only obvious long-term trend occurs in the southern extratropics. Hence, a large portion of the global scale increase is due to changes in this region, related to the intensification of the Antarctic circumpolar circulation (Yang et al. 2007; Fig. 2.23b). The effects of ENSO are difficult to discern in part because averaging over all available longitudes deemphasizes the east–west movement of circulation features during ENSO.

Plate 2.1, panel 8 reveals several notable anomalies in 2008. A large positive anomaly occurred in the central tropical Pacific, associated with the La Niña.

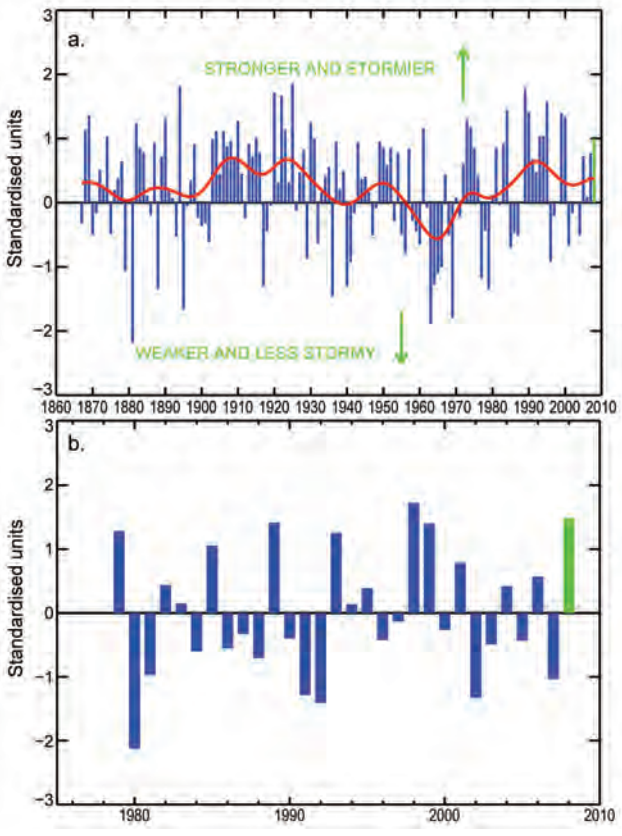

Fig. 2.23. (a) The annual historical instrumental [Ponta Delgada (Azores) minus Stykkisholmur (Iceland), normalized] NAO series from the mid-1860s to present (blue); the 21-point binomial filter run through the data three times (red). The green bar shows the average for the 2007/08 boreal winter. (b) Standardized 3-month running-mean value of the SAM or AAO index from 1979. The loading pattern of the SAM/AAO is defined as the leading mode of EOF analysis of monthly mean 700-hPa height during the 1979–2000 period. The monthly SAM/AAO index is constructed by projecting the monthly mean 700-hPa height anomalies onto the leading EOF mode. The resulting time series are normalized by the std dev of the monthly index (1979–2000 base period). Source: www.cpc.ncep.noaa.gov/products/precip/CWlink/daily_ao_index/aao/aao.shtml.

A large negative anomaly affected most of the Northeastern Pacific, and there was a large positive anomaly over most of the Southern Ocean. In the North Atlantic, the positive anomalies near Iceland and in the trade wind region are consistent with the positive winter North Atlantic Oscillation (section 2d1; see also Hurrell et al. 2003).

e. Earth radiation budget at top-of-atmosphere—T. Wong, P. W. Stackhouse Jr., D. P. Kratz, and A. C. Wilber

Preliminary analysis suggests that global annual-mean outgoing longwave radiation decreased by

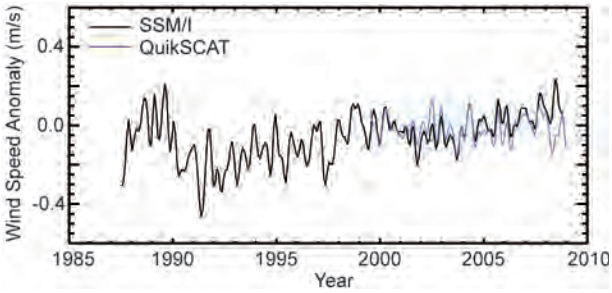

Fig. 2.24. Surface wind speed anomalies averaged over the global ice-free oceans. The time series has been smoothed to remove variability on time scales shorter than 4 months. The reference period for the SSM/I measurements is 1988–2007. For the QuikSCAT measurements the reference period is 2000–07, with the mean adjusted to match the SSM/I anomalies for the 2000–07 period.

~0.75 W m^{-2}, from 2007 to 2008, while there was a decrease of 0.14 W m^{-2} in global-annual mean reflected shortwave radiation (Table 2.3). A small portion of the shortwave decrease was caused by changes in the total solar irradiance since the 11-yr solar cycle was near its minimum during 2007–08. The combined longwave and shortwave changes caused an increase of ~0.89 W m^{-2} in net radiation into the Earth climate system in 2008. However, these initial results are largely derived from the FLASH-Flux dataset (Stackhouse et al. 2006; L'Ecuyer et al. 2009), which still includes instrument drift artifacts between September 2007 and December 2008 that are currently under study by the CERES instrument team and have not yet been removed. Reassessments of these results are expected when newer CERES data are released. Relative to the multidataset average for 2001 to 2008, the 2008 global annual-mean anomalies (Table 2.3) are −0.54/−0.26/+0.80 W m^{-2}

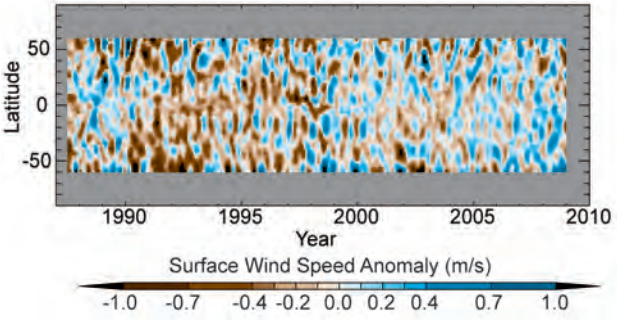

Fig. 2.25. Surface wind speed anomalies by latitude (reference period 1988–2007) over the ice-free oceans. The data have been smoothed in time to remove variability on time scales shorter than 4 months.

Table 2.3. Global annual-mean TOA radiative flux changes between 2007 and 2008, the 2008 global annual-mean radiative flux anomalies relative to their corresponding 2001–08 mean climatological values, and the 2σ interannual variabilities of 2001–08 global annual-mean fluxes (units in W m^{-2}).

	One year change (2008 minus 2007)	2008 anomaly (relative to climatology)	Interannual variability (2001 to 2008)
Longwave	−0.75	−0.54	±0.56
Shortwave	−0.14	−0.26	±0.41
Net	+0.89	+0.80	±0.82

respectively for longwave/shortwave/net radiation. These are within their corresponding 2σ interannual variabilities (Table 2.3) for this period.

Time series of global monthly mean deseasonalized anomalies since March 2000 have been constructed by merging ERB datasets from three sources: CERES EBAF (Loeb et al. 2009); CERES ERBE-like (Wielicki et al. 1999); and FLASHFlux (Fig. 2.26). The 2σ monthly uncertainties of the merge procedure is ±0.23/±0.93/±1.11 W m^{-2}, respectively, for the longwave/shortwave/net radiation. A decrease in longwave and increase in net radiation are noticeable in 2008 and are partly related to the switch to the 2007–08 La Niña, which altered the global distribution of clouds, total column water vapor, and temperature. Linear trend analyses are inconclusive due to natural fluctuation in ERB relating to ENSO activity, large uncertainty from the data-merging process, and instrument drift issues in the 2007–2008 FLASHFlux data. A long-term homogeneous data source with in-depth instrument stability analysis (e.g., CERES EBAF) is needed to reduce these uncertainties for future reassessment activity.

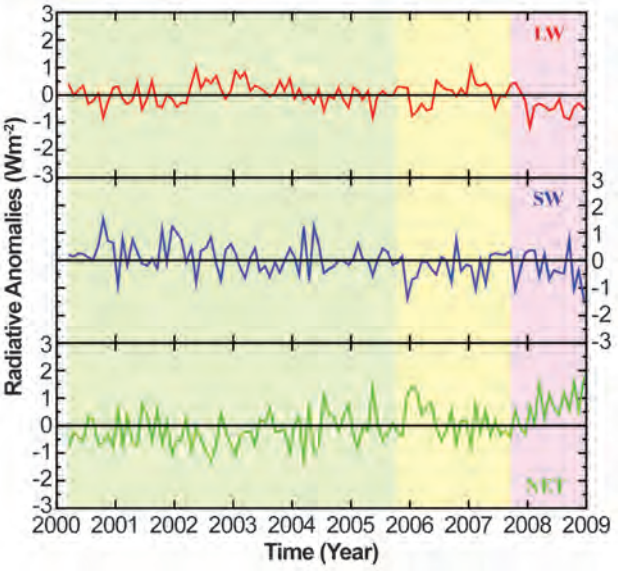

Fig. 2.26. Time series of global monthly mean deseasonalized anomalies of TOA Earth Radiation Budget for longwave (red line), shortwave (blue line), and net radiation (green line) from Mar 2000 to Dec 2008. Anomaly is computed relative to the calendar month climatology derived for the Mar 2000 to Dec 2008 period. The shaded green/yellow/pink area of the figure indicates the portion of the time series that is constructed using the CERES EBAF (Mar 2000 to Oct 2005)/CERES ERBE-like (Nov 2005 to Aug 2007)/FLASHFlux (Sep 2007 to Dec 2008) dataset, respectively. All three datasets are derived directly from CERES measurements. EBAF has been renormalized so that globally averaged top-of-atmosphere net radiation from 2000 to 2005 is consistent with ocean heat storage value (Willis et al. 2004; Hansen et al. 2005; Wong et al. 2006). The green (EBAF) and yellow (ERBE-like) shading indicate high-quality climate data with in-depth on-orbit instrument stability analysis. The pink shading (FLASHFlux) indicates preliminary climate data with possible instrument stability artifacts. Mean differences among datasets were removed using available overlapping data, and the combined ERBE time series was anchored to the absolute value of EBAF before deseasonalization.

f. Atmospheric composition

1) Atmospheric chemical composition—R. C. Schnell

(i) Carbon dioxide, methane, and carbon monoxide—E. J. Dlugokencky

(a) Carbon dioxide

Since 1750, ~335 billion tons of carbon has been emitted into the atmosphere by combustion of fossil fuels and production of cement. About half of these emissions have occurred since the mid-1970s (Marland et al. 2008), and emission rates increased by >3% from 2000 to 2004 (Raupach et al. 2007). This carbon, which is emitted as CO_2, is partitioned into the atmosphere, oceans, and terrestrial biosphere. Atmospheric CO_2 has increased from about 280 ppm (ppm = parts per million by dry-air mole fraction) at the start of the Industrial Revolution to more than

380 ppm today. About half of the emitted CO_2 remains in the atmosphere after a year, and after a millennium, ~20% remains (Archer and Brovkin 2008). The atmospheric increase since the preindustrial era contributes ~1.7 W m^{-2} of radiative forcing (see, e.g., www.esrl.noaa.gov/gmd/aggi/).

The fate of fossil fuel–derived CO_2 is important to climate, because different reservoirs have different residence times and different susceptibilities to human interference. Therefore much current research is dedicated to understanding the partitioning of fossil CO_2 into the ocean and terrestrial biosphere. One key indicator of this is stable C isotopes in atmospheric CO_2. Figure 2.27 (top) shows CO_2 mole fraction and $\delta^{13}C$ in CO_2 from weekly samples at Cape Kumukahi, Hawaii. The long-term decline in $\delta^{13}C$ results from fossil carbon being depleted in ^{13}C relative to atmospheric CO_2. There is a seasonal cycle of opposite phase in CO_2 mole fraction and $\delta^{13}C$. As the biosphere takes up CO_2 in the spring and summer, it favors ^{12}C; this enriches the atmosphere in ^{13}C (less negative $\delta^{13}C$ values). Interannual variation in the balance between photosynthesis and respiration is seen in the subtle variations in the long-term $\delta^{13}C$ trends.

The preliminary globally averaged atmospheric CO_2 mole fraction in 2008 was 384.9 ppm, 2.28 ppm more than in 2007 (see www.esrl.noaa.gov/gmd/ccgg/trends/ for updated data; see Conway et al. 1994 for a description of sampling network and methods). This is significantly greater than the average rate of increase from 1979 through 2008, 1.62 ppm yr^{-1}. Despite fossil CO_2 emissions being predominantly in the Northern Hemisphere, the rate of increase of atmospheric CO_2 is approximately the same everywhere. Figure 2.28 shows monthly mean CO_2 mole fractions from four well-spaced NOAA ESRL observatories. The amplitude of the seasonal cycle varies according to exposure of air masses arriving at the sites to the terrestrial biosphere, but there are no significant differences in long-term trends.

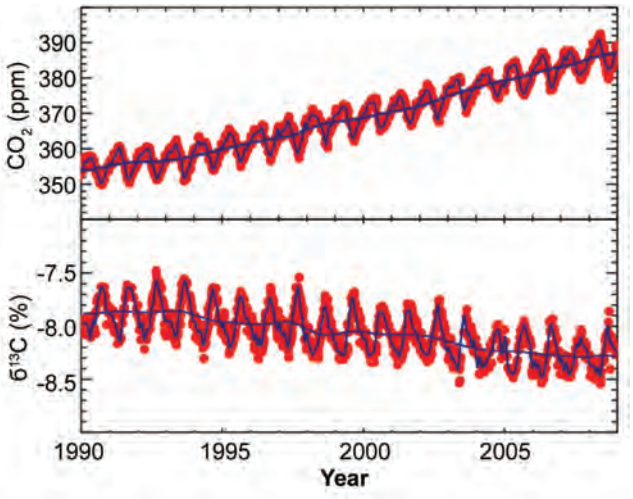

Fig. 2.27. CO_2 dry air mole fractions (top: NOAA ESRL) and $\delta^{13}C$ in CO_2 (bottom: University of Colorado, INSTAAR, courtesy James White) from weekly samples at Cape Kumukahi, HI.

(b) Methane (CH_4)

Methane contributes ~0.7 W m^{-2} to anthropogenic radiative forcing, when direct and indirect effects are included. While ~2/3 of CH_4 emissions are from anthropogenic sources, natural emissions of CH_4, predominantly from wetlands, are especially susceptible to climate change because they depend strongly on temperature and precipitation. In the Arctic, where surface temperatures are increasing at twice the global rate (Solomon et al. 2007), there is the potential for increases in CH_4 emissions from wetlands. The Arctic also contains large stores of organic carbon in permafrost (Zimov et al. 2006) and in hydrates (Kvenvolden 1993). Rapid destabilization of hydrates could release enormous amounts of CH_4 in a short time, although this scenario is unlikely. Anthropogenic sources such as biomass burning are also susceptible to changing climate through changes in precipitation. Dry conditions during the strong El Niño of 1997–98 resulted in an estimated 50% increase in CH_4 emissions from biomass burning in the tropics and high northern latitudes relative to normal (van der Werf et al. 2006).

After a decade of near-zero growth, atmospheric methane increased globally in 2007 by 7.5 ppb (Rigby et al. 2008), driven by increased Arctic and tropical emissions. Likely causes were anomalously high temperatures and precipitation in wetland regions, particularly in the Arctic: CO measurements indicated little contribution from enhanced biomass burning. In 2008, globally averaged atmospheric CH_4 increased again, with most of the increase driven by the tropics. Arctic emissions returned to normal despite continued warmth. The 2007–08 La Niña, with excess precipitation in Indonesia and parts of Amazonia (Plate 2.1, panel 6) , may be responsible for increased tropical emissions, but the current atmospheric CH_4 observing network, including in situ and remotely sensed observations, is insufficient to determine with certainty the causes of the CH_4 increases in 2007 and 2008.

(c) Carbon monoxide

Carbon monoxide does not strongly absorb terrestrial infrared radiation, but it impacts climate

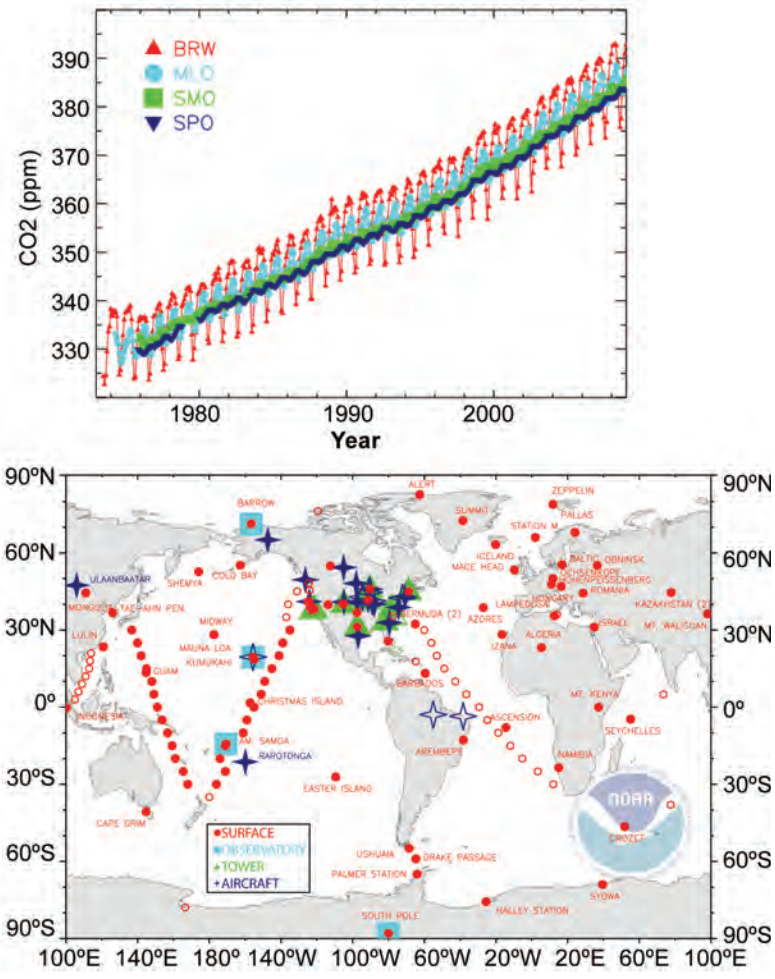

Fig. 2.28. (a) CO_2 monthly mean mole fractions determined from NOAA ESRL observatories at Barrow, AK; Mauna Loa, HI; American Samoa; and South Pole, part of the larger global carbon-cycle monitoring network shown in (b). 2008 results are preliminary. Data are courtesy of Kirk Thoning, NOAA ESRL. Current CO_2 trends at MLO are available at www.esrl.noaa.gov/gmd/ccgg/trends/. Additional plots can be found at www.esrl.noaa.gov/gmd/ccgg/iadv/ and www.esrl.noaa.gov/gmd/Photo_Gallery/GMD_Figures/ccgg_figures/.

through its chemistry. This affects OH (which influences the lifetimes of CH_4 and HFCs) and tropospheric O_3 (itself a greenhouse gas), so emissions of CO can be considered equivalent to emissions of CH_4 (Prather 1996). Current emissions of CO may contribute more to radiative forcing over decadal time scales than emissions of anthropogenic N_2O (Daniel and Solomon 1998).

There has been no long-term CO trend since ESRL measurements began in 1990 (Novelli et al. 2003), but CO enhancements occurred during 1997 to 1998, and again in 2002 to 2003. These are likely the result of tropical (Langenfelds et al. 2002) and boreal biomass burning (Kasischke et al. 2000). Because the lifetime of CO is only a few months, the CO enhancements quickly disappeared.

The preliminary globally averaged CO mole fraction in 2008 of 83 ppb is 12 ppb lower than in 1998 when there was a large contribution from biomass burning. ESRL's surface sampling network is less sensitive to biomass-burning emissions of CO than remotely sensed CO observations such as MOPITT (Pan et al. 1998), because emissions are rapidly transported away from the surface where the sampling sites are located. The combination of surface measurements and MOPITT retrievals may improve our understanding of the contribution of biomass burning to atmospheric CH_4.

(ii) Ozone-depleting gases and their replacements—S. A. Montzka

Long-lived halocarbons affect the radiative balance of the atmosphere because they efficiently absorb terrestrial IR radiation (see next section). Long-lived halocarbons containing bromine and chlorine also influence the radiative atmospheric balance indirectly through their destruction of stratospheric ozone. So production of many halocarbons has been restricted following the 1987 Montreal Protocol on Substances that Deplete the Ozone Layer. As a result, mixing ratios of most of the potent ozone-depleting gases have been declining at Earth's surface; this decline continued in 2008 (Fig. 2.29).

The mixing ratios of some halogenated gases continue to increase globally (Fig. 2.29). The most rapid increases are observed for HCFCs and HFCs, which are common replacements for CFCs, halons, and other ozone-depleting gases. Increases in HCFCs have recently accelerated because of enhanced use in developing countries (Montzka et al. 2009). Both HCFCs and HFCs are efficient absorbers of infrared radiation (Table 2.4). Although HCFCs contain chlorine and deplete ozone with a reduced efficiency compared to CFCs, HFCs do not participate in ozone-destroying reactions.

The influence of halocarbon trace-gas trends on future levels of stratospheric ozone can be estimated

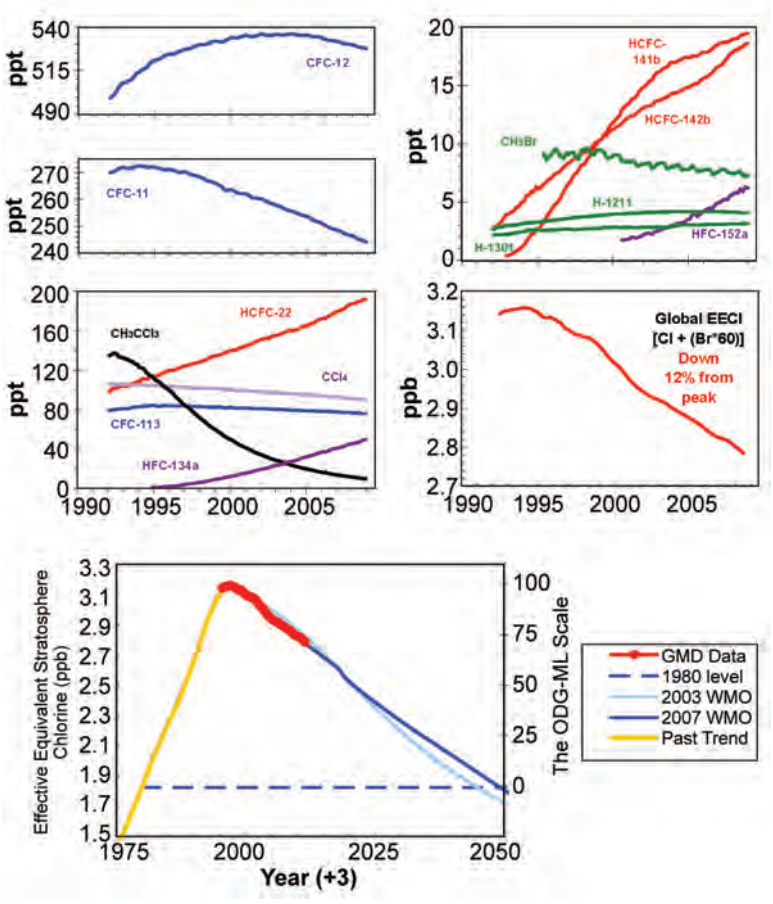

FIG. 2.29. Changes in global mean tropospheric mixing ratios (ppt, or pmol mol^{-1}) of the most abundant CFCs, HCFCs, HFCs, chlorinated solvents, and brominated gases. The middle right-hand panel shows secular changes in atmospheric equivalent chlorine (EECl; ppb or nmol mol^{-1}), which is an estimate of the ozone-depleting power of these atmospheric halocarbons. EECl is derived from observed mixing ratios of ozone-depleting gases appearing in the other four panels, and it is derived from the sum of [Cl + (Br×60)] contained in these gases. The bottom shows the recent changes in EESC observed by the NOAA/GMD global network relative to the secular changes observed in the past, including the level observed in 1980 when the ozone hole was first observed, and a projected future. The Ozone Depleting Gas Index for midlatitudes is derived (right-hand axis) from rescaling EESC. EESC is derived from EECl by simply adding 3 yr to the time axis to represent the lag associated with mixing air from the troposphere to the middle stratosphere, where the ozone layer resides [Source: Montzka et al. (1996, 1999.)]

from weighted sums of Cl and Br in long-lived halocarbons provided that the enhanced efficiency for Br to destroy ozone is considered [a factor of 60 is used here (Clerbaux and Cunnold et al. 2007)]. For midlatitudes this sum is expressed as EECl (Fig. 2.29) and is derived from surface-based measurements. It provides an estimate of the near-future ozone-depleting power of trace gases, when air at Earth's surface will have become mixed into the midlatitude stratosphere. A second metric, ECl, provides an estimate of the ozone-depleting power of trace gases in the near future for the stratosphere over the polar regions.

The EECl content of the lower atmosphere has declined fairly steadily since the peak in 1994 at a mean rate of 28 parts per trillion yr^{-1}. Despite these substantial changes, full recovery of stratospheric ozone is not expected until the mid- to late-twenty-first century due to the long lifetime of many of these chemicals [Fig. 2.29 (bottom); Table 2.4]. Progress toward EECl reductions can now be readily assessed with the NOAA ODGI (see www.cmdl.noaa.gov/odgi/; Hofmann and Montzka 2009), which is derived from EECl. It is scaled so that a value of 100 represents the EECl abundance at its peak, and 0 represents the 1980 level (when ozone depletion was thought to have been small). In 2008 the ODGI–Midlatitudes was 70.8 (Fig. 2.29). Less progress is evident in ECl; the ODGI-Antarctica derived from ECl estimates was 84.5 in 2008.

(iii) The combined influence of long-lived trace gases on the radiative balance of the atmosphere—S. A. Montzka

The direct radiative influence of a trace gas is directly proportional to its atmospheric abundance and how efficiently it absorbs infrared radiation in specific regions of the electromagnetic radiation spectrum (its radiative efficiency; Table 2.4). High-precision measurements of CO_2, CH_4, N_2O, CFC-12, CFC-11 (the major long-lived greenhouse gases) and 10 minor greenhouse gases (CFC-113, HCFCs, HFCs, etc., see Table 2.4 for complete list) from the NOAA global air sampling network have been used to calculate the overall change in the direct radiative climate forcing (Hofmann et al. 2006) (Fig. 2.30). This is calculated from changes in the abundances of these gases since 1750, and by mid-2007 amounted to approximately 2.69 W m^{-2}, of which changes in the abundance of CO_2 accounted for 63%.

Table 2.4. Radiative efficiencies and lifetimes of chemicals considered in the AGGI and OGDI.

Industrial Designation or Common Name	Chemical Formula	AGGI	ODGI	Radiative Efficiency (W m^{-2} $ppbv^{-1}$) *	Mixing ratio [change from 2006 to 2007]**	Lifetime
Carbon Dioxide	CO_2	Y	N	$1.41x10^{-5}$	382.6[1.7]	
Methane	CH_4	Y	N	$3.7x10^{-4}$	1781.4[6.0]	12.0
Nitrous oxide	N_2O	Y	N	$3.03x10^{-3}$	321.9[0.7]	114
Chlorofluorocarbons						
CFC-11	CCl_3F	Y	Y	0.25	247.3[−2.3]	45
CFC-12	CCl_2F_2	Y	Y	0.32	530.6[−1.8]	100
CFC-113	CCl_2FCClF_2	Y	Y	0.30	77.4[−0.8]	85
Hydrochlorofluorocarbons						
HCFC-22	$CHClF_2$	Y	Y	0.20	182.9[7.7]	12.0
HCFC-141b	CH_3CCl2F	Y	Y	0.14	18.7[0.6]	9.3
HCFC-142b	CH_3CClF_2	Y	Y	0.20	17.2[1.2]	17.9
Hydrofluorocarbons						
HFC-134a	CH_2FCF_3	Y	N	0.16	43.2[4.3]	14
HFC-152a	CH_3CHF_2	N	N	0.09	5.3[0.7]	1.4
Chlorocarbons						
Methyl Chloroform	CH_3CCl_3	Y	Y	0.06	12.9[−2.5]	5.0
Carbon Tetrachloride	CCl_4	Y	Y	0.13	92.1[−1.2]	26
Methyl Chloride	CH_3Cl	N	Y	0.01	548[7.3]	1.0
Bromocarbons						
Methyl Bromide	CH_3Br	N	Y	0.01	7.6[0.0]	0.7
Halon 1211	$CBrClF_2$	Y	Y	0.30	4.1[−0.03]	16.0
Halon 1301	$CBrF_3$	Y	Y	0.32	3.1[0.03]	65
Halon 2402	$CBrF_2CBrF$	N	Y	0.33	0.47[−0.01]	20
Fully fluorinated species						
Sulfur Hexafluoride	SF_6	Y	N	0.52	6.16[0.26]	3,200

* Radiative forcings and lifetimes are taken from Daniel and Velders et al. (2007) and Clerbaux and Cunnold et al. (2007).

** Mixing ratios are measured global surface means determined from NOAA global cooperative sampling network (Hofmann et al. 2006). Changes indicated in brackets are simply the difference between the 2007 and 2006 annual global surface mean mixing ratios. Units are ppm for CO_2, ppb for CH_4 and N_2O, and ppt for all others.

The NOAA AGGI is based on the direct radiative forcing calculated from these NOAA measurements (Hofmann et al. 2006). It is calculated as a ratio relative to the direct radiative forcing calculated from these gases for 1990, the Kyoto Protocol baseline year; indirect effects (e.g., arising from ozone depletion or water-vapor feedbacks) are not considered. By 2007, the AGGI was 1.241 (Fig. 2.30). Increases in the atmospheric abundance of CO_2 accounted for 80% of the increase since 1990.

(iv) Nitrous oxide and sulfur hexafluoride—J. W. Elkins and G. S. Dutton

Nitrous oxide (N_2O) and sulfur hexafluoride (SF_6) are important atmospheric trace gases. Atmospheric N_2O has the third-strongest radiative forcing since

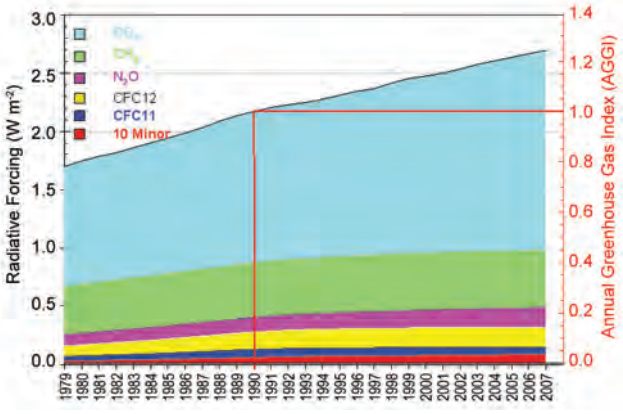

FIG. 2.30. The NOAA AGGI shows radiative forcing relative to 1750, of all the long-lived greenhouse gases indexed to 1 for the year 1990. Since 1990, radiative forcing from greenhouse gases has increased 24%.

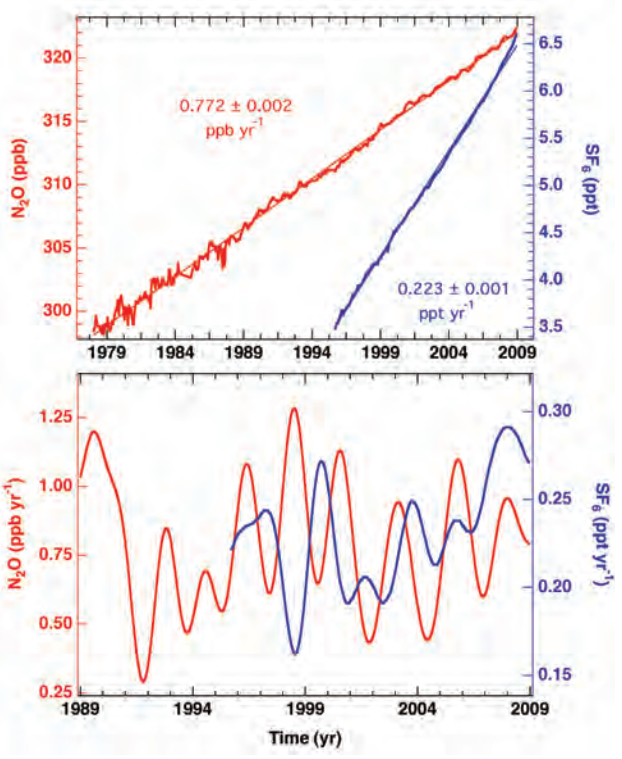

FIG. 2.31. (top) Global monthly means along with estimates for the linear growth rate of atmospheric nitrous oxide (N_2O, red) in ppb and sulfur hexafluoride (SF_6, blue) in ppt from the NOAA/ESRL halocarbon network. (bottom) Instantaneous growth rate of N_2O and SF_6 using a smoothing algorithm with a 2-yr filter; note the rapid rise of the atmospheric SF_6 growth rate after 2003. Atmospheric data for N_2O prior to 1989 and for SF_6 prior to 1999 were analyzed from flasks instead of continuously operating instruments at NOAA/ESRL baseline observatories.

the beginning of the Industrial Revolution after carbon dioxide and methane, while SF_6 represents the fourth-strongest forcing (Table 2.4). Atmospheric N_2O is also a source of stratospheric nitric oxide that is involved in stratospheric ozone depletion, and 30% of its sources are man made (fertilizers, industrial by-products, human and animal waste, and catalytic converters). SF_6 is 100% man made; it is used primarily for insulation in the distribution of electric power. Nitrous oxide has been growing since 1978 at a relatively constant growth rate of 0.772 ppb yr^{-1} with important biennial oscillations in its growth rate resulting from atmospheric transport (Fig. 2.31). Sulfur hexafluoride's growth rate has been increasing since 2003; note the recent deviation from a linear growth rate of 0.223 ppt yr^{-1} over 11 yr in Fig. 2.31, due to the world's growing demand for electricity.

2) Global aerosols—J. Haywood, N. Bellouin, and A. Jones

Aerosols impact climate by scattering and absorbing solar and terrestrial radiation (direct effects) and by influencing the microphysical and optical properties of clouds, thereby influencing cloud development (indirect effects). The effects of anthropogenic aerosols remain major uncertainties in driving climate change. The global distribution of aerosols in 2008 was generally in line with that from climatology and with that from 2007 as demonstrated by aerosol optical depths derived from the MODIS sensor on the *Aqua* platform (Fig. 2.32). Except for the biomass-burning plume over the rain forests of Brazil in 2007 and the increased aerosol optical depths over northeastern Eurasia in 2008, the global distributions (and the global means) are very similar.

The reduced Amazonian optical depth in 2008 is more in line with anomalously clear skies also noted in 2006 (Koren et al. 2007), than with the increasing trend seen from 2000 to 2007 (Evan 2007). Increased aerosol optical depths over northeastern Eurasia appear to arise from intense, large-scale boreal forest fires during April and July 2008. The number of acres burned by wildfires in the United States was significantly less (5.2 million) than the peak in 2006 (9.9 million).

Aerosol algorithm development continues apace with many improved products since the early ocean-only 2-channel retrievals of AVHRR (e.g., Mishchenko et al. 2007). Algorithms can now determine the fine-mode fraction of aerosols (e.g., MODIS; Remer et al. 2005) and speciated aerosol optical depths (e.g., MISR; Kahn et al. 2005). The use of multisensor algorithms allows estimation of the anthropogenic aerosol optical depth, which is important in determining

the radiative forcing of aerosols (Forster et al. 2007) as well as any anthropogenically influenced trend. Figure 2.32c shows the anthropogenic aerosol optical depth determined from MODIS using the retrieval algorithm of Bellouin et al. (2008). The anthropogenic aerosol optical depth consists primarily of industrial pollution (mainly sulfate, nitrate, organic carbon, and black carbon) and biomass-burning smoke (mainly volatile organic carbon, black carbon, and inorganic compounds). It averages around 0.03 over the ocean but exceeds 0.1 over many land areas.

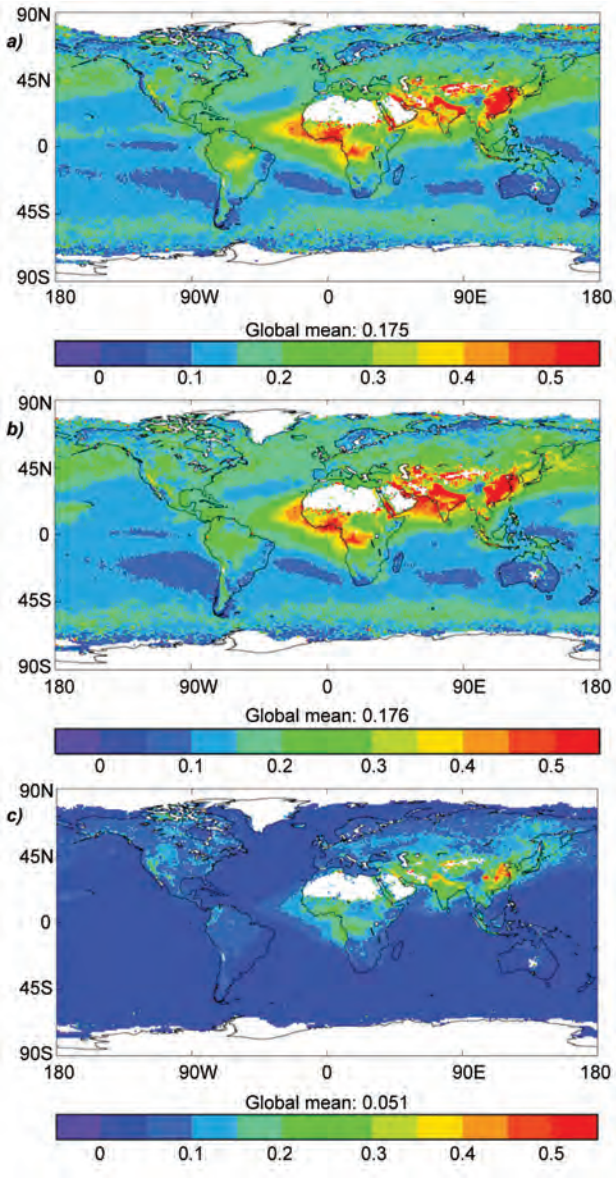

Fig. 2.32. Annual mean total aerosol optical depth derived from the MODIS *Aqua* sensor for (a) 2007, (b) 2008. (c) The anthropogenic aerosol optical depth derived from MODIS aerosol optical depths and fine-mode fractions for 2008, following Bellouin et al. (2008). Missing data areas are white.

Decreases (increases) in sulfur dioxide emissions over Europe and eastern Asia continue to be linked to increases (decreases) in surface solar radiation leading to brightening (dimming) (e.g., Wild et al. 2005). These dimming/brightening features are explicitly modeled in climate scenarios by including the effects of aerosol on radiation as shown in Fig. 2.33. Over Europe the brightening since the mid-1980s evident in the observations and in the modeling shown in Fig. 2.33 also appears well correlated with changes in atmospheric visibility (e.g., Vautard et al. 2009). The analysis of visibility trends attributes some, but not all, of the recent warming trend in the region to this phenomenon.

3) Stratospheric ozone—M. Weber

The Antarctic ozone hole area with total column ozone below 220 DU reached a maximum of 26 million km^2 by the end of September 2008; among the largest on record (www.temis.nl/protocols/o3hole/data/fd-o3area220.pdf). October total ozone above Antarctica and the tip of South America was up to 30 DU below the long-term mean. The annual anomaly was negative for most parts of the globe except for a narrow band in the tropics and a small region near the North Pole with positive anomalies of up to 10 DU (Plate 2.1, panel 9). Large negative annual anomalies were observed above Russia due to a shift of the Arctic polar vortex into this region during spring as well as lower ozone during fall. The positive tropical anomaly is related to the QBO (Baldwin et al. 2001), which was mainly in the west phase near 50 hPa. The QBO signal as well as the 11-yr solar cycle signature in the tropics is clearly evident in the total ozone anomaly time series (Fig. 2.34).

The long-term evolution of total ozone (Fig. 2.34) is dominated by lower stratospheric ozone (~30–100 hPa or 15–25 km) and can be divided into two phases. A steady decline at mid- to high latitudes from satellite record inception lasted until about the mid-1990s, followed by a sharp increase, then leveling off in recent years in the Northern Hemisphere and a leveling off with some enhanced interannual variability in the Southern Hemisphere (Fig. 2.35). Important factors are the 11-yr solar cycle, major volcanic eruptions, the QBO, and chemical ozone loss (Staehelin et al. 2001). The total ozone changes since the mid-1990s can be attributed in part to changes in the halogen load [section 2f1(iv); Dhomse et al. 2006; Froidevaux et al. 2006; Newman et al. 2006, 2007; Stolarski and Frith 2006; Yang et al. 2005]. However, changes in stratospheric circulation pattern and atmospheric dynamics, for example, Brewer–Dobson

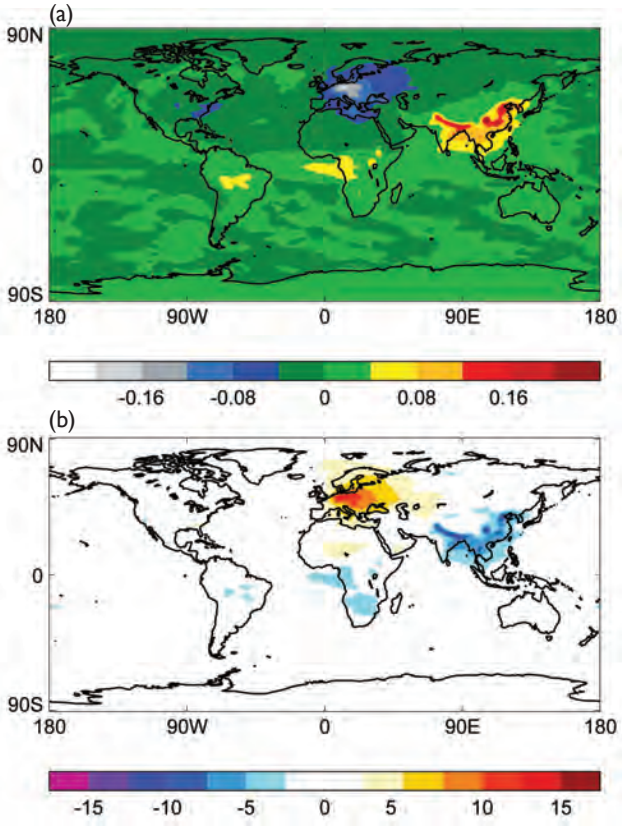

Fig. 2.33. (a) The change in aerosol optical depth simulated by the Met Office HadGEM1 over the period 1980 to 2000. Blue and gray represent a decrease in aerosol optical depths over Europe and the eastern United States due to more stringent emission controls, while red and yellow represent emissions from increasingly industrialized regions. (b) The modeled change in sunlight received at the surface (W m^{-2}) for the same period—"brightening" is shown in yellow/orange, while "dimming" is shown in the blue colors.

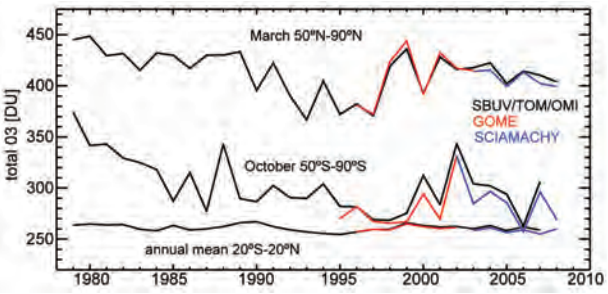

Fig. 2.34. Time series of SBUV/TOMS/OMI (black), GOME (red), and SCIAMACHY (blue) total ozone in the bands 50°–90°N in Mar, 20°S–20°N (annual mean), and 50°–90°S in Oct. Anomalies were calculated from area-weighted monthly mean zonal mean data in 5° latitude steps by removing the seasonal mean from the period 1979–89.

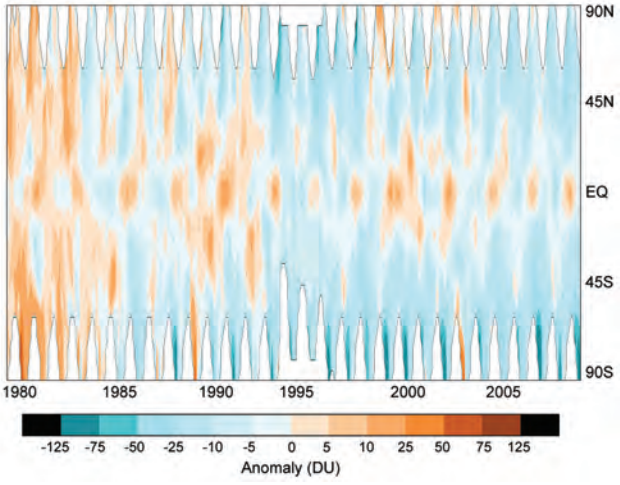

Fig. 2.35. Time variation (1979–2008) of zonally averaged total ozone anomalies. Anomalies are based on the merged SBUV/TOMS/OMI up to Jun 1995 (Frith et al. 2004), GOME from Jul 1995 to May 2003, and SCIAMACHY data from Jun 2003 to Dec 2008 (Weber et al. 2007).

circulation (Weber et al. 2003; Dhomse et al. 2006), teleconnection patterns such as the North Atlantic Oscillation (Appenzeller et al. 2000; Orsolini et al. 2004), and atmospheric advection (Wohltmann et al. 2007), all contribute to winter ozone transport from the tropical production region into middle and high latitudes and explain the large observed interannual variability in extratropical ozone (Fig. 2.35). A record-high chemical ozone loss in Arctic winter 2004/05 (Rex et al. 2006; Newman and Rex 2007) and record-size ozone hole above Antarctica in 2006 indicate that stratospheric halogen load still remains high. The rate of recovery in coming decades will strongly depend on the influence of climate change on stratospheric circulation and temperatures in addition to the expected decrease in ozone-depleting substances (Waugh et al. 2009).

The upper stratosphere is a more favorable region to investigate ozone recovery because long-term changes are larger than observed in column ozone and atmospheric dynamics are less influential (Newchurch et al. 2003). By the end of the 1990s ozone near 40-km altitude had decreased by ~8% $decade^{-1}$ at middle latitudes and then leveled off after that or slightly increased, in agreement with changes in the halogen load (Steinbrecht et al. 2009; Jones et al. 2009). In this region an eventual "super recovery" (Newman and Rex 2007) to ozone levels greater than 1960 levels can be expected if stratospheric temperatures continue to cool (Eyring et al. 2006). Surprisingly, there are indications that upper stratospheric temperatures

near 40-km altitude have not changed significantly over the past 20 yr (Steinbrecht et al. 2009), though temperature trends in this altitude region are not consistent among different datasets (section 2b3).

g. Land surface properties

1) Alpine glaciers and ice sheets—M. S. Pelto

The WGMS (WGMS 2007, 2008) provides annual global indices based on alpine glacier mass balance and terminus position, as these reflect annual volume change (Oerlemans 1994). However, a 9-month time lag prevents immediate assessment of the global state of alpine glaciers in 2008.

Worldwide retreat of mountain glaciers is one of the clearest signals of climate change (Haeberli and Hoelzel 1995). It reflects strongly negative mass balances over the last 30 yr (WGMS 2007). Mass balance is the most appropriate climate parameter for glaciers because it is an annual integral of local weather conditions (Pelto and Hedlund 2001). The change in glacier length is a smoothed and delayed response to the mass balance changes (Haeberli and Hoelzle 1995). The recent rapid retreat and prolonged negative balances have led to some glaciers disappearing (Pelto 2006).

Glacier mass balance is the difference between accumulation and ablation. Variations in temperature and/or snowfall alter the mass balance. A glacier with a sustained negative (positive) balance will retreat (advance) to reestablish equilibrium by decreasing (increasing) the area at lower elevations where ablation is highest. If a glacier lacks a consistent accumulation zone, it is in disequilibrium with climate and will disappear (Pelto 2006; Paul et al. 2007).

In 2007 the mean mass balance of all the WGMS reporting glaciers was −528-mm water equivalent; it was −673 mm for 30 reference glaciers with 30 yr of record, the 17th consecutive year of negative mass balance (Fig. 2.36a). A loss of 0.9 m of water equivalent is the same as the loss of 1.0 m of glacier thickness, since ice is less dense than water. The trend demonstrates why alpine glaciers are currently retreating. The cumulative loss of the last 30 yr (Fig. 2.36b) is the equivalent of cutting a 12–14-m-thick slice off of the average glacier. The trend is remarkably consistent from region to region (WGMS 2007), and the results from the 30 reference glaciers are not appreciably different from those for all monitored glaciers (Fig. 2.36b).

The WGMS glacier terminus position data overemphasize the European Alps, but the overall global and regional records are very similar, except for New Zealand. The proportion of advances in Europe, Asia, and North America reached a minimum in 2005 when of 442 glaciers examined, 26 advanced, 18 were stationary, and 398 (90%) retreated. Overall there has been a substantial volume loss of 11% of New Zealand glaciers from 1975 to 2005 (Salinger NWIA).

In 2008 New Zealand snowlines were 130 m above the elevation for equilibrium leading to negative mass balances and a new record minimum total ice volume for the southern Alps since records began in 1976. In Switzerland negative balances ranged from −0.6 to −1.6 m, and of the 80 glacier termini reporting to date 73 were retreating, 2 advancing, and 5 stationary (Bauder, VAW/ETH). In Norway, of 32 glaciers observed in 2008, 24 retreated, 3 advanced, and 5 were stationary (H. Elvehoi, NVE). The Pacific Northwest of North America experienced strong La Niña conditions with extra snowfall, so mass balances of North Cascade and southeast Alaska glaciers were positive in 2008.

In northern Greenland, ice melt in 2008 lasted 18 days longer than the previous maximum and the melt

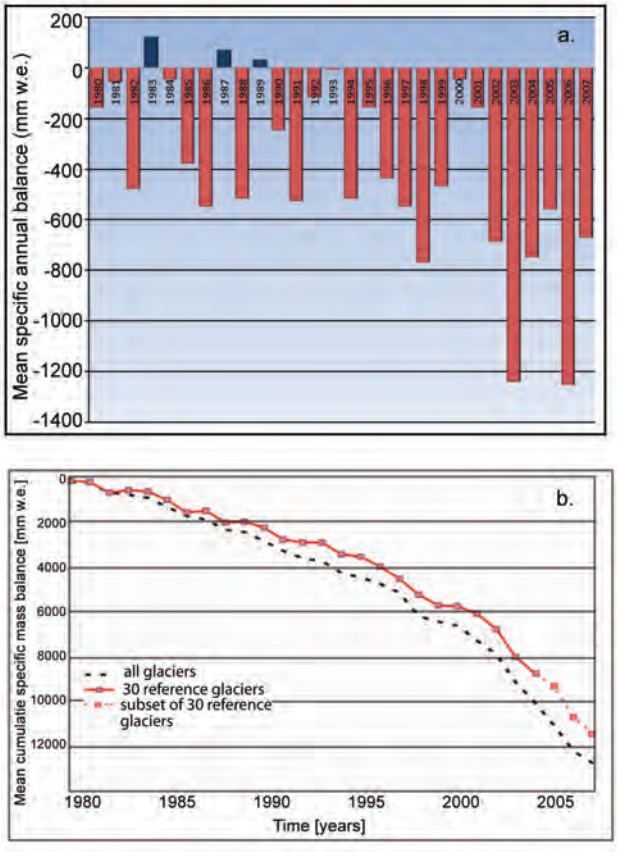

Fig. 2.36. (a) The mean annual mass balance (mm water equivalent) of 30 WGMS reference glaciers, 1980–2007. (b) The mean cumulative mass balance for the 30 reference glaciers and all monitored glaciers. The dashed line is for subset of 30 reference glaciers because not all 30 glaciers have final data for the last few years.

index was 300% of the 1979–2007 average (Tedesco et al. 2008). The record ablation in northern Greenland reflected regional warmth that led to the breakup of 29 km^2 of the floating terminus lobe of Petermann Glacier (Box and Howat, Ohio State), as well as the breakup of Arctic ice shelves on the north coast of Ellesmere Island. Ward Hunt lost 22 km^2, Serson Ice Shelf lost 122 km^2—60% of its area—and Markham lost all 50km^2 of its area (Muller, Trent University).

In Antarctica, Wilkins ice shelf lost 400 km^2 in a rapid February collapse. Humbert and Braun (2008) noted that ongoing thinning had preconditioned it for collapse and that existing rifts in February 2008 suggested that an additional 2000 km^2 was in imminent danger of collapse. During the austral winter an additional 1350 km^2 was lost.

2) Land cover—A. S. Belward, E. Bartholomé, F. Achard, and A. B. Brink

We have begun to make significant progress in documenting the climate-forcing effects of land cover, through increasingly accurate mapping of the global distribution of land-cover types and ongoing changes. At the turn of the millennium a quarter of the land surface was unvegetated (barren, permanent snow and ice, or urban), 30% was grass and shrubland, 29% was forest, and the remaining 16% was devoted to agriculture (Bartholomé and Belward 2005; Fig. 2.37).

In 2008 the U.S. Geological Survey made the Landsat archives—which extend back to 1972—freely available. These data are being used to measure rates and patterns of land cover change, first on a continental and pan-tropical scale, and eventually glob-

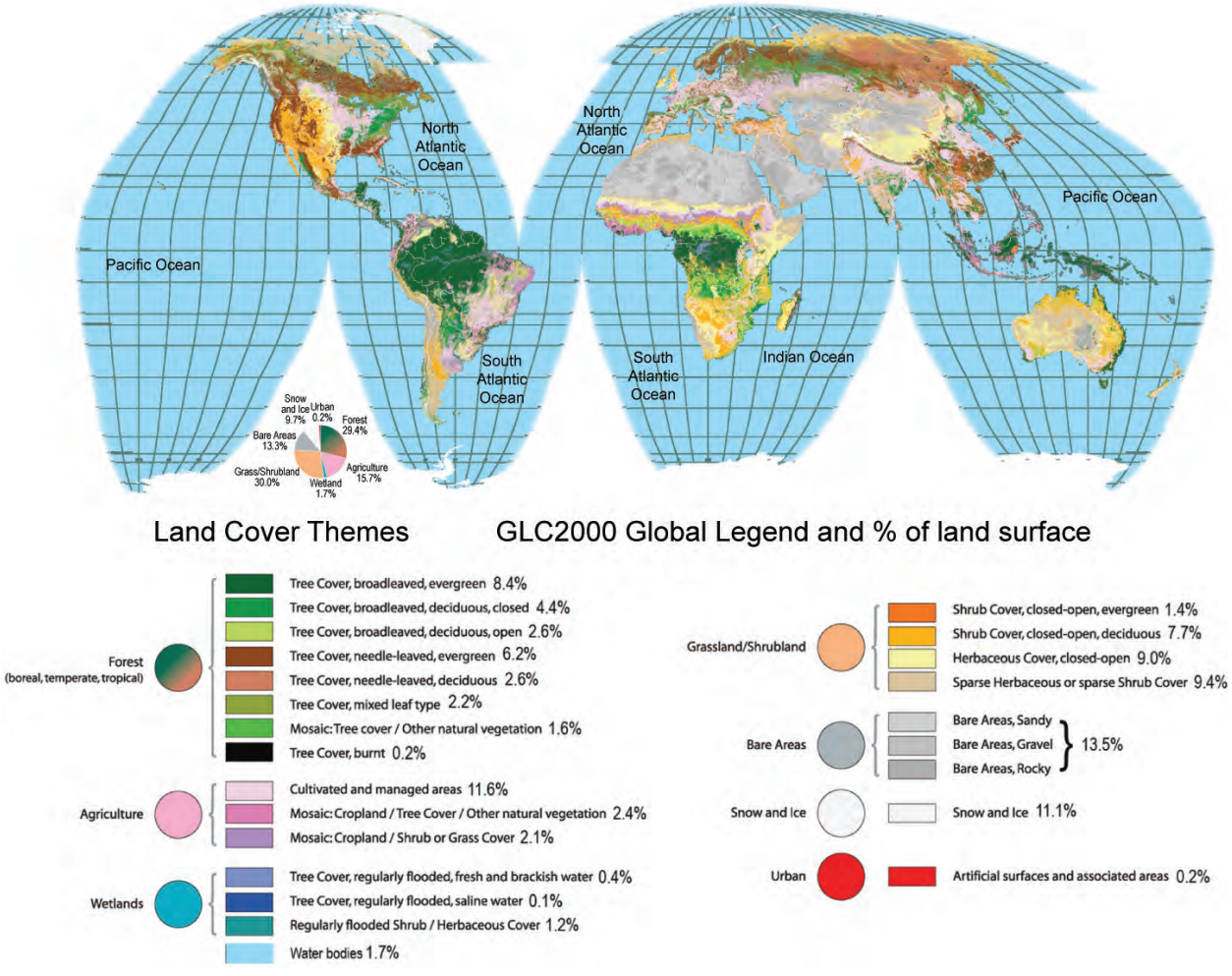

Fig. 2.37. Global land cover at the turn of the millennium: 22 land-cover classes, legend compatible with the FAO Land Cover Classification System (Di Gregorio and Jansen 2000). Projection Interrupted Goode Homolosine Classification derived from daily SPOT VGT satellite observations, 1 × 1 km grid cell, between Nov 1999 and Dec 2000. Map and independent reference data agree 68.6% of the time (Mayaux et al. 2006). Twenty-two percent of the misclassified areas occur in the mixed classes (e.g., some areas known from reference data to be broad-leaved deciduous forest have been mapped as mixed forest).

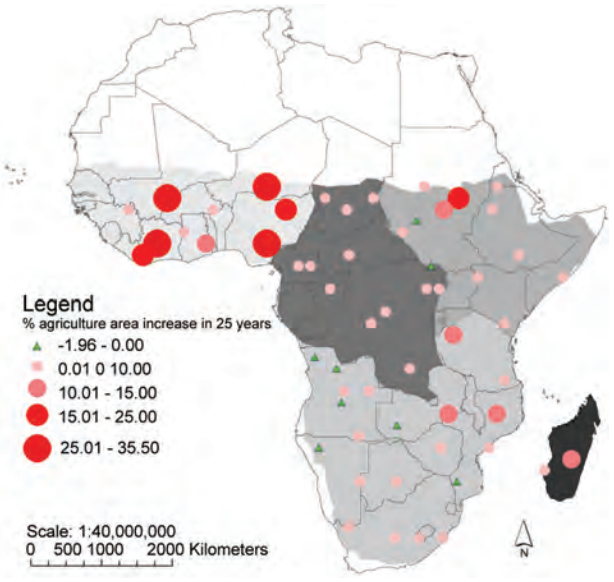

Fig. 2.38. Conversion of natural vegetation to agriculture and reversion of agriculture to natural vegetation between 1975 and 2000 for Africa; rates range from −1.96% to 35.5%

ally. Results for Africa, shown in Fig. 2.38, indicate that since 1975 around 5 million hectares of Africa's natural vegetation have been converted to agriculture each year. This affects albedo, roughness, evapotranspiration, carbon exchange, and aerosol emissions on a continental scale, though the magnitude of the effects relative to natural variability and other external forcing influences has yet to be determined. "Hotspots" of savanna clearance in West Africa are particularly evident, as are the low rates of change in the African humid forest biome (Brink and Eva 2008).

Using a combination of Landsat and MODIS data, Hansen et al. (2008) estimated humid tropical forest clearance between 2000 and 2005 to be 27.2 million hectares or a 2.36% reduction in area. Forest clearing is highly localized, with 55% of the loss being concentrated in just 6% of the humid tropical forest biome—mostly in Latin America and southeast Asia. The Americas lost 2.56% of their humid tropical forest between 2000 and 2005 and Asia lost 2.9%, while Africa lost less than 0.8%.

The ESA has released new global land cover data for 2005, based on MERIS observations and with a spatial resolution of 300 m (Arino et al. 2008). NASA has released for evaluation a new global land cover dataset for 2001–05 based on MODIS observations at a spatial resolution of 500 m (Strahler et al. 1999). These datasets will form a basis for extending cover-change analysis beyond Africa and the tropics and are evidence of renewed attention to land cover by space agencies. The changes in global land cover reported here are anthropogenic in origin, driven by the increasing need of our growing population for land to supply food, fuel, fiber, and shelter. Land cover is also in part determined by regional climate, and as climates change so too does the distribution of vegetation, barren land, water bodies, snow, and ice. Population growth—and climate change—makes future changes in land cover inevitable.

3) Global vegetation condition—N. Gobron and A. S. Belward

The Fraction of Absorbed Photosynthetically Active Radiation is crucial for the energy and carbon balances of ecosystems. It can be used in quantifying CO_2 assimilation by plants and the release of water through evapotranspiration. Daily observations of FAPAR provide a basis for monitoring the seasonal cycle and long-term trends of vegetation, and the data have been used in diagnostic models, for example, to examine the role of the terrestrial biosphere in climate-carbon feedbacks (Knorr et al. 2007).

Rates of photosynthesis are affected by temperature and precipitation, so favorable temperatures and soil moisture availability (extreme heat and/or drought) are accompanied by higher- (lower-) than-average FAPAR. Other influences on plant physiology and plant health, such as pollution, disease, insect attack, wind-throw, and fire, also affect FAPAR. Such perturbations tend to be episodic, though the savanna fires of Africa, for example, are a yearly feature.

Since 1998 FAPAR has been derived from a range of polar-orbiting platforms (Knyazikhin et al. 1998;

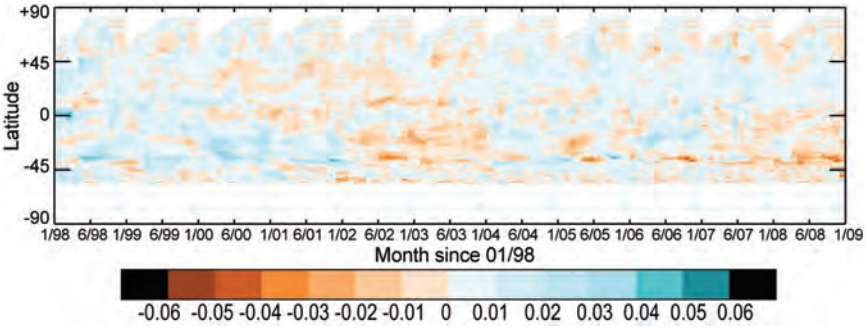

Fig. 2.39. Zonal-average FAPAR anomalies 1998–2008. Values range from −0.06 to 0.06.

Gobron et al. 2006, 2008). Figure 2.39 is derived from SeaWiFS (NASA 1998 to 2006) and MERIS (ESA 2002 to 2008), both of which have been subject to rigorous comparison with reference data (Gobron et al. 2006, 2008). Global vegetation dynamics, as represented by FAPAR, show considerable interannual variations. The Southern Hemisphere generally shows more variability than the Northern Hemisphere, reflecting the greater impact of ENSO events on vegetation at these latitudes. The Northern Hemisphere shows the impacts of the major heat waves of 2003 (Europe) and 2007 (western and central Russia). In 2008 (Plate 2.1, panel 10) the strongest negative anomaly reflected severe drought in Argentina's steppe and grassland. Southeastern Amazonia had negative anomalies, arising partly from intense land-use transformations (Malhi et al. 2008). There were also major negative anomalies in Australia and central Asia. In contrast, much of China, southern Africa's savannas, and northern high latitudes enjoyed better-than-average vegetation vigor in 2008.

FAPAR products (Fig. 2.39), along with reprocessed historical archives and planned missions, have the potential to greatly improve our understanding of vegetation–climate interactions.

Table 2.5. Sources of those datasets used in this chapter that are publicly available for bona fide research purposes.

Source	Datasets
http://www.hadobs.org	HadCRUT3 (surface temperatures), HadAT (radiosonde temperatures), HadSLP2r (SLP and derived indices)[a]
http://www.ncdc.noaa.gov/oa/climate/research/anomalies/anomalies.html	NCDC (surface temperatures)
http://data.giss.nasa.gov/gistemp/	GISS (surface temperatures)
http://www.ncdc.noaa.gov/oa/climate/ratpac/index.php	RATPAC (radiosonde temperatures)
http://earth.geology.yale.edu/~sherwood/radproj/	IUK (radiosonde temperatures)[b]
http://www.univie.ac.at/theoret-met/research/raobcore/	RAOBCORE and RICH (radiosonde temperatures)
http://vortex.nsstc.uah.edu/data/msu/	UAH MSU record (satellite temperatures)
http://www.remss.com	RSS MSU record (satellite temperatures), RSS SSM/I record (winds, precipitation and TCWV over the oceans), TMI and AMSR-E (precipitation)[c]
http://www.star.nesdis.noaa.gov/smcd/emb/mscat/mscatmain.htm	STAR MSU record (satellite temperatures)
On request from junhong@ucar.edu	Land-based GPS TCWV
http://www.geo.unizh.ch/wgms/mbb/mbb10/sum07.html	Glacial Mass Balance data
http://gem.jrc.ec.europa.eu/index.php	Global land cover[a]
http://www.ncdc.noaa.gov/oa/climate/ghcn-monthly/index.php	GHCN monthly (precipitation)[d]
http://www.ncdc.noaa.gov/oa/climate/ghcn-daily/	GHCN daily[d]
http://www.cdc.noaa.gov/data/gridded/data.gpcc.html	GPCC (VasClimO and Full v.3) (precipitation)
http://precip.gsfc.nasa.gov	GPCP (precipitation)
http://www.cpc.noaa.gov/products/global_precip/html/wpage.cmap.html	CMAP (precipitation)
http://climate.rutgers.edu/snowcover	Snowcover extent
http://www.atmos.washington.edu/~ignatius/CloudMap	SOBS cloud
http://www.ssec.wisc.edu/~donw/PAGE/CLIMATE.HTM	HIRS-W cloud
http://isccp.giss.nasa.gov	ISCCP D2 cloud
http://cimss.ssec.wisc.edu/patmosx	PATMOS-x cloud
http://ladsweb.nascom.nasa.gov	MODIS cloud
http://www.cdc.noaa.gov/data/reanalysis	NCEP–NCAR reanalysis
http://www.gth-h.net	Runoff data
http://eosweb.larc.nasa.gov/	CERES EBAF, CERES ERBE-like, and FLASHFlux data (satellite broadband earth radiation budget; outgoing longwave, reflected shortwave, and net radiation)[e]
http://www.esrl.noaa.gov/gmd/aggi/	Greenhouse gas index
http://www.esrl.noaa.gov/gmd/ccgg/trends/	Carbon dioxide monitoring
www.esrl.noaa.gov/gmd/ccgg/towers/	ESRL carbon monoxide monitoring
http://www.cmdl.noaa.gov/odgi/	Ozone-depleting gas index
http://www.esrl.noaa.gov/gmd/dv/ftpdata.html	ESRL halocarbon network
http:// www.iup.uni-bremen.de/gome/wfdoas/	SBUV/TOMS/OMI, GOME, SCIAMACHY ozone
http://fapar.jrc.ec.europa.eu/	FAPAR

[a]Many additional land datasets available
[b]May move as site owner has changed institute
[c]Entire SSM/I record only available on hard disk.
[d]Also other variables
[e]Many additional datasets available; including clouds and aerosols

3. GLOBAL OCEANS—J. M. Levy, Ed.

a. *Overview*—J. M. Levy

As the global ocean observing system matures and climatologies of essential climate variables grow more robust, observations of anomalous departures continue to shed light on the evolving behavior of the coupled ocean–atmosphere system. 2008 was characterized by the following findings.

The global mean SST in 2008 was slightly cooler than that in 2007, largely due to the cooling in the central tropical Pacific, the Arctic Ocean, and the regions extending from the Gulf of Alaska to the west coast of North America. The yearly mean SST anomaly in 2008 was dominated by a negative PDO pattern. The yearly mean PDO index in 2008 was the lowest since 1971.

Global integrals of upper-ocean heat content for the last several years have reached values consistently higher than for all prior times in the record, demonstrating the dominant role of the oceans in the Earth's heat budget. 2008 basin-scale upper-ocean heat content patterns are consistent with current phasing of familiar climate indices such as ENSO.

The basin-averaged latent and sensible heat fluxes in 2008 decreased slightly from 2007, continuing the broad downward trend that started in 1999. There seems to be a tendency toward reversing the upward trend that had dominated the decades of the 1980s and 1990s. Changes in latent and sensible heat fluxes in the Pacific responded to the SST anomalies of the cool PDO phase, with enhanced heat loss over positive SST anomalies and reduced heat loss over negative SST anomalies. By contrast, the ocean heat fluxes in the Atlantic Ocean were an important forcing for SST variability: SST increased as a result of reduced heat loss at the sea surface and decreased as a result of enhanced heat loss at the surface.

Tropical cyclone heat potential values in the north-central Gulf of Mexico were lower in August 2008 than in August 2005.

Outside the tropics, the anomalously salty surface salinity values in climatologically drier locations and anomalously fresh values in rainier locations observed in recent years generally persisted in 2008, suggesting an increase in the hydrological cycle, consistent with climate model predictions for global warming scenarios. Within the tropics, 2008 sea surface salinity anomalies can be largely related to recent La Niña conditions.

Eastward surface current anomalies in the tropical Pacific Ocean in early 2008 played a major role in adjusting the basin from strong La Niña conditions to ENSO-neutral conditions by July–August. Long-term trends in geostrophic eddy kinetic energy continue to indicate interannual-to-decadal shifts in major current systems such as the Gulf Stream and the Brazil–Malvinas Confluence.

Direct observations of the strength of the meridional overturning circulation show substantial variability on short time scales, with some evolving evidence of a pronounced seasonal variation. Indirect observations from subsurface water properties suggest a recent strengthening of deep-water formation in the Labrador Sea and a decrease in deep-water transport from the Antarctic that is both warmer and fresher than in the past.

The La Niña event of 2007–08 affected not only regional sea level anomalies but GMSL as well. GMSL has been persistently low during the La Niña event relative to a linear trend of approximately 3.3 mm yr^{-1}. The correspondence between GMSL and the Multivariate ENSO Index highlights the strong influence of ENSO variability on global sea level. Once this interannual variability is accounted for, the inferred rate of GMSL change remains remarkably constant.

The global mean air–sea CO_2 flux for the period 1983 to 2007, including ENSO effects, gives an average uptake of 1.74 Pg-C yr^{-1}. The global mean CO_2 uptake for 2007 is estimated to be 1.67 Pg-C, about 0.07 Pg-C lower than the long-term average, making it the third-largest anomaly determined since 1983. Unlike long-term findings, the North Atlantic has not had the largest increase in anthropogenic carbon storage over the last decade. The rate of carbon inventory increase in the eastern Indian Ocean was significantly higher between 1995 and 2008 than it was between 1978 and 1995.

Global phytoplankton chlorophyll concentrations were slightly elevated in 2008 relative to 2007, but regional changes were substantial (ranging to about 50%) and followed long-term patterns of net decreases in chlorophyll with increasing sea surface temperature.

b. *Sea surface temperatures in 2008*—Y. Xue and R. W. Reynolds

The global SSTs in 2008 were analyzed using the OISST v.2, which is a weekly analysis on a 1° grid derived by combining in situ and satellite observations for the period of November 1981 to present (Reynolds et al. 2002). To put the 2008 SST in a historical perspective, we also analyzed the ERSST v.3b, which is a monthly merged land–ocean surface temperature analysis on a 2° grid for the period of 1854 to present (Smith et al. 2008). SSTA were

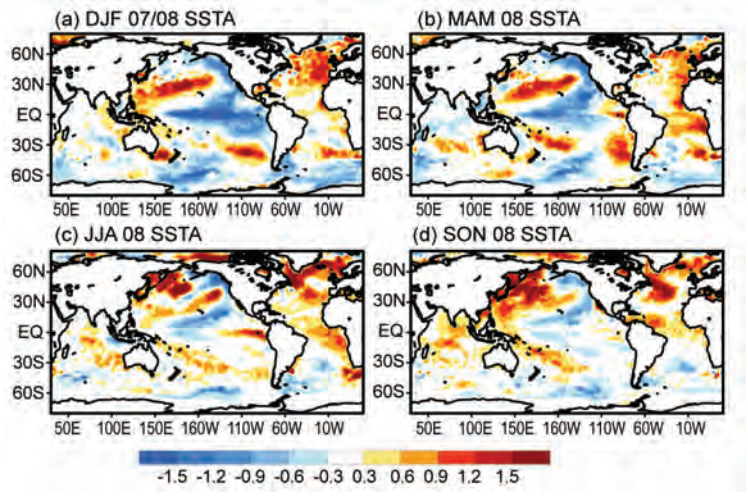

Fig. 3.1. Seasonal mean SST anomalies (°C) for (a) Dec 2007 to Feb 2008, (b) Mar to May 2008, (c) Jun to Aug 2008 ,and (d) Sep to Nov 2008. SSTs are the monthly fields interpolated from the weekly 1° OI analyses of Reynolds et al. (2002). All anomalies are defined as departures from the 1971–2000 climatology (Xue et al. 2003).

defined as departures from the 1971–2000 climatology described by Xue et al. (2003).

The seasonal evolution of SSTAs in 2008 is shown in Fig. 3.1 The SSTAs were generally positive in the Atlantic. In the Pacific basin, SSTAs were negative in the tropics related to the termination of a moderate La Niña. The 2007–08 La Niña started in August 2007, reached its mature phase during December 2007 to February 2008, and then dissipated quickly with the return of ENSO-neutral conditions in June 2008. La Niña conditions, however, reemerged during November 2008 to January 2009 (see NOAA's ENSO definition at www.cpc.ncep.noaa.gov/products/analysis_monitoring/ensostuff/ensoyears.shtml). Both the demise and the reemergence of La Niña lagged associated surface current anomalies (see Fig. 3.14 and accompanying discussion).

During the first half of 2008, strong negative anomalies were present off the west coast of North America, while positive anomalies occurred along a rough sideways "V" pattern connecting the far western equatorial Pacific to 160°W at both 30°N and 30°S. Strong positive anomalies were also present north of 30°N in the Atlantic and western Pacific. These northern positive anomalies were strongest between July and October, with associated positive anomalies in the Arctic Ocean between the date line and 120°W. The Arctic Ocean SST was above normal in 2008, but it was about 1.3°C lower than its historical high of 2.5°C observed in 2007 (not shown). Consistently, the sea-ice extent in 2008 was larger than its historical low in 2007 (http://nsidc.org/arcticseaicenews/index.html).

In the North Atlantic, SST has been persistently above normal since 1995. In the tropical North Atlantic, SST was near normal in the first half of 2008 but increased to about 0.6°C above normal during the Atlantic hurricane season from June to November (see details in the Tropical Cyclones section of chapter 4 of this report). In the eastern tropical Atlantic, SST has been persistently above normal during the past three years.

The yearly mean SSTA in 2008 was dominated by a negative PDO pattern (Mantua et al. 1997), which featured below-normal SST near the Gulf of Alaska and along the west coast of North America and above-normal SST in the central North Pacific (Fig. 3.2a). (The PDO spatial pattern and associated temporal PDO index are defined at http://jisao.washington.edu/pdo.) Monthly and annual time series of the PDO index are shown in Fig. 3.3. The negative PDO phase began in September 2007 and

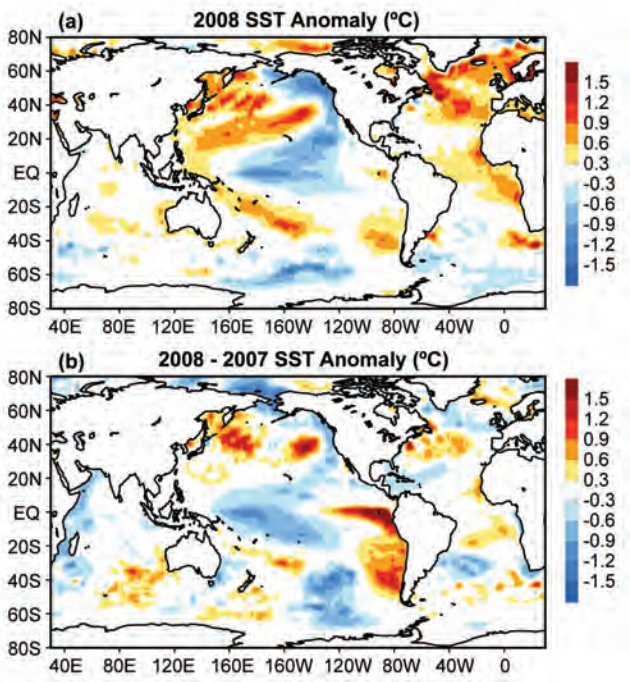

Fig. 3.2. (a) Yearly mean SSTA in 2008 and (b) SSTA differences between 2008 and 2007. SSTs are the monthly fields interpolated from the weekly 1° OI analyses of Reynolds et al. (2002). All anomalies are defined as departures from the 1971–2000 climatology (Xue et al. 2003).

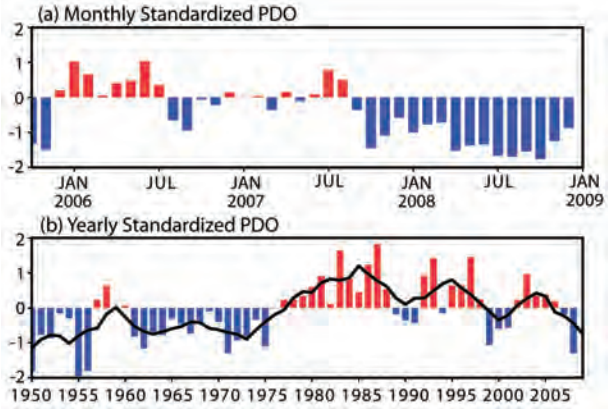

Fig. 3.3. (a) Monthly standardized PDO index (bar) in the past four years and (b) yearly mean of the monthly PDO index (bar) overlapped with the 5-yr running mean of the index (black line) in 1950–2008. The PDO index was downloaded from University of Washington at http://jisao.washington.edu/pdo.

persisted through calendar year 2008 (Fig. 3.3a). The longer-term yearly mean PDO index illustrates prominent low-frequency variability with a downward trend from the mid-1980s to the present (Fig. 3.3b). Interestingly, the PDO value in 2008 was the lowest since 1971. Along with the negative PDO phase, upwelling along the west coast of North America was also well above normal during the 2008 upwelling season, which favored high biological productivity during the past year (Frank Schwing 2009, personal communication).

The global mean SST in 2008 was slightly cooler than that in 2007 (Fig. 3.4a), largely due to the cooling in the central tropical Pacific, the Arctic Ocean, and the regions extending from the Gulf of Alaska to the west coast of North America (Fig. 3.2b). The 2008 minus 2007 SSTA differences largely resemble the negative PDO pattern, which is also reflected in the anomaly differences of surface latent plus sensible heat flux (Fig. 3.8b). The tripole SST pattern in the North Atlantic is also reflected in the heat fluxes.

The global mean SST in 2007 and 2008 was much cooler than that during 2002–06 (Fig. 3.4a). The cooling in the past two years was largely due to the cooling in the tropical Pacific (Fig. 3.4b), which is associated with the 2007–08 La Niña and persistent negative PDO (Fig. 3.3a). The cooling in the tropical Pacific contributed to the cooling in the global tropical oceans in the past two years, although the contributions from the tropical Indian and Atlantic Oceans were less evident (Figs. 3.4c–e). From a historical perspective, the global mean SST was below normal (1971–2000 average) during 1950–76 and has been persistently above normal since 1997. Although the global mean and tropical mean SSTAs all have a prominent upward trend from 1950 to 2008, similar trends are not evident in the North Pacific and North Atlantic (Figs. 3.4f–g).

c. Ocean heat content—G. C. Johnson, J. M. Lyman, J. K. Willis, S. Levitus, T. Boyer, J. Antonov, C. Schmid, and G. J. Goni

Storage and transport of heat in the ocean are central to aspects of climate such as El Niño (e.g., Zebiak 1989), the North Atlantic Oscillation (e.g., Curry

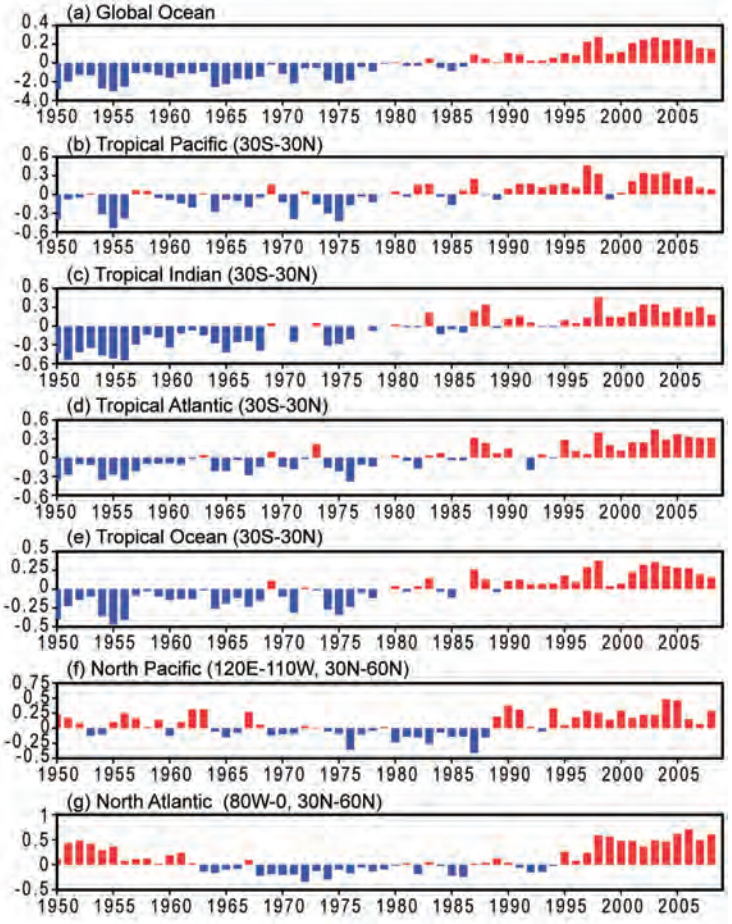

Fig. 3.4. Yearly mean SST anomalies (°C) averaged in (a) the global ocean, (b) tropical Pacific Ocean, (c) tropical Indian Ocean, (d) tropical Atlantic Ocean, (e) all three tropical oceans, (f) North Pacific, and (g) North Atlantic in 1950–2008. SSTs are the ERSST v.3b of Smith et al. (2008). All anomalies are defined as departures from the 1971–2000 climatology (Xue et al. 2003).

and McCartney 2001), hurricanes (e.g., Mainelli et al. 2008; Vecchi et al. 2008), sea level rise (e.g., Domingues et al. 2008), and global warming (e.g., Hansen et al. 2005).

We begin by discussing an estimate of upper (0–750 m) OHCA for the period 1 January–31 December 2008 (Fig. 3.5a) computed from a combination of in situ ocean temperature data and satellite altimetry data, following Willis et al. (2004) but relative to a 1993–2008 baseline, hereafter the combined estimate. We also discuss changes in the combined estimate between 2008 and 2007 (Fig. 3.5b). We contrast these combined estimate changes with changes of mixed layer OHCA (Fig. 3.6) derived from in situ observations (Schmid 2005), hereafter the mixed layer estimate. We also put the estimates of recent upper-OHCA variability into a longer-term context using a time series of global integrals of 0–700-m in situ OHCA from 1955 through 2008 (Fig. 3.7), a time period much longer than the satellite altimeter record, estimated following Levitus et al. (2009), hereafter the in situ estimate.

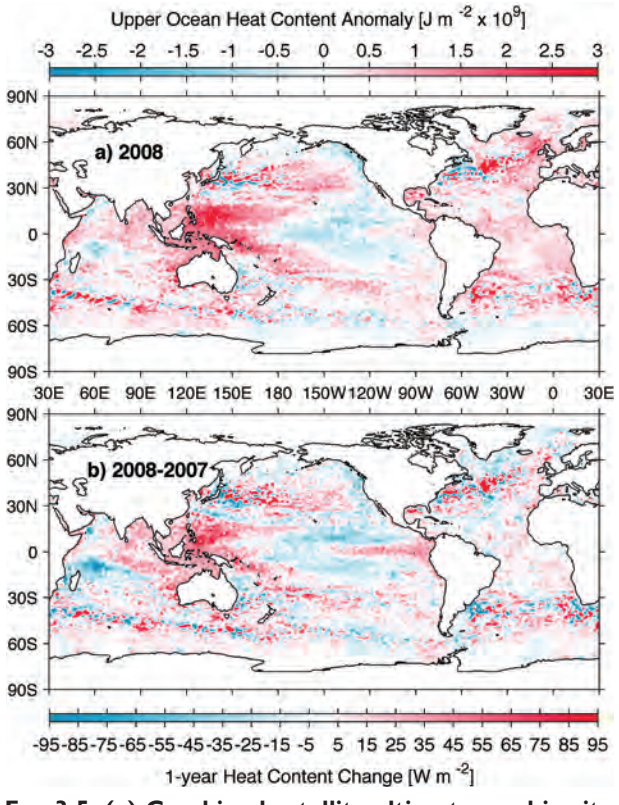

Fig. 3.5. (a) Combined satellite altimeter and in situ ocean temperature data estimate of upper- (0–750 m) ocean heat content anomaly OHCA (10^9 J m^{-2}) for 2008 analyzed following Willis et al. (2004) but relative to a 1993–2008 baseline. (b) The difference of 2008 and 2007 combined estimates of OHCA expressed as a local surface heat flux equivalent (W m^{-2}). For panel comparisons, note that 95 W m^{-2} applied over one year results in a 3 × 10^9 J m^{-2} change of OHCA.

In recent years many of the globally distributed in situ subsurface ocean temperature data are from Argo (Roemmich et al. 2004). Data from Argo floats with the potential for as yet uncorrected systematic pressure biases (www.argo.ucsd.edu/Acpres_drift_apex.html) have been removed from the combined estimate presented here. In addition, annual estimates of XBT fall-rate corrections have been applied for deep- and shallow-probe data following Wijffels et al. (2008) for the combined estimate, but with no XBT data used after 2005. A somewhat different set of corrections to MBTs and XBTs for all years is applied for the 0–700-m in situ estimate following Levitus et al. (2009). The mixed layer estimate uses Argo and GTSPP (www.nodc.noaa.gov/GTSPP/) data subject to Argo real-time quality-control criteria followed by local statistical checks to eliminate remaining outliers. Details of all the fields analyzed here may change after data from floats with potential pressure biases are corrected and made available, after more real-time data are subject to delayed-mode scientific quality control, and as XBT and MBT corrections improve.

The 2008 0–750-m combined estimate of OHCA (Fig. 3.5a) shows eddy and meander variability down to the 100-km mapping scales, as does, to a greater extent, the difference of the 2008 and 2007 combined estimates (Fig. 3.5b). Strong small-scale spatial variability in OHCA fields is associated with the western boundary currents in every gyre, as well as the Antarctic Circumpolar Current. The difference in combined estimates between 2008 and 2007 (Fig. 3.5b) illustrates the large year-to-year variability in ocean heat storage, with changes reaching or exceeding the equivalent of a 95 W m^{-2} magnitude surface flux applied over one year (~3 × 10^9 J m^{-2}). Ocean advection likely plays a significant role in many of these changes. Upper OHCA, deep variability, freshwater, and mass signals all contribute to sea level anomalies. Despite this, there are many large-scale visual similarities between upper-OHCA (Fig. 3.5) and sea level (Fig. 3.21) fields in 2008, even relative to their differing baseline periods.

Large-scale patterns are evident in OHCA for 2008 (Fig. 3.5a) and its difference from 2007 (Fig. 3.5b). The central equatorial Pacific is still low in heat content, as it was during 2007 due to a La Niña (Levinson and Lawrimore 2008), and the off-equatorial central and eastern tropical Pacific OHCA values also fell from 2007 to 2008. However, the eastern equatorial Pacific heat content has risen to values slightly above

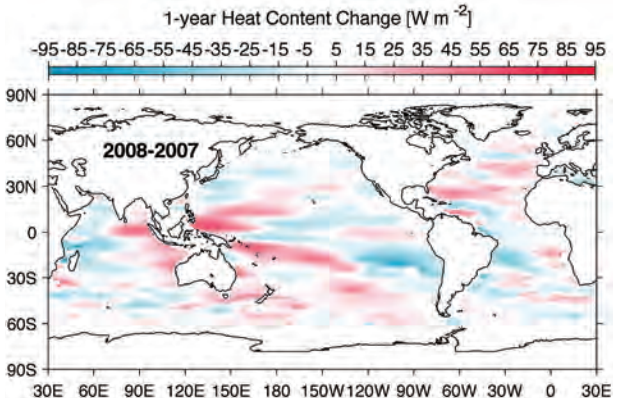

Fig. 3.6. Change of ocean mixed layer heat content estimated following Schmid (2005) expressed as a surface heat flux equivalent (W m^{-2}). The map is based on subtraction of a yearly mean of ocean mixed layer content for calendar year 2008 from that for calendar year 2007.

the mean in that interval, and the western tropical Pacific heat content has risen to levels well above the mean. While the annual averaging period presented here is too long for detailed study of the movement of heat associated with ENSO dynamics, certainly the change on the equator and perhaps those in the off-equatorial regions are related to those processes (e.g., Zebiak 1989).

Like the western tropical Pacific, the northeastern Indian Ocean continued gaining heat between 2007 and 2008 (Fig. 3.5b), as both regions did between 2006 and 2007 (Levinson and Lawrimore 2008). As a result, OHCA in the northeastern Indian Ocean in 2008 is above the mean (Fig. 3.5a), contrasting clearly with below-average values found in 2006 (Aguez et al. 2007). Around 10°S in the Indian Ocean heat was lost in the western half and gained in the east from 2007 to 2008 (Fig. 3.5b), largely the reverse of the tendency in this region from 2006 to 2007 (Levinson and Lawrimore 2008), leaving the area around the Seychelles slightly below the mean for OHCA in 2008 (Fig. 3.5a).

The North Pacific shows high OHCA in its center in 2008, and low OHCA off the west coast of North America (Fig. 3.5a). This pattern is consonant with a strongly negative Pacific decadal oscillation (Mantua et al. 1997) during 2008, and hence mirrored in sea surface temperature anomalies for 2008 (Fig. 3.2). The band of high OHCA near 35°S in the South Pacific (Fig. 3.5a) appears to have steadily migrated south from lower subtropical latitudes in 2007 (Fig. 3.5b), and even lower tropical latitudes in 2006 (Aguez et al. 2007).

In the subpolar North Atlantic, the Labrador and Irminger Seas cooled between 2007 and 2008 (Fig. 3.5b), returning OHCA values in these areas to near the 1993–2008 mean (Fig. 3.5a), consonant with a return of deep wintertime convection there in early 2008 (Våge et al. 2009). A strong warming centered near 45°N, 45°W (Fig. 3.5b) suggests a local northwestward shift in the North Atlantic Current in 2008 relative to the previous year. The continued high OHCA values in the eastern subpolar North Atlantic (Fig. 3.5a) suggest that subtropical influences are still strong there, consistent with anomalously salty surface conditions in that region in 2008 (Fig. 3.13). The subtropical and tropical Atlantic in both hemispheres remains slightly warmer than the mean, with little change from 2007 to 2008.

Near the Antarctic Circumpolar Current, OHCA is highly variable (Fig. 3.5a) and appears anomalously cool in the Pacific, warm in the Indian, and mixed in the Atlantic in 2008, a less coherent pattern than in the previous few years (Arguez et al. 2007; Levinson and Lawrimore 2008). This lack of coherence may be related to a shift in the Antarctic Oscillation Index to positive in 2008, after several years of negative values.

A map of year-to-year changes in mixed layer OHCA (Fig. 3.6) shows many similarities to the map of 2008–07 0–750-m combined OHCA (Fig. 3.5b). However, the figures are not directly comparable. The mixed layer map (Fig. 3.6) is much smoother than the analogous combined OHCA map (Fig. 3.5b) because

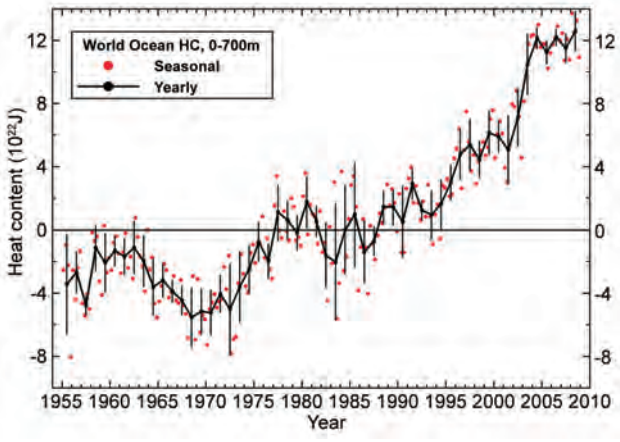

Fig. 3.7. Time series of quarterly (red dots) and annual average (black line) global integrals of in situ estimates of upper OHCA (10^{22} J) for the 0–700-m layer from 1955 to 2008, following Levitus et al. (2009). Error bars for the annual values are 1 std dev of the four quarterly estimates in each year. Additional error sources include sampling errors (Lyman and Johnson 2008) and remaining uncorrected instrument biases (Levitus et al. 2009).

the former map uses much longer decorrelation length scales (20° lon and 4° lat) than the latter. The difference in scales arises because the combined maps of 0–750-m OHCA use altimeter data to increase resolution and fill in where in situ data are sparse.

These methodological differences notwithstanding, the magnitudes of year-to-year changes in the mixed layer (Fig. 3.6) are generally smaller than those from the combined estimates for 0–750 m (Fig. 3.5b). This reduction in magnitude is expected because year-to-year OHCA changes can extend below the mixed layer. In addition, there are a few regions with qualitative differences in the two quantities, such as on either coast of South America around 20°S, where the mixed layer heat content anomaly has fallen over the course of a year (Fig. 3.6), but there is no such change evident in the combined map of upper OHCA (Fig. 3.5b). Changes in mixed layer depth can have large impacts on the heat content in the mixed layer even if there is no change in the mixed layer temperature, and that fact could be the reason for such striking differences.

Over a multidecadal period, upper-ocean estimates (0–700 m) of in situ ocean heat content following Levitus et al. (2009) reveal a large increase in global integrals of that quantity (Fig. 3.7). Global integrals of the in situ estimates for the last several years have reached consistently higher values than for all prior times in the record. The recent several-year plateau has smaller variability than the rest of the record, probably because of the effects of the excellent data coverage (Lyman and Johnson 2008) as provided by Argo floats (Roemmich et al. 2004). However, there are also long stretches in the record prior to 2000 that also exhibit little upward trend in OHCA.

Finally, around Antarctica and in the northern North Atlantic, near-surface water becomes dense enough to sink to the abyssal ocean, spreading around the globe (e.g., Lumpkin and Speer 2007). The ocean below the 2-km target depth for Argo profiles is not frequently sampled, making quantitative annual global estimates of abyssal ocean heat content changes impossible. However, there is observational evidence that the deep oceans, including the North Atlantic, have gained heat at least to 3,000 m over the past few decades (Levitus et al. 2005). Furthermore, analyses of recent repeated hydrographic observations in the deep South Atlantic (Johnson and Doney 2006), Pacific (Johnson et al. 2007), and South Indian Oceans (Johnson et al. 2008a) suggest that Antarctic Bottom Water has warmed over the last decade and that this warming could make a contribution to the global heat budget on the order of 10%–20%.

d. Global ocean heat fluxes—L. Yu and R. A. Weller

Much of the solar energy absorbed at the top ocean layer is released back to the atmosphere by two heat exchange processes at the air–sea interface: evaporation that releases latent heat and conduction and convection that releases sensible heat. These air–sea heat exchanges cool the ocean but warm the air, supplying the heat energy needed to drive the atmospheric circulation and global weather patterns. Clearly, air–sea heat fluxes (i.e., the amount of air–sea heat exchange) are a key measure of the role that the ocean plays in global climate, and their changes on short-term and long-term time scales may have important climate implications.

The global distribution of latent and sensible heat fluxes in 2008 (Fig. 3.8a) shows that on an annual basis the largest ocean heat losses occur over the regions associated with major WBCs and their extensions (e.g., the Kuroshio off Japan, the Gulf Stream off the United States, and the Agulhas Current off the African coast). The magnitude of the annual mean LHF + SHF in these regions exceeds 250 W m^{-2}, produced largely during the fall-to-winter seasons by strong winds and cold and dry air masses coming from the land (Bigorre and Weller 2008). The second-largest heat loss (~180 W m^{-2}) is located over the broad subtropical southern Indian Ocean, where the large air–sea heat exchange is sustained primarily by the strong southeast trade winds in the monsoon months June–September.

The estimates of LHF + SHF were produced by the OAFlux project (Yu et al. 2008) at WHOI. The computation of the OAFlux products uses the state-of-the-art bulk flux algorithm version 3.0 by Fairall et al. (2003), with the surface meteorological variables determined from an optimal blending of satellite retrievals and atmospheric reanalysis/forecast models of NCEP and ECMWF. The accuracy of the OAFlux LHF and SHF estimates was evaluated using 105 buoys available over the global oceans (Yu et al. 2008, manuscript submitted to *J. Climate*). The averaged root-mean-square differences between OAFlux and buoy calculated over the buoy locations are 9.6 W m^{-2} for LHF and 2.6 W m^{-2} for SHF.

The plot of the LHF + SHF differences between 2008 and 2007 (Fig. 3.8b) shows that LHF + SHF had significant changes in the tropical Pacific and Indian Oceans. Positive anomalies are observed in the equatorial eastern Pacific and central tropical Indian Oceans, while negative anomalies are found in the central tropical Pacific. These changes appear to result from the direct response of LHF to SST. The equatorial Pacific in the second half of 2008 was in

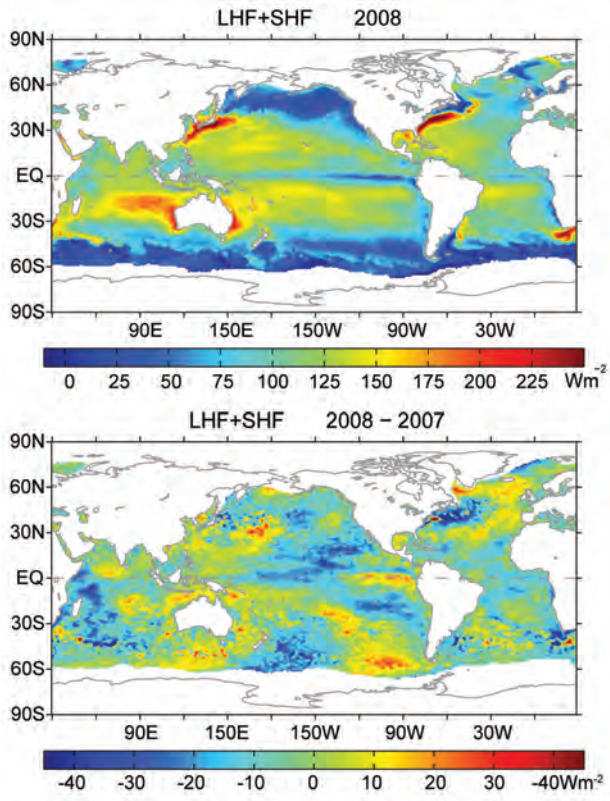

Fig. 3.8. (top) Annual mean latent plus sensible heat fluxes in 2008. The sign is defined as upward (downward) positive (negative). (bottom) Differences between the 2008 and 2007 annual mean latent plus sensible heat fluxes.

ENSO-neutral conditions after a La Niña faded in the spring. The eastern equatorial Pacific warmed following the cool La Niña conditions and the central equatorial Pacific cooled (Fig. 3.2b). Because a warmer (cooler) sea surface increases (reduces) the rate of heat transfer by evaporation, more (less) latent heat was lost in the eastern (central) equatorial Pacific as the basin evolved from a cold ENSO phase to an ENSO-neutral phase. On the other hand, unlike the Pacific counterpart, SST was not the leading cause of the larger LHF in the central tropical Indian Ocean. Persistent dry westerly wind anomalies associated with enhanced convection over the Maritime Continent contributed to a faster rate of evaporation over the warm tropical Indian Ocean waters.

While the tropical Pacific returned to an ENSO-neutral state, the basin-scale pattern of the Pacific was locked in a cool phase of the PDO (Mantua et al. 1997) that started in 2007 (http://jisao.washington.edu/pdo/PDO.latest). The PDO in 2008 was the most negative since 1971. Compared to 2007, SST had trended downward in a much broader area off the coast of North America from Alaska to the equator, forming a cool horseshoe-shape region around a core of warmer SST anomalies to the west (Fig. 3.2b). Interestingly, the LHF + SHF 2008 minus 2007 difference pattern in the Pacific bears a broad resemblance to the classic pattern of the cool PDO phase, with enhanced (reduced) latent and sensible heat loss over positive (negative) SST anomalies. The positive correlation between SST and LHF + SHF is indicative of the atmospheric response to SST, underlying the dominant role of the ocean in the large-scale atmospheric circulation in the Pacific.

For the North Atlantic Ocean, the LHF + SHF difference anomalies between 2008 and 2007 show a tripole structure, with negative anomalies off the east coast of North America (between 30° and 60°N) and positive anomalies to its north and south. The pattern is similar to that of the SST difference anomalies (Fig. 3.2b), but the sign is opposite. This negative correlation between SST and LHF + SHF implies that the variability of the Atlantic SST in 2008 was driven primarily by the atmospheric forcing: SST increases (decreases) as a result of reduced (enhanced) latent and sensible heat loss at the sea surface. That heat fluxes are important forcing for the North Atlantic Ocean variability in 2008 was best demonstrated by a recent study by Våge et al. (2009), who reported a remarkable deep convective overturning event in the Labrador and Irminger Seas in the winter of 2007/08 (defined as December 2007 to February 2008), triggered by rapid, intensive sea surface cooling under unusually cold westerly winds. Deep convection in the northern North Atlantic is regarded as a pump that drives the Atlantic meridional overturning circulation, and it has been suggested that its onset depends on strong westerly winds across this ocean basin that occur during the positive phase of the NAO (Hurrell et al. 1995). Våge et al. (2009) showed that winter 2007/08 was unusual. Though the NAO index was lower than in the previous winters, the westerly winds were unusually strong and cold, resulting in very large latent and sensible heat loss at the sea surface and subsequently a mixing of the water column to depths that had not been reached since the mid-1990s. This enhanced flux of ocean heat in the 2007/08 winter, which was more than 100 W m^{-2} above the winter climatology (Våge et al. 2009), left a clear mark even on the difference plot based on the 2007 and 2008 annual means (Fig. 3.8b): a band of positive LHF + SHF anomalies extends eastward from the ice edge in the Labrador Sea into the Irminger Sea.

The changing relationships between air–sea fluxes and SST from the Pacific to the Atlantic Oceans provide a clear example that the global climate system is

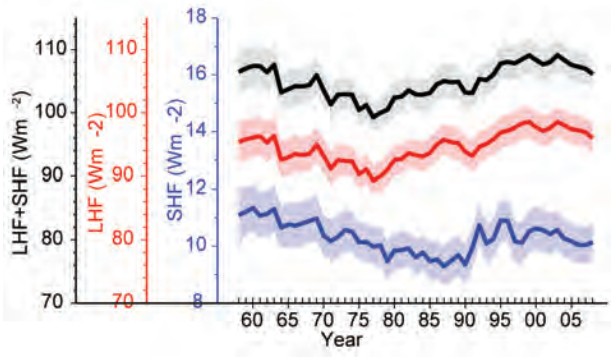

Fig. 3.9. Year-to-year variations of global-averaged annual mean latent plus sensible heat flux (blue line), latent heat flux (red line), and sensible heat flux (black line). The shaded areas indicate the upper and lower limits at the 90% confidence level.

ruled by intricate feedbacks between the ocean and the atmosphere. The oceans modulate large-scale climate variability and change, while short-term weather events could impose significant impact on ocean variability and thus impart an indelible signature on the long-term climate of the ocean circulation. It is worth noting that changes in air–sea heat fluxes also affect the hydrological cycle and hence ocean salinity, as the evaporation releases not only latent heat but also water vapor to the atmosphere. The structure of LHF + SHF anomalies, in particular the tripole shape in the North Atlantic Ocean, was in broad agreement with that of surface salinity anomalies (Fig. 3.13b). The freshening of the sea surface (i.e., negative surface salinity anomalies) over the Gulf Stream was in tune with the local weakened evaporation (i.e., negative LHF + SHF anomalies), while the increased surface salinity to the north and south coincided with enhanced evaporation forcing (positive LHF + SHF anomalies).

The basin-averaged LHF + SHF in 2008 was slightly down from 2007, continuing the broad downward trend that started in 1999 (Fig. 3.9). There seems to be a tendency toward reversing the upward trend that had dominated the decades of 1980s and 1990s.

e. *Tropical cyclone heat potential*—G. J. Goni and J. A. Knaff

Tropical cyclones occur in seven regions in all ocean basins: tropical Atlantic, northeast Pacific, northwest Pacific, southwest Indian, north Indian, southeast Indian, and South Pacific. While SST plays a role in the genesis of TCs, the ocean heat content contained between the sea surface and the depth of the 26°C isotherm, also referred to as TCHP, has been shown to play a more important role in TC intensity changes (Shay et al. 2000), provided that atmospheric conditions are also favorable. The TCHP shows high spatial and temporal variability associated with oceanic mesoscale features. Sea surface height observations derived from satellite altimetry can be used to compute the TCHP (Goni et al. 1996; Shay et al. 2000). In general, the real-time forecast of TC intensity is highly dependent on track forecasts, and many of the errors introduced in the track forecast are translated into the intensity forecast. Clearly, areas with high values of TCHP may be important only when TCs travel over them.

To examine the interannual variability of TCHP with respect to tropical cyclones, TCHP anomalies are computed during the months of TC activity in each hemisphere: June through November in the Northern Hemisphere and November through April in the Southern Hemisphere. Anomalies are defined as departures from the mean TCHP calculated during the same months for the period 1993 to 2008. These anomalies show large variability within and among the tropical cyclone basins (Fig. 3.10).

The west Pacific basin exhibits the anomalies from the signature of the negative phase of the 2007 ENSO event (La Niña). The South Pacific basin showed mostly positive anomalies. The north Indian Basin exhibited positive values in the Bay of Bengal and in the eastern Arabian Sea and negative values in the

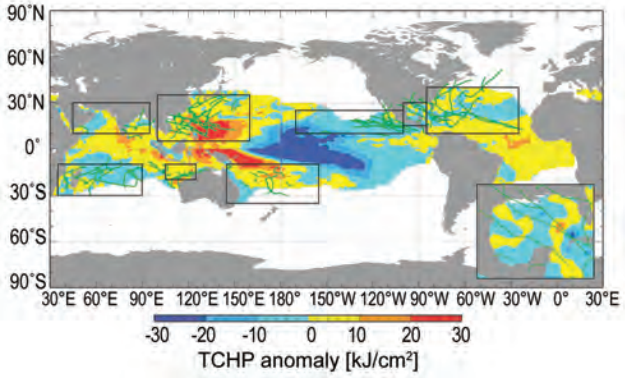

Fig. 3.10. Global anomalies of TCHP corresponding to 2008 computed as described in the text. The boxes indicate the seven regions where TCs occur: (left to right) southwest Indian, north Indian, west Pacific, southeast Indian, South Pacific, east Pacific, and North Atlantic (shown as Gulf of Mexico and tropical Atlantic separately). The black lines indicate the trajectories of all tropical cyclones Category 1 and above during Nov 2007 through Dec 2008 in the Southern Hemisphere and Jan through Dec 2008 in the Northern Hemisphere. The Gulf of Mexico conditions during Jun through Nov 2008 are shown in detail in the insert shown in the lower right corner.

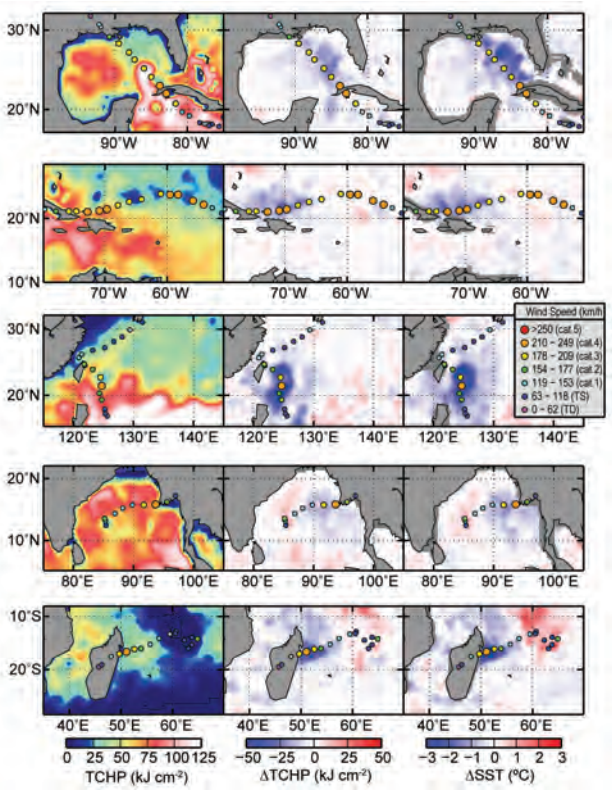

Fig. 3.11. (left) Tropical cyclone heat potential and surface cooling given by the difference between post- and prestorm values of (center) tropical cyclone heat potential and (right) sea surface temperature, for (from top to bottom) Hurricane Gustav, Hurricane Ike, Typhoon Sinlaku, Tropical Cyclone Nargis, and Tropical Cyclone Ivan.

western Arabian Sea. The Gulf of Mexico (insert) showed an alternation of regions with positive and negative values. The tropical Atlantic exhibited positive values to the north of 30°N and south of 15°N. The most evident changes that happened between 2008 and 2007 are the increase of values in the southern region of the western Pacific basin.

During 2008 several TCs were identified to have gained strength when traveling into regions of very high or higher values of TCHP. Some examples of these intensification events are shown in Fig. 3.11. The results presented here correspond to five intense (Categories 4 and 5) TCs, where the location of their intensification coincided with an increase of the values of TCHP along their tracks. Additionally, the cooling associated with the wake of the TCs, which can reach values of 30 kJ cm^{-2} in tropical cyclone heat potential and 3°C in sea surface temperature, is important because it influences the upper-ocean thermal structure on regional scales within weeks to months after the passage of the cyclones. These TCs were Gustav in the Gulf of Mexico, Ike in the Caribbean Sea, Sinlaku in the western Pacific, Nargis in the northern Indian, and Ivan in the southwest Indian region. A brief description of each of these storms is now presented.

In the Atlantic basin, Hurricanes Gustav and Ike are good examples of major hurricanes that interacted with TCHP features. Hurricane Gustav (25 August–2 September) reached its maximum estimated intensity of 125 kt prior to making landfall in Cuba on 30 August and at a time when its track was traversing some of the highest values of TCHP west of Jamaica. The storm's impact was felt throughout the northern Caribbean in Hispanola, Jamaica, the Cayman Islands, and Cuba. On the other hand, Hurricane Ike (1–14 September) experienced three separate peak intensities. The first and maximum peak intensity, 125 kt, was obtained in the central Atlantic, northwest of the Leeward Islands. In the next day or so, the storm weakened and moved southwest. The second peak shown in Fig. 3.11 occurred in a region of elevated TCHP. The third peak intensity occurred in the Gulf of Mexico before making landfall in Texas (not shown in Fig. 3.11). This storm resulted in major impacts throughout the northern Caribbean, making landfall twice in Cuba (110, 115 kt) and once in Texas (95 kt).

Typhoon Sinlaku (8–22 September), in the western North Pacific, obtained its maximum intensity (125 kt) following an encounter with a warm ocean eddy. Following its peak intensity, the storm weakened slightly as it turned toward Taiwan and moved over lower values of TCHP. Following this weakening, Sinlaku showed a slight intensification as it tracked to the northwest and moved over larger TCHP values. The storm eventually brushed the northeast coast of Taiwan on 13 September with an estimated intensity between 90 and 95 kt.

In the north Indian Ocean, Tropical Cyclone Nargis (27 April–3 May) made landfall in Myanmar on 2 May with an estimated intensity of 115 kt. The storm resulted in a devastating surge that killed an estimated 146,000 people. The storm intensified over the high TCHP waters of the Bay of Bengal. One aspect of the storm's forecast is that for the 48 h prior to landfall the storm was forecasted to have a more northward track than was observed, which not only allowed the storm to track over higher TCHP values but to make landfall in the low-lying Irrawaddy River delta. This storm occurred in early May and likely contributed to the negative anomalies in Fig. 3.10 in the northern part of the Bay of Bengal.

Tropical Cyclone Ivan (7–22 February) is a good example of a very strong and rather large Southern Hemisphere tropical cyclone, which reached its

maximum intensity of 115 kt just as it made landfall in Madagascar. Ivan also tracked across the warmest TCHP during the day or so prior to landfall on 17 February when intensification was occurring. Initial reports indicated that 26 deaths occurred and more than 300,000 persons were affected, particularly by the heavy general rainfall and subsequent floods in the north and east of the island of Madagascar.

Hurricane Gustav (2008) is now contrasted with Hurricane Katrina (2005) (Fig. 3.12). Both hurricanes made landfall in a region in the Gulf of Mexico. There are some similarities as they both traveled directly over the Loop Current. Katrina was energized by its passage over the Loop Current and continued to intensify as it moved from the Loop Current region into a region occupied by a warm ring shed by the Loop Current. The storm also became larger as it went through an eyewall replacement cycle (Maclay et al. 2009). Gustav, in contrast, tried to reorganize over the Loop Current region following a landfall in western Cuba, but instead of moving over a warm eddy as Katrina did, Gustav moved into a region of relatively low TCHP and did not reintensify despite being in favorable environmental conditions (200–850-hPa vertical wind shear <15 kt and SST >29°C). As a likely consequence, Gustav did not become nearly as large or as intense as Katrina. And while both storms weakened as they approached the Louisiana coast, Katrina with its larger and more intense wind field and landfall in a more populated area produced more property damage. The difference in the intensity of these two hurricanes translates into a difference in sea surface cooling. Maximum cooling by Katrina was approximately 30 kJ cm^{-2} in tropical cyclone heat potential and 4°C in sea surface temperature, almost double that observed for Hurricane Gustav.

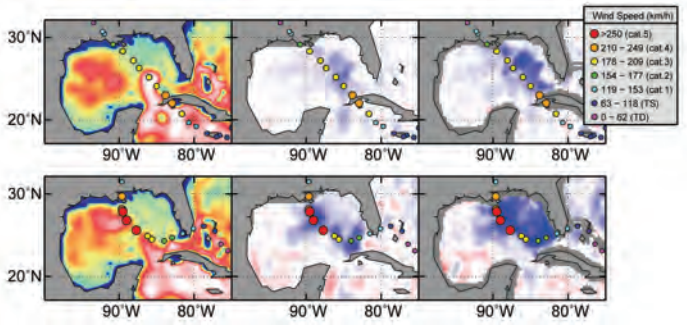

Fig. 3.12. (left) Tropical cyclone heat potential and surface cooling given by the difference between post- and prestorm values of (center) tropical cyclone heat potential and (right) sea surface temperature, for Hurricanes (bottom) Katrina in 2005 and (top) Gustav in 2008. The scales are the same as in Fig. 3.11.

f. Sea surface salinity—G. C. Johnson and J. M. Lyman

Ocean storage and transport of freshwater are intrinsic to aspects of global climate including the water cycle (e.g., Wijffels et al. 1992), El Niño (e.g., Maes et al. 2006), and anthropogenic climate change (e.g., Held and Soden 2006). In the past, in situ ocean salinity data have been too sparse and their reporting too delayed for an annual global perspective of ocean freshwater and its complement, salinity. However, over the past few years, the now mature Argo array of profiling floats, which measures temperature and salinity year-round in the upper 2 km of the ice-free global ocean (Roemmich et al. 2004), has remedied this situation. In addition, remote sensing of SSS by satellite is planned for 2010 (http://aquarius.gsfc.nasa.gov/).

The near-global Argo data are analyzed here to determine an annual average SSS anomaly for 2008 relative to a climatology and to describe how annual SSS anomalies have changed in 2008 relative to 2007. In this work the shallowest near-surface (<25 m) salinity data flagged as good from each available Argo profile for 2007 and 2008 were subjected to a statistical check to discard outliers. After this statistical check, the remaining data were then cast as differences from a climatological mean surface salinity field from the *WOA* based on historical data reported through 2001 (*WOA* 2001; Boyer et al. 2001). The resulting anomalies were then mapped (Bretherton et al. 1976) assuming a Gaussian covariance function with 6° latitude and longitude decorrelation length scales and a noise-to-signal variance ratio of 2.2. While some delayed-mode scientific controlled (final) Argo data are available for the 2007–08 time period, many real-time (preliminary) Argo data were used in both years. The real-time estimates of SSS made here could change after all the data have been subjected to careful scientific quality control.

Climatological SSS patterns are correlated with surface freshwater flux: the sum of evaporation, precipitation, and river runoff (e.g., Bäranger et al. 1999) where advection processes are not dominant. In each ocean basin, subtropical salinity maxima centered between roughly 20° and 25° in latitude are signatures of the predominance of evaporation over precipitation. Conversely, in most regions where climatological surface salinities are relatively fresh, such as the high latitudes and the ITCZs, precipitation generally dominates over evaporation.

The 2008 anomalies from *WOA* 2001 (Fig. 3.13a) reveal some large-scale patterns

that also hold in 2005 through 2007 (not shown). The regions around the subtropical salinity maxima are mostly salty with respect to *WOA* 2001. Most of the high-latitude climatologically fresh regions appear fresher than *WOA* 2001, including most of the ACC near 50°S and the subpolar gyre of the North Pacific. These patterns may be consistent with an increase in the hydrological cycle (i.e., more evaporation in drier locations and more precipitation in rainy areas), as seen in simulations of global warming. These simulations suggest this signal might be discernible over the last two decades of the twentieth century (Held and Soden 2006), consistent with the multiyear nature of these anomalies. In addition, a study of global subsurface salinity anomalies comparing 2000 Argo data to those from the 1990 World Ocean Circulation Experiment and prior historical data suggests that these patterns are persistent and decadal (K. P. Helm et al. 2009, manuscript submitted to *Nature Geosci.*).

Nonetheless, there may be alternate explanations. It is possible that the climatology, being based on relatively sparse data distributions in many parts of the oceans, may tend to underestimate regional extrema that the well-sampled Argo array can better resolve, or that the climatology contains regional biases on seasonal or longer time scales that are not present in the Argo data. Also, some of these patterns might be explained by interannual variability in large-scale oceanic currents or atmospheric features such as the ITCZs.

For example, in contrast to the other high-latitude areas, the subpolar North Atlantic and Nordic Seas in 2008 are anomalously salty with respect to *WOA* 2001 (Fig. 3.13a), as they have been since at least 2005 (not shown). This salty subpolar anomaly is inconsistent with a simple increase in the strength of the hydrological cycle. However, the pattern may have less to do with local evaporation and precipitation fields than with northward spread of saltier waters from the south. The salty anomaly in this region is consistent with a stronger influence of subtropical gyre waters in the northeastern North Atlantic in recent years and a reduced extent of the subpolar gyre (Hátún et al. 2005).

Salinity in the tropics exhibits strong interannual variability due to influences of phenomena such as the ENSO cycle (e. g., Ando and McPhaden 1997). For instance, the ITCZ in the central and eastern tropical Pacific is anomalously salty in 2008 (Fig. 3.13a), with some of that anomaly due to changes since 2007 (Fig. 3.13b), probably caused by an ongoing La Niña in 2008 reducing atmospheric convection and thus changing patterns of evaporation (Fig. 3.8) and precipitation in the region. In contrast, freshening in the far western tropical Pacific is evident, as is freshening in the Atlantic ITCZ. In addition, a strong fresh anomaly south of India in the tropics in 2007 (not shown) is absent in 2008 (Fig. 3.13a), again due to changes taking place over a 1-yr interval (Fig. 3.13b).

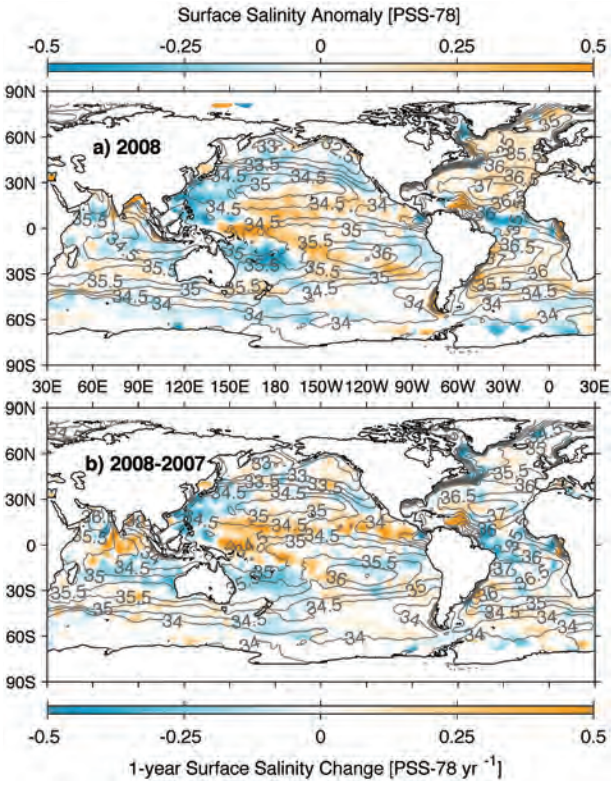

Fig. 3.13. (a) Map of the 2008 annual surface salinity anomaly estimated from Argo data (colors in PSS-78) with respect to a climatological salinity field from *WOA* 2001 (gray contours at 0.5 PSS-78 intervals). (b) The difference of 2008 and 2007 surface salinity maps estimated from Argo data [colors in PSS-78 yr^{-1} to allow direct comparison with (a)]. White areas are either neutral with respect to salinity anomaly or too data poor to map. While salinity is often reported in PSU, it is actually a dimensionless quantity reported on the PSS-78.

g. Surface current observations—R. Lumpkin, G. Goni, and K. Dohan

Near-surface currents are measured in situ by drogued[1] satellite-tracked drifting buoys and by current meters on moored ATLAS buoys. (Drifter

[1] A drogued buoy is attached to a large cylindrical canvas sea anchor. The drogue (sea anchor) dominates the surface area of the drifter and ensures that it follows currents at the drogue depth of 15 m rather than being blown by the wind.

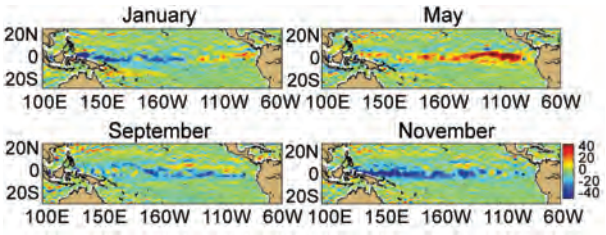

Fig. 3.14. OSCAR monthly averaged zonal current anomalies (cm s^{-1}), positive eastward, with respect to seasonal climatology for Jan, May, Sep, and Nov 2008.

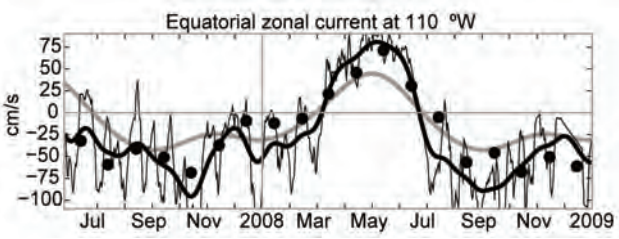

Fig. 3.15. Daily (thin black) and 15-day low-passed (thick black) zonal currents (positive eastward) measured at the equatorial TAO mooring at 110°W, at a depth of 10 m. Also shown are the mean seasonal cycle (gray) and OSCAR monthly mean zonal currents (black dots) at this location.

data are distributed by NOAA/AOML at www.aoml.noaa.gov/phod/dac/gdp.html. Moored data are distributed by NOAA/PMEL at www.pmel.noaa.gov/tao. OSCAR gridded currents are available at www.oscar.noaa.gov/. AVISO gridded altimetry is produced by SSALTO/DUACS and distributed with support from CNES, at www.aviso.oceanobs.com/.) During 2008, the drifter array ranged in size from a minimum of 918 drogued buoys to a maximum of 1,065, with a median size of 966 drogued buoys (undrogued drifters continue to measure SST but are subject to significant wind slippage; Niiler et al. 1987). The moored array included 35 buoys with current meters, all but two between 10°S and 21°N. Tropical moorings are maintained by the Pacific Ocean TAO, Atlantic Ocean PIRATA, and Indian Ocean RAMA projects. The two nontropical moored current meter sites of the Global Ocean Observing System are the Kuroshio Extension Observatory (32°N, 145°E) and Ocean Station Papa (50°N, 145°W).

Satellite-based estimates of ocean currents are produced by NOAA's OSCAR project, which uses satellite altimetry, winds, and SST to create 1° resolution surface current maps for the 0–30-m layer of the ocean (Bonjean and Lagerloef 2002). Anomalies are calculated with respect to the time period 1992–2002.

1) Surface current anomalies in 2008

The instantaneous distribution of current anomalies from the 1992–2002 mean mainly reflects the distribution of eddy kinetic energy associated with mesoscale eddies (cf., Stammer 1998; Lumpkin and Pazos 2007). To be significant, we require that anomalies must exceed the mean standard deviation (square root of eddy kinetic energy) with a distribution extending over several Eulerian length scales (Stammer 1998). By this definition, the only significant short-term (seasonal to annual) anomalies in 2008 occurred in the tropical Pacific Ocean. Longer-term variations can be resolved elsewhere and are discussed in the next section.

In the equatorial Pacific, the year began with large westward current anomalies in the western basin, associated with strong La Niña conditions, extending to 140°W (Fig. 3.14). In the eastern basin, weak eastward anomalies were seen from 120°W to the South American coast. These eastward anomalies grew in intensity and spatial coverage despite enhanced easterly surface winds (Fig. 4.4) At 110°W, this eastward anomaly pattern peaked in early May (Fig. 3.15), when the seasonal cycle typically reaches its maximum eastward speed. The eastward anomalies were 20–40 cm s^{-1} above typical May values and extended from South America to 160°E (Fig. 3.14). These anomalies deepened the thermocline in the eastern equatorial Pacific (Fig. 4.3),

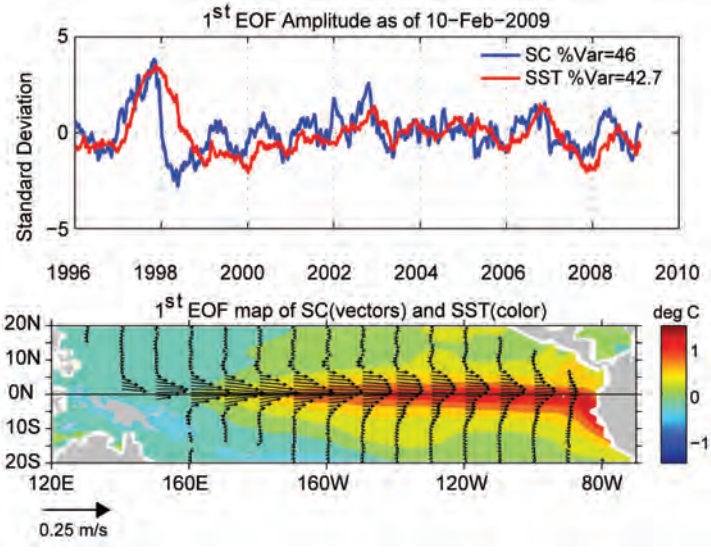

Fig. 3.16. Principal EOF of surface current ("SC") and SST anomaly variations in the tropical pacific. (top) Amplitude time series of the EOFs normalized by their respective std devs. (bottom) Spatial structures of the EOFs.

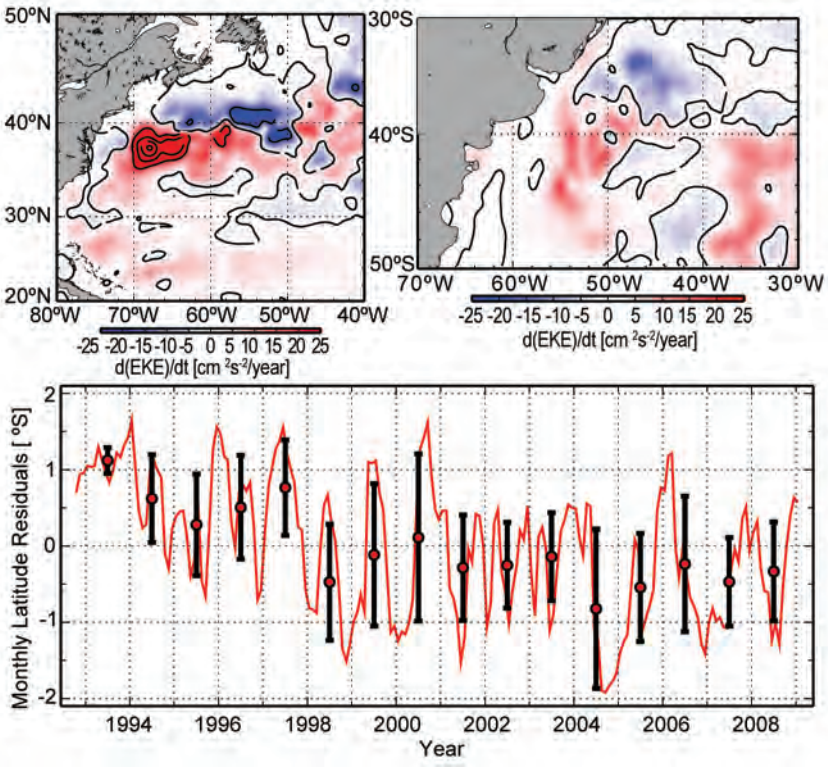

Fig. 3.17. Trends in geostrophic EKE for 1993–2008 in (top left) the Gulf Stream region and (top right) the Brazil–Malvinas Confluence, calculated from satellite altimetry. (bottom) Location of the Brazil Current separation with respect to its mean position over the period 1993–2008. Circles with bars indicate annual means and 2 std devs of the values in each calendar year.

increasing upper-ocean heat content and resulting in warm SST anomalies (Fig. 4.2). Warm SSTs were concentrated west of 120°W on the equator in May, when the Niño-3.4 index (which had been negative from January–April) became neutral (Fig. 4.1).

This El Niño–like surface current pattern, associated with the transition from La Niña to ENSO-neutral conditions, weakened in early boreal summer and had disappeared by early fall when warm SST anomalies in the eastern equatorial Pacific peaked and the monthly averaged Niño-3 and Niño-3.4 indices reached their maximum 2008 value (Fig. 4.1).

Through midboreal summer, westward current anomalies developed in the eastern part of the Pacific basin, reaching a peak of 40 cm s^{-1} (with respect to seasonal climatology) in September at 110°W (Fig. 3.15; anomaly is difference between the black and gray curves). This pattern spread westward in late 2008, reaching the western Pacific with maximum anomalies of 65–75 cm s^{-1} in November (Fig. 3.14). The resulting shallower thermoclines in the eastern Pacific were associated with cool SST anomalies and decreases in the Niño-3 and Niño-3.4 indices over the period October–December (Fig. 4.1).

Surface current anomalies in the equatorial Pacific typically lead SST anomalies by several months, with a magnitude that scales with the SST anomaly magnitude. Recovery to normal current conditions is also typically seen before SST returns to normal. Thus, current anomalies in this region are a valuable predictor for the evolution of SST anomalies and their related climate impacts. This leading nature can be seen clearly in the first principal EOF of surface current anomaly and separately of the SST anomaly in the tropical Pacific basin (Fig. 3.16), extending back to 1996.

2) Long-term changes in surface currents

Geostrophic EKE can be derived from gridded AVISO altimetry fields and reveals long-term trends in the Atlantic Ocean over the period 1993–2008 that may indicate a change of intensity and location of major surface currents. Along the axis of the Gulf Stream (Fig. 3.17) an increase in EKE to the south and a decrease to the north may indicate a long-term shift to the south in the current. In the southwestern Atlantic, a similar situation occurs, where the linear trend of EKE exhibits negative (positive) values to the north (south) of 38°S in the Brazil–Malvinas Confluence region. As with the Gulf Stream, this linear trend may indicate a shift in the surface current field to the south. Altimetry observations (bottom, Fig. 3.17) also show that the separation of the Brazil Current from the continental shelf break (Goni and Wainer 2001) has shifted south over the period 1993–2008. However, since 2004 (when the Brazil Current reached its southernmost separation point) it has tended to shift to the north.

h. The meridional overturning circulation—M. O. Baringer, C. S. Meinen, G. C. Johnson, T. O. Kanzow, S. A. Cunningham, W. E. Johns, L. M. Beal, J. J.-M. Hirschi, D. Rayner, H. R. Longworth, H. L. Bryden, and J. Marotzke

The meridional redistribution of mass and heat associated with the large-scale vertical circulation with-

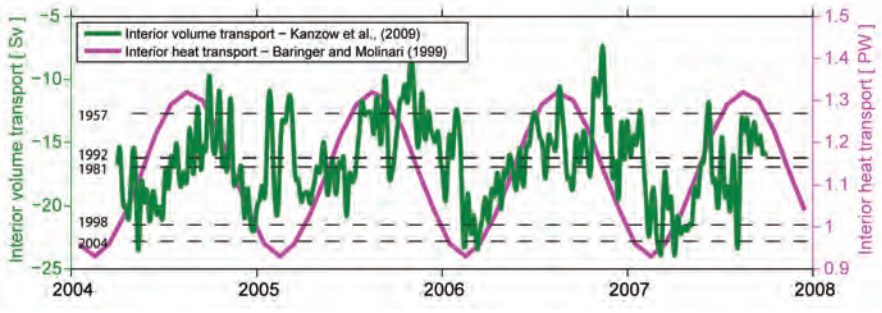

Fig. 3.18. Daily estimates of the strength of the upper 1,000-m transport (green solid) as measured by the United Kingdom's NERC Rapid Climate Change Program, the National Science Foundation's Meridional Overturning and Heat transport Array, and the long-term NOAA-funded Western Boundary Time Series Program. The interior volume transport estimate (accurate to 1 Sv; Cunningham et al. 2007) is based on the upper-ocean transport from Mar 2004 to Oct 2007 (adapted from Fig. 7 from Kanzow et al. 2009), with a 10-day low-pass filter applied to the daily transport values. Dashed black horizontal lines are the Bryden et al. (2005) upper-ocean transport values from the 1957, 1981, 1992, 1998, and 2004 transatlantic hydrographic sections. The total heat transport (estimated error 0.2 PW for monthly averages) is adapted from Baringer and Molinari (1999), including the mean heat transport components from Molinari et al. (1990).

in the oceans is typically called the MOC. The most common definition of the strength of the MOC at any particular latitude is the maximum of the vertically integrated basin-wide streamfunction, which changes as a function of location and time and is influenced by many physical systems embedded within it. There are several available estimates of the steady-state global mass, freshwater, and heat transport based on the best available hydrographic data (Talley 2008; Lumpkin and Speer 2007; Ganachaud and Wunsch 2003), as well as a few local estimates of the MOC from one-time full water column hydrographic sections and western boundary arrays (e.g., McDonagh et al. 2008; Kanzow et al. 2008b); however, true time series observations of basin-wide MOC transports are logistically very challenging to collect.

Presently, observing systems capable of quantifying changes in the MOC are at fledgling stages, and most existing systems at best observe only one component (e.g., a specific current or ocean layer) of the global MOC at discrete locations. Long-time series necessary for fully capturing the MOC variability and hence understanding the variations do not yet exist for the global MOC. As such, estimates of the state of the MOC must be inferred from time series of the complete MOC at one particular location (e.g., at 26°N in the Atlantic; Cunningham et al. 2007; Kanzow et al. 2007; Johns et al. 2008), through individual components of the MOC, or from indirect measurements influenced by the strength of the MOC, such as deep property fields like temperature or salinity.

The only observing system currently in place that measures the MOC spans the subtropical gyre in the North Atlantic near 26°N since April 2004 (called the RAPID Climate Change Program by the U.K. contributors and the MOCHA by the U.S. contributors; see Kanzow et al. 2008a); hence this note concentrates on those observations. During the first year of this new MOC monitoring array, the mean MOC transport was 19.1 Sv[2] with a standard deviation of 5.6 Sv (Kanzow et al. 2007; Cunningham et al. 2007). Observations of the strength of the MOC from this array are available only with a time delay as the moorings are recovered over 12- to 18-month intervals. The MOC can be divided into three components: the northward western boundary Florida Current, the wind-driven Ekman transport, and the southward "interior" transport (0–1,000 m deep geostrophic flow between the Bahamas and Africa). Recently, Kanzow et al. (2009) extended the analysis of the interior transport time series through October 2007 (Fig. 3.18). As with the results from the first year of this array, the time series indicates a surprising amount of variability at a range of time scales, including the emergence of a possible annual cycle that looks similar to the annual cycle postulated on the basis of all available section data in Baringer and Molinari (1999). Of note is that all the interior transport values estimated from five repeated CTD[3] sections by Bryden et al. (2005) can be found within the seasonal range of the interior transport time series (Fig. 3.18). These results do not disprove the presence of a long-term trend in the strength of the MOC (e.g., as suggested by Bryden et al. 2005; Wunsch and Heimbach 2006), but they do suggest a careful error analysis must be performed that includes the impact of the

[2] Sv is a Sverdrup or 10^6 m^3/s, a unit commonly used for ocean volume transports.

[3] CTD sensors are used to obtain vertical profiles of temperature, salinity, and density in the ocean.

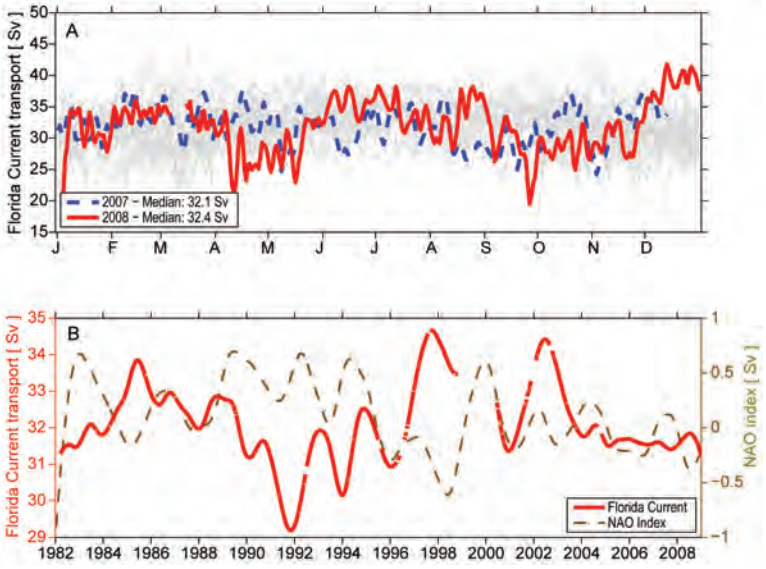

FIG. 3.19. (a) Daily estimates of the transport of the Florida Current for 2008 (red solid line) compared to 2007 (dashed blue line). The daily values of the Florida Current transport for other years since 1982 are shown in light gray. The median transport in 2008 increased slightly relative to 2007 and 2006 and is slightly above the long-term median for the Florida Current (32.2 Sv). (b) Two-year smoothed Florida Current transport (red) and NAO index (dashed orange). The daily Florida Current transport values are accurate to 1.1–1.7 Sv (Meinen et al. 2009, manuscript submitted to *J. Geophys Res.*) and the smoothed transport to 0.25 Sv (a priori estimate using the observed 3–10-day independent time scale).

underlying higher-frequency variability of the MOC on trend estimates (e.g., Baehr et al. 2008; Baehr et al. 2007; Brennan et al. 2008). Other related studies of the MOC trend are so far contradictory, with some reporting a decrease in the MOC or components of the MOC (e.g., Wunsch and Heimbach 2006; Koltermann et al. 1999; H. R. Longworth et al. 2008, unpublished manuscript), while others suggest no change or even an increase (e.g., Kohl and Stammer 2008; Zhang 2008; Olsen et al. 2008; Lumpkin et al. 2008; Schott et al. 2006). Clearly, while disagreement remains over the details of findings from any particular observing system (e.g., Kanzow et al. 2009), agreement exists that longer time series at multiple locations, particularly of the deep transport components, are needed (e.g., Wunsch 2008).

The longest transport time series of an ocean circulation feature directly linked to the MOC exists at 27°N in the Atlantic, where the bulk of the warm upper limb of the Atlantic MOC is thought to be carried in the Florida Current through the Straits of Florida and the majority of the cold lower limb is believed to be carried to the south in the DWBC just east of the Bahamas (e.g., Meinen et al. 2009, manuscript submitted to *J. Geophys. Res.*; Baringer and Larsen 2001). Since 1982, variations in the upper limb of the Atlantic MOC have been monitored by measuring the Florida Current transport using a submarine cable across the Straits of Florida in combination with regular hydrographic sections. In 2008 the median transport through the Straits of Florida was 32.4 Sv, well within the middle range of mean annual values (32.2 Sv median transport of the Straits of Florida from 1982 to 2008 with 50% of the annual means within ±2.2 Sv). There were, however, several unusual high-frequency events during the year (Fig. 3.19): three anomalously low (outside of 2–3 standard deviations of the daily averaged values) transport events during 4–6 January, 7 April–17 May, and 24–29 September, with values as low as about 20 Sv, and an unusually high transport 10–31 December, with values as high as about 42 Sv. Because these events were relatively short lived, it is likely they are local responses to upstream atmospheric forcing and coastally trapped wave processes and are not particularly indicative of a climatically important shift (e.g., Mooers et al. 2005). Interannual fluctuations in the Florida Current show a negative correlation ($r \sim 0.6$) with the NAO during the 1982–98 time period (Baringer and Larsen 2001); however, while the NAO has been tending to decrease over the past 20 years, the Florida Current transport shows no corresponding long-term trend through 2008 (Meinen et al. 2009, manuscript submitted to *J. Geophys. Res.*; Peng et al. 2009; Beal et al. 2008).

Trends in the global MOC can also be determined through proxies of the MOC strength, such as paleo observations (e.g., Carlson et al. 2008), tracers (e.g., LeBel et al. 2008), and characteristic water masses (e.g., Lohmann et al. 2008; Hawkins and Sutton 2007). For example, during the past year, temperature and salinity observations in the Labrador Sea showed an abrupt return of deep convection between 2007 and 2008 (Våge 2009). Yashayaev and Yoder (2009) showed that the enhanced deep convection in the Labrador Sea in the winter of 2008 was the deepest since 1994 and included the largest heat loss from the ocean to the atmosphere since the mid-1990s, exceeding the long-term mean by 50% (see also Fig. 3.8b). Such anomalous local events may be a precursor to changes in the MOC

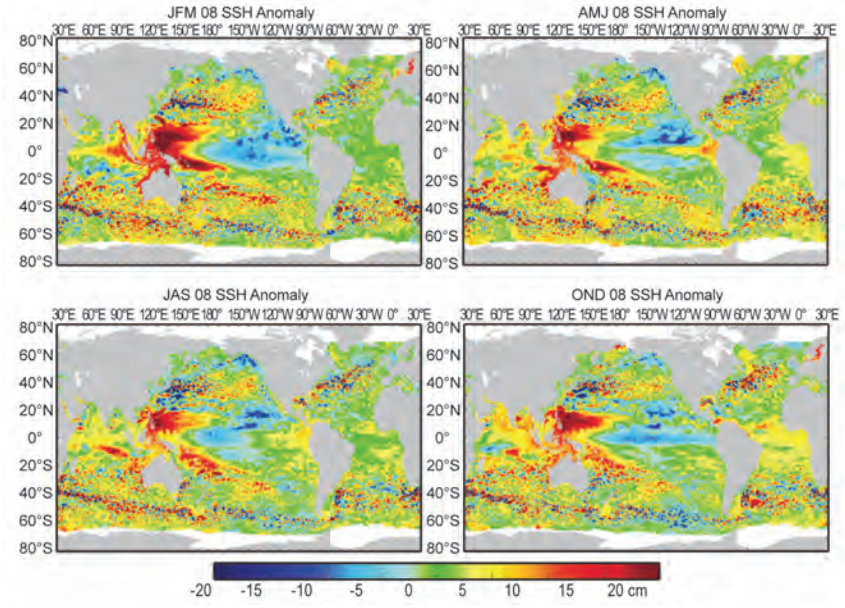

Fig. 3.20. Seasonal SSH anomalies for 2008 relative to the 1993–2007 baseline average are obtained using the multimission gridded sea surface height altimeter product produced by Ssalto/Duacs and distributed by Aviso, with support from CNES (www.aviso.oceanobs.com).

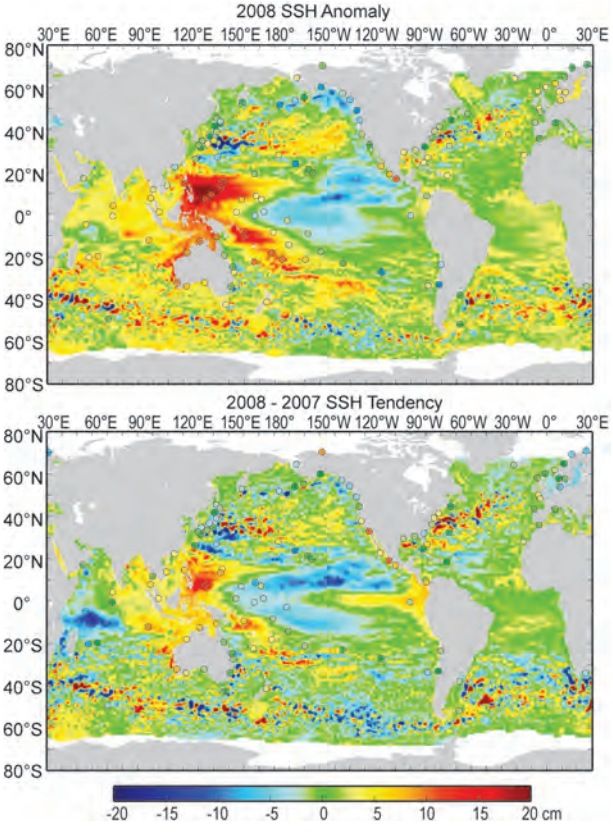

Fig. 3.21. (top) The 2008 SSH anomaly (Ssalto/Duacs product) from the 1993–2007 baseline is compared to the 2008 anomaly computed for tide gauge data (dots) obtained from the University of Hawaii Sea Level Center (http://uhslc.soest.hawaii.edu/). (bottom) The difference between 2008 and 2007 annual means.

strength (e.g., Lohmann et al. 2009; Bellucci et al. 2008).

While the MOC is often discussed in terms of the large-scale, full-depth circulation in the North Atlantic Ocean, surface water also sinks into the abyssal ocean around Antarctica (e.g., Orsi et al. 1999). The Antarctic and North Atlantic limbs of the MOC appear to be of similar magnitude (e.g., Lumpkin and Speer 2007), and the Antarctic Bottom Water fills more of the deepest parts of the global ocean than does the North Atlantic Deep Water (e.g., Johnson 2008b). Comparisons of deep hydrographic observations with respect to earlier data reveal some interesting changes associated with Antarctic Bottom Water. For instance, bottom waters of Antarctic origin in the deep South Atlantic (e.g., Johnson and Doney 2006), Pacific (e.g., Fukasawa et al. 2004; Kawano et al. 2006; Johnson et al. 2007), and south Indian Oceans (e.g., Johnson et al. 2008a) have all warmed over the last decade, indicating a change in the Antarctic contribution to the MOC. Furthermore, bottom waters close to Antarctica, at least in the Indian Ocean sector, also appear to have freshened (Rintoul 2007; Johnson et al. 2008a), consistent with decadal time scale freshening in the source regions for this bottom water (Jacobs et al. 2002). Finally, there are suggestions in both the North Atlantic (Johnson et al. 2008b) and North Pacific (Kouketsu et al. 2009) that the MOC associated with Antarctic Bottom Water may have slowed. Above the bottom water, Argo float data document a large-scale warming and freshening around Antarctica, but there is no accompanying change in horizontal gradients and hence no suggestion of a response to the large-scale increases in westerly winds that have been observed and are projected to continue under a warming climate (e.g., Boning et al. 2008).

i. Sea level variations, 2008 annual assessment—M. A. Merrifield, R. S. Nerem, G. T. Mitchum, L. Miller, E. Leuliette, S. Gill, and P. L. Woodworth

Sea level variations in 2008 are strongly influenced by the persistent, but apparently weakening, La Niña event. We will begin with a description of the associated quarterly sea level anomalies, turning then to

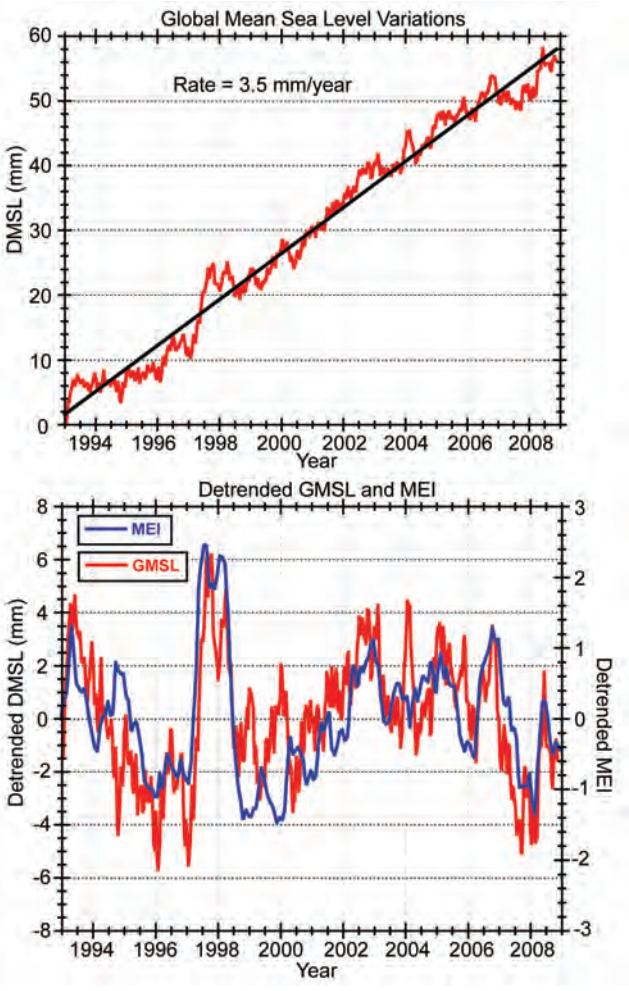

Fig. 3.22. (top) Monthly GMSL (seasonal cycle removed) relative to a linear trend of 3.5 mm yr^{-1}. (bottom) Monthly GMSL (linear trend removed, red) versus the MEI (blue). SSH data provided by the NASA PO.DAAC at the Jet Propulsion Laboratory/California Institute of Technology (http://podaac.jpl.nasa.gov/).

the mean of 2008 relative to a long-term mean, and then relative to the 2007 mean, the latter difference being interpreted as the present sea level tendency. We will conclude with an evaluation of global sea level changes in the context of the recent La Niña conditions, and a brief description of sea level extremes observed at tide gauges in 2008.

The La Niña event that developed during 2007 persisted during 2008 with strong positive anomalies in the western tropical Pacific (Fig. 3.20). During JFM 2008 positive SSH anomalies extended throughout the Indonesian Archipelago into the tropical Indian Ocean and southward along the west coast of Australia. The La Niña weakened noticeably during AMJ 2008 with the arrival of a Kelvin wave in the eastern equatorial Pacific.

The annual mean SSH (Fig. 3.21, top) depicts the dominant La Niña state in the Pacific, and the negative-phase PDO pattern in the North Pacific with negative anomalies along the west coast of North America and positive anomalies in the central North Pacific. The shift to a negative PDO began in late 2007. In general, sea level appears to be higher in most regions relative to the 1993–2002 baseline, with the exception of the mid- to high-latitude North Pacific and North Atlantic. The coastal tide gauge and adjacent SSH deviations are similar at most stations.

The SSH tendency (Fig. 3.21, bottom), measured as the difference in annual mean SSH between 2008 and 2007, shows a net increase in sea level in the warm-pool region despite the weakened state of the La Niña during the Kelvin wave event (AMJ; Fig. 3.20). The SSH increase in this region is associated with zonal wind anomalies directed toward the Indonesian Archipelago from both the Indian and Pacific Oceans. A decrease in sea level occurs in the central equatorial

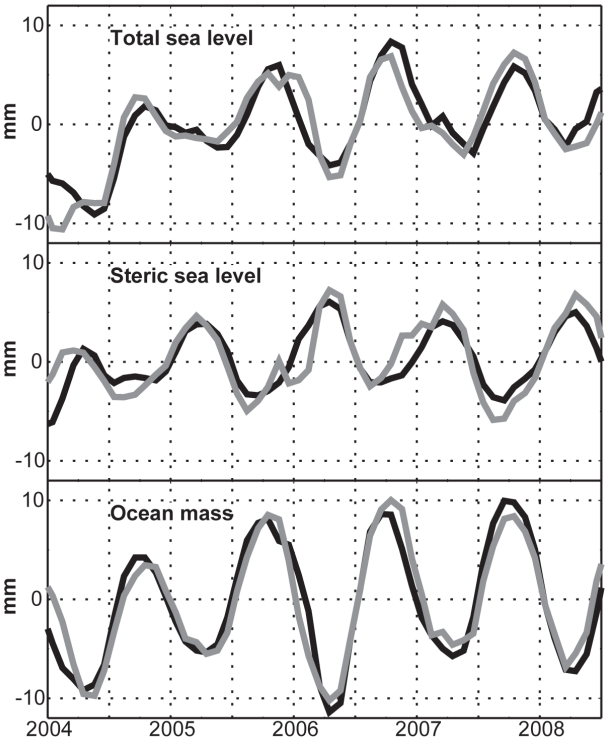

Fig. 3.23. Time series of GMSL, or total sea level, is compared with the two principal components of sea level change, upper-ocean steric change from Argo measurements, and mass change from GRACE measurements (Leuliette and Miller 2009). In this figure, black lines show the observed values and gray lines the inferred values from the complementary observations (e.g., the inferred steric sea level is obtained from observed total sea level–observed ocean mass).

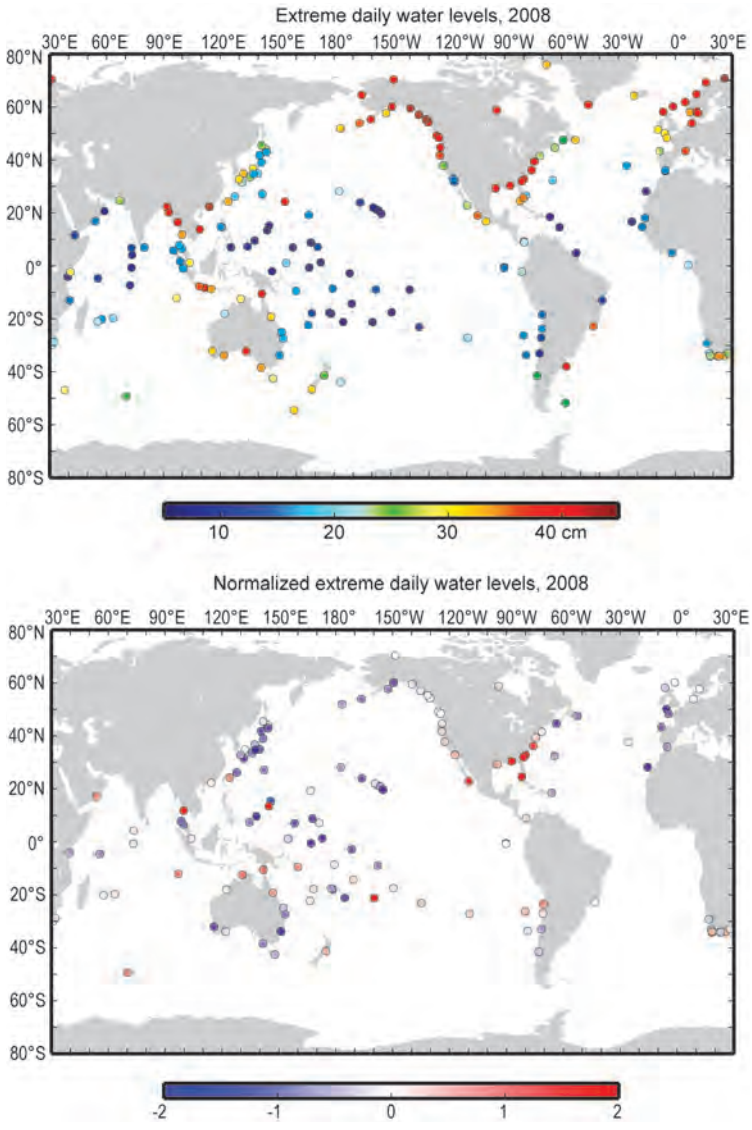

Fig. 3.24. (top) Extreme sea level variability is characterized using the average of the top 2% mean daily sea levels during 2008 relative to the annual mean at each station. (bottom) The extreme values are normalized by subtracting the mean and dividing by the std dev of past-year extreme values for stations with at least 15-yr record lengths.

Pacific and in the eastern tropical Pacific. There is, however, a positive anomaly along Central and South American coasts associated with the Kelvin wave. A strong positive anomaly that occurred during 2007 in the western Indian Ocean fell sharply in 2008, and this region is now substantially below normal. SSH changes in the Atlantic Ocean were weak compared to other regions.

The La Niña event of 2007–08 affected not only regional sea level anomalies but GMSL as well. GMSL has been persistently low during the La Niña event relative to a linear trend of approximately 3.5 ± 0.4 mm yr^{-1} (Fig. 3.22.) (R. S. Nerem et al. 2009, unpublished manuscript). The correspondence between GMSL and the MEI (www.cdc.noaa.gov/people/klaus.wolter/MEI/mei.html) shows that El Niño and La Niña events have a strong influence on global sea level. Once this interannual variability is accounted for, the inferred rate of GMSL change remains remarkably constant, suggesting that La Niña may partially explain the flattening of the GMSL curve over the past one to two years.

Variations in GMSL due to changes in ocean density (steric sea level) and ocean mass are currently under investigation using satellite altimeters, the Argo array (ocean thermal), and the GRACE time series (ice melt and other hydrological variations), and preliminary investigations are beginning to document these changes (e.g., Willis et al. 2008; Leuliette and Miller 2009). On seasonal time scales (Fig. 3.23), the steric and mass components of GMSL are 180° out of phase due to differences in continental surface area in the Northern and Southern Hemispheres, which leads to asymmetries in net ocean heat flux and river runoff (Willis et al. 2008). These analyses of seasonal variations demonstrate the power of the present system for observing and interpreting sea level variations. As the time series from Argo and GRACE lengthen, the contributions to interannual GMSL change will become increasingly clear.

Extreme sea level variability during 2008 is examined using daily averages obtained from a global set of tide gauges (Fig. 3.24). Extreme sea levels, taken as the average of the 2% highest daily values relative to the annual mean level (top), were high along the coasts of North America, Europe, and Southeast Asia, and low at most of the islands in the tropics. For time series with at least 15 years of record length, we normalize the levels by removing the mean and dividing by the standard deviation of extreme sea levels for all available years (Fig. 3.24, bottom). By this measure, extremes along the southeast coast and Gulf Coast of the United States were notably higher than normal. Other areas of unusually high values include northern Australia and isolated stations south of the

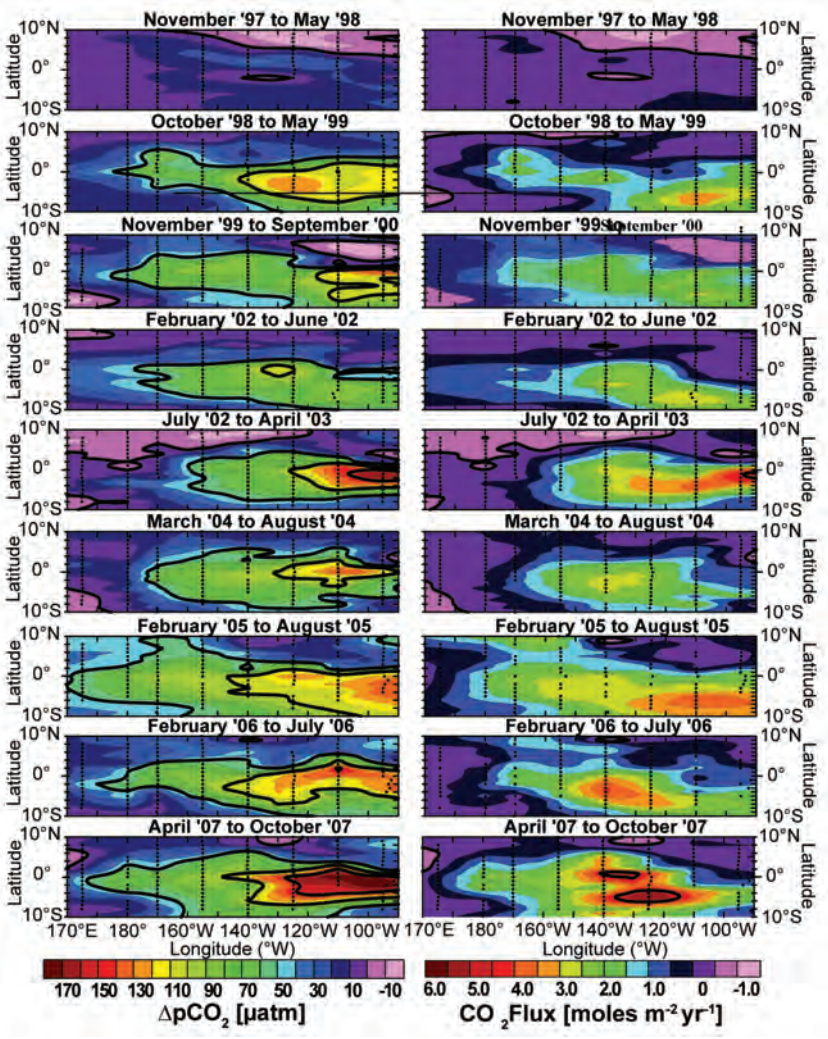

FIG. 3.25. Plots of sea–air pCO_2 difference and air–sea CO_2 flux in the equatorial Pacific between 1997 and 2007 based on underway CO_2 measurements collected on the TAO service cruises. The nominal cruise track lines are shown in black. A complete survey of the region is completed approximately every six months. The black and dark purple areas indicate where the atmosphere and seawater pCO_2 values are nearly balanced. The pink areas indicate ocean uptake of CO_2, and the blue to red colors indicate areas of ocean CO_2 out-gassing.

equator in the tropical Pacific. Extremes in Europe, Japan, and South Australia, and at island stations in the equatorial Pacific, were well below normal.

j. The global ocean carbon cycle—C. L. Sabine, R. A. Feely, R. Wanninkhof, and T. Takahashi

1) AIR–SEA CARBON DIOXIDE FLUXES

The time and space scales of variability in the air–sea CO_2 flux make it challenging to assess global fluxes based on in situ surface observations. The latest global flux map is based on approximately 3 million measurements collected between 1970 and 2007 (Takahashi et al. 2009). The annual mean contemporary CO_2 flux over the global oceans in 2000 is estimated to be a net uptake of 1.4 ± 0.7 Pg-C yr^{-1}. As with the previous maps, the estimate is for a "normal" year when there are no significant El Niño signals in the equatorial Pacific. Because the loss of CO_2 from the equatorial Pacific to the atmosphere is depressed during El Niños (Feely et al. 2006), these conditions result in a net increase in the global ocean CO_2 uptake for that year. Seasonal-to-annual estimates of net air–sea CO_2 fluxes are needed to better understand the changing role of the ocean in the global carbon cycle. The updated empirical approach to quantifying the air–sea CO_2 exchange utilizing in situ, climatological, and satellite data is described in Sabine et al. (2008). The diverse data streams and lags in availability of quality-controlled atmospheric CO_2, satellite, and assimilation products preclude real-time analysis such that quarterly air–sea CO_2 flux maps are only available for the period from 1983 to 2007. The global mean air–sea CO_2 flux for this period, including the ENSO effects, gives an average uptake of 1.74 Pg-C yr^{-1}. Assuming the preindustrial steady-state ocean was a source of 0.4 Pg-C yr^{-1} (Jacobson et al. 2007), the estimated average flux equates to a net ocean anthropogenic CO_2 uptake of 2.14 Pg-C yr^{-1}. This is consistent with the oceanic anthropogenic CO_2 sink estimate of 2.2 ± 0.5 Pg-C yr^{-1} from Bindoff et al. (2007), based on several different approaches. Gruber et al. (2009) analyzed the oceanic uptake rates of anthropogenic CO_2 for the period of 1990 to early 2000, which were estimated from observations (sea–air pCO_2 difference, sea–air ^{13}C disequilibrium, and atmospheric O_2/N_2) and general circulation models (ocean data inversion, atmospheric data inversion, and ocean biogeochemical models). Multiple techniques for estimating ocean anthropogenic CO_2, including observational approaches, numerical models, and techniques that blend observations and models, were found to be mutually consistent within their respec-

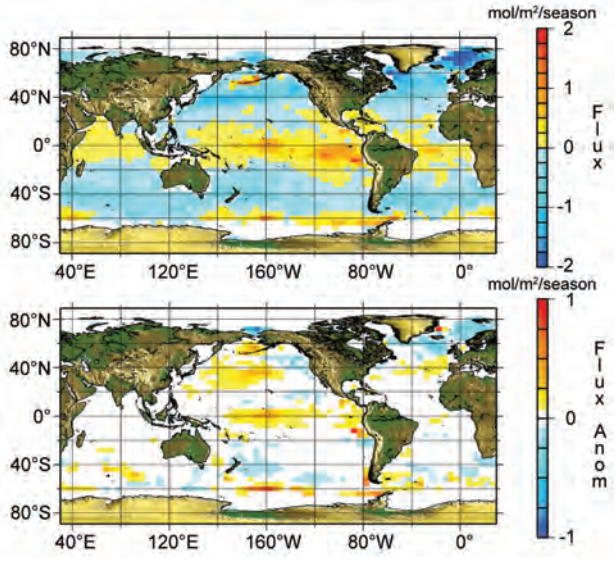

Fig. 3.26. Maps of (a) net air–sea CO_2 fluxes and (b) air–sea CO_2 flux anomaly for Sep–Dec 2007. Coastal pixels and those with ice cover are masked in gray. Negative fluxes represent uptake of CO_2 by the ocean. Output and graphic provided by J. Trinanes.

tive uncertainties, ranging from 1.5±0.9 Pg-C yr^{-1} to 2.4±0.5 Pg-C yr^{-1} (Gruber et al. 2009).

Figure 3.25 shows the measured sea–air CO_2 differences and net fluxes in the equatorial Pacific for a 10-yr period from 1997 to 2007. The top, from the fall of 1997 and spring of 1998, shows the very low out-gassing conditions of the 1997/98 El Niño. This is in contrast to the bottom, which shows very strong out-gassing during the 2007 La Niña shown by the Multivariate ENSO Index (www.cdc.noaa.gov/enso/enso.mei_index.html). The difference in the estimated flux between the top (November 1997–May 1998) and the bottom panels (April 2007–October 2007) is 0.39 Pg-C, or about 20% of the long-term average annual global air–sea CO_2 flux.

The global pattern of the net air–sea CO_2 flux for October–December 2007 is presented in Fig. 3.26a based on seasonal correlations between sea surface temperature and pCO_2 for each 4° by 5° pixel of the Takahashi et al. (2009) map (see Lee et al. 1998; Park et al. 2006; and Sabine et al. 2008 for methods). The interannual variability in air–sea CO_2 fluxes is determined from these relationships and global interannual sea surface temperature and wind speed anomalies derived from satellite and assimilation products. It shows the characteristic global pattern of net release of CO_2 in the tropics and regions of upwelling and CO_2 uptake in the mid- and high latitudes. Of note are the regions of efflux near the Antarctic ice edge that partially offset the sink strength of the Southern Ocean. Figure 3.26b shows the difference between the September–December 2007 air–sea fluxes and the average September–December flux pattern for the whole record (1983–2007). The large positive anomaly in the equatorial Pacific means that there was enhanced out-gassing of CO_2 consistent with the measurements shown in the bottom of Fig. 3.25. These estimates suggest the La Niña effect impacted a much larger area of the Pacific than the region measured from the cruises to service the TAO moorings. Very strong positive local anomalies are determined off the coast of Peru associated with intensified upwelling and stronger winds. Positive anomalies are also estimated for the subtropical North Pacific. The cause of the North Pacific anomaly, and to a lesser extent in the North Atlantic, is being validated and is under investigation. Observations from volunteer observing ships in the North Atlantic suggest that this is an actual anomaly rather than an artifact of the approach. It is a continuation of the depressed North Atlantic CO_2 sink in this region, albeit of lesser magnitude than that observed in the mid-1990s (Schuster and Watson 2007). Due to changing shipping routes there were no measurements in that region of the North Pacific to validate the results for the North Pacific, but the strong positive air–sea CO_2 flux anomaly off the coast of Peru was confirmed with measurements from the flux reference buoy deployed as part of the VOCALS (www.eol.ucar.edu/projects/vocals/) project and ship-based observations from NOAA ship R/V *Ronald H. Brown* servicing the buoy.

A negative correlation (r^2~0.6) between the Multivariate ENSO Index and global air–sea CO_2 fluxes is observed in the long-term flux record. Positive MEI indicates El Niño conditions and low CO_2 outgassing. The boreal winter of 2007 showed a negative MEI (<–1) corresponding to an increased equatorial Pacific CO_2 flux to the atmosphere, or depressed net global oceanic uptake of CO_2 (Fig. 3.26b). The global mean CO_2 uptake for 2007 is estimated at 1.67 Pg-C, about 0.07 Pg-C lower than the long-term average. This seasonal anomaly is the third-largest determined with this method since 1983. The low global uptake is attributed, in large part, to the La Niña that was observed in the equatorial Pacific at that time. It intensified toward the end of 2007 as observed with sea surface temperature observations (Reynolds and Xue 2008).

2) Subsurface carbon inventory

In 2003, the U.S. CLIVAR/CO_2 Repeat Hydrography Program began reoccupying a subset of lines from the WOCE/JGOFS global ocean survey con-

ducted in the 1990s. The program has identified 19 hydrographic sections distributed around the global ocean that will be surveyed approximately every 10 years to examine changes in ocean carbon and other physical and biogeochemical tracers. In 2008 two lines were completed: I6S in the southwestern Indian Ocean, nominally along 30°E, and P18 in the southeastern Pacific, nominally along 105°W.

Figure 3.27 shows sections of DIC along P18 in 2008 and 1994. To first order the distributions look similar for both years, but the difference plot (Fig. 3.27, bottom) shows patchy increases as large as 50 μmol kg^{-1}. This patchy pattern does not simply reflect a secular increase in CO_2 but is also influenced by variability in the natural carbon distributions at interannual and shorter time scales. Aliasing from mesoscale eddies and frontal oscillations that displace isopycnal surfaces (Haine and Gray 2001; Peacock et al. 2005), as well as variations in water mass properties associated with climate modes such as the El Niño–Southern Oscillation (Feely et al. 2002), can be significant when comparing two cruises separated in time.

To correct for these variations and isolate the changes due to uptake of CO_2 from the atmosphere, we use the multiple linear regression approach first introduced by Wallace (1995). The application of these corrections varies depending on data quality and the oceanographic conditions along the section; thus each section must be evaluated separately. A full global assessment of ocean DIC changes cannot be made until the resurvey of the oceans is completed in the next few years. However, each updated ocean section provides incremental insight into how carbon uptake rates are evolving spatially and temporally.

Table 1 summarizes the current best estimates of anthropogenic CO_2 accumulation along representative north–south cruise tracks in the Atlantic, Pacific, and Indian Oceans over the last decade. If these values are representative of the basin averages, then the changes over the last decade are somewhat different from the pattern of long-term accumulation. For example, Sabine et al. (2004) found that the largest accumulation of anthropogenic CO_2 over the last 200 years was in the North Atlantic. This was attributed to the transport of waters rich in anthropogenic CO_2 into the ocean interior by the formation of North Atlantic Deep Water. The repeat hydrography results, however, indicate that over the last decade the North Atlantic has not had the largest increase in anthropogenic carbon storage. This finding is consistent with other independent estimates that the North Atlantic uptake rate has decreased over

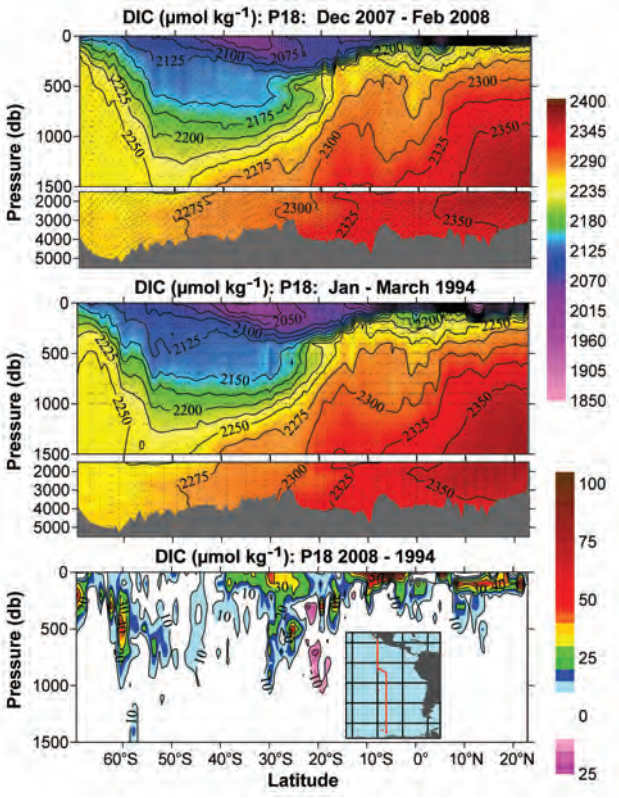

Fig. 3.27. Sections of dissolved inorganic carbon (μmol kg^{-1}) nominally along 105°W in (top) 2008 and (middle) 1994. The bottom section shows the DIC change between the two cruises (2008–1994). Black dots show sample locations. Inset map shows cruise track in red.

Table 3.1. Estimates of ocean column inventory changes in anthropogenic carbon (mol C m^{-2} yr^{-1}) over the last decade.

	Atlantic (25°W) 1993–2005	Pacific (152°W) 1991–2006	Indian (90°E) 1995–2007
Northern Hemisphere	0.63	0.25	0.63
Southern Hemisphere	0.75	0.41	0.83

the last decade (Schuster and Watson 2007; Thomas et al. 2008). The largest increases in anthropogenic carbon accumulation along these sections appear to be in the Southern Hemisphere oceans.

Figure 3.28 shows the change in carbon column inventories between the CLIVAR (2008), WOCE (1995), and GEOSECS (1978) cruises in the eastern Indian Ocean along 90°E. The pattern of average annual carbon increases between 1995 and 2008 were similar to the pattern of increases between 1978 and 1995, but the magnitude of the increases over the last decade are about twice the increases prior to 1995. These findings appear to contradict some recently published model results and surface ocean pCO_2 observations that have suggested that the Southern Ocean uptake of CO_2 has decreased over the last few decades (Le Quéré et al. 2007; Lovenduski et al. 2007; Takahashi et al. 2009). There are still more lines that need to be examined in the Southern Ocean, but these initial results illustrate the importance of studying the linkages and differences between CO_2 uptake from the atmosphere and the ultimate storage of carbon in the ocean interior.

Because atmospheric CO_2 concentrations are growing at a nearly exponential rate, it is not surprising to find that the rate of carbon storage is increasing with time. However, there are two processes that control the rate of anthropogenic carbon increases in the ocean: the equilibration time between the ocean and the atmosphere and the rate at which waters containing anthropogenic carbon are moved into the ocean's interior. In most places the surface ocean CO_2 values are increasing at roughly the same rate as the atmosphere (Takahashi et al. 2009). This means that anthropogenic CO_2 is accumulating in surface waters everywhere at approximately the same rate. There are only a few locations, however, where surface waters are moving into the ocean interior.

North of about 55°S the difference between the two curves in Fig. 3.28 is reasonably consistent. Because both curves show the largest overall accumulations of carbon in the southern subtropical gyre, the percent change in the carbon accumulation rate is much larger north of 10°S (from 0.2–0.3 to ~0.6 mol m^{-2} yr^{-1}, or roughly a 100% increase) compared to the region south of approximately 10°S (from 0.7–0.9 to 1.0–1.2 mol m^{-2} yr^{-1}, or about a 30% increase). This observation is consistent with the idea that surface layer accumulation of anthropogenic carbon has increased at all latitudes, but the rate of transport of anthropogenic carbon into the ocean interior has not changed dramatically along this section. The anthropogenic carbon penetration is still

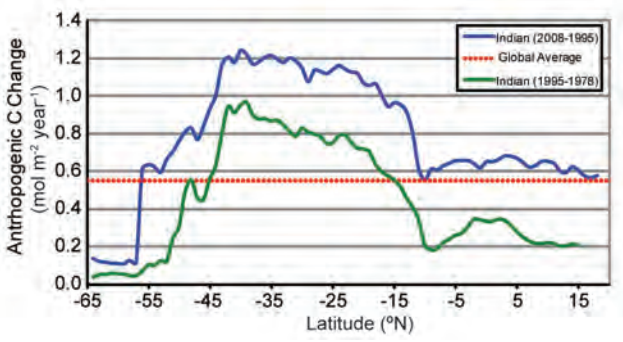

Fig. 3.28. Column Inventory changes as a function of latitude along ~90°E in the eastern Indian Ocean. The blue line is the average annual change between 2007 and 1995. The green line is the average annual change between 1995 and 1978. The red dotted line is the global-average annual uptake of anthropogenic CO_2 divided by the surface area of the ocean.

relatively shallow north of 10°S, thus the increase in surface uptake resulted in a significant increase in the total carbon column inventory. South of 10°S, however, much of the anthropogenic carbon is found in the intermediate waters. An increase in the surface accumulation rate without a subsequent increase in the rate at which CO_2 is moved into the ocean interior, therefore, would result in a smaller percent increase in the total column inventory as observed.

These latest results show conclusively that anthropogenic CO_2 is continuing to accumulate in the Atlantic, Pacific, and Indian Oceans and suggest that the accumulation rates can vary over decadal time scales. However, a single transect through an ocean basin is not sufficient for characterizing the full patterns of anthropogenic CO_2 storage. More in-depth analyses will be undertaken once the global survey is complete. Because circulation and biological processes changes can vary in cycles often associated with ocean climate reorganizations such as ENSO, North Atlantic Oscillation, Pacific decadal oscillation, and southern annular mode, it is critical to continue to monitor the changes in carbon inventories and how they interact with the secular increases in anthropogenic CO_2.

k. Global ocean phytoplankton—M. J. Behrenfeld, D. A. Siegel, R. T. O'Malley, and S. Maritorena

Photosynthesis by the free-floating, single-celled phytoplankton of the upper sunlit "photic" layer of the global ocean is the overwhelmingly dominant source of organic matter fueling marine ecosystems. Phytoplankton contribute roughly half of annual biospheric (i.e., terrestrial and aquatic) NPP (gross photosynthesis minus plant respiration), and their

NEW EVIDENCE FOR OCEAN ACIDIFICATION IN COASTAL WATERS OF NORTH AMERICA—R. A. FEELY AND A. G. DICKSON

Over the past two centuries the release of CO_2 from humankind's combined industrial and agricultural practices has resulted in atmospheric CO_2 concentrations that are now higher than experienced on the Earth for at least the last 800,000 years (Lüthi et al. 2008). During this period the oceans have taken up approximately one-third of the total amount of CO_2 produced by human activities (Sabine et al. 2004). This addition of anthropogenic CO_2 to the ocean has reduced the surface ocean pH by about 0.1 to date (a process known as ocean acidification) and is expected to reduce pH by a further 0.3 units by the end of this century (Feely et al. 2004). It now appears likely that the level of CO_2 in the atmosphere might double over its preindustrial levels by the middle of this century. This rapid change in ocean chemistry is more dramatic than at any time in the past 20 million years (Feely et al. 2004). This pH decrease will lead to a reduction in the saturation state of seawater with respect to calcite and aragonite, which are the two most common types of calcium carbonate formed by marine organisms (Feely et al. 2004). These changes in seawater chemistry have consequences for a wide variety of marine organisms in coastal and open ocean ecosystems. Many species of marine calcifiers, such as clams, oysters, mussels, sea urchins, and corals, have exhibited reduced calcification rates in response to elevated CO_2 levels (Kleypas et al. 2006; Fabry et al. 2008; Doney et al. 2009). On the other hand, other noncalcifying species, including sea grasses (Palacios and Zimmermann 2007; Hall-Spencer et al. 2008), and nitrogen-fixing bacteria (Hutchins et al. 2007) appear to produce increased biomass under increased CO_2 levels.

Recent studies have provided new findings that organisms growing in estuaries or in coastal upwelling zones, such as near river mouths or along the continental shelf of the west coast of North America, may already be experiencing significant biological effects resulting from the combined impacts of freshwater input, coastal upwelling, and ocean acidification (Salisbury et al. 2008; Feely et al. 2008). For example, Salisbury et al. (2008) demonstrated that discharge of acidic river water over the continental shelf may result in poor conditions for shell formation. When the low-alkalinity river water mixes into the surface ocean it can significantly reduce the aragonite or calcite saturation state. For many rivers, this process could inhibit the development of certain shellfish larvae such as the commercially valuable clam Mya arenaria.

On the west coast of North America, the seasonal upwelling of subsurface waters along the coast brings CO_2-enriched waters onto the shelf and, in some instances, into the surface ocean (Fig. 3.29). It appears that this water, in addition to its original high level of CO_2 resulting from natural respiration processes in the subsurface layers, is also significantly contaminated with anthropogenic CO_2 as it was last in contact with the atmosphere about 50 years ago when it took up additional CO_2 from the atmosphere. An immediate consequence of this additional CO_2 is that the CO_2 concentrations in these upwelled waters will be significantly greater than they would have been in preindustrial times. Furthermore, each ensuing year will draw on water that has been exposed to the atmosphere still more recently, resulting in yet higher CO_2 levels. Because these "ocean-acidified" upwelled waters are undersaturated with respect to aragonite, they are already a potential threat to many of the calcifying aragonitic species that live along such coasts.

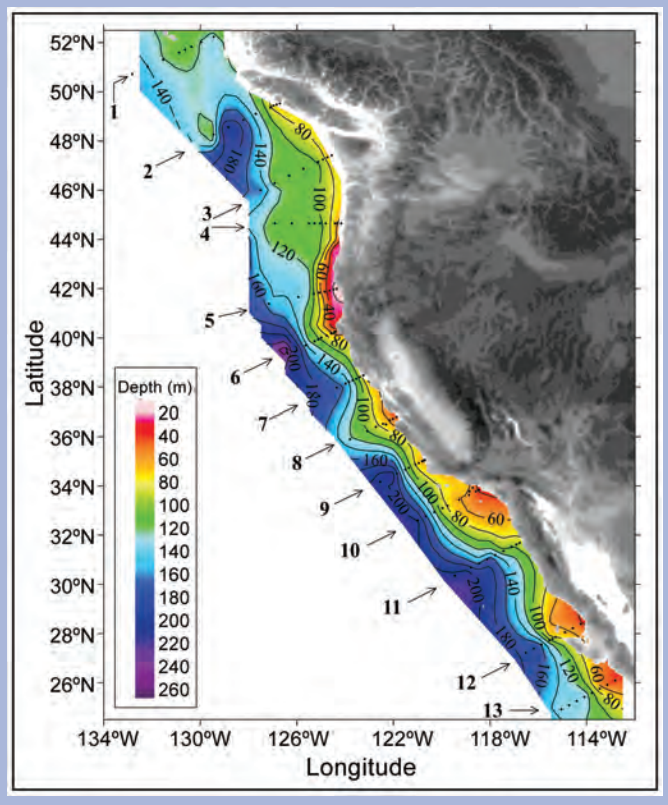

FIG. 3.29 (after Feely et al. 2008). Distribution of the depths of "ocean acidified" undersaturated water (aragonite saturation <1.0; pH <7.75) on the continental shelf of western North America from Queen Charlotte Sound, Canada, to San Gregorio Baja California Sur, Mexico. On transect line 5, the corrosive water reaches all the way to the surface in the inshore waters near the coast. The black dots represent station locations.

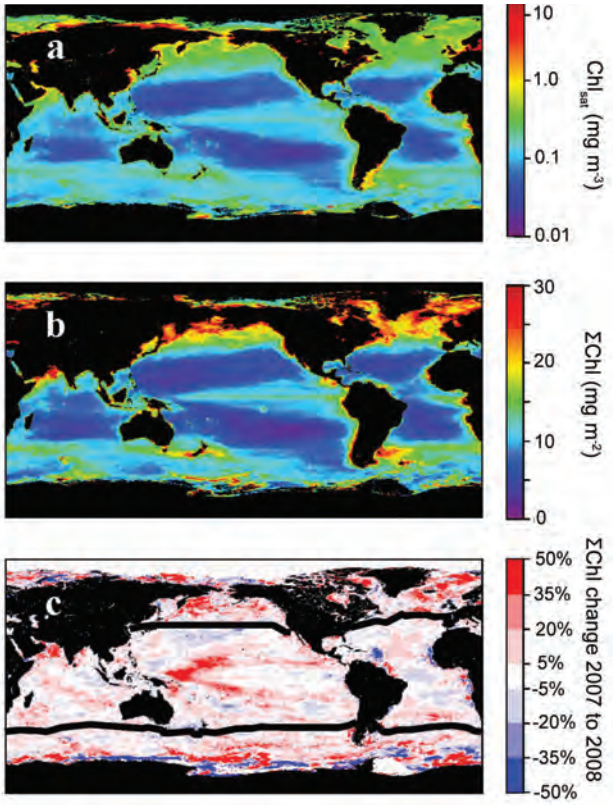

FIG. 3.30. (a) Average MODIS–*Aqua* Chl_{sat} for 2008. (b) Average MODIS-*Aqua* ΣChl for 2008. (c) Percentage change in ΣChl from 2007 to 2008. Heavy black lines demark permanently stratified oceans (2007 average SST >15°C) from higher-latitude regions (2007 average SST < 15°C). Because data were only available through day 320 of 2008 at the time of our analysis, here and in the main text annual values are for Julian dates 321 of a given year to 320 of the following year (e.g., the 2008 period = Julian day 321, 2007 to Julian day 320, 2008). Photic zone chlorophyll content calculated following Behrenfeld et al. (2006).

photosynthetic carbon fixation is the primary conduit through which atmospheric CO_2 is transferred into ocean organic carbon pools. Thus, these tiny suspended ocean "plants" play a vital role in world fisheries and the Earth's biogeochemical cycles.

The productivity of phytoplankton depends on the availability of sunlight, macronutrients (e.g., nitrogen, phosphorous), and micronutrients (e.g., iron), and thus is sensitive to climate-driven changes in these resources. Since 1997, a continuous satellite record of global climate-quality ocean color data has existed, allowing quantification of phytoplankton properties and investigation of broad relationships between upper-ocean environmental conditions and biology (e.g., McClain 2009). The ecosystem property most often derived from ocean color observations is the surface chlorophyll concentration (Chl_{sat}) (Fig. 3.30a), which can be taken as representative of the upper mixed layer and is a complex expression of phytoplankton standing stock (biomass) and physiological responses to prevailing light and nutrient levels. Chl_{sat} varies globally by three orders of magnitude (roughly 0.03 to >30 mg m^{-3}). A relevant property for ocean biology and biogeochemistry is the chlorophyll standing stock integrated over the photic zone (ΣChl; e.g., Behrenfeld et al. 2006), where the photic zone is traditionally defined as the layer between the surface and 1% light depth. Qualitatively, ΣChl exhibits a similar global distribution as Chl_{sat} (Fig. 3.30b), but ΣChl is roughly proportional to the square root of Chl_{sat}, so its value range is constrained to only 1.3 orders of magnitude (Behrenfeld et al. 2008a; Behrenfeld and Falkowski 1997).

Since the beginning of the satellite ocean color record, a striking correspondence has emerged between global variations in ΣChl and SST (Gregg et al. 2005; Behrenfeld et al. 2006). In 2008, our ability to monitor, refine, and interpret this relationship weakened. For the past decade, the SeaWiFS provided an unbroken time series of well-characterized global ocean data, but multiple satellite system failures this past year yielded temporal discontinuities in the record, with data gaps extending several months. Consequently, continuation of the long-term satellite record requires merging SeaWiFS data with products from the MODIS on the *Aqua* EOS satellite, which unavoidably introduces a potential for intersensor artifacts in the time series. Data from the MODIS sensor on the *Terra* EOS satellite are not used because the MODIS–*Terra* sensor has many technical issues that limit its utility for climate applications (e.g., Kwiatkowska et al. 2008).

SeaWiFS and MODIS–*Aqua* observations overlap continuously between July 2002 and December 2007. Over this 66-month period, global-average Chl_{sat} for SeaWiFS is 0.302 mg m^{-3}, average photic zone chlorophyll (ΣChl) is 13.5 mg m^{-2}, and total global chlorophyll standing stock for the photic zone averages 4.6 Tg. Sixty-one percent of this global chlorophyll stock is found in the permanently stratified oceans (approximated here as waters with annual average SST in 2007 of >15°C), which cover 72% of the ocean surface. The remaining 39% of global chlorophyll stock is found in the more productive seasonal seas at higher latitudes. By comparison, MODIS–*Aqua* data for the same 66-month period give a global-average Chl_{sat} of 0.266 mg m^{-3}, an average ΣChl of 12.1 mg m^{-2}, and an average global chlorophyll stock of 4.1 Tg, with 62% of this stock found in the

permanently stratified oceans. The elevated values of chlorophyll for SeaWiFS relative to MODIS–*Aqua* reflect a persistent bias between the two datasets, as clearly seen in the time series of monthly chlorophyll stocks for the permanently stratified oceans (Fig. 3.31a). On average, SeaWiFS chlorophyll values are 13.2% higher than MODIS–*Aqua*. When applied to the Vertically Generalized Production Model (Behrenfeld and Falkowski 1997), SeaWiFS data yield annual ocean NPP estimates ranging from 51.2 to 52.3 Pg C y^{-1}, while MODIS-*Aqua* gives values of 45.6 to 46.9 Pg C y^{-1} (average intersensor bias between NPP values is 12.3%).

Sensor gains for SeaWiFS and MODIS–*Aqua* are determined through comparison with the same in situ dataset (e.g., Franz et al. 2007), but no deliberate effort has been specifically made to date to minimize discrepancies between the resulting satellite data products. In 2009, both datasets will undergo a complete reprocessing, after which issues of bias between the two sensors should be reevaluated.

For 2008, the complete annual record provided by MODIS–*Aqua* gives an average Chl_{sat} of 0.271 mg m^{-3} and an average ΣChl of 12.4 mg m^{-2}. While the MODIS–*Aqua* globally integrated chlorophyll standing stock for 2008 of 4.1 Tg is only 1.4% higher than the 2007 value, regional changes in ΣChl were substantial and ranged to ±50% (Fig. 3.30c). Pixel-level comparison of these ΣChl changes with coincident changes in MODIS–*Aqua* SST data yields an inverse relationship for 66% of the stratified ocean (i.e., ΣChl decreases with increasing SST, and vise versa), while only 34% of the region exhibits a positive correlation. This result can be viewed in the broader context of the full satellite record by merging SeaWiFS, MODIS–*Aqua*, and AVHRR data and comparing monthly chlorophyll and SST anomalies for the permanently stratified, northern high-latitude, and southern high-latitude zones.

Monthly chlorophyll anomalies for the stratified oceans exhibit a remarkable coherence between the two records (r^2 = 0.81) (Fig. 3.31b), despite the bias between SeaWiFS and MODIS–*Aqua* data (e.g., Fig. 3.31a). Similar intersensor agreement in chlorophyll anomalies is also found for the two high-latitude zones (i.e., annual average SST <15°C). While these results do not diminish the impact of SeaWiFS/MODIS–*Aqua* biases on quantitative analyses of phytoplankton standing stocks and rates, they do imply that anomaly trends can be evaluated across the merged dataset. With respect to SST and in contrast to chlorophyll, AVHRR and MODIS–*Aqua* data for the 2002–07 period do not show significant intersensor

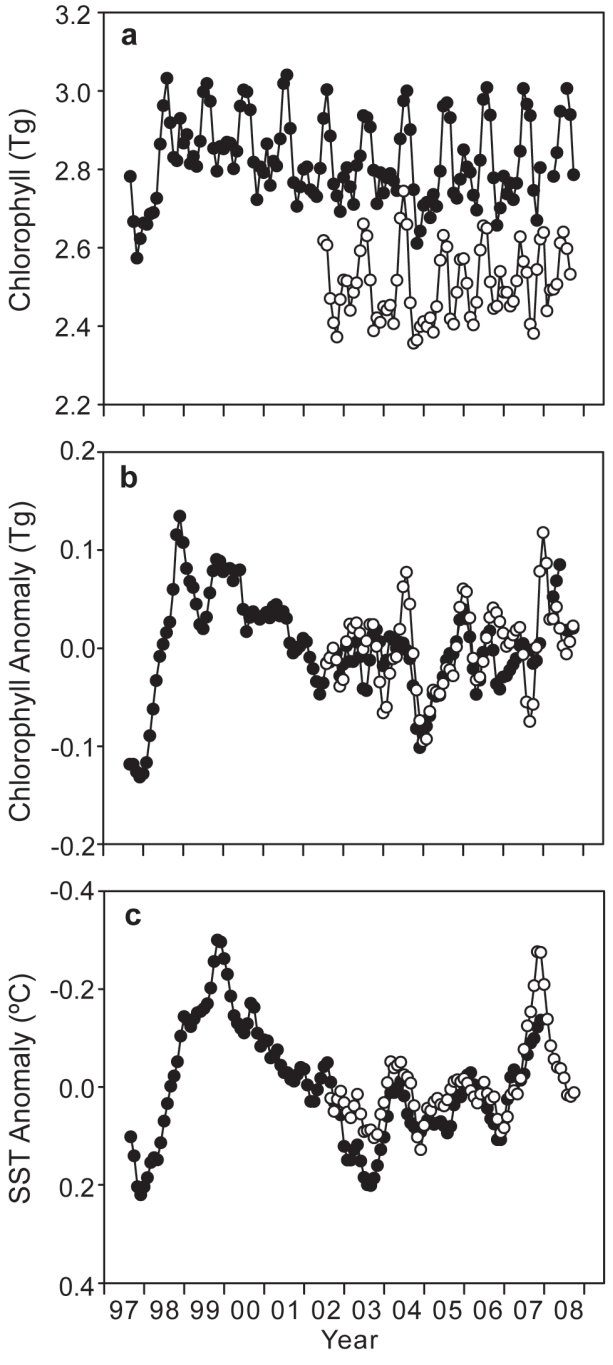

Fig. 3.31. (a) Monthly photic zone chlorophyll concentrations (= average ΣChl times area) for the permanently stratified oceans (SST >15°C; Fig. 1c). Solid symbols are SeaWiFS data. Open symbols are MODIS–*Aqua* data. (b) Monthly anomalies in stratified ocean photic zone chlorophyll for SeaWiFS (solid symbols) and MODIS–*Aqua* (open symbols). Anomalies represent the difference between photic zone chlorophyll for a given month and the average value for that month for a given sensor record. (c) Monthly anomalies in mean SST for the stratified oceans based on AVHRR-quality 5–8 data (solid symbols) and MODIS SST4 data (open symbols).

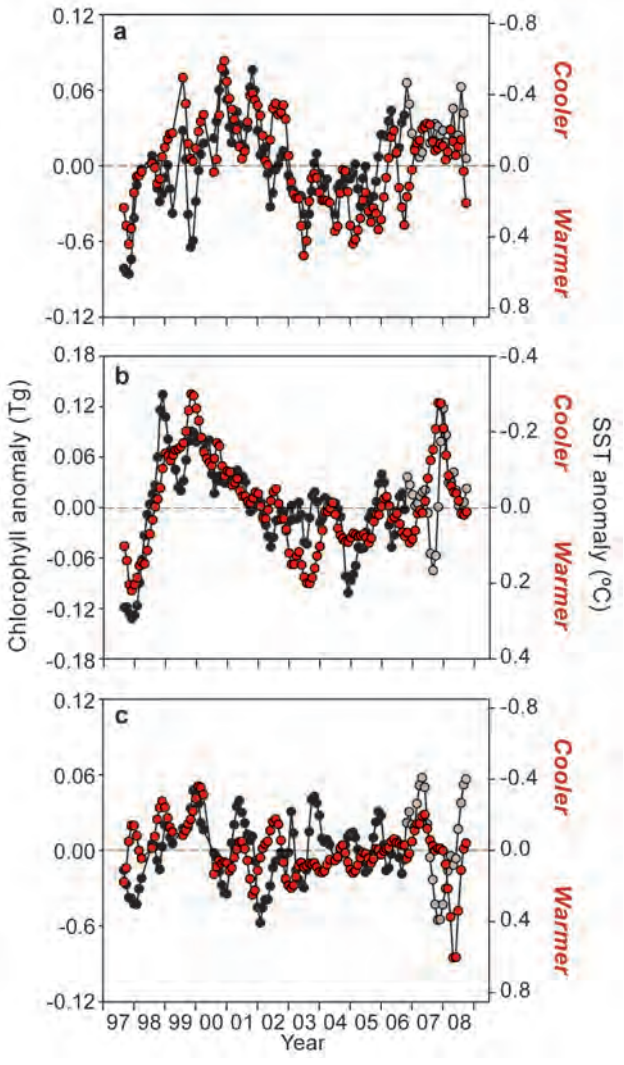

Fig. 3.32. Comparison of monthly anomalies in photic zone chlorophyll (black and gray symbols, left axis) and SST (red symbols, right axis). (a) Northern waters with 2007 average SST < 15°C. (b) Permanently stratified waters with 2007 average SST > 15°C. (c) Southern waters with 2007 average SST < 15°C. (a–c) Solid black symbols are SeaWiFS data. Gray symbols are MODIS–*Aqua* data. MODIS–*Aqua* data are spliced into the SeaWiFS record beginning on Julian day 321, 2006, to be consistent with Fig. 1. Horizontal dashed line in each panel corresponds to monthly climatological average values. (Note, left axes increase from bottom to top, while right axes decrease from bottom to top.)

biases and their SST anomalies are highly correlated ($r^2 = 0.91$) (Fig. 3.31c).

From the merged datasets, we find that the chlorophyll–SST relationship observed during 2008 is consistent with longer-term patterns observed since the first SeaWiFS images in September 1997 (Fig. 3.32). At northern high latitudes, oscillations in monthly chlorophyll anomalies are inversely correlated with SST anomalies (linear regression slope $p < 0.01$) (Fig. 3.32a). Note that the SST anomaly scale in all panels of Fig. 3.32 is the right-hand axes, with cooling at the top and warming at the bottom (as in Fig. 3.31c). Similarly, chlorophyll and SST anomalies are inversely related in the permanently stratified oceans (linear regression slope $p < 0.001$) (Fig. 3.32b). At high southern latitudes, weaker temporal trends in chlorophyll and SST are found, but an inverse relationship is still apparent and significant (linear regression slope $p < 0.05$). Combining the two polar regions, we find that the slope of the chlorophyll–SST relationship is a factor of 3 steeper (i.e., greater change in chlorophyll per unit change in SST) than in the permanently stratified zone.

Despite all three of our global zones exhibiting inverse chlorophyll–SST relationships, it is important to recognize their correlative, not causative, underpinnings. Ninety percent of the SST anomalies shown in Fig. 3.32 are within ±0.3°C of the 11-yr record monthly mean values (s.d. = 0.11°C), and the full range of anomaly values barely span a 1°C range. The direct physiological consequences (e.g., enzymatic reaction rates) of such minute temperature changes are negligible. Thus, correlations between SST and chlorophyll anomalies emerge because SST acts as a surrogate for other environmental factors that vary with SST and directly impact phytoplankton chlorophyll levels. Two such factors are nutrients (including iron) and mixed layer light levels. In general, surface layer warming is associated with stronger surface layer stratification and shallower mixing depths, which in turn increase average mixed layer phytoplankton light exposure and can hamper vertical nutrient exchange (Behrenfeld et al. 2005; Siegel et al. 2005). Decreased nutrient availability suppresses phytoplankton cellular chlorophyll levels and can diminish phytoplankton biomass. Likewise, acclimation to enhanced mixed layer light exposure entails reductions in cellular chlorophyll. Changes in seasonal surface mixing cycles can also influence chlorophyll levels by altering predator–prey interactions and thereby phytoplankton biomass and species composition. Thus, it is the correlation between SST and the summed expression of these direct nutrient, light, and ecosystem effects that gives rise to inverse chlorophyll–SST relationships. The relative importance of these controlling factors, however, varies over space and time (e.g., Behrenfeld et al. 2008b) and is expressed through variations in the slope of the chlorophyll–SST relationship.

Conclusions of the 2008 analysis are that 1) continuation of the satellite-based climate record for

global chlorophyll anomalies was possible, despite prolonged 2008 gaps in SeaWiFS data, because of a substantial and continuous overlap period between SeaWiFS and MODIS–*Aqua* observations; 2) the rise in chlorophyll for the stratified oceans between 2007 and 2008 corresponds with an ENSO shift toward La Niña conditions; 3) net inverse relationships between anomalies in chlorophyll and SST for the merged data are consistent with SeaWiFS-only trends since 1997; 4) intersensor biases in ocean products, while not preventing extension of anomaly trends, do have a significant impact on quantitative assessments of global chlorophyll concentrations and NPP; and 5) continuity of satellite ocean color observations is essential for understanding global ocean biosphere changes and feedbacks (Siegel et al. 2008).

4. THE TROPICS—H. J. Diamond, Ed.

a. *Overview*—H. J. Diamond

This tropics section consists of five topics: 1) ENSO and the tropical Pacific; 2) the MJO; 3) TC activity for the 2008 season in seven basins: the North Atlantic, eastern North Pacific, northwest Pacific, north Indian and south Indian, South Pacific, and Australia; 4) ITCZ behavior in the Pacific and Atlantic basins; and 5) the IOD.

The year was characterized by fluctuating conditions throughout the tropical Pacific that began with a strong La Niña episode that ended in June. This was followed by ENSO-neutral conditions during the middle and latter half of the year, and a return to La Niña conditions late in December. The predominant La Niña conditions had significant impacts on the activity of the Atlantic and northeast Pacific TC seasons.

The 2008 Atlantic hurricane season was the 14th busiest on record and significantly more active than the 2006 and 2007 seasons. Conversely, activity in the northwest Pacific was considerably below normal during 2008. While activity in the north Indian Ocean was only slightly above average, the season was punctuated by Cyclone Nargis, which was the seventh-strongest cyclone ever in the basin.

Since the weak negative IOD in 2005, there have been three consecutive seasons from 2006–08 with a positive IOD.

b. *ENSO and the tropical Pacific*—M. L'Heureux, G. Bell, and M. Halpert

1) Oceanic conditions

ENSO is a coupled ocean–atmosphere phenomenon centered in the equatorial Pacific Ocean. ENSO features two opposing phases, El Niño and La Niña, which are responsible for considerable interannual climate variability in the global tropics and mid-to-high latitudes. NOAA defines these ENSO phases using the Niño-3.4 index, which reflects area-averaged SST anomalies between 5°N–5°S and 170°–120°W.

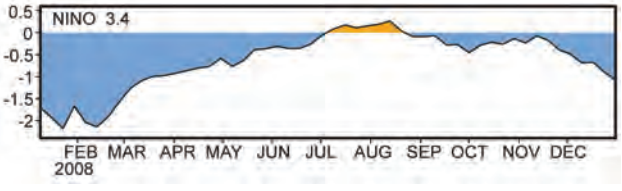

Fig. 4.1. Time series of SST anomalies (°C) in the Niño-3.4 region (5°N–5°S, 170°–120°W). Anomalies are departures from the 1971–2000 base period weekly means and are obtained from the adjusted OI dataset (Smith and Reynolds 1998).

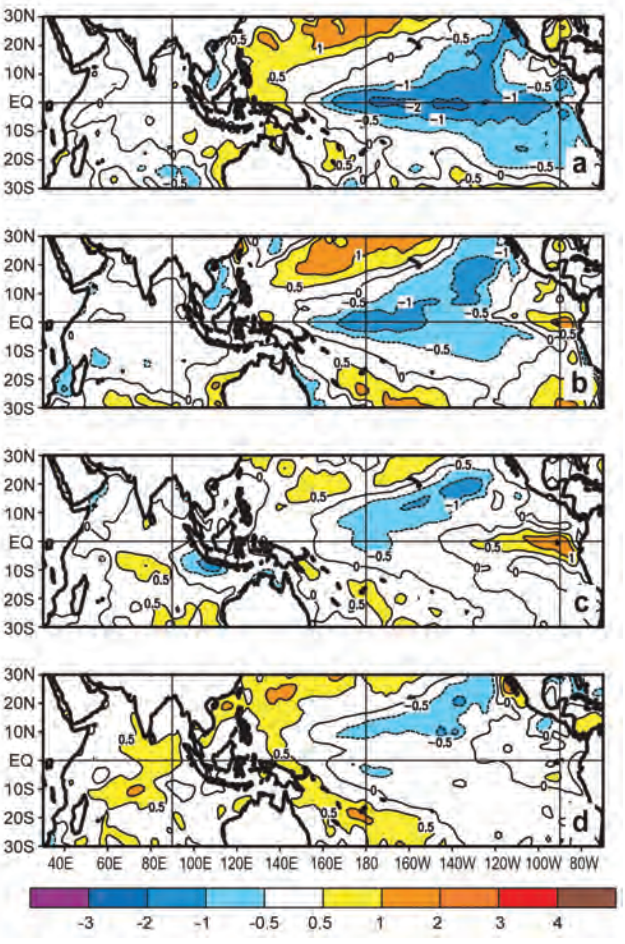

Fig. 4.2. SST anomalies (°C) during (a) Dec–Feb 2007–08, (b) Mar–May 2008, (c) Jun–Aug 2008, and (d) Sep–Nov 2008. Anomalies are departures from the 1971–2000 adjusted OI climatology (Smith and Reynolds 1998).

El Niño occurs when the 3-month running mean value of the Niño-3.4 index (ONI) is greater than or equal to +0.5°C, while La Niña occurs when the ONI is less than or equal to −0.5°C.

During 2008, conditions throughout the tropical Pacific reflected a strong La Niña episode that ended in June. This was followed by ENSO-neutral conditions during the middle and latter half of the year, and a return to La Niña conditions late in December (Fig. 4.1). During the peak of the event, the DJF 2007–08 ONI value was −1.4°C, with weekly values of the Niño-3.4 index dropping below −2°C. These measures indicated the strongest La Niña episode since 1999–2000.

The seasonal surface and subsurface temperature anomalies associated with the 2007–08 La Niña episode are summarized in Figs. 4.2, 4.3. SSTs during the peak of the event were at least 1°C below average

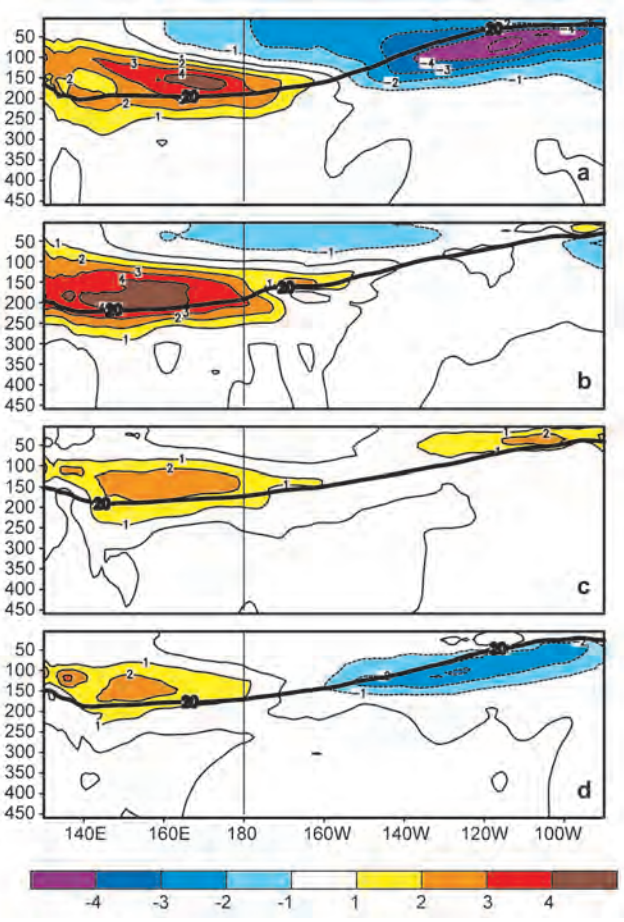

Fig. 4.3. Equatorial depth-longitude section of ocean temperature anomalies (°C) averaged between 5°N and 5°S during (a) Dec–Feb 2007–08, (b) Mar–May 2008, (c) Jun–Aug 2008, and (d) Sep–Nov 2008. The 20°C isotherm (thick solid line) approximates the center of the oceanic thermocline. The data are derived from an analysis system that assimilates oceanic observations into an oceanic GCM (Behringer et al. 1998). Anomalies are departures from the 1971–2000 period monthly means.

across the eastern half of the equatorial Pacific, with the largest departures (below –2°C) centered just east of the international date line and in the east-central Pacific (Fig. 4.2a).

The pattern of subsurface temperature anomalies illustrates the large vertical extent of the oceanic cooling during this period (Fig. 4.3a), with departures in some areas of the eastern Pacific at least 5°C below average. In the east-central and eastern Pacific, this cooling reflected an exceptionally shallow thermocline. In contrast, in the western half of the basin temperatures were significantly above average at thermocline depth (100–250 m), although negative anomalies resided close to the ocean surface (0–100 m). These subsurface temperature anomalies and the associated increased slope of the oceanic thermocline are typical of a mature La Niña.

During March–May 2008, a wide swath of below-average but somewhat weaker SST anomalies remained across the equatorial Pacific, except for the far eastern portion of the basin (Fig. 4.2b). The most significant evolution during this period occurred below the ocean surface, where the negative temperature anomalies in the east-central and eastern equatorial Pacific dissipated in response to a deepening of the oceanic thermocline (Fig. 4.3b). Subsequent additional warming and a westward expansion of positive SST anomalies in the eastern Pacific contributed to a rapid weakening of La Niña during May and June, and to the appearance of positive anomalies in the Niño-3.4 region by early July.

The dissipation of the anomalous subsurface temperature structure occurred in conjunction with oceanic Kelvin waves initiated during January and May (Fig. 4.7). These waves were triggered by low-level westerly wind events associated with MJO activity (section 4c). Major impacts of the final Kelvin wave in May included a weakening of the record-high (dating back to the start of the historical record in 1980) oceanic heat content anomalies in the western Pacific, and the development of positive surface (Fig. 4.2c) and subsurface (Fig. 4.3c) temperature anomalies in the eastern Pacific.

During SON 2008, near-average SSTs were evident throughout the equatorial Pacific Ocean (Fig. 4.2d). However, a more La Niña–like subsurface temperature pattern and thermocline structure became re-established (Fig. 4.3d), which when combined with subsequent cooling of the SSTs, led to the reemergence of La Niña in December.

2) Atmospheric circulation

During DJF 2007–08 and MAM 2008 the below-average SSTs were strongly coupled to the atmosphere (Figs. 4.4a,b). For example, convection was suppressed over the central and east-central equatorial Pacific (brown shading), and enhanced over Indonesia and the far western Pacific (green shading). This pattern reflects a westward contraction of the equatorial convection toward the western Pacific and a complete disappearance of convection from the central Pacific.

These conditions were associated with enhanced easterly trade winds at 850 hPa (vectors, Figs. 4.4a,b) and anomalous upper-level westerly winds at 200 hPa (not shown) across the central and western equatorial Pacific Ocean, along with anomalous low-level westerly winds over the IO. This combination reflects

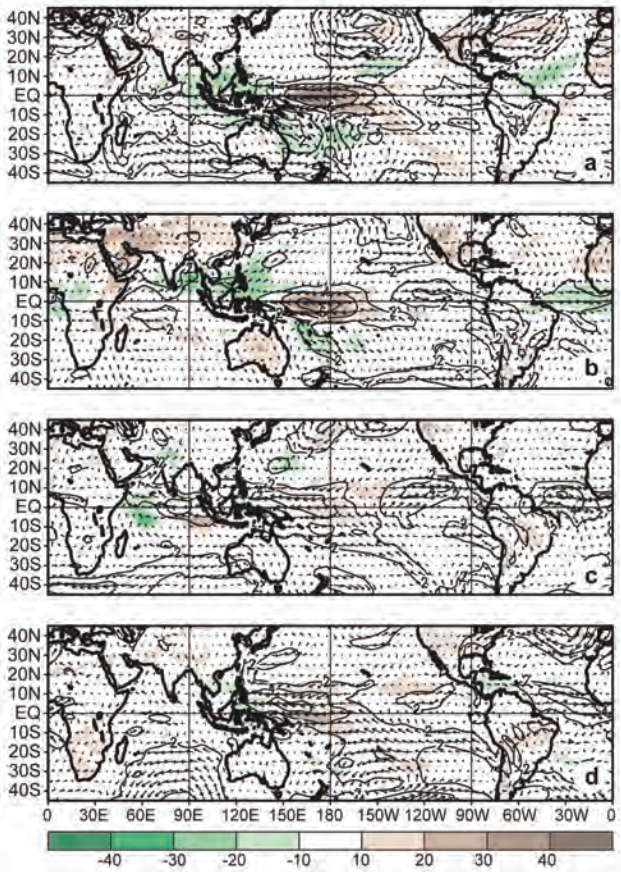

Fig. 4.4. Anomalous 850-hPa wind vector and speed (m s^{-1}) and anomalous OLR (shaded, W m^{-2}) during (a) Dec–Feb 2007–08, (b) Mar–May 2008, (c) Jun–Aug 2008, and (d) Sep–Nov 2008. Anomalies are departures from the 1979–95 period monthly means.

an enhanced equatorial Walker circulation that was confined to the western half of the Pacific Ocean, which is typical of La Niña.

In both hemispheres the subtropical circulation during DJF and MAM 2008 was also typical of La Niña, with cyclonic anomalies over the central and east-central Pacific and anticyclonic anomalies over Australasia (shading, Fig. 4.5a). This pattern reflected enhanced mid-Pacific troughs and a westward retraction of the subtropical ridges toward the western Pacific (contours, Fig. 4.5b). In the Northern Hemisphere, these conditions were associated with a westward retraction of the East Asian jet core, and a westward shift of the mean North American ridge to the eastern North Pacific and the mean Hudson Bay trough to western North America.

During JJA and SON the anomalous convection over the tropical Pacific weakened as La Niña dissipated (Figs. 4.4c,d). However, the low-level easterlies remained enhanced in the western and central Pacific Ocean, and convection remained suppressed near the date line.

3) La Niña impacts

Regional La Niña impacts during DJF 2007–08 and MAM 2008 included above-average rainfall across much of the Maritime Continent (e.g., Indonesia, Philippines, Malaysia, and Borneo) extending to northernmost portions of Australia. An enhanced and extreme southwestward displacement of the SPCZ in April 2008 contributed to increased rainfall over the southwestern Pacific Ocean, including significant flooding in Vanuatu (Island Climate Update 2008a).

Also consistent with La Niña, rainfall was enhanced in northeastern Brazil and in the South African monsoon region. Over the United States, La Niña led to drier-than-average conditions across much of the South and to increased precipitation in the Pacific Northwest and in the Ohio and Tennessee valleys. A persistent La Niña–like circulation contributed to an above-normal Atlantic hurricane season (section 4d2) and to below-average hurricane activity in the northeast Pacific (section 4d3).

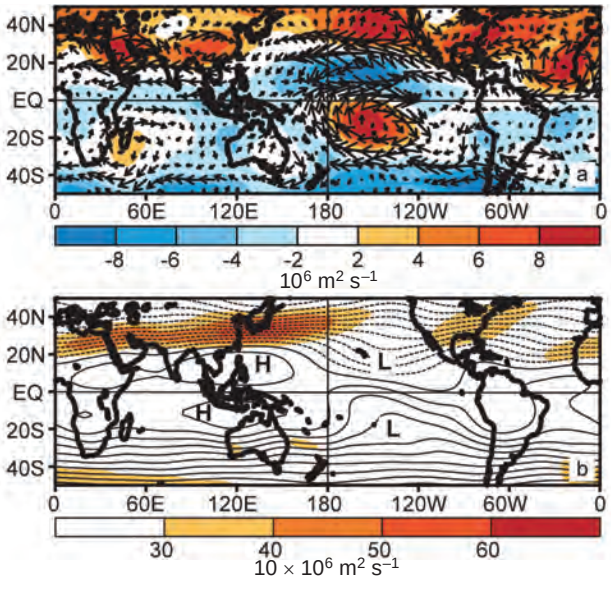

Fig. 4.5. 200-hPa circulation during Dec 2007–May 2008: (a) anomalous streamfunction (shading) and vector winds (m s^{-1}) and (b) total streamfunction (contours) and wind speed (shading). In (a), anomalous ridges are indicated by positive values (red) in the NH and negative values (blue) in the SH. Anomalous troughs are indicated by negative values in the NH and positive values in the SH. In (b), "L" indicates mid-Pacific trough and "H" indicates western Pacific subtropical ridge. Anomalies are departures from the 1971–2000 period monthly means.

c. The Madden–Julian Oscillation—J. Gottschalck and G. Bell

The MJO (Madden and Julian 1971, 1972, 1994) is a leading climate mode of tropical convective variability that occurs on intraseasonal time scales. The convective anomalies associated with the MJO often have the same spatial scale as ENSO, but differ in that they exhibit a distinct eastward propagation and generally traverse the globe in 30–60 days. The MJO can strongly affect the tropical and extratropical atmospheric circulation patterns, and sometimes produces ENSO-like anomalies (Mo and Kousky 1993; Kousky and Kayano 1994; Kayano and Kousky 1999). The MJO is often quite variable in a given year, with periods of moderate-to-strong activity sometimes followed by little or no activity. Overall, the MJO tends to be most active during neutral and weak ENSO periods and is often absent during strong El Niño events (Hendon et al. 1999; Zhang and Gottschalck 2002; Zhang 2005).

The MJO is seen by continuous propagation of 200-hPa velocity potential anomalies around the globe. A time–longitude section of this parameter shows three distinct periods during 2008 with at least moderate MJO activity (Fig. 4.6). These include 1) a continuation during January to early March of strong activity that began in late 2007, 2) moderate-to-strong activity from May through July, and 3) moderate-to-strong activity during September and October.

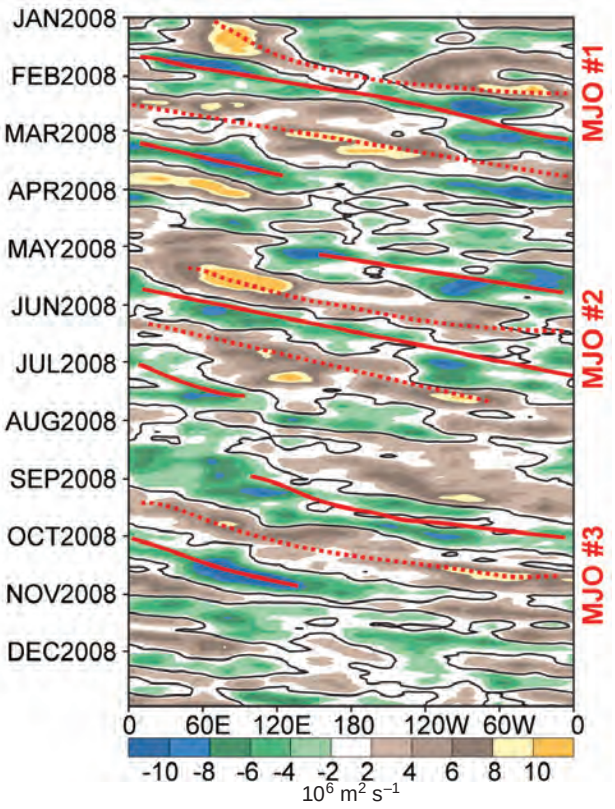

Fig. 4.6. Time–longitude section of filtered 200-hPa velocity potential anomaly (5°N–5°S) for 2008. Green (brown) shading represents anomalous divergence (convergence). Red lines highlight the MJO signal. The three MJO episodes are marked. Anomalies are departures from the 1971–2000 base period daily means.

The early and midyear activity was particularly interesting due to its interplay with La Niña. For example, during late December 2007, February–March and early May, the MJO and La Niña–related convective anomalies were in-phase, making it appear that La Niña and its associated downstream circulation anomalies were particularly strong. Conversely, during January, late May, and late June, the MJO and La Niña–related convective anomalies were out-of-phase, resulting in a masking of the underlying La Niña signals.

These varying climate conditions had several impacts in the Pacific/North American sector. During late December 2007, enhanced convection across Indonesia (in response to both the MJO and La Niña) resulted in a strong upper-level ridge over the high latitudes of the central North Pacific and an amplified trough over the eastern North Pacific. This circulation led to heavy precipitation across sections of central and Southern California in early January 2008, regions that normally receive little or no wintertime precipitation during La Niña.

Other periods when La Niña and the MJO were in-phase resulted in recurring jet stream patterns that favored exceptionally heavy precipitation events and eventual June flooding in the U.S. Midwest (see section 7b2). Also, consistent with the results of Mo (2000) and Maloney and Hartmann (2000), periods during 2008 with suppressed MJO-related convection near the date line were more La Niña–like and were associated with lower northeast Pacific and greater Atlantic hurricane activity.

Other interactions between the MJO and La Niña were related to two equatorial oceanic Kelvin waves that were triggered by the MJO during January and May 2008. In both events, the MJO completely masked La Niña's convective signal by producing suppressed convection over the Indian Ocean and Indonesia, and enhanced convection across the western Pacific and within the SPCZ. In each case, Kelvin waves were initiated by a dramatic weakening of the low-level easterly winds as the area of suppressed convection propagated into the western Pacific Ocean (dotted lines, Fig. 4.7).

The Kelvin wave triggered in January acted to lower the oceanic thermocline across the central and east-central equatorial Pacific, thereby substantially weakening the negative heat content anomalies as-

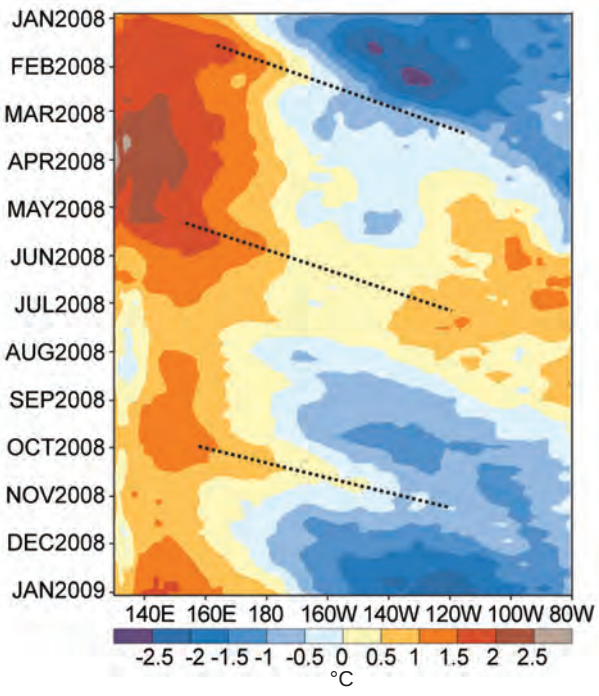

Fig. 4.7. Time–longitude section of the upper ocean (0–300 m) heat content anomaly (5°N–5°S) for 2008. Blue (yellow/red) shading indicates below- (above) average heat content. The downwelling phases (solid lines) of oceanic Kelvin waves are indicated. Anomalies are departures from the 1982–2004 base period pentad means.

sociated with La Niña. A similar warming due to the Kelvin wave triggered in May led to positive heat content anomalies across much of the Pacific basin during June and July, and to the end of La Niña (Fig. 4.3c).

A third equatorial Kelvin wave was triggered by the MJO in late September, again in response to the propagation of suppressed convection from the Indian Ocean to the western Pacific. This wave counteracted the anomalous cooling that was becoming reestablished across the central and east-central equatorial Pacific, and likely delayed the reemergence of La Niña until later in the year. The timing of La Niña's reemergence was also likely related to the opposite phase of the MJO in November, which featured significantly enhanced convection and stronger low-level easterlies over the western Pacific Ocean.

d. Tropical cyclones

1) Overview—H. J. Diamond

The global tallying of total storm numbers is always challenging and involves more than simply adding up basin totals, as there are a number of storms that cross basin boundaries. Averaged across all basins, the 2008 TC season (2007–08 in the Southern Hemisphere) saw a near-normal (1981–2000 base) number of tropical or NSs (≥ 34 kt) and a below-average number of HTCs (≥ 64 kt) and major HTCs (≥ 96 kt) than average. Globally, 96 NSs developed during 2008 (1 below average), and 46 became HTCs (9 below average). Of these, 20 (compared with 26 in 2006 and 18 in 2007) attained major/intense status (global average is 25.4).

The 2008 season was significantly above average in two basins (North Atlantic and south Indian); near to slightly above average in the NIO, and near to below average in the remaining basins (eastern North Pacific, northwest Pacific, southwest Pacific, and Australian region). The North Atlantic season was also active in terms of landfalling storms. The island of Hispaniola was affected by several storms (two direct hits); Cuba experienced two landfalls by major hurricanes; the continental United States experienced a total of six landfalling storms (including three hurricanes); and one hurricane made a very rare landfall in Nova Scotia, Canada. The NIO season was punctuated by a severe Category-5 storm (Cyclone Nargis), which was responsible for over 145,000 deaths and $10 billion (USD) in damages in Myanmar; Nargis is also ranked as the seventh-strongest storm ever in that basin. TC activity in the western North Pacific basin was also shifted farther westward and northward than normal and was unusually tranquil (see sidebar "Unusually Quiet West Pacific Typhoon Season Ends with a Dolphin Kick").

2) Atlantic basin—G. D. Bell, E. Blake, S. B. Goldenberg, T. Kimberlain, C. W. Landsea, R. Pasch, and J. Schemm

(i) Seasonal activity

The 2008 Atlantic hurricane season produced 16 NSs, of which 8 became Hs and 5 became MHs (J. Beven and D. Brown 2009, unpublished manuscipt). The 1950–2000 averages are 11 NSs, 6 Hs, and 2 MHs. For 2008 the ACE (Bell et al. 2000) was 167% of the median (Fig. 4.8).This value is the 14th most active since 1950 and is well into the above-normal range (see www.cpc.noaa.gov/products/outlooks/background_information.shtml), consistent with the ongoing active Atlantic hurricane era that began in 1995 (Goldenberg et al. 2001). It is the only season on record in which an MH existed in every month from July through November.

Consistent with other active seasons, 11 NSs formed in the MDR (Goldenberg and Shapiro 1996) during 2008 (green box, Fig. 4.9a). These systems accounted for seven Hs, all five MHs, and 88% of the ACE value. The season was also active in terms of landfalling NSs. The nations in and surrounding

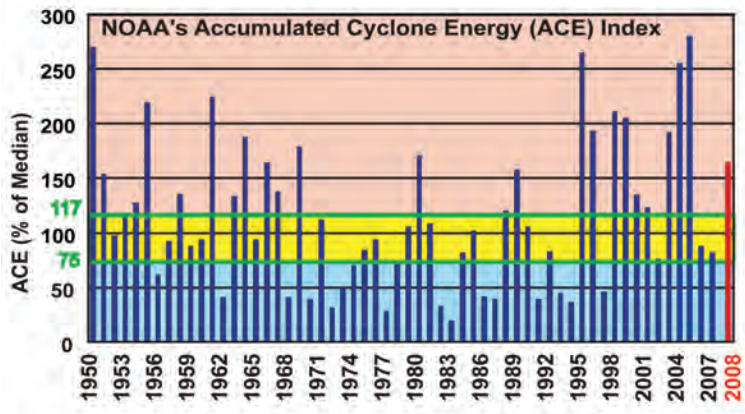

Fig. 4.8. ACE values expressed as percent of the 1950–2000 median value (87.5×10^4 kt^2). ACE is a wind energy index that measures the combined strength and duration of the NSs. ACE is calculated by summing the squares of the 6-hourly maximum sustained surface wind speed in knots (Vmax2) for all periods while the storm has at least TS strength. Pink, yellow, and blue shades correspond to NOAA's classifications for above-, near-, and below-normal seasons, respectively.

the Caribbean Sea were severely impacted by four TSs and four Hs. Cuba experienced three hurricane landfalls (including two MHs, Gustav and Ike), while Hispaniola was affected by several NSs including direct strikes by TS Fay and H Hanna. The continental United States was struck by three TSs and three Hs, with all but one TS making landfall along the Gulf Coast. Elsewhere, H Kyle made landfall in Nova Scotia, Canada.

(ii) SSTs

For the ASO climatological peak months of the season, SSTs were generally 0.5°–1.0°C above average in the MDR (Fig. 4.9a). The area-averaged SST anomaly in the MDR was 0.60°C, the fifth warmest since 1950 (Fig. 4.9b).

This warmth partly reflects the warm phase of the AMO (Enfield and Mestas-Nuñez 1999), which accompanied the 1995 transition to the active Atlantic phase of the tropical multidecadal signal (Goldenberg et al. 2001; Bell and Chelliah 2006). It also reflects reduced mixing and reduced evaporation from the ocean surface in response to weaker northeasterly trade winds (anomalous southwesterly flow) across the southern half of the MDR (Fig. 4.10a).

(iii) Atmospheric circulation

An interrelated set of atmospheric anomalies typical of recent active hurricane seasons (Landsea et al. 1998; Bell et al. 1999, 2000, 2004, 2006; Goldenberg et al. 2001; Bell and Chelliah 2006; Kossin and Vimont 2007) set the stage for the active 2008 hurricane season. These conditions are also known to greatly increase the probability of hurricane landfalls, as was seen in 2008.

During ASO 2008, weaker trade winds and high values of CAPE covered the southern half of the MDR (Fig. 4.10a), and sea level pressure was below average across the MDR (blue shading, Fig. 4.10b). These conditions were associated with a more northward position of the Atlantic ITCZ (section 4e2) and with an enhanced West African monsoon system.

The low-level westerly anomalies extended past 700 hPa, the approximate level of the African Easterly Jet, and were associated with a 5° northward shift of the AEJ core (black arrow) compared to climatology. As a result, the bulk of the African easterly wave energy (Reed et al. 1977) was often centered within the MDR. The AEJ also featured increased cyclonic shear along its equatorward flank, which dynamically favors stronger easterly waves and provides an inherent cyclonic rotation to their embedded convective cells.

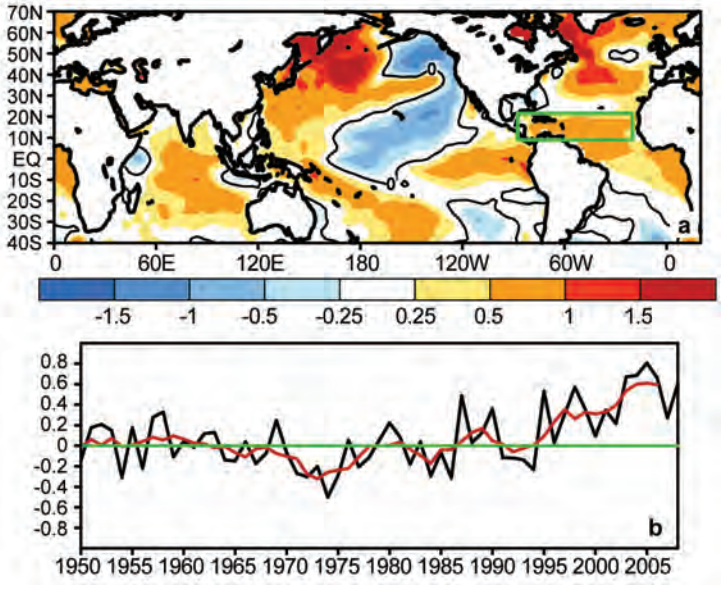

Fig. 4.9 (a) SST anomalies (°C) during Aug–Oct 2008. (b) Consecutive Aug–Oct area-averaged SST anomalies in the MDR. Red line shows the corresponding 5-yr running mean. Green box in (a) denotes the MDR. Anomalies are departures from the 1971–2000 monthly means.

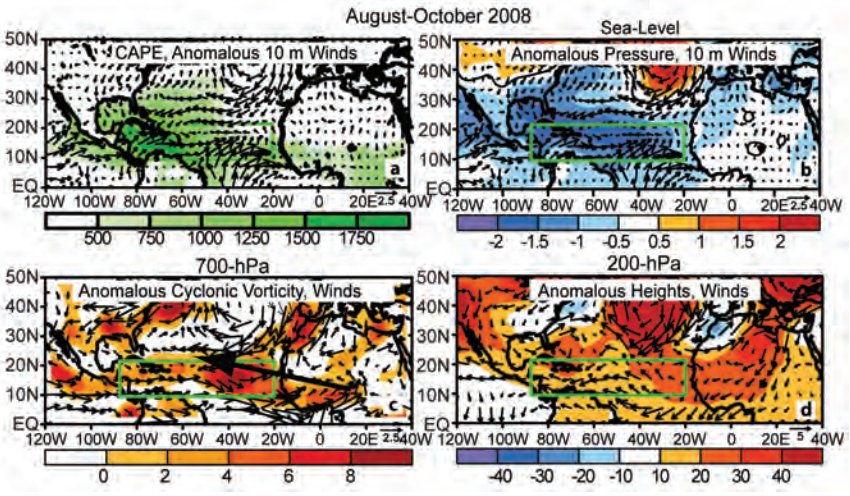

Fig. 4.10. Aug–Oct 2008: (a) total CAPE (J kg^{-1}) and anomalous vector winds (m s^{-1}) at 10 m; (b) anomalous sea level pressure (shading, hPa) and vector winds at 10 m; (c) 700-hPa anomalous cyclonic relative vorticity (shading) and vector winds, with thick arrow indicating the observed AEJ core; (d) 200-hPa anomalous heights and vector winds. Green boxes denote the MDR. Anomalies are departures from the 1971–2000 monthly means.

below normal and only three were above normal.

The transition to the current active era was associated with a phase change in the tropical multidecadal signal, which reflects the leading modes of tropical convective rainfall variability occurring on multidecadal time scales (Bell and Chelliah 2006; Bell et al. 2007). This signal highlights the convectively driven nature of the atmospheric anomalies across the central and eastern MDR, and links them to an east–west oscillation in anomalous convection between western Africa (Landsea and Gray 1992; Goldenberg and Shapiro 1996) and the Amazon basin. As seen in 2008, the combination of an enhanced West African monsoon and suppressed convection in the Amazon basin (Fig. 4.12a) is consistent with the ongoing high-activity era (Fig. 4.12b), as is the anomalous low-level inflow into the West African monsoon region

At 200 hPa, the wind and height anomalies reflected an enhanced upper-level ridge and a stronger, more westward extension of the tropical easterly jet (Fig. 4.10d). The result was weak (less than 8 m s^{-1}) vertical wind shear between 200 and 850 hPa across much of the MDR (shading, Fig. 4.11a), with the most anomalously weak shear spanning the central tropical Atlantic Ocean and Caribbean Sea (Fig. 4.11b).

This combination of conditions meant that many TSs developed from amplifying African easterly waves in an environment of below-average pressure and increased cyclonic shear. Those waves were also embedded within an extended region of weak vertical wind shear, which enabled further intensification as they moved westward over progressively warmer SSTs.

Two prominent climate phenomena can account for the interrelated set of anomalies associated with the 2008 Atlantic hurricane season. These are the ongoing active Atlantic phase of the tropical multidecadal signal and lingering La Niña signals.

(iv) Conditions associated with the ongoing active Atlantic hurricane era

2008 marks the 10th above-normal Atlantic hurricane season since the current high-activity era began in 1995. During 1995–2008 only the strong El Niño year of 1997 had below-normal activity. The increased activity since 1995 contrasts with the preceding low-activity era 1971–94, when half of the seasons were

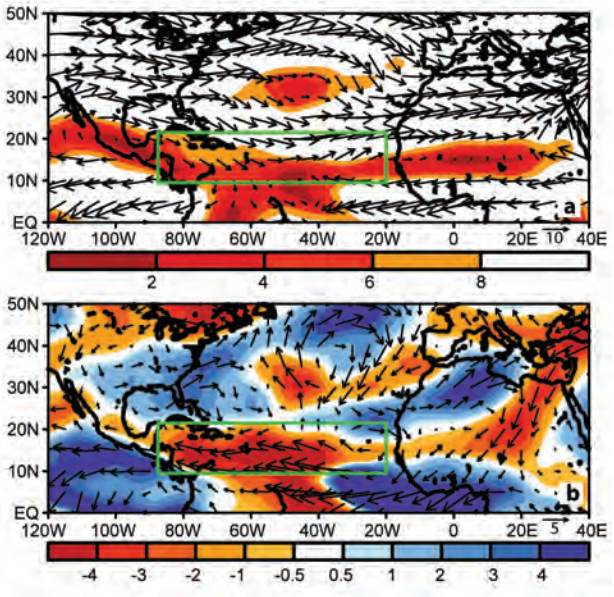

Fig. 4.11. Aug–Oct 2008: 200–850-hPa vertical wind shear magnitude (m s^{-1}) and vectors (a) total and (b) anomalies. In (a), shading indicates values below 8 m s^{-1}. In (b), red (blue) shading indicates below- (above) average magnitude of the vertical shear. Green boxes denote the MDR. Anomalies are departures from the 1971–2000 monthly means.

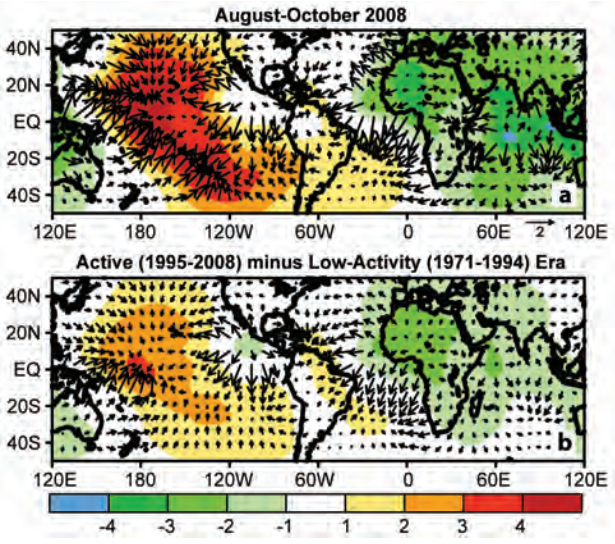

Fig. 4.12. 200-hPa velocity potential (shading) and divergent wind vectors (m s^{-1}): (a) Aug–Oct 2008 anomalies and (b) high-activity (1995–2008) period means minus low-activity (1971–94) period means. Anomalies are departures from the 1971–2000 monthly means.

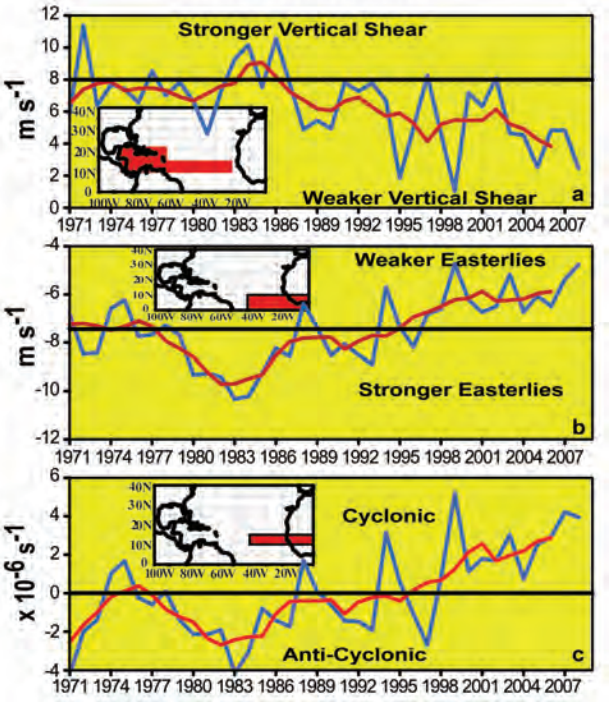

Fig. 4.13. Time series showing consecutive Aug–Oct values of area-averaged (a) 200–850-hPa vertical shear of the zonal wind (m s^{-1}), (b) 700-hPa zonal wind (m s^{-1}), and (c) 700-Pa relative vorticity (× 10^{-6} s^{-1}). Blue curves show unsmoothed values, and red curves show a 5-pt running mean of the time series. Averaging regions are shown in the insets.

(Fig. 4.11a) and enhanced upper-level outflow from that region (Figs. 4.10d, 4.12a).

Consistent with these conditions are dramatic differences in the vertical wind shear (Fig. 4.13a), 700-hPa zonal winds (Fig. 4.13b), and 700-hPa relative vorticity (Fig. 4.13c), within the MDR between the high-activity and low-activity era.

An enhanced West African monsoon system has major impacts on the 200-hPa Northern Hemispheric circulation, as seen in 2008 by the pronounced interhemispheric symmetry of streamfunction anomalies across the eastern subtropical Atlantic Ocean and Africa (Fig. 4.14a). This pattern reflects enhanced upper-level ridges in the subtropics of both hemispheres and a stronger tropical easterly jet, both of which have prevailed throughout this high-activity era (Fig. 4.14b) (Bell and Chelliah 2006).

(v) La Niña

La Niña acts to reduce the vertical wind shear in the western MDR, thus favoring increased Atlantic hurricane activity (Gray 1984). During 2008, SSTs in the Niño-3.4 region returned to normal in June (Fig. 4.1). However, tropical convection remained suppressed near the date line throughout ASO (e.g., Fig. 4.4c), which favored cyclonic anomalies at 200 hPa over the western subtropical Pacific and anticyclonic anomalies over the eastern subtropical Pacific and Caribbean Sea (Fig. 4.14a). The associated anomalous easterly winds extended from the eastern Pacific to the tropical Atlantic, and contributed to reduced vertical wind shear in the western MDR. Historically, the presence of these conditions during a high-activity era greatly increases the probability of an above-normal Atlantic hurricane season.

During 2008, the window of opportunity for TC formation widened, as the above circulation anomalies (Figs. 4.12–4.14) were present before the peak of the season. For example, a large area of anomalous upper-level divergence and enhanced convection (indicated by the core of negative velocity potential anomalies; Fig. 4.15a) was already present during April–June over the eastern tropical Atlantic Ocean and West Africa (Fig. 4.15a). Impacts from this anomalous convection can be seen in the pattern of 200-hPa streamfunction anomalies (Fig. 4.15b), which shows amplified ridges in the subtropics of both hemispheres flanking the region of enhanced convection. As shown by Bell et al. (2009), the associated upper-level easterly anomalies and reduced vertical wind shear contributed to the development of two TCs (including long-lived MH Bertha) within the MDR during July, a month when conditions are normally unfavorable for low-latitude TC formation (DeMaria et al. 2001).

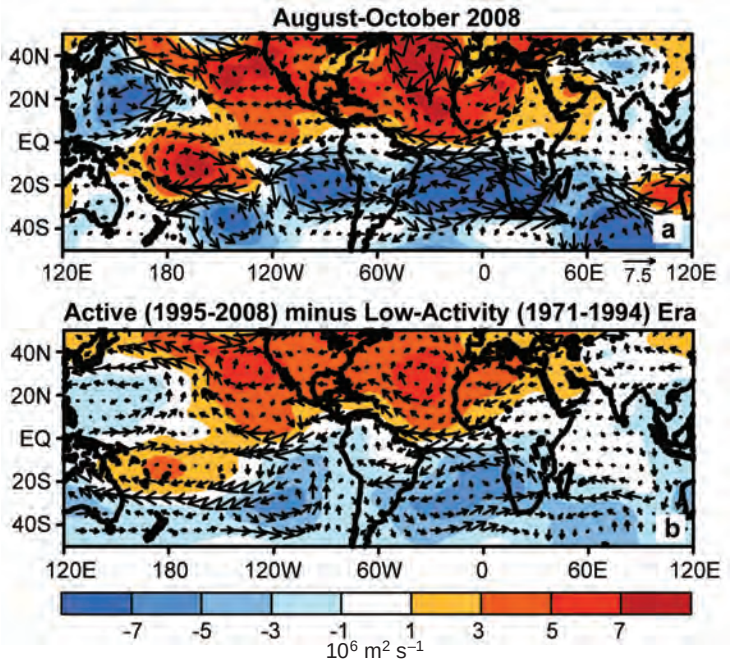

Fig. 4.14. 200-hPa streamfunction (shading) and vector wind (m s^{-1}): (a) Aug–Oct 2008 anomalies and (b) high-activity (1995–2008) period means minus low-activity (1971–94) period means. In (a), anomalous ridges are indicated by positive values (red) in the NH and negative values (blue) in the SH. Anomalous troughs are indicated by negative values in the NH and positive values in the SH. Anomalies are departures from the 1971–2000 monthly means.

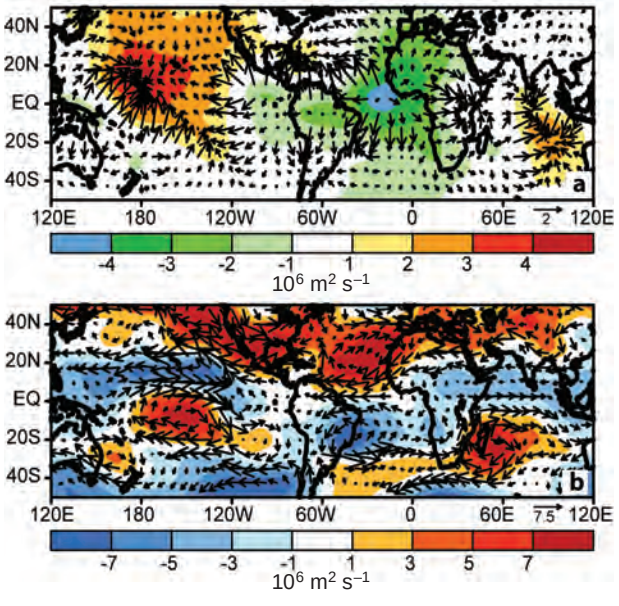

Fig. 4.15. Apr–Jun 2008 anomalies at 200 hPa: (a) velocity potential (shading) and divergent wind vectors (m s^{-1}) and (b) streamfunction and total wind vectors (m s^{-1}). In (b), anomalous ridges are indicated by positive values (red) in the NH and negative values (blue) in the SH. Anomalous troughs are indicated by negative values in the NH and positive values in the SH. Anomalies are departures from the 1971–2000 monthly means.

3) Eastern North Pacific basin—M. C. Kruk, D. H. Levinson, and J. Weyman

(i) Seasonal activity

The ENP basin includes two regions officially designated by NOAA's NWS for issuing NS and H warnings and advisories. The ENP warning area extends from the West Coast of North America to 140°W and is the responsibility of NOAA's NHC in Miami, Florida, while the central Pacific warning area between 140°W and 180° is the responsibility of the CPHC in Honolulu, Hawaii. The 2008 TC activity in both these warning areas is covered using combined statistics, along with information summarizing activity and impacts in the central North Pacific region.

The ENP hurricane season officially lasts from 15 May to 30 November. The peak activity for the central (eastern) part of the region normally occurs in August (September). The 2008 ENP hurricane season produced 17 NSs, 7 Hs, and 2 MHs (Fig. 4.16a). These values are generally below the 1971–2005 averages of 16.2 NSs, 9.1 Hs, and 4.3 MHs.

The 2008 season began on schedule with NS Alma (29–30 May), which was also the first NS to develop east of 90°W since 1970. For the season as a whole, the number of NSs that developed was above average, although few of these systems became hurricanes. As a result, the seasonal ACE (Bell et al. 2000; Bell and Chelliah 2006) was only 81.4×10^4 kt^2, which was shy of the 1971–2005 mean (126.3×10^4 kt^2) but higher than occurred during the 2007 season (Fig. 4.16b).

Only one system (Kika) was observed in the central North Pacific region during 2008, which is well below the 1971–2005 average of 4–5 TCs.[1] TS Kika entered the region from the east and stayed well south of the Hawaiian Islands before dissipating.

(ii) Historical context of the 2008 ENP hurricane season

Since 1995, the number of NSs in the ENP basin has been near average, fluctuating around the long-term mean (Fig. 4.16a). However, the numbers of Hs and MHs have been generally below normal, with above-normal H activity seen in only two seasons

[1] CPHC includes TDs in its climatological statistics for the central North Pacific region.

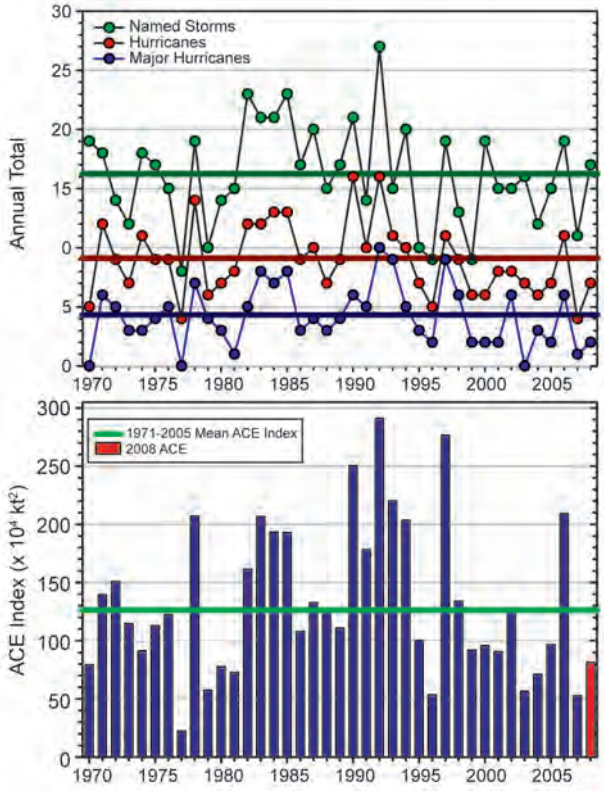

Fig. 4.16. Seasonal TC statistics for the east North Pacific Ocean during 1970–2008: (a) number of NS, H, and MH and (b) ACE (× 10^4 kt^2) with the seasonal total for 2008 highlighted in red. Both time series include the 1971–2005 base period means.

(2000 and 2006). NOAA has identified 9 of the 14 ENP seasons during 1995–2008 as being below normal, with only the 1997 and 2006 El Niño–influenced seasons producing above-normal activity as measured by ACE. In contrast, higher activity seen during the preceding 1970–94 period had 6 of 25 (24%) below-normal seasons and 9 of 25 (36%) above-normal seasons as measured by ACE.

These active and inactive ENP eras are opposite to those observed over the North Atlantic. Such east–west oscillations in activity reflect the large-scale atmospheric circulation anomalies that extend across both basins (Bell and Chelliah 2006). The spatial scale of these atmospheric anomalies is far larger than the area of warmer Atlantic SSTs (Lander and Guard 1998; Landsea et al. 1998, 1999; Goldenberg et al. 2001), suggesting this warmth alone is not a primary direct cause for the 1995 transition to generally below-normal (above normal) ENP (Atlantic) hurricane seasons.

(iii) Environmental influences on the 2008 season

Seasonal TC activity (both frequency and intensity) in the ENP basin is influenced by several large-scale environmental factors, including SSTs, 200–850-hPa vertical wind shear, the phase of the ENSO in the equatorial Pacific region (Whitney and Hobgood 1997), and possibly the phase of the equatorial QBO in the tropical lower stratosphere. ENSO is known to strongly modulate both the SSTs and vertical wind shear on seasonal time scales (Whitney and Hobgood 1997). Multidecadal fluctuations in ENP activity are less well understood, but they show a strong relationship to the phase of the tropical multidecadal signal (Bell and Chelliah 2006) and Atlantic hurricane activity.

El Niño typically favors an above-normal ENP season, while La Niña favors a below-normal season (Irwin and Davis 1999; Frank and Young 2007; Camargo et al. 2008). These ENSO impacts are modulated by the multidecadal signal, with the combination of La Niña during an inactive hurricane era greatly increasing the probability of a below-normal season. During 2008, the weakening state of La Niña to a more neutral phase during the climatological peak of the hurricane season (August–October) resulted in near-average SSTs (−0.5° to +0.5°C anomalies) in the MDR[2] during most of the season (Figs. 4.2c,d). In the absence of a strong ENSO signal, neutral years tend to favor below-normal hurricane activity in the ENP.

Another contributing factor to the below-normal season was above-average vertical wind shear between 200 and 850 hPa in the MDR during JJA (Fig. 4.17a). The largest shear anomalies (exceeding 9–12 m s^{-1}) were observed during JJA (Fig. 4.17a), followed by negative anomalies of 6–12 m s^{-1} during SON (Fig. 4.17b). This stronger-than-normal shear early in the season likely prevented systems from intensifying very quickly, and as a result 2008 had shorter-lasting and fewer-than-average Hs and MHs.

Previous studies have shown some statistically significant correlations between ENP hurricane activity and the phase of the QBO (Gray 1984; Shapiro 1989; Whitney and Hobgood 1997). In the ENP, TCs may attain a higher intensity when the QBO is in its westerly phase at 30 hPa, but there is also a corresponding decrease in the observed seasonal frequency (Whitney and Hobgood 1997). During May, the phase of the QBO was westerly, as indicated by westerly winds at 30 and 50 hPa. The winds were again westerly at both levels in June, and thereafter

[2] For the eastern North Pacific basin the MDR covers the area 10°–20°N and 90°–130°W (green boxes, Fig. 4.17).

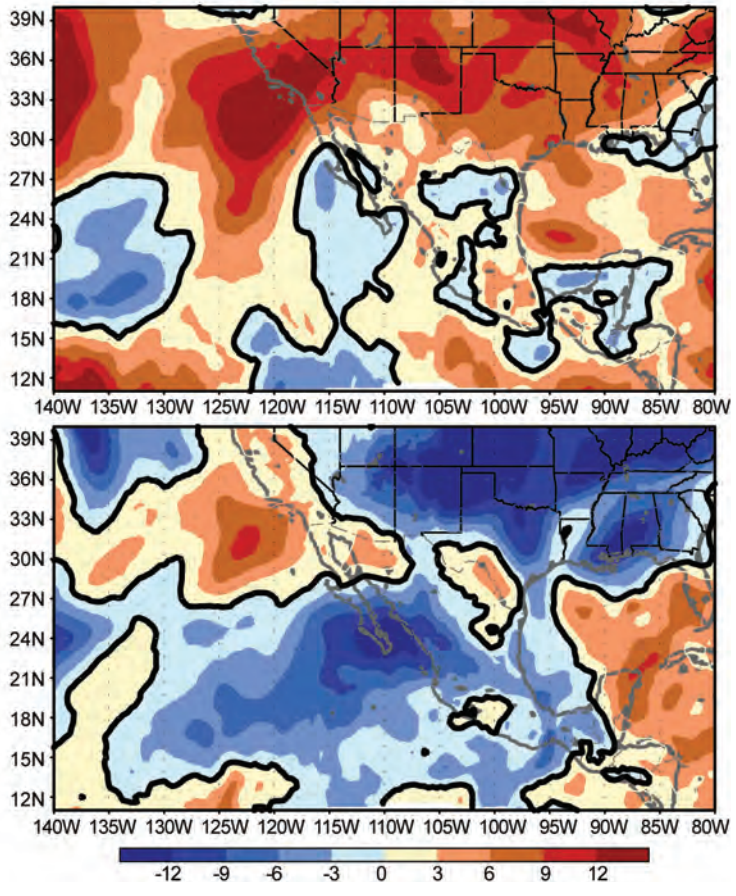

Fig. 4.17. The 200–850-hPa vertical wind shear anomaly (m s^{-1}) during (top) Jun–Aug and (bottom) Sep–Nov 2008. Anomalies are departures from the 1979–2004 period means. (Source: NOAA NOMADS NARR dataset.)

remained constant throughout the remainder of the hurricane season (not shown). Therefore, the westerly phase of the QBO may have aided in allowing more TCs to develop in the ENP basin in 2008.

(iv) Tropical cyclone impacts in 2008

Three TSs made landfall along the Pacific coast of Mexico during 2008 [NS Julio, NS Lowell (as a tropical depression), and Category-2 H Norbert]. This is well above the 1951–2000 average of 1.34 landfalling TSs and near the average of 1.3 landfalling Hs (Jauregui 2003).

In Central America, NS Alma made landfall along the northwestern coast of Nicaragua on 29 May with maximum sustained winds of 55 kt. The wind and rain from NS Alma forced the evacuation of 25,000 residents, and many homes were destroyed and flooded.

On 23 August, NS Julio made landfall on the coast of Mexico with maximum sustained winds of 40 kt and moved northwestward paralleling the coastline. Two persons were killed in the southern tip of Baja California by the heavy rains and flash flooding. Roughly two weeks later, NS Lowell made landfall in Baja California on 11 September. No significant damage was caused by the excessive rains from Lowell, which had peak winds near 30 kt at landfall.

The strongest storm of the ENP 2008 season was Category-4 MH Norbert, which made landfall in Baja California on 11 October as a Category-2 H, and again as a Category-1 H in Sonora, Mexico. Maximum sustained winds during Norbert's peak intensity were measured at 115 kt, becoming only the second MH of the ENP 2008 season (after Category-3 MH Hernan, which remained over the open waters). MH Norbert was the first October hurricane to strike the western Baja California peninsula since H Pauline (1968). MH Norbert was responsible for five deaths as it made landfall in Mexico.

There was no direct landfall or strike associated with NS Kika (7–12 August) in the central North Pacific. Kika formed east of 150°W and moved westward before dissipating near 165°W. Maximum sustained winds from NS Kika topped out at 35 kt as it stayed over open waters, well south of Hawaii.

4) Western North Pacific basin—S. J. Camargo

The 2008 season featured 27 TCs, with 25 reaching TS intensity (though 4 were not named), 12 becoming TYs, and only 2 reaching STY intensity (see Fig. 4.18a). TC data are from the JTWC, and the climatology is defined as 1971–2000.

There were significant differences between the 2008 warnings by JTWC and the RSMC in Tokyo. The RSMC did not name four TCs that the JTWC considered to have reached TS intensity (01W, 14W, 16W, and 22W). Halong was considered a TY by JTWC, but not by Tokyo. In contrast, Phanfone was considered a TS by RSMC, but not by JTWC (Chan 2009).

The 2008 season started in January with unnamed TS (01W). In April, TY Neoguri was the earliest TY to make landfall in China in the historical record.[3] There was a historical record number of TYs (three)

[3] China Meteorological Agency statement in the Chinese media.

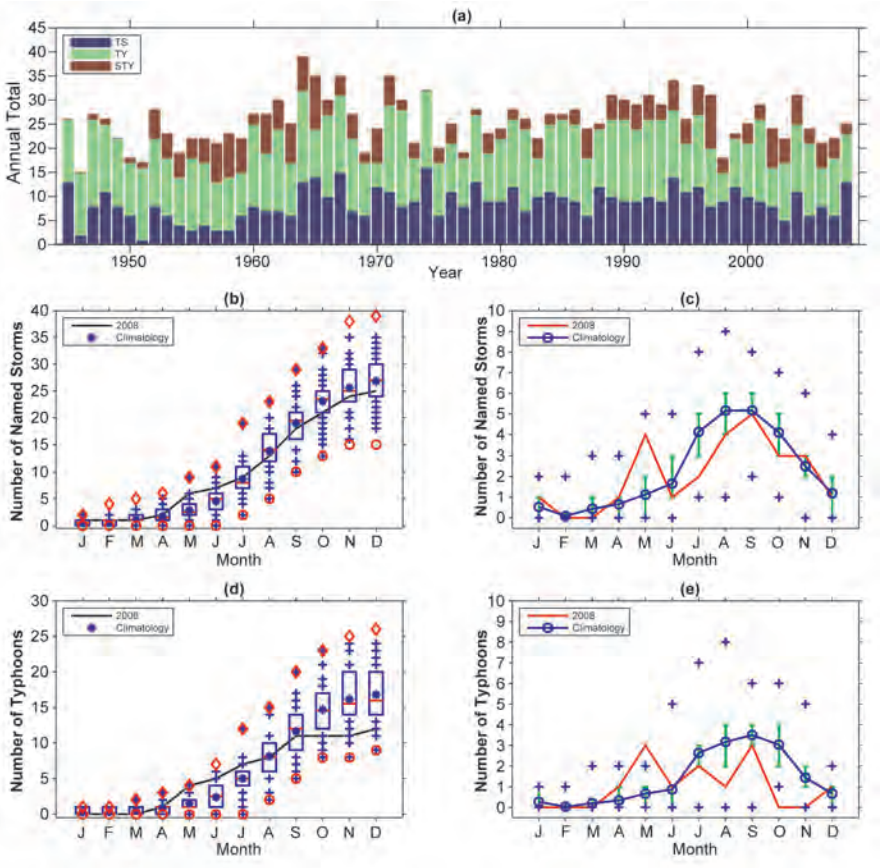

Fig. 4.18. (a) Number of TSs, TYs, and STYs per year in the WNP 1945–2008. (b) Cumulative number of TCs with TS intensity or higher (NS) per month in the WNP: 2008 (black line) and climatology (1971–2000) shown as box plots [interquartile range: box, median; red line, mean; blue asterisk, values in the top or bottom quartile; blue crosses, high (low) records in the 1945–2006 period; red diamonds (circles)]. (c) Number of NSs per month in 2008 (black curve); mean climatological number of NSs per month (blue curve); the blue plus signs denote the maximum and minimum monthly historical values (1945–2008); and green error bars show the interquartile range for each month. In the case of no error bars, the upper and/or lower percentiles coincide with the median. (d) Cumulative number of TYs per month in the western North Pacific: 2008 (black line) and climatology (1971–2000) shown as box plots. (e) Number of TYs per month in 2008 (black curve); mean climatological number of TY per month (blue curve); the blue plus signs denote the maximum and minimum monthly historical values (1945–2008); and green error bars show the interquartile range for each month. (Source: 1945–2007 JTWC best-track dataset, 2008 JTWC preliminary operational track data.)

in May (Fig. 4.18e, climatological median 1), including STY Jangmi. June, July, and August featured TSs and TYs in the bottom quartile of the distribution. The number of NSs in September was equal to the climatological median, but the number of TYs was in the bottom quartile of the distribution. October 2008 was the first October in the historical record with no TYs (climatological median is 3). The previous record was October 1976, with one STY. In November, three TSs occurred. TY Dolphin, in December, closed the 2008 season (see sidebar "Unusually Quiet West Pacific Typhoon Season Ends with a Dolphin Kick").

The total number of TCs, TYs, and STYs were all in the bottom quartile of the climatological distributions (median: 30.5 TCs, 16 TYs, and 3 STYs). The number of TSs was below the median (27). The cumulative distribution of NSs (Figs. 4.18b,d) shows above-normal activity in the early season, and below-normal activity for the rest of the season, especially for TYs. The number of TYs in 2008 is in the lowest 15th percentile. The number of NSs in the season was only slightly below the median. The number of STYs in 2008 (two) was in the bottom quartile of the distribution (median is 3). The low activity in 2008 is therefore mainly due to lack of intensification of the TCs to TY intensity.

The 2008 ACE (Bell 2000) was below the bottom 15th percentile of the climatological distribution (Fig. 4.19a). Reflecting the occurrence of TYs, the ACE for the early season (April–June) was in the top 10th percentile of the distribution (Fig. 4.19b), while the ACE for the peak season (July–October) was in the bottom 5th percentile. The ACE value in May was in the top quartile, mainly due to the occurrence of STY Rammasun (77% of the May ACE value). September was the only peak-season month with an ACE value near the climatological median. STY Jangmi (30% of September ACE) was the most intense TY in 2008 with peak winds near 135 kt.

There is a known relationship between ACE and ENSO, with low values of ACE usually occurring in La Niña years, when the TCs tend to be short lived

and less intense (Wang and Chan 2002; Camargo and Sobel 2005; Camargo et al. 2007a). According to the Niño-3.4 and Niño-3 indices, the 2007–08 La Niña ended during the boreal summer and reemerged toward the end of the year. However, in the Niño-4 region, anomalously cool SSTs never warmed, despite the occurrence of warming SSTs in the eastern Pacific (not shown). The Southern Oscillation index was briefly neutral during the summer months but was positive after September. Key TC environmental conditions in the western North Pacific were consistent with La Niña events. Most notably, the eastern portion of the monsoon trough was confined to a small region west of the Philippines (Fig. 4.20a) (Camargo et al. 2007a), and the Pacific decadal oscillation was strongly negative throughout 2008.

During 2008, the median duration of NSs was only 4.75 days (bottom 15th percentile of the distribution). The median lifetime of NSs during La Niña is 6.75 days. The duration of 14 TCs was in the bottom quartile of the distribution, and only 2 TCs had lifetimes above the median (8 days). As a result, the number of days with TS was only 92.5 (median is 144.25). There were only 75.5 TY days (median is 120.4) and 9.25 STY days (median is 19.4 days), both in the bottom quartiles of the distributions.

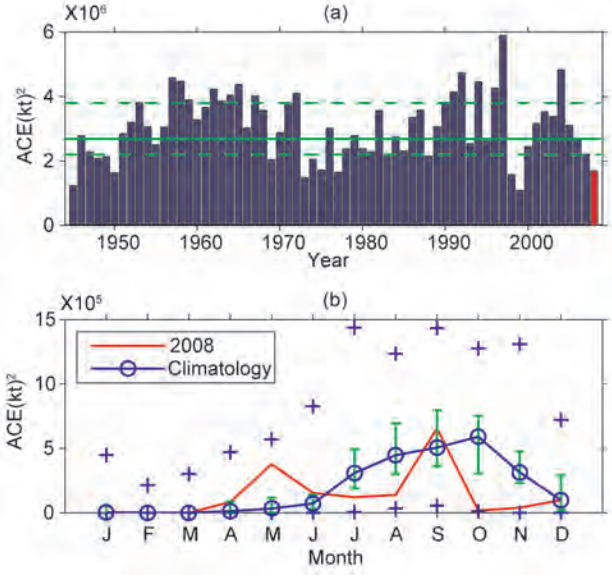

Fig. 4.19. (a) ACE values per year in the WNP for 1945–2008. The solid green line indicates the median for 1971–2000 climatology, and the dashed green lines show the 25th and 75th percentiles. (b) ACE values per month in 2008 (red line) and the median in 1971–2000 (blue line), where the green error bars indicate the 25th and 75th percentiles. In the case of no error bars, the upper and/or lower percentiles coincide with the median. The blue plus signs denote the maximum and minimum values during the period 1945–2008. (Source: 1945–2007 JTWC best-track dataset, 2008 JTWC preliminary operational track data.)

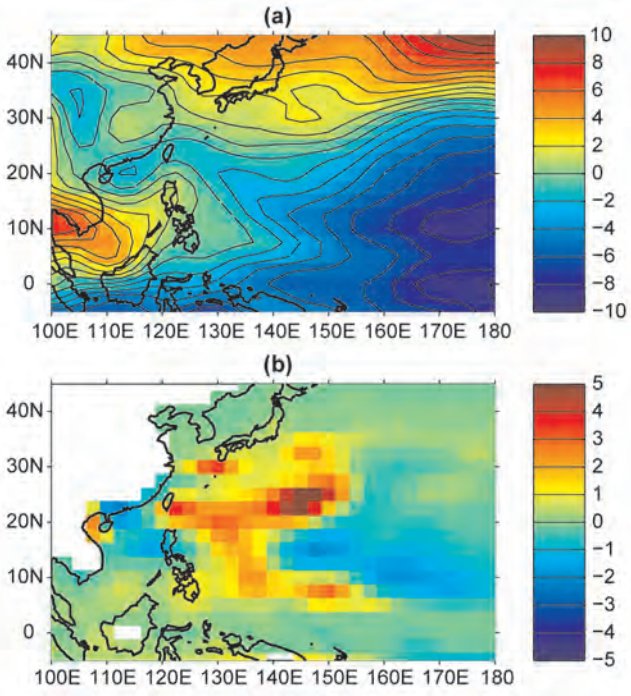

Fig. 4.20. (a) Zonal 850-hPa winds (m s^{-1}) from JASO 2008. The contour interval is 1 m s^{-1}. (b) Genesis potential index (Camargo et al. 2007b) anomalies for JASO 2008. (Source: atmospheric variables—NCEP reanalysis data; Kalnay et al. 1996; SST—Smith and Reynolds 2005.)

Fourteen TCs made landfall during 2008, which is just below the 1951–2000 median of 15.[4] Two systems made landfall as a TD (median is 3), six made landfall as a TS (median is 6), six struck as a TY (median is 4), and none as a STY (median is 0).

The Philippines were affected by four TCs in 2008: TYs Neoguri and Fengshen, and TSs Halong and Higos. The largest impacts resulted from TY Fengsheng, which brought more than 1,300 deaths.

Taiwan was hit by four TYs in 2008: Kaelmaegi and Fung-wong in July, and Sinlaku and Jangmi in September. They brought heavy rainfall amounts to Taiwan, causing large losses to agriculture and infrastructure. Both TYs Kaemaegi and Fung-wong also affected mainland China, after crossing Taiwan and becoming weaker. TYs Kammuri, Nuri, and Hagupit and TS Higos also made landfall in China. Vietnam

[4] Here we consider only one landfall per TC. If a TC makes more than one landfall, the landfall event with the highest wind speed is considered.

was also affected in this typhoon season, with three landfalls (TS Mekkhala, 22W, and Noul).

The GPI (Emanuel and Nolan 2004) during 2008 was above normal in the western portion of the WNP and below normal near the date line and in the South China Sea (Fig. 4.20b), which is also consistent with the presence of La Niña (Camargo et al. 2007b). The decreased GPI near the date line in La Niña events is mainly attributed to the low-level vorticity, while the increased GPI near the Asian continent is attributed to an increase in midlevel relative humidity (Camargo et al. 2007b).

5) Indian Ocean basins—K. L. Gleason and M. C. Kruk

(i) NIO

The NIO TC season typically extends from April to December, with two peaks in activity during May–June and November when the monsoon trough is positioned over tropical waters in the basin. TCs in the NIO basin normally develop over the Arabian Sea and Bay of Bengal between latitudes 8° and 15°N. These systems are usually short lived and relatively weak, and they often quickly move into the Indian subcontinent. However, strong and "severe cyclonic storms"[5] can develop with winds exceeding 130 kt (Neumann et al. 1993).

The 2008 TC season produced seven NSs, one CYC, and one MCYC (Fig. 4.21a). These values are near the 1981–2005 averages of 4.6 NSs, 1.4 CYCs, and 0.5 MCYCs. The season produced an ACE value of 19×10^4 kt^2, which is slightly above the 1981–2005 mean of 16×10^4 kt^2 (Fig. 4.21b).

The 2008 season was most noted for MCYC Nargis, which made landfall on the Irrawaddy Delta of Myanmar on 2 May. Nargis began as a disturbance east of the Nicobar Islands on 24 April. As it migrated to the northwest, it entered a region of low vertical wind shear and began to intensify. By 28 April, Nargis was a Category-1 CYC and continued to intensify as it turned toward the Myanmar coast. The storm rapidly intensified over a period of 24 h (1–2 May), with peak maximum sustained winds reaching 115 kt. This storm caused catastrophic destruction and significant loss of life, with estimates of 146,000 fatalities and thousands missing. The massive storm surge inundated the low-lying coastal region and was the reason for the majority of the fatalities. Extreme winds and high storm surge were responsible for damage estimates of over $10 billion (USD). MCYC Nargis was the most damaging cyclone recorded in this basin and the seventh-deadliest cyclone of all time.

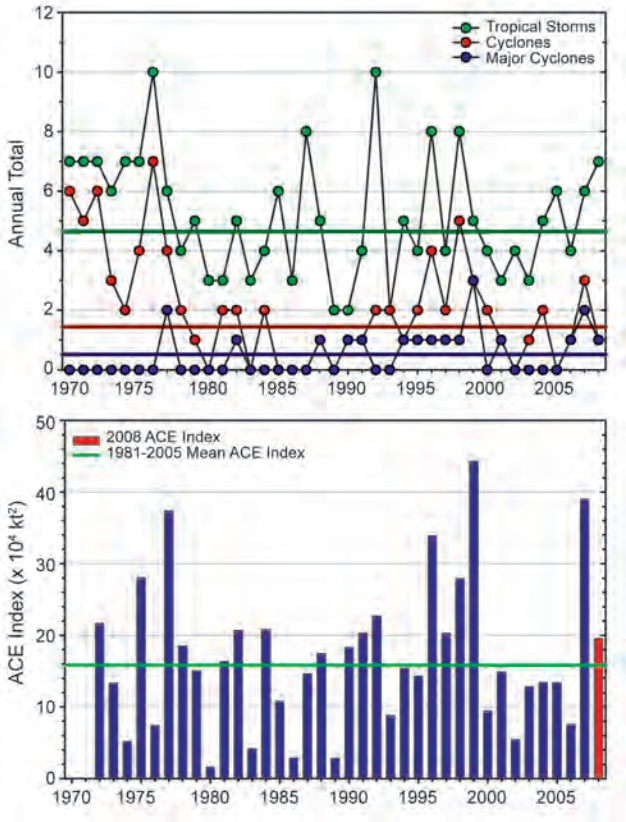

Fig. 4.21. Annual TC statistics for the NIO over the period 1970–2008: (a) number of TSs, CYCs, and MCYCs, and (b) the estimated annual ACE (× 10^4 kt^2) for all TCs during which they were at least TS or greater intensities (Bell et al. 2000). The 1981–2005 base period means are included in both (a) and (b). Note that the ACE values are estimated due to a lack of consistent 6-h-sustained winds for every storm.

(ii) Southern Indian Ocean

The SIO basin extends south of the equator from the African coastline to 105°E, with most CYCs developing south of 10°S. The SIO TC season extends from July to June encompassing equal portions of two calendar years (e.g., the 2008 season is composed of storms from July to December 2007, and January to June 2008). The peak activity occurs during December–April when the ITCZ is located in the Southern Hemisphere and is migrating equatorward. Historically, the vast majority of the landfalling CYCs in the SIO impact Madagascar, Mozambique, and the Mascarene Islands, including Mauritius and Réunion.

[5] The Bangladesh Supercyclone of 1970 produced perhaps the greatest human death toll (300,000 persons) on record, primarily from storm surge flooding of low-lying deltas (Holland 1993).

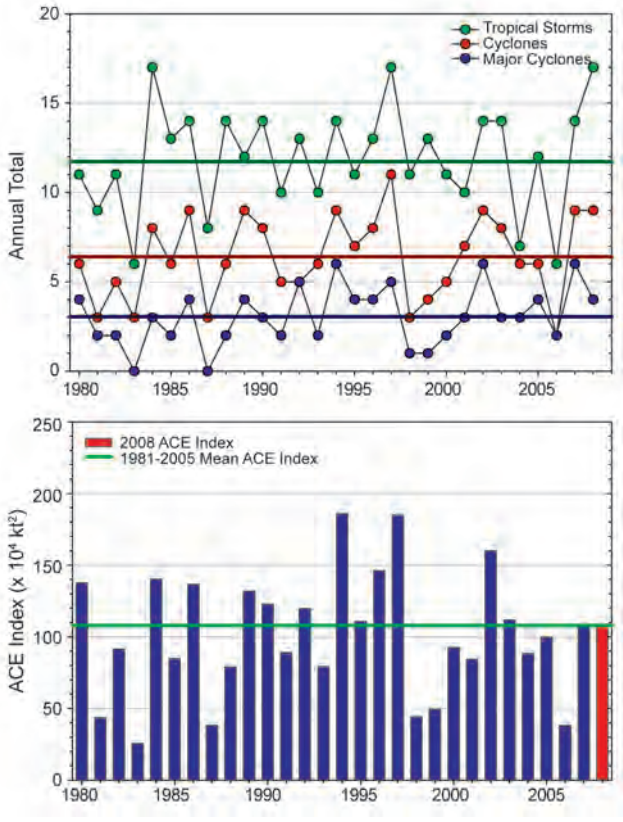

Fig. 4.22. Same as in Fig. 4.21, but for TCs in the SIO over the period 1980–2008.

The historical SIO TC data are probably the least reliable of all the TC basins (Atkinson 1971; Neumann et al. 1993), primarily due to a lack of historical record keeping by individual countries and no centralized monitoring agency; however, the historical dataset for the region has been updated (Kruk et al. 2009, manuscript submitted to *J. Atmos. Oceanic Technol.*; Knapp et al. 2009). The historical data are noticeably deficient before reliable satellite data were operationally implemented in the region beginning about 1983.

The 2007–08 season produced 17 NSs and above-average numbers of CYCs (9) and MCYCs (4) (Fig. 4.22a). The 1981–2005 averages are 11.8 NSs, 6.4 CYCs, and 3 MCYCs. However, the 2007–08 ACE (109 $\times 10^4$ kt^2) was near the 1981–2005 average (Fig. 4.22b). Over the last 10 years, only the 2001–02 season had above-average ACE. Previous to that, the most recent period with above-average ACE occurred during the period from 1994 to 1997.

The strongest storm during the 2007–08 season was MCYC Hondo, which reached peak strength of 125 kt on 7 February. Hondo formed approximately 560 nm southeast of Diego Garcia on 4 February and began rapid intensification early the next day. As it migrated south over the central Indian Ocean, it continued to organize into a Category-4 MCYC. Over the next couple of days, MCYC Hondo entered a region of higher wind shear and cooler ocean waters and began to weaken.

The strongest landfalling storm of the season formed off the northeast coast of Madagascar on 7 February. The disturbance quickly intensified into CYC Ivan before tracking to the southeast and again entered a region with unfavorable wind shear. After some weakening and meandering, Ivan regained its strength and began a southwestward track toward the east coast of Madagascar. At peak intensity, MCYC Ivan had sustained winds of 115 kt and made landfall north of Fanoarivo, Madagascar, on 17 February. Nearly 100 fatalities were reported and over 330,000 residents were rendered homeless. Damages from Ivan were estimated at more than $30 million (USD).

6) Southwest Pacific basin—M. J. Salinger

The 2007–08 southwest Pacific TC season had 4 TC occurrences (east of 150°E), 5 less than the median of 9 (1976–77 to 2006–07) for the region in the TC season (Fig. 4.23). The first TC of the season occurred on 3 December. The season finished unusually early with the last in late January/early February (the TC season typically runs into May).

The season's NSs were clustered nearer the date line in the southwest Pacific region, with three tracking near Fiji (Fig. 4.24). Rather than the normal February–March peak, the season peaked early, with three of the four NSs forming in January and the remainder of the season being unusually quiet. Three of the four TCs in the southwest Pacific region reached H strength, and two reached MH strength.

TC Daman was the first of the season, occurring 5–9 December near Fiji, with maximum sustained winds of 105 kt. Daman produced heavy rainfall over northern Fiji, with destructive winds flattening vil-

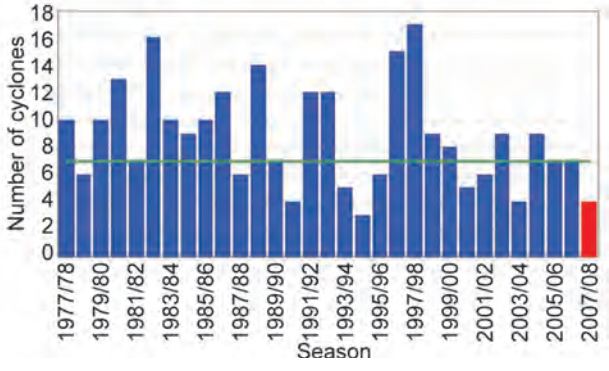

Fig. 4.23. TC frequencies in the southwest Pacific, 1976–2008.

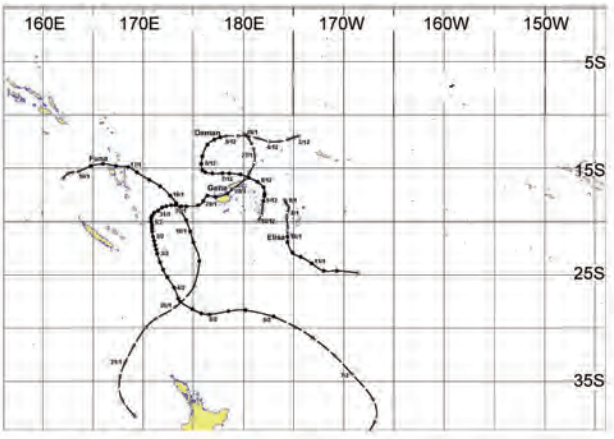

Fig. 4.24. TC tracks in the Southwest Pacific, 2007–08.

lages and causing widespread destruction to roads and property. TC Elisa formed on 10 January near the date line and moved southwest of Nukualofa, Tonga, producing maximum sustained winds of 45 kt. TC Funa developed near Fiji, then moved southeast toward Tonga 16–19 January with maximum sustained winds of 105 kt, causing heavy rain and storm-force winds to Vanuatu, which disrupted communications. TC Gene was the last of the 2007/08 winter season, developing northeast of Fiji and tracking toward New Caledonia. Maximum sustained winds were near 100 kt. This storm caused seven deaths on Fiji, left many without power, and caused estimated damages of $25 million (USD).

7) Australian basin—B. Trewin and A. B. Watkins

(i) Seasonal activity

The 2007–08 TC season was near normal in the broader Australian basin (areas south of the equator and between 90° and 160°E,[6] which includes Australian, PNG, and Indonesian areas of responsibility). The season produced 10 TCs, equal to the long-term average. There were three TCs in the eastern sector[7] of the Australian region during 2007–08, and seven TCs in the western sector. The number of landfalls was relatively low, with only two landfalls during the season.

(ii) Landfalling and other significant TCs

The most intense TC during the season was TC Pancho, which formed off the northwest coast on 25 March. It reached peak intensity (Category-4, 95-kt sustained winds with 135-kt gusts, 934-hPa central pressure; see www.bom.gov.au/weather/cyclone/faq/index.shtml for a definition of Australian TC categories) at 0000 UTC 27 March. It weakened below TC intensity before making landfall as a tropical low near Shark Bay on 29 March, bringing heavy rain to parts of southwestern Western Australia. An intense midlatitude low that absorbed the remnants of Pancho was responsible for widespread wind damage in Victoria and Tasmania on 2 April.

TC Nicholas was the sole landfalling TC in the western sector. It formed on 12 February and peaked as a Category-3 system (80-kt sustained winds with 115-kt gusts, central pressure 948 hPa) on 16–17 February. It eventually crossed the coast south of Coral Bay as a Category-1 system on 20 February. No significant damage was reported on land, but widespread shutdowns of the offshore oil and gas industry resulted in economic losses of several hundred million USD.

The other landfalling system of the season was TC Helen, which formed off the west coast of the top end of the Northern Territory and made landfall on 4 January about 100 km southwest of Darwin as a Category-2 system (50-kt sustained winds with 65-kt gusts, central pressure 975 hPa). There was some minor wind damage in the Darwin area. While Helen was short lived as a TC, long-lived remnants of the system moved into Queensland and contributed to major flooding in central Queensland in mid-January. Helen's track was also unusual, being the first landfall from the west on the top end coastline since Tracy in 1974–75.

TC Guba, which moved over waters east of Queensland from 14 to 20 November (2007) and peaked as a Category-3 system, was significant in that it approached the Queensland coast more closely than any other recorded November cyclone, although it did not ultimately make landfall. Guba's antecedent low caused severe flooding, with numerous deaths, in PNG on 12–13 November.

e. *Intertropical Convergence Zones*

1) Pacific—A. B. Mullan

There are two prominent convergence zones in the Pacific: the ITCZ in the Northern Hemisphere, which lies approximately parallel to the equator, with its position varying seasonally from around 5° to 7°N in February–May to 7° to 10°N in August–November

[6] The Australian Bureau of Meteorology's warning area overlaps both the SIO and SWP.

[7] The western sector covers areas between 90° and 125°E. The eastern sector covers areas east of the eastern Australian coast to 160°E, as well as the eastern half of the Gulf of Carpentaria. The northern sector covers areas from 125° E east to the western half of the Gulf of Carpentaria.

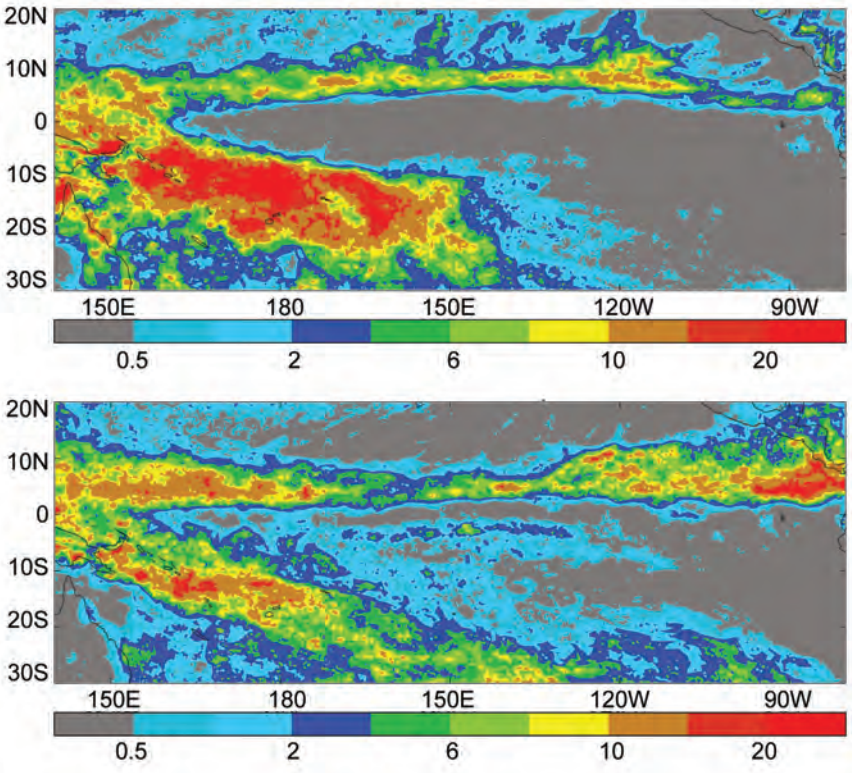

Fig. 4.25. Annual average rainfall rate from TRMM 0.25° analysis for (top) Jan 2008 and (bottom) May 2008. Note the uneven contour intervals (0.5, 1, 2, 4, 6, 8, 10, 15, and 20 mm day^{-1}).

(Fig. 4.27); and the SPCZ, which extends diagonally from around Solomon Islands (10°S, 160°E) to near 30°S, 140°W, and is most active in the November–April half-year.

Figure 4.25 shows the monthly rainfall in the tropical Pacific for two selected months in 2008, as derived from the 0.25° resolution NASA TRMM rainfall data (3B-43 product; Huffman et al. 2007). The year 2008 began with a continuation of strong to moderate La Niña conditions, and the January 2008 rainfall shows a clear separation between the ITCZ and SPCZ around the date line, with a region of suppressed convection extending from western to eastern Kiribati, which resulted in low rainfall in the northern Cooks and the Marquesas of French Polynesia. The SPCZ was well south and west of its normal position and very active through the first quarter of 2008 (Fig. 4.26, left), resulting in much-above-average rainfall in Vanuatu, New Caledonia, Tonga, Niue, and southern Cooks.

In May (Fig. 4.25, bottom), the SPCZ was still active and south of its normal position. A very clear southern branch of the ITCZ is apparent between 180° and 120°W, while the ITCZ in the Northern Hemisphere appears somewhat weaker than usual over the same longitudes. To the north of this section of the ITCZ, there is suppressed convection to at least 20°N, which was typical of the second quarter of 2008, contributing to the drought conditions that were declared in many parts of the Hawaiian Islands by midyear. The May rainfall also highlights a more intense ITCZ around 90°W. This continued into October, coinciding with several months of above-normal SSTs in the far eastern equatorial Pacific.

Unusually persistent trade winds dominated the weather across Micronesia and the equatorial South Pacific during the third quarter of 2008 (Pacific ENSO Applications Center 2008; Island Climate Update 2008b,c), and the ITCZ lay on the equatorward edge of its climatological distribution (Fig. 4.26, right). The SPCZ was fairly inactive in the third quarter, but convective activity increased in October and the SPCZ ended the year as it began—south of its normal position. The ITCZ spent much of the year, April through November (Figs. 4.26, right, 4.27), equatorward of its normal position, especially over the central Pacific (180° to 120°W).

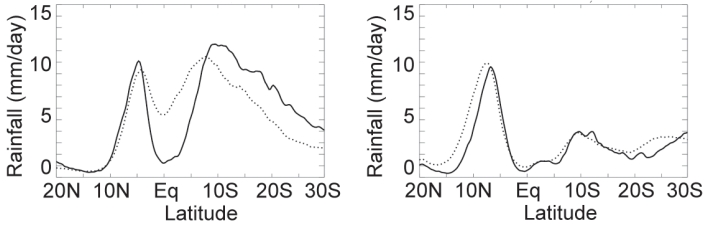

Fig. 4.26. Latitudinal cross-sections of TRMM rainfall (mm day^{-1}): Jan to Mar quarter averaged across the sector (left) 150°E–180°, and Jul to Sep quarter averaged across the sector (right) 180°–150°W. Profiles are given for 2008 (solid line) and the 1998–2007 average (dotted line).

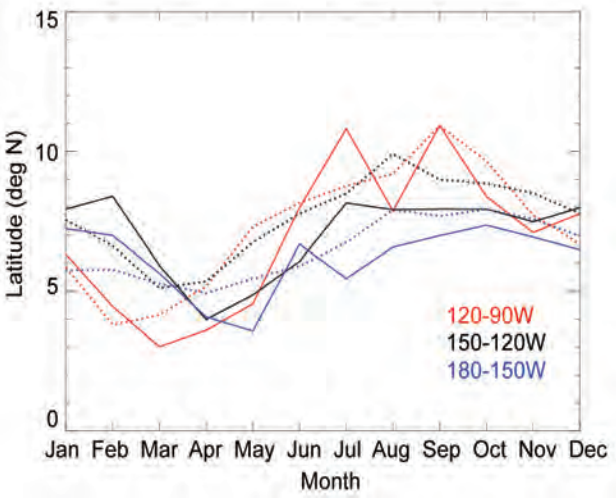

Fig. 4.27. Monthly variation in latitude of peak ITCZ rainfall over three longitude sectors: 180°–150°W (blue), 150°–120°W (black) and 120°–90°W (red). Annual cycle variations given for 2008 (solid lines) and the 1998–2007 climatology (dotted).

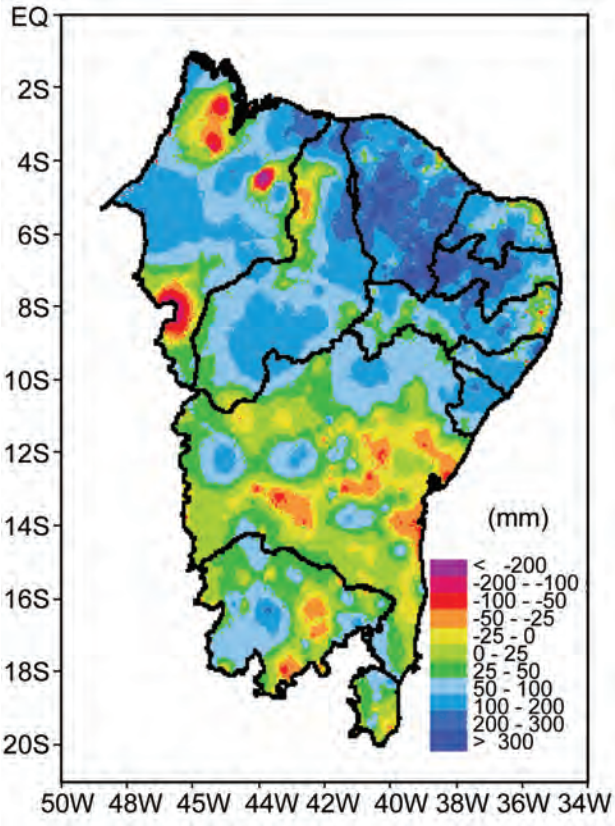

Fig. 4.28. Northeastern Brazil Mar 2008 precipitation anomalies (mm) with respect to 1961–90 climatology based on high-resolution station data.

2) Atlantic—A. B. Pezza and C. A. S. Coelho

The Atlantic ITCZ is a well-organized convective band that oscillates approximately between 5° and 12°N during July–November and 5°N and 5°S during January–May (Waliser and Gautier 1993; Nobre and Shukla 1996). As equatorial Kelvin waves can modulate the ITCZ's interannual variability, ENSO is also known to influence it on a seasonal scale (Münnich and Neelin 2005).

In the semiarid area of northeastern Brazil a sudden southward burst of the Atlantic ITCZ can produce heavy rains (monthly anomalies above 300 mm) as observed in March 2008 (Fig. 4.28). This pattern is facilitated during La Niña and when the South Atlantic is predominantly warmer than the North Atlantic Ocean, as observed in the first half of 2008.

The Atlantic ITCZ reached its southernmost annual position (5°S) during the second half of March in 2008 (Fig. 4.29a). This positioning is within the climatological range (Waliser and Gautier 1993). The ITCZ then migrated rapidly back to the North Atlantic from May (Fig. 4.29b), reaching its northernmost position (10°–15°N) during late August in association with intense convective activity near the African coast (Fig. 4.29c). The resulting convective band during the boreal summer was aligned from southwest–northeast over the North Atlantic (Fig. 4.29c), different from the quasihorizontal alignment observed in May (Fig. 4.29b). This pattern was modulated by strong low-level wind anomalies demarcating the mass convergence between South America and Africa, and further reinforced by a semistationary upper-level vortex over the South Atlantic near northeastern Brazil in August.

For the remainder of the year the Atlantic ITCZ was close to its climatological average, slowly returning to the south and reaching 5°S in December. As a result, a large area of the tropical South Atlantic recorded above-average rainfall in 2008 compared to the 1998–2007 annual mean (Fig. 4.30), contrasting with the below-normal conditions observed in 2006 and 2007.

f. Indian Ocean Dipole—J. J. Luo

The IOD is a coupled ocean–atmosphere phenomenon in the tropical IO. Following a weak negative IOD in 2005, three consecutive positive IODs occurred from 2006 to 2008 (Fig. 4.31a). The SSTs have warmed persistently (Fig. 4.31b) in the central equatorial IO. In contrast, SSTs along the west coast of Sumatra have not increased and are slightly cooler. This indicates the impact of frequent positive IOD on the long-term climatological SST state. The trends of warmer SST in the central and western IO and relatively colder SST west of Sumatra may favor the occurrence of positive IOD.

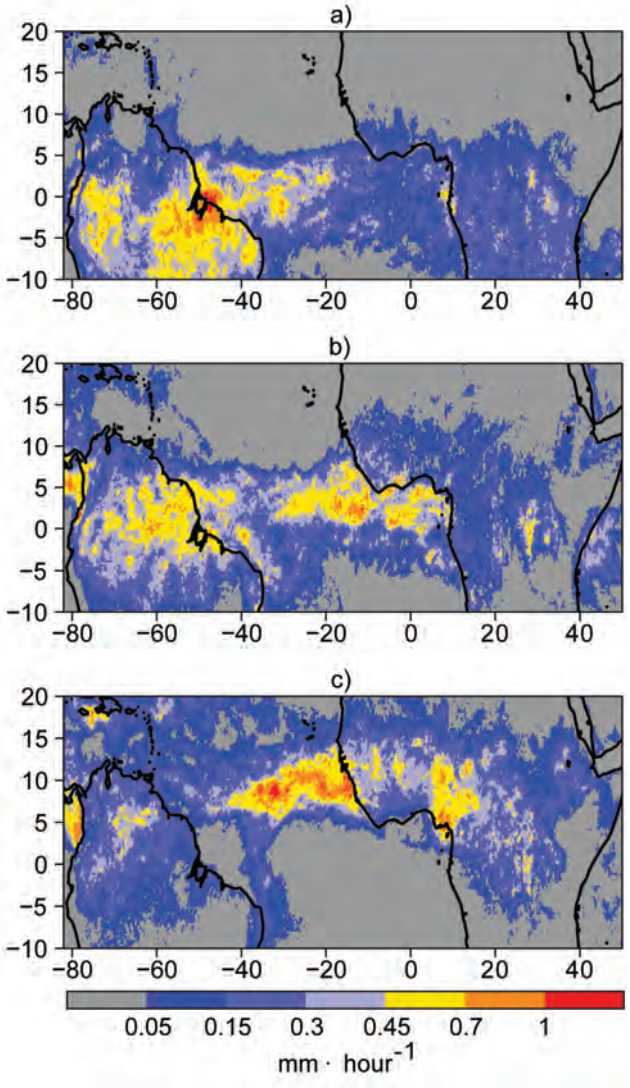

Fig. 4.29. Average rainfall rate (mm h^{-1}) from high-resolution (0.25° lat × 0.25° lon) TRMM analysis for (a) Mar, (b) May, and (c) Aug 2008.

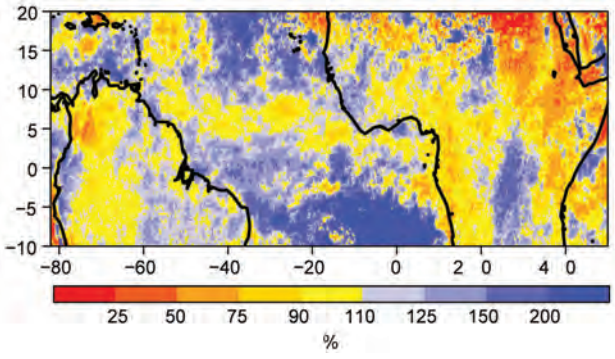

Fig. 4.30. Percentage of the 1998–2007 mean annual rainfall during 2008. Data are TRMM estimates calculated from a 0.25° lat/lon grid.

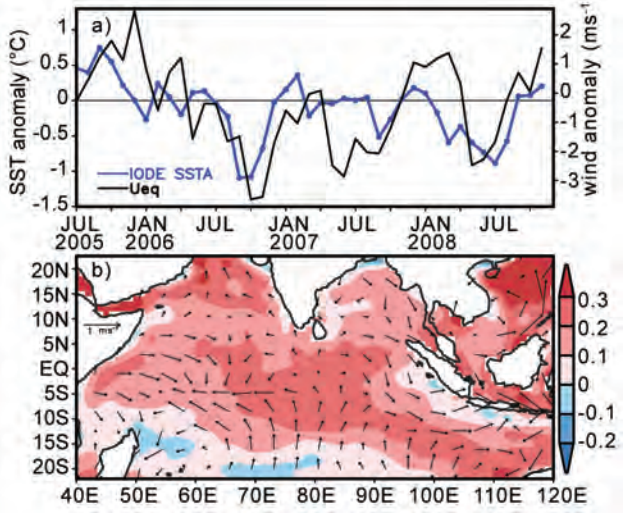

Fig. 4.31. (a) Monthly anomalies of SST (°C) in the eastern pole of IOD (IODE, 90°–110°E, 10°S–0°) and surface zonal wind (m s^{-1}) in the central Indian Ocean (Ueq, 70°–90°E, 5°S–5°N). (b) SST and surface wind differences between the period 1995–2008 and 1982–95. The anomalies were calculated relative to the climatology over the period 1982–2007. These are based on NCEP optimum interpolation SST (Reynolds et al. 2002) and NCEP atmospheric reanalysis data. Here, we used the IODE SST anomaly for IOD definition. Unstable growth of strong surface cooling in this region was found to be closely related to the Bjerknes feedback associated with strong coastal upwelling west of Sumatra, which plays a key role in initiating the positive IOD evolution.

The strong IOD in 2006 coincided with a weak-to-intermediate El Niño, and its evolution is consistent with large-scale IOD dynamics (Luo et al. 2007, 2008). The cold SST anomaly west of Sumatra causes anomalous easterlies in the central Indian Ocean (Fig. 4.31a) in association with the unstable Bjerknes feedback. In contrast, the 2007 weak and short-lived IOD occurred alongside a La Niña (Luo et al. 2008; Luo and Bell 2008). The strong easterlies in the central IO during May–June 2007 played a key role in driving this weak IOD, and in 2008 IOD underwent a unique evolution. During December 2007 to February 2008, anomalous westerlies blew over the IO basin (Fig. 4.32a), particularly between 10°S and the equator, in response to the strong La Niña. Weak cold SST anomalies appeared in the western IO accompanied by weak warming in the east following the demise of the 2007 positive IOD. Correspondingly, more rainfall appeared in the east with drought in the western IO (East Africa). During March–May 2008 (Fig. 4.32b), basin-wide cooling was well developed under the influence of the La Niña. The strong cold

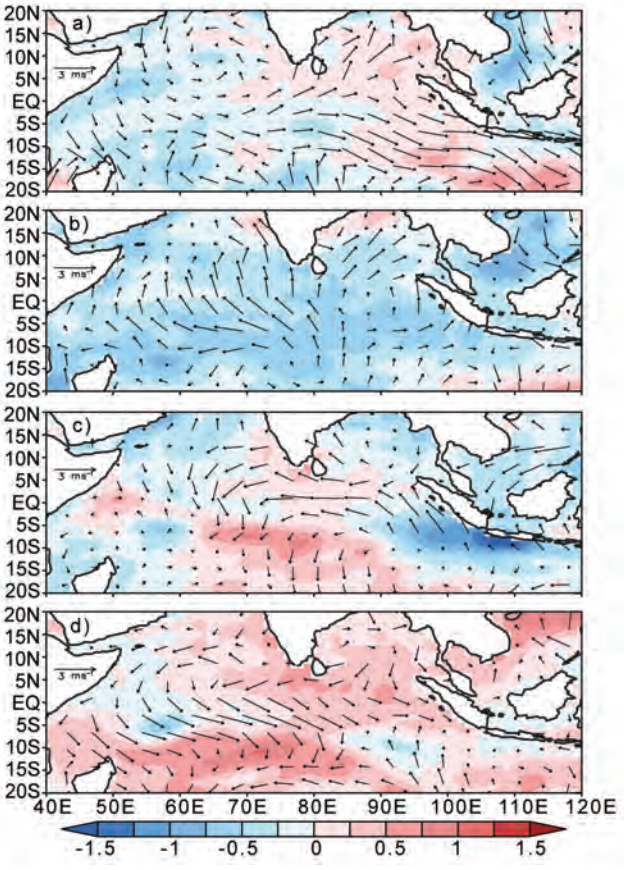

Fig. 4.32. SST (°C) and surface wind anomalies during (a) Dec–Feb 2007–08, (b) Mar–May 2008, (c) Jun–Aug 2008, and (d) Sep–Nov 2008.

SST anomalies in the southwestern IO at 15°–10°S, which caused local drought and anomalous easterlies near the equator, gradually expanded eastward. During May 2008, associated with the arrival of the strong cold SST anomalies and severe drought in the eastern IO at ~10°S, strong equatorial easterly anomalies appeared across the whole basin. This drove an eastward-propagating equatorial upwelling Kelvin wave (Fig. 4.33a) and favored the onset of IOD in the following season.

The positive IOD was well developed during June–August 2008. Strong SST cooling appeared along the west coast of Sumatra with weak warming located in the central IO (Fig. 4.32c). Stronger alongshore southeasterlies enhanced the coastal upwelling and hence favored the development of cold SST and easterly anomalies toward the central Indian Ocean. Such an SST anomaly dipole pattern caused flooding (drought) in the western (eastern) IO. Rainfall over the Indonesia Sea, however, was above normal in association with the La Niña. Due to the IOD influence, Australia again suffered from sustained drought in 2008 despite the prospect of rains resulting from La Niña conditions. During September, the IOD collapsed, in contrast to the usual peak in boreal fall terminating in early winter. Initial westerly wind anomalies appeared in the central equatorial IO during August and intensified in September. This forced a downwelling equatorial Kelvin wave during August–September (Fig. 4.33a) and ended this IOD. During November, the situation in the IO became similar to that during a La Niña year: drought in the west and flooding over the eastern IO, Indonesia, and large parts of Australia.

The concurrence of the positive IOD and La Niña in 2007 and 2008 clearly suggests that potential predictability of IOD may reside in the IO itself. Underlying mechanisms for the 2008 IOD appear to be different from those for the 2006–07 events. Following the demise of the 2007 IOD, a warm subsurface signal persisted in the equatorial eastern IO until May 2008 (Fig. 4.33a). The MJO-related strong cross-basin equatorial easterly anomalies in May appear to have played an important triggering mechanism similar to 2007. Apart from the MJO impact, a clear westward-propagating cold oceanic Rossby wave at 10°–5°S can be seen from November 2007 to May 2008 (Fig. 4.33b). The cold Rossby wave reflected as an eastward-propagating equatorial upwelling Kelvin wave and favored the positive IOD development. Therefore, both the large-scale oceanic process and MJO influences appeared to play important roles in the 2008 IOD development.

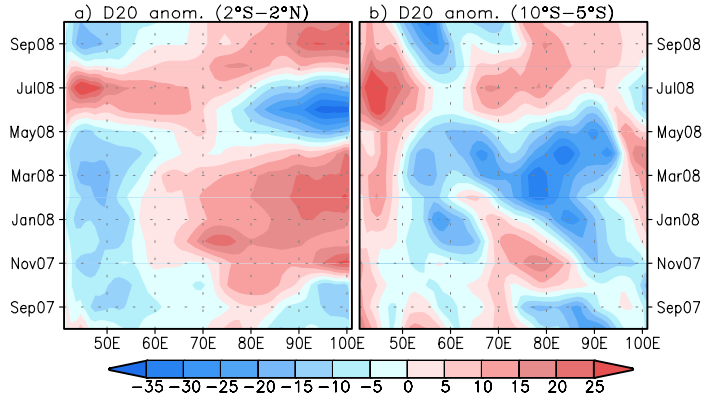

Fig. 4.33. 20°C isotherm depth (D20, m) anomalies in (a) the equatorial Indian Ocean (2°S–2°N) and (b) off-equatorial south Indian Ocean (10°–5°S). The data are derived from the NCEP ocean assimilation system.

UNUSUALLY QUIET WEST PACIFIC TYPHOON SEASON ENDS WITH A DOLPHIN KICK—M. A. LANDER, B. WARD, AND H. J. DIAMOND

In the WNP basin, climatic effects typical of La Niña were noted for much of 2008. These included well-known La Niña–related anomalies such as below-normal TC activity across most of Micronesia, TC activity shifting well to the west and north of normal, a weak (or absent) monsoon, higher-than-normal sea level, and abnormally strong and widespread TW in the lower latitudes (Fig. 4.34).

The 2008 TY season came to an apparent end after STY Jangmi recurved east of Japan in September. There were no TYs in the WNP basin in October for only the second time since JTWC records began in 1959. After the demise of TS Noul in mid-November, TWs of unprecedented persistence and wide coverage seemed to preclude the formation of any more TCs for the remainder of the year. This would have contributed to several statistical extremes of low TC activity in a year, but nature had one more peculiar scenario to play out.

In early December, a midlatitude cyclone east of Japan intensified, matured, and evolved into a warm seclusion. This isolated vortex was then steered southward by a surge of northerly gales. Starting near 30°N, it plunged southward into the deep tropics (12°N), turned west, and became the seed for the season's final TY, Dolphin. Including the early phases of its subtropical existence, Dolphin's track was very unusual (Fig. 4.35).

As Dolphin's seed vortex was driven southward, it was accompanied by an unusual pattern of northerly gale-to-TY-force winds located in the subtropics of the WNP near the date line. These winds generated oceanic swells that traveled southward and caused phenomenal surf at Wake Island, many of the islands and atolls of Micronesia, and the Marshall Islands—and then south to Kiribati, the Solomon Islands, and the northern coast of Papua New Guinea. Breaking surf heights at more than 20 ft were reported on some atolls. Substantial inundation from wave run up was experienced in many locations, with damage to infrastructures, personal property, and crops. Inundation was exacerbated by a combination of extreme wave height, high tides, and high sea levels related to La Niña.

News reports implicated the developing TY Dolphin in the generation of this very high and destructive surf. Dolphin played only a small role in the wave event, but the struggling incipient vortex that became Dolphin defied expectations and intensified to a TS, and then to a TY. As Dolphin intensified, it passed south of Guam, requiring the issuance of the only TC watches and warnings for all of 2008 within the Guam Weather Forecast Office's area of responsibility (equator to 25°N and 130°E to 180°). After passing Guam, it became a TY. It later recurved toward Iwo Jima, Japan, completing an anomalous giant elliptical path (Fig. 4.35) that ended on 19 December near where it had begun on 4 December. After passing Iwo Jima, Dolphin decayed, thus ending this most unusual WNP TY season.

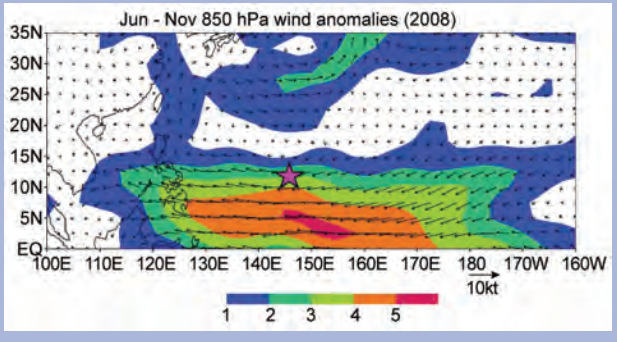

FIG. 4.34. Wind anomaly at 850 hPa for the 6-month period Jun through Nov 2008. This vast easterly wind anomaly in the deep tropics of the western North Pacific was of sufficient magnitude to eliminate the normal monsoon trough of the region and to stifle the normal development of tropical cyclones eastward of the longitude of Guam (purple star). (Figure adapted and used with permission of J–C.L. Chan, City University of Hong Kong.)

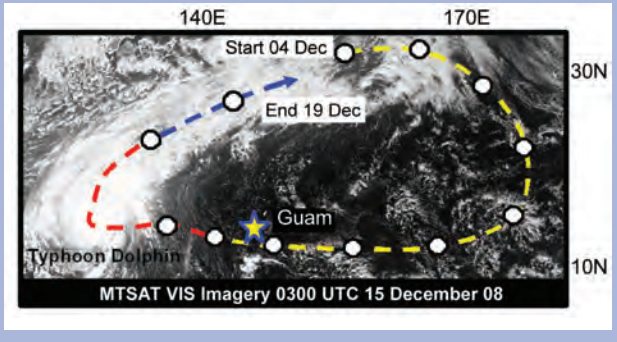

FIG. 4.35. The highly unusual track of TY Dolphin. Filled circles show 24-hr positions, with some circles left out so as not to cover the image of the typhoon. Dolphin is a typhoon in this MTSAT visible imagery of 0300 UTC 15 Dec 2008. Imagery obtained from the geostationary archive of the University of Dundee, U.K. (www.sat.dundee.ac.uk/).

5. THE ARCTIC—J. Richter-Menge

a. Overview

In 2008 there continued to be broad evidence of the impact of a general, Arctic-wide warming trend in surface air temperatures over land, apparent since the mid-1960s. Record-setting summer (JJA) air temperatures were observed throughout Greenland. The northern region of Greenland and adjacent areas of Arctic Canada experienced a particularly intense melt season, even though there was an abnormally cold winter across Greenland's southern half. On land there was a continued Arctic-wide trend toward a shorter snow season, highlighted by the shortest snow cover duration on record (beginning in 1966) in the North American Arctic. There has been a general increase in land-surface temperatures and in permafrost temperatures during the last several decades throughout the Arctic region. New permafrost data from Russia show striking similarity to observations made in Alaska, with permafrost temperature typically having increased by 1° to 2°C in the last 30 to 35 years. One of the most dramatic signals of the general warming trend was the continued significant reduction in the extent of the summer sea-ice cover and, importantly, the decrease in the amount of relatively older, thicker ice. The extent of the 2008 summer sea-ice cover was the second-lowest value of the satellite record (beginning in 1979) and 36% below the 1979–2000 average. Summer temperature anomalies in the ocean surface layer remained relatively high, reaching above +3°C in the Beaufort Sea. Significant losses in the mass of ice sheets and the area of ice shelves continued, with several fjords on the northern coast of Ellesmere Island being ice free for the first time in 3,000–5,500 years.

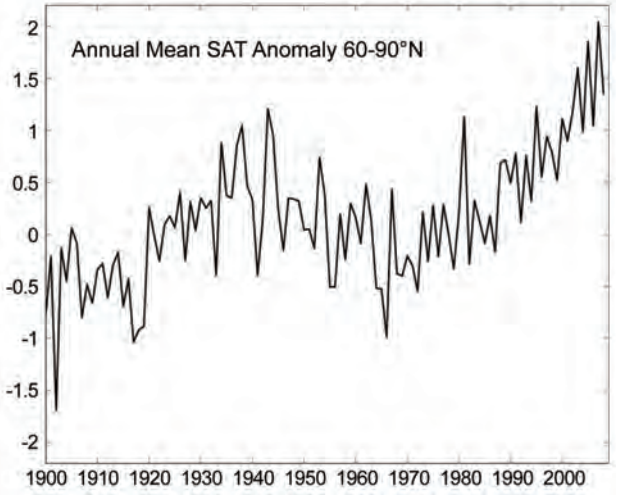

Fig. 5.1. Arctic-wide annual averaged surface air temperature anomalies (60°–90°N) based on land stations north of 60°N relative to the 1961–90 mean. From the CRUTEM 3v dataset (available online at www.cru.uea.ac.uk/cru/data/temperature/). Note: this curve does not include marine observations.

Documented signs of connectivity between the various elements of the Arctic system are beginning to emerge. For instance, a comparison of ocean surface temperatures during the summer of 2007 and 2008 provides clear evidence that the timing in the loss of the summer sea-ice cover plays a significant role in determining the magnitude and distribution of ocean surface temperatures. It is apparent that the heating of the ocean in areas of extreme summer sea-ice loss is directly impacting surface air temperatures over the Arctic Ocean, where surface air temperature anomalies reached an unprecedented +5°C during October through December 2008. Direct observations confirm model predictions that the effects of the retreating sea ice influence the temperature and vegetation of adjacent lands. Temporal analyses generally show that within a specific region, periods of lower sea-ice concentration are correlated with higher land-surface temperatures and an increase in the amount of live green vegetation in the summer.

b. Atmosphere—J. Overland, M. Wang, and J. Walsh

The annual mean Arctic temperature for 2008 was the fourth-warmest year for land areas since 1990 (Fig. 5.1). This continued the twenty-first century positive Arctic-wide SAT anomalies of greater than 1.0°C, relative to the 1961–90 reference period. The mean annual temperature for 2008 was cooler than 2007, coinciding with cooler global and Pacific temperatures (Hansen et al. 2009).

Similar to the previous years of the twenty-first century, in 2008 the spatial extent of positive SAT anomalies in winter and spring of greater than +1°C was nearly Arctic-wide (Fig. 5.2a), in contrast with more regional patterns in the twentieth century (Chapman and Walsh 2007). The exception was the Bering Sea/southwestern Alaska, which experienced a fourth-consecutive cold or average winter associated with a strong negative PDO as 2008 came to a close.

The summer of 2008 ended with nearly the same extreme minimum sea-ice extent as in 2007, characterized by extensive areas of open water (see section 5d). This condition allows extra heat to be absorbed by the ocean from longwave and solar radiation throughout the summer season, which is then released back to the atmosphere the following autumn (Serreze et al. 2009). As a result, during October through December 2008 SAT anomalies

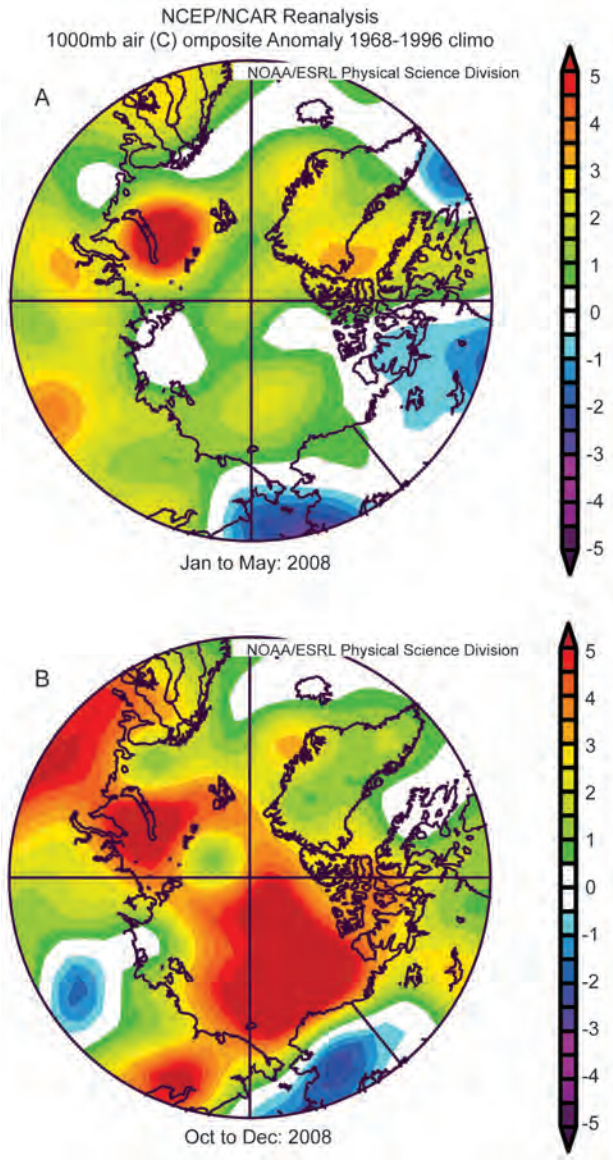

Fig. 5.2. Near-surface air temperature anomalies for (a) Jan–May 2008 and (b) Oct through Dec 2008. Anomalies are relative to 1968–96 mean. Data are from the NCEP–NCAR reanalysis through the NOAA/ Earth Systems Research Laboratory, generated online at www.cdc.noaa.gov.

remained above an unprecedented +5°C across the central Arctic (Fig. 5.2b).

The climate of the Arctic is influenced by repeating patterns of SLP that can either dominate during individual months or represent the overall atmospheric circulation flow for an entire season. 2008 continued twenty-first-century conditions where both the types of patterns and their frequency have shifted in comparison to the twentieth century. The main pattern of primarily zonal winds is known as the Arctic Oscillation. A second more meridional wind pattern that is more prevalent in the twenty-first century is known as the Arctic Warm pattern (Wu et al. 2006; Overland et al. 2008). The AW pattern has anomalous high SLP pressure on the North American side of the Arctic and low SLP on the Eurasian side, and it implies increased transport of heat into the central Arctic Ocean (e.g., Fig. 5.3). 2007 exhibited an unusually persistent positive AO pattern in the winter and AW pattern in all summer months, which helped to support the major 2007 summer reduction in sea-ice extent (Overland et al. 2008). 2008 was more typical of past patterns, characterized by month-to-month variability in the presence of these climate patterns, with no single pattern showing seasonal dominance.

There is evidence that by creating a new major surface heat source, the recent extreme loss of summer sea-ice extent is having a direct feedback effect on the general atmospheric circulation into the winter season (Francis et al. 2009). Fall air temperature anomalies of greater than +1.0°C were observed well up into the troposphere (Fig. 5.4a), when averaged over 2003–08 relative to a 1968–96 base period. The

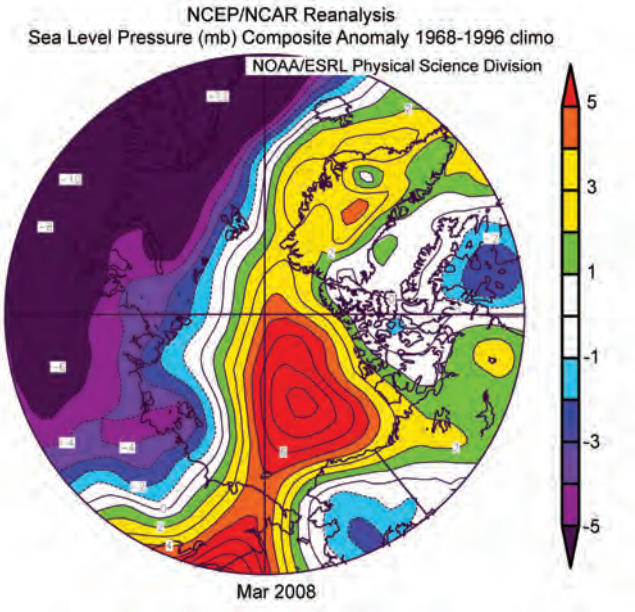

Fig. 5.3. An example of a positive AW pattern of SLP anomalies from Mar 2008. Purple/blue regions have relative low SLP and orange regions have high SLP. Anomalous winds tend to blow parallel to the contour lines, creating a flow from north of eastern Siberia across the North Pole. The orientation of the pressure dipole can shift; other examples have the anomalous geostrophic wind flow coming from north of the Bering Strait or Alaska. Data are from the NCEP–NCAR reanalysis available online at www.cdc.noaa.gov.

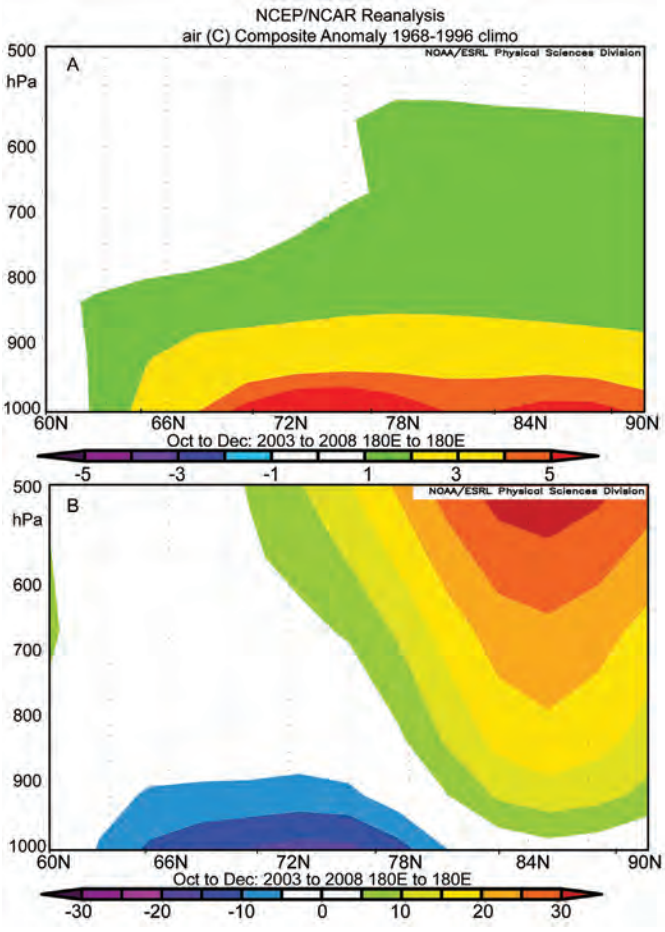

Fig. 5.4. Vertical cross section from 60° to 90°N along 180° longitude averaged for Oct–Dec 2003 through 2008 (years for which summertime sea-ice extent fell to extremely low values) for (a) air temperature and (b) geopotential height. Data are from the NCEP–NCAR reanalysis available online at www.cdc.noaa.gov.

higher temperatures in the lower troposphere increase the atmospheric geopotential thickness and raise upper-air geopotential heights above the Arctic Ocean (Fig. 5.4b). Increased geopotential heights north of 75°N weaken the normal north–south pressure gradient driving the polar vortex that creates west–east airflow aloft. In this sense, the effect of higher air temperatures in the lower troposphere is contributing to changes in the atmospheric circulation in the subarctic by reducing the potential impacts from the positive phase of the AO pattern, and perhaps contributing to the increased occurrence of the AW pattern.

c. Ocean—A. Proshutinsky, R. Krishfield, M. Steele, I. Polyakov, I. Ashik, M. McPhee, J. Morison, M.-L. Timmermans, J. Toole1, V. Sokolov, I. Frolov, E. Carmack, F. McLaughlin, K. Shimada, R. Woodgate, and T. Weingartner

1) Circulation

In 2008, the ocean surface circulation regime in the central Arctic was anticyclonic (clockwise) in winter and summer (Fig. 5.5). The intensity of motion was weaker than observed in 2007, consistent with changes in the observed sea level atmospheric pressure patterns (see section 5b). In winter the major flow stream removed sea ice from the Kara and Laptev Seas, while in the summer sea ice from the Canada Basin was transported toward the Fram Strait. Data from satellites and drifting buoys (Proshutinsky et al. 2009) indicate that the entire period of 1997–2008 has been characterized by a relatively stable anticyclonic ocean surface circulation regime. This circulation pattern was the result of a higher sea level atmospheric pressure over the Arctic Ocean, relative to the 1948–2008 mean, and the prevalence of anticyclonic winds. These conditions have significantly influenced the sea-ice cover, oceanic currents, and ocean freshwater and heat content.

2) Water temperature and salinity

Upper-ocean temperatures in summer 2008 were not quite as high as in the record-breaking summer of 2007. Although the position of the September ice edge did not change significantly in 2008 relative to 2007, the timing of ice retreat was different. Early ice retreat from the Beaufort

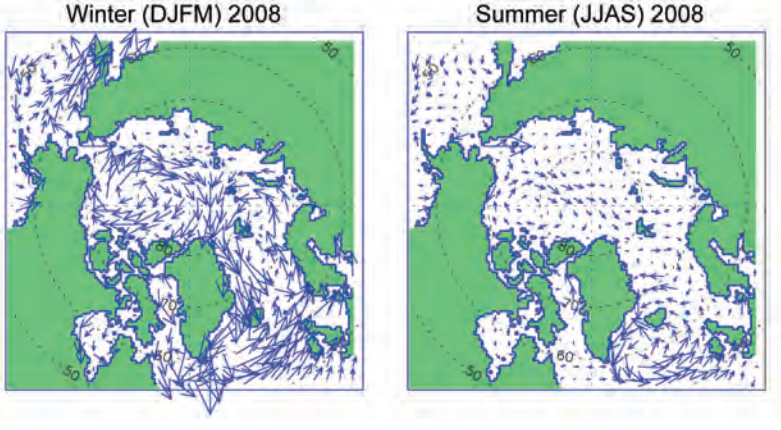

Fig. 5.5. Simulated circulation patterns of the upper-ocean wind-driven circulation in (left) winter and (right) summer in 2008. Both patterns are identified as anticyclonic (clockwise). The intensity of anticyclonic circulation in summer 2008 has reduced relative to 2007 (see Proshutinsky and Johnson 1997 for details).

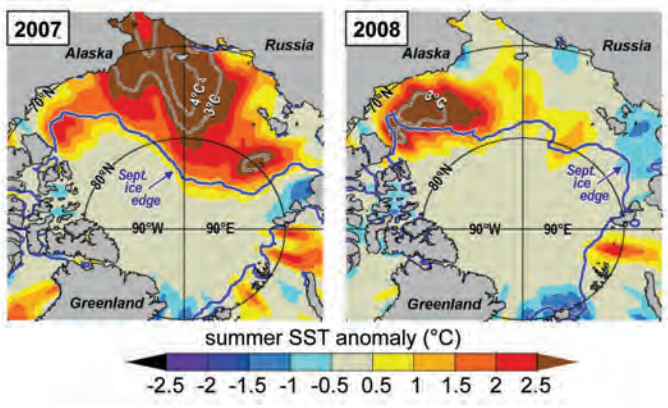

Fig. 5.6. Satellite-derived summer (JAS) SST anomalies (Reynolds et al. 2002) in (left) 2007 and (right) 2008, relative to the summer mean over 1982–2006. Also shown is the Sep mean ice edge (thick blue line).

Sea in 2008 led to anomalously high sea surface temperatures that exceeded even those in 2007 in this region (Fig. 5.6). However, ice retreat in the Chukchi and east Siberian Seas occurred relatively late in the summer, leading to near-normal or only slightly above-normal ocean warming (Fig. 5.6). This difference illustrates that the warming of the upper ocean is dependent not only on the position of the September ice edge but also on the time history of the ice cover over the summer. More specifically, ocean surface warming depends on the time history of atmospheric heat input to the sea surface, which depends both on atmospheric conditions (winds, clouds) and on the presence of the ice cover that acts to block this heat input (Steele et al. 2009, manuscript submitted to *J. Geophys. Res.*).

Changes in the AWCT varied regionally in 2008, reflecting temporal pulses in the Atlantic water flow volume, temperature, and salinity in the Fram Strait. The Atlantic water propagates cyclonically (counterclockwise) along the Arctic Ocean continental slope, entering the Arctic Ocean via the Fram Strait west of Spitsbergen and leaving the Arctic via the Fram Strait east of Greenland. Observations at a NABOS (http://nabos.iarc.uaf.edu/) mooring in the vicinity of Spitsbergen (Fig. 5.7) along the entry point of the AWCT showed that the monthly mean AWCT at 260 m reached a maximum of ~3.8°C in November–December 2006. Subsequently, the temperature at this location has declined or cooled, reaching ~2.8°C in 2008. Observations at sections crossing the continental slope in the vicinity of Severnaya Zemlya also revealed cooling of AWCT by approximately 0.5°C (Fig. 5.7). This cooling signal has not reached central parts of the Arctic Ocean and the Beaufort Gyre of the Canada Basin (Proshutinsky et al. 2009). In the Beaufort Gyre region, the AWCT in 2008 was 0.80°–0.90°C, which is 0.10°C above AWCT observed in 2007 and 0.50°C above AWCT from pre-1990s climatology. In spring of 2008, data collected at the NPEO (http://psc.apl.washington.edu/northpole/index.html) indicate that the AWCT increased to nearly 1.4°C, which is about 0.1°C higher than observed in a 2007 survey and about 0.7°C higher than pre-1990s climatology.

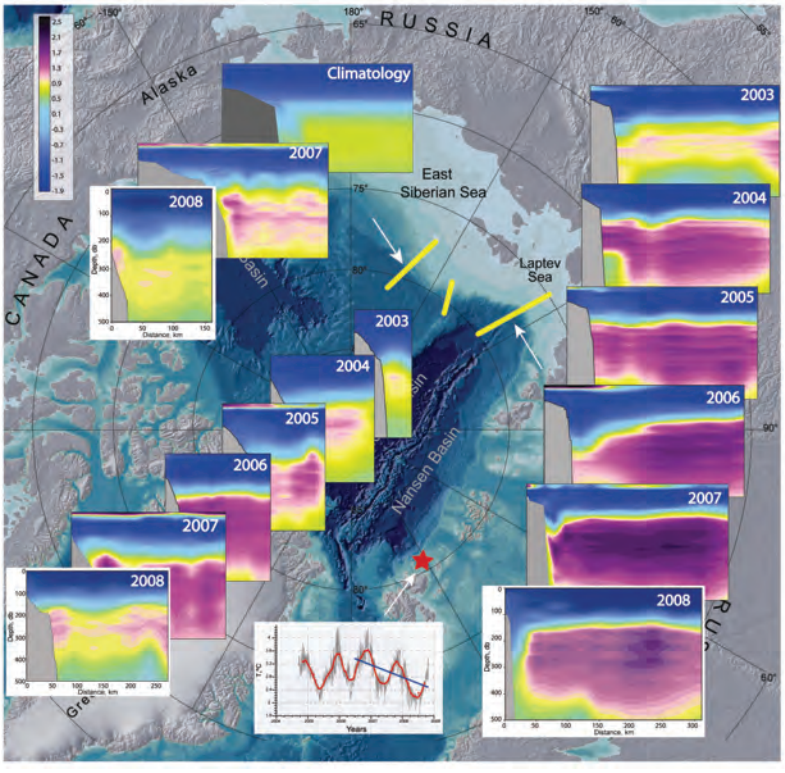

Fig. 5.7. Temporal (°C) and spatial variability of the AWCT. Locations of sections are depicted by yellow thick lines. Mooring location north of Spitsbergen is shown by a red star. There is a decline of Atlantic water temperature at 260 m at mooring locations with a rate of 0.5°C per year starting at the end of 2006. Some cooling in 2008 is also observed at the sections crossing the continental slope in the vicinity of Severnaya Zemlya and in the east Siberian Sea (Polyakov et al. 2009, manuscript submitted to *Geophys. Res. Lett.*).

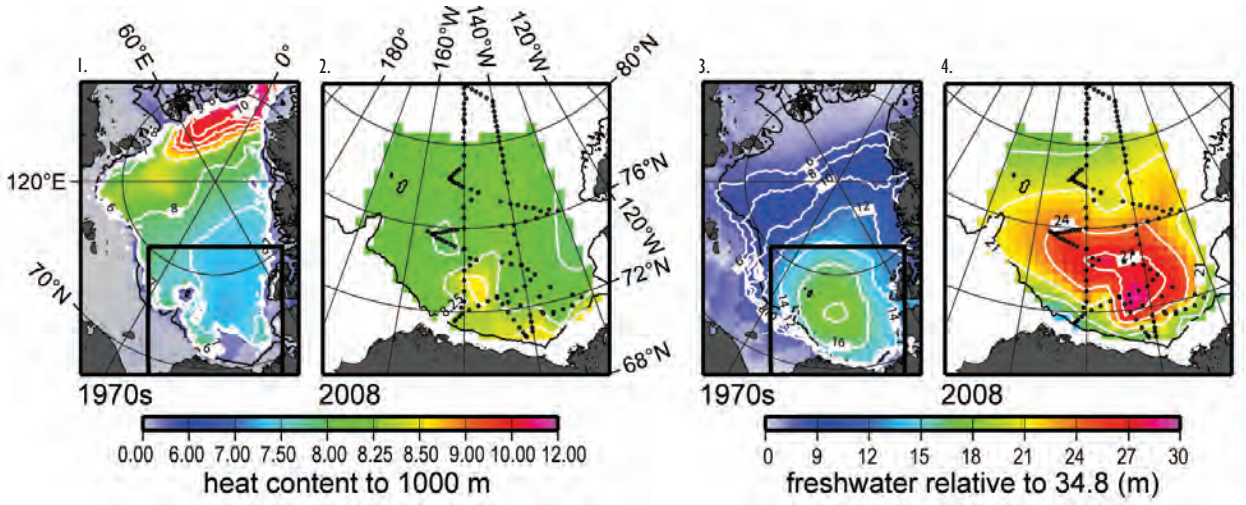

Fig. 5.8. (left) Summer heat (1×10^{10} J m^{-2}) and (right) freshwater (m) content. Panels 1 and 3 show heat and freshwater content in the Arctic Ocean based on 1970s climatology (Arctic Climatology Project 1997, 1998). Panels 2 and 4 show heat and freshwater content in the Beaufort Gyre in 2008 based on hydrographic survey (black dots depict locations of hydrographic stations). For reference, this region is outlined in black in panels 1 and 3. The heat content is calculated relatively to water temperature freezing point in the upper 1000-m ocean layer. The freshwater content is calculated relative to a reference salinity of 34.8.

Summer 2008 ship-based hydrographic surveys (Ashik, Sokolov, Frolov, and Polyakov 2008, personal communications) in different regions of the Arctic Ocean showed a continued freshening of the upper 20-m ocean layer, similar to 2007. In the 25–75-m layer, some salinification was observed in the central regions of Amundsen and Makarov Basins, while along the continental slope the water salinity remained unchanged relative to salinities observed in 2007. There was also some freshening of the deeper water layers in the Beaufort Gyre in 2008, as the surface freshening in this region was accompanied by Ekman pumping (Proshutinsky et al. 2009).

Data collected as part of the BGOS (www.whoi.edu/beaufortgyre/index.html) show that in 2000–08 the total freshwater summer content in the Beaufort Gyre has significantly increased relative to climatology of the 1970s (Arctic Climatology Project 1997, 1998; Fig. 5.8). In 2008, the center of the freshwater maximum remained shifted toward Canada as in 2007 but significantly intensified relative to 2007 (Fig. 5.8). As a result, the northwest part of the region is much saltier and the southeast region of the Beaufort Gyre is much fresher than in 2006–07 and, also, compared to 30 years ago. At some stations in the southeast of the Canada Basin the FWC reached the maximum observed value, increasing by as much as 11 m, which is 60% above climatology values. The freshening extends northward through the Canada and Makarov Basins to the Lomonosov Ridge (not shown). On the Eurasian side of the Lomonosov Ridge, the FWC anomaly is negative (water salinity was increased relative to climatology) with minimum FWC values of about −4 m (McPhee et al. 2009). The Beaufort Gyre heat content is significantly elevated relative to 1970s climatology (Arctic Climatology Project 1997, 1998; Fig. 5.8), but no significant changes relative to 2007 heat content were registered by the BGOS in 2008.

The Bering Strait is an important gateway to the Arctic Ocean. Preliminary observations from a mooring site, established and maintained since 1990 (Woodgate et al. 2006), suggest the 2007 annual mean transport through the Bering Strait is around 1 Sv (1 Sv = 10^6 m^3 s^{-1}), greater than 2006 but comparable with previous high years, such as 2004. The same is true of the freshwater flux through the strait. The heat flux, being largely determined by the total volume flux, is also high, but in this case it appears to be somewhat higher than the 2004 values.

3) Sea Level

Figure 5.9 shows SL time series from nine coastal stations in the Siberian Seas, having representative records for the period of 1954–2008 (Arctic and Antarctic Research Institute data archives). For the nine stations, the rate for 1954–89, after the GIA, was 1.94 ± 0.47 mm yr^{-1}. This compares to an estimated rate of 1.85 ± 0.43 mm yr^{-1} along the Arctic coastlines over the same period, based on 40 arctic coastal stations (Proshutinsky et al. 2004). Addition of 1990–2008 data increases the estimated rate of SL rise for the

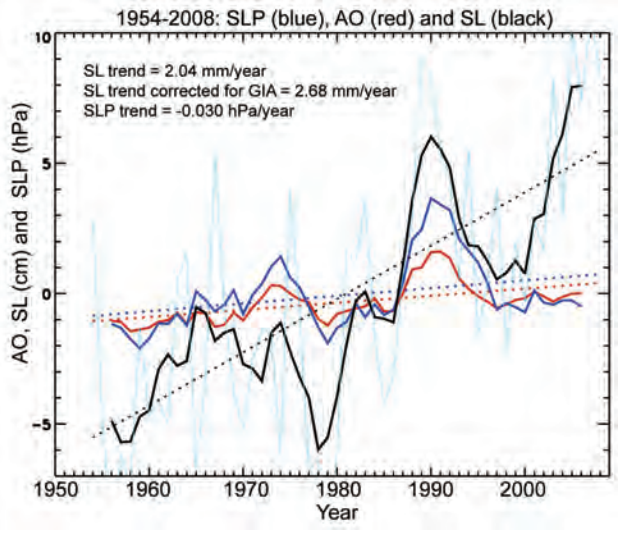

Fig. 5.9. The 5-yr running mean time series: annual mean sea level at nine tide gauge stations located along the Kara, Laptev, east Siberian, and Chukchi Seas' coastlines (black line). The red line is the anomalies of the annual mean AO Index multiplied by 3. The dark blue line is the sea surface atmospheric pressure at the North Pole (from NCAR–NCEP reanalysis data) multiplied by −1. Light blue line depicts annual sea level variability.

nine stations in the Siberian seas, beginning in 1954, to 2.68 ± 0.45 mm yr^{-1} (after correction for GIA).

Until 1996, SL correlates relatively well with the times series of the AO Index and sea level atmospheric pressure at the North Pole (Fig. 5.9). In contrast, from 1997 to 2008 the SL has generally increased, despite the more or less stable behavior of AO and SLP. Possible reasons for the rapidly rising sea level are ocean expansion, due to heating and freshening of the Arctic Ocean, and increased rates of the Greenland ice sheet melt (see section 5f).

d. Sea-ice cover—D. K. Perovich, W. Meier, and S. V. Nghiem

1) Sea-ice extent

Sea-ice extent has become the primary parameter for summarizing the state of the Arctic sea-ice cover. Microwave satellites have routinely and accurately monitored the extent since 1979. There are two periods that define the annual cycle and are thus of particular interest: March, at the end of winter when the ice is at its maximum extent, and September, when it reaches its annual minimum. Maps of ice coverage in March 2008 and September 2008 are presented in Fig. 5.10. The magenta line in the maps denotes the median ice extent for the period 1979–2000. The total area coverage in March was 15.2 million km^2, only 4% less that the 1979–2000 average of 15.8 million km^2. The area of reduced winter ice extent was located largely in the Barents Sea and the Sea of Ohkotsh. The 2008 September summer minimum ice extent was 4.5 million km^2 and was not a record minimum. However, it was the second-lowest ice extent on record, only 0.3 million km^2 greater than 2007 and 36% below the 1979–2000 average. The largest retreats in September 2008 were found in the Beaufort and east Siberian Seas.

The time series of the anomalies in sea-ice extent in March and September for the period 1979–2008, computed with respect to the average from 1979 to 2000, are plotted in Fig. 5.11. The large interannual variability in September ice extent is evident. Both winter and summer ice extent exhibit a negative (decreasing) trend, with values of –2.8% per decade for March and –11.1% per decade for September.

2) Sea-ice age and thickness

The age of the ice is another key descriptor of the state of the sea-ice cover, since older ice tends to be

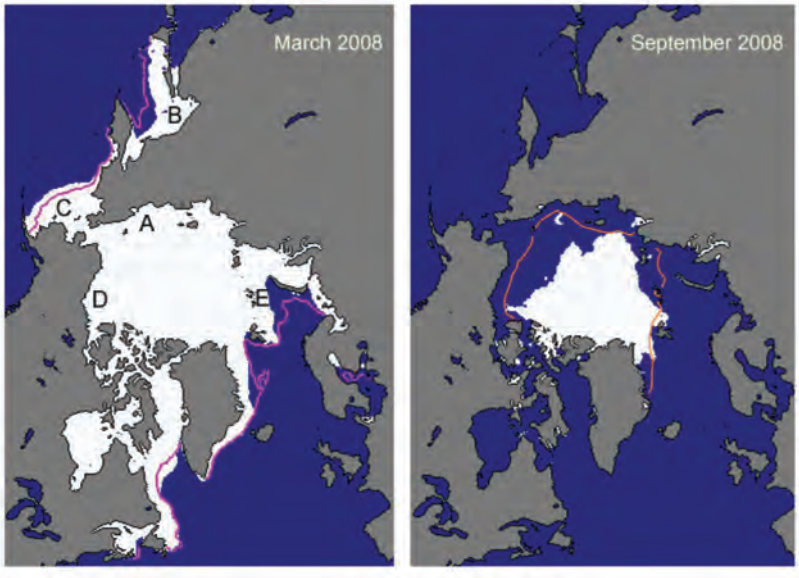

Fig. 5.10. Sea-ice extent in (left) Mar 2008 and (right) Sep 2008, illustrating the respective winter maximum and summer minimum extents. The magenta line indicates the median maximum and minimum extent of the ice cover, for the period 1979–2000. A—east Siberian Sea, B—Sea of Ohkotsh, C—Bering Sea, D—Beaufort Sea, and E—Barent's Sea. (Figures from the NSIDC Index: nsidc.org/data/seaice_index.)

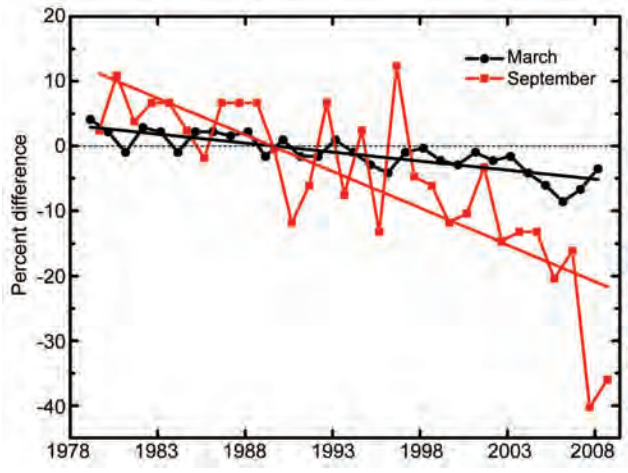

Fig. 5.11. Time series of the percent difference in ice extent in Mar (the month of ice-extent maximum) and Sep (the month of ice-extent minimum) from the mean values for the period 1979–2000. Based on a least-squares linear regression, the rate of decrease for the Mar and Sep ice extents was −2.8% and −11.1% per decade, respectively.

thicker and more resilient than younger ice. A simple two-stage approach classifies sea ice as seasonal or perennial. Seasonal ice freezes in the winter and melts in the summer, while perennial ice can last for several years. Satellite-derived maps of ice age for March and September in 2007 and 2008 are presented in Fig. 5.12.

QuikSCAT data show the Arctic perennial sea-ice extent on 1 March 2008. A combination of the satellite and surface drift data records (Rigor and Wallace 2004) confirmed that the 2008 winter perennial ice extent was a minimum compared to data over the last half-century. The extent of perennial sea ice on 1 March 2008 was reduced by 1 million km^2 compared to that at the same time last year (Fig. 5.12, top). This decrease of perennial ice continues a decade-long sharp decline, caused in part by enhanced wind-driven transport of perennial ice out of the Arctic Basin via the Fram and Nares Straits (Nghiem et al. 2006, 2007).

A noteworthy, albeit explicable, aspect of the 2008 summer melt season was the higher-than-average retention of first-year sea ice, with much more first-year ice surviving in 2008 than in 2007 (Fig. 5.12, bottom). This observation is counterintuitive because relatively thin first-year ice is typically prone to complete melting. One cause of the large first-year ice survival rate was that early summer 2008 was cooler than in 2007 and the lower air temperatures slowed the melt rate in the early part of the season (NSIDC, http://nsidc.org/news/press/20081002_seaice_pressrelease.html). Conditions in August favored rapid ice loss, but this did not make up for the modest early season melt. Furthermore, much of this year's first-year ice was located at higher latitudes than in 2007, covering even the geographic North Pole. These far north regions receive less solar energy and have less melting.

The total volume of sea ice depends on the ice area and the ice thickness. Unfortunately, ice thickness is difficult to monitor. Surface-based measurements are few in number and submarine observations are at irregular temporal spacing. Satellite-based techniques (Laxon et al. 2003; Kwok et al. 2004, 2007) offer the promise of complete spatial and temporal coverage but are not yet fully operational. Thickness data from these various sources indicate a net thinning of the Arctic sea-ice cover. Submarine-based observations indicate that over the period 1975 to 2000, the annual mean thickness of the ice cover declined

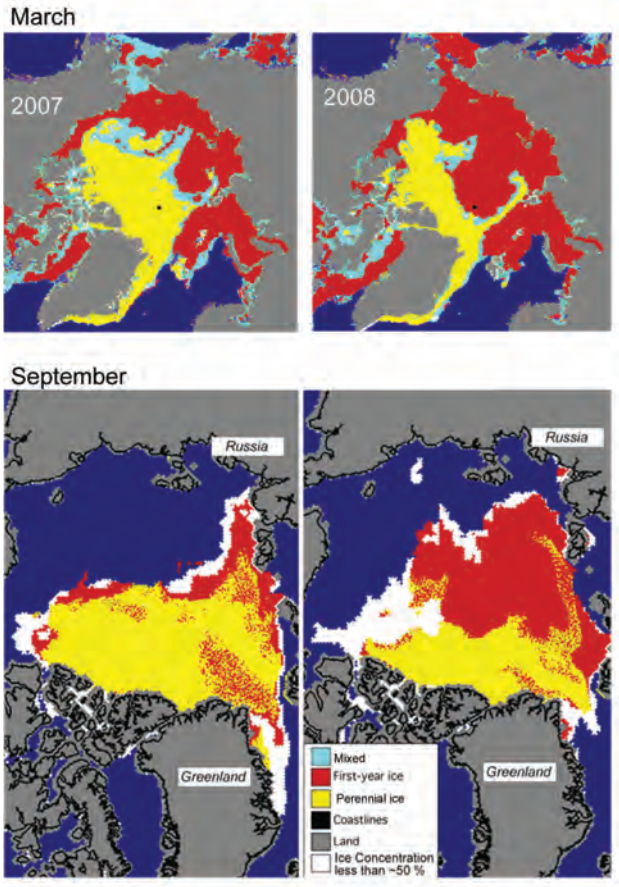

Fig. 5.12. Maps of age of Arctic sea ice for (left) 2007 and (right) 2008 in (top) Mar and (bottom) Sep. (top) Derived from QuikSCAT data (Nghiem et al. 2007). (bottom) Courtesy of C. Fowler, J. Maslanik, and S. Drobot, NSIDC, and are derived from a combination of AVHRR and SSM/I satellite observations and results from drifting ice buoys.

from 3.71 m in 1980 to 2.46 m in 2000, a decrease of 1.25 m (Rothrock et al. 2008). Maslanik et al. (2007) generated a proxy ice-thickness record for 1982–2007 by combining satellite estimates of sea-ice age and thickness, and the record indicates significant thinning between 1982 and 2007. A reduction of modal and mean sea ice thicknesses in the region of the North Pole of up to 53% and 44%, between 2001 and 2007, has been observed by Haas et al. (2008) using helicopter-borne electromagnetic ice-thickness profilers. Using satellite radar altimetry data, covering the Arctic Ocean up to 81.5°N, Giles et al. (2008) observed that after the melt season of 2007, the average sea-ice thickness was 0.26 m below the 2002/03 to 2007/08 average. In contrast to the central Arctic, measurements of the seasonal and coastal ice cover do not indicate any statistically significant change in thickness in recent decades (Melling et al. 2005; Haas 2004; Polyakov et al. 2003), indicating that the thinning of the ice cover is primarily the result of changes in perennial ice thickness.

e. *Land*—D. A. Walker, U. S. Bhatt, M. K. Raynolds, J. E. Comiso, H. E. Epstein, and G. J. Jia

1) Vegetation

Models have predicted that the retreating sea ice (see section 5d) should affect the temperature and ecosystems of adjacent lands (e.g., Lawrence et al. 2008). Time series of sea-ice area and land temperatures, as well as an index of greening, were investigated for trends and variability during the period 1982–2007 along the coastlines of 14 Arctic seas (Fig. 5.13). Temporal analyses of these regional time series (not shown) consistently indicate that higher land-surface temperatures and higher NDVI values correspond to below-average sea-ice concentration (Bhatt et al. 2008, 2009, manuscript submitted to *Earth Interactions*).

The trend analysis shows that coastal sea ice declined in all regions, with a decrease of 25% for the Northern Hemisphere as a whole (Fig. 5.13, top blue bar). The largest declines were along the northern Beringia region, including the west Chukchi, east Chukchi, and east Siberia Seas. This portion of the Arctic saw large areas of summer ice retreat in 2005 and 2007.

Land temperatures as measured by the summer warmth index (sum of the monthly mean temperatures that are above freezing) increased 24% for the Northern Hemisphere as a whole (Fig. 5.13, top red bar). However, the coastal areas of the North America Arctic have experienced a 27% increase in land temperatures, while Eurasia experienced only a 16% increase. The largest increases occurred in the Beringia region (east Siberia, west Chukchi, west Bering, and east Chukchi) and in the Greenland and Baffin Island regions (Greenland Sea, Baffin Bay, and Davis Strait). The smallest increases were seen along

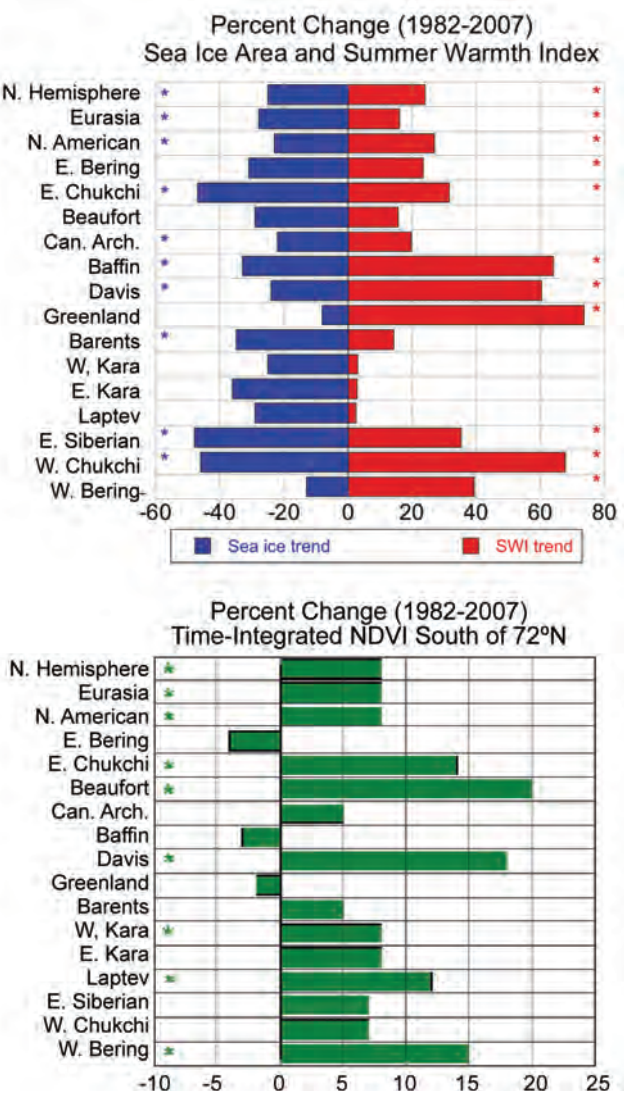

Fig. 5.13. (top, blue bars) Percentage change in sea-ice area in late spring (when the long-term mean 50% concentration is reached) during 1982–2007 along the 50-km-seaward coastal margin in each of the major seas of the Arctic using 25-km-resolution SSMI passive microwave Bootstrap sea-ice concentration data (Comiso and Nishio 2008). (top, red bars) Percentage change in the summer land-surface temperature along the 50-km-landward coastal margin as measured by the SWI [sum of the monthly mean temperatures above freezing (°C mo)] based on AVHRR surface-temperature data (Comiso 2003). (bottom, green bars) Percentage change in greenness for the full tundra area south of 72°N as measured by the TI-NDVI based on biweekly GIMMS NDVI (Tucker et al. 2001). Asterisks denote significant trends at $p < 0.05$. Based on Bhatt et al. (2008).

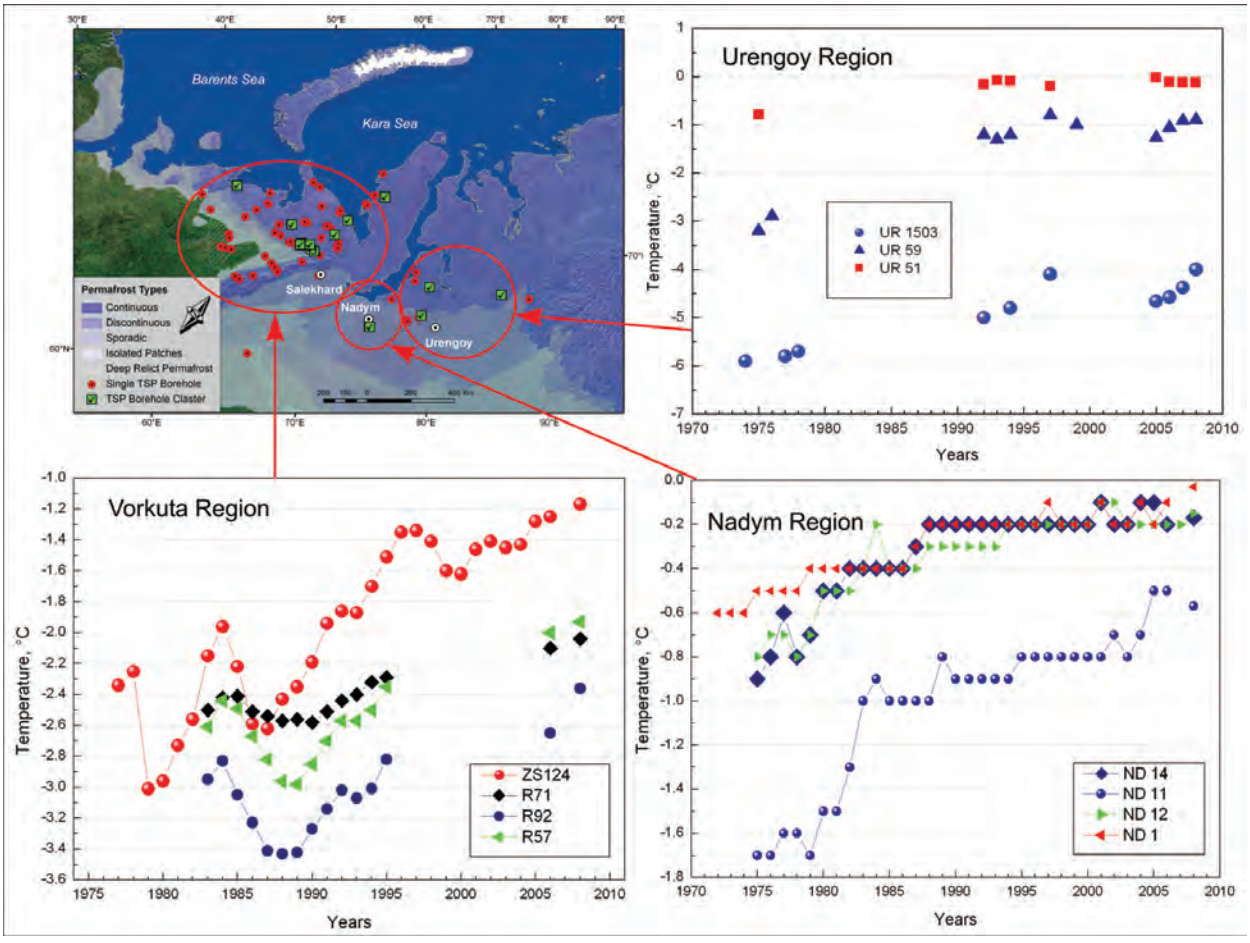

Fig. 5.14. (top left) Location of the long-term MIREKO and the Earth Cryosphere Institute permafrost observatories in northern Russia. (bottom left) Changes in permafrost temperatures at 15-m depth during the last 20 to 25 years at selected stations in the Vorkuta region (updated from Oberman 2008). (top right) Changes in permafrost temperatures at 10-m depth during the last 35 yr at selected stations in the Urengoy and Nadym (bottom right) regions (updated from Romanovsky et al. 2008).

the northern coast of Russia (Laptev Sea, east Kara Sea, and west Kara Sea).

Greenness was determined using the TI-NDVI derived from the GIMMS data. TI-NDVI is an index of the productivity of the vegetation each summer that is derived from Earth's reflectance in the visible and near-infrared portions of the spectrum. The TI-NDVI analysis was limited to the area south of 72°N (covers primarily the low Arctic) because of a discontinuity in the GIMMS data at this latitude. TI-NDVI increased 8% for the Arctic as a whole (Fig. 5.13, top green bar) but was variable. The largest increase was along the Beaufort Sea coast (20%). Other large increases occurred adjacent to the Davis Strait and the east Chukchi and west Bering Seas. Smaller increases occurred in much of northern Russia (Barents, Kara, east Siberian, and west Chukchi Seas), generally where summer temperature increases were lower. A few nonsignificant negative trends occurred in the east Bering Sea, Baffin Bay, and Greenland Sea. The NDVI changes noted here are in general agreement with other analyses of NDVI trends in the Arctic (Jia et al. 2003; Goetz et al. 2005; Verbyla 2008; Raynolds et al. 2008) and ground observations (Tape et al. 2006; Walker et al. 2008; Epstein et al. 2008).

2) Permafrost—V. Romanovsky, N. Oberman, D. Drozdov, G. Malkova, A. Kholodov, and S. Marchenko

Observations show a general increase in permafrost temperatures during the last several decades in Alaska (Romanovsky et al. 2002, 2007; Osterkamp 2008), northwest Canada (Couture et al. 2003; Smith et al. 2005), Siberia (Oberman and Mazhitova 2001; Oberman 2008; Drozdov et al. 2008; Romanovsky et al. 2008), and northern Europe (Isaksen et al. 2000; Harris and Haeberli 2003).

Most of the permafrost observatories in Alaska show a substantial warming during the last 20 years.

The detailed characteristic of the warming varies between locations, but it is typically from 0.5° to 2°C at the depth of zero seasonal temperature variations in permafrost (Osterkamp 2008). It is worth noting that permafrost temperature has been relatively stable on the North Slope of Alaska during 2000–08.

Permafrost temperature has increased by 1° to 2°C in northern Russia during the last 30 to 35 years (Fig. 5.14). This increase is very similar in magnitude and timing to what has been observed in Alaska. Also, a common feature for Alaskan and Russian sites is more significant warming in relatively cold permafrost than in warm permafrost. An especially noticeable permafrost temperature increase in the Russian Arctic was observed during the last two years. The mean annual permafrost temperature at a 15-m depth increased by more than 0.3°C in the Tiksi area and by 0.25°C at a 10-m depth in the European north of Russia.

The last 30 years of generally increasing permafrost temperatures have resulted in thawing of permafrost in areas of discontinuous permafrost in Russia (Oberman 2008). At one of the locations, the upper boundary of permafrost lowered to 8.6 m in 30 years. It lowered even more, to almost 16 m, in an area where a newly developed talik (a volume or layer of all-year-round unfrozen soil above or within the permafrost) coalesced with an already existing lateral talik. The average increase in depth of the permafrost table in the Vorkuta and Nadym regions in Russia ranged from 0.6 to 6.7 m, depending on the geographical location, ice content, lithological characteristics of sediments, hydrological, hydrogeological, and other factors.

3) River discharge—A. Shiklomanov

A general increase of river discharge to the Arctic Ocean from Eurasia was observed over the period 1936–2007, with a rate of annual change (defined from the linear trend) of 2.7 ± 0.5 km^3 yr^{-1} (Fig. 5.15). The most pronounced positive (increasing) trend for the six largest Eurasian rivers is observed during the last 21 years (1987–2007), at a rate of 11.8 km^3 yr^{-1}. The rate of discharge has continued to increase in the twenty-first century. The mean 2000–07 discharge was 171 km^3 higher (10%) than the long-term average over the period 1936–99. A new historical maximum for Eurasian river discharge to the Arctic Ocean was observed in 2007, reaching 2250 km^3 yr^{-1} or 30% higher than the long-term mean discharge from 1936–99, reported in Peterson et al. (2002).

The mean annual discharge to the ocean over 2000–07 from the five large North American Arctic rivers, based on data from the Environment Canada and USGS, was about 6% (31 km^3) greater than the long-term mean from 1973 to 1999. The river discharge during 2007 was higher than the long-term mean and, taking into account that this year had extremely high freshwater discharge from Greenland (Mernild et al. 2009), we can estimate that 2007 showed record-high total freshwater input to the Arctic Ocean from the terrestrial land surface.

Provisional estimates, made using techniques developed by Shiklomanov et al. (2006), indicate that the 2008 annual river discharge to the Arctic Ocean from the Russian rivers was significantly greater than the long-term mean but lower than the historical maximum observed in 2007 (Fig. 5.15).

4) Terrestrial snow—C. Derksen, R. Brown, and L. Wang

The 2007/08 Arctic snow season was characterized by close-to-normal snow cover onset over North America and Eurasia, with above-normal seasonal accumulation over Siberia and much of North America. The Arctic spring melt was characterized by close-to-normal conditions over Eurasia, but the earliest snow cover disappearance in the period of record (1966–present) over North America.

Various satellite and conventional measurements provide a comprehensive perspective on terrestrial snow including SCD, SD, and melt timing/duration (Brasnett 1999; Brown et al. 2007; Helfrich et al. 2007;

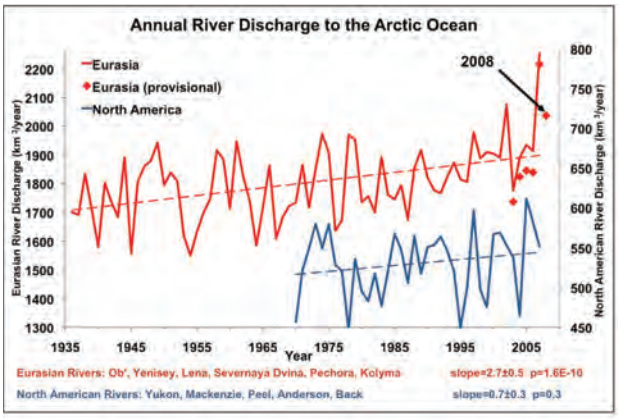

Fig. 5.15. Total annual river discharge to the Arctic Ocean from the six largest rivers in the Eurasian Arctic for the observational period 1936–2007 (updated from Peterson et al. 2002) (red line) and from the five large North American pan-Arctic rivers over 1973–2006 (blue line). The least-squares linear trend lines are shown as dashed lines. Provisional estimates of annual discharge for the six major Eurasian Arctic rivers, based on near-real-time data from http://RIMS.unh.edu, are shown as red diamonds.

Wang et al. 2008a). SCD anomalies for the 2007/08 snow season, derived from NOAA weekly snow charts (available online at climate.rutgers.edu/snowcover/), illustrate a reduced snow cover season over the eastern Canadian Arctic, most of Europe, and eastern Siberia, compared to a longer-than-normal snow season in central China and the midlatitudes of North America (Fig. 5.16a). The period 1988–2007 is selected as the historical reference period for this assessment to place anomalies in the context of more recent snow cover conditions following a rapid reduction in hemispheric snow cover during the 1980s. Time series of SCD anomalies across the North American and Eurasian sectors of the Arctic (north of 60°N) are illustrated in Fig. 5.16b. SCD anomalies are generally in-phase for both sectors, with the 2007/08 snow cover season close to the 1988–2007 normal for snow cover onset (fall SCD). For snowmelt (spring SCD) the Eurasian average was close to normal, while the North American Arctic had the earliest disappearance of snow in the NOAA record (since 1966). This is a continuation of shorter snow seasons observed since the rapid reductions in the 1980s. Unlike summer sea-ice concentration, however, there is no linear decrease in Arctic spring SCD over the past decade.

Annual maximum SD anomalies for 2007/08 (1998–2008 reference period), determined from the CMC analysis (Brasnett 1999), are shown in Fig. 5.16c. Over Siberia, positive SD anomalies coincide with below-normal SCD, indicating above-average snowfall but early spring melt—a continuation of recent trends reported in Kitaev et al. (2005).

The main melt onset date for 2008 across the pan-Arctic land mass was derived from Ku-band scatterometer measurements available from QuikSCAT using the algorithm of Wang et al. (2008a). The melt onset anomaly relative to the 9-yr QuikSCAT record (2000 to 2008) confirms regional early melt onset over the North American Arctic that agrees with early dates of snow disappearance identified from the NOAA record (Fig. 5.16d). In the Eurasian region there was a pattern of generally late melt onset between approximately 60°–65°N, anomalously early melt across 65°–70°N, and then a transition to late melt onset again across the northern portion of Eurasia.

5) Glaciers outside Greenland—M. Sharp and G. Wolken (with acknowledge data contributions from D. Burgess, G. Cogley, P. Glowacki, J. Jania, S. O'Neel, D. Puczko, A. Arendt, and S. Luthcke)

Glacier shrinkage is a major contributor to global sea level change (Meier et al. 2007). Surface mass

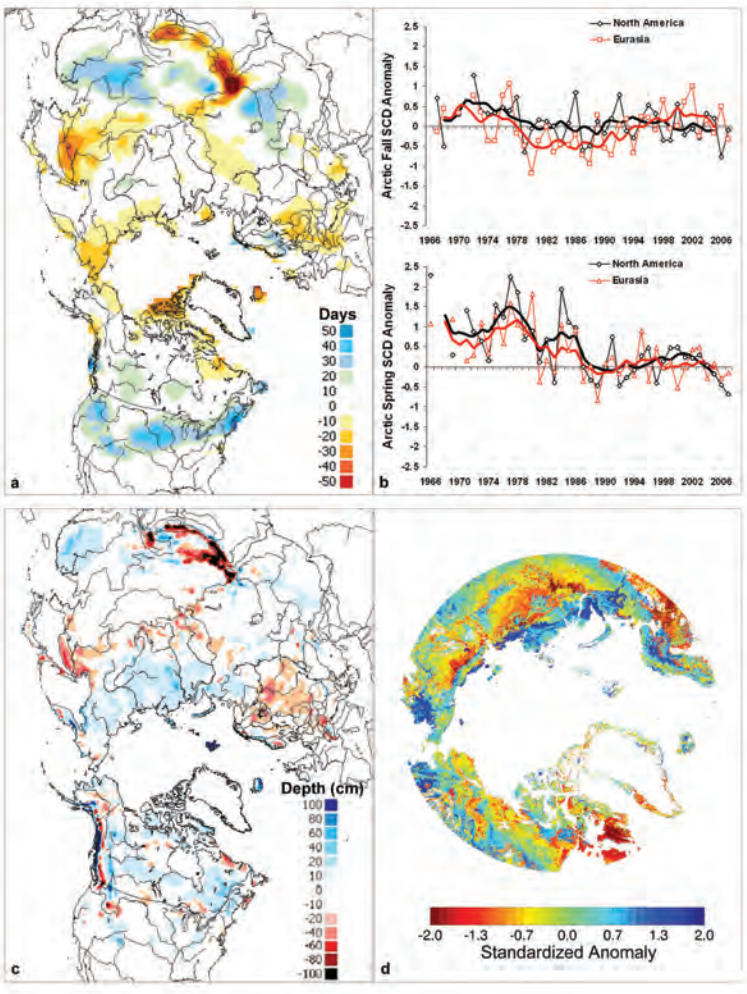

Fig. 5.16. (a) SCD anomalies (with respect to 1988–2007) for the 2007/08 snow year and (b) Arctic seasonal SCD anomaly time series (with respect to 1988–2007) from the NOAA record for the first (fall) and second (spring) halves of the snow season. Solid lines denote 5-yr moving average. (c) Maximum seasonal snow depth anomaly for 2007/08 (with respect to 1998/99–2007/08) from the CMC snow depth analysis. (d) Terrestrial snowmelt onset anomalies (with respect to 2000–08) from QuikSCAT data derived using the algorithm of Wang et al. (2008a). The standardized anomaly scales the date of onset of snowmelt based on the average and the magnitude of the interannual variability in the date at each location. A negative anomaly (shown in red-yellow) indicates earlier onset of snowmelt in the spring.

balance (annual net balance and its summer/winter components) measures how climate affects the health of Arctic glaciers. As most 2007–08 measurements are not yet available, we report results for the 2006–07 balance year (Svalbard: 4 glaciers, Iceland: 6, Alaska: 3, Arctic Canada: 4). Annual surface balances were negative for 14 glaciers, positive for 2 (1 each in Iceland and Alaska), and zero for 1 (in Svalbard) (WGMS 2009).

Summer (JJA 2008) 700-hPa air temperature and winter (September 2007–May 2008) precipitation data from the NCEP–NCAR reanalysis serve as climatic indices for regions centered over each of the Arctic's major glaciated regions (excluding Greenland) (Table 5.1). Sixteen discrete regions form four groups (Alaska, Arctic Canada, Iceland, and the Eurasian Arctic) based on correlations between 1948 and 2008 NCEP summer temperature series. These indices suggest that the 2008 annual mass balance was likely extremely negative in Arctic Canada, due to unusually high summer air temperatures, and positive in Alaska due to strong positive winter precipitation anomalies (confirmed by GRACE satellite gravimetry; S. Luthcke 2009, personal communication). Annual balance was likely near zero or slightly positive in the Eurasian Arctic (relatively cool summers and generally high winter precipitation) and negative in Iceland (higher-than-average summer temperatures and below-average winter precipitation).

Melt onset and freeze-up dates and 2008 melt season duration were determined from temporal backscatter variations measured by QuikSCAT's SeaWinds (Table 5.1). In Arctic Canada, melt duration anomalies (relative to 2000–04 climatology) on the North Ellesmere, Agassiz, and Axel Heiberg ice caps ranged from +17.6 to +22.5 days, largely due to late freeze-up. Here, summer 2008 was the longest melt season in the 2000–08 record. Melt duration anomalies were also strongly positive on northern Prince of Wales Icefield and Severnaya Zemlya, and positive in central and southern Arctic Canada, Franz Josef Land, and Iceland. The melt season in southwest Alaska was the shortest in the 9-yr record, with strongly negative melt duration anomalies, mostly due to early freeze-up.

The total ice shelf area in Arctic Canada decreased by 23% in summer 2008 (Mueller et al. 2008). The Markham ice shelf disappeared completely and the Serson ice shelf lost 60% of its area. In the past century, 90% of the Arctic ice shelf area has been lost. Several fjords on the north coast of Ellesmere Island are now ice free for the first time in 3,000–5,500 years (England et al. 2008).

f. Greenland—J. E. Box, L.-S. Bail, R. Benson, I. Bhattacharya, D. H. Bromwich, J. Cappelen, D. Decker, N. DiGirolamo, X. Fettweis, D. Hall, E. Hanna, T. Mote, M. Tedesco, R. van de Wal, and M. van den Broeke

1) Summary

An abnormally cold winter across the southern half of Greenland led to substantially higher west coast sea ice thickness and concentration. Even so, record-setting summer temperatures around Greenland, combined with an intense melt season (particularly across the northern ice sheet), led the 2008 Greenland climate to be marked by continued ice sheet mass deficit and floating ice disintegration.

2) Regional surface temperatures

Temperature anomalies were mixed and exhibited seasonal variability (Fig. 5.17). Annual mean temperatures for the whole ice sheet were +0.9°C, but were not abnormal, given a rank of 23 of 51 years over the 1958–2008 period (Box et al. 2006). Persistent warm anomalies were evident over the northern ice sheet in all seasons. Temperatures were abnormally cold over the southern ice sheet in winter. Coastal meteorological stations around Greenland with a consistent 51-yr period (1958–2008) (Cappelen 2009) indicate a record-setting warm summer in 2008. The Upernavik (Nuuk) summer temperature was the warmest (second warmest) on record since 1873, respectively.

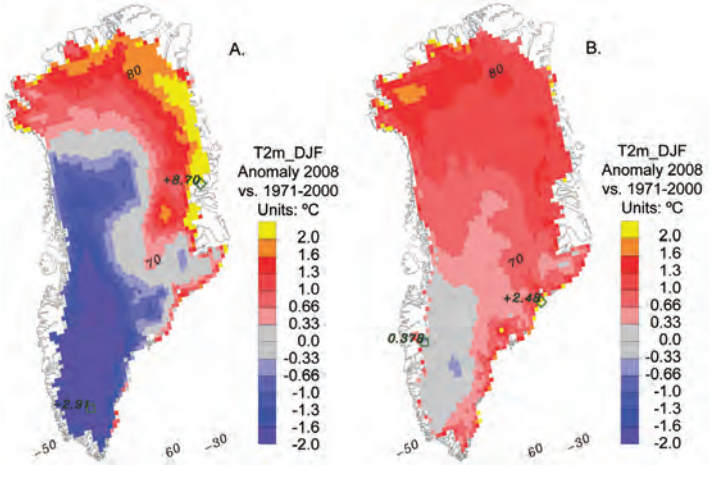

Fig. 5.17. 2008 (a) winter and (b) summer near-surface (2 m) air temperature anomalies with respect to the 1971–2000 base period, simulated by Polar MM5 after Box et al. (2006).

Table 5.1. 2008 Summer 700-hPa temperature and winter precipitation anomalies (relative to 1948–2008 NCEP reanalysis means) for glaciated regions of the Arctic (excluding Greenland). Inferred sign of surface mass balance is based on comparison of historical mass balance records for each region with NCEP reanalysis temperature and precipitation anomalies. Anomalies in melt duration and the timing of melt onset and freeze-up (relative to 2000–04 climatology) derived from QuikSCAT data. For timing, negative anomalies indicate an earlier-than-normal date.

Region	Sub-region	Latitude (°N)	Longitude (°E)	JJA 700-hPa T Anomaly	2008 Rank	Sep–May Ppt Anomaly	2008 Rank	Inferred Surface Balance	Melt Onset Anomaly	Freeze-up Anomaly	Melt Duration Anomaly
				(°C)	(*N* = 60)	(mm)	(*N* = 60)		days	days	days
Arctic Canda	North Ellesmere Island	80.6–83.1	267.7–294.1	2	4	12.3	10	−−	−1.8	9.8	19.3
	Axel Heiberg Island	78.4–80.6	265.5–271.5	1.67	5	0	30	−−	−2.9	11.4	17.6
	Agassiz Ice Cap	79.2–81.1	278.9–290.4	2.11	3	−9.2	44	−−	5.4	24.0	22.5
	Prince of Wales Icefield	77.3–79.1	278–284.9	1.77	7	−11.4	42	−−	2.1	7.8	10.2
	Sydkap	76.5–77.1	20.7–275.8	1.53	6	−58.5	59	−−	3.0	3.8	1.4
	Manson Icefield	76.2–77.2	278.7–282.1	1.71	7	−62.5	56	−−	6.4	5.7	0.0
	Devon Ice Cap	74.5–75.8	273.4–280.3	1.47	6	−8	33	−−	0.8	−0.8	5.8
	North Baffin	68–74	278–295	1.97	2	12.4	17	−−	−26.9	−14.4	4.9
	South Baffin	65–68	290–300	2.39	1	5.9	25	−−	−2.8	−1.6	−1.1
Eurasian Arctic	Severnaya Zemlya	76.25–81.25	88.75–111.25	−0.36	41	38.9	17	+	−0.2	13.4	10.6
	Novaya Zemlya	68.75–78.75	48.75–71.25	0.29	24	78	6	+	21.5	−5.3	−4.2
	Franz Josef Land	80–83	45–65	−0.77	46	110	3	++	8.4	−2.4	6.1
	Svalbard	76.25–81.25	8.75–31.25	0.13	31	58.5	7	+	−6.6	−2.8	−0.8
Iceland		63–66	338–346	0.13	27	−29.3	46	−	−4.2	−14.4	6.5
Alaska	SW Alaska	60–65	210–220	−0.33	40	117.4	14	+	3.5	−15.6	−17.7
	SE Alaska	55–60	220–230	−0.91	50	237	5	++	*	*	*

3) Upper-air temperatures

Upper-air sounding data available from the Integrated Global Radiosonde Archive (Durre et al. 2006) indicate a continued pattern of lower tropospheric warming and lower stratospheric cooling 1964-onward (Box and Cohen 2006). Lower tropo-

spheric warm anomalies in all seasons, particularly in spring along western Greenland, were accompanied by relatively small midtropospheric cool anomalies. Winter tropopause temperatures (200 hPa) were above normal. Lower stratospheric (above 100 hPa) temperatures were lower than normal.

4) Surface melt extent and duration

Passive (SMMR and SSM/I, 1979–2008) and active (QuikSCAT, 2000–08) microwave remote sensing (Bhattacharya et al. 2009, submitted to *Geophys. Res. Lett.*; Liu et al. 2005) indicate abnormally high melt duration over the north and northeast ice sheet and along the east and west coasts above Greenland's most productive three outlet glaciers in terms of ice discharge into the sea: Kangerlussuaq; Helheim; and Jakobshavn (Fig. 5.18). Lower-than-normal melt duration is evident over much of the upper elevations of the ice sheet. New records of the number of melting days were observed over the northern ice sheet, where melting lasted up to 18 days longer than previous maximum values. Anomalies near the west coast are characterized by melting up to 5–10 days longer than the average (Tedesco et al. 2008).

The average daily melt extent, after Mote and Anderson (1995) and Mote (2007), for 2008 was 424,000 km^2, about 2.4% greater than the 1989–2008 average of 414,000 km^2, representing the lowest average melt extent since 2001. Significantly more melt occurred in 2008 in the northeast (45.6% greater than the 1989–2008 average) and northwest (29.7%), but less occurred in the two east-central regions (–16.8% and –25.4%) and in the southeast (–21.1%). Melt extent in 2008 was also above the 1979–2007 average. The trend in the total area of melt during 1979–2008 is approximately +15,900 km^2 yr^{-1} and is significant at the 95% confidence interval ($p < 0.01$).

5) Precipitation anomalies

Annual PT anomalies in 2008, determined using Polar MM5 data assimilation modeling (Bromwich et al. 2001; Cassano et al. 2001; Box et al. 2006), were positive (negative) up to 750 mm (–250 mm) over the eastern (western) ice sheet, respectively. More PT than normal occurred in isolated areas in extreme southeast, east, north, and northwestern Greenland. The overall anomaly indicated approximately 41 Gt more PT than normal for the 1971–2000 standard normal period.

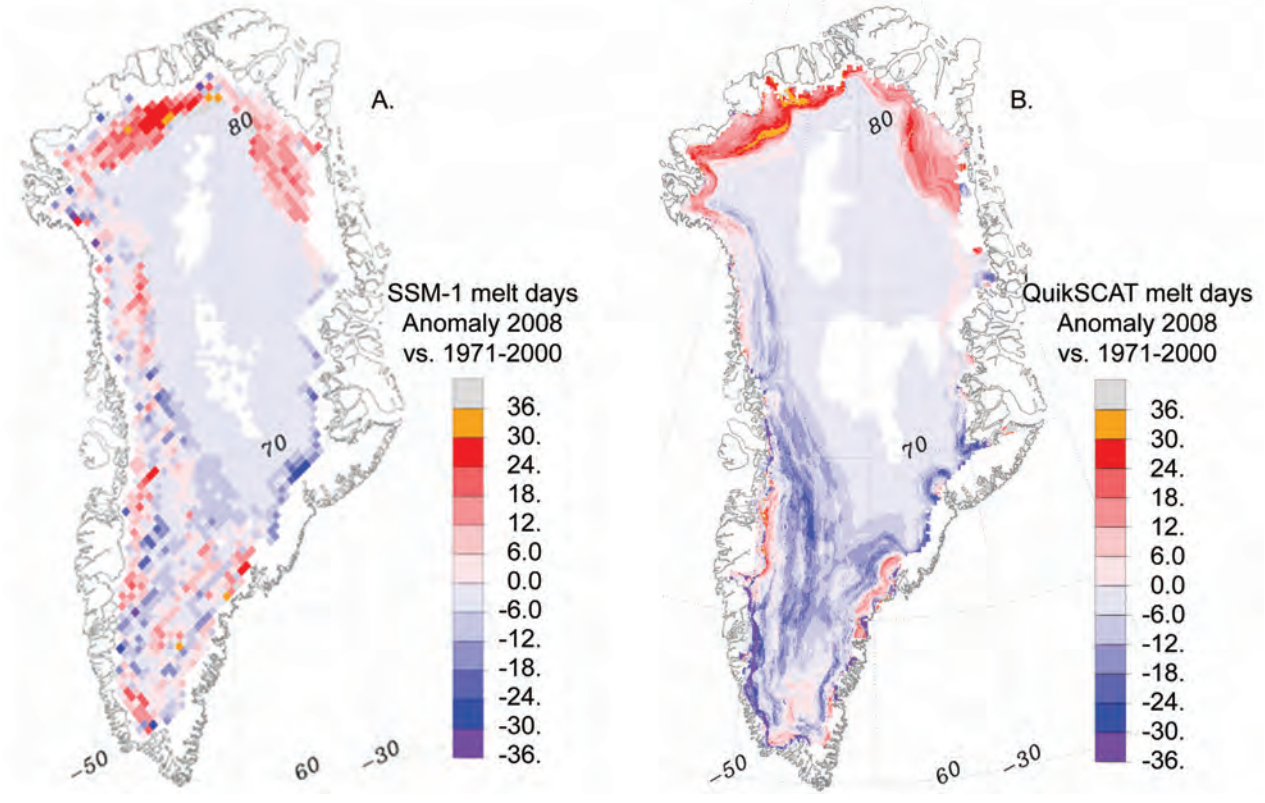

Fig. 5.18. 2008 Greenland ice sheet surface melt duration anomalies relative to the 1989–2008 base period based on (a) SSM/I and (b) QuikSCAT (2000–08 base period), after Bhattacharya et al. (2009, submitted to *Geophys. Res. Lett.*).

Table 5.2. Greenland ice sheet surface mass balance parameters: 2008 departures from 1971–2000 average (adapted from Box et al. 2006). Estimates by Hanna et al. (2008) are included for comparison.

	Box			Hanna		
	Mean (1971–2000)	% of normal	2008 Anomaly (Gt)	Mean (1971–2000)	% of normal	2008 Anomaly (Gt)
Total Precipitation	710.7	105%	38.5	624.16	108%	52
Liquid Precipitation	16.8	142%	7.1	27.01	147%	13
Surface Water Vapor Flux	66.7	100%	−0.2	40.59	74%	−11
Blowing Snow Sumblimation	39.6	99%	−0.3			
Snow Accumulation	604.5	106%	39.0	556.56	109%	50
Meltwater Volume	330.1	159%	194.1	333.95	133%	110
Meltwater Runoff	214.9	186%	184.3	277.91	142%	116
Surface Mass Balance	389.6	63%	−145.3	305.66	83%	−53
Mean T	−19.0		0.9	−21.4		1.1
AAR	0.920	0.905%	−0.087	0.859	0.933%	−0.007

6) Surface albedo

Melt season (day 92–274) surface albedo anomalies, derived using the Liang et al. (2005) algorithm applied to daily cloud-free MODIS imagery, indicate a lower surface albedo around the ablation zone (except the east ice sheet) (Fig. 5.19) resulting from the combined effect of the positive summer surface melt intensity anomaly and, in most areas, less winter snow coverage. A positive albedo anomaly is evident for the ice sheet accumulation zone and is consistent with above-average solid precipitation and/or less-than-normal melting/snow grain metamorphism.

7) Surface mass balance

Polar MM5 climate data assimilation model runs spanning 51 years (1958–2008), calibrated by independent in situ ice-core observations (Bales et al. 2001; Mosley-Thompson et al. 2001; Hanna et al. 2006) and ablation stakes (van de Wal et al. 2006), indicate that 2008 total precipitation and net snow accumulation was slightly (6%–8%) above normal (Table 5.2). In accordance with a +0.9°C 2008 annual mean surface temperature anomaly, the fraction of precipitation that fell as rain instead of snow, surface meltwater production, and meltwater runoff were 142%–186% of the 1971–2000 mean. Consequently, and despite 6%–9% (39–50 Gt) more snow accumulation than normal, the surface net mass balance was substantially (145 Gt) below normal. 2008 surface mass balance ranked ninth-least positive out of 51 years (1958–2008).

Surface mass balance anomalies indicate a pattern of increased marginal melting with noteworthy departures in excess of 1-m water equivalence per year from normal across the northern ice sheet (Fig. 5.20). The pattern of steepening mass balance profile is consistent with observations from satellite altimetry (Zwally et al. 2005) and airborne altimetry (Krabill et al. 2000); satellite gravity retrievals (e.g., Luthcke et al. 2006); and climate projections (Solomon et al. 2007).

8) Floating glacier ice changes

Daily surveys of Greenland ice sheet marine terminating outlet glaciers from cloud-free MODIS imagery (http://bprc.osu.edu/MODIS/) indicate that the 32 widest glaciers collectively lost 184.1 km^2 of mostly floating ice between the end of summer 2007 and the end of summer 2008. The 2008 area loss was 3 times that of the previous summer (2006–07 area

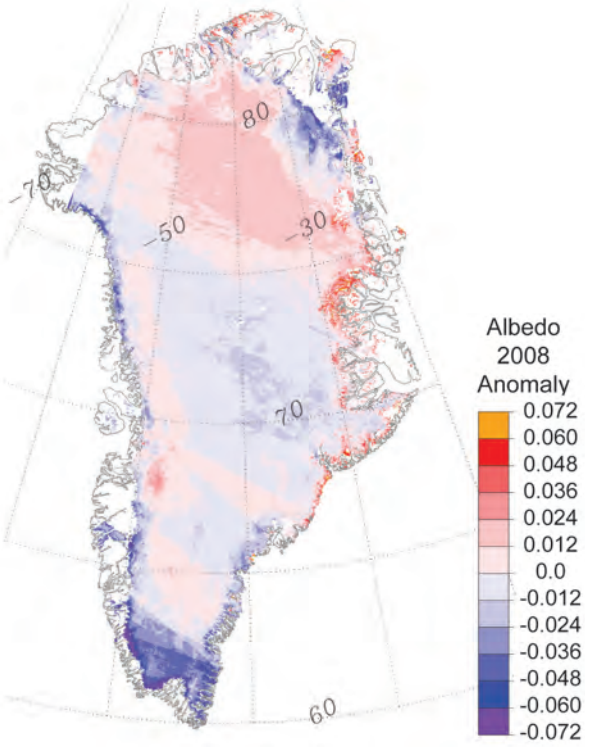

Fig. 5.19. Surface albedo anomaly Jun–Jul 2008 relative to a Jun–Jul 2000–08 base period.

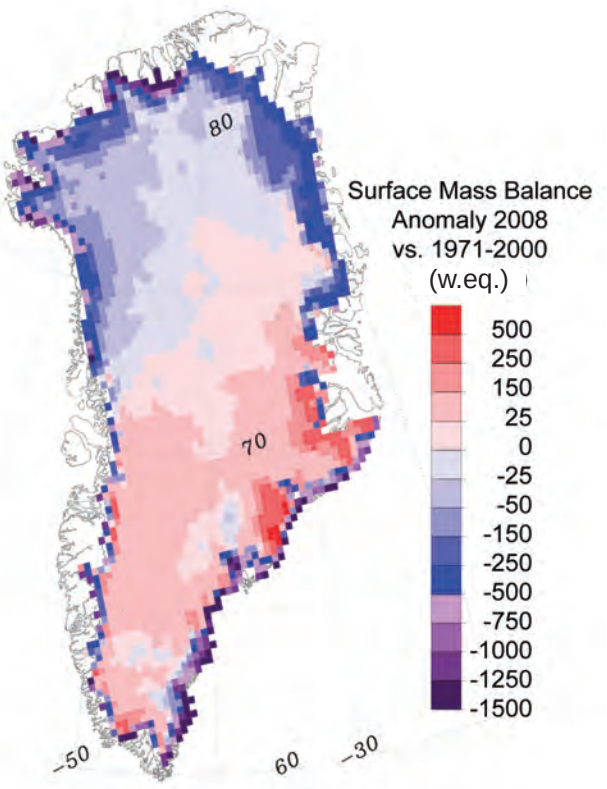

Fig. 5.20. 2008 surface mass balance anomalies with respect to the 1971–2000 base period, simulated by Polar MM5 after Box et al. (2006).

change was −60.8 km^2) and 1.7 times greater than the 8-yr trend, beginning in 2000 when MODIS data became available. In 2008, 18 of the 32 glaciers retreated relative to their end-of-summer 2007 position. The total net effective length change of these glaciers was −9.1 km. These losses marked a continuation of a deglaciation trend of −106.4 km^2 yr^{-1} area change (R = −0.98) since 2000. In other words, between 2007 and 2008, glaciers around Greenland lost an area more than 2 times the size of Manhattan Island, New York. The cumulative area change from end-of-summer 2000 to 2008 is −920.5 km^2, an area loss equivalent to 10 times the area of Manhattan Island.

6. ANTARCTICA

a. Overview—R. L. Fogt and T. A. Scambos

In comparison to other regions of the globe, detailing Antarctic climate variability is not an easy task, mainly due to the quantity and quality of available data. Atmospheric reanalysis datasets, which fill in large spatial data voids across Antarctica, are strongly dependent on satellite data (Bromwich et al. 2007), thereby effectively limiting large-scale climate analysis in the high southern latitudes to post-1979. In light of this comparatively short record, several interesting Antarctic climate anomalies during 2008 are described in this section.

Overall, the year was dominated by a positive phase of the Southern Hemisphere Annular Mode. There was strong warming along the Antarctic Peninsula and West Antarctica in 2008, most marked in September and December, and also pockets of warming along coastal East Antarctica. Moderate La Niña events occurred during the austral summers of 2007–08 and 2008–09, and the simultaneous occurrence of these events with positive SAM phases amplified the regional response in West Antarctica and the Antarctic Peninsula region (e.g., Fogt and Bromwich 2006). This is particularly noted in changes in sea-ice concentration in the Amundsen/Bellingshausen Seas, which continued to show decline in 2008, in concert with and possibly contributing to the warming of the region. Precipitation anomalies were also above normal along portions of the Antarctic Peninsula in austral spring due to the SAM/La Niña influence. The positive phase of the SAM led to record-high total Antarctic sea-ice extent for much of early 2008 through enhanced equatorward Ekman transport. With colder continental temperatures at this time, the 2007–08 austral summer snowmelt season was dramatically weakened, making it the second-shortest melt season since 1978 when the record began. The lower stratosphere was anomalously cold throughout the polar night, with the 2008 ozone hole being the sixth worst on record and unusually persistent.

Another significant event during 2008 was the disintegration and retreat of the Wilkins Ice Shelf in the southwest peninsula area (Fig. 6.1). Three breakup events took place: one near the end of the summer melt season (29 February to 6 March, Fig. 6.1a) and two more in the 2008 autumn and winter (27–31 May, Fig. 6.1b; 28 June to mid-July, Fig. 6.1c). The shelf lost 431 km^2 in the first event and 160 km^2 in the second, and it saw calving and rifting of nearly 6,000 km^2 in the winter event (out of a total area of 13,680 km^2 just prior to the breakups; Fig. 6.1). Analysis of the breakups and the evolution of the Wilkins Ice Shelf leading up to these events suggested either that melt- and brine-layer-driven enhancement of fracturing led to the retreats or that basal melting from warmer near-surface and sub-shelf ocean layers caused weakening of the ice plate (Scambos et al. 2009; Padman et al. 2009; Braun et al. 2008). A further suspected contributing factor is ocean wave action. The extended period of ice-free conditions near the Wilkins Ice Shelf for much of the first half of the year exposed the shelf front directly to the open ocean swell. All of these models and hypotheses point to the glaciological consequences of the continuing climate warming and sea-ice decline in the peninsula region.

There were also recent advances in Antarctic climate science during 2008, most notably in prominent papers in *Nature Geoscience* by Gillett et al. (2008) and in *Nature* by Steig et al. (2009). Gillett et al. (2008) analyze fully coupled climate model simulations and demonstrate that human activity has contributed

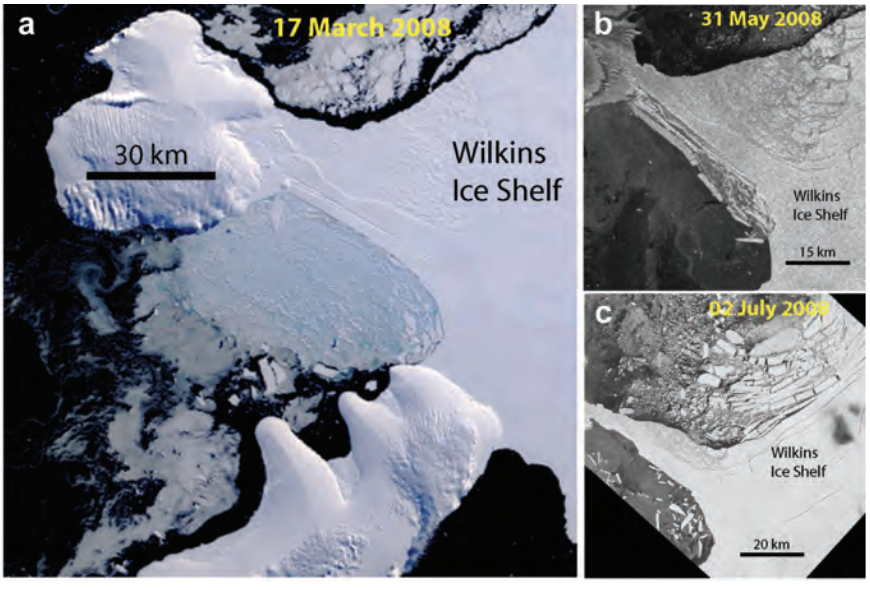

Fig. 6.1. Wilkins Ice Shelf breakup events of 2008. (a) MODIS band 1 image 10 days after the end of the first event; (b) *Envisat* ASAR image during the second event; (c) *Envisat* ASAR image during the third event. (*Envisat* ASAR images © European Space Agency.)

to the warming not only in the Arctic but also in the Antarctic. Steig et al. (2009) demonstrate that significant warming since the IGY (1957–58)—previously thought confined to the Antarctic Peninsula—is much broader in spatial extent, expanding to include West Antarctica. Additionally, a synthesis report (Mayewski et al. 2009) of the relevant mechanisms and long-term changes in the full Antarctic climate system also appeared recently. Such manuscripts help to place contemporaneous Antarctic climate variations described herein in the context of global climate change. However, the large interannual variability in the southern high latitudes complicates this matter by making trend detection difficult. Therefore, the record seasonal highs in Antarctic sea-ice extent in early and late 2008, for example, are not evidence against global change, because conclusions about long-term trends in Southern Hemisphere sea-ice extent cannot be drawn from monthly seasonal observations taken out of spatial and temporal contexts.

b. Atmospheric circulation—R. L. Fogt and S. Barreira

The large-scale Antarctic circulation anomalies during 2008 based on NCEP–NCAR reanalyses are highlighted through a zonal mean perspective, covering both the troposphere and stratosphere (Fig. 6.2), and spatially at the Antarctic surface (Fig. 6.3). During the beginning of the year (January–March), low geopotential height anomalies over high latitudes and strong zonal wind anomalies at midlatitudes throughout the troposphere and stratosphere were observed, indicative of the positive SAM phase. The lower-than-average surface pressures in the Antarctic circumpolar trough in this period (Fig. 6.3a) resulted from an increase in individual cyclonic activity, while the strengthened circumpolar westerly wind anomalies (Fig. 6.2c) aided in isolating the Antarctic continent from the warmer midlatitudes, generating the colder temperatures over most of coastal Antarctica (Fig. 6.3b). In many places, these temperature anomalies were more than two standard deviations below the January–March mean. During April–May, high pressure anomalies over Antarctica as well as throughout much of the Pacific Ocean, in conjunction with predominantly negative anomalies in the midlatitudes of the Eastern Hemisphere, generated only a weakly negative SAM index (Fig. 6.3c). The overall weaker circumpolar westerly winds (Fig. 6.2c) at this time allowed for more intrusions of warmer air from the north, leading to low-level warm temperature anomalies across much of the Antarctic continent, especially over East Antarctica (Figs. 6.2b, 6.3d). The pressure anomaly in the Amundesn/Bellingshausen Seas in Fig. 6.3c indicates that many low-pressure systems formed in this region; however, due to the presence of a strong high-pressure anomaly in the Pacific, they were impeded from traveling north toward South America.

A strong positive SAM anomaly occurred in June [3.00 on the Marshall (2003) index, the second-highest Jun positive SAM anomaly since 1957; www.antarctica.ac.uk/met/gjma/sam.html], with corresponding strong circumpolar winds (Fig. 6.2c). Throughout the remaining winter season, however,

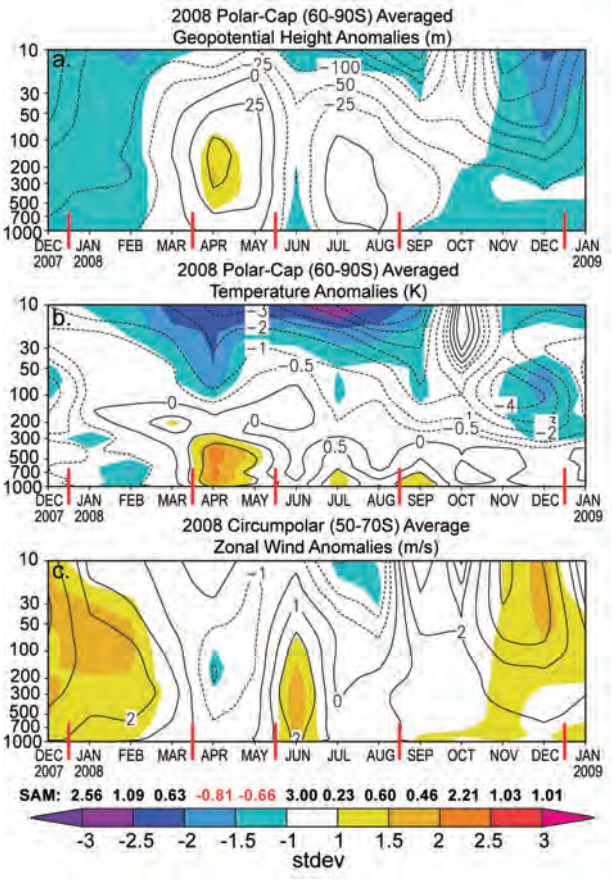

Fig. 6.2. Zonally averaged climate parameter anomalies for the southern polar region in 2008 relative to the 1979–2007 period. (a) Polar cap averaged geopotential height anomalies (m); (b) averaged temperature anomalies (K); (c) averaged wind anomalies (m s^{-1}). Absolute anomaly values are contoured, and the panels are shaded according to how many std devs the anomalies are from the 1979–2007 mean (color bar at bottom for scale). Red vertical bars indicate the four separate periods shown as spatial climate anomalies for 2007 in Fig. 6.3. Primary contour interval is 50 m in (a), 1 K in (b), and 2 m s^{-1} in (c), with additional contours at ±25m, ±0.5K, ±1 m s^{-1} in (a), (b), and (c), respectively. Values for the SAM index (www.antarctica.ac.uk/met/gjma/sam.html) are shown along the bottom in black and red. Data are from the NCEP–NCAR reanalysis.

the tropospheric circulation anomalies were relatively weak, although the pressure anomalies continued to indicate the positive phase of the SAM (Fig. 6.3e). At the end of the year (September–December), the positive SAM began to increase at the same time a La Niña began to develop in the tropics, peaking in December 2008. The simultaneous occurrence of positive SAM and La Niña was characterized by anomalously low geopotential height throughout the atmosphere and strong circumpolar zonal flow (Fig. 6.2), similar to the anomalies in December of 2007. At the surface, the low pressure anomalies (>2 std devs from the mean) were most marked in the Amundsen/Bellingshausen Seas, the region strongly influenced by both SAM and ENSO (Fig. 6.3g). The altered circulation brought stronger northwesterly flow to the Antarctic Peninsula and portions of West Antarctica, leading to the marked warming there (Fig. 6.3h), also more than two standard deviations above the late-year mean. In addition, the strong negative pressure anomalies in the South Pacific enhanced the off-continent flow in the eastern Ross Sea, leading to much cooler-than-normal conditions farther over the South Pacific Ocean. The strong ridge in the subtropical Atlantic deterred the low-pressure systems forming in the Amundesn/Bellingshausen Seas away from southern South America, leading to very dry conditions there at the end of 2008.

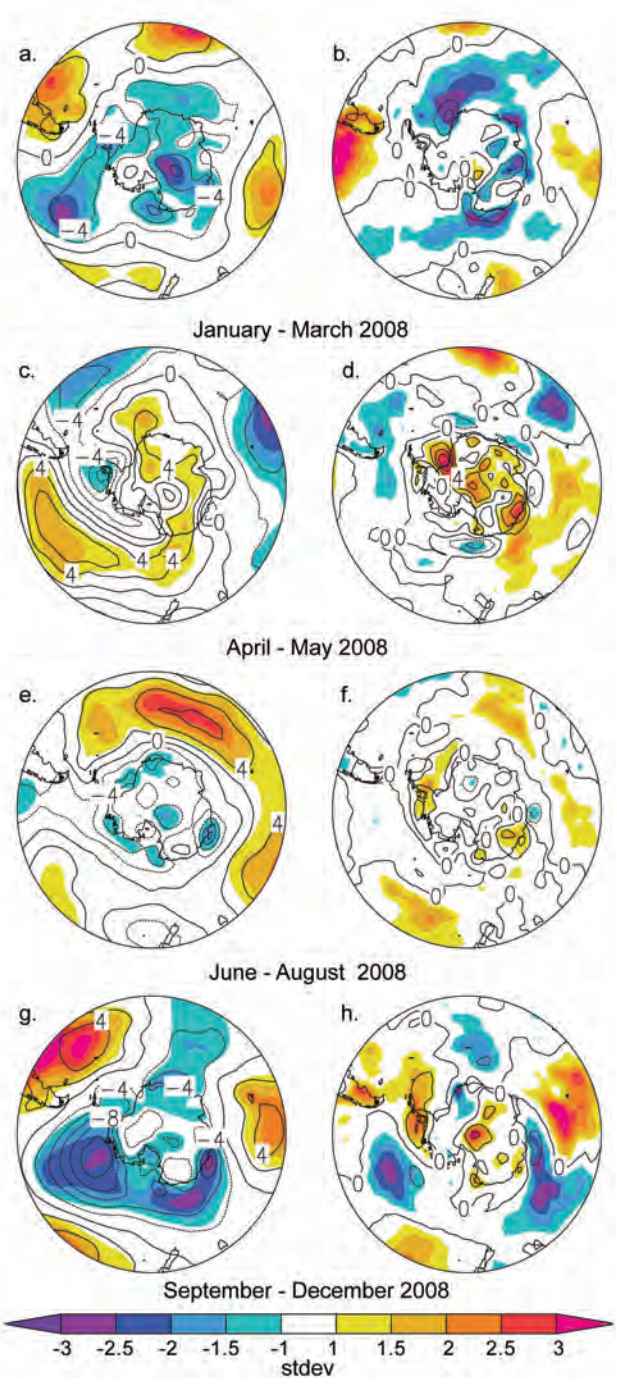

Fig. 6.3. (left) Surface pressure anomalies and (right) surface temperature anomaly contours relative to 1979–2007 climatology for four distinct periods. The shaded regions correspond to the number of std devs the anomalies are from the 1979–2007 mean, as in Fig. 6.2. Data are from the NCEP–NCAR reanalysis.

The Antarctic upper stratosphere (above 50 hPa) remained anomalously cold during the polar night, from March to September (Fig. 6.2), which allowed for high levels of polar stratospheric cloud formation (especially during the autumn). During the early and late portions of 2008, there is strong evidence that the stratosphere and troposphere were dynamically coupled during the positive phase of the SAM, as both low geopotential height and positive circumpolar wind anomalies extend up to 10 hPa.

c. *Surface station observations*—S. Colwell and J. Turner

Figure 6.4 highlights the temperature, MSLP, and wind speed anomalies at six representative Antarctic stations in 2008. Rothera (67.5°S, 68.1°W) and Marambio Base (64°S, 56°W) are situated along the west and east sides of the Antarctic Peninsula, respectively; Halley V Station (75°S, 26°W) lies in the Weddell Sea region of West Antarctica; Davis (68.6°S, 78.0°E) and Dumont d'Urville (66.7°S, 140.0°E) are in coastal East Antarctica; and McMurdo Station (77°S, 166°E) lies more inland near the junction of the Ross Ice Shelf/Ross Sea. All-time record anomalies are highlighted with plus signs in Fig. 6.4, while asterisks mark the second-highest anomaly. Station records extend back until at least the 1970s, although most extend to 1956–57 (see caption for details).

In January, record cold was observed at Halley, and at McMurdo the MSLP was the second lowest. At Dumont d'Urville a mean monthly minimum tem-

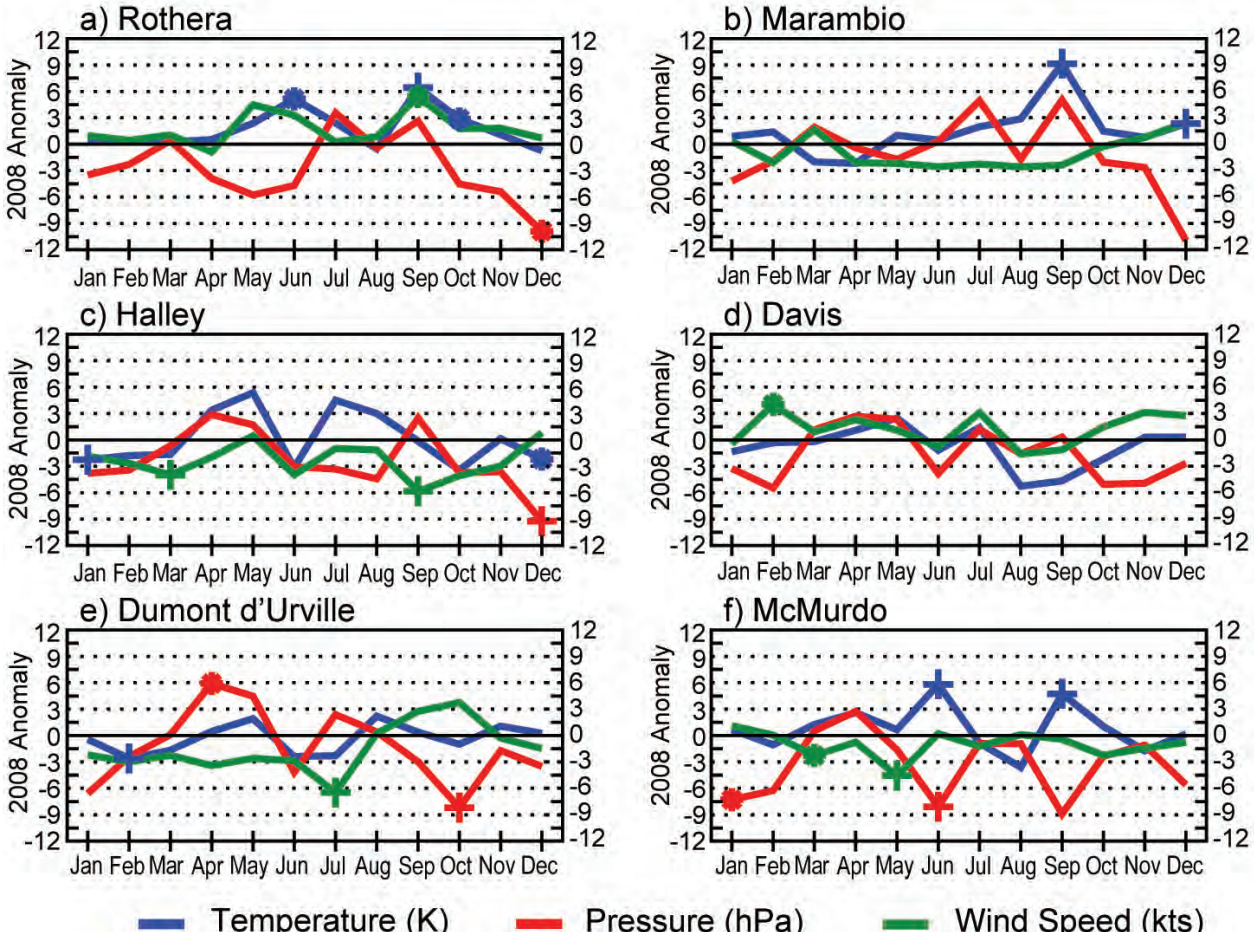

Fig. 6.4. 2008 Antarctic station anomalies. Monthly mean anomalies for temperature (K), MSLP (hPa), and wind speed (m s^{-1}) are shown for six representative stations. Plus signs denote all-time record anomalies, while asterisks denote the second-highest record anomaly for each station. Climatological station data starts in 1976 for Rothera; 1970 for Marambio (1983 for Marambio wind speeds); and 1956–57 for the other stations. The base period for calculating the anomalies was 1979–2007 for all but Rothera, where the base period was 1976–2007.

perature of −6.7°C was recorded in February, 0.8°C colder than any previous February value. Although winds were anomalously weak at Halley in March and at McMurdo from March through May, the only other notable anomaly in March–May across all stations was the second-highest pressure at Dumont d'Urville in May. During the June SAM maxima, MSLP was at a record low at McMurdo, confirmed in the more complete Scott Base record (which is within a few kilometers). At the same time, temperatures there were at a record high, opposite of the pronounced cooling expected in interior Antarctica during positive SAM phases (Marshall 2007). However, Rothera observed the second-warmest June, consistent with the impact of the positive SAM.

There were many record anomalies from August through October. In September the temperature at Rothera was 1.8°C above the previous highest September value and more than 6°C above normal (Fig. 6.4a). At Marambio the mean temperature was 2.3°C above the previous highest September mean and 9°C above normal (Fig. 6.4b); anomalously warm conditions were also observed at McMurdo in September (Fig. 6.4f). At Davis in East Antarctica the temperatures were colder than average (but not a record) in August, September, and October (Fig. 6.4d).

There is also some reflection of the positive SAM in December. Rothera observed the second-lowest pressure anomaly in December since the record began in 1976. At Marambio, the December temperature was the warmest on record, while December temperatures were the second coldest at Halley and pressures were the record lowest.

d. Surface mass balance—D. H. Bromwich, S.-H. Wang, and A. J. Monaghan

Precipitation-minus-evaporation (P–E) closely approximates the surface mass balance over most of Antarctica, with precipitation being the dominant term at regional and larger scales, especially near the coast (e.g., Bromwich et al. 2004; van den Broeke et al. 2006). Precipitation and evaporation fields from the JRA (Onogi et al. 2005) and NCEP–DOE Reanalysis II (NCEP2; Kanamitsu et al. 2002) were examined to assess Antarctic snow accumulation for 2008. The evaporation in JRA was calculated from the surface latent heat flux. Both JRA and NCEP2 (not shown) give similar findings. The mass balance is summarized by the annual mean and spring (SON) P–E anomalies (Fig. 6.5; anomalies are calculated from the 1980–2007 average), as the spring season dominates the annual mean, especially over the Antarctic Peninsula.

In general, the annual anomalies (Fig. 6.5a) over the high interior of the continent are small and negative. However, most coastal regions have positive anomalies, especially the Antarctic Peninsula (~400 mm) and near Casey (~700 mm) at 110° E. The annual P–E anomalies are consistent with the mean atmospheric circulation dominated by the SON MSLP anomalies (Fig. 6.3g): two strong negative pressure anomaly centers (~105° W and ~120° E) produced higher-than-normal precipitation in these regions. Negative P–E anomalies are observed over the Amundsen Sea and the Antarctic coast between 140° E and 180°. Both are linked to the secondary negative anomaly of MSLP near 180° longitude.

Over the Antarctic Peninsula the SON anomalies (~175 mm) contribute nearly 50% of annual P–E anomalies. The strong negative MSLP anomaly pattern over the Amundsen Sea (Fig. 6.3g, <2.5 std devs from the mean) indicates greater-than-normal storm activity during the 2008 SON season that results in the large P–E anomaly. As noted in section 6b, the enhanced SON storm activity is consistent with strong positive anomalies of both the SAM and La Niña during austral spring 2008.

e. Seasonal melt extent and duration—L. Wang and H. Liu

The extent, onset date, end date, and duration of snowmelt on the Antarctic ice sheet during 2007–08 summer was derived using a wavelet-transform-based edge detection method (Liu et al. 2005). The 19-GHz horizontal polarization channel of SSM/I data are utilized for the melt information extraction. Figure 6.6 shows the melt extent and duration during the austral

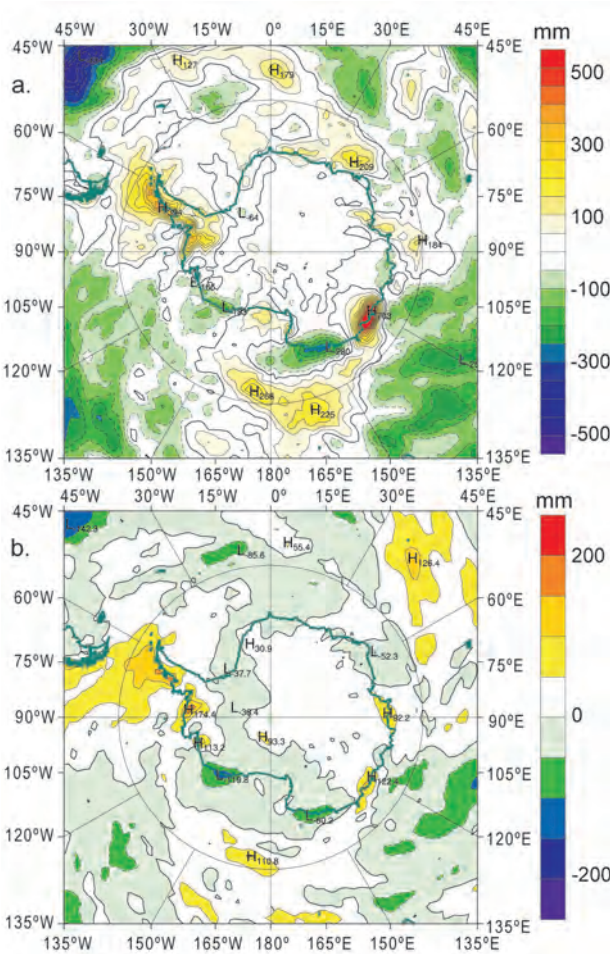

Fig. 6.5. JRA 2008 anomalies of P−E (in mm) from the 1980–2007 average: (a) annual and (b) spring (SON).

summer 2007–08. The total melt extent, including all areas with at least one day of surface melting, is 800,000 km^2, covering only 5.8% of the continent (Figs. 6.6a–c). The melt index (sum of total melt extent for each day in the melt season) during 2007–08 is 24,353,750 day km^2. The melt extent during 2007–08 is significantly smaller than the average melt extent (1.277 million km^2) of the past 25 years, or 9.34% of the continent's area (Liu et al. 2006). This places the austral summer of 2007–08 as the second lowest since 1978 in terms of both melt extent and melt index, behind only the 1999–2000 melt season. Also, it should be noted that a decreasing trend in melt extent and melt index is apparent for the past six years.

Surface melt during 2007–08 primarily occurred on the Antarctic Peninsula, Abbot Ice Shelf, West Ice Shelf, and Shackleton Ice Shelf (see Fig. 6.6 for locations). Surface melt events primarily took place in December and January (Figs. 6.6a,b,d), and the maximum one-day melt extent occurred on 21 December. All the regions in Antarctica have a considerably

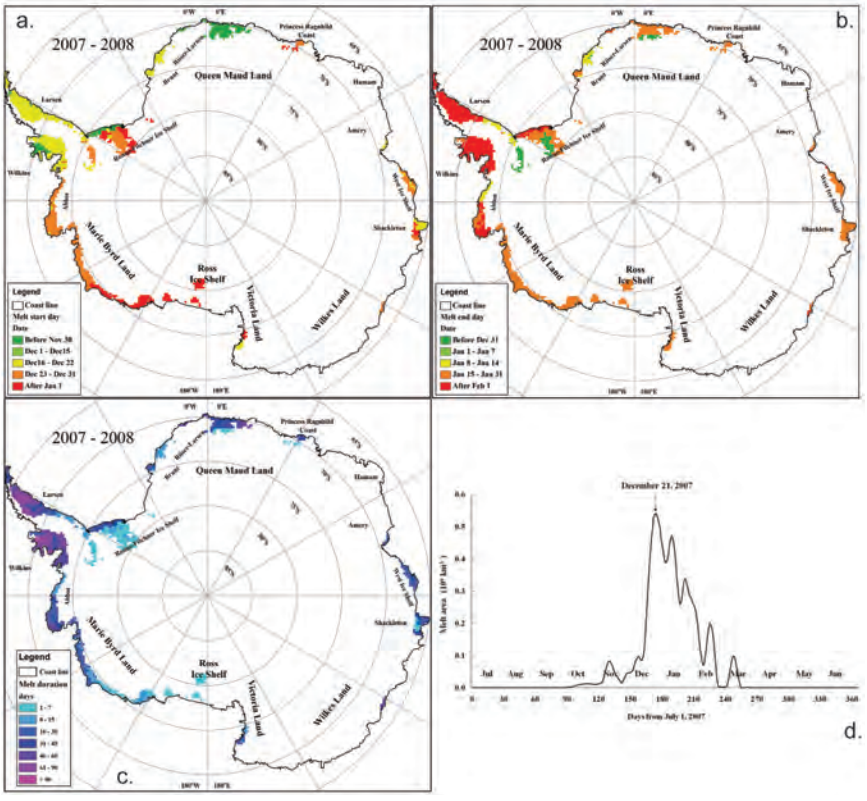

Fig. 6.6. Surface snow (a) onset date, (b) end date, (c) duration in days, and (d) melt area, for the austral 2007–08 melt season.

lower melt extent than the average of the past 25 years, which is consistent with weak surface cold temperature anomalies in December 2007 (Fig. 6.2) and January 2008 (Fig. 6.4). The Amery Ice Shelf, Queen Maud Land, Wilkes Land, and Ross Ice Shelf have an extremely low melt extent and melt intensity, which is likely associated with the strong positive sea-ice extent anomalies in these regions and the influence of the strong positive SAM and 2007–08 La Niña event.

f. Sea-ice extent and concentration—R. A. Massom, P. Reid, S. Stammerjohn, and S. Barreira

2008 was a year of exceptional seasonal variability in Antarctic sea-ice coverage, characterized by three distinct phases of overall sea-ice extent anomalies: i) well above average (January–April inclusive and December), ii) moderately above average (May–June), and iii) average to slightly below average (July–November), but with substantial regional variability that reflects patterns of atmospheric circulation.

The analysis is based on monthly mean Nimbus-7 SMMR (1979–87) and DMSP SSM/I (1987–present) sea-ice concentration data from the NSIDC Sea Ice Index project (Fetterer et al. 2008). Note that 2008 data are processed from a combination of NSIDC's preliminary (Meier et al. 2006) and NRTSI data that have lower quality control, but they must be used because the quality-controlled data are unavailable at the time of writing. According to Fetterer et al. (2008), however, this effect is likely to be of the order of less than 10,000 km^2.

Monthly ice extent and concentration anomalies for 2008 display a distinct zonal asymmetry (Figs. 6.7a–d), largely in response to the location and intensity of climatological low and high pressure centers described in the atmospheric circulation section. The January–April period was characterized by the persistence of anomalously high sea-ice concentrations in the Weddell Sea and almost the entire zone from the Indian Ocean through the western Pacific Ocean and western Ross Sea sectors (from ~40°E eastward to ~160°W; Figs. 6.7a,b), resulting in record and near-record zonally averaged monthly ice extents during January–April. With an ice extent anomaly of 3.4 std devs (+33% or 1.7×10^6 km^2) above the long-term (1979–2000) mean of 5.1×10^6 km^2, January 2008 continued from December 2007 as being a record high for that month (Fig. 6.7e), that is, ~11% greater than the previous record high for January (in 1996). Major positive anomalies of +28% occurred in both February and March (3.31 and 3.16 std devs above the mean, respectively) and +18% in April (2.27 std devs above the mean). Record monthly high values were also recorded in March and April: the March 2008 anomaly exceeded the previous record (in 2001) by about 10%, and April was about 5% greater than the previous highs in 1979 and 1982 (Fig. 6.7f). February 2008 saw the second-highest monthly sea-ice extent on record. The persistence of unusually compact sea ice in many regions into the summer melt period led to difficulties in ship navigation during the critical shipping (base resupply) and tourist season of early 2008 (especially in accessing the Ross Sea). More

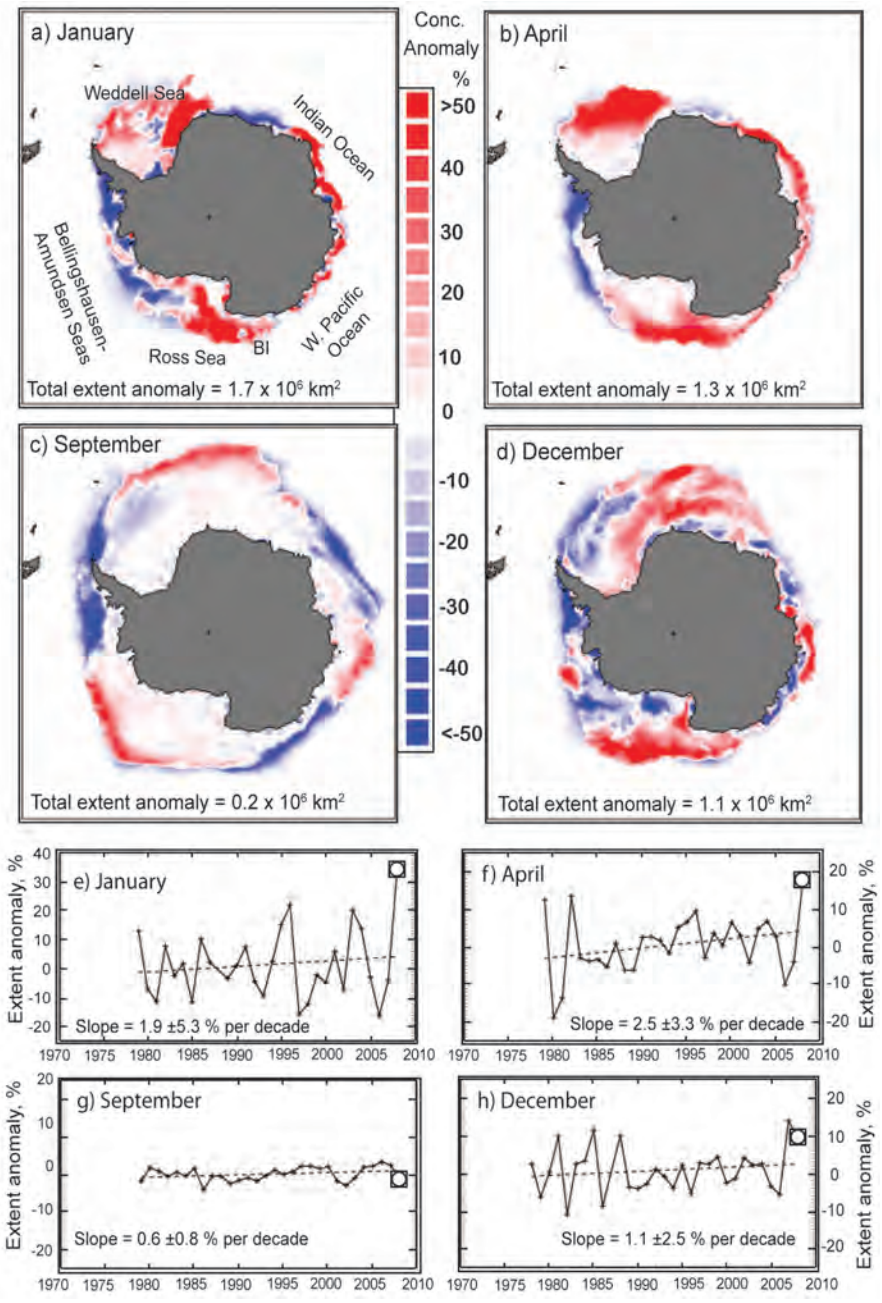

Fig. 6.7. Antarctic sea-ice extent and concentration anomalies for (a) Jan, (b) Apr, (c) Sep, and (d) Dec, and coincident trends in (e–h) sea-ice extent, all for 2008. The bold black line represents the long-term monthly mean sea ice extent (1979–2000) for that particular month, while the dashed black line is the monthly mean for the month in 2008 (both equivalent to the 15% ice concentration isoline). The ice concentration anomaly is computed from the monthly mean ice concentration relative to the long-term mean (1979–2000) for that particular month. The ice concentration anomaly is only calculated for the area covered by sea ice for the month (in 2008) in question. BI is Balleny Islands.

extensive sea ice also occurred in the May–June period (late autumn to early winter), but at lower levels compared to the previous four months.

In contrast, sea-ice extent was generally close to (i.e., within ±2%) the long-term mean for July through November, although it was again characterized by marked regional variability. Negative anomalies in the Amundsen/Bellingshausen and northwest Weddell Seas, the Indian, and west Pacific Ocean sectors were compensated for by positive anomalies in the northeast Weddell and Ross Sea sectors. The sea-ice extent during December, 12.2×10^6 km^2, was well above the long-term average of 11.1×10^6 km^2.

A major feature throughout the year is anomalously low sea-ice extent for every month in the Bellingshausen/Amundsen Seas (west Antarctic Peninsula) sector. This represents a continuation in the long-term trend in this region (Stammerjohn et al. 2008). The juxtaposition of this major sea-ice "indentation" to strong positive (ice growth) anomalies in the adjacent Ross Sea sector is largely due to the dominant impact of surface winds associated with a persistent deep low pressure system centered on approximately 240°E, 68°S (the "Amundsen Sea Low"; Fig. 6.3g). This leads to sustained west-northwesterly airflow across the west Antarctic Peninsula sector to hold back autumnal ice-edge advance and accelerate the spring retreat, causing dynamic sea-ice compaction against the coast and islands (Massom et al. 2008). It is most strongly seen in 2008 during October and November. By the same token, the more southerly outflow of cold air from continental Antarctica along the western flank of this system

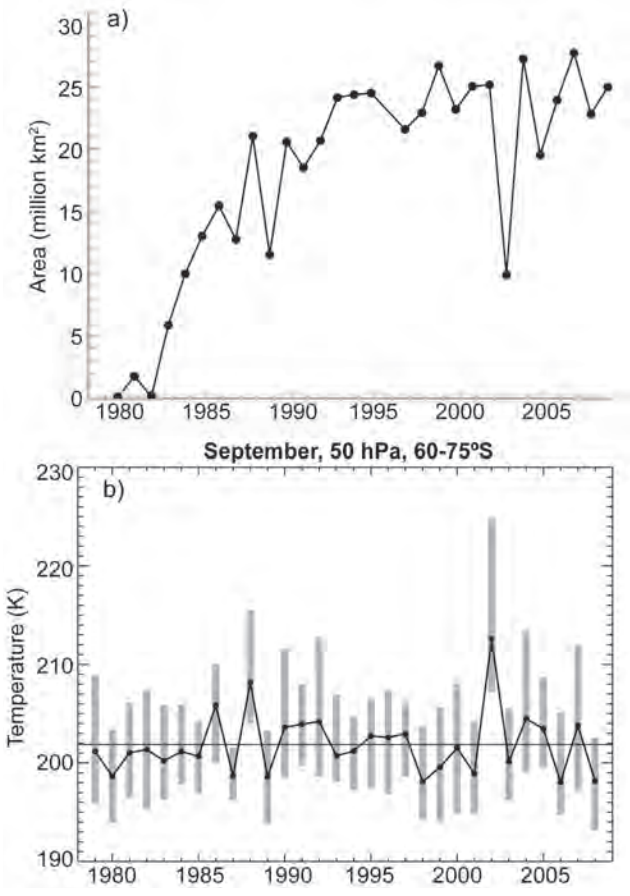

Fig. 6.8. (a) Ozone hole area, 1979–2008. The area is calculated by first calculating the area enclosed by the 220 DU value over the Southern Hemisphere for each day from 21 to 30 Sep, and then averaging these 10 days. The area of the North American continent is indicated by the horizontal bar (24.71 million km^2). (b) Temperature at 50 hPa from 60° to 75°S during Sep 1979–2008. The vertical bars represent the range of values from the individual days of Sep. The Sep average over the 1979–2008 period is indicated by the horizontal line.

creates a strong ice-edge advance, and in 2008 led to a positive ice concentration and extent anomaly across the Ross Sea sector from April through December. The increased occurrence of an intensified Amundsen Sea Low is contemporaneous with an increase and poleward shift of the westerly circulation in the high-latitude South Pacific, which happened in 2008 in response to La Niña and/or positive SAM conditions, as well as a wave-3 atmospheric circulation pattern. Finally, the 2008 continuation of decreased sea ice in the Amundsen/Bellingshausen Seas is particularly noteworthy given the recent association of the decreasing regional trend with amplified surface warming of the West Antarctic ice sheet during the last 30 years (Steig et al. 2009).

g. Ozone depletion—P. A. Newman

Analysis of the 2008 ozone concentrations is based on data from the NASA Aura satellites, in particular, the KNMI OMI and the JPL MLS. PSC information was obtained from the NASA LaRC CALIPSO instrument. NOAA/NCEP provided analyses of satellite and balloon stratospheric temperature observations. NOAA/ESRL regularly launches ozone- and temperature-measuring balloon instruments from the South Pole. Figure 6.8a displays the average area of the Antarctic ozone hole from 1979 to 2008, estimated by first summing the area of the daily total column ozone values less than 220 DU from the Aura OMI observations, and then averaging these estimates from 21–30 September. Based on these measurements, the Antarctic ozone hole was the sixth worst on record for 2008, fifth worst when using SBUV total ozone from the NOAA polar orbiter satellites. The area of the hole was approximately 25 million km^2 (9.65 million mi^2), somewhat smaller than the 2006 record of 27.7 million km^2 (10.7 million mi^2). The very large ozone hole area is consistent with severe depletion caused by the high levels of chlorine and bromine in the Antarctic stratosphere. At present, ODSs are estimated to have only decreased by about 4% from the peak levels in the 2000–02 period.

The total ozone values over Antarctica steadily decreased from July to early October 2008. Aura OMI observations showed ozone values of about 230 DU near the edge of Antarctica (inside the stratospheric polar vortex in early July) and a low value of 100 DU on 4 October 2008. Balloon-borne ozonesonde observations from NOAA/ESRL at the South Pole also showed similar behavior. On 22 August total ozone estimated from these sondes was 260 DU, with a decrease to 107 DU on 28 September. The ozonesonde profile information showed that the large losses occurred in the lower stratosphere by late September, with a near complete loss of ozone in the 14–20-km layer on 8 October.

Figure 6.8b shows the temperature average (based on the NCEP–NCAR reanalysis) for September at 50 hPa averaged from 60°–75°S (edge of the polar vortex). The September 2008 period was nearly the coldest on record, but comparable to 1980, 1987, 1989, 1998, and 2006. The cold temperatures result in an increased frequency of PSCs, where chlorine molecules are converted from their nonreactive forms into their reactive forms; the latter leads to rapid ozone destruction. In terms of season-integrated totals, CALIPSOs indicate that the 2008 season PSC volume started on par with the record 2006 season but dropped off significantly in August. The overall PSC volume in

2008 ended about 16% lower than in 2006 (Pitts et al. 2009). The cold stratospheric temperatures in winter and spring (Fig. 6.2b), particularly in September 2008 (Fig. 6.8b), were due to weaker-than-normal (5% below the average for the August–September period) wave activity.

The 2008 ozone hole was unusually persistent, with low ozone values extending into the late-December period. The Antarctic ozone hole causes the spring-like conditions to persist because the ozone-depleted air cannot absorb shortwave radiation. Hence, temperatures in the Antarctic spring and early summer are colder, and the vortex transitions to summer conditions at a later date. In addition, lack of wave forcing to dynamically warm the stratosphere can lead to colder spring conditions. In November 2008, ozone depletion combined with a lack of wave driving to produce a cold and stable vortex that persisted well into the December period (Fig. 6.2b). In fact, the polar vortex in 2008 persisted beyond any previous year dating to 1979. Consequently, the area of depleted ozone below 220 DU also persisted to the latest date.

7. REGIONAL CLIMATES

a. Overview—A. B. Watkins and L. A. Vincent

This chapter provides the local perspective of the global climate in 2008. Analyses have been made for a number of individual nations, most broad geographic regions, and all continents. In the vast majority of cases, information for a specific region has been compiled by local scientists, and hence the source of the data used is typically the agency affiliated with the lead author, unless otherwise noted. While acknowledging that the recommended World Meteorological Organization's standard reference period is 1961–90, a number of other reference periods are also used in this chapter for the computation of local climate normals. This is largely due to insufficient data being available in some regions to cover one selected reference period, while in some cases local reference periods are more suitable for domestic purposes. Please also note that while this chapter covers the climate of 2008, information may include data from the previous year to accurately cover appropriate climate events. For example, in southern Africa, the rainy season is from October until the following April, and hence information is provided for the entire period and not just the months from 2008. Likewise, descriptions of the austral summer and boreal winter seasons include data from December 2007.

Annual mean temperatures were generally well above average in Canada, South America, northern and southern Africa, Iceland, Europe, Russia, South Asia, and Australia. Winter 2008 (December 2007 to February 2008) was remarkably mild in most northern European regions. In contrast, an exceptional cold outbreak occurred during January across Eurasia, over southern European Russia, and southern western Siberia.

The year 2008 was also characterized by heavy precipitation in a number of regions including South America, Africa, and South Asia. In contrast, a prolonged and intense drought occurred during most of 2008 in northern Argentina, Paraguay, Uruguay, and southern Brazil, causing severe impacts to agriculture and affecting many communities.

Where not explicitly described in the following text, the background atmospheric state for this local perspective is provided in chapter 2.

b. North America

1) Canada—R. Whitewood and D. Phillips

The year 2008 was another warm year (relative to the 1951–80 reference period). It was wet across Canada, especially in southern regions of Ontario and Quebec where some locations set records for both the wettest winter and summer. It was another year of significant ice loss in the Arctic. For several growers from British Columbia to Ontario, hail storms took a significant toll on grain and fruit crops and properties.

(i) Temperature

Canada experienced its 16th-warmest year in 2008, 0.7°C above normal (Fig. 7.1). The warmest year remains 1998 at 2.5°C above normal, since reliable nationwide records began in 1948. Although not as warm as recent years, most of the warming occurred in the arctic region (Fig. 7.2a) where temperatures were more than 1°C above normal north of 60°N. Most of the populated south was within half a degree of normal.

Temperatures have shown a pronounced warming since records began. Figure 7.1 shows that temperatures have been above the 1951–80 normal period for 12 consecutive years, with 5 of the warmest 10 years occurring in the last decade. The dashed line indicates a trend of 1.3°C for the 1948–2008 period.

Seasonally, anomalies for summer and fall were higher than for the cold seasons. Summer temperatures were 1.0°C above normal, ranking it the third warmest since records began in 1948. Fall ranked sixth warmest with temperatures 1.4°C above normal. For both seasons, most of the above-normal temperatures occurred in the north. Nunavut averaged about 2°C above normal. Nationally, winter and spring were closer to normal, within about half a degree above normal.

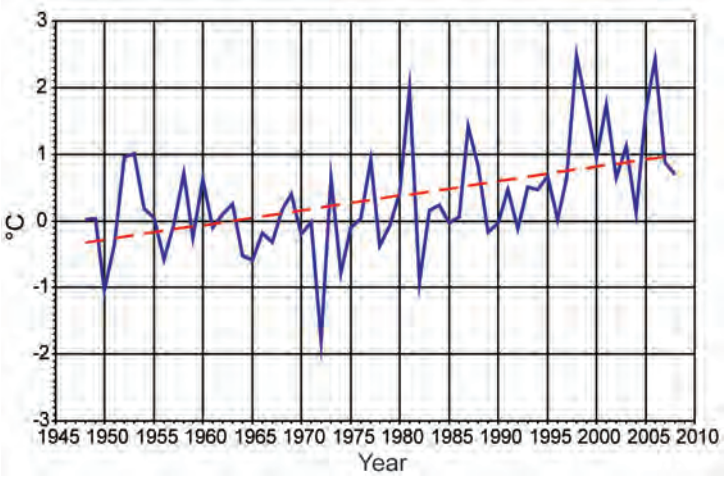

Fig. 7.1. Annual mean temperature anomalies for Canada, 1948–2008. (Source: Environment Canada.)

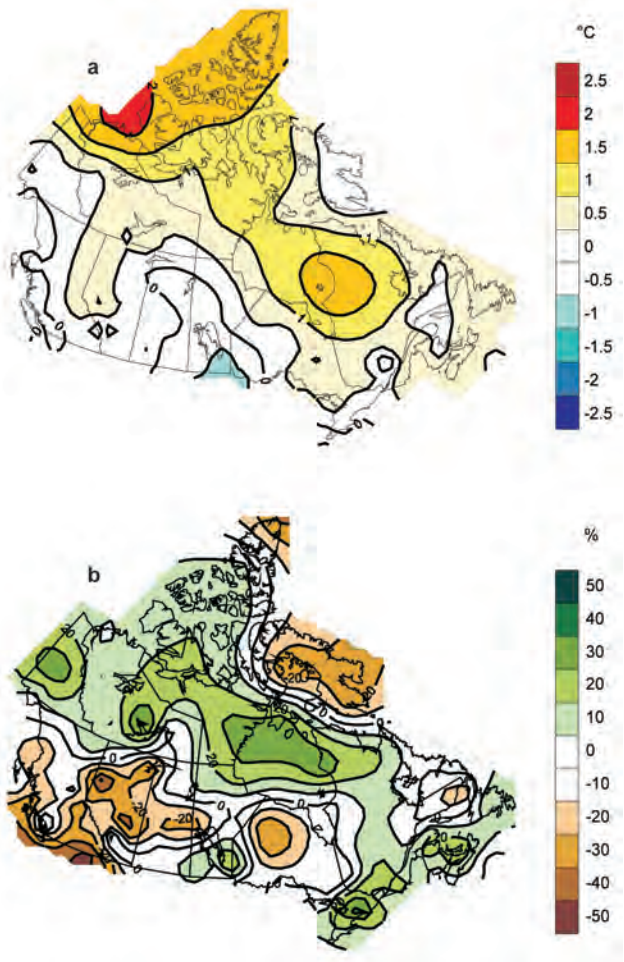

Fig. 7.2. (a) 2008 annual mean temperature anomalies and (b) 2008 annual total precipitation anomalies (percent of 1951–80 average) for Canada. (Source: Environment Canada.)

(ii) Precipitation

Nationwide, Canada experienced its 13th-wettest year in 2008, 4.6% above average. The wettest regions (>20% wetter than normal) included the Arctic, and from southern Ontario through the Maritimes (Fig. 7.2b). In the west, British Columbia through Saskatchewan, it was at least 20% drier than normal. Of note, southern Ontario and southern Quebec experienced their wettest year, 20.4% above normal. Conversely, the region covering the interior mountains of British Columbia was 18.5% below normal, ranking as the fifth-driest year on record (1948–2008).

Since the 1970s, precipitation across Canada has tended to be less than the 1951–80 average. The last drier-than-normal year was 2001. The wettest year on record occurred in 2005 (13.4% above normal), and the driest was 1956 (7.3% below normal).

Seasonally, the summer was exceptionally wet nationally, 13.3% above normal, ranking this season the third-wettest on record. Autumn, on the other hand, was on the dry side, 1.0% below normal, ranking as the 22nd driest on record. Both winter and spring were close to normal (0.5% above normal, and 0.5% below normal, respectively).

(iii) Notable events

The loss of sea ice in the Arctic meant that 2008 was the first time in the satellite era that both the Northwest and the Northeast Passages were open simultaneously, with Arctic sea ice melting to the second-lowest coverage (4.13 million km^2) since records began in 1979 (see chapter 5).

Although not a single event, the total amount of snow that fell during the winter of 2007/08 eclipsed many records across eastern Canada. Snow totals for several locations were in excess of 500 cm, including Quebec City, Quebec (558 cm), Muskoka, Ontario (558 cm), and Gander, Newfoundland (534 cm). The excessive amount of snow led to large snow removal costs, the collapse of several buildings leading to four deaths, and near-record floods.

Costly hail storms damaged crops across Canada during the spring–summer of 2008, despite the lack of hot, humid weather normally associated with such events. Crop damage across the prairies amounted to $341 million (Canadian), the most ever reported. A July storm damaged the fruit-growing region of British Columbia, with some orchards experiencing losses of up to 40% of their tender fruit. Southern Ontario had a series of hail storms that bruised and battered fruit and crops, amounting to 4 times the previous 5-yr average for both number of reports and acreage damaged.

2) United States—S. E. Stephens, R. R. Heim, Jr., K. L. Gleason, C. Fenimore, G. D. Bell, M. Shulski, and R. A. Ballard

Reliable monthly, seasonal, and annual weather records for the United States exist from 1895 to the present, enabling the climate of 2008 to be placed in a 114-yr context for the contiguous United States. Based on preliminary data, the year 2008 was near the twentieth-century mean, with a nationally averaged temperature of 11.7°C. This ended a string of 10 consecutive much-warmer-than-average years. Spatial distribution of annual temperature anomalies included above-average temperatures in the northeast and southwest, with below-average temperatures in the central states and Pacific Northwest.

The year was characterized by dry conditions in the West, portions of Texas, and the Southeast,

with unusually wet conditions from the plains into the Northeast. New Hampshire and Missouri experienced their wettest year on record, punctuated by historic flooding in June in the Midwest. Exceptional drought, as defined by the U.S. Drought Monitor (Svoboda et al. 2002), was ameliorated in the Southeast by late in the year, while areas affected by drought expanded in parts of south-central Texas. Above-average snowpack in the West provided relief to some areas experiencing multiyear drought.

(i) Temperature

For the contiguous United States, 2008 was the coolest year since 1997 with an annual temperature that was 0.1°C above the twentieth-century (1901–2000) mean (Fig. 7.3).

The contiguous United States had the 53rd-warmest winter season (December 2007–February 2008), 45th-coolest spring (March–May), 30th-warmest summer (June–August), and 32nd-warmest fall (September–November) in 2008. A persistent trough brought below-normal temperatures to the West Coast into the central plains, with warmer-than-average temperatures from the Deep South into the Northeast. Below-average spring temperatures occurred across the plains and westward, with only Texas, New Jersey, Delaware, Connecticut, and Rhode Island warmer than normal. Indicative of a weakening La Niña, temperature anomalies during the summer season were much above average in the West, where California experienced its sixth-warmest summer on record. New Jersey and Rhode Island experienced their eighth- and sixth-warmest summers, respectively. The western United States had a warmer-than-normal fall, while the eastern United States was cooler than average. California experienced its third-warmest fall on record, while Georgia observed the eighth coolest.

California and the Southwest experienced above-normal annual temperatures, while New Jersey and Delaware had their 10th- and 11th-warmest annual period, respectively. Temperatures across the Midwest were below average for 2008, with Iowa recording its 11th-coolest year (Fig. 7.4a).

The annual temperature for Alaska in 2008 was 0.4°C below average, representing a return to cool anomalies after above-normal conditions for eight consecutive years. The strongest negative tempera-

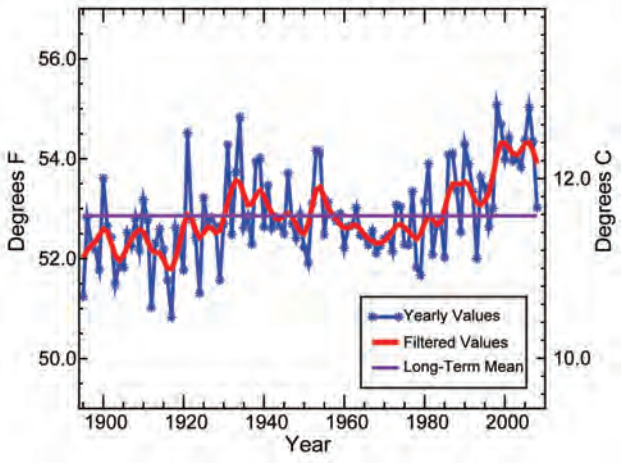

Fig. 7.3. Annual mean temperature for the contiguous United States, 1895–2008. (Source: NOAA/NCDC.)

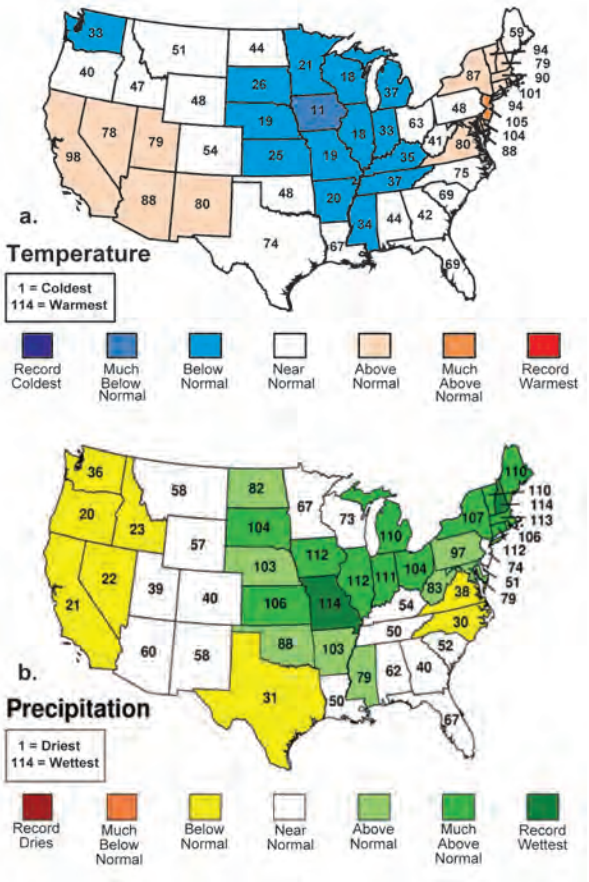

Fig. 7.4. Statewide ranks of (a) annual 2008 temperatures and (b) annual 2008 precipitation. A rank of 114 represents the warmest/wettest year since 1895. Much-above-normal temperature/precipitation is defined as occurring in the top 10% of recorded years, which corresponds to a rank of 104–113. Above-normal temperature/precipitation is defined as occurring in the warmest/wettest third of recorded years (ranks 77–103). Much-below-normal temperature/precipitation is likewise the bottom 10% of coolest/driest years since 1895, and below normal is defined as the remaining coolest/driest third of the distribution. (Source: NOAA/NCDC.)

ture anomalies were in the southwest portion of the state, with a notable warmer-than-normal exception along the central Arctic coast. Alaskan temperatures in winter (December–February) were near the 1971–2000 average. Spring temperatures were above average, while summer and fall both averaged below the 1971–2000 mean.

(ii) Precipitation and snowpack

Record amounts of rainfall in the Northeast and historic flooding in the Mississippi and Ohio River valley regions occurred during 2008 (Fig. 7.4b). Nationally, four months were wetter than average, contributing to the 27th-wettest year on record. Persistent precipitation events throughout the year resulted in record precipitation for the Northeast. Connecticut, Massachusetts, Rhode Island, and Vermont each had the wettest February, while New York experienced its wettest winter. New Hampshire ranked wettest for the summer and annual periods.

During June, significant flooding affected the states of Illinois, Indiana, Michigan, Minnesota, Missouri, and Wisconsin. Record-high flows were recorded in major rivers, including the Des Moines, Cedar, and Wisconsin Rivers, with peak levels in some locations exceeding the 500-yr return interval. The Cedar River crested at over 9.8 m, flooding 1,300 city blocks of Cedar Rapids, Iowa. Local flash floods also occurred as rainfall totals at times exceeded 127 mm day^{-1}, with more than 1,100 daily rainfall records broken during the month. Factors contributing to the floods included well-above-average precipitation during January–May, followed by significant rainfall for nearly two weeks in June as a persistent area of low pressure and well-defined cold and warm fronts affected the central plains. Preconditioning heavy rainfall events earlier in 2008, culminating with the heavy June rainfall, occurred while the convection patterns associated with the MJO and La Niña were in-phase (Bell 2008). Additionally, excess soil moisture and elevated river levels preceded the floods. The atmospheric circulation during the main flood event was typical of other major floods, including the great Midwest floods of 1993 (Bell and Janowiak 1995).

During winter 2007/08, snowpack levels were above average in much of the Rockies, Cascades, and Sierra Nevada. Some areas in Oregon, Washington, Arizona, New Mexico, Nevada, and southern Colorado had levels above 180% of normal. Conversely, parts of Wyoming, Montana, and Nevada had levels below normal, as did much of eastern Alaska and southern New Mexico. Mountain snowpack remained substantial with most of the intermountain region and Pacific Northwest reporting above-normal snowpack at the end of the winter season. February brought a series of large winter storms across much of the northern two-thirds of the nation. Madison, Wisconsin, set a new record for seasonal snowfall with 257.6 cm. Snowfall at Caribou, Maine, was 502.4 cm, a new seasonal record.

The beginning of the 2008/09 snow season was below normal in the Sierra Nevada and many California reservoirs were at their lowest levels in over 30 years. Snow conditions in the rest of the West were near normal. In October, a major snowstorm over the western United States dumped as much as 124 cm of snow in Cole Creek, Montana, and 76 cm of snow in Lander, Wyoming. In Alaska, Barrow reported the heaviest October snowfall on record with 58.9 cm. During the month of December, more than 2,200 daily and monthly snowfall records were broken across the United States, with the most notable events in the upper Midwest, southern Nevada, and southwest Louisiana.

(iii) Drought and wildfires

The year was characterized by persistently dry conditions across much of the West, Southeast, northwestern Great Lakes, southern plains, and Hawaii. For California, which had its driest spring (March–May) and March–August periods on record, October 2007–September 2008 was the second consecutive dry hydrological year. Nevada had its driest March–September period on record.

Three-quarters of the Southeast was in moderate-to-exceptional drought when the year began, with low stream flows and water restrictions affecting many communities. Beneficial precipitation in the waning months of the year contracted the drought area to about 15% of the region. Drought plagued the southern plains for most of 2008, depleting soil

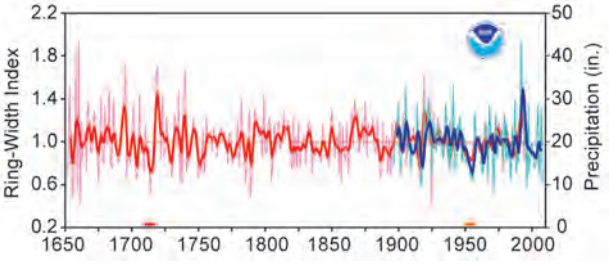

Fig. 7.5. South-central Texas Dec–Jun precipitation (1896–2008, blue curves) and proxy precipitation from tree rings (1652–1995, red curves). Annual values are shown as thin curve; 5-yr smoothed values are shown as thick curves. (Source: NOAA/NCDC/Paleoclimatology Branch.)

FACTORS CAUSING THE 2008 U.S. COOLNESS—NOAA CSI TEAM

The near-normal 2008 U.S. annual temperature was a departure from the unusual warmth of the previous 10 years (Fig. 7.6). However, the decline relative to 2007 was only about one standard deviation of the historical interannual variability. Two sets of climate models—CMIP model data and atmospheric general circulation models forced with the monthly evolution of observed SSTs (AMIP experiments)—were used to assess the influence of external climate forcings (greenhouse gas concentrations and other forcings) and SSTs on U.S. temperatures.

Figure 7.6 (middle) shows the time series of the CMIP ensemble mean annual U.S. temperatures for 1895–2008 and the 2008 projection of +0.73°C, which is considerably warmer than the observed anomaly. Further, the observed coolness appears to have been a low-probability outcome: only 5% of the model runs (7 of 144) are as cold as observed for 2008, despite the considerable spread among ensemble members.

The 2008 ocean conditions were persistently cool in the tropical Pacific, which was not predicted due to external forcing (CMIP runs). Global SSTs as a whole have cooled in recent years, possibly due to strong natural internal coupled variability. The time series of AMIP ensemble mean annual U.S. temperatures for 1895–2008 is shown in Fig. 7.6 (bottom). The observed anomaly was also colder than the expected SST-forced signal (+0.45°C), though the probability of exceedence of such coolness in the AMIP realizations was 15% (23 of 150), threefold greater than implied by the CMIP runs.

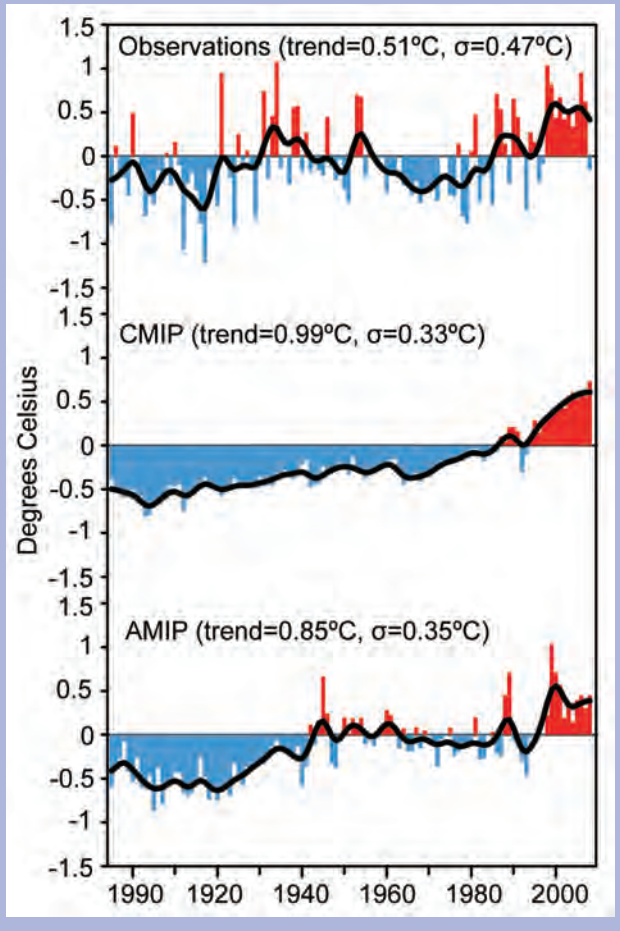

FIG. 7.6. Time series of annual land temperature departures (°C) for the contiguous United States during 1895–2008 based on (top) NCDC climate division observational analyses, (middle) the ensemble of CMIP simulations forced with observed greenhouse gas, aerosol, solar, and volcanic aerosol variability, and (bottom) the ensemble of AMIP simulations forced with observed global sea surface temperature variability. Bars plot the annual departure, computed relative to a 1971–2000 reference period, and the black curve is a 9-point Gaussian filter applied to the annual values.

This preliminary assessment has not taken other potentially important factors into account (e.g., land surface conditions, uncertainties in external climate forcings in the CMIP runs, observed values of solar forcing for 2008). Nonetheless, a key outcome of the model diagnosis is that the average spread among individual simulations for both CMIP and AMIP runs is roughly 0.50°C, a value close to the observed historical interannual variability. As such, the observed coolness over the United States appears consistent with a scenario of moderate-intensity atmospheric internal variability masking the warming influences of boundary forcings. In other words, although the United States was colder than many recent years, temperatures in 2008 were well within the range of variability associated within natural internal climate fluctuations. Indeed, the model simulations suggest that even stronger cooling could have resulted—one AMIP run using observed SSTs for 2008 generated colder U.S. temperatures than any prior observed year since 1895.

moisture, lowering river and lake levels, and ravaging crops. Southern Texas had the driest October–June in its 114-yr record. December 2007–June 2008 ranked as the fourth-driest December–June in the 114-yr precipitation record for south-central Texas. A precipitation index for this region based on tree-ring data covers the period 1652–1995. In the approximately 250 years prior to 1896, the tree-ring record shows about a dozen individual years

that likely had very low December–June precipitation similar to the lowest values in the past century, such as 2008 (Fig. 7.5). The 1950s drought is the drought of record for the twentieth century, with seven consecutive years (1950–56: orange bar) having below-normal December–June precipitation. The 1950s drought appears to have been matched and possibly exceeded by one that occurred in the early 1700s (red bar), in which the ring-width index was below average for seven years in a row (1711–17) and the cumulative ring-width anomaly for those seven years was slightly lower than that for 1950–56.

Although there were heavy rains and serious flooding over Hawaii in February and again in mid-December, these episodes were separated by a long, severe dry spell that produced significant drought conditions by late summer. Although beneficial rains did fall by year's end, some areas in Hawaii continued to suffer from lingering drought conditions.

The United States had a relatively mild wildfire season in 2008 when compared to 2007 and 2006. However, some areas of the nation—primarily in the western and southeastern regions—experienced significant and costly fire activity in 2008. The majority of fire activity occurred during the months of July and August. For the year as a whole, nearly 80,000 wildland fires burned more than 2 million hectares, according to preliminary year-end statistics from the NIFC. These values rank 2008 near average in terms of the number of fires and above average for area burned.

(iv) Tornadoes

Across the United States, 2008 was a very active year for tornadoes. As of January 2009, confirmed tornado reports and estimates for the end of 2008 indicated that there were 1,630 tornadoes from January–December 2008, which is above the 10-yr average of 1,270 and the second-highest total in the 1953–2008 record. In 2004, 1,817 tornadoes were confirmed across the contiguous United States. The number of strong-to-violent tornadoes (rated EF3–EF5)[1] reported in 2008 was 36, which is equivalent to the average number reported over the period 1950–2008. (See: www.spc.noaa.gov/faq/tornado/ef-ttu.pdf for additional details.) The total number of tornado-related fatalities for 2008 was 125, the 10th highest in the 1953–2008 record. Nearly all of these fatalities occurred during the first five months of the year.

The beginning of 2008 was an active severe weather period. There were 54 confirmed reports of tornadoes and five deaths across the Midwest on 7–8 January 2008, making it the second-largest January tornado outbreak on record. On 5 February, 87 tornadoes were confirmed. This deadly event, nicknamed the "Super Tuesday Outbreak," was responsible for 57 deaths in the southeastern United States. The number of tornado-related fatalities reported in February across the United States was the second highest on record for the month.

May was also an active month with 460 confirmed tornadoes, making it the third-most-active May on record. For the period January–May, a total of 112 tornado fatalities were reported, which ties 2008 and 1968 for the eighth-deadliest January through May period since reliable records began in 1953. Severe weather continued into June when two outbreaks spawned 289 confirmed tornadoes. The severe weather season began to slow down over the summer months and into the fall with over 300 tornadoes confirmed from July–October and only five additional fatalities reported during the remainder of the year.

3) Mexico—V. Davydova-Belitskaya and F. Romero-Cruz

For Mexico, 2008 was slightly warmer than normal, with an annual mean temperature of 21.4°C, 0.7°C above the long-term climate average. Annual total precipitation was the 17th wettest since records began in 1941, with 900.7 mm, compared with the long-term (1941–2000) average of 771 mm. Extreme weather took a toll with several deaths and monetary losses in the millions (USD) across the agricultural sector. Hardest hit were areas near Coahuila, north of Chihuahua and Tamaulipas, Durango, Nayarit, south of Sinaloa, and west of Jalisco, which started the year with severe drought conditions and continued with extended wildfires through the spring. In contrast, Aguascalientes, Zacatecas, San Luis Potosi, Durango, south of Tamaulipas, Chihuahua, and Veracruz registered heavy rain and flooding during July and August, with dam levels in these zones more than 100% of capacity at year's end.

(i) Temperature

The annual mean temperature anomaly over much of Mexico was near 0°C, however across the northwestern region temperatures were 1° to 3°C above normal (Fig. 7.7a). During the spring and the begin-

[1] Prior to 2007, statistics were compiled using the original Fujita scale, which classified tornadoes based on wind strength, estimated by associated damage. The Enhanced F-scale is also a set of wind estimates based on damage. It uses 3-second gusts estimated at the point of damage based on a judgment of 8 levels of damage to 28 specified indicators.

U.S. RIVER DISCHARGE FOR 2008—A. MACDONALD, L. BOWLING, B. FEKETE, R. LAMMERS, AND R. LAWFORD

For the 2008 water year (1 October 2007 through 30 September 2008), streamflow across the contiguous United States was slightly above the long-term annual median (1930–2008), with pronounced regional differences (Jian et al. 2009). Annual streamflow was much above normal throughout the upper Midwest and central Plains, due primarily to wet winter and early spring conditions. Wet winter and summer conditions led to above-normal annual streamflow in New England. Much-below-average annual flows existed in the Southeast, due to low flows in the fall and winter that slowly recovered in the spring and summer (Jian et al. 2009). Streamflow in Alaska was low in all seasons, with record-low values in the spring, summer, and annual totals.

Transporting nutrients, pollutants, heat, and low salinities, river discharge is important to the ocean on both regional and basin scales. Milliman et al. (1995) identified 61 rivers in the contiguous United States that discharge directly into ocean basins. Of these, 40 are active USGS stations with record lengths sufficient to compute 2008 streamflow as a percentile of normal flow (1964–2008). As illustrated (Table 7.1), total discharge into the Gulf of Mexico was higher than normal in 2008 (84th percentile) due to summer flooding in the U.S. Midwest, while discharge into the Pacific and Atlantic Oceans was lower than normal (32nd and 36th percentiles, respectively).

Table 7.1. Estimates of observed and extrapolated discharge volume.

Basin receiving water	U.S. land area (km^2)[a]	Gauged land area (km^2)	Observed 2008 discharge volume (km^3)	Percentile (1964–2008)	Extrapolated 2008 discharge volume (km^3)[b]
Atlantic Ocean[c]	795,256	277,847	102	36th	292
Pacific Ocean[d]	1,022,605	749,933	215	32nd	293
Gulf of Mexico[e]	4,053,225	3,251,813	588	84th	733

[a] Estimated using the published areas of the 21 USGS water resources regions (Seaber et al. 1987)

[b] Calculated from observed annual runoff (observed discharge/gauged land area) times the total land area draining to each water body.

[c] Excludes Great Lakes drainage through the St. Lawrence River.

[d] Includes the Canadian portion of the Columbia River basin.

[e] Excludes the Rio Grande.

ning of summer, anomalies from +1° to +4°C were observed in the northwestern, northern, northeastern, and the southern Pacific Coast regions. Monsoon conditions starting in the north and moving eastward brought heavy rain from July to September. This was accompanied by temperatures 2° to 4°C below normal in the northern, central, southern, and southeastern regions of Mexico. The northwestern and western regions of the country experienced temperatures 1° to 3°C above normal during the rainy season (June–September). During the fall, in the southeast and the Yucatán Peninsula, unusually low temperatures were reported (11°C and 13°C in Campeche and Yucatán, respectively), resulting in low mean temperatures for these regions during October and November.

(ii) Precipitation

The year started drier than normal during the winter and spring, but significant precipitation occurred during the rainy season. Normal precipitation started in July, particularly in the north and northeast of Mexico and the central part of the country. The rainy

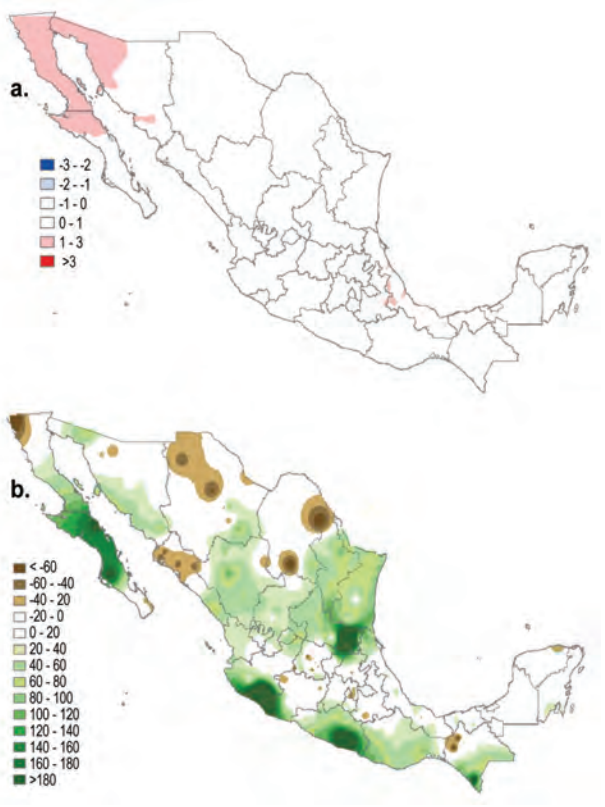

Fig. 7.7. (a) Annual mean temperature anomalies for Mexico (°C, based on 1971–2000); (b) seasonal total precipitation anomalies (May–Oct) (percent of 1971–2000). (Source: National Meteorological Service of Mexico.)

season ended abruptly at the beginning of October, and the end of the year was exceptionally dry.

Annual total precipitation for Mexico was 116.8% of the 1941–2000 mean. The largest anomalies were registered in Aguascalientes and Coahuila (49% above normal), Nayarit (48%), San Luis Potosi (47%), Baja California (44%), Nuevo Leon (43%), Campeche (40%), Chihuahua (35%), Tamaulipas (34%), Durango (33%), and Guanajuato and Chiapas (25%). Four of the 32 states of Mexico reported some rainfall deficit: Mexico City (23% below normal), Yucatán (14%), Tlaxcala (3%), and Sinaloa (2%). The rainy season in Mexico was mostly wet. Only the northern regions of the country and the Yucatán Peninsula reported precipitation slightly below normal (Fig. 7.7b).

(iii) Wildfires

According to the CONAFOR reports, less than 10,000 wildfires were detected during 2008. Most of them were registered during the period from February through June. May had the most wildfires, almost 26% of the total, while April and March accounted for 24% and 21% of the annual total, respectively. Wildfires occurred mainly in the western, northern, southeastern, and northeastern parts of the country, as well as along the Gulf of Mexico and the Yucatán Peninsula. In the north, northwest, and west regions of the country, the North American monsoon helped extinguish these fires during the 2008 rainy season.

c. Central America and the Caribbean

1) Central America—J. A. Amador, E. J. Alfaro, E. R. Rivera, and B. Calderon

(i) Temperature

To illustrate the behavior of the 2008 climate across Central America in the context of its long-term mean, four stations were analyzed for the Pacific region, namely San José (Guatemala), Choluteca (Honduras), Liberia (Costa Rica), and David (Panamá), and three along the Caribbean Sea; Philip Goldson (Belize), Puerto Lempira (Honduras), and Puerto Limón (Costa Rica). All four Pacific stations recorded below-normal annual mean temperature with respect to their climatological values (1971–2000 average). Of all the stations, the largest anomaly was for Liberia, whose annual mean temperature was about 2°C below normal. In contrast, two stations on the Caribbean side (Philip Goldson and Puerto Limón) reported above-normal mean temperatures, while Puerto Lempira was near normal. Puerto Limón recorded an annual mean temperature of about 1°C above normal.

(ii) Precipitation

All stations reported below-normal annual total precipitation for 2008, though it is worth noting that most stations had some missing data. In most regions, daily precipitation was generally less than 20 mm, with very few events recording totals above 40 to 50 mm. The start and end dates of the Caribbean rainy season were near normal; however, a slightly late start was observed for Choluteca and David.

(iii) Notable events

2008 was very active for tropical storms. From 16 named storms observed in the Atlantic, 10 entered the Caribbean basin, four of which were very strong. Despite the fact that Pacific hurricanes rarely affect Central America, the first hurricane of the season, Alma, reached land in Leon (Nicaragua), producing significant economic and social damage.

2) Cuba—C. Fonseca, R. Pérez, B. Lapinel, V. Cutié, I. Gonzáles, D. Boudet, and M. Hernandez.

(i) Temperature

The annual mean temperature for Cuba was 0.3°C above its long-term average, with 2008 being

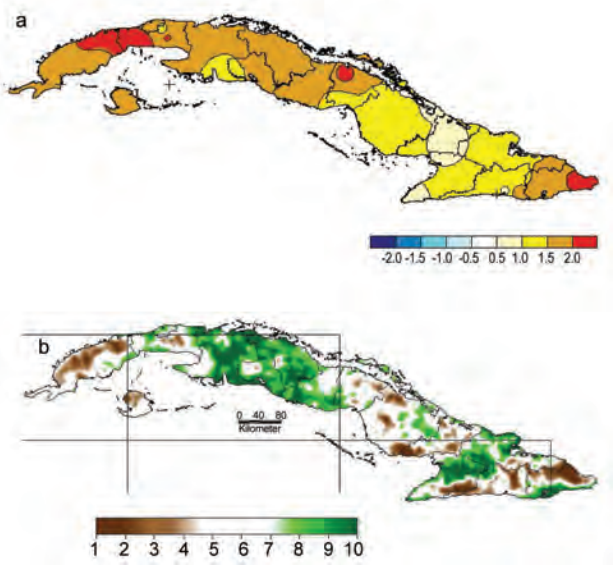

Fig. 7.8. (a) Feb mean temperature anomalies for Cuba (°C; based on 1971–2000); (b) annual total rainfall expressed as deciles (based on 1971–2000; preliminary analysis). (Source: Institute of Meteorology of Cuba.)

its ninth-warmest year since records began in 1951. February was much warmer than normal, with an anomaly of +1.8°C; the second warmest on record (Fig. 7.8a). The summer season was also very warm. November was the only month below average, with temperatures of 0.9°C below normal. Several weather stations reported new record-low nighttime during that month.

(ii) Precipitation

Annual total precipitation for 2008 was either above or near normal for most provinces across the country, with only a few small regions recording below-normal precipitation (Fig. 7.8b). During the first seven months of the year, rainfall deficits were recorded across the country, contributing to a significant drought event over eastern Cuba; however, rainfall associated with hurricanes during August, September, and November ended this drought.

(iii) Notable events

Cuba was affected by four tropical cyclones, which included one tropical storm (Fay) and three hurricanes (Gustav, Ike, and Paloma). Ike was the sixth major hurricane (Category 3 or above) to impact Cuba since 2001, a record for any 8-yr period. The three hurricanes caused extensive damage, estimated at about $10 million (USD), and while seven deaths were reported, actions taken to mitigate the impact of hurricanes on Cuba prevented many more.

3) Jamaica—T. S. Stephenson, M. A. Taylor, and J. M. Spence

(i) Temperature

Positive surface air temperature anomalies were recorded at coastal stations during most of 2008, consistent with the warmer-than-average ocean temperatures. Some inland stations, however, experienced below-normal temperatures over the same period.

(ii) Precipitation

The annual total rainfall for 2008 was slightly above average. This was the cumulative effect of negative anomalies for half of the year, near-normal precipitation for four months, and well-above-normal precipitation for two months (August and November) (Fig. 7.9). August rainfall was the highest August total (357 mm) since 1971. It was primarily attributed to the passage of TS Gustav, and to a lesser extent to tropical waves and surface troughs. Other notable rainfall features included February being the fourth driest since 1971 and the delay of the characteristic May peak in rainfall to June. December rains were below the 1971–2000 mean, but this may be related to a reduction in station density across the island.

(iii) Notable events

The main event in 2008 was the passage of TS Gustav in late August, which produced considerable rainfall over the island. The Mavis Bank station in rural St. Andrew recorded 419 mm of rain on 28 August (495% of the 1951–80 climatological monthly mean) and a 3-day total of 534.6 mm between 27 and 29 August. The rainfall rate at this station peaked at 80 mm h^{-1}. Jamaica also experienced the effects of Hurricane Fay (August) and TSs Ike and Paloma (September and November, respectively).

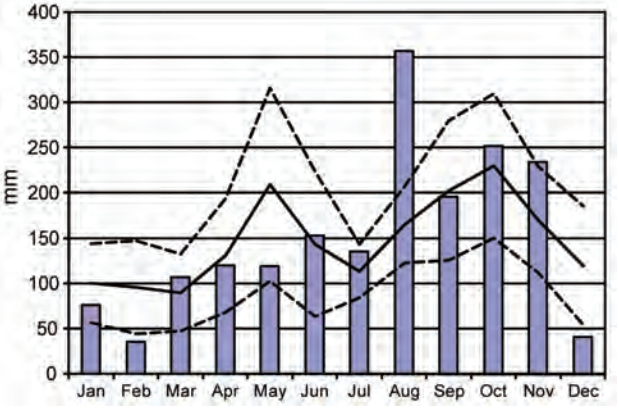

Fig. 7.9. Monthly Jamaican rainfall for 2008 (bars), climatology (black), and one std dev from climatology (dashed). The reference period is 1971–2000. (Source: Meteorological Service of Jamaica.)

4) Puerto Rico and the U.S. Virgin Islands—S. Rossi and J. P. Cupo

(i) Temperature

Annual mean temperatures in San Juan (Puerto Rico) during 2008 were 0.2°C below the 1971–2000 mean. The average maximum temperature of 29.8°C was the coolest recorded since 1996. The highest daily maximum temperature occurred in Juana Diaz, on the south coast, where the temperature reached 37.2°C on 18 July. The lowest daily minimum temperature occurred in Aibonito, over the central interior, where the temperature fell to 6.1°C on 30 January. The temperatures in San Juan were fairly consistent with those observed across the U.S. Virgin Islands, with both the Cyril E. King Airport on Saint Thomas and the Henry E. Rohlsen Airport on Saint Croix reporting their coolest average maximum temperatures of the decade (29.6°C and 29.8°C, respectively). Minimum temperatures were also below their 30-yr means across the U.S. Virgin Islands, resulting in an annual mean temperature anomaly of –0.7°C.

(ii) Precipitation

The annual total precipitation across Puerto Rico (average of 30 sites) was near normal during 2008, with 98% of the expected yearly rainfall for the island (100% was recorded for the U.S. Virgin Islands). San Juan recorded 1,389 mm of rain, nearly identical to the accumulated rainfall of the previous year, and marking its sixth consecutive year of above-normal precipitation. This recent string of wet years in San Juan has resulted in a total rainfall surplus of 1,554 mm recorded so far this decade, exceeding one year's worth of precipitation; the 30-yr annual average rainfall in San Juan is about 1,289 mm.

Of the six geographical sectors that make up Puerto Rico, the driest sector was the eastern interior, which received only 81% of its average precipitation in 2008. The wettest sector was the south coast, which received 132% of its average precipitation in 2008 (Fig. 7.10). There were several spikes in the averaged weekly rainfall across Puerto Rico in 2008, with each of these spikes representing a significant weather event that affected the island.

(iii) Notable events

The first significant weather event of the year was associated with a pair of fragmented cold fronts during the month of January that brought widespread rainfall to much of the northern half of the island. The remnants of two additional fragmented frontal boundaries, combined with a weakening of the persistent upper-level ridge across the region, led to an additional pair of significant rainfall events in the spring. However, these rainfall events were not enough to prevent large sections of the southern and eastern regions from entering into dry-to-moderate drought conditions by late March, which persisted until mid-September.

Relief from heavy rainfall associated with three strong tropical waves during the second half of August (which eventually developed into Tropical Storm Fay, Hurricane Gustav, and Hurricane Hanna), helped to relieve the drought conditions across the region. However, short-term drought conditions did not end until the passage of a strong tropical disturbance, which meandered around Puerto Rico for several days during September, dropping torrential rainfall across much of the southern and eastern sections of the island. Specifically, an unprecedented 560 mm fell in Patillas, 559 mm in Guayama, 406 mm in Cabo Rojo, and 377 mm in Yabucoa, all within a 24-hr period ending at 1200 UTC 22 September.

The only named tropical system that directly impacted Puerto Rico and the U.S. Virgin Islands came in mid-October when Hurricane Omar moved across the Caribbean, eventually tracking northeast through the Anegada Passage. While a spike in rainfall associated with this storm can be seen across Puerto Rico in Fig. 7.10, Puerto Rico was largely spared the brunt of Hurricane Omar. Across the U.S. Virgin Islands, however, damage from the hurricane-force winds, heavy rainfall, and large surf was reported on the island of Saint Croix, with less damage reported across Saint Thomas and Saint John.

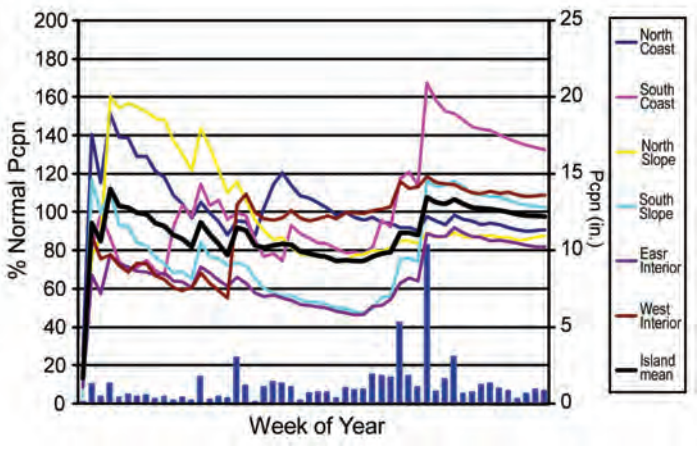

Fig. 7.10. Weekly precipitation expressed as percentage of normal rainfall (left-hand side) for six distinct sectors of Puerto Rico. The average for the island is in bold and the weekly average totals are given on the bottom.

d. South America

1) Northern South America and Tropical Andes —R. Martínez, D. Pabón, G. León, E. Jaimes, A. Quintero, and A. Mascarenhas

(i) Temperature

2008 was characterized by mean temperatures below the 1971–2000 normal for the coast of Suriname, Guyana, Columbia, Ecuador, and Peru, while elsewhere temperatures were near normal (Fig. 7.11a). Temperatures were generally above normal from January to May in most countries, while from July to September temperatures were above normal in the coastal regions. From October to December, the temperatures along the coastal zone were below normal, while they were above normal in the highlands and Amazonia. Temperatures in Peru were near normal with highly localized cold anomalies. In the Galapagos Islands, temperatures were predominantly above normal, except in March when monthly anomalies of −0.5°C were observed.

(ii) Precipitation

Annual total rainfalls were mainly above normal along the coast of Suriname, Guyana, Columbia, and Ecuador, while they were below normal in the north of Venezuela, northeast Columbia, and south of Peru (Fig. 7.11b).

In Venezuela, most of the country experienced below normal precipitation during 2008; however, locally intense rainfall occurred during February, April, and May, while above-normal precipitation occurred over most of the country in October and November. Despite some positive precipitation anomalies in May, the start of the rainy season was delayed. Positive precipitation anomalies in October were mainly associated to the passage of Tropical Storm Omar. This event produced floods and landslides in different parts of the country, with emergency actions taking place in several states and in the Capital District. In November, heavy rainfall caused eight deaths and damaged houses and other infrastructures in Ocumare in Aragua state.

For Colombia, 2008 showed above-normal precipitation. From January to March, most areas experienced positive anomalies, with the wetter conditions contributing to fewer bushfires than expected at that time of year. During the remaining months, generally above-normal precipitation predominated, with the exception of April, September, and December. In the north, central, and west, May, August, October, and November saw many extreme events such as sudden storms, floods, and landslides. The landslides and floods in October and November had considerable human and economic impacts. According to the institution of the National System for Disaster Prevention, 165 people were killed, 213 were wounded, and nearly 1.8 million people

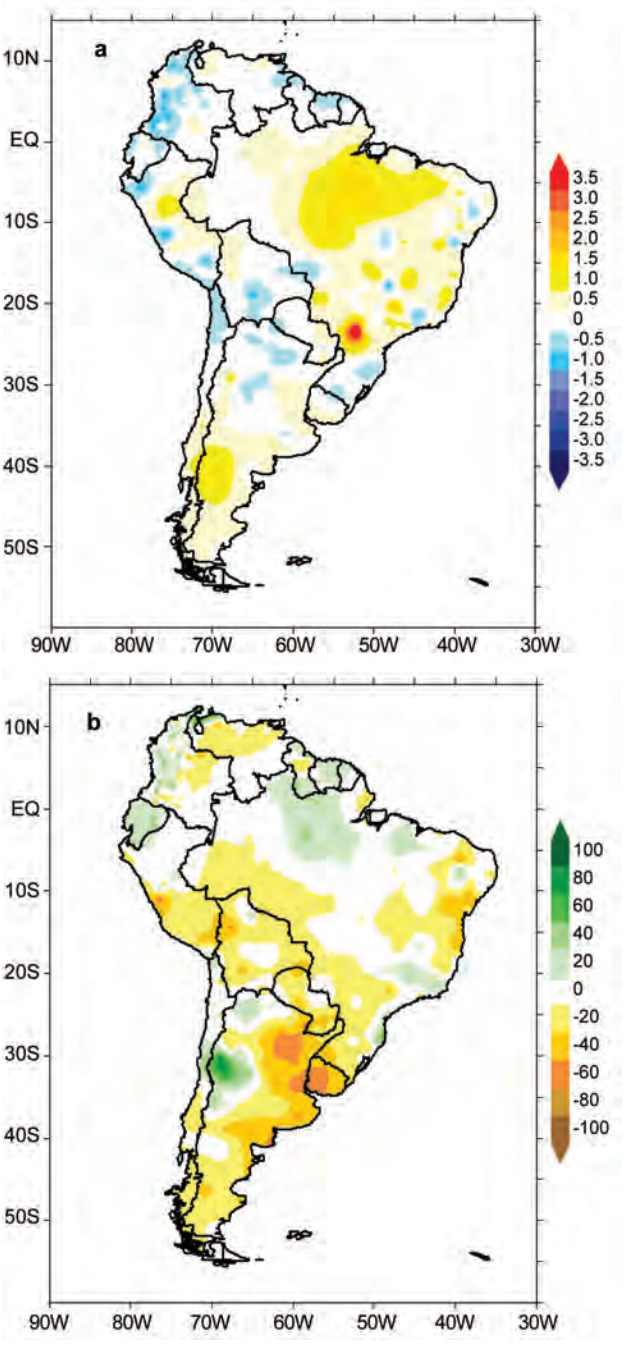

Fig. 7.11. (a) Annual mean temperature anomalies for South America for 2008 (°C); (b) annual total precipitation anomalies (% normal). The reference period is 1971–2000. [Sources: National Meteorological Services of Argentina, Brazil, Bolivia, Chile, Columbia, Ecuador, Guyana, Paraguay, Peru, Uruguay, Venezuela, and CPTEC (Brazil). Data compilation and processing by CIIFEN 2008.]

(approximately 360,000 families) experienced damage to their houses. Losses were estimated at over $26 million (USD).

In Ecuador, the annual total precipitation anomalies were about 20% above normal during 2008. With the La Niña event peaking during December 2007, the rainy season over Ecuador experienced its earliest start in the last seven years. During January and February 2008, while La Niña was diminishing, heavy rainfall was registered over most of the country with the coastal regions affected by floods and the central and northern highlands affected by landslides, leading to a state of emergency being declared across the country. During March and April, rainfall remained above normal along the coast and the Andean region, but it was below normal in Amazonia. In May and June, conditions in the coastal region switched to a rainfall deficit, while in the southern and northern highlands heavy rainfall was reported. The second half of the year was characterized by normal conditions in the coastal zone. During the last trimester of 2008, rainfall was above normal in the central highlands and southeastern Ecuador. In the Galapagos Islands, precipitation was significantly below normal in January and February, mostly associated with negative sea surface temperature anomalies; however, precipitation was twice the monthly normal in March and 27% above normal in April. The rest of the year was characterized by normal to slightly below-normal precipitation.

In Peru, significant rainfall was observed in January. Heavy rainfall occurred in the coastal area of Ica (17 mm in 5 days; 4 mm is usually observed for the month) and in the highlands of Arequipa, where more than 80 mm of rain was observed in the first 20 days of the month. In February and March, there was significant rainfall along the northern coast of Peru, resulting in an emergency declared in the flooded areas. In April, cold and dry air moved into the tropical latitudes inducing rainfall and thunderstorms over the southern jungle of Peru, Bolivia, and Amazonia. This also resulted in a significant drop in air temperature over the tropics. In the remaining months, the precipitation was slightly below normal. During 2008, the precipitation over Peru showed a deficit of about 20% compared to the long-term average (1971–2000).

(iii) Notable events

Of 16 tropical cyclones, only Omar passed near the Caribbean coast of Venezuela on 13 and 14 October, intensifying precipitation over much of the country.

2) Tropical South America East of the Andes—J. A. Marengo, J. Baez, and J. Ronchail

(i) Temperature

Most of tropical South America east of the Andes and south of 23°S experienced a warm 2008, with annual mean temperatures 2° to 3°C warmer than normal. Likewise, warm conditions (1° to 2°C above normal) were observed in northern Venezuela, interior Brazil between Amazonia and Northeast Brazil, and in eastern Peru (Fig. 7.11a). Cooler-than-normal conditions (anomalies of −0.5 to −1°C) were observed in southeast Brazil. From January to April, warm temperature anomalies were detected in eastern Amazonia, Northeast Brazil, southern Paraguay, and northern Argentina. In the interior of Northeast Brazil, mean temperatures reached 32° to 34°C, exceeding the mean by more than 4°C. Negative daily maximum temperature anomalies of 2° to 3°C were reported in Uruguay, southern Brazil, and the Brazilian highlands, associated with the penetration of a cold air mass.

In May, negative air temperature anomalies (–1° to –2°C) were observed in the Peruvian Andes and western Bolivia. A cold outbreak, due to an early northward penetration of a polar air mass, occurred in May in southern South America. Very cold temperatures were registered over the Peruvian–Bolivian Altiplano from March to May 2008. Mean minimum temperatures fell considerably to 2.7°, −0.2°, and 3.9°C in La Paz in March, April, and May, respectively. Early frosts and hail resulted in poor harvests in Andean crops (30%–40% below normal) and affected high-altitude hay making, leaving breeders with no alternative food for their herds. Mean maximum temperatures dropped by 3° to 4°C in those regions while minimum temperatures dropped by 1° to 2°C. The sharp falls in temperature were related to two episodes of cold-air penetration, which occurred at the beginning and end of May, with lower temperatures in the highlands of southern Brazil.

In June, colder temperatures (1° to 2°C below normal) were reported over a large area between Paraguay, northern Argentina, and northern Brazil. In July, positive temperature anomalies were detected across almost all tropical South America, east of the Andes. Temperatures 4°C warmer than normal were recorded in eastern Bolivia, Paraguay, northern Argentina, and southern Brazil, making it the warmest July in the last 50 years for many locations. In July, maximum and minimum air temperature anomalies reached 4°C above normal over most of central and southeastern South America, including Brazil. Clearer-than-normal skies also favored

intense overnight heat losses, which in turn lowered minimum air temperatures, especially in west-central and southeastern Brazil. In Campos de Jordão, in the highlands of São Paulo, the temperature fell to −0.2°C on 14 July, and in southern Brazil, some cities experienced three consecutive days with minimums near 0°C from 17 to 19 July.

From August to October almost all of tropical South America was about 1°C warmer than normal, while in September and October, negative maximum and minimum temperature anomalies (1° to 3°C below normal) were detected in southern Brazil and eastern South America. High daily maximum temperatures were detected on 26 August in west-central Brazil (38.4°C at Cacoal; 39.3°C at Diamantino; and 39.6°C at Cáceres). In other regions, minimum temperatures were near normal due to the cloudiness associated with a cold front. However, in November warm temperatures were detected in regions of southern Bolivia, Paraguay, southern Brazil, and northern Argentina, with temperatures 3°C warmer than normal. In November, maximum mean temperature anomalies reached +2° to +3°C over large parts of tropical South America while mean minimum temperatures were 3°C warmer than normal.

(ii) Precipitation

In the tropical region east of the Andes, rainfall was 40% to 60% above normal in the Amazon region and central-southeastern Brazil (Fig. 7.11b), a situation fairly typical of La Niña years. The opposite was observed in central and southern Paraguay, with rainfall 20% to 80% below normal. In Bolivia, heavy rainfall, which began in November 2007, continued into January, causing floods that affected around 25,000 people and resulted in 30 fatalities. More than 10,000 hectares of crops were damaged by the floods, causing an estimated $30 million (USD) in losses. Mudslides destroyed many homes in the capital city of La Paz. In Rio de Janeiro, torrential rain produced floods that affected around 50,000 people and caused four deaths.

As for January, most of the summer and autumn months were characterized by episodes of intense rainfall and floods in large cities such as São Paulo and Rio de Janeiro. In the Peruvian upper Amazon, excessive rains in February produced floods and landslides in various states. The heights of the Ucayali and Madre de Dios Rivers, as well as the Beni and Mamoré Rivers in the lowlands of Bolivia, were all above normal. On the Altiplano, severe flooding and high river levels were detected in the Desaguadero and Pilcomayo Rivers. In tropical Brazil, wetter conditions in the austral summer of 2007/08 resulted in above-normal river levels for the Amazon, Tocantins, and São Francisco Rivers. In northern Paraguay, rainfall was almost twice the normal amount in February 2008; however, for the rest of summer and fall rainfall was deficient.

In Northeast Brazil, the pre–rainy season between January and February was wetter than normal, while the peak of the rainy season from March to May was also normal to above normal. Both March and April were between 20% and 40% wetter than normal. As a consequence, widespread floods killed 15 people, displaced more than 30,000 from their homes, and destroyed corn and bean crops in the Piaui state of Northeast Brazil. In June and July, wetter conditions were observed in northern Brazil and French Guiana, while drier conditions persisted in eastern Colombia and western Venezuela. In August, hailstorms were observed in southern Brazil due to the penetration of a cold front.

Rainfall in the Andean region of Colombia was about 40%–60% above normal between January and September 2008, and, as a consequence of the intense rainfall, about 56% of the country suffered the impacts of the rainfall excesses. Landslides accounted for 70% of deaths and 46% of injuries. In May, dangerous floods caused by torrential rains affected more than 100,000 people, damaged thousands of homes, and were responsible for nine fatalities. In December, rainfall was 20% to 60% above normal over the entire region, and the subsequent overflowing of the Magdalena River broke the retaining wall in the town of Plato (580 km north of Bogotá) and affected about 20,000 people. Power systems and drinking water were restricted in several areas of the municipality.

In areas east of the Andes, a large part of northern Argentina, Paraguay, Uruguay, and southern Brazil experienced a prolonged and intense drought during most of 2008, causing severe impacts to agriculture. From April to August 2008 (including September for Paraguay), Bolivia, Paraguay, and most of northern Argentina were affected by severe rainfall deficits, in some cases 60% to 80% below normal. The presence of a dry air mass that covered most of central and northern South America inhibited the formation of rain and produced above-normal maximum temperatures and, in some areas, a reduction in minimum (overnight) temperatures.

In August 2008, two cold fronts produced intense rainfall in southern and southeastern Brazil. In Paraguay, the states of Alto Paraguay, Boquerón, and Presidente Hayes were affected by a severe drought (rainfall

INTENSE RAINFALL AND FLOODS CLAIM AT LEAST 120 LIVES IN SOUTHERN BRAZIL—J. A. MARENGO

In southern Brazil, 22 to 24 November saw heavy rainfall over Santa Catarina state, which caused severe floods and deadly mudslides. Around 1.5 million people (a quarter of Santa Catarina's total population) were directly impacted, with 69,000 people left homeless, 120 fatalities reported, and a state of emergency declared. Mudslides and flooding caused by the storms blocked almost all highways in the region and cut off water and electricity to many thousands of homes. Most of the fatalities were caused by mudslides that swept away homes and businesses. The storms broke a stretch of pipeline that carries Bolivian natural gas to southern Brazil and forced the suspension of the fuel supply to part of Santa Catarina and to the entire neighboring Rio Grande do Sul state. Some cities reported looting of supermarkets and pharmacies by hungry and desperate flood victims. This event has been described as the region's worst hydrometeorological disaster since at least 1862.

The meteorological causes were associated with an atmospheric blocking over the South Atlantic that formed in the preceding week. High rainfall was linked to the intensification of the subtropical Atlantic high, which produced a steep pressure gradient along the coast that favored strong moisture transport from the ocean to the continent. Over land, a cyclonic vortex at the middle levels of the atmosphere between eastern Paraná and Santa Catarina favored the ascent of the moist air along the Sierra do Mar mountains. This unusual combination of phenomena favored the intensification of rainfall along the coastal region of Santa Catarina (Fig. 7.12). Unofficial estimates of the losses due to this extreme rainfall event and subsequent floods and landslides are of the order of $350 million (USD).

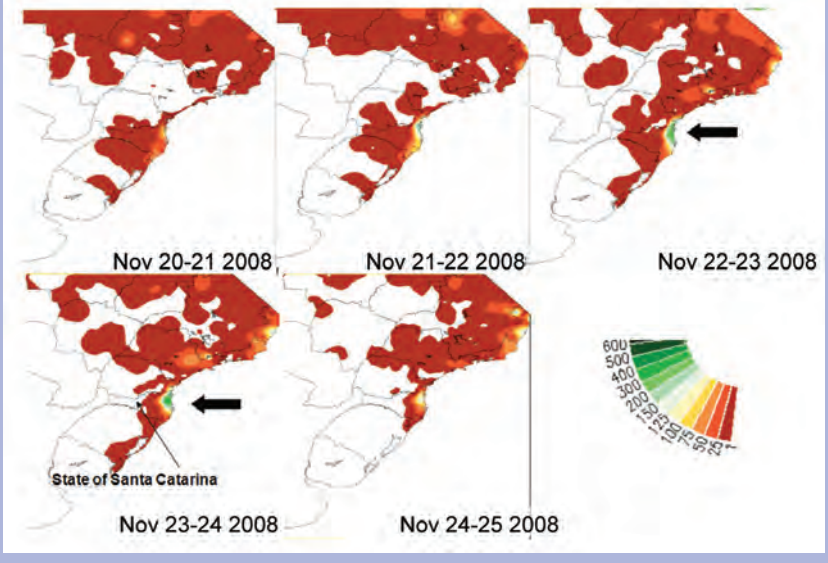

Fig. 7.12. Accumulated precipitation (mm) in southern Brazil during 20–25 Nov 2008. (Source: CPTEC/INPE.)

80%–100% below normal), and by September 2008 the government had declared a regional emergency (Paraguayan Chaco), with thousands of families, as well as cattle and agriculture, strongly affected.

3) Southern South America—P. Aceituno, M. Bidegain, J. Quintana, M. Skansi, and M. Rusticucci

(i) Temperature

Temperatures above the 1971–2000 average were observed over most of southern South America during 2008, with mean anomalies of between +0.5 and +1°C (Fig. 7.11a). Mean temperatures in July were more than 3°C above average over large parts of northern Argentina, Paraguay, northern Uruguay, and southern Brazil, making this month the warmest of the last 50 years for many locations. Mean temperature anomalies larger than 3°C were also reported during November, when the average daily maximum temperature in central Argentina and southwestern Uruguay was more than 4°C above the climatological mean. For many cities in southeastern South America, including Montevideo and Buenos Aires, this was the warmest November in the last 50 years.

The annual mean temperature for 2008 was also above average along the extratropical west coast of the continent southward from 30°S, with annual mean anomalies of 1.0°C in the region from 35° to 41°S. Above-average daily maximum temperatures were prevalent during the early (January to March) and late (September to December) parts of the year. Most were associated with rainfall deficits and clear sky conditions. In the region from 39° to 46°S, monthly mean maximum temperature anomalies were above +2.0°C during January and March and above 4.0°C

in February. However, the most extreme conditions occurred during January when maximum temperatures on some days exceeded 35°C in southern Chile for some days. In particular, 37.3°C was registered at Temuco (38.8°S) on 28 January, which was the highest daytime temperature in 37 years. The beginning of the 2008/09 austral summer was anomalously warm in the southern region of Chile, with daily maximum temperature anomalies greater than +3.0°C reported during December (4.7°C above the 1971–2000 average at Coyhaique, 46°S). As a result of strong positive anomalies in daily minimum temperature for central Chile during winter, a relatively low incidence of freezing days was reported for this rich agricultural region during 2008.

(ii) Precipitation

Large and persistent rainfall anomalies in southern South America are typically associated with the occurrence of La Niña or El Niño episodes. During the first quarter of 2008, the regional climate was strongly affected by La Niña conditions.

Southeastern South America, including a large part of Argentina, Uruguay, Paraguay, and southern Brazil, experienced a prolonged and intense drought during most of 2008 (Fig. 7.11b). This caused severe impacts to agriculture and hydropower generation. Dry conditions in Uruguay reinforced a drought that started in November 2007, with the western province of Soriano experiencing its driest annual total in 65 years. These conditions exacerbated water shortages for agriculture in this main crop-growing area of the country, with the annual rainfall deficit reaching 57% below average in Mercedes, Soriano (Fig. 7.13). In the rest of the country the rainfall ranged from 20% to 40% below the 1971–2000 mean. Further exceptionally dry conditions occurred in March and November when mean rainfall deficits of 71% and 86%, respectively, were reported for the whole country. All months during 2008 were drier than average in Uruguay, resulting in the driest year in the past 65 years.

In Argentina, annual total precipitation was 40% to 60% below average in the eastern region of the country, including the province of Entre Rios and part of the provinces of Corrientes, Santa Fe, and Buenos Aires. In some areas, the precipitation during 2008 was the lowest recorded in the last 50 years.

Along the western margin of the continent, dry conditions that had prevailed in Chile during 2007 continued during the 2007/08 summer, with rainfall deficits around 50% occurring from 37° to 46°S. Early uncertainty about the evolution of a La Niña

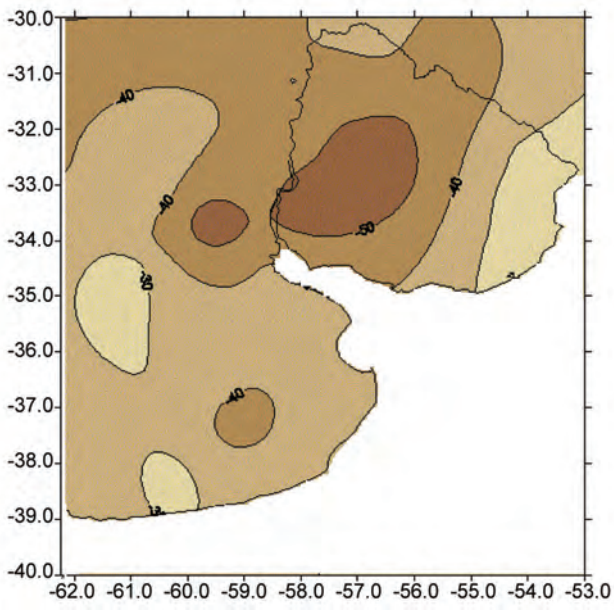

Fig. 7.13. Annual total rainfall deficit in central-east Argentina and Uruguay during 2008. The reference period is 1961 to 1990. (Source: CIIFEN 2008.)

event raised concerns about drought and hence about a severe shortage of energy in Chile, where hydroelectrical power plants have a large share in the industry of energy production. However, the relatively abrupt weakening of La Niña during the autumn saw intense storms in central Chile during May, producing considerable damage due to extensive flooding, and an autumn surplus of rainfall at most stations. The 127.6 mm of rainfall measured at Concepción (36.9°S) on 18 May was the largest daily value for this month since 1971. The rainfall regime during winter was characterized by a large intraseasonal variability with a marked contrast between anomalously dry conditions during June and July and above the 1971–2000 average rainfall in August, mainly as the result of an intense storm that affected the central portion of the country around the middle of the month. The 103.4 mm of rainfall registered at Valparaiso (33°S) on 15 August was the highest daily value since 1971. Winter ended with near-average rainfall, except at the southernmost station of Punta Arenas (53.3°S), where a surplus of 39% was recorded.

As for other regions in the southern portion of the continent, very dry conditions prevailed over Chile during the spring, with rainfall ranging from 40% to 90% below average. As the drought was intensified by a very warm austral fall and winter, considerable impacts on agriculture and a large number of forest fires were reported for central and southern portions of the country.

SEVERE DROUGHT IN CENTRAL ARGENTINA AND URUGUAY—M. BIDEGAIN

Precipitation was below the 1971–2000 mean during the period November 2007 to December 2008 over a large region in central-east Argentina and Uruguay. This severe drought, which is considered the worst in the last 65 years, affected key agricultural areas in Argentina and Uruguay, producing a sharp decline in grain and meat output. The drought especially hit the 600,000 km^2 of grassland in the Pampas region. The Rural Association estimated that Argentinean grain production would drop by 39% and 1.5 million livestock would be lost, with poor meat and dairy production from the surviving animals. Drought assistance measures adopted by the governments of Argentina and Uruguay included delivery of livestock fodder.

The severe rainfall deficit in this region was illustrated by the record of daily and accumulated precipitation at Salto, located near the border with Argentina in northern Uruguay, where 2008 ended with an annual rainfall total that was 47% below the 1971–2000 mean (Fig. 7.14).

In Uruguay, the hydroelectric sector was also severely affected, with precipitation more than 60% below the long-term mean over the Uruguay (reference period 1979–2005) and Negro (reference period 1950–2000) river basins. During 2008, the level of the reservoirs, which normally are responsible for 80% of the country's energy production along these basins, reached values lower than 20% of their long-term mean. During the 2007 winter, hydroelectric plants satisfied all domestic demand; however, in 2008 the continuing drought forced oil-fired plants into full operation, burning expensive imported oil to feed the power grid.

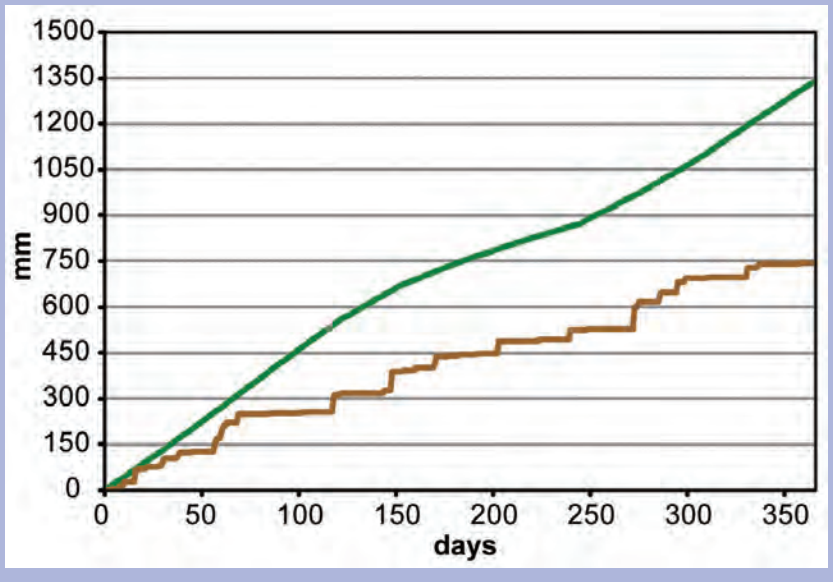

Fig. 7.14. Accumulated rainfall at Salto (Uruguay) during 2008 (brown) an accumulated normal (green). (Source: CIIFEN 2008.)

e. *Africa*

1) Northern Africa—K. Kabidi, A. Sayouri, R. Sebbari, S. Attaher, A. Khalil, and M. Medany

The year 2008 was characterized by several extreme weather events, including periods of heavy rainfall, heat waves, cold outbreaks, and strong winds. Several records were broken and the annual mean temperature for northern Africa continued to rise.

(i) Temperature

In northwest Africa (mainly Morocco, Algeria, Tunisia, and Libya), the annual mean temperature was 1° to 2°C above the 1968–96 normal in many regions. Winter was exceptionally cold with temperatures generally 0.5° to 3°C below normal and daily minimum temperature records broken at many locations. In contrast, spring was more than 2°C above the long-term average over most parts of Morocco. During the summer, exceptional heat waves occurred across the region, with above-average maximum temperatures in several locations. Tanger (Morocco) experienced summer temperatures 3.3°C above normal.

In Egypt, the annual mean temperature was 1.9°C above the 1961–90 reference period (Fig. 7.15). All weather stations across Egypt indicated an annual mean minimum temperature of 1.3° to 5.7°C above normal. Stations on the northern coast recorded annual mean temperature anomalies of –0.5° to –1.2°C, whereas all other stations indicated annual mean temperatures that were 1.2° to 5.6°C above normal. Annual mean maximum temperatures were below normal for northern Egypt with anomalies ranging from –0.2° to –3.9°C. In the central region, the annual mean maximum temperature was 1.3° to 5.5°C above normal.

(ii) Precipitation

In northwest Africa, spring and summer 2008 were characterized by low rainfall totals, with March expe-

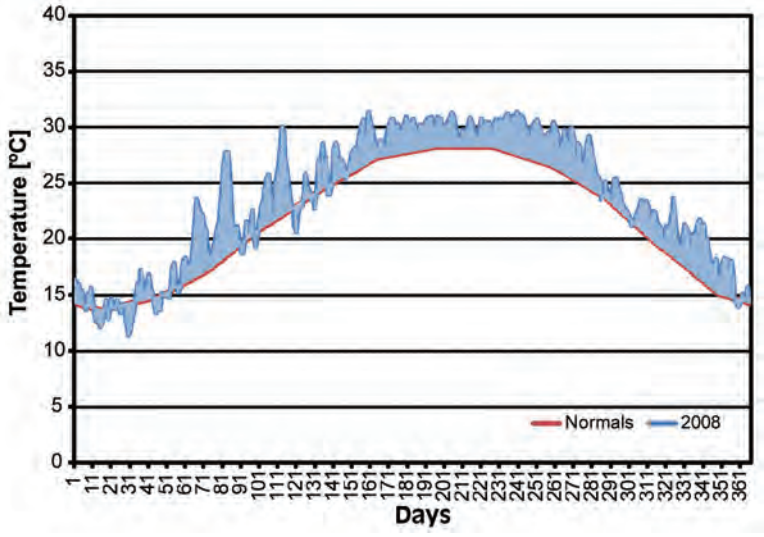

Fig. 7.15. Daily mean temperature for 2008 and the long-term average for Egypt. (Source: Weather Service in Egypt.)

riencing a deficit of more than 90%. However, autumn and winter 2007/08 were characterized by significant rainfall, especially across the northern regions. For October, many weather stations in Morocco, Algeria, and Tunisia reported 24-hr rainfall totals exceeding 200 mm. In Algeria, September, October, and November saw many locations registering monthly rainfalls 4 to 7 times their monthly average. Similarly in Morocco, October and November brought rainfall that was more than 300% of the monthly means. However, in Egypt both the number of the rainy days and the total precipitation for 2008 were near normal.

(iii) Notable events

Several high daytime temperature records were set over the region in 2008. New records were set for Kenitra (Morocco) with a temperature of 49.8°C on 1 July (Fig. 7.16), Tanger Aero with 37°C on 27 June, and 24.4°C on 3 April for Tanger Port. A number of low nighttime records were also broken. For example, Tanger Port recorded 9.7°C on 13 April, and Housaima and Taourirte had a minimum temperature of 7.6°C and 6.8°C, respectively, in October. Heavy precipitation occurred in October, with 24-hr rainfall records set in Larache and Chefchaouen at 108 and 117 mm, respectively, on 31 October, while 200 mm was observed at Tanger Port on 23 October.

In Egypt, strong winds (known as "The Khamaseen") and sandstorms typically occur during February to April. In 2008, there was a large number of these events, with an average wind speed of 8 m s^{-1} and an average horizontal visibility of 4 to 6 km. On 8 June, a sandstorm hit Cairo at noon with wind speeds reaching 11 m s^{-1} and maximum temperatures around 4°C above normal.

2) Western Africa—L. N. Njau, M. A. Bell, and W. M. Thiaw

Western Africa extends from the Guinea coast to Chad and the Central African Republic. 2008 was characterized by above-average rainfall in the west, while below-average rainfall was observed in the southeast.

(i) Temperature

Overall, the annual mean temperature for most of the western Africa countries was near average in 2008. In August 2008, mean temperature anomalies above 1.5°C were observed in northeast Niger, northwest Chad, and western Nigeria and across into Benin, while mean temperature anomalies below –1.5°C were observed in south Mauritania across into Mali.

(ii) Precipitation

Precipitation totals during the May–October 2008 rainy season were mostly near or above the 1971–2000 average in the western sections of the region, except for southeastern Côte d'Ivoire and central Guinea. However, they were below average in several areas farther east, including southeastern Nigeria, Cameroon, eastern Chad, and the central region of the Central African Republic (Fig. 7.17).

The evolution of the rainy season in western Africa was extremely variable. Areas with precipitation deficits during one month would often receive above-

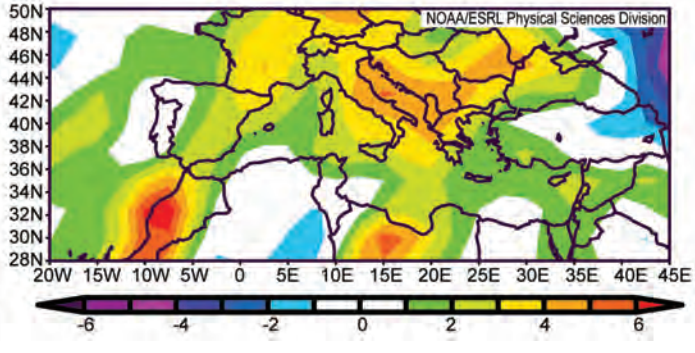

Fig. 7.16. Daily maximum temperature anomalies on 1 Jul 2008 for northern Africa (°C, 1968–96 reference period). (Source: CDC, NOAA.)

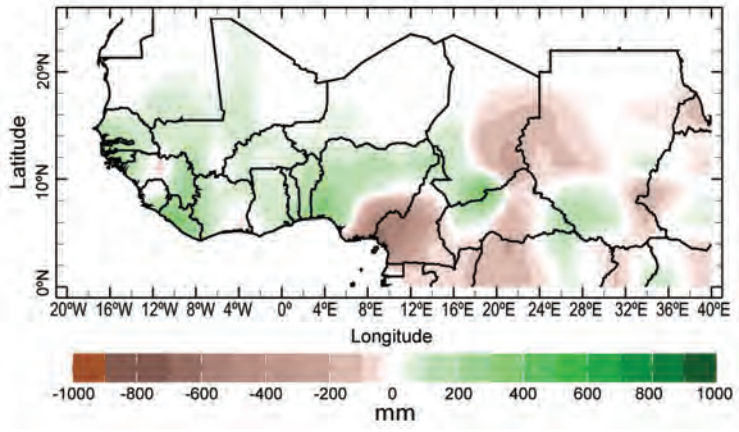

Fig. 7.17. May to Oct 2008 accumulated precipitation anomalies (mm) for western African (1971–2000 reference period). (Source: GPCC, Version 2 Monitoring Product.)

average rainfall during the following month. In April, at the start of the rainy season, monthly precipitation values were as much as 50 mm below the 1971–2000 normal in southern Benin and neighboring areas of Nigeria and Togo. In May, there was a general increase in precipitation totals in the western regions of the Guinea coast (with the exception of southeastern Liberia), with mixed anomalies observed farther east. With the exception of southern Benin and surrounding areas, where precipitation was as much as 150 mm above average at some stations, precipitation along the Guinea coast was below average in June. In contrast, rainfall in the western Sahel, and particularly in Senegal, was well above average, with some stations receiving two and one-half times their mean June total. July also brought significant rainfall to much of western Africa, with notably large accumulations, and some flooding in southern Chad, the western sections of the Central African Republic, and Senegal. Dry conditions continued to develop in July in southeastern Nigeria and much of Cameroon. In August, above-average precipitation was observed across the region but was followed by mixed conditions in September, including another round of heavy precipitation in southern Chad and a general reinforcement of dry conditions in eastern Nigeria and much of Cameroon that persisted into October.

3) Eastern Africa—B. Osman-Elasha, C. Oludhe, and L. Ogallo

Eastern Africa can be divided into three main sectors: southern, equatorial, and northern. The southern sector, which comprises central and southern Tanzania, normally experiences a unimodal type of rainfall regime, with rainfall occurring between December and April. The equatorial sector, made up of northern Tanzania, Kenya, southern Ethiopia, southern Sudan, and southern Somalia, generally exhibits a bimodal rainfall regime, with the "Long Rains" season occurring from March to May and the "Short Rains" occurring between October and December. In the northern sector, comprising central and northern Sudan, northern Ethiopia, Eritrea, and Djibouti, the major rainy season occurs during the months of June to September.

(i) Temperature

In Sudan, the mean temperature was near to below normal from January to April. For the rest of

HEAVY RAINS AND FLOODS IN WESTERN AFRICA—L. N. NJAU

Heavy rainfall across western Africa brought flooding to the region, threatening the homes and livelihoods of more than 50,000 people in seven western African countries during the period from 15 July to 4 August. Six fatalities were reported in Mali, while the rising waters of the Senegal River displaced about 4,600 people in southern Mauritania. In Togo, 10,000 people were displaced by the swollen Hao and Zio Rivers. At least nine deaths were reported as floods submerged several villages in Togo.

In early July, the Red Cross estimated 7,000 people in Benin were affected by floods. Storms during the last week of July affected 9 out of 13 districts in Benin with entire neighborhoods under water. From 30 July to 3 September, the World Health Organization reported 192 cases of cholera in three districts of Cotonou with more than 10,000 people displaced by floods.

On 18 July, at least seven deaths were reported and 2,000 displaced after heavy rains in the Zinder region in Niger, while on 8 August, 30 people died in Burkina Faso after a landslide. In Chad, during the period 20 July to 25 August, over 10,000 people were displaced by floods around the southern town of Sahr.

On 20 July, intense rainfall over the Liberian capital Monrovia resulted in one of the worst floods on record, with nearly 1,000 people forced out of their houses.

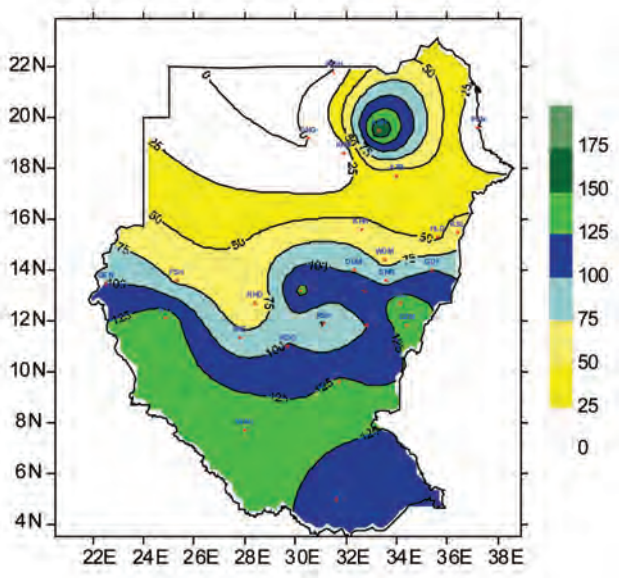

Fig. 7.18. Jun to Sep 2008 Sudan total rainfall expressed in percentage of normal (1971–2000 reference period). (Source: National Weather Service of Sudan.)

the year, mean temperatures were near to above the 1971–2000 average. The highest temperature for the year (48.0°C) was recorded in July at Dongola, located in the northern region, and at Port Sudan on the Red Sea coast. The lowest temperature was 4.0°C reported in February at Dongola.

(ii) Precipitation

In Sudan, the rainy season usually extends from June to September. Rainfall started early in some regions and late in others. From mid-July to mid-August, delayed below-average rains were recorded in the western regions of Kordofan, Gezira, and Kassala states. This resulted in negative impacts to agricultural crops, particularly those planted after the onset of the rains. Timely rainfall with good distribution was experienced in many areas of eastern Sudan, including the Blue Nile, Sennar, and Gadaref states. From mid-August onward, most areas received normal-to-above-normal rainfall, largely compensating for the low rainfall in July and enabling a late planting of crops and hence a general improvement in food security. Normal-to-above-normal rainfall continued until mid-September but shifted to drier-than-average conditions toward the end of the season (Fig. 7.18). Overall, the June to September total rainfall was above the 1971–2000 average in the south, while it was below average in the north of Sudan. In Djibouti, only 3.5 mm of rain was received for the year until 29 October, after which 136 mm fell in the next six days, including 110 mm in the two days 3–4 November, exceeding the annual average.

The GHA consists of southern Sudan, Ethiopia, Uganda, Kenya, Somalia, and Tanzania. In January, much of the southern region (including Uganda, Kenya, and Tanzania) received from 10 mm to over 100 mm of rainfall. March marked the beginning of the "Long Rains" season over the equatorial sector, while most rainfall for the northern GHA occurred in the period from June to August. This season was marked by wet conditions over the central areas of the northern GHA, namely western Ethiopia and southwestern Sudan, where more than 100 mm was recorded during the month of August.

The accumulated totals for selected stations indicate near-average rainfall for the northern sector (Fig. 7.19a), below-average rainfall for the equatorial sector (Fig. 7.19b), and above-average rainfall for the southern sector (Fig. 7.19c). These cumulative rainfalls are used to evaluate water stress over various parts of the GHA regions.

In September, rainfall conditions were associated with poor pastures and water stress for livestock in the eastern and northern regions, improved agricultural

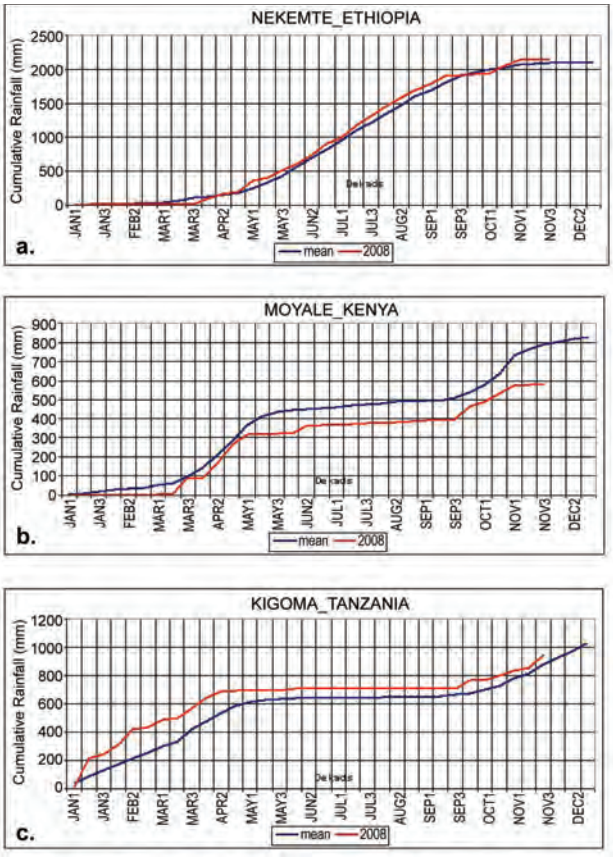

Fig. 7.19. Cumulative rainfall over (a) the northern sector (Nekmite, Ethiopia), (b) the equatorial sector (Moyale, Kenya), and (c) the southern sector (Kigoma, Tanzania). (Source: ICPAC 2008.)

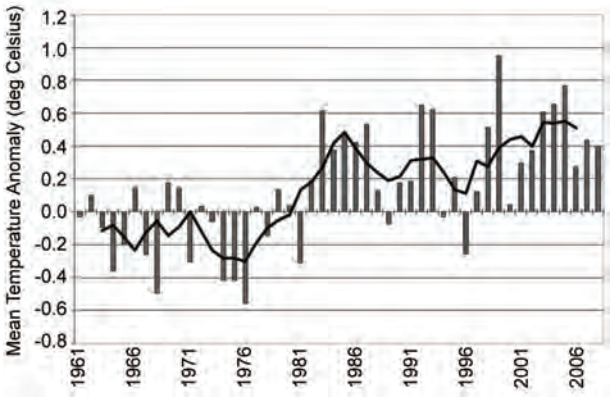

Fig. 7.20. Annual mean temperature anomalies for South Africa, 1961–2008 (1961–90 reference period). The dark line represents a 5-yr running mean. (Source: South African Weather Service.)

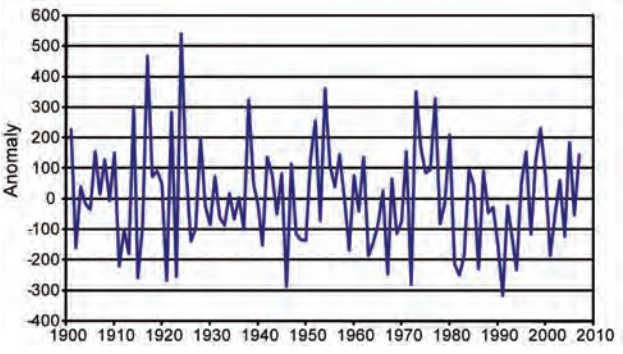

Fig. 7.21. Annual total rainfall anomalies for Zimbabwe, 1900–2008 (mm; 1971–2000 reference period). (Source: Meteorological Service Department of Zimbabwe.)

productivity over the western and northern regions, floods in most parts of the northern and western equatorial regions, and increasing cases of malaria in the western equatorial sector and parts of the northern regions due to an increase in moisture availability and breeding places for mosquitoes.

4) Southern Africa—A. Mhanda, W. Zhakata, C. Mutasa, M. S. Gamedze, A. Kruger, W. M. Thiaw, and C. McBride

(i) Temperature

In Zimbabwe, monthly mean temperatures were close to their long-term (1971–2000) average with no records broken in 2008. However, in Swaziland, the temperatures were warmer than average over most parts of the country. In Lesotho, the year was generally warm, with the annual mean temperature about 0.3°C above normal.

For South Africa, 2008 was approximately the 13th-warmest year since nationwide averages began in 1961 (Fig. 7.20). Monthly mean temperatures were near the 1971–2000 average in most regions. In March, the maximum temperature anomalies were mostly negative over the greater part of the country. Extremely cold conditions over the western and northern interior resulted in numerous new lowest maximum and minimum temperature records for the month. In contrast, May brought mostly positive temperature anomalies over the country. In September, temperatures followed the rainfall pattern with mostly below-average temperatures in the wetter western regions, and above-normal temperatures over the remainder of the country where it was dry. With the exception of the southern and eastern coastal regions, the country experienced above-average temperatures during December.

(ii) Precipitation

In Zimbabwe, the rainy season extends from October to the following April. The Zimbabwe national average rainfall for October 2007 to April 2008 of 795.8 mm was well above the 1971 to 2000 average of 650.7 mm (Fig. 7.21). Although most of the country received normal-to-above-normal rainfall, the temporal distribution was skewed, with the bulk of the rain falling in the first part of the season (October to December 2007), with the second part of the season (February to April) recording below-average totals.

In Swaziland, the rainy season is typically from October until April. The 2007/08 rainy season started late, with drier-than-average conditions during the

Fig. 7.22. Annual total rainfall anomalies for South Africa (expressed as percentage of the 1961–90 average) for Jul 2007 to Jun 2008. (Source: South African Weather Service.)

EXTREME WEATHER IN SOUTH AFRICA—A. KRUGER AND C. MCBRIDE

A number of significant weather events took place in South Africa during 2008 with associated humanitarian and economic consequences. Strong winds with associated wildfires occurred in the Western Cape in January and February. Heavy rains with flooding occurred in the eastern interior in January and cases of heavy rainfall and gale-force winds occurred in February, causing loss of life and building collapses. February also saw one person killed and more than 500 left homeless when a suspected tornado struck in the Eastern Cape, while freak waves on the east coast at Durban drowned one person with 18 others rescued. Incidents of heavy rainfall and flooding in the east continued in March, while in Cape Town a gale-force southeasterly wind fanned wildfires, leaving more than 100 people homeless. In June, floods in the Western Cape displaced a number of residents, while in the eastern province of KwaZulu-Natal, rivers burst their banks and media reported that four people perished. Incidents of heavy rainfall and flooding in the Western Cape continued throughout July.

In August, incidents of wildfires increased over the dry central and eastern regions. In October, unseasonable hailstorms caused widespread destruction in the east in the Mpumalanga province, with significant impacts on the fruit export industry. Several devastating storms, including reports of a tornado, hit the Free State province during November. Eight people died, homes were destroyed, and roads damaged. In December at least 10 wildfires raged over the Cape peninsula, causing extensive damage.

months of December 2007 and January 2008. As this dry spell coincided with the warmest months of the season, a major crop failure occurred in the eastern half of the country. In Lesotho, rainfall amounts were near normal.

In South Africa, the rainy season is October to March over much of the country, but May to September in the southwest. The rainy season from July 2007 to June 2008 was near average for most of the country, with the noteworthy exception of the southwest, which received 150%–200% of its average rainfall. In contrast, locations in the east received less than 75% of their rainy season totals (Fig. 7.22).

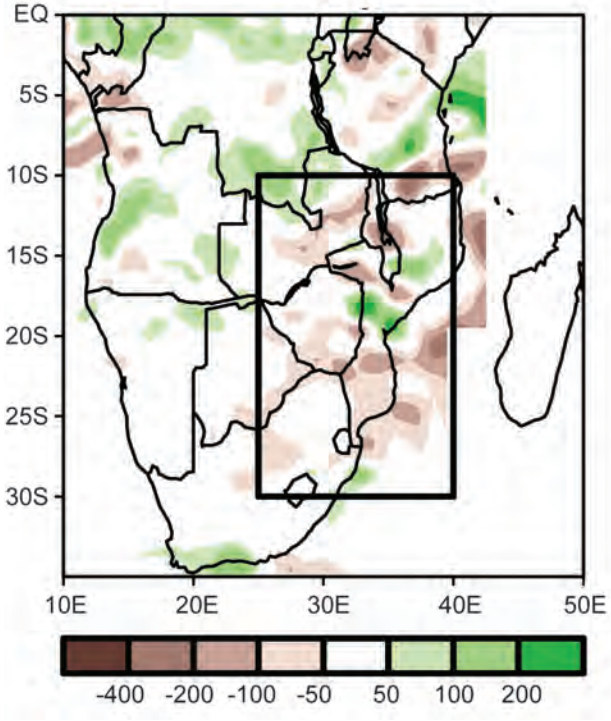

Fig. 7.23. Total rainfall anomalies over southern Africa for Nov 2007 to Apr 2008 (mm). The black box denotes areas that are climatologically wet during summer. (Source: NOAA.)

The southern Africa summer features two basic climate zones. The climatologically wet zone (shown as a box in Fig. 7.23) registered rainfall amounts between 300 and 1,200 mm. Rainfall in the climatologically dry zone, the area that encompasses western South Africa, much of Namibia, and western Botswana, received 100 to 300 mm. Overall, the November to April rainfall season for southern Africa did not exhibit a significant departure from climatology during the 2007–08 season (Fig. 7.23). However, the southern areas of Mozambique and Zimbabwe, southern Zambia, Malawi, and southern Tanzania recorded rainfall totals 50 to 200 mm below normal, while areas of central Mozambique received amounts about 200 mm above average.

f. Europe

1) Overview—A. Obregón, P. Bissolli, J. J. Kennedy, and D. E. Parker

Europe commenced the year under a strong zonal (positive) North Atlantic Oscillation (NAO) pattern, which continued until March, when a blocking pattern developed over Russia resulting in a strong meridional pattern during April. May saw high pressures dominate northern and central Europe, followed by cyclonic conditions during summer across central Europe with frequent thunderstorms. A negative phase of the Arctic Oscillation brought cold Arctic air into

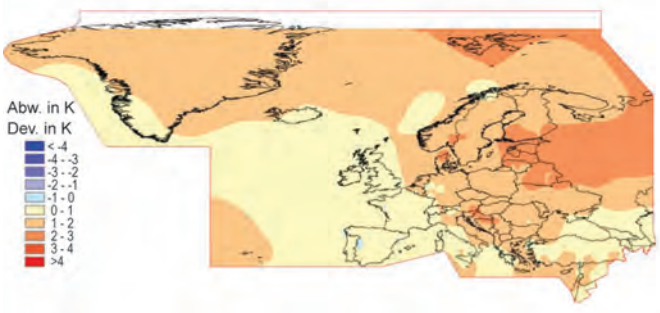

Fig. 7.24. Annual mean temperature anomalies in Europe and over the North Atlantic, 2008 (°C, 1961–90 base period) based on CLIMAT and ship observations. [Source: DWD.]

northeastern, and at times central and southern, Europe from April to September. Conversely, southwesterly flow during summer across southeastern Europe resulted in several heat waves. In October, a blocking pattern established over Russia and remained for much of the year, producing mild conditions over eastern Europe and colder air masses over western Europe. In November, a deep trough extended from Scandinavia to Iberia. The year ended with very cold air flowing from the high latitudes to southeastern Europe and the Middle East on the eastern flank of a central European high pressure system.

Overall, warmer-than-average conditions in 2008 extended across most of Europe.[2] The mean land surface temperature for the European region (35°–75°N, 10°W–30°E), derived from the CRUTEM3 dataset (Brohan et al. 2006), was 1.16° ± 0.17°C above the 1961–90 mean. This made 2008 (with 2006) the fourth-warmest year for Europe since 1850. The highest temperature anomalies occurred in Svalbard, the Baltic countries, eastern Europe, and parts of southern Fennoscandia, where anomalies exceeded +2°C (Fig. 7.24). Lithuania reported its warmest year, while Latvia and Denmark experienced their second-warmest year since records began. Only a few places in southwestern Europe reported a cooler-than-average temperature in 2008.

Rainfall for Europe during 2008 was unevenly distributed both spatially and temporally (Figs. 7.25a–d), and the year was characterized by several notable storm events with some extremely intense and heavy precipitation. Annual precipitation (Fig. 7.26) was mainly above the long-term (1951–2000) average in northern and western parts of Europe and below average in southern Europe. Less than 80% of normal precipitation was observed in Bulgaria, Greece, and the Middle East. Some areas of Finland, Sweden, the United Kingdom, and Ireland received over 125% of normal precipitation.

Winter featured a dipole structure, with warmer-than-normal conditions and above-average rainfall in northern parts of Europe and closer-to-average temperatures and very dry conditions in southern Europe (Figs 7.27a, 7.25a). Iberia in particular was affected by severe drought conditions during February. Southwesterly winds were predominant during the winter and coincided with anomalously high sea surface temperatures in the North Atlantic. This led to an exceptionally warm winter in most of northern Europe with many temperature records broken. In contrast, unusually cold and dry conditions prevailed during winter across the Middle East (see section 7g).

During spring, temperatures were mostly above average across Europe with the highest positive anomalies over eastern Europe (Fig. 7.27b). Temperatures during May were well above average in central and western Europe (Fig. 7.28). Eastern Europe, France, and Iberia received above-normal rainfall during the spring, while precipitation in central Europe and

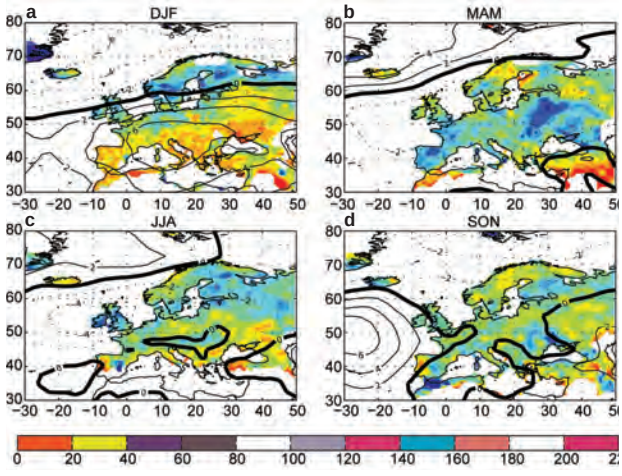

Fig. 7.25. Seasonal anomalies (1961–90 reference period) of sea level pressure (contour, hPa) using data from the NCAR–NCEP reanalysis. The colored shading represents percentage of accumulated seasonal precipitation compared with the 1951–2000 climatology using the seasonal GPCC precipitation data set: (a) winter (Dec 2007–Feb 2008), (b) spring (Mar–May 2008), (c) summer (Jun–Aug 2008), and (d) autumn (Sep–Nov 2008). Some intense precipitation anomalies in the southern Mediterranean during seasons when it usually rains very small amounts are filtered out.

[2] The standard reference period used for European averages is 1961–90 for temperature, and 1951–2000 for precipitation, unless otherwise expressly identified.

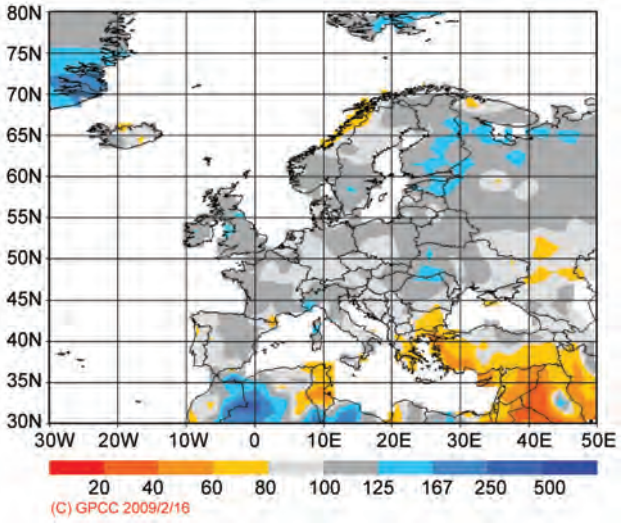

Fig. 7.26. European precipitation totals (percentages of normal, 1951–2000 base period) for the whole year 2008. (Source: GPCC; Rudolf et al. 2005.)

parts of northern Europe was close to or below the long-term average. Precipitation was particularly low in central Europe during May (Fig. 7.29).

During summer 2008, eastern Europe and northern parts of the Balkan Peninsula experienced well-above-average temperatures, with August being a particularly hot month. Conversely, August was colder than normal over northeastern Europe, particularly in Finland and northern Russia (Fig. 7.30). Summer was dry for the southern parts of Europe, particularly over western Iberia and Turkey [see section 7g4(iii)], while northern European regions received mainly above-average rainfall.

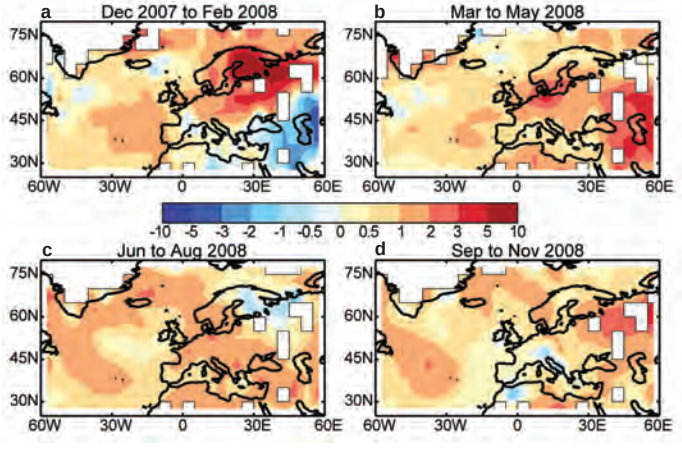

Fig. 7.27. European surface air temperature anomalies (°C, 1961–90 base period) from HadCRUT3 for (a) Dec 2007–Feb 2008, (b) Mar–May 2008, (c) Jun–Aug 2008, and (d) Sep–Nov 2008.

During autumn, the highest temperature anomalies occurred over the Arctic and the eastern and southeastern parts of Europe, while western Europe was average to colder than average. Iberia in particular had an extremely cold November.

The year ended with colder-than-average conditions over virtually all of western Europe and the Middle East. Anomalous warmth was widespread over northern, eastern, and southeastern Europe. December was drier than normal in most parts of Europe, but very wet south of the Alps and over the central Mediterranean.

2) Central and Western Europe—A. Obregón, P. Bissolli, J. J. Kennedy, and D. E. Parker

(i) Temperature

Warmer-than-average temperatures affected central Europe during 2008. At stations in Slovakia, 2008 was the warmest year since records began in 1871. In most parts of Austria, 2008 ranked among the five warmest years. Due to frequent southerly foehn events, valleys in the northern Alpine region experienced temperature anomalies above +1.3°C. In Germany, Austria, Switzerland, and the Czech Republic, September was the only month that recorded below-average temperatures.

Over western Europe, annual temperature anomalies were generally lower than in central regions. For the United Kingdom and Ireland, despite temperatures 0.6°C above normal, 2008 was one of the coldest years in the last decade. France experienced mean temperature anomalies of around +0.4°C, while the Netherlands recorded +0.8°C.

In Germany, the mean winter anomaly of +2.7°C was the sixth warmest on record. Belgium reported its fourth-warmest winter (+2.1°C anomaly), while the winter temperature anomaly for the United Kingdom was +1.6°C, which, although high, was cooler than in 2006/07. January was particularly mild throughout western and central Europe.

Much of Europe was also warmer than average during May (Fig. 7.28). It was the warmest May on record in the United Kingdom, at most stations in Ireland, Uccle (Belgium), and Luxembourg. May was also exceptionally warm across Switzerland and the Netherlands—it was the warmest May in De Bilt for more than a century—and it was the fourth-warmest May on record for France. On 28 May, a heat wave in Graz (Austria) saw a new May record temperature of 34.9°C.

In contrast, summer was one of the coldest since the turn of the century, particularly over

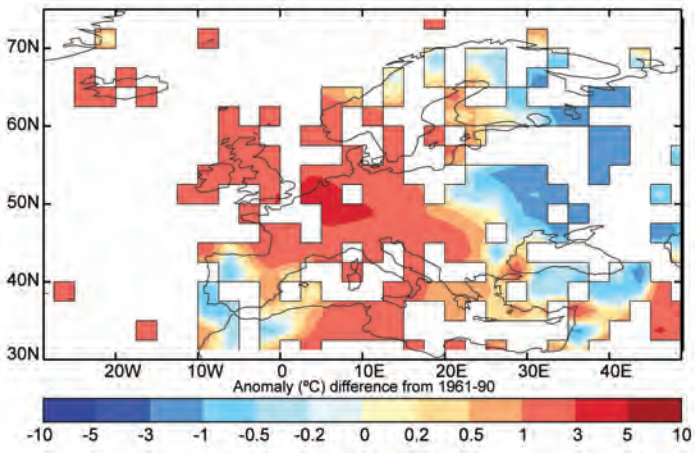

Fig. 7.28. May 2008 mean temperature anomalies in Europe, (°C, 1961–90 base period), based on CRUTEM3 dataset (Source: Brohan et al. 2006).

western Europe. Despite such relatively cold conditions, temperatures were still above the 1961–90 average throughout most of central and western Europe, with anomalies generally around +1°C.

In September, most countries were approximately 1°C cooler than average. In western Europe, the cold conditions continued into October. It was the coldest autumn at many stations in Ireland for 10 years and in the United Kingdom for 15 years. During the last week of October, some stations in the United Kingdom set new October records for low maximum temperatures. In contrast, Switzerland was warmer than average, with temperatures up to 20°C on the plains and 15°C at elevations of 1500 m. November ended with a cold spell across western and central Europe. On 29 November, the average Northern Ireland maximum temperature (1.9°C) was the lowest November maximum temperature since such records began in 1960.

December 2008 was colder than normal over western Europe (–2°C and below in western France) and up to +3°C warmer than normal in the east. It was the coldest December since 1996 for Northern Ireland. It was also a sunny month especially in northern parts of central Europe. In the Netherlands (station De Bilt) it was the sunniest December since records began in 1901.

(ii) Precipitation

In 2008, above-average precipitation was recorded over most of western Europe and northern parts of central Europe. The United Kingdom experienced its third-wettest year in a national rainfall series that begins in 1914, with 118% of the 1961–90 annual mean rainfall. Rainfall totals in Ireland were well above average. Shannon Airport recorded its highest precipitation total since observations began in 1945. In central Europe, precipitation was close to or slightly below average, with the exceptions being eastern Austria (>110%) and the southern Alpine region (120%–140%).

Due to mild temperatures during the winter, no snowfall was measured during all three winter months at most locations in central and western lowland parts of Switzerland. Basel and Geneva registered their first snowfall of the year at the end of March, the latest arrival of snow since measurements began in 1931. Austria, too, received little snow, just 10%–30% of the winter average.

During January, precipitation exceeded 250% of average in parts of northern England and southern Scotland. It was the wettest January in eastern Scotland and the second wettest in Northern Ireland since 1914. Poland was also exceptionally wet during January. In contrast, February was dry over Austria, especially in the southeast (<25% of the 1961–90 mean) and in parts of Switzerland and southern France (around 50% or less).

England experienced its wettest March since 1981, Scotland since 1994. Luxembourg reported 185% of normal rainfall in March, the Czech Republic 153%, northeastern Poland and parts of upper Austria more than 200%, while March brought more snow to Austria than the preceding winter months. In contrast, May was exceptionally dry in Ireland, most of the United Kingdom except the south, and most of central Europe. It was the third-driest May in Germany since 1901 and the driest since 1919.

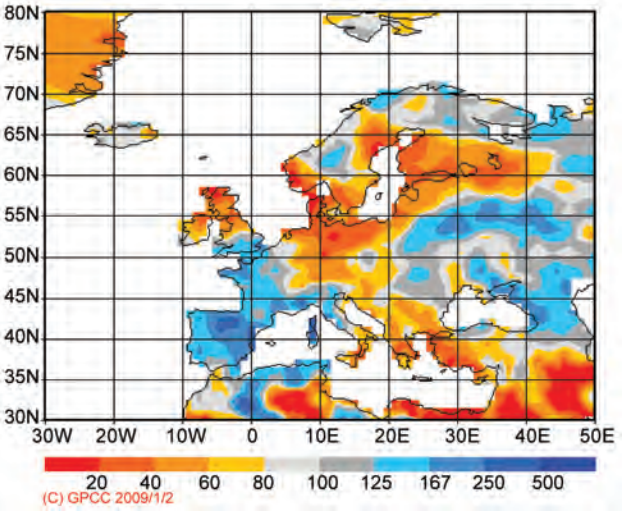

Fig. 7.29. European precipitation anomalies (percentages of normal, 1951–2000 base period) in May 2008. (Source: GPCC; Rudolf et al. 2005.)

Summer precipitation was more than 167% of normal in eastern Ireland. Dublin Airport experienced its wettest summer in 50 years. In June, 300% of the 1961–90 normal precipitation fell south of Vienna and parts of eastern Austria registered their wettest summer on record. Poland was very dry in June. In Lugano, Switzerland, it was the second-wettest July since 1864 (359 mm). The Netherlands reported 111 mm of rainfall in July (70 mm average) and 100 mm in August (82 mm average). August was very wet across northern and central France, much of the United Kingdom (154%), and Ireland. In Northern Ireland, it was the wettest August since records began in 1914 (anomaly 213%).

In September, some stations in England recorded around 300% of their monthly normal (1961–90) rainfall. Scotland experienced its fourth-wettest October on record and the wettest since 1954. Luxembourg Airport reported 162% of average (1971–2000) precipitation in September and set new records for hourly and daily rainfall amounts. During a cold spell at the end of October, snow was registered in many places. London received snow in October for the first time since 1934. New record fresh snow depths for this month were also measured on 30 October in many places in Switzerland; October snow events are extremely rare in the lowlands of Switzerland. A fresh snow depth of 20 cm in Zurich beat the previous October record of 14 cm set in 1931. Between 31 October and 2 November, France was affected by flooding after up to 500 mm of precipitation fell in the region west of the Rhône River in the southeast of the country.

December brought a record snow depth for that month of 38 cm in Switzerland's capital Bern. In Austria, a new record snow depth for December of 125 cm was reported from eastern Tyrol's capital Lienz. December precipitation was also well above average in southeast France and was up to 400% of normal over southern Austria, largely due to persistent low pressure in the Gulf of Genoa. Southern Alpine regions experienced heavy snowfalls until the middle of the month.

(iii) Notable events

Heavy storms occurred over central Europe between 26 and 28 January. Gusts of up to 46 m s^{-1} were measured in Austria, where the storm Paula caused massive forestry losses. On 1 March, another storm, Emma, brought strong winds to western and central areas, reaching hurricane strength over the mountains and bringing heavy precipitation with local flooding. Infrastructure disruptions and at least 14 fatalities were reported. Strong winds also affected the United Kingdom, France, and Germany on 10–12 March and a pressure of 953.6 hPa was recorded in Northern Ireland, the lowest since 1995.

Snow fell over much of the region during a cold spell on 20–26 March. In some places over central Europe, it was the coldest Easter on record. Temperatures remained below 0°C at many stations in Germany and Switzerland on Easter Sunday.

Tennis-ball-size hail was reported in western Germany on 30 May. On 22 June, thundery showers with strong gusts and hailstones of approximately 5-cm diameter caused much damage in the eastern Netherlands. Unusually heavy thunderstorms with hailstorms occurred in Austria in all three summer months, causing flooding and large agricultural losses. During August, several tornadoes occurred in northern Germany and France, Belgium, and the Netherlands.

3) The Nordic and Baltic countries—C. Achberger, A. Walther, D. Chen, A. Obregón, P. Bissolli, J. J. Kennedy, and D. E. Parker

(i) Temperature

Similar to recent years, annual temperatures over the Nordic region (Denmark, Finland, Iceland, Norway, and Sweden, including the European Arctic) and the Baltic countries were characterized by positive anomalies. They ranged between 0° and +1°C for Iceland and the Faroe Islands, +1° and +2°C in most of Fennoscandia and Denmark, and +2° and +3°C for Svalbard, southeastern Norway, southern Finland, and most of the Baltic States (Fig. 7.24). This was mainly due to exceptionally high temperatures during the winter of 2007/08 (Fig. 7.27).

Widespread anomalous warmth was present over the European Arctic in 2008. The island Hopen, in the Svalbard archipelago, experienced a temperature anomaly of +2.8°C. The island of Jan Mayen (northeast of Iceland) had an annual average temperature of 0.7°C, 2.1°C above normal.

For Iceland, 2008 was the 13th consecutive warmer-than-average year. The Icelandic capital Reykjavik reported an annual temperature anomaly of +1.0°C. Temperatures during May to September were unusually high in the south and west. Reykjavik reported a new all-time record of daily maximum temperature at 25.7°C on 30 July. In September, Reykjavik was more than 3°C warmer than normal. October was the only colder-than-average month on Iceland.

In Norway, Sweden, and Denmark, annual mean temperatures were well above normal (Norway:

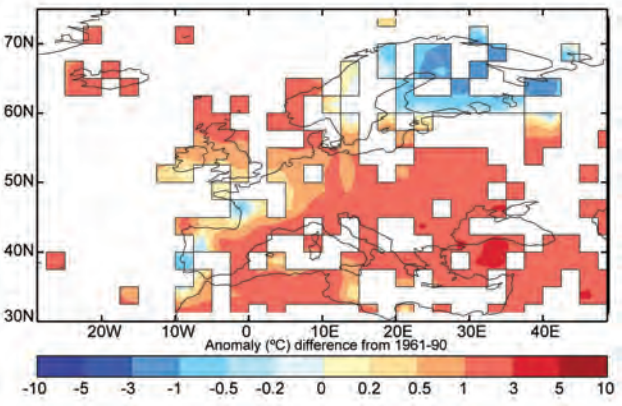

Fig. 7.30. Aug 2008 mean temperature anomalies in Europe (°C, 1961–90 base period), based on CRUTEM3 dataset (Source: Brohan et al. 2006).

+1.4°C; Sweden: +1° to +2.5°C). It was the second-warmest year in Denmark (along with 2006), with an annual mean temperature of 9.4°C, +1.7°C above normal. The last three years were the warmest ever recorded in Denmark.

For Finland, 2008 was among the six warmest years since measurements started in 1850. Southwestern and most of southern Finland experienced the warmest year in those areas since 1961, while the capital, Helsinki, set a new mean temperature record (7.6°C). For the first time since temperature measurements started in Helsinki in 1829, all monthly mean temperatures were above 0°C.

It was the warmest year in Lithuania, where the annual mean air temperature of 8.2°C was 2°C higher than the 1961–90 average. Latvia reported its second-warmest year over the last 85 years (+1.8°C anomaly).

(ii) Precipitation

Precipitation during 2008 was mostly above the long-term average. The highest anomalies occurred in southeastern and southwestern Finland, where precipitation was 150%–200% of the 1961–90 normal. In Kemiö, 1,064 mm of precipitation was recorded, the second-highest total recorded in Finland in the last hundred years. However, due to mild temperatures, only 20–30 snow days (where a snow day is a day with at least 1 cm of snow lying on the ground) were recorded in southern and southwestern Finland during winter, well below the normal of more than 70 days. Latvia had an annual precipitation total of 757 mm (115% of normal). In Sweden, precipitation totals locally reached 175% of normal partly due to a wet winter. Denmark received 110% of normal precipitation; a very dry May partly compensated for wet conditions during January, March, and August. Annual precipitation was close to normal in Norway, although some southern parts received 50% more than normal. Parts of the European Arctic experienced well-above-average precipitation. Ny-Ålesund on Svalbard reported 128% of average precipitation. On Iceland, precipitation was close to normal in the north and east, but for the southwest of the island, 2008 was a wet year (Reykjavik 117%). Tórshavn on the Faroe Islands had 115% of the 1961–90 normal rainfall.

Winter 2007/08 proved to be much wetter than normal across the Nordic countries. Norway experienced over 145% of normal, parts of eastern and northern Norway over 200%; Denmark received 125% of normal. Lithuania recorded more than 150% of the normal (1961–90) monthly total in both January and February. April was dry in Iceland, with Stykkishólmur experiencing its driest April since 1951. May was a significantly dry month in most of the Nordic region, especially Denmark, southern Finland, and the Baltic States (Fig. 7.29). Denmark had its fourth-driest May on record with only 13 mm of precipitation averaged over the country (normal 48 mm).

Summer was wetter than average in Finland, most of Sweden, and Denmark, mainly due to an exceptionally wet August (218% anomaly from 1961–90 in Denmark, the wettest August in 40 years). June was exceptionally dry in Reykjavik (30% of normal).

Large parts of Sweden received less than 25 mm of precipitation in September, which is less than 40% of normal. Lithuania saw less than half its normal (1961–90) precipitation in September. In contrast, September was a very wet month for Reykjavik (>250% of the normal), and Stykkishólmur on the west coast recorded its wettest September since 1856.

The year ended with a drier-than-normal December, especially on the west coasts of Norway, Sweden, and Denmark.

(iii) Notable events

Norway's capital Oslo was affected by some heavy storms in 2008. On 1 February, a snowstorm forced Oslo's airport to close for several hours. On 5 July, the city was again affected by an intense thunderstorm causing heavy rainfall and flooding. Gusts up to 27 m s^{-1} were reported. Gothenburg, Sweden, was hit by a heavy storm with hurricane-strength winds on 22 February, disrupting power for many hours. The severe storm also reached the coast of Lithuania with local wind speeds of 28–30 m s^{-1}.

MILD WINTER IN NORTHERN EUROPE—C. ACHBERGER, A. WALTHER, D. CHEN, A. OBREGÓN, P. BISSOLLI, J. J. KENNEDY, AND D. E. PARKER

Winter (December 2007–February 2008) was remarkably mild in the northern European region, mainly due to a dominant southwesterly flow, in conjunction with anomalously high sea surface temperatures in the North Atlantic. This was consistent with an ongoing positive phase of the winter North Atlantic Oscillation, which was +1.37 for December 2007–March 2008 (Jones et al. 1997; Fig. 7.31).

Mean temperature anomalies ranged between +3° and +4°C in southern Scandinavia and exceeded +4°C in eastern Sweden and most parts of Finland and the Baltic countries (Fig. 7.27a; please note the inclusion of SST anomalies in this map is likely to have diluted the coastal land air temperature anomalies in cases of sharp local anomaly contrasts, e.g., Norway). Finland experienced temperatures 4° to 6.5°C above the 1971–2000 average, some 1°C higher than the previous record set in 1925. The number of winter days (daily mean temperature below 0°C) was significantly lower than normal through central and southern Finland. There was hardly any ice cover in the Baltic Sea and no permanent snow cover in most of southern Finland. Average temperatures in Latvia were 5°C above the long-term mean. Svalbard Airport reported temperature anomalies of +7.8° and +7.3°C in January and February, respectively.

In most parts of Finland, Sweden, and the Baltic States, winter 2007/08 was the warmest in recorded history. In Norway, it was the third-warmest winter on record for the country as a whole; Denmark experienced its fourth-warmest winter and had only 18 frost days on an areal average (normal is 53). In the vicinity of Stockholm, winter was the warmest in some local series going back to the eighteenth century.

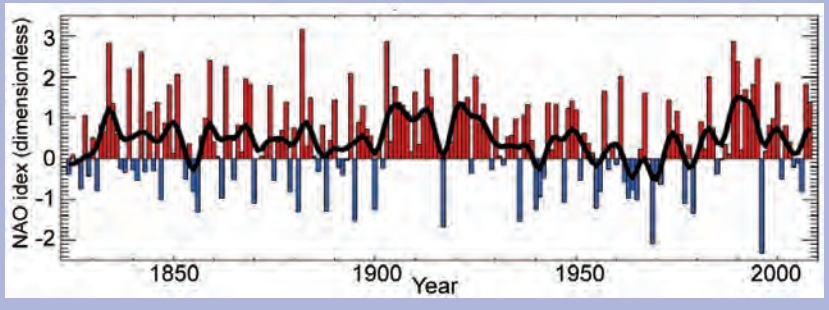

FIG. 7.31. Time series of winter NAO (after Jones et al. 1997, Dec to Mar average). Image from www.cru.uea.ac.uk/~timo/projpages/nao_update.htm, updated 27 Jan 2009.

4) IBERIA—R. M. Trigo, D. Barriopedro, C. C. Gouveia, A. Obregón, P. Bissolli, J. J. Kennedy, and D. E. Parker

(i) Temperature

Although annual temperatures in Spain were slightly above average, it was the coldest year since 1996. Portugal was about 0.2°C cooler than the 1971–2000 average.

However, these annual anomalies conceal important spatial and seasonal differences. Winter 2007/08, for instance, was much warmer than average, with Seville experiencing its warmest winter since 1951. January was a particularly warm month throughout Iberia. For Portugal, the January anomaly of +1.5°C was the second warmest since 1931 (Instituto de Meteorologia 2009). Averaged over continental Spain, January mean temperatures were 1.7°C above the 1971–2000 average. The month of February was extremely mild for the southern Spanish cities of Seville, Cordoba, and Cadiz as well as for the northwestern (Galicia) stations of Santiago and La Coruña, which registered new monthly records in time series longer than 60 years.

In contrast, autumn brought significant negative anomalies with minimum temperatures in Portugal being the third coolest since 1931 (Instituto de Meteorologia 2009), largely dominated by an extremely cold November, particularly in the later days of the month. Monthly mean temperature anomalies in Portugal generally ranged between –1.5° and –2.5°C, while Spain experienced its coldest autumn since 1993.

Spring was relatively warm (+0.44°C) over Iberia and was followed by a slightly warmer-than-average summer (+0.22°C). In Portugal, it was the 15th consecutive spring with temperature anomalies above the 1971–2000 average. June was exceptionally warm over the Atlantic Spanish archipelago of Canary Islands. Monthly records were broken, including in the approximately 90-yr series of Santa Cruz de Tenerife.

(ii) Precipitation

The Iberian Peninsula generally experienced below-average rainfall in 2008, with the largest anomalies more than 20% below the long-term mean over the northern half of Portugal. In the northeast-

ern regions of Spain, annual precipitation was slightly above average. The 2008 accumulated precipitation over the Iberian Peninsula was slightly less (around 5%) than the 1961–90 average. The year was generally characterized by periods of drought interspersed with local heavy rainfalls. From April to June and September to November, a new record daily precipitation for the respective month was set for at least one Spanish station.

Iberia experienced drier-than-average conditions during winter 2007/08, with large areas receiving less than 60% of the average (Fig. 7.25). These conditions were related to positive mean sea level pressure anomalies over western Europe and northern Africa, which, combined with 500-hPa geopotential height anomalies, suggested the northern European blocking pattern was shifted slightly southward, a feature that limits the natural progression of Atlantic low pressure systems bound for southern Europe (Trigo et al. 2004). Portugal suffered its most severe winter drought since 1917. Drought conditions in Spain prevailed until mid-April, making it Spain's worst drought for over half a century.

The following seasons revealed a very different pattern, with most of Iberia recording above-average spring rainfall (Fig. 7.25b), while there were below- (above) normal values over western (eastern) Iberia in summer and autumn. Most of the rainfall in spring occurred in the latter part of the season, although northeastern Spain was wet during March. Spring rainfall exceeded 125% of normal over most parts of Iberia, with several new records of monthly precipitation. Records set in March were largely confined to the Basque country stations of Bilbao (215 mm) and San Sebastián (238 mm); however, during the following months several new all-time records of accumulated monthly precipitation were observed over a wider area of southern (April) and coastal Mediterranean (May) provinces, including stations with more than 100 years of data (e.g., Tortosa). May was the wettest since 1971 in Spain. Heavy precipitation caused flooding in the northeast of the country.

Summer in the southwestern half of Iberia was markedly dry. Southern Portugal received less than 10 mm of precipitation, less than 20% of average. In contrast, parts of eastern Iberia were characterized by above-average summer precipitation totals, although it must be remembered that Iberia is typically extremely dry in summer.

During autumn, Portugal experienced locally very heavy rainfalls. Faro on the southern Atlantic coast set a new record of 80.4 mm within 24 hr from 28 to 29 September, while its monthly total of 147.3 mm was also its highest rainfall for September since records began in 1965. At the end of September, the heaviest rainfall for 30 years in eastern Spain caused local flooding. Valencia received an hourly rainfall amount of 144 mm, and 390 mm over 24 hr. The Gibraltar Strait also registered an extremely wet period during autumn. New daily records were set for the Spanish enclave city of Melilla (60-yr time series), with 92.7 mm on 26 September far surpassing the previous maximum of 29.4 mm. New monthly record values were also set in September (Melilla and Cadiz) and October (Melilla; see also section 7e for details on Morocco).

Despite locally heavy rainfall in Portugal, it was generally very dry between October and December. From 28 November to 3 December, there was snow during a cold spell in areas above 600 m in Portugal. The southernmost coast of Iberia was (relative to normal) much drier than the rest of Iberia in spring and much wetter in autumn.

5) Mediterranean, Italian, and Balkan Peninsulas and Eastern Europe—A. Obregón, P. Bissolli, J. J. Kennedy, and D. E. Parker

(i) Temperature

2008 was 1° to 2°C warmer than normal over most of eastern and southeastern Europe. In Belarus, anomalies exceeded +2°C, while anomalies in southern Greece, Sicily, and parts of the Italian peninsula were below +1°C. On the Balkan Peninsula, the highest departures from the normal were observed in Bosnia and Herzegovina and northern parts of Croatia. Across most of Croatia, temperatures exceeded the 98th percentile of the 1961–90 distribution. In Zagreb, 2008 was the third-warmest year after 2000 and 2007, and in Split, it was the fifth. New records of absolute maxima were recorded in Serbia in February, May, and September for several locations throughout the country.

In winter, anomalies exceeded +2°C in northern parts of Ukraine and +3°C in Belarus and northern Russia (Fig. 7.27a). Temperatures across Italy and the Balkan Peninsula were closer to the long-term mean. However, an exceptionally low number of freezing days was recorded during January in Serbia, while January was also the mildest in Moscow for 130 years (see section 7g).

Over the rest of the year, the highest temperature anomalies generally occurred over eastern Europe and northern parts of the Balkan Peninsula, while anomalies farther to the south were less pronounced. March was a particularly warm month in parts of the Balkan Peninsula and eastern Europe. In most

parts of eastern Europe, monthly mean temperature anomalies exceeded +3°C. Out of all months in Athens, the highest positive anomaly was observed in March (>3°C). In Italy, the cities of Verona (27.2°C) and Ferrara (27.6°C) reported new record high March temperatures. Spring temperatures in Montenegro were in the upper decile of the 1961–90 distribution in coastal areas and northeastern parts. Farther south, a maximum temperature of 37.4°C was recorded on Crete on 22 April, one of the highest April temperatures ever measured there. At the end of May, warm Saharan air led to high temperatures in southeastern Europe. Chirpan, Bulgaria, experienced 36.2°C, and Palermo, Sicily, 38.9°C.

The summer was very warm in parts of the northern Balkan Peninsula, although heat waves were less severe than in 2007. Serbia recorded heat waves from 26 May to 3 June and from 20–27 June, while in August, its number of tropical days (>20°C) was twice the long-term average. Mean temperature anomalies in Serbia, Bosnia, and Herzegovina as well as in Montenegro ranged around +2°C and exceeded the 98th percentile in most parts. Summer temperatures were also well above average in Athens, with highest deviations in August, which was also particularly hot in Ukraine, Romania, and Bulgaria (Fig. 7.30).

For many areas, September was the only cooler-than-average month of 2008. However, Serbia experienced a heat wave at the beginning of the month with widespread new record maximum September temperatures of more than 37°C, although cooler conditions prevailed in the second half of the month. October was unusually warm across eastern Europe. Unusually high temperatures of around 30°C occurred in southern Greece on 2 November. In December, monthly mean temperature anomalies of more than +2°C were observed across most of the Balkan Peninsula, locally reaching more than +3°C.

(ii) Precipitation

In 2008, rainfall deficits were observed across the Italian and Balkan Peninsulas, while precipitation was above average in Belarus and parts of Russia and Romania. Corsica in the western Mediterranean was wet in 2008; annual rainfall totals were the highest in more than 40 years. The annual total rainfall in Athens was 87% of the 1961–90 average. Croatia, too, had a deficit in annual rainfall, especially in northern parts and southern coastal areas. Precipitation in Dubrovnik was below the 10th percentile (1961–90 base period). It was also dry in most parts of Serbia, where the annual total, as well as the number of rain and snow days, was low.

Winter was characterized by significantly below-normal rainfall across most of the region (Fig. 7.25a). At some locations in Montenegro and Croatia, seasonal rainfall was 40% of average. February was exceptionally dry in Romania and parts of Bulgaria, Greece, Serbia, and Croatia, where less than 20% of normal precipitation fell in many places. Much of Romania received less than 10%, while Sofia received only 1 mm during the whole month. Monthly precipitation in Athens was about 25% of normal.

April was exceptionally wet across the Ukraine and large parts of Bulgaria and Greece. Precipitation across Bulgaria was mainly above 150% of normal, while Athens received double the normal amount of rainfall. Northern Italy experienced two very intense rain periods in May and June. It was the fifth-wettest May in Bologna since 1937. Summer was very dry in the south of the region, particularly in Bulgaria and Greece (Fig. 7.25c). September was exceptionally wet in the Ukraine (>200% of the 1961–90 normal over most of the country), Bulgaria, and parts of Greece. Athens received 300% of the September normal. Precipitation from October onward was generally closer to average, except for anomalously high totals in Italy and Croatia during December.

(iii) Notable events

Southeastern Europe was hit by an intense storm with heavy snowfall on 3 January, with the Black Sea harbors and the main airports of Romania closed. On 17 February, more than 25 villages in Greece were cut off by heavy snowfall, and Athens was covered by several centimeters of snow. During 22–29 July, torrential rainfall affected parts of Ukraine and Romania. Farmland was destroyed and 50,000 houses were affected by flooding. Thirty-four fatalities were reported, while 350 mm of precipitation fell over northern Italy close to Bologna between 28 October and 1 November.

Between 10 and 12 December, a storm system brought heavy rainfall and strong winds to Italy causing flooding in several places. Rainfall around Rome was particularly high. Cumulative rainfall totals over three days exceeded the monthly average.

6) Middle East—A. Obregón, P. Bissolli, J. J. Kennedy, and D. E. Parker

Detailed summaries for Turkey, Iran, and Iraq may be found in part 4 (Southwest Asia) of section g (Asia) of this chapter.

(i) Temperature

Annual temperatures across the Middle East were generally 0° to 1°C above normal, although anoma-

lies in Cyprus, southern Turkey, and parts of Syria, Lebanon, and Israel exceeded +1°C.

In contrast to most of continental Europe, the Middle East region experienced well-below-average temperatures during winter (Fig. 7.27a). Mean temperature anomalies were generally between –2° and –1°C in Georgia and Armenia, with local values in some areas below –2°C. In parts of Syria, Israel, and Jordan, mean temperatures were between 0° and 1°C below the long-term average. During the first weeks of the year, extreme low temperatures prevailed across much of the Middle East region. In January, parts of Georgia experienced one of the coldest nights for 10 years, with temperatures dropping to –10°C in the capital Tbilisi and to –25°C in mountainous areas. Severe frost was also reported in southern Israel and Jordan. In Syria's capital Damascus (608 m above sea level) nighttime temperatures fell to –11°C in mid-January, 11.5°C below the average minimum temperature for January and the lowest January temperature since 1982. Mean temperatures across Cyprus were around 1°C below normal in January, with widespread ground frost during the first half of the month causing damage to crops.

Spring temperature anomalies were generally positive across the region and exceeded +2°C in the eastern Caucasus, Syria, and Jordan. March temperatures were around 4°C above normal in Cyprus, where temperatures reached 33°C at the end of the month. In April, several heat waves occurred across the Middle East, while temperatures exceeding 40°C affected Cyprus in the second half of July and during the last week of August. The remainder of the year was generally warmer than average across the region, though anomalies tended to be smaller than at other times of the year.

(ii) Precipitation

Drier-than-average conditions affected most of the Middle East region in 2008 (Fig. 7.26). Precipitation anomalies ranged between 40% and 60% of normal in Cyprus and in parts of Jordan and Syria. For Cyprus, it was its second-driest year since 1901, with the country now suffering three consecutive years of drought and, as a result, severe water shortages. Long dry spells in Cyprus during winter caused a decrease in crop production, while snow fell in areas above 100 m elevation several times in January and February. Annual rainfall was 60%–80% of average in Lebanon, Israel, and parts of Turkey. In other areas of Turkey and in the Caucasus region, annual precipitation was generally close to the long-term mean, while December was particularly dry across much of the Middle East.

(iii) Notable events

During a storm on 30 January, Jerusalem was covered by snow, with a recorded depth of 20 cm. Likewise, Jordan's capital Amman received 30 cm of snow, while Lebanon, Syria, and even Cyprus were affected by severe cold conditions.

On 17 February, heavy snowfall across much of Turkey led to thousands of villages becoming isolated, while on 18 February the storm reached Israel, bringing snow, hail, rain, and strong winds. Five centimeters of snow was reported in Jerusalem. Thunderstorms with hail affected southern Lebanon.

On 8 May and again in October, severe hailstorms with heavy rainfall affected Cyprus, causing floods.

g. Asia

1) Russia—O. N. Bulygina, N. N. Korshunova, and V. N. Razuvaev.

2008 was very warm over Russia, with a mean air temperature anomaly (relative to 1961–90) of 1.9°C; the second warmest since observations began in 1891 (Fig. 7.32). Anomalies of mean air temperatures were positive for all seasons: winter, +2.4°C; spring, +2.0°C; summer, +0.9°C; and autumn, +2.1°C (second only to 2005).

January air temperature anomalies were in the range from –9° to +12°C (Fig. 7.33). Conditions were very warm in the north of the country, including most of the Yakutia-Sakha Republic, the Amur region, and the southern Khabarovsk Territory. Maximum temperature anomalies in excess of 12°C were recorded on the Arctic coast, where records were set at a number of stations. These large anomalies are associated with significant deviations from the normal surface pressure field. The Icelandic low, which slightly shifted northeastward, was considerably deeper than normal, as was the trough going from

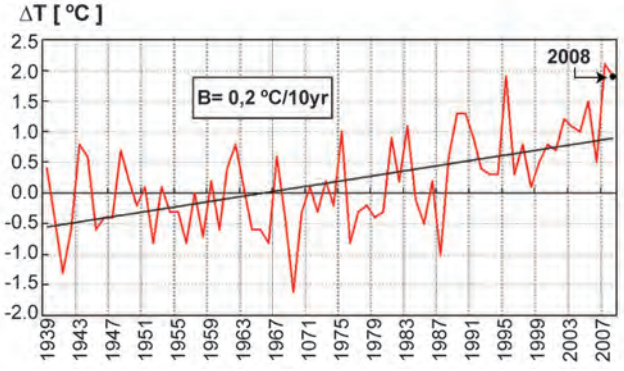

Fig. 7.32. Anomalies of mean annual air temperatures averaged over the Russian Territory, 1939–2008 (against 1961–90 normals).

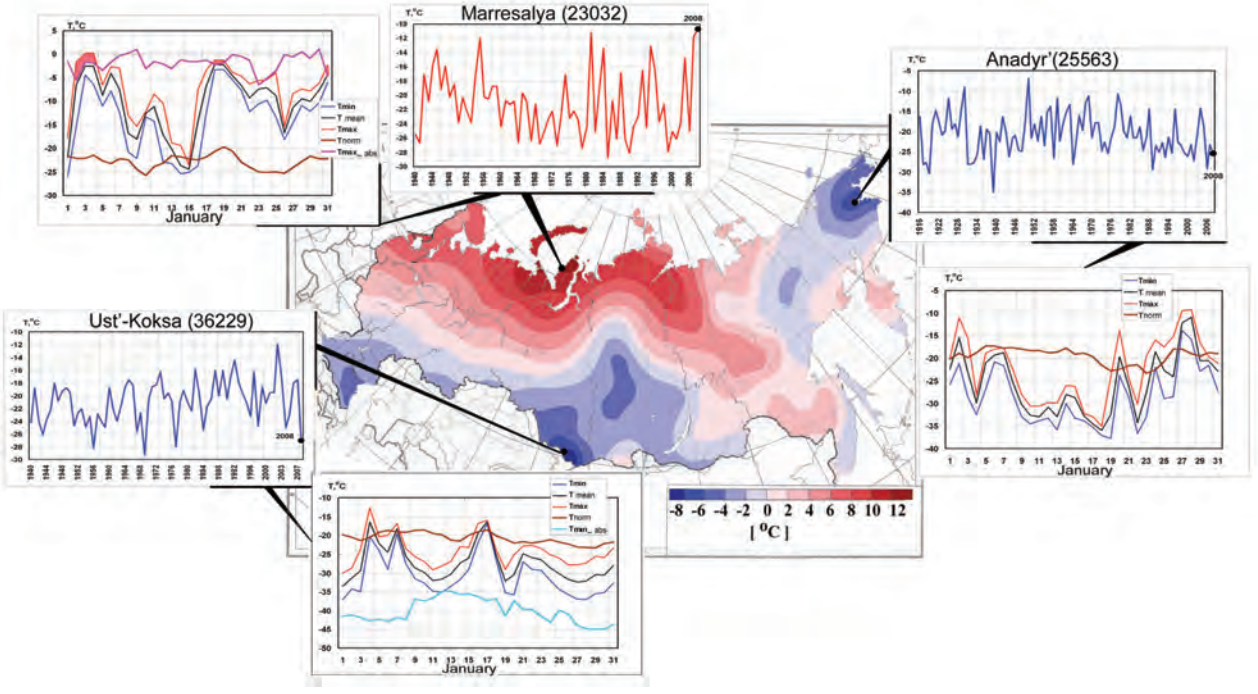

Fig. 7.33. Air temperature anomalies in Jan 2008. Insets show mean monthly and mean daily air temperatures in Jan 2008 at meteorological stations Marresalya, Anadyr', and Ust'-Koksa.

the Iceland depression along the northern coast of Eurasia. Throughout January, the Atlantic cyclones passed over the northern seas around Eurasia, contributing to the formation of warm and wet air masses in the coastal regions.

In contrast, over southern European Russia and southern western Siberia it was very cold. Such cold weather was due to the Siberian anticyclone being southwest of its climatological position, being more intense, covering a larger area than normal, and forming a common high with the Azores anticyclone. In the first 10 days of January, abnormally cold weather with mean daily air temperatures 7°–15°C below normal was recorded in central Chernozem regions. In the Volgograd region, the Stavropol Territory, and the Chechen Republic, minimum air temperatures were as low as –25° to –28°C. In the south of western Siberia, severe frosts (–35° to –42°C) were recorded in the second 10-day period of January. On the coldest days, the mean daily air temperature was 7°–16°C below normal. In some areas of the Krasnoyarsk Territory, the Irkutsk region, and Transbaikalia, the air temperature reached –46° to –50°C.

In European Russia, with the exception of the Black Sea coast, and over most of Siberia, mean February temperatures were above normal. Maximum anomalies (in excess of 10°C) were recorded in southwestern Yakutia. The warmest weather in European Russia was recorded in the west, where mean monthly air temperatures were 6°–7°C above normal. In eastern Siberia, mean monthly temperature anomalies around Evenkia were +8 to +9°C. Precipitation was also twice the monthly mean over the northwestern region, the southwestern Arkhangelsk region, and the southern Urals. At the beginning of the second 10-day period, the Sverdlovsk region and Bashkortostan experienced severe snow storms, with wind speed attaining 24 m s^{-1} and visibility being as poor as 300–500 m. In the southern Far East, the Maritime Territory and the Amur region recorded no precipitation for two months.

Mean monthly air temperatures in March were 1°–2°C below normal in northern European Russia and northern western Siberia. In the rest of the Russian Territory, March was very warm. In the east of the country, mean monthly temperatures were up to 10°C above normal over the eastern Yakutia-Sakha Republic, while in the southern Khabarovsk Territory, mean monthly air temperature anomalies were 7°–8°C. High temperatures in these regions were accompanied by a large amount of precipitation. In the vicinity of Yakutsk and Khabarovsk, precipitation was 3 times as high as the monthly average.

In April, the largest temperature anomalies were recorded over European Russia, where mean monthly air temperatures were generally above normal.

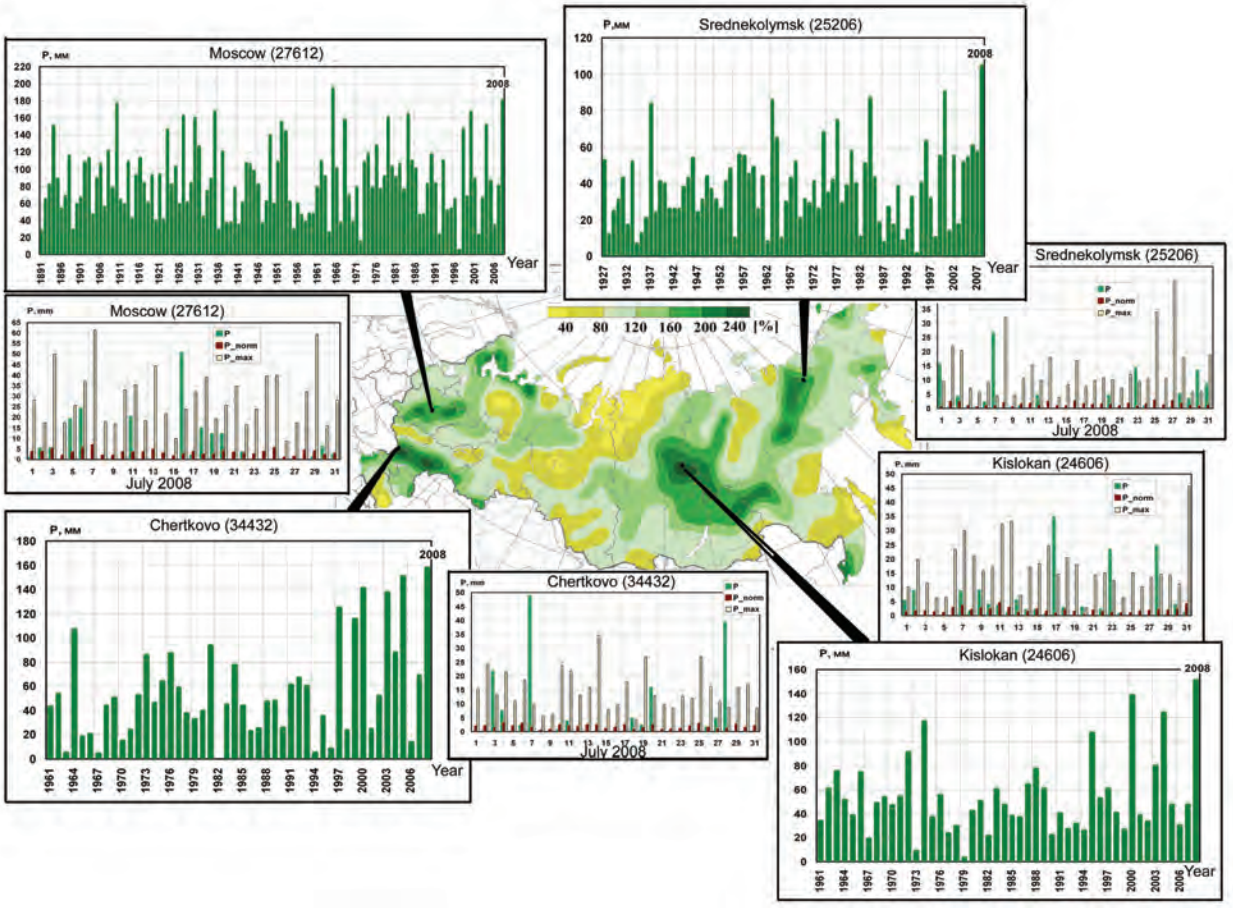

Fig. 7.34. Precipitation total in Jul 2008 against normal. Insets show monthly precipitation total series in Jul and daily precipitation in 2008 at meteorological stations Moscow, Chertkovo, Kislokan, and Srednekolymsk.

Significant precipitation deficits were recorded in the southern Far East (western Amur region, eastern Maritime Territory, and southern Sakhalin) against the background of positive temperature anomalies (3°–4°C).

In May, the division between negative and positive anomalies in the temperature field coincided with the border between the two continents. In European Russia, mean monthly temperatures were below normal, with some regions recording record low daily minima. In contrast, nearly the whole of the territory east of the Urals experienced warmer weather than the long-term average, with many regions of Siberia and the Far East setting new daily maximum air temperature records. In late May, air temperatures rose to +25°C in Yakutia and to +35°C in southern Siberia.

In June, negative temperature anomalies persisted in European Russia. In the first 10-day period, ground and air frosts were recorded in most locations. June was very warm in Eastern Siberia and southern Yakutia. Very hot weather, predominantly without precipitation, also prevailed in the Amur region and the southern Khabarovsk Territory. These weather conditions caused railway accidents and numerous forest fires. The city of Khabarovsk was wrapped with dense smog from forest fires that gave rise to poor visibility. In the republics of Northern Caucasia, the Krasnodar, and Stavropol Territories precipitation of 75–96 mm occurred in one to three hours.

In July, no significant broadscale temperature anomalies were recorded; however, precipitation in some regions exceeded long-term records (Fig. 7.34). Heavy rains were reported in the central region of European Russia and in the northwestern Rostov region (200%–300% of monthly average). In contrast, August was warm over most of the Russian Territory. Hot winds were observed in the Altai Territory by the end of the first 10-day period, while very hot and dry weather occurred in the second half of August in southern European Russia. In some regions maximum air temperatures were above 30°C for 24–25 days, peaking at 36°–40°C. Drought conditions, defined as a period with precipitation of less than 5 mm, persisted for 31 days.

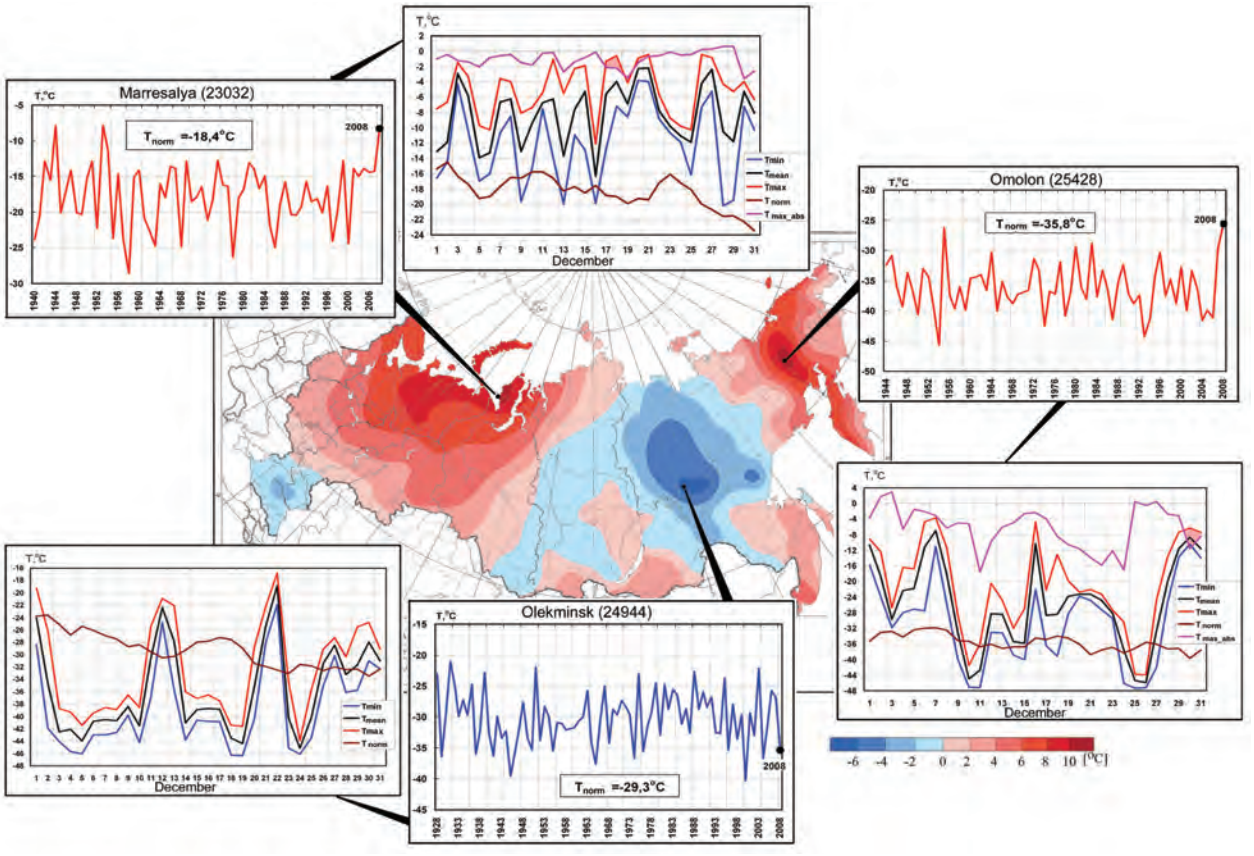

Fig. 7.35. Air temperature anomalies in Dec 2008. Insets show mean monthly and mean daily air temperatures in Dec 2008 at meteorological stations Marresalya, Omolon, and Olekminsk.

September 2008 in European Russia will be remembered for both abnormal heat and cold. For example, on 11 September, Voronezh city reached a record-high temperature, 30.7°C, and in the neighboring city of Tambov, on 27 September, air temperature dropped to a record-breaking low value of –2.6°C. In the Magadan region, Chukotka, and Kamchatka, the weather was considerably warmer throughout the month, as compared with normal values.

October 2008 was the warmest October on record for Russia, with a mean air temperature anomaly of 2.9°C. This record was achieved despite few individual stations reaching record levels (maximum anomalies were no higher than 6°C), but rather by the fact that virtually the entire country was consistently warm. Over most of European Russia, warm weather in October was generally accompanied by below-normal precipitation. Conversely, Transbaikalia received above-average precipitation, with monthly averages exceeded by 2 to 3 times, and heavy snowfalls producing a snow cover as deep as 30–35 cm. Heavy snowstorms also took place on Taimyr and in Khakassia.

November also proved warm for Russia, with abnormally warm weather prevailing over European Russia, particularly in the Urals, with mean monthly air temperature anomalies reaching 6–7°C. Western Siberia experienced anomalies of more than 8°C. Central regions of Sakhalin received precipitation that was twice the monthly mean.

In December, northern regions of European Russia and western Siberia and continental regions of the Magadan and Chukotka all recorded exceptional warm anomalies—up to 10°C in places. For example, at Omolon, whose normal value is –35.8°C, mean monthly air temperatures rose to –25.6°C. Conversely, over western Yakutia (Fig. 7.35), daily air temperatures were below normal for most of the month, with anomalies reaching –15° to –20°C.

2) East Asia—Y. Guo, Y. Sakai, S. Zhao, X. Wang, and H. Lee

(i) Overview

Over most of East Asia, the annual mean surface air temperature during 2008 was near or above normal (Fig. 7.37). Temperatures were significantly below normal for most of East Asia during winter

THE EURASIAN COLD EVENT OF JANUARY 2008—M. ROGERS, S. SENSOY, O. BULYGINA, F. RAHIMZADEH, Y. GUO, S. ATTAHER, AND A. B. WATKINS

During January 2008, an exceptional cold outbreak occurred across Eurasia (Fig. 7.36). Mean monthly temperatures were as low as −8.0°C in Turkey, with nearly 50 extreme weather events recorded. Cold stretched south into Israel, Jordan, and Egypt, where temperatures 5° to 8°C below normal had a severe impact on many vegetable and fruit crops. Jerusalem was covered by 20 cm of snow, Amman received 30 cm of snow, while Lebanon, Syria, and even Cyprus were affected by severe cold conditions. Iraq experienced record cold, with snow being reported on at least six days at Mosul in northern Iraq and temperatures near record lows in many areas. On 11 January, snow fell in Baghdad for the first time in living memory. The lowest recorded temperature was −10°C at Al Qaim in the western desert. Over northern Iran, mean January temperatures were generally 5° to 10°C below normal. Some areas that had not observed minimum temperatures below freezing since records began in 1951, experienced subzero temperatures on multiple days. In the south of western Siberia, severe frosts (−35° to −42°C) were recorded in mid-January, with temperatures generally 7° to 16°C below normal. In some areas of the Krasnoyarsk Territory, the Irkutsk region, and Transbaikalia, temperatures dropped to between −46° and −50°C. Western regions of Afghanistan experienced their coldest winter in nearly 30 years. Nearly two-thirds of China was affected by the event, with southern China experiencing a once-in-a-hundred-year cold snap. Maximum temperatures were 2° to 6°C below average. Averaged across southern China, 19 successive days occurred with a daily mean temperature of below 1°C. This, and an accumulated mean snowfall of 42.4 mm, were both records since observations began in 1952. Snow cover for Eurasia was at all-time record levels for the month of January. Snow coverage exceeded 32 million km^2, just over 3 million km^2 above the long-term average; further details in chapter 2. Sadly, many hundreds died from the extremely cold conditions across Eurasia in early 2008.

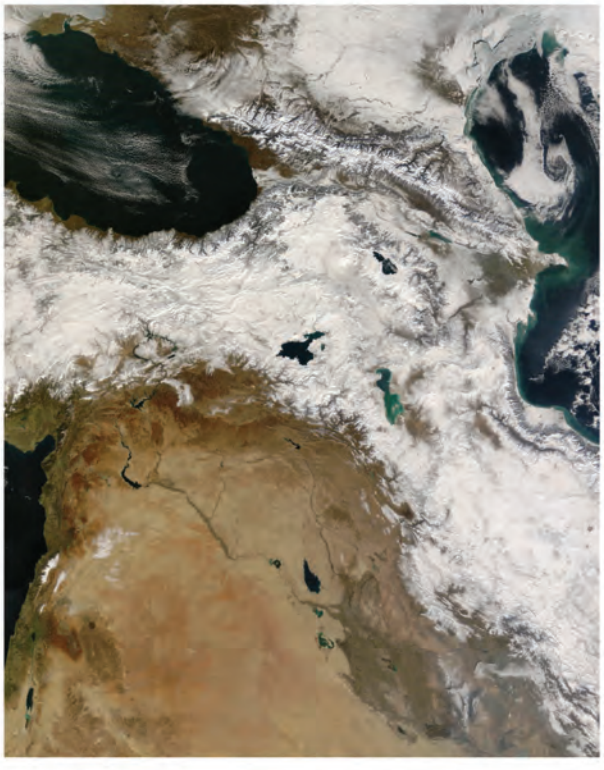

Fig. 7.36. Snow covers the region of southwest Asia, from Turkey in the west to Iran in the east, on 15 Jan 2008. NASA image courtesy Jeff Schmaltz, MODIS Rapid Response Team at NASA GSFC (http://earthobservatory.nasa.gov/NaturalHazards/view.php?id=19555).

(December 2007–February 2008) and were above normal in the spring (March–May 2008) and autumn (September–November 2008). In China, the mean temperature in spring was the warmest since national average records commenced in 1951. In Japan, 2008 was the 11th-warmest year since 1898. Annual precipitation totals were above normal in eastern northwest China, the Tibetan Plateau, and the regions from southern China to the northeastern Indochina peninsula, while it was below normal in the regions from western northwest China to western Mongolia and the northeast part of East Asia (Fig. 7.38). Two extreme floods occurred in southern China in late May to June, and again during late October to early November. Widespread droughts expanded across most of northern China from January to March 2008. Parts of Japan were affected by localized torrential rainfall during summer.

(ii) Temperature

The average temperature over China for 2008 was 9.5°C, 0.7°C above the 1971–2000 normal and the seventh highest since 1952, and the 12th above-average year since 1997. Annual mean temperatures for 2008

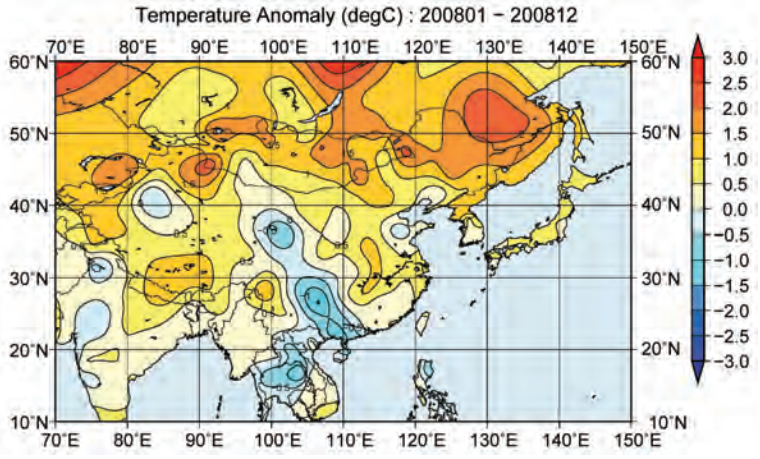

Fig. 7.37. Annual mean temperature anomalies (°C; 1971–2000 base period) over East Asia in 2008. (Source: JMA.)

were near normal over most of China, and 1°–2°C above normal in northeastern and northwestern China. The average temperature in China for winter 2007/08 was −4.4°C, which was 0.2°C below normal and the coolest winter since 1986/87. Extreme low temperatures, freezing rain, and snow persisted over most of southern China from 10 January to 2 February, resulting in the worst severe weather event in five decades, the loss of 107 people, and over $15 billion (USD) in damage (Gao 2009; Wang et al. 2008b). For spring, the average temperature was 11.4°C, 1.8°C above normal and the warmest spring since 1951. The seasonal mean temperatures for summer and autumn were 0.5°C and 1.0°C above normal, respectively.

The average temperature over Japan (averaged over 17 observatories confirmed as being relatively unaffected by urbanization) in 2008 was 0.46°C above normal (based on the 1971–2000 average), making it the 11th warmest year since 1898. Area-averaged annual mean temperature anomalies were +0.6°C in northern and eastern Japan, +0.5°C in western Japan, and +0.4°C in Okinawa/Amami.

(iii) Precipitation

Total precipitation for 2008 in China was 651.3 mm, which was 38.4 mm above normal and the highest since 1999. The spatial and seasonal precipitation distributions were uneven across the country. Summer rainfall was the third highest since 1955. Annual precipitation was 20%–50% above normal in western Inner Mongolia, southwestern, and southern China, while deficits of 20%–50% were recorded in parts of northwestern China. From 26 May to 19 June, heavy rainfall persisted over southern China, causing severe flooding. From 21 October to 8 November, heavy rains occurred frequently in southern China, resulting in an average precipitation of 94.9 mm, 160% above normal and the highest value since regional records began in 1951. In contrast, from 1 January to 18 March, widespread droughts expanded across much of northwest and North China, with precipitation 30% to 80% below normal.

Annual precipitation amounts over Japan were near normal nationwide, except for northern Japan and over parts of eastern Japan, where totals were significantly below normal. Some mainland areas experienced localized torrential rainfall in summer.

(iv) Atmospheric circulation

In winter, both the polar front jet and the subtropical jet were stronger than normal over Eurasia. Blocking highs were prevalent around western Siberia, and the Siberian high developed in January and February, when cold spells affected East Asia, and particularly China. Extremely low temperature anomalies were observed in the lower troposphere over China.

During spring and summer, positive 500-hPa height anomalies occurred over the Arctic Ocean and the midlatitudes of Asia, while negative anomalies

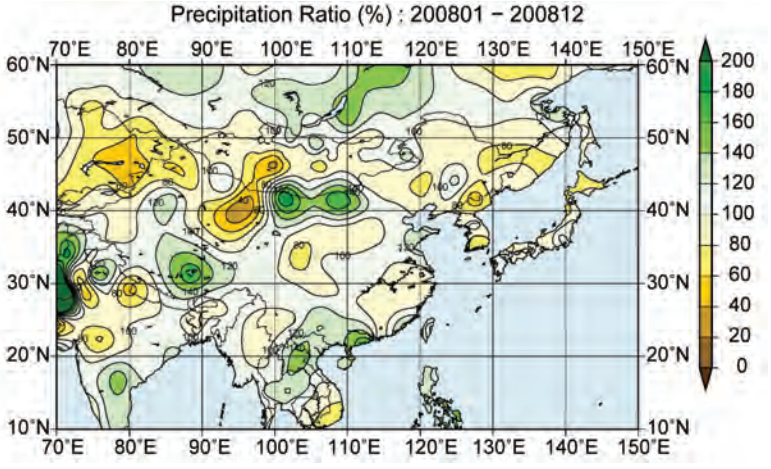

Fig. 7.38. Annual precipitation ratio as percentage of normal (1971–2000 base period) over East Asia in 2008. (Source: JMA.)

occurred from Europe to central Siberia. A stationary ridge over eastern Siberia was also observed. These features were consistent with the southward-shifted polar front jet and the weaker-than-normal or slightly northward–shifted subtropical jet, corresponding to most parts of East Asia experiencing a warm spring and a hot summer. Though the Okhotsk high appeared over the Sea of Okhotsk several times, it brought a cool wind to northern Japan only in late August. The Pacific high was weaker than normal over the northwestern Pacific during August.

In September and November, positive 500-hPa height anomalies prevailed over East Asia. Southerly winds were dominant in the lower troposphere, resulting in a warm autumn for most parts of East Asia. In November and December, westerly jets meandered and the trough stayed over the East China Sea. Wet weather was observed at the south and east side of the trough, while dry conditions were observed to the north and west.

(v) Monsoon

The onset of the SCS summer monsoon was in the first pentad of May and earlier than normal. Subsequently, southwesterlies moved northward to regions south of the Yangtze River. During mid-June, southwesterlies extended northward to the Jianghuai area, and warm and humid air was prevalent south of the Huanghuai area. Southwesterlies moved northward to North China during mid-July. After mid-August, warm and moist air swiftly withdrew southward and moved back to the middle to lower reaches of the Yangtze River, withdrawing further to South China by mid-September and remaining until early October. The summer monsoon withdrew from the SCS during the second pentad[3] of October 2008, two pentads later than normal. Overall, the SCS summer monsoon index during 2008 was –1.37 and weaker than normal. Pentad intensities of the SCS summer monsoon were stronger than normal during May and the period from the third pentad of September to the first pentad of October, but they were weaker than normal during most of the period June–August (Fig. 7.39). Over eastern China, precipitation totals for summer (June–August) were more than 30% above normal in the Jianghan area, the eastern Huanghuai area, and South China.

Onsets of the Bai-u (the rainy season over Japan during the late spring and summer) were earlier than

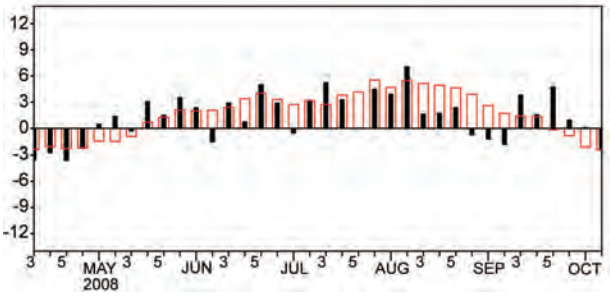

Fig. 7.39. Variation of pentad zonal wind index over monitoring region(10°–20°N, 110°~120°E), red open bars stand for climatology (Unit: m s^{-1}) (Source: CMA.)

normal in western and eastern Japan. In western Japan, the Bai-u withdrew on 6 July, one to two weeks earlier than normal. This was followed by sunny and hot days until mid-August. Over western Japan, July received only 29% of its normal rainfall, which was the least recorded since 1946. Meanwhile, isolated heavy rains caused by developed cumulonimbus were sporadically observed in eastern and western Japan from the end of July to the beginning of September. Total precipitation amounts exceeded 400 mm in the Tokai region resulting in floods and land slides.

(vi) Aeolian dust

In spring 2008, China was affected by nine dust and sand events, far fewer than in 2007 (15). The average number of dust days in northern China was 1.7 days (3.8 days less than normal). During 26–28 May, the worst event of 2008 saw a 3-day dust storm blanketed northern China.

The Republic of Korea was affected by six dust events in spring (March, April, May) 2008, with the strongest peaking on 2 March, affecting most of Korea over a 2-day period. The average number of dust days over the 28 recording stations was 4 days, which was near normal (3.6 days). The number of dust days in April was 0.3 days, which was significantly below normal (2 days) and is likely to be due to anomalous easterlies and southwesterlies. The last dust event was observed on 29–31 May, which was the latest occurrence observed since 1979.

In Japan, the number of days when yellow sand, or aeolian dust, was observed was 10 from January to May 2008, which was the lowest number since 1987. The total number of days that meteorological stations recorded aeolian dust during 2008 was 125, which was also the lowest number since 1997. Of special interest is that the total number of days when yellow sand was observed during April (one) was far below the normal value of 7.9.

[3] Pentad refers to blocks of five days, starting on the first day of the month.

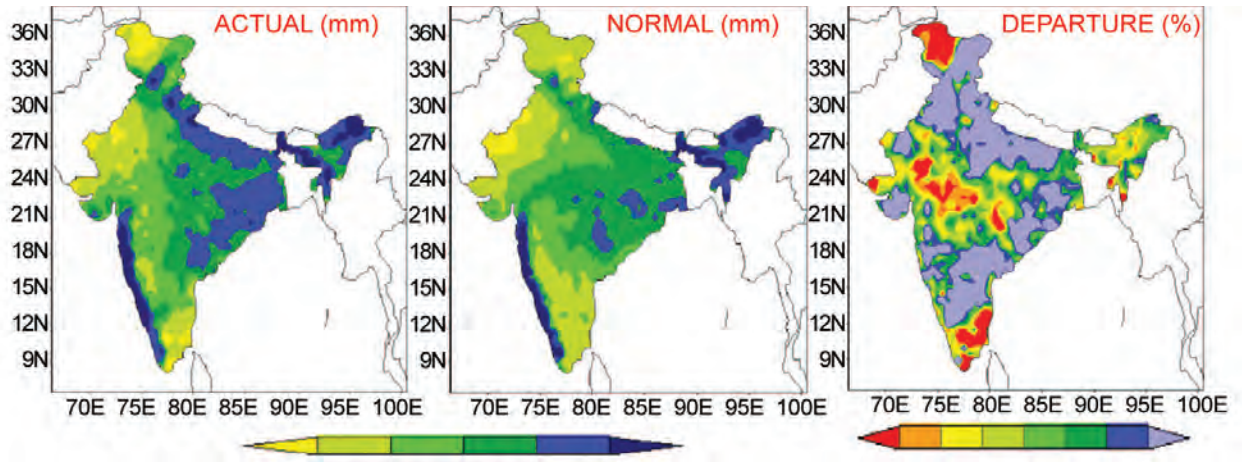

Fig. 7.40. Monsoonal (Jun–Sep) rainfall (mm) and anomalies (percentage departure from normal) over India in 2008.

3) South Asia—M. Rajeevan and J. Revadekar

(i) Overview

During 2008, South Asia experienced many extreme precipitation and temperature events. During the last week of January, parts of northern India experienced severe cold-wave conditions. Delhi, the capital city of India, recorded a minimum of 2.5°C on 28 January, its lowest temperature in five years. During the premonsoon season (March to May), a severe heat wave affected many parts of northern India and Pakistan. During March, unprecedented heavy rainfall occurred over southern parts of India and Sri Lanka associated with the passage of easterly waves in the lower troposphere. The area-weighted average rainfall over the southern peninsular India was 915% of its long period average value, an all-time record. Record-high rainfall was reported at more than 20 stations over southern India. In Sri Lanka, flash floods associated with heavy rains affected more than 50,000 families.

A cyclonic storm (Nargis) developed over the Bay of Bengal during the last week of April, which intensified into a very severe cyclonic storm (Category 4) on 29 April. Along with its intensification, it recurved and moved toward Myanmar. On 2 May, it crossed the southwest coast of Myanmar, resulting in the worst disaster ever for that country. Nargis was the most devastating cyclonic storm to strike South Asia since 1991. According to reports, the storm left nearly 78,000 people dead and almost 56,000 missing.

(ii) South Asian summer monsoon (June to September)

The summer monsoon season (June to September) typically contributes 60%–90% of the annual mean rainfall over major portions of South Asia. The onset phase of the monsoon in 2008 was characterized by a normal onset over southern peninsular India. Further progress of the monsoon over the country was satisfactory, except for a brief hiatus during the third week of June. The monsoon covered the whole country by 10 July, about five days ahead of normal.

The all-India summer monsoon rainfall (June to September) was 2% below its long-term (1901–2000) mean of 890 mm. However, rainfall was unevenly distributed over both space and time (Fig. 7.40). Seasonal rainfall was above normal over the far northern parts of India and its north peninsula, while totals were deficient over most of central and extreme southern parts of India. The 2008 summer monsoon was also characterized by strong intraseasonal variability as seen in Fig. 7.41. During the month of June, area-weighted rainfall over the country as a whole was 24% above average. However, rainfall activity was confined to the extreme northern parts of India, in association with the interaction between the midlatitude westerly system and the monsoon

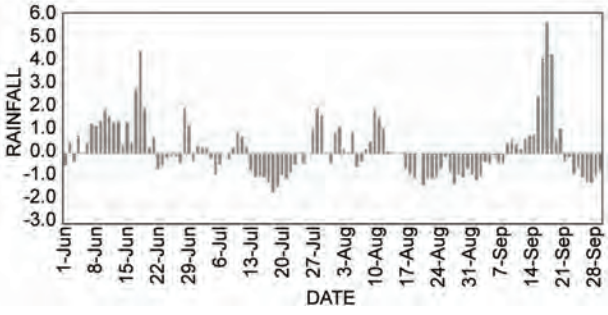

Fig. 7.41. Daily standardized rainfall time series averaged over the monsoon zone over India (1 Jun to 30 Sep 2008).

circulation. Conversely, during the second and third weeks of July, the monsoon circulation was weak, most likely due to enhanced convection over the equatorial eastern Indian Ocean and midlatitude circulation anomalies.

During the summer monsoon season, 2 of the 36 meteorological subdivisions in India recorded excess rainfall, 31 subdivisions received normal rainfall, and the remaining 3 subdivisions received deficient rainfall. Out of 516 meteorological districts for which rainfall data were available, 76% of the meteorological districts received excess/normal rainfall, and the remaining 24% of districts received deficient rainfall (rainfall deficiency more than 19%). During the season, 65 districts (13%) experienced moderate drought conditions (rainfall 26% to 50% below normal) and 17 districts (3%) experienced severe drought conditions (rainfall deficiency 51% or more).

A notable feature during the monsoon season was less-frequent occurrence of cyclonic disturbances such as monsoon depressions, although this suppressed activity is consistent with the observed decreasing trend in the frequency of monsoon depressions over the Indian region during recent decades. Only four monsoon depressions formed during the season, against the long-term average of around seven. Depressions that did occur were short lived with an average life period of only 2.2 days.

The area-weighted seasonal (July to September) rainfall over Pakistan was slightly below normal. Rainfall in July was deficient, while it was in excess during August. Seasonal rainfall was above normal over northwest Frontier Province and Punjab. Over the Sindh region, seasonal monsoon rainfall was largely deficient. Monsoon rainfall over western Nepal was consistently above normal until August.

During the monsoon season, heavy rainfall and flash floods affected many parts of India, Bangladesh, Nepal, and Pakistan, impacting hundreds of thousands of people and causing more than 2,000 deaths. Record rainfall was reported in many cities and towns in India. On 2 July, the city of Varanasi recorded 330 mm of rainfall in just 24 hr, an all-time record for the city. In neighboring Nepal, heavy rainfall in August caused the Kosi River to spill over its banks, flooding villages and leaving several people missing. During September, in eastern Orissa, heavy monsoon rains triggered widespread floods that affected nearly 2.4 million people and damaged crops and property.

Another notable feature was the strong zonal dipole structure of precipitation observed over the tropical Indian Ocean, with positive anomalies over the west and negative anomalies over the east. This pattern was consistent with the strong and persistent dipole structure in the SST pattern observed during the same period. This favorable SST pattern may be responsible for the observed excess of monsoon rainfall along the west coast of India and the northern peninsula, at least during August.

(iii) Northeast monsoon

The NEM sets in over southern peninsular India in October and in Sri Lanka in late November. The NEM contributes 30%–50% of the annual average rainfall over southern peninsular India and Sri Lanka as a whole, and up to 70% of the annual rainfall in the dry northern and eastern regions of Sri Lanka.

During the season, the storm activity over the North Indian Ocean was above normal with three cyclonic storms and one deep depression. In November, Tropical Storm Nisha caused disaster in Sri Lanka and India and resulted in fatalities of at least 200 people. The storm caused heavy rain and flooding that displaced more than 50,000 people in Vanni and Jaffna districts in Sri Lanka. Associated with this storm, Jaffna recorded 520.1 mm of rainfall, which is an all-time record. Orathanadu, a small town in Tamil Nadu received more than 990 mm of rainfall in just 48 hr. On 28 November, Chennai airport recorded 280 mm of rainfall in just 24 hr. The NEM seasonal rainfall was, however, above normal only over the eastern parts of the south peninsula, while it was deficient over the western parts of the region.

4) Southwest Asia

(i) Iraq—M. Rogers

(a) Overview

The main features of the climate of Iraq in 2008 were the cold January, the very dry winter and spring, and the relatively wet autumn. The dry spring, and overall dry year, has extended one of the worst droughts in the past 10 years and has had a massive effect on the wheat and barley production within the country.

(b) Seasonal Review

The winter period, Iraq's wet season, was drier than normal with most locations receiving less than 50% of their normal winter rainfall (see Fig. 7.42). December and February were drier than average with generally near-normal temperatures. January, however, had near-normal rainfall in many central and southern areas, locally above-normal in the west, but mean temperatures were between 2° and 3°C below normal. Basra Airport was 3.3°C colder

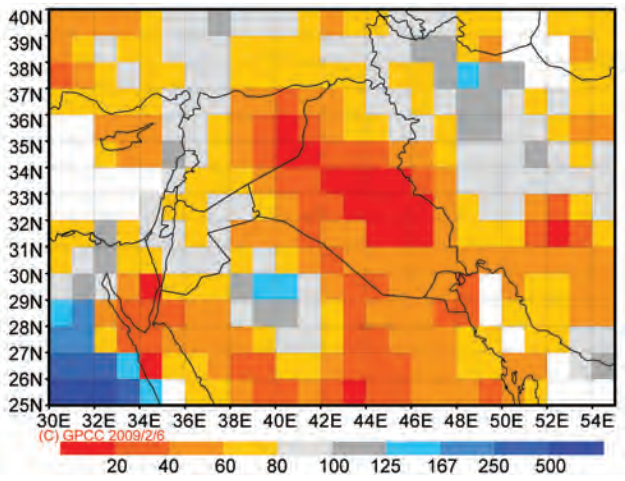

Fig. 7.42. Percentage of normal precipitation (base period 1951–2000) for seasons Dec–Feb. (Source: GPCC.)

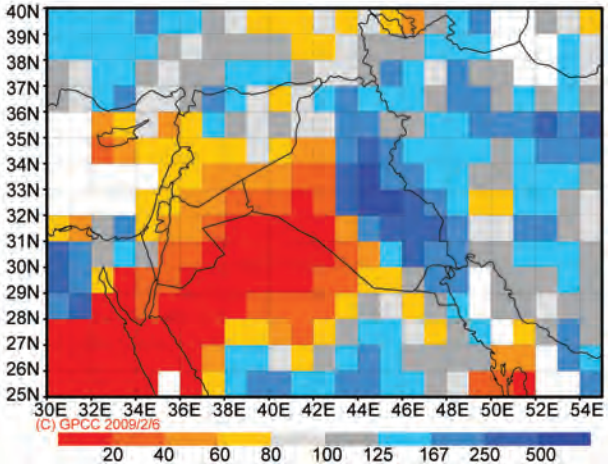

Fig. 7.43. Percentage of normal precipitation (base period 1951–2000) for seasons Sep–Nov. (Source: GPCC.)

than average during January and 1.8°C colder for the winter as a whole.

Temperatures recovered during the spring, with most areas experiencing mean temperatures between 2° and 4°C above the 1961–90 normal, with many places reaching record-breaking temperatures during March (e.g., 39.4°C at Basra Airport). The high temperatures, brought about by generally settled weather conditions across the country, led to an extension of the very dry conditions experienced during winter. Most areas received less than 40% of their normal rainfall with some places having less than 10% (e.g., around 6% at Baghdad). With the drier-than-normal ground and the lack of crops in the fields due to their failure through lack of irrigation, there was a higher occurrence of dense lifted dust.

Summer in Iraq was fairly typical with fine, dry, and dusty conditions across most areas, although temperatures were generally above normal. The northwesterly Shamal winds dominated conditions, bringing occasional dense lifted dust.

An unsettled period of weather during October and November led to above-average rainfall in many places, especially in central and eastern areas (see Fig. 7.43), with Baghdad receiving nearly 180% of the normal rainfall during the September to November period. Temperatures were generally between 1° and 2°C above normal. A drier-than-average December with near-normal temperatures ended the year.

(c) Annual Review

Overall, 2008 in Iraq was drier and warmer than average. On the whole temperatures were between 1° and 2°C above normal with rainfall less than 65% of the expected levels (Table 7.2).

(ii) Iran—M. Khoshkam and F. Rahimzadeh

Temperature anomalies during 2008 in Iran were mixed (Table 7.3). Cooler-than-average conditions prevailed during winter, when Iran experienced temperatures generally 0°–4°C below the long-term mean, with areas in the northeast of the country recording temperatures up to 6°C below average (Fig. 7.44). During spring, temperatures were generally up to 4°C above long-term average over most parts of Iran, though some regions experienced maximums up to 6.3°C above the mean. During summer, below-average temperatures were observed in the south, southeast, and northwest. In autumn, cooler-than-average temperatures persisted across the northwest, southern, and central parts of the

Table 7.2. Precipitation anomaly (percentage of 1951–2000 normal). (Source: USAF, 14th Weather Squadron.)

	Mar–May	Sep–Nov	Annual
Mosul	32.0	188.9	62.4
Baghdad	5.9	179.9	58.5
Basra	32.9	118.6	53.8

Table 7.3. Seasonal amount of precipitation and temperature over Iran.

Parameter	Season		Winter	Spring	Summer	Autumn
Precipitation	Average (mm)		69	14	9.5	56.2
	Respect to (%)	Long term	−42%	−76%	−15%	−14%
		Previous year	−27%	−84%	−37%	49%
	Range from–to (mm)		6 to 578	0 to 180	0 to 227	0 to 954
Temperature	Respect to long term (°C)		−6 to 0	2 to +4	0 to 1	−2 to −1
	Range from–to (°C)		−10 to 25	10 to 35	15 to 45	3 to 28

country, while warmer-than-average conditions were limited to the east and some parts of the northwest and central regions.

Iran experienced drier-than-normal conditions in all four seasons of 2008 (Table 7.3), with the country receiving only 58%, 24%, 85%, and 86% of its long-term winter, spring, summer, and autumn rainfall, respectively. Winter, spring, and summer also received less rainfall in 2008 than that received in the previous year, the only exception (autumn) being due to exceptionally low rainfall in 2007. Areas with above-average winter rainfall were confined to the southeast and small parts over the northwest, while the rest of the country received precipitation amounts that were at most 75% of the long-term mean. Total rainfall for winter 2008 across the Caspian Sea and through the western parts of the country was generally more than 200 mm. The largest total of 578 mm was observed in Bandar Anzali (northern Iran). Through the middle of the country, and through isolated regions in other parts, rainfall was less than 35 mm. Averaged precipitation over the country was below the long-term mean during the spring of 2008 (Fig. 7.45).

During the summer, most parts of the eastern half of the country received below-normal precipitation, while areas in the south received no rainfall at all. During autumn, northwest, northeast, south, and southeast parts of the country received 60% of their long-term mean rainfall.

During winter, spring, and summer, significant dust storms spread out over large parts of the southern half of Iran. While this is fairly typical for the southeastern regions, it is only in the past few years that these conditions have spread into the southwest of the country, although it is worth noting that the source region differs for the two areas.

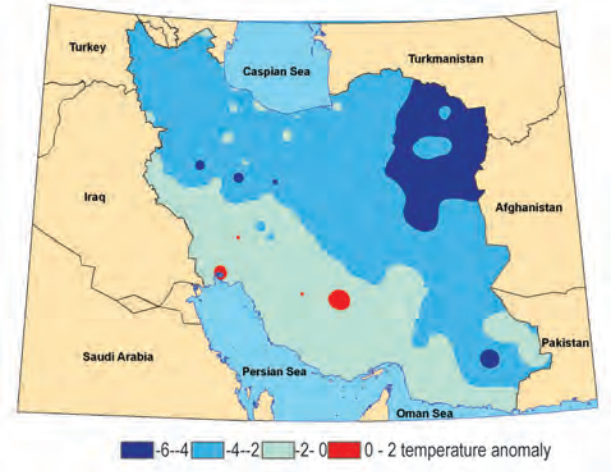

Fig. 7.44. Winter mean temperature anomaly (°C) for Iran. (Source: IRIMO.)

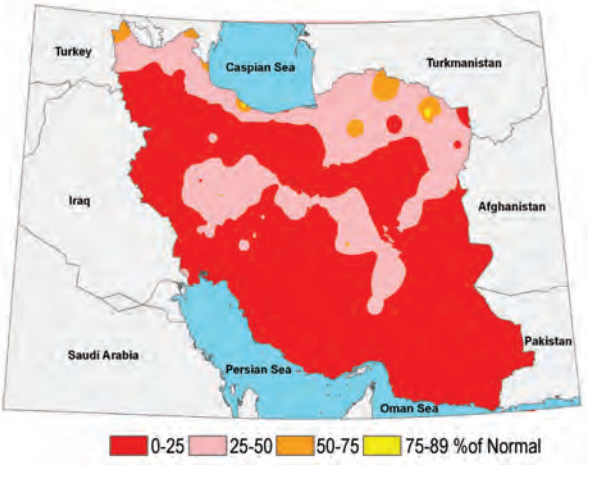

Fig. 7.45. Spring precipitation anomaly (percentage of normal) for Iran. (Source: IRIMO.)

(iii) Turkey—S. Sensoy

The annual surface temperature anomaly averaged over Turkey in 2008 was 0.8°C above the 1961–90 average (13.6°C). Coastal areas and the western part of the country recorded temperatures above the mean, while areas around Sivas, Erzurum, and Kars experienced below-average temperatures. Positive temperature anomalies for Turkey have now occurred over all years (with the exception of 1997) since 1994. This increase is observed not only in the mean temperature but also in maximum and minimum temperatures. Middle East and Turkish climate indices studies show that the number of summer days (Tmax ≥ 25°C) and tropical nights (Tmin ≥ 20°C) has been increasing over Turkey, while cool nights (Tmin < 10th percentile) and cool days (Tmax < 10th percentile) have been decreasing (Sensoy et al. 2008; Zhang et al. 2005).

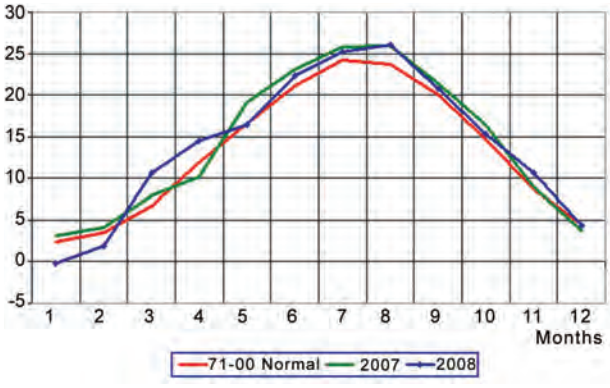

Fig. 7.46. Monthly mean temperatures (°C) for Turkey in 2008.

In 2008, January and February mean temperatures were below the 1971–2000 mean, while March, April, June, July, August, and November were above it. All other months saw mean temperatures that were near normal (Fig. 7.46). January 2008 mean temperatures were significantly below the 1971–2000 mean, reaching –8.0°C in areas around Sivas, Erzurum, and Kars (Fig. 7.47). Forty-nine extreme events, including heavy snowfall, storms, and frosts, were reported in January and February 2008. This exceptional cold was thought to be due to the Siberian high-pressure system that affected Turkey, combined with prevailing La Niña conditions.

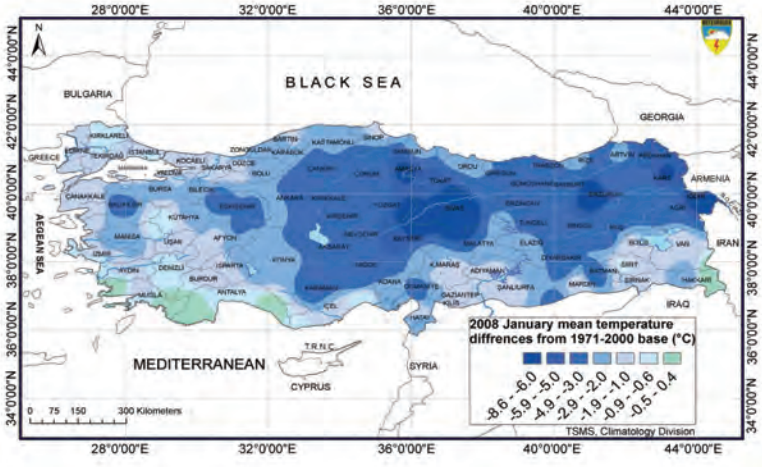

Fig. 7.47. Jan 2008 temperature anomalies (°C; base period 1971–2000) for Turkey.

Total precipitation was below the mean in Antalya, Muğla, Mardin, and Bitlis, which all broke records in 2008. In contrast, slightly above-average precipitation occurred in the central Black Sea region, Sivas, Bayburt, and Kars. Overall, total precipitation for the country was 128 mm below the 1961–90 mean, and hence large areas suffered drought conditions during all seasons of 2008 except autumn. Despite the drought conditions, 42 extreme rainfall and flood events occurred during 2008.

h. Oceania

1) Australia—B. C. Trewin and A. B. Watkins

(i) Overview

Australia in 2008 was generally warmer than normal, with near-normal rainfall, despite the presence of a strong La Niña early in the year (see chapter 4 for a description of the ENSO state, and chapter 3 gives a broader view of oceans), something that historically brings above-normal rainfall to northern and eastern Australia. Rainfall averaged over Australia for 2008 was 466 mm (44th highest of 109 years, 1% below normal),[4] and, while much of the north and east was wet, dry conditions in the southeast reinforced long-term drought over much of that region. This exacerbated severe water shortages in the agriculturally important Murray-Darling basin.

[4] Anomalies are calculated with respect to the 1961 to 1990 average. High-quality *annual* Australia-wide temperature anomalies have been calculated for all years since 1910 (Della-Marta et al. 2004), while high-quality *monthly* anomalies are available from 1950. This report's rankings use the monthly values. High-quality nationwide rainfall measurements commenced in 1900 (Lavery et al. 1997).

Mean temperatures for the year were 0.41°C above normal, making 2008 the 14th-warmest year on record, despite being the coolest year since 2001. Australian temperatures are generally below average in years in which a La Niña event finishes. Unusual for a La Niña year, the Australian mean diurnal temperature range was larger than normal.

(ii) Temperature

Temperatures were above normal for much of Australia during 2008, but to a lesser extent than they have been in some recent years, with the largest anomalies in the central and western interior.

Only the south-central Northern Territory and the eastern interior of western Australia experienced maximum temperature anomalies of more than +1°C through the year (Fig. 7.48), while only a few areas had below-normal maxima. Averaged over Australia, the mean maximum temperature was 0.52°C above normal (13th highest on record), with positive anomalies in all states. However, only the Northern Territory (10th) ranked in the top 10.

Minima were closer to normal, with the national average anomaly of +0.29°C ranking 19th highest. Only a few areas had annual anomalies with a magnitude of more than 1°C. The most consistent signals were in northern parts of the Northern Territory and western Australia, where annual anomalies were between −0.5° and −1.0°C, and in the northern half of New South Wales, which was similarly cool.

While the annual temperatures were mostly unexceptional, there were some notable monthly and seasonal anomalies. January was Australia's warmest on record and was particularly hot in the central and western interior, which missed out on wet season rains. Maximum temperatures in March were exceptionally warm over much of southern Australia, largely due to a prolonged heat wave [see section 7h1(iv)]. However the early end to the wet season and persistent southerly flow saw low autumn minimum temperatures over much of northern Australia.

Winter temperatures were generally close to normal, with a cold August offsetting a mild June. Parts of the southeast had their lowest winter mean maximum temperatures since 1998, although anomalies were still near zero. Mount Hotham set an Australian record when the temperature failed to rise above 0°C for 53 consecutive days between 7 July and 28 August, and Eyre set a western Australian state record with −7.2°C on 17 August.

September and October were generally warm, continuing the pattern of recent years (September maximum temperature anomalies have been +0.8°C or above in 13 of the last 15 years, and positive in all 15), with Victoria and South Australia setting October records for mean maxima and minima, respectively. The year had a reasonably cool finish, especially in the west, although December was hot in much of Queensland.

(iii) Precipitation

Australian precipitation was generally close to normal during 2008. While some areas affected by long-term drought had their best rains for several years, others saw a continued deterioration of conditions during the year.

The tropical wet season in the first part of 2008 was one of contrasts. In the northern tropics, much of the eastern half of Queensland, and NSW, it was wet with flooding at times, although only limited areas had January–March totals in the highest decile. Conversely, with no significant incursions of tropical moisture into the interior, rainfall was well below normal in the Northern Territory south of 18°S, the far west of Queensland, and all of South Australia. The wet conditions around the NSW/Queensland border, following heavy rains at the end of 2007, provided the northern Murray-Darling basin with its best inflows since 2000/01, although little of this water reached lower parts of the basin.

The tropical wet season came to an early end and dry conditions dominated over most of the country from March to October, with 87% of the country experiencing below-median rainfall. Autumn was especially dry, with the national average the eighth lowest on record, May was the driest on record, and all states and territories were below normal in all three months.

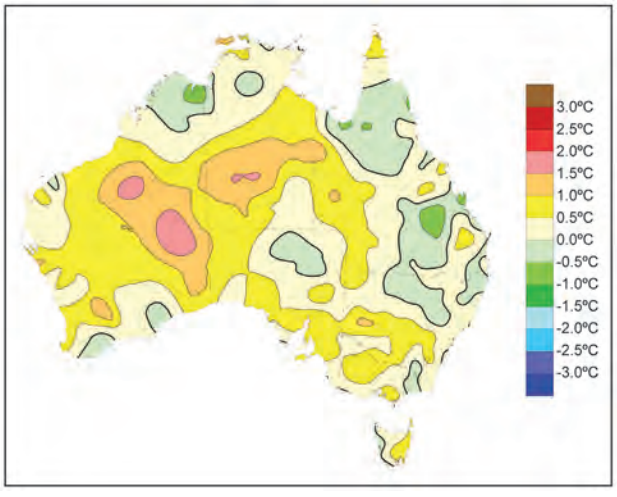

Fig. 7.48. Australian mean annual maximum temperature anomalies (°C; 1961–80 base period) for 2008.

The winter rainfall areas of southeastern Australia experienced near-normal totals in July and August but were otherwise dry, especially in September and October, which were the driest on record over large parts of Victoria and South Australia.

There was a marked shift in the rainfall regime in November, with above-normal rains extending through most of the continent. The contrast was especially marked in South Australia and the southern half of the Northern Territory, much of which experienced its driest January–October on record, with many stations below 50 mm for the period (and a few below 20 mm). South Australia followed its second-driest January–October on record, with its wettest November–December.

For the year as a whole (Fig. 7.49), rainfall was above normal in northern New South Wales and eastern Queensland, the Top End of the Northern Territory and the Kimberley region of western Australia, and most of the western half of western Australia. The most consistent below-normal values were in the central Northern Territory and adjoining western Queensland, as well as in the southeast, covering Victoria, Tasmania, and southern South Australia. In the latter region, the low rainfall exacerbated long-term rainfall deficits. The last 12 years have now been the driest such period on record in much of southern Victoria, while record 3-yr rainfall deficits have also developed in many areas, particularly on the northwest slopes of the Australian Alps, which are critical for inflows into the Murray-Darling basin.

(iv) Notable events

The most significant feature of the early weeks of 2008 in Australia was flooding in the north and east. While several regions were affected, the two most severe events affected the Emerald area in eastern Queensland in mid-January and Mackay in mid-February. The Emerald floods resulted from several days of heavy rain associated with the remnants of Tropical Cyclone Helen. The Mackay event, in contrast, was mostly flash flooding, which resulted from extremely heavy rain in a low-level convergence zone. East Mackay received 625 mm on 15 February, most of it in five hours. A full description of Australian and southwest Pacific basin cyclones is given in chapter 4.

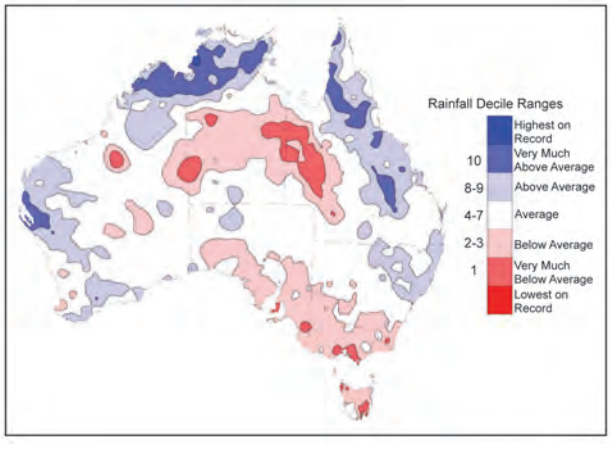

Fig. 7.49. Australian annual rainfall deciles for 2008.

Perhaps the most notable event of 2008 was the exceptional prolonged heat wave that affected southern Australia during March (National Climate Centre 2008). Adelaide experienced 15 consecutive days above 35°C from 3 to 17 March (including a run of 13 consecutive days above 37.8°C/100°F), nearly double the previous record of 8 days. The heat wave was more exceptional for its duration than any individual extreme days, but a Tasmanian state record for March was still set when Campania reached 38.0°C on 14 March.

There were several severe thunderstorm outbreaks in southeastern Queensland in the second half of November. The most damaging occurred on 16 November, when storms crossed metropolitan Brisbane and a suspected microburst caused major damage in the northwestern suburbs.

Tropical cyclone activity in the Australian region in the 2007/08 season was close to normal with a total of 10 systems (including those of late 2007).

2) New Zealand—M. J. Salinger

New Zealand's climate for 2008 was sunny and warm with many extremes. Most significantly, drought from January to March in the west of the North Island was estimated to have cost at least $1 billion (NZ), while floods in central North Island areas caused loss of life.

Overall, mean sea level pressures were near average over New Zealand, with more anticyclones than average to the east of the country, resulting in frequent winds from the north and northeast. Warmer-than-normal sea surface temperatures prevailed around New Zealand from January to May, becoming cooler during late spring before warming up again by early summer.

The national average temperature in 2008 was 12.9°C, 0.3°C above the 1971–2000 normal (Fig. 7.50). Temperatures were generally between 0.5° and 1.0°C above average in the west of the North Island and Nelson. The warmest location was Leigh (northeast North Island), with a mean temperature for the year of 16.5°C, 0.3°C above normal.

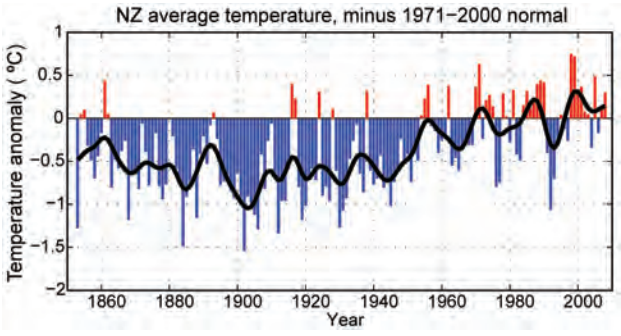

Fig. 7.50. Mean annual temperature anomalies (°C) over New Zealand, from 1853 to 2008 inclusive, based on between 2 (from 1853) and 7 (from 1908) long-term station records. The blue and red bars show annual differences from the 1971–2000 average; the solid black line is a smoothed time series.

Rainfall was close to normal in many areas of New Zealand. Annual rainfall was more than 135% of normal at the northern tip of New Zealand and in central New Zealand (Wellington and in central Marlborough), and more than 120% of normal in the far northern areas of the country, central New Zealand, and parts of the east of South Island. Annual rainfall was less than 90% of normal in the southwest of South Island, and the east of North Island, with parts of Fiordland, eastern Otago, and southern Hawke's Bay recording less than 80% of normal.

It was a sunny year everywhere, with nowhere in New Zealand recording below-normal sunshine totals. Sunshine hours were more than 115% of normal in central areas of North Island, the east of North Island, and in the east and south of South Island, with Turangi, Dannevirke, Waipawa, and Invercargill experiencing their sunniest years on record.

From January–March it was very extremely dry, with monthly totals of less than 10 mm in many areas. In Waikato it was the driest January in over 100 years of records. The dryness continued through February and March, and as a result, severe soil moisture deficits persisted in Waikato, parts of Bay of Plenty, South Taranaki, and northern Manawatu, Hawke's Bay, Wairarapa, and Marlborough, as well as parts of south Canterbury, Otago, and Southland. January also saw heat wave conditions occur across inland areas of South Island, sometimes reaching the coast.

April was a month of extremes, with floods in northern New Zealand, while it remained dry in the south. Heavy rainfalls alleviated the significant soil moisture deficits for most of North Island. It was the coldest May since 1992, with the national average temperature of 9.6°C being 1.1°C below average.

May to August were stormy months. Late June saw thunderstorms, hail, lightning, and high winds affecting much of North Island. In the last week of July, New Zealand was hit by two intense storms that caused flooding and the loss of five lives. Winter rainfall was over twice as high as normal in the northeast of South Island, with several high rainfall/flood-producing events. On 26 July heavy rainfall in Northland and Coromandel (166 mm was recorded in Paeroa, the highest 1-day total for July since records commenced in 1914) caused severe flooding. On 29 July, heavy rainfall caused more flooding, slips, and damage in Thames/Coromandel, Auckland, Nelson, and Marlborough. More severe flooding occurred on 26 August, when 126 mm of rain fell at Kaikoura, the second-highest 1-day August rainfall for this location since 1898, resulting in several landslides, damage, and the death of many livestock. Rainfall totals were greater than 150% of normal for much of North Island in August. Mt. Ruapehu in the central North Island recorded a snowpack of 3.5 m, the deepest since records began in 1992.

September brought a shift back to much more settled weather conditions for the country. Temperatures were above average, while rainfall was less than 50% of normal for many areas.

The period October to December was dry, with the southeast of South Island recording its highest October sunshine values on record. November and December were sunny months over much of the country, and rainfall was once again less than 50% of normal in eastern areas and between 50% and 80% of normal for much of North Island. Soil moisture levels in eastern areas and in Waikato were between 30 and 50 mm lower than normal at the end of December. Double the normal rainfall for November fell in the northwest of South Island and for December in inland Canterbury and Banks peninsula.

The highest New Zealand temperature of the year (34.8°C) occurred in the east of South Island at Timaru Airport on 12 January and 19 March and at Waione (eastern North Island) on 22 January, while the lowest temperature was –9.5°C recorded at Mt. Cook on 20 August. The highest-recorded wind gust was 183 km h^{-1} at Mokohinau Island on 11 May and at Hicks Bay on 18 June. The driest location was Alexandra in Central Otago with 376 mm of rain for the year, while, of the regularly reporting gauges, Cropp River in the Hokitika River catchment in the west of South Island recorded the highest rainfall with 10,940 mm. Of the major cities, Wellington was by far the wettest with 1,662 mm; in contrast, Christchurch

and Dunedin were the driest of the five main centers with a mere 704 and 705 mm, respectively. Auckland received 1,226 mm and Hamilton 1,220 mm.

3) Southwest Pacific—S. McGree

The year began with La Niña conditions firmly established in the equatorial Pacific (see chapter 4), the event reaching maturity in February, with the first signs of weakening apparent in March. Neutral conditions existed in May and continued for the rest of 2008, although some indices were more typical of a weak La Niña in November and December. The surface equatorial (trade) winds were generally enhanced from January to April, and again later in the year between September and December. Sea surface temperature anomalies along the equator in January were the coolest since 2000. Broadscale anomalies were as low as –2°C, with small areas of –3°C, and extended along the equator from the South American coast to west of the date line central; eastern equatorial SSTs increased from March to August. In September, slight cooling took place with further cooling from October to December, especially in the eastern Pacific.

From early January, the SPCZ was southwest of its normal position, typical of a cool ENSO phase. In March to May the SPCZ was well south, over Vanuatu and occasionally south of Fiji (Fig. 7.51). In June it extended from PNG over northern Fiji to Niue and across to the southern Cook and Austral Islands. Over the next five months, the SPCZ was generally north of Fiji, but it was usually weak and inactive; however, there were instances when troughs of low pressure would merge with the SPCZ, resulting in enhanced activity. In late December, the SPCZ was again south of its climatological position, particularly in the areas near Samoa and the Cook Islands. From January to May a large region of suppressed convection existed near the equator, including western and eastern Kiribati, Nauru, Tokelau, Tuvalu, and northern Cook and Marquesas Islands. Over the next three months the area of suppressed convection contracted but still included Kiribati and the region immediately to the south of these islands. Suppressed convection covering an area similar to that from January to May also existed from October to December.

Positive sea surface temperature anomalies existed around Vanuatu, New Caledonia, west of Fiji, eastern French Polynesia, and Pitcairn Island in January. These positive SST anomalies expanded in February to cover the band from PNG to Vanuatu, south of Fiji, to a large region south of the Cook and Austral Islands. Anomalies above +2.0°C existed at the center of this large region. The area of positive SST anomalies increased in March to include the Solomon Islands, Fiji, Tonga, and the southern Cook Islands. Cooling occurred from April to June. Warming resumed in July, and by November positive SST anomalies existed from northern PNG to French Polynesia. Positive SST anomalies extended as far north as Tuvalu and Samoa in December and were greater than +2.0°C from southern Vanuatu to south of Fiji and in a large region south of the Cook Islands. This pattern is typical of positive (cool) ENSO conditions caused by a strengthening of the South Pacific high and the southwest displacement of the SPCZ.

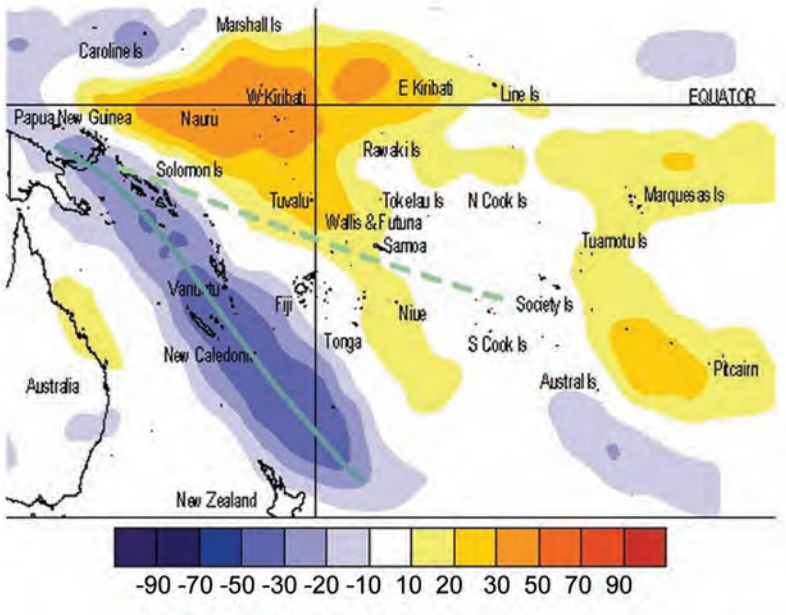

Fig. 7.51. Outgoing longwave radiation anomalies (W m^{-2}) in the southwest Pacific for Apr 2008. Solid line indicates the location of the SPCZ. Dashed line indicates the normal location of the SPCZ in Apr.

Annual rainfall was greater than 120% of normal across most of the Solomon Islands, central Vanuatu, most of Fiji, and Tonga. Near-normal rainfall was received elsewhere in these countries and the southern parts of Tuvalu, Niue, American Samoa, and the southern Cook Islands. Below-normal rainfall was recorded at Nanumea in northern Tuvalu (36% of normal, lowest in 68 years), the whole of Kiribati (44%–59%), and Penrhyn in the northern Cook Islands (56%). This pattern of drier conditions in

the north and east, and wetter conditions in the south and west, is broadly consistent with the neutral-to-cool ENSO conditions that were experienced through 2008.

Maximum and minimum air temperatures in American Samoa were above normal year-round. In Fiji, maximum and minimum temperatures were normal or above normal, except in January and May—and March in the case of minimum temperatures.

Three tropical cyclones formed in the southwest Pacific in 2008 (for full details see chapter 4). TC Funa developed near northern Vanuatu on 16 January, resulting in maximum winds to 195 km h^{-1}, causing damage to agricultural crops, villages, and tourist resorts in the provinces of Torba, Sanma, and Penama. TC Gene developed over Fiji on 28 January with winds to 185 km h^{-1}, resulting in significant damage to agricultural crops and the loss of seven lives. The financial cost of the damage in Fiji exceeded $22 million (USD). More than 50% of agricultural crops were damaged by high winds as the cyclone passed close to the island of Futuna in Vanuatu.

Satellite observations show generally positive sea level in the western South Pacific throughout the year. In March, the region of +20-cm anomalies had expanded east as far as Tuvalu, with all-time monthly mean sea level records set in the PNG and the Solomon Islands region. Reasonably large tidal ranges were observed early in May and June due to the astronomical positions of the moon and the sun. Record-high sea level was observed by the Vanuatu Tide Gauge in November, with the monthly mean exceeding the October 2008 record by 5 cm. Large waves generated by weather systems in the far North Pacific caused flooding along coastlines of a number of Pacific Island countries in December. By the end of the month, positive sea level anomalies existed across much of the region, from 160°E–160°W and 5°–22°S, with the highest +20-cm anomalies off the PNG coastline.

Other notable meteorological events included hail on three separate days and a small 15-min tornado during November in Fiji. Incidences of hail and tornados are very rare in the southwest Pacific and are usually associated with afternoon thunderstorm activity.

4) Northwest Pacific, Micronesia—C. Guard and M. A. Lander

(i) Overview

This assessment covers the area from the date line west to 130°E, between the equator and 20°N. It includes the U.S.-affiliated islands of Micronesia but excludes the western islands of Kiribati. The weather throughout Micronesia was generally tranquil, with no destructive wind events and few extremes of rainfall. This is generally typical of the weather experienced during La Niña, although the prevailing state of the climate was ENSO neutral. As in 2007, trade winds and low-latitude easterly winds were stronger than normal, while the monsoon trough spent most of the boreal summer and fall west of Micronesia, rarely pushing eastward beyond Palau and Yap. This caused a shift of tropical cyclone activity in the basin, with most tropical cyclones developing west of Guam and north of Yap, and not significantly intensifying until they were nearer to the Philippines, Taiwan, or East Asia. In addition, sea levels were significantly higher than normal across all of Micronesia. In fact, the most dramatic climate extreme of the year occurred during the week of 8–15 December 2008, when an unusual pattern of gale-force winds located in the subtropics of the western North Pacific near the date line generated an oceanic swell that traveled to the south and caused phenomenal surf throughout eastern Micronesia and the northern coast of Papua New Guinea.

(ii) Temperature

Except for the Mariana Islands (e.g., Guam and Saipan), average monthly maximum temperatures across most of Micronesia were lower than normal. At the Guam International Airport, monthly average maximum temperature anomalies were +0.40°C from January through June and +0.19°C for the entire year. For Palau, at the western end of the area, the average monthly maximum temperature anomalies were −0.35°C for the first six months and −0.27°C for the entire year. Values at Yap were −0.34°C for the first six months and −0.42°C for the entire year. In central Micronesia, south of 10°N, Chuuk had average monthly maximum temperature anomalies of −0.22°C for the first 6 months and 12-month anomalies of −0.28°C. Farther east, Pohnpei experienced January through June anomalies of −0.15°C and for the year they were −0.16°C. Still farther east, maximum temperature anomalies at Kosrae were larger, with 6-month and 12-month values being −0.74°C and −0.65°C, respectively.

The cause of the persistently below-normal maximum temperatures across most of Micronesia may have been related to the persistent tongue of colder-than-normal SSTs that extended from California to south of Hawaii, and then to Micronesia, for much of the year. In addition, trade winds were much stronger than normal over Micronesia, likely increasing

cooling via evaporation. Temperature anomalies for the first six months and for all of 2008 for selected Micronesian locations are summarized in Table 7.4.

(iii) Precipitation

Precipitation at the major island stations during the first half of 2008 was fairly typical of La Niña conditions. The stronger-than-normal and converging northeast and southeast trade winds allowed the trade wind trough to become well developed, keeping the western North Pacific islands between 4° and 8°N wet during the first half of the year. The trough axis typically passes very close to Kosrae, which had 3101.1 mm or 112% of normal rainfall during the first half of 2008. In general, rainfall for the first six months of 2008 in Micronesia fell between 75% and 125% of average throughout most of the area. With the exception of the Marshall Islands, locations north of 8°N were drier than normal, while those south of 8°N were generally wetter than normal. In the Marshall Islands, locations north of 6°N were drier than normal and those south of 6°N were wetter. During the third quarter (July–September), almost all locations in Micronesia were considerably drier than normal. This was the result of monsoon and tropical cyclone activity being displaced well to the north and west, and high pressure generally dominating Micronesia. The annual rainfall for the major islands in Micronesia ranged from a high of 5,661.7 mm or 108% of normal at Kosrae to a low of 1,697.2 mm or 88% of normal at Saipan in the Commonwealth of the Northern Mariana Islands. Palau at the western edge of the area had 4,038.3 mm or 107% of normal, while Majuro at the eastern edge of the area had 2,933.7 mm, 88% of normal for the year. Generally, islands north of 8°–9°N and east of 165°E were drier than normal, while those to the south and west were wetter than normal. The six-month and annual rainfall for selected locations are summarized in Table 7.4. Figure 7.52 shows the annual rainfall amount and percent of normal for American Samoa and the major Micronesian islands.

(iv) Tropical cyclone activity

Tropical cyclone activity in 2008 in the western North Pacific and across Micronesia was below nor-

Table 7.4. Maximum (max) temperature (temp) anomalies and rainfall anomalies for selected Micronesian locations for Jan–Jun and Jan–Dec 2008. "N" is the normal rainfall taken from the NCDC 1971–2000 base period. Locations (lat and lon) are approximate.

		Max Temp		Rainfall					
		Jan–Jun	Jan–Dec	Jan–Jun			Jan–Dec		
Station	**Location**	°C	°C	N mm	2008 mm	2008 %	N mm	2008 mm	2008 %
Guam	13°N, 145°E	+0.40	+0.19	612.1	618.2	99	2167.6	1838.2	81
Yap	9°N, 138°E	−0.34	−0.42	1168.9	950.7	81	2987.5	2710.4	89
Palau	7°N, 134°E	−0.35	−0.27	1724.7	1841.8	107	3768.6	4038.3	107
Chuuk	7°N, 152°E	−0.22	−0.28	1538.0	1801.4	117	3402.8	3262.1	97
Pohnpei	7°N, 158°E	−0.15	−0.16	2277.6	2794.8	123	4689.1	4767.1	100
Kosrae	5°N, 163°E	−0.74	−0.65	2765.3	3101.1	112	5236.7	5661.7	108
Kwajalein	9°N, 168°E	−0.69	−0.63	959.6	822.5	86	2550.2	2164.6	83
Majuro	7°N, 171°E	+0.62	+0.25	1455.4	1289.6	89	3344.2	2933.7	88

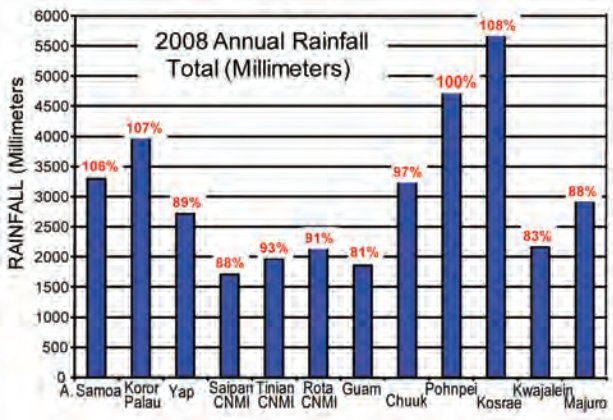

Fig. 7.52. Annual rainfall (mm) for American Samoa and selected Micronesian islands for Jan through Dec 2008. Numbers above the bars indicate the annual rainfall as a percent of normal as determined from the NCDC 1971–2000 base period.

mal (see chapter 4d4), and was even more meager than in 2007. For nearly the entire year, low-level easterly wind anomalies dominated low latitudes of the western North Pacific. The monsoon trough was weak and displaced to the west, and as a result, tropical cyclone genesis was affected in two fundamental ways: a reduction of the number of tropical cyclones that developed in the deep tropics and a major shift to the west and north of the tropical cyclone genesis area. It was not until the first week of December that a midlatitude cyclone east of Japan intensified and developed a warm-cored vortex and became the seed for Typhoon Dolphin. Prior to Dolphin, every 2008 storm that began to develop in Micronesia never intensified beyond tropical depression intensity until it passed west of Palau, Yap, Guam, or the Commonwealth of the Northern Mariana Islands.

(v) Sea level

The high sea levels of 2007 that occurred across Micronesia continued through all of 2008. The persistent La Niña–like conditions kept trade winds strong, and hence the wind stress caused water to mound up in the west of the basin. In addition, clearer-than-normal skies allowed the ocean to absorb abundant incoming solar radiation, which added heat content, and hence thermal expansion, to the upper 300 m of the western North Pacific Ocean. As a result, coastal flooding and inundation affected many of the low islands from the Marshall Islands in the east to Palau in the west. Sea levels were highest from January through April and in November and December. From January 2008 through the end of the year, sea levels averaged 15 to 25 cm above their normal monthly averages, but during full and new moon phases, the high tide levels were sometimes as high as 80–110 cm above expected high tide levels. The high astronomical tides coupled with the affect of La Niña caused considerable coastal inundation in the Chuuk and Pohnpei states, contaminating drinking water and destroying food crops.

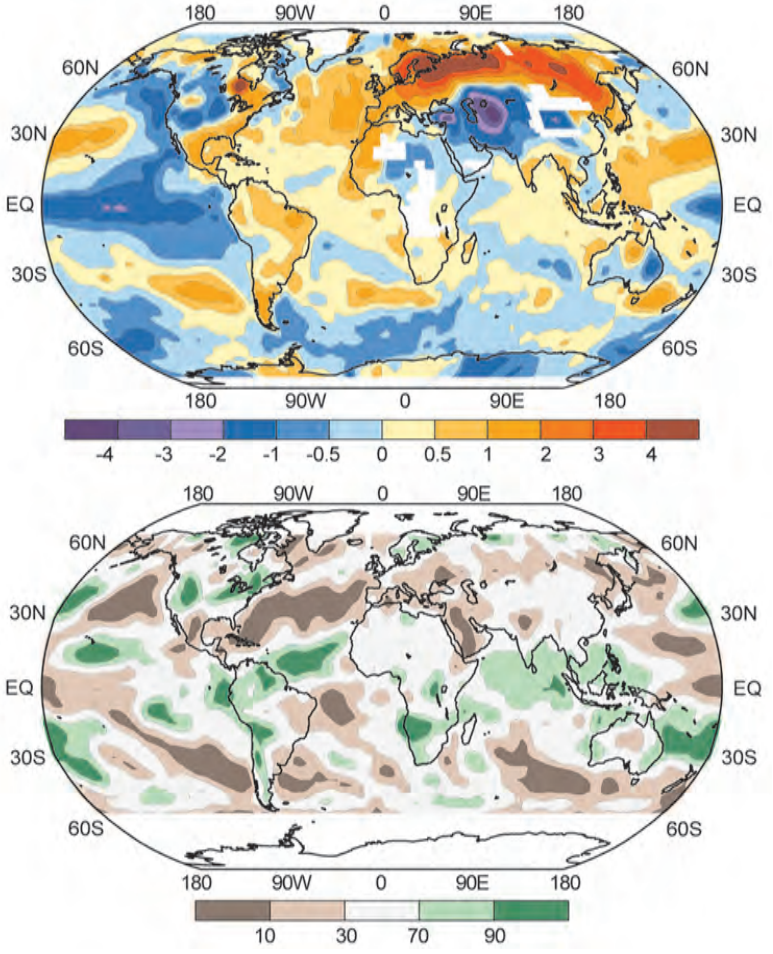

Fig. 8.1 .Dec 2007–Feb 2008 (top) surface temperature anomalies (°C) and (bottom) precipitation percentiles based on a gamma distribution fit to the 1979–2000 base period. Temperature anomalies (1971–2000 base period) are based on station data over land and SST data over water. Precipitation data were obtained from the CAMS-OPI dataset that is a combination of rain-gauge observations and satellite-derived estimates (Janowiak and Xie 1999). Analysis was omitted in data-sparse regions (white areas).

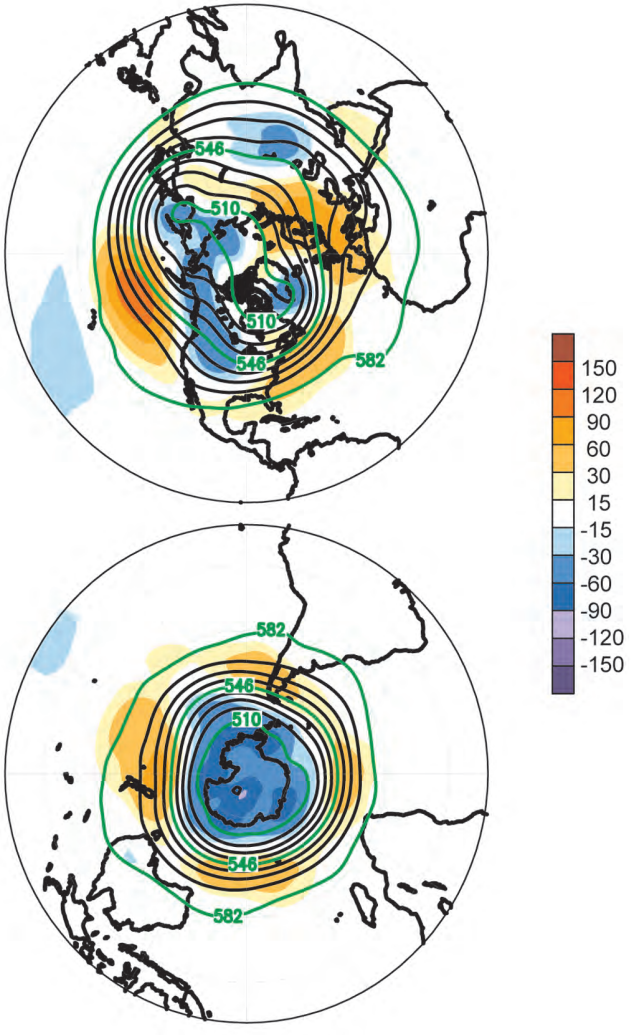

Fig. 8.2. Dec 2007–Feb 2008 (top) Northern Hemisphere and (bottom) Southern Hemisphere 500-hPa geopotential heights (9-dam contour interval) and anomalies (shading) determined from the 1979–2000 base period means.

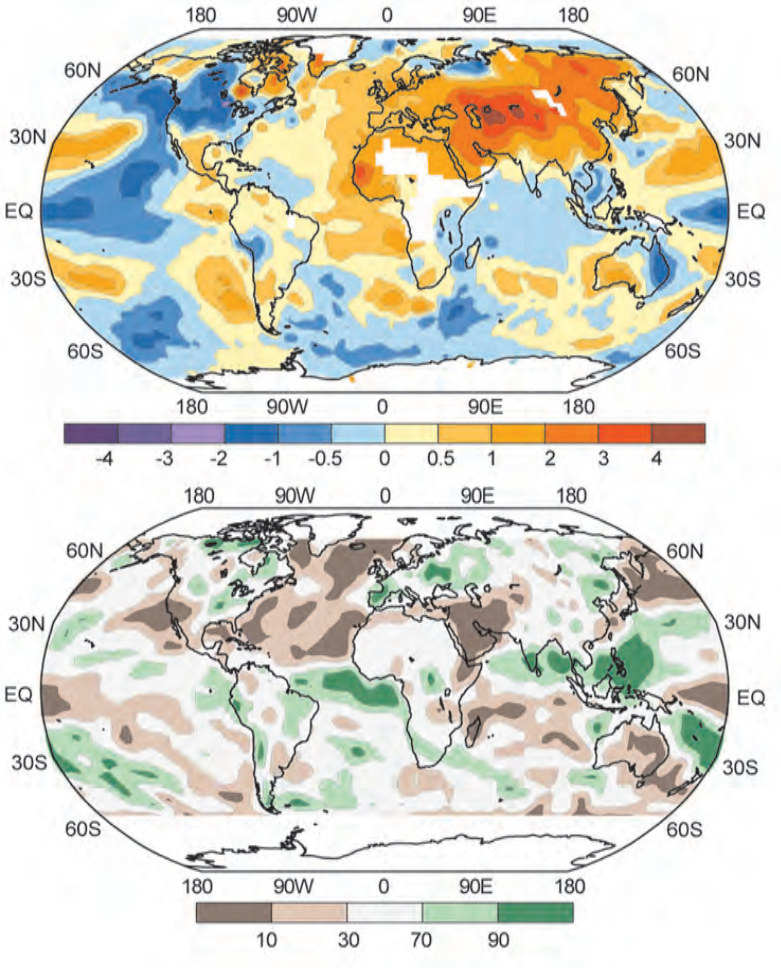

Fig. 8.3. Mar–May 2008 (top) surface temperature anomalies (°C) and (bottom) precipitation percentiles based on a gamma distribution fit to the 1979–2000 base period. Temperature anomalies (1971–2000 base period) are based on station data over land and SST data over water. Precipitation data were obtained from the CAMS-OPI dataset that is a combination of rain-gauge observations and satellite-derived estimates (Janowiak and Xie 1999). Analysis was omitted in data-sparse regions (white areas).

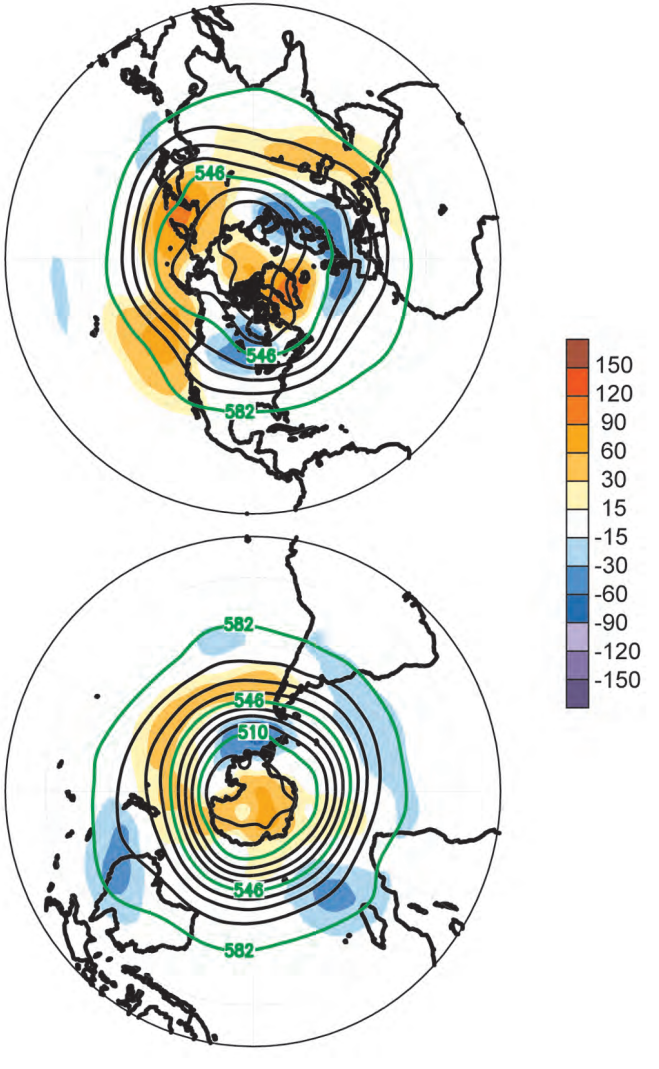

Fig. 8.4. Mar–May 2008 (top) Northern Hemisphere and (bottom) Southern Hemisphere 500-hPa geopotential heights (9-dam contour interval) and anomalies (shading) determined from the 1979–2000 base period means.

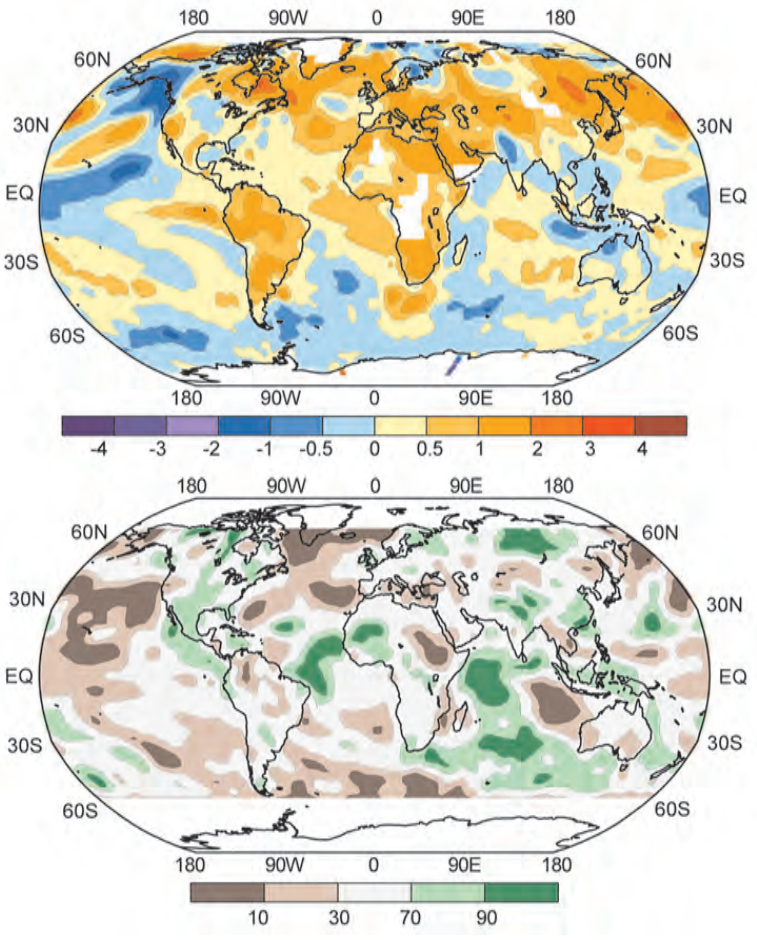

Fig. 8.5. Jun–Aug 2008 (top) surface temperature anomalies (°C) and (bottom) precipitation percentiles based on a gamma distribution fit to the 1979–2000 base period. Temperature anomalies (1971–2000 base period) are based on station data over land and SST data over water. Precipitation data were obtained from the CAMS-OPI dataset that is a combination of rain-gauge observations and satellite-derived estimates (Janowiak and Xie 1999). Analysis was omitted in data-sparse regions (white areas).

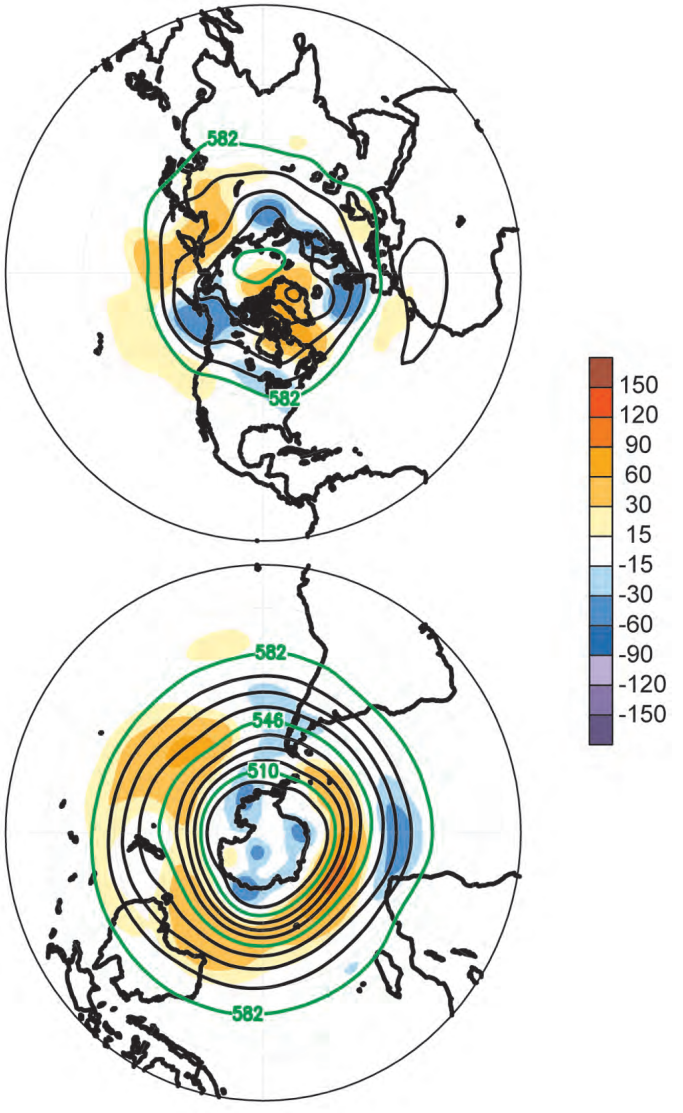

Fig. 8.6. Jun–Aug 2008 (top) Northern Hemisphere and (bottom) Southern Hemisphere 500-hPa geopotential heights (9-dam contour interval) and anomalies (shading) determined from the 1979–2000 base period means.

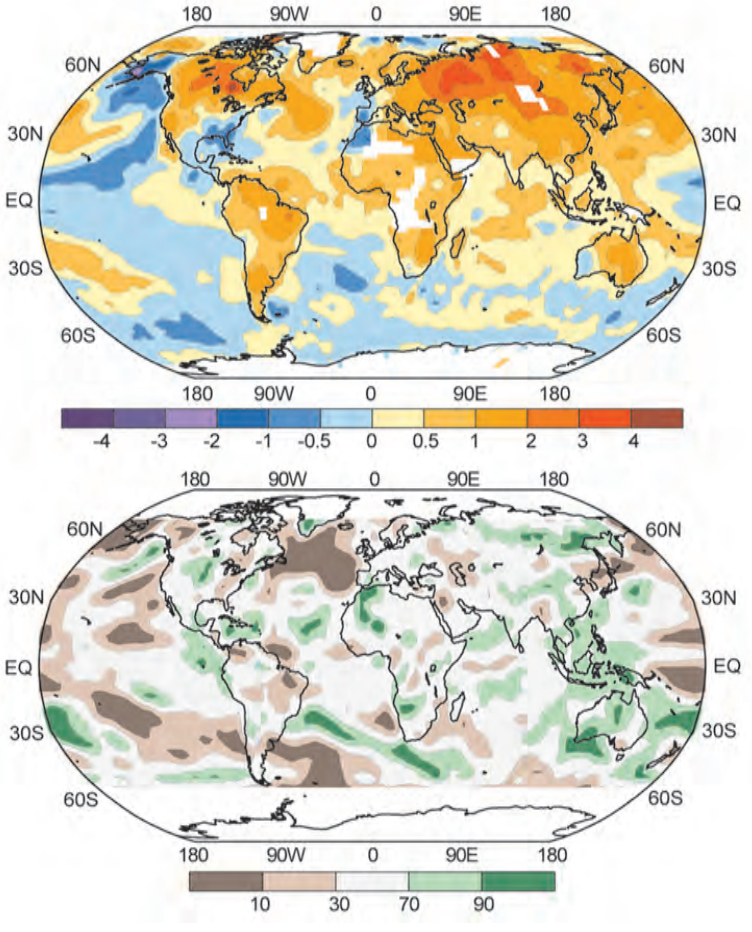

Fig. 8.7. Sep–Nov 2008 (top) surface temperature anomalies (°C) and (bottom) precipitation percentiles based on a gamma distribution fit to the 1979–2000 base period. Temperature anomalies (1971–2000 base period) are based on station data over land and SST data over water. Precipitation data were obtained from the CAMS-OPI dataset that is a combination of rain-gauge observations and satellite-derived estimates (Janowiak and Xie 1999). Analysis was omitted in data-sparse regions (white areas).

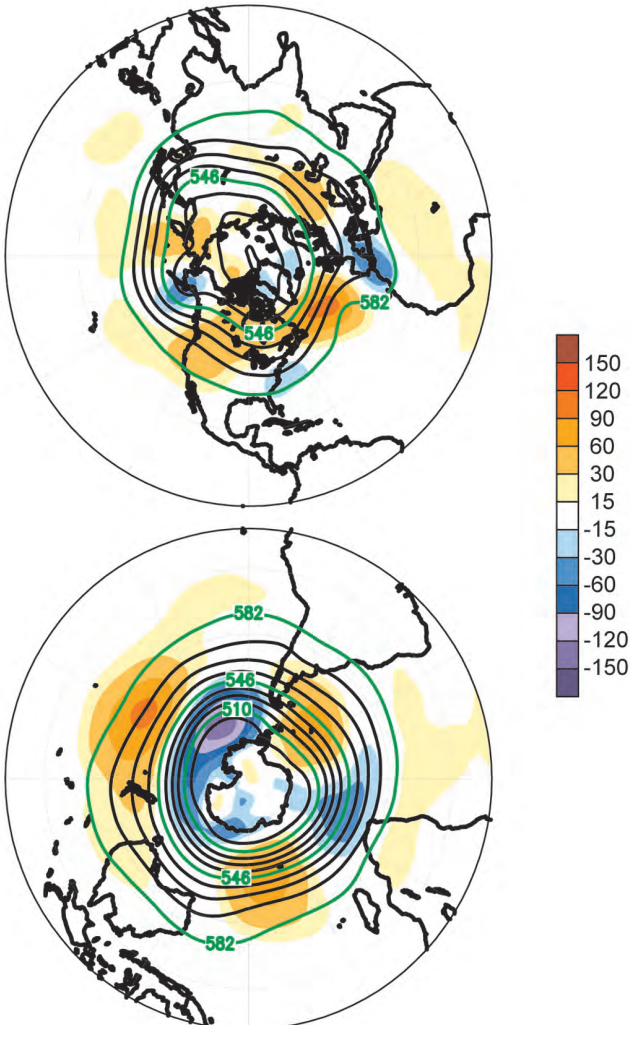

Fig. 8.8. Sep–Nov 2008 (top) Northern Hemisphere and (bottom) Southern Hemisphere 500-hPa geopotential heights (9-dam contour interval) and anomalies (shading) determined from the 1979–2000 base period means.

ACKNOWLEDGMENTS. We would like to acknowledge our sincere appreciation for the many anonymous reviewers who worked under tight deadlines and whose insights made this and future issues of the State of the Climate better.

APPENDIX: ACRONYMS

A	Anticyclonic days
AAO	Atlantic Oscillation
ACC	Antarctic Circumpolar Current
ACE	NOAA's Accumulated Cyclone Energy Index
AEJ	African Easterly Jet
AGCM	Atmospheric general circulation model
AGGI	NOAA's Annual Greenhouse Gas Index
AMIP	Atmospheric Model Intercomparison Project
AMJ	April–May–June
AMO	Atlantic Multidecadal Oscillation
AMSR-E	Advanced Microwave Scanning Radiometer for Earth Observing System
AMSU	Advanced Microwave Sounding Unit
ANEEL	Agência Nacional de Energia Eléctrica
AO	Arctic Oscillation
AOD	Aerosol optical depth
AOML	Atlantic Oceanographic and Meteorological Laboratory
AR4	Fourth Assessment Report
ASAR	Advanced Synthetic Aperture Radar
ASO	August–September–October
ASTER	Advanced Spaceborne Thermal Emission and Reflection Radiometer
ATLAS	Autonomous Temperature Line Acquisition System
AVHRR	Advanced Very High Resolution Radiometer
AVISO	Archiving, Validating, and Interpretation of Satellite Oceanographic data
AW	Arctic Warm
BC	British Columbia
BGOS	Beaufort Gyre Observing System
BI	Balleny Islands
Br	Bromine
C	Cyclonic days
CALIPSO	Cloud-Aerosol Lidar and Infrared Pathfinder Satellite Observation
CAMS	Climate Anomaly Monitoring System
CAPE	Convective Available Potential Energy
CERES	Clouds and the Earth's Radiant Energy System
CFC	Chlorofluorocarbon
CFC-11	Trichlorofluoromethane
CFC-12	Dichlorodifluoromethane
CH_4	Methane
Chl_{sat}	Surface-layer chlorophyll concentration
CIIFEN	International Research Center on El Niño
Cl	Chlorine
CLIVAR	Climate Variability and Predictability
CMA	China Meteorology Administration
CMAP	Climate Prediction Center (CPC) Merged Analysis of Precipitation
CMC	Canadian Meteorological Centre
CMIP	Coupled Model Intercomparison Project
CNES	Centre National d'Etudes Spatiales
CO	Carbon monoxide
CO_2	Carbon dioxide
CONAFOR	National Forestry Commission, Mexico
CPC	Climate Prediction Center
CPHC	NOAA's Central Pacific Hurricane Center
CPTEC	Center for Weather Forecasting and Climate Studies
CRU	Climate Research Unit
CSI	NOAA Climate Scene Investigation
CTD	Conductivity, Temperature, Depth
CYC	Cyclone
DIC	Dissolved inorganic carbon
DISC	Data and Information Services Center
DJF	December–January–February
DMSP	Defense Meteorological Satellite Program
DOE	Department of Energy
DU	Dobson units
DWBC	Deep western boundary current
DWD	Deutscher Wetterdienst
EBAF	Energy Balanced and Filled
ECl	Equivalent chlorine
ECMWF	European Centre for Medium-Range Weather Forecasts

ECV	Essential Climate Variables
EECl	Effective equivalent chlorine
EESC	Effective equivalent stratospheric chlorine
EKE	Eddy kinetic energy
ENP	Eastern North Pacific (basin)
ENSO	El Niño–Southern Oscillation
EOF	Empirical orthogonal function
EOS	Earth Observatory System
ERB	Earth Radiation Budget
ERBE	Earth Radiation Budget Experiment
ERSST, v3b	Extended Reconstructed Sea Surface Temperature, version 3b
ESA	European Space Agency
ESRL	Earth System Research Laboratory
EU	European Union
FAO	Food and Agriculture Organization
FAPAR	Fraction of Absorbed Photosynthetically Active Radiation
FLASHflux	Fast Longwave and Shortwave Radiative Fluxes
FWC	freshwater content
GCM	General circulation model
GCOS	Global Climate Observing System
GEOSECS	Geochemical Ocean Section Study
GHA	Greater Horn of Africa
GHCN	Global Historical Climatology Network
GIA	Glacial isostatic adjustment
GIMMS	Global Inventory Modeling and Mapping Strides
GISS	NASA's Goddard Institute of Space Studies
GMD	Global Monitoring Division
GMSL	global mean sea level
GOME	Global Ozone Monitoring Experiment
GPCC	Global Precipitation Climatology Centre
GPCP	Global Precipitation Climatology Project
GPI	Genesis potential index
GRACE	Gravity Recovery and Climate Experiment
GRDC	Global Runoff Data Centre
Gt	gigaton
GTSPP	Global Temperature and Salinity Profile Project
H	Hurricane
HadAT	Hadley Centre's radiosonde temperature product
HadCRUT3	Hadley Centre/CRU gridded monthly temperatures dataset
HadGEM1	Hadley Centre global model
HCFC	Hydrochlorofluorocarbon
HFC	Hydrofluorocarbon
HIRS-W	High Resolution Infrared Sounder
hPa	Hectopascal (1 mb)
IGY	International Geophysical Year
INPE	National Institute for Space Research, Brazil
INSTAAR	Institute of Arctic and Alpine Research
IO	Indian Ocean
IOD	Indian Ocean dipole
IODE	eastern pole of the Indian Ocean Dipole
IPCC	Intergovernmental Panel on Climate Change
IPCC AR4	IPCC Fourth Assessment report (published in 2007)
IR	Infrared
IRIMO	Islamic Republic of Iran Meteorological Organization
ISCCP	International Satellite Cloud Climatology Project
ITCZ	Intertropical convergence zone
IUK	iterative universal Kriging
JAS	July–August–September
JASO	July–August–September–October
JFM	January–February–March
JGOFS	Joint Global Ocean Flux Study
JJA	June–July–August
JMA	Japanese Meteorological Agency
JPL	Jet Propulsion Laboratory
JRA	Japanese Reanalysis
JTWC	U.S. Navy's Joint Typhoon Warning Center
KNMI	Royal Netherlands Meteorological Institute
LaRC	Langley Research Center
LHF	Latent heat flux
MAM	March–April–May
MBT	mechanical bathythermograph
MCYC	Major cyclone
MDR	Main Development Region
MEI	Multivariate ENSO Index
MERIS	Medium Resolution Imaging Spectrometer
MH	Major hurricane
MISR	Multiangle Imaging SpectroRadiometer
MJO	Madden–Julian oscillation
MLO	Mauna Loa Observatory

MLS	Microwave Limb Sounder
MM5	Fifth-generation Pennsylvania State University–National Center for Atmospheric Research Mesoscale Model
MOC	Meridional overturning current
MOCHA	Meridional Overturning Circulation Heat Transport Array
MODIS	Moderate Resolution Imaging Specroradiometer
MOPITT	Measurements of Poluution in the Troposphere
MSLP	mean sea level pressure
MSU	Microwave Sounding Unit
MTSAT	Multifunctional Transport Satellites
N_2O	Nitrous oxide
NAM	Northern annular mode
NAMOS	Nansen and Amundsen Basin Observational System
NAO	North Atlantic Oscillation
NARR	North American Regional Reanalysis
NASA	National Aeronautics and Space Administration
NCAR	National Center for Atmospheric Research
NCDC	National Climatic Data Center
NCEP	National Center for Environmental Prediction
NDVI	Normalized difference vegetation index
NEM	Northeast monsoon
NERC	National Environmental Research Council
NH	Northern Hemisphere
NHC	National Hurricane Center
NIFC	National Interagency Fire Center
NIO	Northern Indian Ocean
NOAA	National Oceanic and Atmospheric Administration
NOMADS	National Operational Model Archive and Distribution System
NPEO	North Pole Environmental Observatory
NPP	Net primary production
NRTSI	Near Real-Time SSM/I Plar Gridded Sea Ice Concentrations
NS	Named storm
NSIDC	National Snow and Ice Data Center
NSW	New South Wales, Australia
NWS	National Weather Service
O_3	Ozone
OAFlux	Objectively Analyzed Air–Sea Fluxes
ODGI	Ozone Depleting Gas Index
OH	Hydroxide anion
OHCA	Ocean Heat Content Anomaly
OI	Optimal interpolation
OISST, v2	Optimal Interpolation SST, version 2
OLR	Outgoing longwave radiation
OMI	Ozone Monitoring Instrument
ONI	Oceanic Niño Index
OPI	OLR precipitation index
OSCAR	Ocean Surface Current Analysis–Real Time
PATMOS (-x)	Pathfinder Atmospheres (Extended Product)
pCO_2	Carbon dioxide partial pressure
PDO	Pacific decadal oscillation
Pg	Petagram (1015 g)
PIRATA	Pilot Research Array in the Tropical Atlantic
PMEL	Pacific Marine Environmental Laboratory
PNG	Papau New Guinea
PO.DAAC	Physical Oceanography Distributed Active Archive Center
ppb	Parts per billion
ppbv	Parts per billion by volume
ppm	Parts per million
ppt	Parts per trillion
PSC	Polar stratospheric cloud
PSS	Practical salinity scale
PT	total precipitation
QBO	Quasi-biennial oscillation
QuikSCAT	Quick Scatterometer
RAMA	Research Moored Array for African-Asian-Australian Monsoon Analysis Prediction
RAOBCORE	Radiosonde Observation Correction
RATPAC	Radiosonde Atmospheric Temperature Products for Assessing Climate
RICH	Radiosonde Innovation Composite Homogenization
RSMC	Regional Specialized Meteorological Centre Tokyo
RSS	Remote Sensing Systems
SAM	Southern annular mode
SAT	surface air temperature
SBUV	Solar Backscatter Ultraviolet
SCD	snow cover duration
SCE	Snow cover extent

SCIAMACHY	SCanning Imaging Absorption Spectrometer for Atmospheric Chartography
SCS	South China Sea
SD	snow depth
SeaWiFS	Sea-viewing Wide Field of View
ΣChl	Photic zone chlorophyll
SF_6	Sulfur hexafluoride
SH	Southern Hemisphere
SHF	Sensible heat flux
SIO	Southern Indian Ocean
SL	Sea level
SLP	Sea level pressure
SMMR	Scanning Multichannel Microwave Radiometer
SOBS	surface weather observations
SOI	Southern Oscillation index
SON	September–October–November
SPCZ	South Pacific convergence zone
SPOT	VGT satellite
SRES	Special Report on Emissions Scenarios
SSALTO/DUACS	Segment Sol Multimission Altimetry and Orbitography/ Developing Use of Altimetry for Climate Studies
SSM/I	Special Sensor Microwave Imager
SSS	Sea surface salinity
SST	Sea surface temperature
SSTA	Sea surface temperature anomaly
SSU	Stratosphere Sounding Units
STAR	Center for Satellite Applications and Research
STY	Supertyphoon
Sv	Sverdrups (1 Sv ≡ 10^6 m^3 s^{-1})
SWI	Summer warmth index
SWP	Southwest Pacific
TAO	Tropical Atmosphere Ocean
TATL	Tropical Atlantic
TC	Tropical cyclone
TCHP	Tropical cyclone heat potential
TCWV	Total Column Water Vapor
TD	Tropical depression
TI-NDVI	time-integrated NDVI
TLT	temperature of the lower troposphere
TMI	Tropical Rainfall Measuring Mission Microwave Imager
TOA	top of atmosphere
TOMS	Total Ozone Mapping Spectrometer
TRMM	Tropical Rainfall Measuring Mission
TS	Tropical storm
TSP	Thermal state of permafrost
TMI	Tropical Rainfall Measuring Mission Microwave Imager
TW	trade winds
TY	Typhoon
UAH	University of Alabama Huntsville
USD	U.S. Dollars
USGS	U.S. Geological Survey
VasClimO	Variability Analysis of Surface Climate Observations
VOCALS	VAMOS (Variability of the American Monsoon Systems) Ocean–Cloud–Atmosphere–Land Study
WBC	Western boundary current
WGMS	World Glacier Monitering Service
WHOI	Woods Hole Oceanographic Institute
WMO	World Meteorological Organization
WNP	western North Pacific (basin)
WOA	*World Ocean Atlas*
WOCE	World Ocean Circulation Experiment
WPO	west Pacific Ocean
XBT	Expendable bathythermograph

REFERENCES

Adler, R. F., and Coauthors, 2003: The Version-2 Global Precipitation Climatology Project (GPCP) Monthly Precipitation Analysis (1979–present). *J. Hydrometeor.,* **4,** 1147–1167.

Allan, R. J., and R. D. D'Arrigo, 1999: 'Persistent' ENSO sequences: How unusual was the 1990–1995 El Niño? *Holocene,* **9,** 101–118**.**

——, J. A. Lindesay, and D. E. Parker, 1996: *El Niño, Southern Oscillation & Climatic Variability*. CSIRO Publications, 405 pp.

Alsdorf, D. E., and D. P. Lettenmaier, 2003: Tracking fresh water from space. *Science,* **301,** 1491–1494.

——, E. Rodrígues, and D. P. Lettenmaier, 2007: Measuring surface water from space. *Rev. Geophys.,* **45,** RG2002, doi:10.1029/2006RG000197.

Ando, K., and M. J. McPhaden, 1997: Variability of surface layer hydrography in the tropical Pacific Ocean. *J. Geophys. Res.,* **102,** 23 064–23 078.

Appenzeller, C., A. K. Weiss, and J. Staehelin, 2000: North Atlantic Oscillation modulates total ozone winter trends. *Geophys. Res. Lett.,* **27,** 1131–1134.

Archer, D., and V. Brovkin, 2008: Millennial atmospheric lifetime of anthropogenic CO_2. *Climatic Change,* **90,** 283–297.

Arctic Climatology Project, 1997: *Environmental Working Group Joint U.S.-Russian Atlas of the Arctic Ocean - Winter Period*. L. Timokhov and F. Tanis, Eds. Environmental Research Institute of Michigan in association with the National Snow and Ice Data Center. CD-ROM.

——, 1998: *Environmental Working Group Joint U.S.-Russian Atlas of the Arctic Ocean - Summer Period*. L. Timokhov and F. Tanis, Eds. Environmental Research Institute of Michigan in association with the National Snow and Ice Data Center. CD-ROM.

Arguez, A., A. M. Waple, and A. M. Sanchez-Lugo, 2007: State of the climate in 2006. *Bull. Amer. Meteor. Soc.,* **88,** 929–932.

Arino, O., P. Bicheron, F. Achard, J. Latham, R. Witt, and J. L. Weber, 2008: The most detailed portrait of Earth. ESA Bull. 136, 24–31.

Atkinson, G. D., 1971: *Forecasters' Guide to Tropical Meteorology.* U.S. Air Force Tech. Rep. 240, 360 pp.

Baehr, J., H. Haak, S. Alderson, S. A. Cunningham, J. H. Jungclaus, and J. Marotzke, 2007: Timely detection of changes in the meridional overturning circulation at 26°N in the Atlantic. *J. Climate,* **20,** 5827–5841.

——, K. Keller, and J. Marotzke, 2008: Detecting potential changes in the meridional overturning circulation at 26°N in the Atlantic. *Climatic Change,* **91** (1–2), 11–27, doi: 10.1007/s10584-006-9153-z.

Baldwin, M. P., and Coauthors, 2001: The Quasi-Biennial Oscillation. *Rev. Geophys.,* **39,** 179–229.

Bales, R. C., E. Mosley-Thompson, and J. R. McConnell, 2001: Variability of accumulation in northwest Greenland over the past 250 years. *Geophys. Res. Lett.,* **28,** 2679–2682.

Baringer, M. O., and R. Molinari, 1999: Atlantic Ocean baroclinic heat flux at 24° to 26°N. *Geophys. Res. Lett.,* **26,** 353–356.

——, and J. Larsen, 2001: Sixteen years of Florida Current transport at 27°N. *Geophys. Res. Lett.,* **28** (16), 3179–3182.

Bartholome, E. M., and A. S. Belward, 2005: GLC2000; a new approach to global land cover mapping from earth observation data. *Int. J. Remote Sens.,* **26,** 1959–1977.

Baumgartner, A., and E. Reichel, 1975: *The World Water Balance*. Elsevier, 180 pp.

Beal, L. M., J. M. Hummon, E. Williams, O. B. Brown, W. Baringer, and E. J.Kearns, 2008: Five years of Florida Current structure and transport from the Royal Caribbean Cruise Ship Explorer of the Seas. *J. Geophys. Res.,* **113,** C06001, doi:10.1029/2007JC004154.

Behrenfeld, M. J., and P. G. Falkowski, 1997: Photosynthetic rates derived from satellite-based chlorophyll concentration. *Limnol. Oceanogr.,* **42,** 1–20.

——, E. Boss, D. A. Siegel, and D. M. Shea, 2005: Carbon-based ocean productivity and phytoplankton physiology from space. *Global Biogeochem. Cycles,* **19,** GB1006, doi:10.1029/2004GB002299.

——, and Coauthors, 2006: Climate-driven trends in contemporary ocean productivity. *Nature,* **444,** 752–755.

——, D. A. Siegel, and R. T. O'Malley, 2008a: Global ocean phytoplankton and productivity [in "State of the Climate in 2007"]. *Bull. Amer. Meteor. Soc.*, **89** (7), S56–S61.

——, K. H. Halsey, and A. J. Milligan, 2008b: Evolved physiological responses of phytoplankton to their integrated growth environment. *Philos. Trans. Roy. Soc.,* **B363,** 2687–2703, doi:10.1098/rstb.2008.0019.

Behringer, D. W., M. Ji, and A. Leetmaa, 1998: An improved coupled model for ENSO prediction and implications for ocean initialization. Part I: The ocean data assimilation system. *Mon. Wea. Rev.,* **126,** 1013–1021.

Bell, G. D., cited 2008: Climate factors associated with the Midwest floods of June 2008. [Available online at www.cpc.ncep.noaa.gov/products/expert_assessment/midwest_floods_june2008.pdf.]

——, and J. E. Janowiak, 1995: Atmospheric circulation associated with the Midwest floods of 1993. *Bull. Amer. Meteor. Soc.,* **76,** 681–696.

——, and M. Chelliah, 2006: Leading tropical modes associated with interannual and multidecadal fluctuations in North Atlantic hurricane activity. *J. Climate,* **19,** 590–612.

——, M. S. Halpert, C. F. Ropelewski, V. E. Kousky, A. V. Douglas, R. C. Schnell, and M. E. Gelman, 1999: Climate assessment for 1998. *Bull. Amer. Meteor. Soc.,* **80** (5), S1–S48.

——, and Coauthors, 2000: The 1999 North Atlantic and Eastern North Pacific hurricane seasons [in "Climate Assessment for 1999"]. *Bull. Amer. Meteor. Soc.,* **81** (6), S19–S22.

——, and Coauthors, 2004: Atlantic hurricane season [in "State of the Climate in 2003"]. *Bull. Amer. Meteor. Soc.,* **85** (6), S20–S24.

——, and Coauthors, 2006: Tropical cyclones: Atlantic basin [in "State of the Climate in 2005"]. *Bull. Amer. Meteor. Soc.,* **86** (6), S33–S37.

——, and Coauthors, 2007: Tropical cyclones: Atlantic basin [in "State of the Climate in 2006"]. *Bull. Amer. Meteor. Soc.,* **87** (6), S48–S51.

——, E. Blake, S. B. Goldenberg, T. Kimberlain, C. W. Landsea, R. Pasch, and J. Schemm, 2009: The 2008 North Atlantic hurricane season; A climate perspective. NOAA Climate Prediction Center, Climate Summary. [Available online at www.cpc.ncep.

noaa.gov/products/expert_assessment/hurrsummary_2008.pdf.]

Bellouin, N., A. Jones, J. M. Haywood, and S. A. Christopher, 2008: Updated estimate of aerosol direct radiative forcing from satellite observations and comparison against the Hadley Centre climate model. *J. Geophys. Res.,* **113,** D10205, doi:10.1029/2007JD009385.

Bellucci, A., S. Gualdi, E. Scoccimarro, and A. Navarra, 2008: NAO-ocean circulation interactions in a coupled general circulation model. *Climate Dyn.,* **31** (7–8), doi:10.1007/s00382-008-0408-4.

Beránger, K., L. Siefridt, B. Barnier, E. Garnier, and H. Roquet, 1999: Evaluation of operational ECMWF surface freshwater fluxes of oceans during 1991-1997. *J. Mar. Syst.,* **22,** 13–36.

Bhatt, U., D. A. Walker, M. K. Raynolds, and J. Comiso, 2008: Circumpolar and regional analysis of the relationship between sea-ice variability, summer land-surface temperatures, Arctic tundra greenness and large-scale climate drivers (Abstract ID 363). *NASA Carbon Cycle and Ecosystems Joint Science Workshop,* Adelphi, MD, NASA. [Available online at http://cce.nasa.gov/cgi-bin/meeting_2008/mtg2008_ab_search.pl.]

Bigorre, S., and R. Weller, 2008: Air-sea surface conditions in the Gulf Stream from in-situ observations. *Eos, Trans. Amer. Geophys. Union*, **89** (Fall Meeting Suppl.), Abstract OS13B-1189.

Bindoff, N. L., and Coauthors, 2007: Observations: Oceanic climate change and sea level. *Climate Change 2007: The Physical Science Basis,* S. Solomon et al., Eds., Cambridge University Press, 385–428.

Boning, C. W., A. Dispert, M. Visbeck, S. R. Rintoul, and F. U. Schwarzkopf, 2008: The response of Antarctic Circumpolar Current to recent climate change. *Nat. Geosci.,* **1,** 864–869.

Bonjean, F., and G. Lagerloef, 2002: Diagnostic model and analysis of the surface currents in the tropical Pacific Ocean. *J. Phys. Oceanogr.,* **32,** 2938–2954.

Bowman, K. P., C. R. Homeyer, and D. G. Stone, 2009: A comparison of oceanic precipitation estimates in the tropics and subtropics. *J. Appl. Meteor. Climatol.,* **47,** 1335–1344.

Box, J. E., and A. E. Cohen, 2006: Upper-air temperatures around Greenland: 1964–2005. *Geophys. Res. Lett.,* **33,** L12706, doi:10.1029/2006GL025723.

——, and Coauthors, 2006: Greenland ice sheet surface mass balance variability (1988–2004) from calibrated Polar MM5 output. *J. Climate,* **19,** 2783–2800.

Boyer, T. P., C. Stephens, J. I. Antonov, M. E. Conkright, R. A. Locarnini, T. D. O'Brien, and H. E. Garcia, 2002: *Salinity.* Vol. 2, *World Ocean Atlas 2001,* NOAA Atlas NESDIS 50, 165 pp.

Brasnett, B., 1999: A global analysis of snow depth for numerical weather prediction. *J. Appl. Meteor.,* **38,** 726–740.

Braun, M., A. Humbert, and A. Moll, 2008: Changes of Wilkins Ice Shelf over the past 15 years and inferences on its stability. *Cryosphere Discuss.,* **2,** 341–382.

Brennan, C. E., R. J. Matear, and K. Keller, 2008: Measuring oxygen concentrations to improve the detection capabilities of an ocean circulation observation array. *J. Geophys. Res.,* **113**, C02019, doi:10.1029/2007JC004113.

Bretherton, F. P., R. E. Davis, and C. Fandry, 1976: A technique for objective analysis and design of oceanographic instruments applied to MODE-73. *Deep-Sea Res.,* **23,** 559–582.

Brink, A. B., and H. D. Eva, 2008: Monitoring 25 years of land cover change dynamics in Africa: A sample based remote sensing approach. *Appl. Geogr.,* doi:10.1016/j.apgeog.2008.10.004, in press.

Brohan, P., J. J. Kennedy, I. Harris, S. F. B. Tett, and P. D. Jones, 2006: Uncertainty estimates in regional and global observed temperature changes: A new data set from 1850. *J. Geophys. Res.,* **111,** D12106, doi:10.1029/2005JD006548.

Bromwich, D., J. Cassano, T. Klein, G. Heinemann, K. Hines, K. Steffen, and J. E. Box, 2001: Mesoscale modeling of katabatic winds over Greenland with the Polar MM5. *Mon. Wea. Rev.,* **129,** 2290–2309.

——, Z. Guo, L.-S. Bai, and Q.-S. Chen, 2004: Modeled Antarctic precipitation. Part I: Spatial and temporal variability. *J. Climate,* **17,** 427–447.

——, R. L. Fogt, K. I. Hodges, and J. E. Walsh, 2007: A tropospheric assessment of the ERA-40, NCEP, and JRA-25 global reanalyses in the polar regions. *J. Geophys. Res.,* **112,** D10111, doi:10.1029/2006JD007859.

Brown, R., C. Derksen, and L. Wang, 2007: Assessment of spring snow cover duration variability over northern Canada from satellite datasets. *Remote Sens. Environ.,* **111,** 367–381.

Bryden, H. L., H. R. Longworth, and S. A. Cunningham, 2005: Slowing of the Atlantic meridional overturning circulation at 25°N. ***Nature,*** 438, 655–657.

Camargo, S. J., and A. H. Sobel, 2005: Western North Pacific tropical cyclone intensity and ENSO. *J. Climate,* **18,** 2996–3006.

——, K. A. Emanuel, and A. H. Sobel, 2007a: Use of a genesis potential index to diagnose ENSO effects on tropical cyclone genesis. *J. Climate,* **20,** 4819–4834.

——, A. W. Robertson, S. J. Gaffney, P. Smyth, and M. Ghil, 2007b: Cluster analysis of typhoon tracks. Part II: Large-scale circulation and ENSO. *J. Climate,* **20,** 3654–3676.

——, ——, A. G. Barnston, and M. Ghil, 2008: Clustering of eastern North Pacific tropical cyclone tracks: ENSO and MJO effects. *Geochem. Geophys. Geosyst.,* **9,** Q06V05, doi: 10.1029/2007GC001861.

Cappelen, J., Ed., 2009: DMI monthly climate data collection 1768-2008, Denmark, The Faroe Islands and Greenland. Dansk Meterologisk Institut Tech. Rep. 09-05, 53 pp.

Carlson, A. E., D. W. Oppo, R. E. Came, A. N. LeGrande, L. D. Keigwin, and W. B. Curry, 2008: Subtropical Atlantic salinity variability and Atlantic meridional circulation during the last deglaciation. *Geology,* **36,** 991–994, doi:10.1130/G25080A.1.

Carter, R. M., 2008: Knock, knock: Where is the evidence for dangerous human-caused global warming? *Econ. Anal. Policy,* **38,** 177–202.

Cassano, J., J. E. Box, D. Bromwich, L. Li, and K. Steffen, 2001: Verification of polar MM5 simulations of Greenland's atmospheric circulation. *J. Geophys. Res.,* **106** (D24), 33 867–33 890.

Chan, J. C. L., 1985: Tropical cyclone activity in the northwest Pacific in relation to El Niño/Southern Oscillation phenomenon. *Mon. Wea. Rev.*, **113,** 599–606.

——, 2009: Verification of forecasts of tropical cyclone activity over the western North Pacific in 2008. Laboratory for Atmospheric Research, City University of Hong Kong. [Available online at http://weather.cityu.edu.hk/tc_forecast/2008_Verification.htm.]

Chapman, W. L., and J. E. Walsh, 2007: Simulations of Arctic temperature and pressure by global coupled models. *J. Climate,* **20,** 609–632.

Chen, M., P. Xie, and J. E. Janowiak, 2002: Global land precipitation: A 50-yr monthly analysis based on gauge observations. *J. Hydrometeor.,* **3,** 249–266.

Chia, H. H., and C. F. Ropelewski, 2002: Interannual variability in the genesis location of tropical cyclones in the northwest Pacific. *J. Climate,* **15,** 2934–2944.

Chiang, J. C. H., Y. Kushnir, and A. Giannini, 2002: Deconstructing Atlantic intertropical convergence zone variability: Influence of the local cross-equatorial sea surface temperature gradient and remote forcing from the eastern equatorial Pacific. *J. Geophys. Res.,* **107,** 4004, doi:10.1029/2000JD000307.

Christy, J. R., and R. T. McNider, 1994: Satellite greenhouse signal. *Nature,* **367,** 325.

——, and W. B. Norris, 2009: Discontinuity issues with radiosonde and satellite temperatures in the Australian region 1979–2006. *J. Atmos. Oceanic Technol.,* **26,** 508–522.

——, R. W. Spencer, W. B. Norris, W. D. Braswell, and D. E. Parkeret, 2003: Error estimates of version 5.0 of MSU–AMSU bulk atmospheric temperatures. *J. Atmos. Oceanic Technol.,* **20,** 613–629.

Ciasto, L. M., and D. W. J. Thompson, 2008: Observations of large-scale ocean–atmosphere interaction in the Southern Hemisphere. *J. Climate,* **21,** 1244–1259.

Clerbaux, C., and D. Cunnold, 2007: Long-lived compounds. Scientific assessment of ozone depletion: 2006, Global Ozone Research and Monitoring Project Rep. 50, World Meteorological Organization, 1.1–1.63.

Collins, M., B. B. B. Booth, G. Harris, J. M. Murphy, D. M. H. Sexton, and M. Webb, 2006: Towards quantifying uncertainty in transient climate change. *Climate Dyn.,* **27,** 127–147.

Comiso, J., 2003: Warming trends in the Arctic from clear-sky satellite observations. *J. Climate,* **16,** 3498–3510.

——, and F. Nishio, 2008: Trends in the sea ice cover using enhanced and compatible AMSR-E, SSM/I, and SMMR data. *J. Geophys. Res.,* **113,** C02S07, doi:10.1029/2007JC004257.

Conway, T. J., P. P. Tans, L. S. Waterman, K. W. Thoning, D. R. Kitzis, K. A. Masarie, and N. Zhang, 1994: Evidence for interannual variability of the carbon cycle from the NOAA CMDL global air sampling network. *J. Geophys. Res.,* **99** (D11), 22 831–22 855.

Couture, R., S. Smith, S. D. Robinson, M. M. Burgess, and S. Solomon, 2003: On the hazards to infrastructure in the Canadian North associated with thawing of permafrost. *Proc. Geohazards (2003), Third Canadian Conf. on Geotechnique and Natural Hazards,* Edmonton, AB, Canada, The Canadian Geotechnical Society, 97–104.

Cunninghman, S. A., and Coauthors, 2007: Temporal variability of the Atlantic meridional overturning circulation at 26.5°N. *Science,* **317,** 935–938, doi:10.1126/science.1141304.

Curry, R. G., and M. S. McCartney, 2001: Ocean gyre circulation changes associated with the North Atlantic oscillation. *J. Phys. Oceanogr.,* **31,** 3374–3400.

Curtis, S., and R. Adler, 2000: ENSO indexes based on patterns of satellite-derived precipitation. *J. Climate,* **13,** 2786–2793.

Dai, A., and K. E. Trenberth, 2002: Estimates of freshwater discharge from continents: Latitudinal and seasonal variations. *J. Hydrometeor.,* **3,** 660–687.

Daniel, J. S., and S. Solomon, 1998: On the climate forcing of carbon monoxide. *J. Geophys. Res.,* **103** (D11), 13 249–13 260.

——, and Coauthors, 2007: Halocarbon scenarios, ozone depletion potentials, and global warming potentials. Scientific assessment of ozone depletion: 2006, Global Ozone Research and Monitoring Project Rep. 50, World Meteorological Organization, 8.1–8.39.

D'Arrigo, R. D., R. J. Allan, R. Wilson, J. Palmer, J. Sakulich, J. Smerdon, S. Bijaksana, and L. Ngkoimani, 2008: Pacific and Indian Ocean climate signals in a tree-ring record of Java monsoon drought. *Int. J. Climatol.,* **28,** 1889–1901.

Della-Marta, P. M., D. A. Collins, and K. Braganza, 2004: Updating Australia's high-quality annual temperature dataset. *Aust. Meteor. Mag.,* **53,** 75–93.

DeMaria, M., J. A. Knaff, and B. H. Connell, 2001: A tropical cyclone genesis parameter for the tropical Atlantic. *Wea. Forecasting,* **16,** 219–233.

Dhomse, S., M. Weber, J. P. Burrows, I. Wohltmann, and M. Rex, 2006: On the possible cause of recent increases in NH total ozone from a statistical analysis of satellite data from 1979 to 2003. *Atmos. Chem. Phys.,* **6,** 1165–1180.

Di Gregorio, A., and L. J. M. Jansen, 2000: Land cover classification system, concepts and user manual. GCP/RAF/287/ITA, Africover, Food and Agriculture Organization of the United Nations Publishing Service, Rome, Italy, 179 pp.

Domingues, C. M., J. A. Church, N. J. White, P. J. Gleckler, S. E. Wijffels, P. M. Barker, and J. R. Dunn, 2008: Improved estimates of upper-ocean warming and multi-decadal sea-level rise. *Nature,* **453,** 1090–1093, doi:10.1038/nature07080.

Doney, S. C., V. J. Fabry, R. A. Feely, and J. A. Kleypas, 2009: Ocean acidification: The other CO_2 problem. *Annu. Rev. Mar. Sci.,* **1,** 169–192, doi:10.1146/annurev.marine.010908.163834.

Drozdov, D. S., G. V. Malkova, and V. P. Melnikov, 2008: Recent advances in Russian geocryological research: A contribution to the International Polar Year. *Proceedings of the 9th International Conference on Permafrost, Fairbanks, Alaska, 29 June – 3 July 2008*, Vol. 1, D. L. Kane and K. M. Hinkel, Eds., Institute of Northern Engineering, University of Alaska Fairbanks, 379–384.

Durre, I., R. S. Vose, and D. B. Wuertz, 2006: Overview of the Integrated Global Radiosonde Archive. *J. Climate,* **19,** 53–68.

Easterling, D. R., and M. F. Wehner, 2009: Is the climate warming or cooling? *Geophys. Res. Lett.,* **36**, L08706, doi:10.1029/2009GL037810.

Elsberry, R. L., R. Ferek, S. W. Chang, P. A. Harr, and D. Eleuterio, 2008: Tropical Cyclone Structure (TCS08) field experiment in the western North Pacific during 2008. *Proc. 28th Conf. on Hurricanes and Tropical Meteorology,* Orlando, FL, Amer. Meteor. Soc., 7C.6. [Available online at http://ams.confex.com/ams/28Hurricanes/techprogram/paper_138469.htm.]

Enfield, D. B., and A. M. Mestas-Nuñez, 1999: Multiscale variabilities in global sea surface temperatures and their relationships with tropospheric climate patterns. *J. Climate,* **12,** 2719–2733.

England, J., T. R. Lakeman, D. S. Lemmen, J. M. Bednarski, T. G. Stewart, and D. J. A. Evans, 2008: A millennial-scale record of Arctic Ocean sea ice variability and the demise of the Ellesmere Island ice shelves. *Geophys. Res. Lett.,* **35,** L19502, doi:10.1029/2008GL034470.

Epstein, H. E., D. A. Walker, M. K. Raynolds, G. J. Jia, and A. M. Kelley, 2008: Phytomass patterns across a temperature gradient of the North American arctic tundra. *J. Geophys. Res.,* **113,** G03S02, doi:10.1029/2007JG000555.

Evan, A. T., 2008: Global aerosols [in "State of the Climate in 2007"]. *Bull. Amer. Meteor. Soc.*, **89** (7), S31–S32.

Eyring, V., and Coauthors, 2006: Assessment of temperature, trace species, and ozone in chemistry-climate model simulations of the recent past. *J. Geophys. Res.,* **111,** D22308, doi:10.1029/2006JD007327.

Fabry, V. J., B. A. Seibel, R. A. Feely, and J. C. Orr, 2008: Impacts of ocean acidification on marine fauna and ecosystem processes. *J. Mar. Sci.,* **65,** 414–432.

Fairall, C. W., E. F. Bradley, J. E. Hare, A. A. Grachev, and J. B. Edson, 2003: Bulk parameterization on air–sea fluxes: Updates and verification for the COARE algorithm. *J. Climate,* **16,** 571–591.

Feely, R. A., and Coauthors, 2002: Seasonal and interannual variability of CO_2 in the equatorial Pacific. *Deep-Sea Res. II,* **49,** 2443–2469.

——, C. L. Sabine, K. Lee, W. Berelson, J. Kleypas, V. J. Fabry, and F. J. Millero, 2004: Impact of anthropogenic CO_2 on the $CaCO_3$ system in the oceans. *Science,* **305,** 362–366.

——, T. Takahashi, R. Wanninkhof, M. J. McPhaden, C. E. Cosca, and S. C. Sutherland, 2006: Decadal variability of the air-sea CO_2 fluxes in the equatorial Pacific Ocean. *J. Geophys. Res.*, **111,** C08S90, doi:10.1029/2005JC003129.

——, C. L. Sabine, J. M. Hernandez-Ayon, D. Ianson, and B. Hales, 2008: Evidence for upwelling of corrosive "acidified" water onto the Continental Shelf. *Science,* **320,** 1490–1492.

Fekete, B. M., C. J. Vörösmarty, and R. B. Lammers, 2001: Scaling gridded river networks for macroscale hydrology: Development, analysis, and control of error. *Water Resour. Res.,* **37,** 1955–1967.

Fetterer, F., K. Knowles, W. Meier, and M. Savoie, 2008: Sea ice index. National Snow and Ice Data Center, Boulder, CO, digital media. [Available online at http://nsidc.org/data/seaice_index/.]

Fogt, R. L., and D. H. Bromwich, 2006: Decadal variability of the ENSO teleconnection to the high-latitude South Pacific governed by coupling with the southern annular mode. *J. Climate,* **19,** 979–997.

Forster, P., and Coauthors, 2007: Changes in atmospheric constituents and in radiative forcing. *Climate Change 2007: The Physical Science Basis,* S. Solomon et al., Eds., Cambridge University Press, 129–234.

Francis, J. A., W. Chan, D. J. Leathers, J. R. Miller, and D. E. Veron, 2009: Winter northern hemisphere weather patterns remember summer Arctic sea-ice extent. *Geophys. Res. Lett.*, **36**, L07503, doi:10.1029/2009GL037274.

Frank, W. M., and G. S. Young, 2007: The interannual variability of tropical cyclones. *Mon. Wea. Rev.,* **135,** 3587–3598.

Franz, B. A., S. W. Bailey, P. J. Werdell, and C. R. McClain, 2007: Sensor-independent approach to the vicarious calibration of satellite ocean color radiometry. *Appl. Opt.,* **46,** 5068–5082.

Free, M., and J. Lanzante, 2009: Effect of volcanic eruptions on the vertical temperature profile in radiosonde data and climate models. *J. Climate,* **22,** 2925–2939.

——, D. J. Seidel, J. K. Angell, J. R. Lanzante, I. Durre, and T. C. Peterson, 2005: Radiosonde Atmospheric Temperature Products for Assessing Climate (RATPAC): A new dataset of large-area anomaly time series. *J. Geophys. Res.,* **110,** D22101, doi:10.1029/2005JD006169.

Frith, S., R. Stolarski, and P. K. Barthia, 2004: Implications of Version 8 TOMS and SBUV data for long-term trend. *Proceedings of the Quadrennial Ozone Symposium–2004,* C. Zerefos, Ed., IAMAS, 65–66. [Available online at http://hyperion.gsfc.nasa.gov/Data_services/merged/.]

Froidevaux, L., and Coauthors, 2006: Temporal decrease in upper atmospheric chlorine. *Geophys. Res. Lett.,* **33,** L23812, doi:10.1029/2006GL027600.

Fukasawa, M., H. Freeland, R. Perkin, T. Watanabe, H. Uchida, and A. Nishina, 2004: Bottom water warming in the North Pacific Ocean. *Nature,* **427,** 825–827, doi:10.1038/nature02337.

Ganachaud, A., and C. Wunsch, 2003: Large-scale ocean heat and freshwater transports during the World Ocean Circulation Experiment. *J. Climate,* **16,** 696–705.

Gao, H., 2009: China's snow disaster in 2008, who is the principal player? *Int. J. Climatol.,* doi:10.1002/joc.1859, in press.

Gardner, A. S., and M. Sharp, 2007: Influence of the Arctic circumpolar vortex on the mass balance of Canadian high Arctic glaciers. *J. Climate,* **20,** 4586–4598.

GCOS, 2003: The second report on the adequacy of the global observing systems for climate in support of the UNFCCC. GCOS-82, World Meteorological Organization, 74 pp.

Gedney, N., P. M. Cox, R. A. Betts, O. Boucher, C. Huntingford, and P. A. Stott, 2006: Detection of a direct carbon dioxide effect in continental river runoff records. *Nature,* **439,** 835–838.

Giles, K. A., S. W. Laxon, and A. L. Ridout 2008: Circumpolar thinning of Arctic sea ice following the 2007 record ice extent minimum. *Geophys. Res. Lett.,* **35,** L22502, doi:10.1029/2008GL035710.

Gillett, N. P., D. A. Stone, P. A. Stott, T. Nozawa, A. Y. Karpechko, G. C. Hegerl, M. F. Wehner, and P. D. Jones, 2008: Attribution of polar warming to human influence. *Nat. Geosci.,* **1,** 750–754, doi:10.1038/ngeo338.

Gobron, N., and Coauthors, 2006: Evaluation of fraction of absorbed photosynthetically active radiation products for different canopy radiation transfer regimes: Methodology and results using Joint Research Center products derived from SeaWiFS against ground-based estimations. *J. Geophys. Res.,* **111,** D13110, doi:10.1029/2005JD006511.

——, and Coauthors, 2008: Uncertainty estimates for the FAPAR operational products derived from MERIS: Impact of top-of-atmosphere radiance uncertainties and validation with field data. *Remote Sens. Environ.,* **112,** 1871–1883.

Goetz, S. J., A. G. Bunn, G. J. Fiske, and R. A. Houghton, 2005: Satellite-observed photosynthetic trends across boreal North America associated with climate and fire disturbance. *Proc. Natl. Acad. Sci. USA,* **102,** 13 521–13 525.

Goldenberg, S. B., and L. J. Shapiro, 1996: Physical mechanisms for the association of El Niño and West African rainfall with Atlantic major hurricane activity. *J. Climate,* **9,** 1169–1187.

——, C. W. Landsea, A. M. Mestas-Nuñez, and W. M. Gray, 2001: The recent increase in Atlantic hurricane activity: Causes and implications. *Science,* **293,** 474–479.

Goni, G., and I. Wainer, 2001: Investigation of the Brazil Current front variability from altimeter data. *J. Geophys. Res.,* **106,** 31 117—31 128.

——, S. Kamholz, S. Garzoli, and D. Olson, 1996: Dynamics of the Brazil-Malvinas confluence based on inverted echo sounders and altimetry. *J. Geophys. Res.,* **101,** 16 273–16 289.

Gordon, C., C. Cooper, C. A. Senior, H. Banks, J. M. Gregory, T. C. Johns, J. F. B. Mitchell, and R. A. Wood, 2000: The simulation of SST, sea ice extents and ocean heat transports in a version of the Hadley Centre coupled model without flux adjustments. *Climate Dyn.,* **16,** 147–168.

Gray, W. M., 1984: Atlantic seasonal hurricane frequency. Part I: El Niño and 30 mb quasi-biennial oscillation influences. *Mon. Wea. Rev.,* **112,** 1649–1668.

GRDC, cited 2004: GRDC runoff estimate in km^3/a. [Available online at http://grdc.bafg.de.]

Gregg, W. W., N. W. Casey, and C. R. McClain, 2005: Recent trends in global ocean chlorophyll. *Geophys. Res. Lett.,* **32,** L03606, doi:10.1029/2004GL021808.

Gruber, N., and Coauthors, 2009: Oceanic sources, sinks, and transport of atmospheric CO_2. *Global Biogeochem. Cycles,* **23,** GB1005, doi:10.1029/2008GB003349.

Haas, C., 2004: Late-summer sea ice thickness variability in the Arctic Transpolar Drift 1991–2001 derived from ground-based electromagnetic sounding. *Geophys. Res. Lett.,* **31,** L09402, doi:10.1029/2003GL019394.

——, A. Pfaffling, S. Hendricks, L. Rabenstein, J.-L. Etienne, and I. Rigor, 2008: Reduced ice thickness in Arctic Transpolar Drift favors rapid ice retreat. *Geophys. Res. Lett.,* **35,** L17501, doi:10.1029/2008GL034457.

Haeberli, W., and M. Hoelzle, 1995: Application for inventory data for estimating characteristics of and regional climate-change effects on mountain glaciers: A pilot study with the European Alps. *Ann. Glaciol.,* **21,** 206–212.

——, J. Cihlar, and R. Barry, 2000: Glacier monitoring within the Global Climate Observing System. *Ann. Glaciol.,* **31,** 241–246.

Haigh, J. D., 2003: The effects of solar variability on the Earth's climate. *Philos. Trans. Roy. Soc. London,* **A361,** 95–111.

Haimberger, L., 2007: Homogenization of radiosonde temperature time series using innovation statistics. *J. Climate,* **20,** 1377–1403.

——, C. Tavolato, and S. Sperka, 2008: Toward elimination of the warm bias in historic radiosonde temperature records—Some new results from a comprehensive intercomparison of upper-air data. *J. Climate,* **21,** 4587–4606.

Haine, T. W. N., and S. L. Gray, 2001: Quantifying mesoscale variability in ocean transient tracer fields. *J. Geophys. Res.,* **106,** 13 861–13 878.

Haines, K., L. Hermanson, C. Liu, D. Putt, R. Sutton, and D. Smith, 2009: Decadal climate prediction (project GCEP). *Philos. Trans. Roy. Soc. London,* **A367,** 925–937.

Hall-Spencer, J. M., and Coauthors, 2008: Volcanic carbon dioxide vents show ecosystem effects of ocean acidification. *Nature,* **454,** 96–99.

Hanna, E., J. McConnell, S. Das, J. Cappelen, and A. Stephens, 2006: Observed and modeled Greenland Ice Sheet snow accumulation, 1958–2003, and links with regional climate forcing. *J. Climate,* **19,** 344–358.

——, and Coauthors, 2008: Increased runoff from melt from the Greenland Ice Sheet: A response to global warming. *J. Climate,* **21,** 331–341.

Hansen, J., R. Ruedy, M. Sato, M. Imhoff, W. Lawrence, D. Easterling, T. Peterson, and T. Karl, 2001: A closer look at United States and global surface temperature change. *J. Geophys. Res.,* **106** (D20), 23 947–23 963.

——, and Coauthors, 2005: Earth's energy imbalance: Confirmation and implications. *Science,* **308,** 1431–1435.

——, M. Sato, R. Ruedy, and K. Lo, cited 2009: 2008 global surface temperature in GISS analysis. [Available online at **www.columbia.edu/~jeh1/mailings/2009/20090113_Temperature.pdf.**]

Hansen, M. C., and Coauthors, 2008: Humid tropical forest clearing from 2000 to 2005 quantified by using multitemporal and multiresolution remotely sensed data. *Proc. Natl. Acad. Sci. USA,* **105,** 9439–9444.

Harris, C., and W. Haeberli, 2003: Warming permafrost in European mountains. *Global Planet. Change*, **39,** 215–225.

Hátún, H., A. B. Sandø, H. Drange, B. Hansen, and H. Valdimarsson, 2005: Influence of the Atlantic subpolar gyre on the thermohaline circulation. *Science,* **309,** 1841–1844, doi:10.1126/science.1114777.

Hawkins, E., and R. Sutton, 2007: Variability of the Atlantic thermohaline circulation described by three-dimensional empirical orthogonal functions. *Climate Dyn.,* **29**, 745–762, doi:10.1007/s00382-007-0263-8.

Held, I. M., and B. J. Soden, 2006: Robust response of the hydrological cycle to global warming. *J. Climate,* **19,** 5686–5699.

Helfrich, S., D. McNamara, B. Ramsay, T. Baldwin, and T. Kasheta, 2007: Enhancements to, and forthcoming developments in the Interactive Multisensor Snow and Ice Mapping System (IMS). *Hydrol. Processes,* **21,** 1576–1586.

Hendon, H., C. Zhang, and J. Glick, 1999: Interannual variation of the Madden–Julian oscillation during austral summer. *J. Climate,* **12,** 2538–2550.

Hilburn, K. A., and F. J. Wentz, 2008: Intercalibrated passive microwave rain products from the unified microwave ocean retrieval algorithm (UMORA). *J. Appl. Meteor. Climatol.,* **47,** 778–794.

Hofmann, D. J., and S. A. Montzka, 2009: Recovery of the ozone layer: The ozone depleting gas index. *Eos, Trans. Amer. Geophys. Union,* **9,** 1–2.

——, J. H. Butler, E. J. Dlugokencky, J. W. Elkins, K. Masarie, S. A. Montzka, and P. Tans, 2006: The role of carbon dioxide in climate forcing from 1979–2004. *Tellus,* **58B,** 614–619.

Huffman, G. J., and Coauthors, 2007: The TRMM Multisatellite Precipitation Analysis: Quasi-global, multiyear, combined-sensor precipitation estimates at fine scale. *J. Hydrometeor.,* **8,** 38–55.

Humbert, A., and M. Braun, 2008: Wilkins Ice Shelf – break-up along failure zones. *J. Glaciol.,* **55,** 943–944.

Hurrell, J. W., 1995: Decadal trends in the North Atlantic Oscillation: Regional temperatures and precipitation. *Science,* **269,** 676–679.

——, Y. Kushnir, G. Ottersen, and M. Visbeck, 2003: An overview of the North Atlantic Oscillation. *The North Atlantic Oscillation: Climatic Significance and Environmental Impact,* J. W. Hurrell et al., Eds., Amer. Geophys. Union, 1–36.

Hutchins, D. A., F.-X. Fe, Y. Zhang, M. E. Warner, Y. Feng, K. Portune, P. W. Bernhardt, and M. R. Mulholland, 2007: CO_2 control of *Trichodesmium* N2 fixation, photosynthesis, growth rates, and elemental ratios: Implications for past, present, and future ocean biogeochemistry. *Limnol. Oceanogr.,* **52,** 1293–1304.

Instituto de Meteorologia, 2009: Annual climatological bulletin for 2008 (in Portuguese). Portuguese Meteorological Office, 9 pp.

Irwin, R. P., and R. Davis, 1999: The relationship between the southern oscillation index and tropical cyclone tracks in the eastern North Pacific. *Geophys. Res. Lett.,* **26,** 2251–2254.

Isaksen, K., D. Vonder Mühll, H. Gubler, T. Kohl, and J. L. Sollid, 2000: Ground surface temperature reconstruction based on data from a deep borehole in permafrost at Janssonhaugen, Svalbard. *Ann. Glaciol.,* **31,** 287–294.

Island Climate Update, 2008a: *The Island Climate Update 92*. National Institute of Water and Atmospheric Research, New Zealand, 6 pp. [Available online at www.niwa.co.nz/ncc/icu.]

——, 2008b: *The Island Climate Update 97*. National Institute of Water and Atmospheric Research, New Zealand, 6 pp. [Available online at www.niwa.co.nz/ncc/icu.]

——, 2008c: *The Island Climate Update 98*. National Institute of Water and Atmospheric Research, New Zealand, 6 pp. [Available online at www.niwa.co.nz/ncc/icu.]

Jacobs, S. S., C. F. Giulivi, and P. A. Mele, 2002: Freshening of the Ross Sea during the late 20th century. *Science,* **297,** 386–389.

Jacobson, A. R., S. E. Mikaloff Fletcher, N. Gruber, J. S. Sarmineto, and M. Gloor, 2007: A joint atmosphere-ocean inversion for surface fluxes of carbon dioxide: 1. Methods and global-scale fluxes. *Global Biogeochem. Cycles,* **21,** GB1019, doi:10.1029/2005GB002556.

Janowiak, J. E., and P. Xie, 1999: CAMS–OPI: A global satellite-rain gauge merged product for real-time precipitation monitoring applications. *J. Climate*, **12**, 3335–3342.

Jauregui, E., 2003: Climatology of landfalling hurricanes and tropical storms in Mexico. *Atmósphera,* **16,** 193–204.

Jia, G. J., H. E. Epstein, and D. A. Walker, 2003: Greening of arctic Alaska, 1981–2001. *Geophys. Res. Lett.,* **30,** 2067, doi:10.1029/2003GL018268.

Jian, X., D. M. Wolock, H. F. Lins, and S. Brady, 2009: Streamflow of 2008—Water year summary. FS-2009-3003, U.S. Geological Survey, Reston, VA, 8 pp. [Available online at http://water.usgs.gov/waterwatch/2008summary/fs_2009_3003.pdf.]

Johns, W. E., L. M. Beal, M. O. Baringer, J. R. Molina, S. A. Cunningham, T. Kanzow, and D. Rayner, 2008: Variability of shallow and deep western boundary currents off the Bahamas during 2004–05: Results from the 26°N RAPID–MOC array. *J. Phys. Oceanogr.,* **38,** 605–623.

Johnson, G. C., 2008: Quantifying Antarctic Bottom Water and North Atlantic Deep Water volumes. *J. Geophys. Res.,* **113,** C05027, doi:10.1029/2007JC004477.

——, and S. C. Doney, 2006: Recent western South Atlantic bottom water warming. *Geophys. Res. Lett.,* **33,** L14614, doi:10.1029/2006GL026769.

——, S. Mecking, B. M. Sloyan, and S. E. Wijffels, 2007: Recent bottom water warming in the Pacific Ocean. *J. Climate,* **20,** 5365–5375.

——, S. G. Purkey, and J. L. Bullister, 2008a: Warming and freshening in the abyssal southeastern Indian Ocean. *J. Climate,* **21,** 5351–5363.

——, ——, and J. M. Toole, 2008b: Reduced Antarctic meridional overturning circulation reaches the North Atlantic Ocean. *Geophys. Res. Lett.,* **35,** L22601, doi:10.1029/2008GL035619.

Jones, A., and Coauthors, 2009: Evolution of stratospheric ozone and water vapour time series studied with satellite measurements. *Atmos. Chem. Phys. Discuss.,* **9,** 1157–1209.

Jones, P. D., T. Jónsson, and D. Wheeler, 1997: Extension to the North Atlantic Oscillation using early instrumental pressure observations from Gibraltar and South-West Iceland. *Int. J. Climatol.,* **17,** 1433–1450.

Kahn, R., B. Gaitley, J. Martonchik, D. Diner, K. Crean, and B. Holben, 2005: MISR global aerosol optical depth validation based on two years of coincident AERONET observations. *J. Geophys. Res.,* **110,** D10S04, doi:10.1029/2004JD004706.

Kalnay, E., and Coauthors, 1996: The NCEP/NCAR 40-Year Renalysis Project. *Bull. Amer. Meteor. Soc.,* **77,** 437–471.

Kanamitsu, M., W. Ebisuzaki, J. Woollen, S.-.K Yang, J. J. Hnilo, M. Fiorino, and G. L. Potter, 2002: NCEP–DOE AMIP-II Reanalysis (R-2). *Bull. Amer. Meteor. Soc.,* **83,** 1631–1643.

Kanzow, T., and Coauthors, 2007: Observed flow compensation associated with the meridional overturning circulation near 26.5ºN in the Atlantic. *Science*, **317,** 938–941, doi: 10.1126/science.1141293.

——, and Coauthors, 2008a: A prototype system for observing the Atlantic Meridional Overturning Circulation – Scientific basis, measurement and risk mitigation strategies, and first results. *J. Oper. Oceanogr.,* **1** (1), 19–28.

——, U. Send, and M. McCartney, 2008b: On the variability of the deep meridional transports in the tropical North Atlantic. *Deep-Sea Res.,* **55,** 1601–1623, doi:10.1016/j.dsr.2008.07.011.

——, H. Johnson, D. Marshall, S. A. Cunningham, J. J.-M. Hirschi, A. Mujahid, H. L. Bryden, and W. E. Johns, 2009: Basinwide integrated volume transports in an eddy-filled ocean. *J. Phys. Oceanogr.,* in press.

Karl, T. R., S. J. Hassol, C. D. Miller, and W. L. Murray, Eds., 2006: Temperature trends in the lower atmosphere: Steps for understanding and reconciling differences. U.S. Climate Change Science Program Final Rep., Synthesis and Assessment Product 1.1, Subcommittee on Global Change Research, Washington, DC, 164 pp. [Available online at www.climatescience.gov/Library/sap/sap1–1/finalreport/default.htm.]

Kasischke, E. S., and Coauthors, 2000: Contributions of 1998 fires in the boreal forest to atmospheric concentrations of carbon monoxide and methane. *Eos, Trans. Amer. Geophys. Union,* **81,** 260.

Kawano T., M. Fukasawa, S. Kouketsu, H. Uchida, T. Doi, I. Kaneko, M. Aoyama, and W. Schneider, 2006: Bottom water warming along the pathway of lower circumpolar deep water in the Pacific Ocean. *Geophys. Res. Lett.,* **33,** L23613, doi:10.1029/2006GL027933.

Kay, J. E., T. L'Ecuyer, A. Gettelman, G. Stephens, and C. O'Dell, 2008: The contribution of cloud and radiation anomalies to the 2007 Arctic sea ice extent minimum. *Geophys. Res. Lett.,* **35,** L08503, doi:10.1029/2008GL033451.

Kayano, M., and V. Kousky, 1999: Intraseasonal (30-60 day) variability in the global tropics: Principal modes and their evolution. *Tellus,* **51,** 373–386.

Kitaev, L., E. Førland, V. Razuvaev, O. Tveito, and O. Krueger, 2005: Distribution of snow cover over Northern Eurasia. *Nordic Hydrol.,* **36,** 311–319.

Kleypas, J. A., R. A. Feely, V. J. Fabry, C. Langdon, C. L. Sabine, and L. L. Robbins, 2006: Impacts of ocean acidification on coral reefs and other marine calcifiers: A guide for future research. Workshop Report, St. Petersburg, FL, NSF/NOAA/U.S. Geological Survey, 88 pp.

Knapp, K. R., M. C. Kruk, D. H. Levinson, and E. J. Gibney, 2009: Archive compiles new resource for global tropical cyclone research. *Eos, Trans. Amer. Geophys. Union,* **90,** 6, 46.

Knorr, W., N. Gobron, M. Scholze, T. Kaminski, R. Schnur, and B. Pinty, 2007: Impact of terrestrial biosphere carbon exchanges on the anomalous CO_2 increase in 2002–2003. *Geophys. Res. Lett.,* **34,** L09703, doi:10.1029/2006GL029019.

Knyazikhin, Y., J. V. Martonchik, R. B. Myneni, D. J. Diner, and S. W. Running, 1998: Synergistic algorithm for estimation of vegetation canopy leaf area index and fraction of absorbed photosynthetically active radiation from MODIS and MISR data. *J. Geophys. Res.,* **103** (D24), 32 257–32 276.

Kohl, A., and D. Stammer, 2008: Variability of the meridional overturning in the North Atlantic from the 50-year GECCO state estimation. *J. Phys. Oceanogr.,* **38,** 1913–1930.

Koren, I., L. A. Remer, and K. Longo, 2007: Reversal of trend of biomass burning in the Amazon. *Geophys. Res. Lett.,* **34,** L20404, doi:10.1029/2007GL031530.

Korzun, V. I., A. A. Sokolov, A. M. I. Budyko, K. P. Voskresensky, G. P. Kalinin, A. A. Konoplyantsev, and E. S. Lvovich, Eds., 1977: *Atlas of World Water Balance: Explanatory Text.* Gidrometeoizdat, 34 pp.

Kossin, J. P., and D. J. Vimont, 2007: A more general framework for understanding Atlantic hurricane variability and trends. *Bull. Amer. Meteor. Soc.,* **88,** 1767–1781.

Kouketsu, S., M. Fukasawa, I. Kaneko, T. Kawano, H. Uchida, T. Doi, M. Aoyama, and K. Murakami, 2009: Changes in water properties and transports along 24°N in the North Pacific between 1985 and 2005. *J. Geophys. Res.,* **114,** C01008, doi:10.1029/2008JC004778.

Kousky, V., and M. Kayano, 1994: Principal modes of outgoing longwave radiation and 250-mb circulation for the South American sector. *J. Climate,* **7,** 1131–1143.

Krabill, W., and Coauthors, 2000: Greenland ice sheet: High-elevation balance and peripheral thinning. *Science,* **289**, 428–430.

Kruk, M. C., K. R. Knapp, D. H. Levinson, H. J. Diamond, and J. P. Kossin, 2009: An overview of the International Best Track Archive for Climate Stewardship (IBTrACS) project. Preprints, *21st Conf. on Climate Variability and Change*, Phoenix, AZ, Amer. Meteor. Soc., 7B.1. [Available online at http://ams.confex.com/ams/pdfpapers/146864.pdf.]

Kvenvolden, K.A., 1993: Gas hydrates—Geological perspective and global change. *Rev. Geophys.*, **31**, 173–187.

Kwiatkowska, E. J., B. A. Franz, G. Meister, C. R. McClain, and X. Xiong, 2008: Cross calibration of ocean-color bands from Moderate Resolution Imaging Spectroradiometer on Terra platform. *Appl. Opt.,* **47,** 6796–6810.

Kwok, R., 2007: Near zero replenishment of the Arctic multiyear sea ice cover at the end of 2005 summer. *Geophys. Res. Lett.,* **34,** L05501, doi:10.1029/2006GL028737.

——, H. J. Zwally, and D. Yi, 2004: ICESat observations of Arctic sea ice: A first look. *Geophys. Res. Lett.,* **31,** L16401, doi:10.1029/2004GL020309.

L'Ecuyer, T. S., N. B. Wood, T. Haladay, G. L. Stephens, and P. W. Stackhouse, 2008: Impact of clouds on atmospheric heating based on the R04 CloudSat fluxes and heating rates data set. *J. Geophys. Res.,* **113,** D00A15, doi:10.1029/2008JD009951.

Lander, M. A., and C. P. Guard, 1998: A look at global tropical cyclone activity during 1995: Contrasting high Atlantic activity with low activity in other basins. *Mon. Wea. Rev.,* **126,** 1163–1173.

Landsea, C. W., and W. M. Gray, 1992: The strong association between Western Sahel monsoon rainfall and intense Atlantic hurricanes. *J. Climate,* **5,** 435–453.

——, G. D. Bell, W. M. Gray, and S. B. Goldenberg, 1998: The extremely active 1995 Atlantic hurricane season: Environmental conditions and verification of seasonal forecasts. *Mon. Wea. Rev.,* **126,** 1174–1193.

——, R. A. Pielke Jr., A. M. Mestas-Nuñez, and J. A. Knaff, 1999: Atlantic basin hurricanes: Indices of climatic changes. *Climatic Change,* **42,** 89–129.

Langenfelds, R. L., R. J. Francey, B. C. Pak, L. P. Steele, J. Lloyd, C. M. Trudinger, and C. E. Allison, 2002: Interannual growth rate variations of atmospheric CO_2 and its $\delta^{13}C$, H_2, CH_4, and CO between 1992 and 1999 linked to biomass burning. *Global Biogeochem. Cycles,* **16,** 1048, doi:10.1029/2001GB001466.

Lavery, B., G. Joung, and N. Nicholls, 1997: An extended high-quality historical rainfall dataset for Australia. *Aust. Meteor. Mag.,* **46,** 27–38.

Lawrence, D. M., A. G. Slater, R. A. Tomas, M. M. Holland, and C. Deser, 2008: Accelerated Arctic land warming and permafrost degradation during rapid sea ice loss. *Geophys. Res. Lett.,* **35,** L11506, doi:10.1029/2008GL033985.

Lawson, N., 2008: *An Appeal to Reason: A Cool Look at Global Warming*. Gerald Duckworth & Co., 149 pp.

Laxon, S., N. Peacock, and D. Smith, 2003: High interannual variability of sea ice in the Arctic region. *Nature,* **425,** 947–50.

LeBel, D. A., and Coauthors, 2008: The formation rate of North Atlantic deep water and eighteen degree water calculated from CFC-11 inventories observed during WOCE. *Deep-Sea Res.,* **55,** 891–910, doi:10.1016/j.dsr.2008.03.009.

Le Quéré, C., and Coauthors, 2007: Saturation of the Southern Ocean CO_2 sink due to recent climate change. *Science,* **316,** 1735–1738, doi:10.1126/science.1136188.

Lee, K., R. Wanninkhof, T. Takahashi, S. Doney, and R. A. Feely, 1998: Low interannual variability in recent oceanic uptake of atmospheric carbon dioxide. *Nature,* **396,** 155–159.

Leuliette, E., and L. Miller, 2009: Closing the sea level rise budget with altimetry, Argo, and GRACE. *Geophys. Res. Lett.,* **36,** L04608, doi:10.1029/2008GL036010.

Levinson, D. H., and J. H. Lawrimore, 2008: State of the climate in 2007. *Bull. Amer. Meteor. Soc.,* **89** (7), S1–S179.

Levitus, S., J. I. Antonov, and T. P. Boyer, 2005: Warming of the World Ocean, 1955–2003. *Geophys. Res. Lett.,* **32,** L02604, doi:10.1029/2004GL021592.

——, ——, ——, R. A. Locarnini, H. E. Garcia, and A. V. Mishonov, 2009: Global ocean heat content 1955–2008 in light of recently revealed instrumentation problems. *Geophys. Res. Lett.,* **36,** L07608, doi:10.1029/2008GL037155.

Liang S., J. Stroeve, and J. E. Box, 2005: Mapping daily snow/ice shortwave broadband albedo from Moderate Resolution Imaging Spectroradiometer (MODIS): The improved direct retrieval algorithm and validation with Greenland in situ measurement. *J. Geophys. Res.,* **110,** D10109, doi:10.1029/2004JD005493.

Liu, H., L. Wang, and K. Jezek, 2005: Wavelet-based edge detection approach to derivation of snow-melt onset, duration and extent from satellite passive microwave measurements. *Int. J. Remote Sens.,* **26,** 4639–4660.

——, ——, and ——, 2006: Spatiotemporal variations of snowmelt in Antarctica derived from satellite scanning multichannel microwave radiometer and Special Sensor Microwave Imager data (1978–2004). *J. Geophys. Res.,* **111,** F01003, doi:10.1029/2005JF000318.

Liu, K. S., and J. C. L. Chan, 2008: Interdecadal variability of western North Pacific tropical cyclone tracks. *J. Climate,* **21,** 4464–4476.

Livezey, R. E., and W. Chen, 1983: Statistical field significance and its determination by Monte Carlo techniques. *Mon. Wea. Rev.*, **111**, 46–59.

Loeb, N. G., B. A. Wielicki, D. R. Doelling, G. L. Smith, D. F. Keyes, S. Kato, N. Manalo-Smith, and T. Wong, 2009: Toward optimal closure of the earth's top-of-atmosphere radiation budget. *J. Climate,* **22,** 748–766.

Lohmann, G., H. Haak, and J. H. Jungclaus, 2008: Estimating trends of Atlantic meridional overturning circulation from long-term hydrographic data and model simulations. *Ocean Dyn.,* **58,** doi:10.1007/s10236-008-0136-7.

Lohmann, K., H. Drange, and M. Bentsen, 2009: Response of the North Atlantic subpolar gyre to persistent North Atlantic oscillation like forcing. *Climate Dyn.,* **32,** 273–285, doi:10.1007/s00382-008-0467-6.

Lovenduski, N. S., N. Gruber, S. C. Doney, and I. D. Lima, 2007: Enhanced CO_2 outgassing in the Southern Ocean from a positive phase of the Southern Annular Mode. *Global Biogeochem. Cycles,* **21,** GB2026, doi:10.1029/2006GB002900.

Lumpkin, R., and M. Pazos, 2007: Measuring surface currents with Surface Velocity Program drifters: The instrument, its data, and some recent results. *Lagrangian Analysis and Prediction of Coastal and Ocean Dynamics,* A. Griffa et al., Eds., Cambridge University Press, 39–67.

——, and K. Speer, 2007: Global Ocean meridional overturning. *J. Phys. Oceanogr.,* **37,** 2550–2562.

——, ——, and K. P. Koltermann, 2008: Transport across 48°N in the Atlantic Ocean. *J. Phys. Oceanogr.,* **38,** 733–752.

Lungu, T., and P. S. Callahan, 2006: QuikSCAT science data product user's manual: Overview and geophysical data products. D-18053-Rev A, version 3.0, 91 pp. [Available from Jet Propulsion Laboratory, 4800 Oak Grove Dr., Pasadena, CA 91109.]

Luo, J.-J., and G. D. Bell, 2008: Indian Ocean Dipole [in "State of the Climate in 2007"]. *Bull. Amer. Meteor. Soc.,* **89** (7), S81–S83.

——, S. Masson, S. Behera, and T. Yamagata, 2007: Experimental forecasts of the Indian Ocean Dipole using a coupled OAGCM. *J. Climate,* **20**, 2178–2190.

——, S. Behera, Y. Masumoto, H. Sakuma, and T. Yamagata, 2008: Successful prediction of the consecutive IOD in 2006 and 2007. *Geophys. Res. Lett.,* **35,** L14S02, doi:10.1029/2007GL032793.

Luthcke, S. B., and Coauthors, 2006: Recent Greenland ice mass loss by drainage system from satellite gravity observations. *Science,* **24,** 1286–1289.

Lüthi, D., and Coauthors, 2008: High-resolution carbon dioxide concentration record 650,000–800,000 years before present. *Nature,* **435,** 379–382.

Lyman, J. M., and G. C. Johnson, 2008: Estimating global upper-ocean heat content despite irregular sampling. *J. Climate,* **21,** 5629–5641.

Maclay, K. S., M. DeMaria, and T. H. Vonder Haar, 2008: Tropical cyclone inner core kinetic energy evolution. *Mon. Wea. Rev.,* **136,** 4882–4898.

Madden, R., and P. Julian, 1971: Detection of a 40-50 day oscillation in the zonal wind in the tropical Pacific. *J. Atmos. Sci.,* **28,** 702–708.

——, and ——, 1972: Description of global-scale circulation cells in the tropics with a 40-50 day period. *J. Atmos. Sci.*, **29,** 1109–1123.

——, and ——, 1994: Observations of the 40-50 day tropical oscillation: A review. *Mon. Wea. Rev.,* **122,** 814–837.

Maes, C., K. Ando, T. Delcroix, W. S. Kessler, M. J. McPhaden, and D. Roemmich, 2006: Observed correlation of surface salinity, temperature and barrier layer at the eastern edge of the western Pacific warm pool. *Geophys. Res. Lett.,* **33,** L06601, doi:10.1029/2005GL024772.

Mainelli, M., M. DeMaria, L. K. Shay, and G. Goni, 2008: Application of oceanic heat content estimation to operational forecasting of recent Atlantic category 5 hurricanes. *Wea. Forecasting,* **23,** 3–16.

Malhi, Y., J. T. Roberts, R. A. Betts, T. J. Killeen, W. Li, and C. A. Nobre, 2008: Climate change, deforestation, and the fate of the Amazon. *Science,* **319,** 169–172.

Maloney, E. D., and D. L. Hartmann, 2000: Modulation of eastern North Pacific hurricanes by the Madden–Julian oscillation. *J. Climate,* **13,** 1451–1460.

Mantua, N. J., S. R. Hare, Y. Zhang, J. M. Wallace, and R. C. Francis, 1997: A Pacific interdecadal climate oscillation with impacts on salmon production. *Bull. Amer. Meteor. Soc.,* **78,** 1069–1079.

Marland, G., T. A. Boden, and R. J. Andres, 2008: Global, regional, and national CO2 emissions. Trends: A compendium of data on global change, Carbon Dioxide Information Analysis Center, Oak Ridge National Laboratory, U.S. Department of Energy. [Available online at http://cdiac.esd.ornl.gov/trends/emis/em_cont.html.]

Marshall, G. J., 2003: Trends in the southern annular mode from observations and reanalyses. *J. Climate,* **16,** 4134–4143.

——, 2007: Half-century seasonal relationships between the Southern Annular Mode and Antarctic temperatures. *Int. J. Climatol.,* **27,** 373–383.

Maslanik, J. A., C. Fowler, J. Stroeve, S. Drobot, J. Zwally, D. Yi, and W. Emery, 2007: A younger, thin-

ner Arctic ice cover: Increased potential for rapid, extensive sea-ice loss. *Geophys. Res. Lett.,* **34,** L24501, doi:10.1029/2007GL032043.

Massom, R. A., S. E. Stammerjohn, W. Lefebvre, S. A. Harangozo, N. Adams, T. A. Scambos, M. J. Pook, and C. Fowler, 2008: West Antarctic Peninsula sea ice in 2005: Extreme ice compaction and ice edge retreat due to strong anomaly with respect to climate. *J. Geophys. Res.,* **113,** C02S20, doi:10.1029/2007JC004239.

Mayaux, P., and Coauthors, 2006: Validation of the global land cover 2000 map. *IEEE Trans. Geosci. Remote Sens.,* **44,** 1728–1737.

Mayewski, P. A., and Coauthors, 2009: State of the Antarctic and Southern Ocean climate system. *Rev. Geophys.,* **47,** RG1003, doi:10.1029/2007RG000231.

McClain, C. R., 2009: A decade of satellite ocean color observation. *Annu. Rev. Mar. Sci.,* **1,** 19–42.

McDonagh, E. L., H. L. Bruden, B. A. King, and R. J. Saunders, 2008: The circulation of the Indian Ocean at 32°S. *Prog. Oceanogr.,* **79,** 20–36, doi:10.1016/j.pocean.2008.07.001.

McPhee, M. G., A. Proshutinsky, J. H. Morison, M. Steele, and M. B. Alkire, 2009: Rapid change in freshwater content of the Arctic Ocean. *Geophys. Res. Lett.,* **36,** L10602, doi:10.1029/2009GL037525.

Mears, C. A., and F. J. Wentz, 2009a: Construction of the RSS V3.2 lower-tropospheric temperature dataset from the MSU and AMSU microwave sounders. *J. Atmos. Oceanic Technol.,* **26,** 1492–1509.

——, and ——, 2009b: Construction of the Remote Sensing Systems V3.2 atmospheric temperature records from the MSU and AMSU microwave sounders *J. Atmos. Oceanic Technol.,* **26,** 1040–1056

——, B. D. Santer, F. J. Wentz, K. E. Taylor, and M. F. Wehner, 2007: Relationship between temperature and precipitable water changes over tropical oceans. *Geophys. Res. Lett.,* **34,** L24709, doi:10.1029/2007GL031936.

Meier, M. F., M. B. Dyurgerov, U. K. Rick, S. O'Neel, W. T. Pfeffer, R. S. Anderson, S. P. Anderson, and A. F. Glazovsky, 2007: Glaciers dominate eustatic sea-level rise in the 21st century. *Science,* **317,** 1064–1067.

Meier, W., F. Fetterer, K. Knowles, M. Savoie, and M. J. Brodzik, 2006: Sea ice concentrations from Nimbus-7 SMMR and DMSP SSM/I passive microwave data. National Snow and Ice Data Center, Boulder, CO, digital media. [Available online at http://nsidc.org/data/nsidc-0051.html.]

Melling, H., D. A. Riedel, and Z. Gedalof, 2005: Trends in the draft and extent of seasonal pack ice, Canadian Beaufort Sea. *Geophys. Res. Lett.,* **32,** L24501, doi:10.1029/2005GL024483.

Mernild, S. H., G. E. Liston, C. A. Hiemstra, and K. Steffen, 2009: Record 2007 Greenland Ice Sheet surface melt extent and runoff. *Eos, Trans. Amer. Geophys. Union,* **90,** doi:10.1029/2009EO020002.

Milliman, J. D., C. Rutkowski, and M. Meybeck, 1995: River discharge to the sea: A global river index (GLORI). Land-Ocean Interactions in the Coastal Zone Rep., 138 pp. [Available online at www.loicz.org/imperia/md/content/loicz/print/rsreports/2_river_discharge.pdf.]

——, K. L. Farnsworth, P. D. Jones, K. H. Xu, and L. C. Smith, 2008: Climatic and anthropogenic factors affecting river discharge to the global ocean, 1951-2000. *Global Planet. Change,* **62,** 187–194.

Mishchenko, M. I., I. V. Geogdzhayev, W. B. Rossow, B. Cairns, B. E. Carlson, A. A. Lacis, L. Liu, and L. D. Travis, 2007: Long-term satellite record reveals likely recent aerosol trend. *Science,* **315,** 1543.

Mo, K. C., 2000: The association between intraseasonal oscillations and tropical storms in the Atlantic basin. *Mon. Wea. Rev.,* **128,** 4097–4107.

——, and V. E. Kousky, 1993: Further analysis of the relationship between circulation anomaly patterns and tropical convection. *J. Geophys. Res.,* **98** (D3), 5103–5113.

Molinari, R. L., E. Johns, and J. F. Festa, 1990: The annual cycle of meridional heat-flux in the Atlantic Ocean at 26.5°N. *J. Phys. Oceanogr.,* **20,** 476–482.

Montzka, S. A., R. C. Myers, J. H. Butler, J. W. Elkins, L. Lock, A. Clarke, and A. H. Goldstein, 1996: Observations of HFC-134a in the remote troposphere. *Geophys Res. Lett.,* **23,** 169–172.

——, J. H. Butler, J. W. Elkins, T. M. Thompson, A. D. Clarke, and L. T. Lock, 1999: Present and future trends in the atmospheric burden of ozone-depleting halogens. *Nature,* **398,** 690–694.

——, B. D. Hall, and J. W. Elkins, 2009: Accelerated increases observed for hydrofluorocarbons since 2004 in the global atmosphere. *Geophys. Res. Lett.,* **36,** L03804, doi:10.1029/2008GL036475.

Mooers, C. N. K., C. S. Meinen, M. O. Baringer, I. Bang, R. Rhodes, C. N. Barron, and F. Bub, 2005: Cross validating ocean prediction and monitoring systems. *Eos, Trans. Amer. Geophys. Union*, **86,** 269–273.

Mosley-Thompson, E., and Coauthors, 2001: Local to regional-scale variability of annual net accumulation on the Greenland ice sheet from PARCA cores. *J. Geophys. Res.,* **106** (D24), 33 839–33 851.

Mote, T. L., 2007: Greenland surface melt trends 1973-2007: Evidence of a large increase in 2007. *Geophys. Res. Lett.,* **34,** L22507, doi:10.1029/2007GL031976.

——, and M. R. Anderson, 1995: Variations in melt on the Greenland Ice Sheet based on passive microwave measurements. *J. Glaciol.,* **41,** 51–60.

Mueller, D. R., L. Copland, A. Hamilton, and D. Stern, 2008: Examining Arctic ice shelves prior to the 2008 breakup. *Eos, Trans. Amer. Geophys. Union,* **89,** doi:10.1029/2008EO490002.

Münnich, M., and J. D. Neelin, 2005: Seasonal influence of ENSO on the Atlantic ITCZ and equatorial South America. *Geophys. Res. Lett.*, **32,** L21709, doi:10.1029/2005GL023900.

National Climate Centre, 2008: An exceptional and prolonged heatwave in Southern Australia. Bureau of Meteorology Special Climate Statement 15, 7 pp. [Available online at www.bom.gov.au/climate/current/special-statements.shtml.]

Neumann, C. J., B. R. Jarvinen, C. J. McAdie, and J. D. Elms, 1993: *Tropical cyclones of the North Atlantic Ocean,* 1871-1992. Historical Climatology Series 6-2, NOAA/National Climatic Data Center, 193 pp.

New, M., M. Todd, M. Hulme, and P. Jones, 2001: Precipitation measurements and trends in the twentieth century. *Int. J. Climatol.,* **21,** 1899–1922.

Newchurch, M. J., E. S. Yang, D. M. Cunnold, G. C. Reinsel, J. M. Zawodny, and J. M. Russel III, 2003: Evidence for slowdown in stratospheric ozone loss: First stage of ozone recovery. *J. Geophys. Res.,* **108,** 4507, doi:10.1029/2003JD003471.

Newman, P. A., and M. Rex, 2007: Polar Ozone: Past and present. *Scientific assessment of ozone depletion: 2006.* Global Ozone Research and Monitoring Project Rep. 50, World Meteorological Organization, 4.1–4.48. [Available online at www.wmo.ch/pages/prog/arep/gaw/ozone_2006/ozone_asst_report.html.]

——, E. R. Nash, S. R. Kawa, S. A. Montzka, and S. M. Schauffler, 2006: When will the Antarctic ozone hole recover? *Geophys. Res. Lett.,* **33,** L12814, doi:10.1029/2005GL025232.

——, J. S. Daniel, D. W. Waugh, and E. R. Nash, 2007: A new formulation of equivalent effective stratospheric chlorine (EESC). *Atmos. Chem. Phys.,* **7,** 4537–4552.

Nghiem, S. V., Y. Chao, G. Neumann, P. Li, D. K. Perovich, T. Street, and P. Clemente-Colón, 2006: Depletion of perennial sea ice in the East Arctic Ocean. *Geophys. Res. Lett.,* **33,** L17501, doi:10.1029/2006GL027198.

——, I. G. Rigor, D. K. Perovich, P. Clemente-Colon, J. W. Weatherly, and G. Neumann, 2007: Rapid reduction of Arctic perennial sea ice. *Geophys. Res. Lett.,* **34,** L19504, doi:10.1029/2007GL031138.

Niiler, P. P., R. E. Davis, and H. J. White, 1987: Water-following characteristics of a mixed layer drifter. *Deep-Sea Res.,* **34** (11), 1867–1881.

NOAA CPC, cited 2009a: Observations of the 2008 stratospheric sudden warmings. [Available online at www.cpc.ncep.noaa.gov/products/stratosphere/temperature.]

——, cited 2009b: Observations of the size of the 2008 south polar vortex. [Available online at www.cpc.noaa.gov/products/stratosphere/polar/gif_files/vtx_sh.png.]

Nobre, P., and J. Shukla, 1996: Variations of sea surface temperature, wind stress, and rainfall over the tropical Atlantic and South America. *J. Climate,* **9,** 2464–2479.

Novelli, P. C., K. A. Masarie, P. M. Lang, B. D. Hall, R. C. Myers, and J. C. Elkins, 2003: Reanalysis of tropospheric CO trends: Effects of the 1997–1998 wildfires. *J. Geophys. Res.,* **108,** 4464, doi:10.1029/2002JD003031.

Oberman, N. G., 2008: Contemporary permafrost degradation of northern European Russia. *Proceedings of the 9th International Conference on Permafrost, Fairbanks, Alaska, 29 June – 3 July 2008*, Vol. 2, D. L. Kane and K. M. Hinkel, Eds., Institute of Northern Engineering, University of Alaska Fairbanks, 1305–1310.

——, and G. G. Mazhitova, 2001: Permafrost dynamics in the northeast of European Russia at the end of the 20th century. *Norw. J. Geogr.,* **55,** 241–244.

Oerlemans, J., 1994: Quantifying global warming from the retreat of glaciers. *Science,* **264,** 243–245.

Oki, T., and S. Kanae, 2006: Global hydrological cycles and world water resources. *Science,* **313,** 1068–1072.

Olsen, S. M., B. Hansen, D. Quadfasel, and S. Osterhus, 2008: Observed and modelled stability of overflow across the Greenland–Scotland ridge. *Nature,* **455,** 519–522, doi:10.1038/nature07302.

Onogi, K., and Coauthors, 2005: JRA-25: Japanese 25-year re-analysis. *Quart. J. Roy. Meteor. Soc.,* **131,** 3259–3268.

Orsi, A. H., G. C. Johnson, and J. L. Bullister, 1999: Circulation, mixing, and production of Antarctic Bottom Water. *Prog. Oceanogr.,* **43,** 55–109, doi:10.1016/S0079-6611(99)00004-X.

Orsolini, Y. J., 2004: Seesaw ozone fluctuations between the North Pacific and Atlantic in late winter. *J. Meteor. Soc. Japan,* **82,** 941–948.

Osterkamp, T. E., 2008: Thermal state of permafrost in Alaska during the fourth quarter of the twentieth century (plenary paper). *Proceedings of the 9th International Conference on Permafrost, Fairbanks, Alaska, 29 June – 3 July 2008*, Vol. 2, D. L. Kane and K. M. Hinkel, Eds., Institute of Northern Engineering, University of Alaska Fairbanks, 1333–1338.

Overland, J. E., M. Wang, and S. Salo, 2008: The recent Arctic warm period. *Tellus,* **60A,** 589–597.

Pacific ENSO Applications Climate Center, cited 2008: Pacific ENSO update newsletter. [Available online at www.soest.hawaii.edu/MET/Enso.]

Padman, L., D. Costa, M. Dinniman, H. Fricker, T. Scambos, M. Goebel, B. McDonald, and A. Humbert, 2009: Pre-collapse thinning of Wilkins Ice Shelf, Antarctica, by basal melting. *Earth Planet. Sci. Lett.,* in press.

Palacios, S. L., and R. C. Zimmerman, 2007: Response of eelgrass *Zostrea marina* to CO_2 enrichment: Possible impacts of climate change and potential for remediation of coastal habitats. *Mar. Ecol. Prog. Ser.,* **344,** 1–13.

Pan, L. W., J. C. Gille, D. P. Edwards, P. L. Bailey, and C. D. Rodgers, 1998: Retrieval of tropospheric carbon monoxide for the MOPITT experiment. *J. Geophys. Res.,* **103** (D24), 32 277–32 290.

Park, G.-H., K. Lee, R. Wanninkhof, and R. A. Feely, 2006: Empirical temperature-based estimates of variability in the oceanic uptake of CO_2 over the past 2 decades. *J. Geophys. Res.,* **111,** C07S07, doi:10.1029/2005JC003090.

Parker, D. E., T. P. Legg, and C. K. Folland, 1992: A new daily Central England Temperature Series, 1772-1991. *Int. J. Climatol.,* **12,** 317–342.

Parsons, P., I. Szunyogh, and P. Harr, 2008: Scientific program overview: THORPEX Pacific-Asian Regional Campaign (T-PARC). Executive Summary, 21 pp. [Available online at www.ucar.edu/na-thorpex/tparc/SPO_PARC_revised.pdf.]

Paul, F., A. Kääb, and W. Haeberli, 2007: Recent glacier changes in the Alps observed by satellite: Consequences for future monitoring strategies. *Global Planet. Change,* **56,** 102–111.

Peacock, S., M. Maltrud, and R. Bleck, 2005: Putting models to the data test: A case study using Indian Ocean CFC-11 data. *Ocean Modell.,* **9,** 1–22.

Pelto, M. S., 2006: The current disequilibrium of North Cascade glaciers**.** *Hydrol. Processes,* **20,** 769–779.

——, and C. Hedlund, 2001: The terminus behavior and response time of North Cascade glaciers. *J. Glaciol.,* **47,** 497–506.

Peng, G., Z. Garraffo, G. R. Halliwell, O.-M. Smedstad, C. S. Meinen, V. Kourafalou, and P. Hogan, 2009: Temporal variability of the Florida Current transport at 27ºN. *Ocean Circulation and El Nino: The New Research,* J. A. Long and D. S. Wells, Eds., NOVA Science Publishers, in press.

Peterson, B. J., R. M. Holmes, J. W. McClelland, C. J. Vorosmarty, R. B. Lammers, A. I. Shiklomanov, I. A. Shiklomanov, and S. Rahmstorf, 2002: Increasing river discharge to the Arctic Ocean. *Science,* **298,** 2171–2173.

——, J. McClelland, R. Curry, R. M. Holmes, J. E. Walsh, and K. Aagaard, 2006: Trajectory shifts in the arctic and subarctic freshwater cycle. *Science,* **313,** 1061–1066.

Peterson, T. C., and R. S. Vose, 1997: An overview of the Global Historical Climatology Network temperature database. *Bull. Amer. Meteor. Soc.,* **78,** 2837–2849.

Pitts, M. C., L. R. Poole, and L. W. Thomason, 2009: CALIPSO polar stratospheric cloud observations: Second-generation detection algorithm and composition discrimination. *Atmos. Chem. Phys. Discuss.,* **9**, 8121–8157.

Polyakov, I., D. Walsh, I. Dmitrenko, R. L. Colony, and L. A. Timokhov, 2003: Arctic Ocean variability derived from historical observations. *Geophys. Res. Lett.,* **30,** 1298, doi:10.1029/2002GL016441.

Prather, M. J., 1996: Natural modes and time scales in atmospheric chemistry: Theory, GWPs for CH_4 and CO, and runaway growth. *Geophys. Res. Lett.,* **23,** 2597–2600.

Proshutinsky, A. Y., and M. A. Johnson, 1997: Two circulation regimes of the wind-driven Arctic Ocean. *J. Geophys. Res.*, **102** (C6), 12493–12514.

——, I. M. Ashik, E. N. Dvorkin, S. Häkkinen, R. A. Krishfield, and W. R. Peltier, 2004: Secular sea level change in the Russian sector of the Arctic Ocean. *J. Geophys. Res.,* **109,** C03042, doi:10.1029/2003JC002007.

——, and Coauthors, 2009: The Beaufort Gyre Fresh Water Reservoir: State and variability from observations. *J. Geophys. Res.,* **114,** C00A10, doi:10.1029/2008JC005104.

Ramaswamy, V., M. D. Schwarzkopf, W. J. Randel, B. D. Santer, B. J. Soden, and G. L. Stenchikov, 2006: Anthropogenic and natural influences in the evolution of lower stratospheric cooling. *Science,* **311,** 1138–1141.

Randel, W. J., and Coauthors, 2009: An update of observed stratospheric temperature trends. *J. Geophys. Res.,* **114,** D02107, doi:10.1029/2008JD010421.

Raupach, M. R., G. Marland, P. Ciais, C. Le Quéré, J. G. Canadell, G. Klepper, and C. B. Field, 2007: Global and regional drivers of accelerating CO_2 emissions. *Proc. Natl. Acad. Sci. USA,* **104,** 10 288–10 293.

Raynolds, M. K., D. A. Walker, C. A. Munger, C. M. Vonlanthen, and A. N. Kade, 2008: A map analysis of patterned-ground along a North American Arctic Transect. *J. Geophys. Res.,* **113,** G03S03, doi:10.1029/2007JG000512.

Reed, R. J., D. C. Norquist, and E. E. Recker, 1977: The structure and properties of African wave disturbances as observed during Phase III of GATE. *Mon. Wea. Rev.,* **105,** 317–333.

Remer, L. A., and Coauthors, 2005: The MODIS aerosol algorithm, products, and validation. *J. Atmos. Sci.,* **62,** 947–973.

Rex, M., and Coauthors, 2006: Arctic winter 2005: Implications for stratospheric ozone loss and climate change. *Geophys. Res. Lett.,* **33,** L23808, doi:10.1029/2006GL026731.

Reynolds, R. W., and Y. Xue, 2008: Sea surface temperatures in 2007 [in "State of the Climate in 2007"]. *Bull. Amer. Meteor. Soc.,* **89** (7), S37–S39.

——, N. A. Rayner, T. M. Smith, D. C. Stokes, and W. Wang, 2002: An improved in situ and satellite SST analysis for climate. *J. Climate,* **15,** 1609–1625.

Rigby, M., and Coauthors, 2008: Renewed growth of atmospheric methane. *Geophys. Res. Lett.,* **35,** L22805, doi:10.1029/2008GL036037.

Rigor, I. G., and J. M. Wallace, 2004: Variations in the age of Arctic sea-ice and summer sea-ice extent. *Geophys. Res. Lett.,* **31,** L09401, doi:10.1029/2004GL019492.

Rintoul, S. R., 2007: Rapid freshening of Antarctic Bottom Water formed in the Indian and Pacific Oceans. *Geophys. Res. Lett.,* **34,** L06606, doi:10.1029/2006GL028550.

Roemmich, D., S. Riser, R. Davis, and Y. Desaubies, 2004: Autonomous profiling floats: Workhorse for broadscale ocean observations. *J. Mar. Technol. Soc.,* **38,** 31–39.

Romanovsky, V., M. Burgess, S. Smith, K. Yoshikawa, and J. Brown, 2002: Permafrost temperature records: Indicators of climate change. *Eos, Trans. Amer. Geophys. Union*, **83,** 589, doi:10.1029/2002EO000402.

——, S. Gruber, A. Instanes, H. Jin, S. S. Marchenko, S. L. Smith, D. Trombotto, and K. M. Walter, 2007: Frozen ground. *Global Outlook for Ice and Snow*, J. Eamer, Ed., United Nations Publications, 181–200.

——, and Coauthors, 2008: Thermal state and fate of permafrost in Russia: First results of IPY. *Proceedings of the 9th International Conference on Permafrost, Fairbanks, Alaska, 29 June – 3 July 2008*, Vol. 2, D. L. Kane and K. M. Hinkel, Eds., Institute of Northern Engineering, University of Alaska Fairbanks, 1511–1518.

Ropelewski, C. F., and M. S. Halpert, 1987: Global and regional scale precipitation patterns associated with the El Niño/Southern Oscillation. *Mon. Wea. Rev.,* **115,** 1606–1626.

Rothrock, D. A., D. B. Percival, and M. Wensnahan, 2008: The decline in arctic sea ice thickness: Separating the spatial, annual, and interannual variability in a quarter century of submarine data. *J. Geophys. Res.,* **113,** C05003, doi:10.1029/2007JC004252.

Rudolf, B., C. Beck, J. Grieser, and U. Schneider, cited 2005: Global Precipitation Analysis products. [Available online at www.dwd.de/en/FundE/Klima/KLIS/int/GPCC/Reports_Publications/QR/GPCC-intro-products-2005.pdf.]

Sabine, C. L., and Coauthors, 2004: The oceanic sink for anthropogenic CO_2. *Science,* **305,** 367–371.

——, R. A. Feely, R. Wanninkhof, and T. Takahashi, 2008: The global ocean carbon cycle [in "State of the Climate in 2007"]. *Bull. Amer. Meteor. Soc.,* **89** (7), S52–S56.

Sakamoto, M., and J. R. Christy, 2009: The influence of TOVS radiance assimilation on temperature and moisture tendencies in JRA-25 and ERA-40. *J. Atmos. Oceanic Technol.,* **26,** 1435–1455.

Salisbury, J., M. Green, C. Hunt, and J. Campbell, 2008: Coastal acidification by rivers: A threat to shellfish? *Eos, Trans. Amer. Geophys. Union,* **89,** doi:10.1029/2008EO500001.

Santer, B. D., T. M. L. Wigley, J. S. Boyle, D. J. Gaffen, J. J. Hnilo, D. Nychka, D. E. Parker, and K. E. Taylor, 2000: Statistical significance of trends and trend differences in layer-average atmospheric temperature time series. *J. Geophys. Res.,* **105** (D6), 7337–7356.

——, and Coauthors, 2003: Contributions of anthropogenic and natural forcing to recent tropopause height changes. *Science,* **301,** 479–483.

——, and Coauthors, 2007: Identification of human-induced changes in atmospheric moisture content. *Proc. Natl. Acad. Sci. USA,* **104,** 15 248–15 253.

Saravanan, R., and P. Chang, 2000: Interaction between tropical Atlantic variability and El Niño–Southern Oscillation. *J. Climate,* **13,** 2177–2194.

Scambos, T., H. A. Fricker, C.-C. Liu, J. Bohlander, J. Fastook, A. Sargent, R. Massom, and A.-M. Wu, 2009: Ice shelf disintegration by plate bending and hydro-fracture: Satellite observations and model results of the 2008 Wilkins ice shelf break-ups. *Earth Planet. Sci. Lett.,* **280,** 51–60, doi:10.1016/j.epsl.2008.12.027.

Schmid, C., 2005: Impact of combining temperature profiles from different instruments on an analysis of mixed layer properties. *J. Atmos. Oceanic Technol.,* **22,** 1571–1587.

Schott, F. A., J. Fischer, M. Dengler, and R. Zantopp, 2006: Variability of the Deep Western Boundary Current east of Grand Banks. *Geophys. Res. Lett.*, **33,** L21S07, doi:10.1029/2006GL026563.

Schuster, U., and A. J. Watson, 2007: A variable and decreasing sink for atmospheric CO_2 in the North Atlantic. *J. Geophys. Res.,* **112,** C11006, doi:10.1029/2006JC003941.

Seaber, P. R., F. P. Kapinos, and G. L. Knapp, 1987: Hydrologic unit maps. U.S. Geological Survey Water-Supply Paper 2294, 63 pp.

Seidel, D. J., and J. R. Lanzante, 2004: An assessment of three alternatives to linear trends for characterizing global atmospheric temperature changes. *J. Geophys. Res.,* **109,** D14108, doi:10.1029/2003JD004414.

——, and Coauthors, 2009: Reference upper-air observations for climate: Rationale, progress, and plans. *Bull. Amer. Meteor. Soc.,* **90,** 361–369.

Sensoy, S., I. Alan, and M. Demircan, 2008: Trends in Turkey climate extreme indices from 1971 to 2004. *Balwois Conf. on Water Observation and Information,* Ohrid, Republic of Macedonia, Balkan Institute for Water and Environment, 9 pp. [Available online at http://balwois.com/balwois/administration/full_paper/ffp-1000.pdf.]

Serreze, M. C., A. P. Barrett, J. C. Stroeve, D. N. Kindig, and M. M. Holland, 2009: The emergence of surface-based Arctic amplification. *The Cryosphere*, **3**, 11–19.

Shapiro, L. J., 1989: The relationship of the quasi-biennial oscillation to Atlantic tropical storm activity. *Mon. Wea. Rev.,* **117,** 1545–1552.

Shay, L. K., G. J. Goni, and P. G. Black, 2000: Effects of a warm oceanic feature on Hurricane Opal. *Mon. Wea. Rev.,* **128,** 1366–1383.

Sherwood, S. C., C. L. Meyer, R. J. Allen, and H. A. Titchner, 2008: Robust tropospheric warming revealed by iteratively homogenized radiosonde data. *J. Climate,* **21,** 5336–5352.

Shiklomanov A. I., T. I. Yakovleva, R. B. Lammers, I. Ph. Karasev, C. J. Vörösmarty, and E. Linder, 2006: Cold region river discharge uncertainty - estimates from large Russian rivers. *J. Hydrol.,* **326,** 231–256.

Shine, K. P., J. J. Barnett, and W. J. Randel, 2008: Temperature trends derived from Stratospheric Sounding Unit radiances: The effect of increasing CO_2 on the weighting function. *Geophys. Res. Lett.,* **35,** L02710, doi:10.1029/2007GL032218.

Siegel, D. A., S. Maritorena, N. B. Nelson, and M. J. Behrenfeld, 2005: Independence and interdependences among global ocean color properties: Reassessing the bio-optical assumption. *J. Geophys. Res.,* **110,** C07011, doi:10.1029/2004JC002527.

——, J. A. Yoder, and C. R. McClain, 2008: Thoughts about the future of satellite ocean color observations. *OCB Newsletter*, October, Ocean Carbon and Biogeochemistry Project Office, Woods Hole, MA, 7–8. [Available online at www.us-ocb.org/publications/OCB_NEWS_OCT08.pdf.]

Smith, D. M., S. Cusack, A. W. Colman, C. K. Folland, G. R. Harris, and J. M. Murphy, 2007: Improved surface temperature prediction for the coming decade from a global climate model. *Science,* **317,** 796–799.

Smith, S. L., M. M. Burgess, D. Riseborough, and F. M. Nixon, 2005: Recent trends from Canadian permafrost thermal monitoring network sites. *Permafrost Periglacial Processes,* **16,** 19–30.

Smith, T. M., and R. W. Reynolds, 1998: A high-resolution global sea surface temperature climatology for the 1961–90 base period. *J. Climate,* **11,** 3320–3323.

——, and ——, 2005: A global merged land–air–sea surface temperature reconstruction based on historical observations (1880–1997). *J. Climate,* **18,** 2021–2036.

——, ——, T. C. Peterson, and J. Lawrimore, 2008: Improvements to NOAA's historical merged land–ocean surface temperature analysis (1880–2006). *J. Climate,* **21,** 2283–2296.

Solomon, S., D. Qin, M. Manning, M. Marquis, K. Averyt, M. M. B. Tignor, H. L. Miller Jr., and Z. Chen, Eds., 2007: *Climate Change 2007: The Physical Sciences Basis.* Cambridge University Press, 996 pp.

Stackhouse, P. W., Jr., D. P. Kratz, G. R. McGarragh, S. K. Gupta, and E. B. Geier, 2006: Fast Longwave and Shortwave Radiative Flux (FLASHFlux) products from CERES and MODIS measurements. *Proc. 12th Conf. on Atmospheric Radiation,* Madison, WI, Amer. Meteor. Soc., P1.10. [Available online at http://ams.confex.com/ams/pdfpapers/113479.pdf.]

Staehelin, J., N. R. P. Harris, C. Appenzeller, and J. Eberhard, 2001: Ozone trends: A review. *Rev. Geophys.,* **39,** 231–290.

Stammer, D., 1998: On eddy characteristics, eddy transports, and mean flow properties. *J. Phys. Oceanogr.,* **28,** 727–739.

Stammerjohn, S. E., D. G. Martinson, R. C. Smith, X. Yuan, and D. Rind, 2008: Trends in Antarctic annual sea ice retreat and advance and their relation to El Niño–Southern Oscillation and Southern Annular Mode variability. *J. Geophys. Res.,* **113**, C03S90, doi:10.1029/2007JC004269.

Steig, E. J., D. P. Schneider, S. D. Rutherford, M. E. Mann, J. C. Comiso, and D. T. Shindell, 2009: Warming of the Antarctic ice-sheet surface since the 1957 International Geophysical Year. *Nature,* **457,** 459–462, doi:10.1038/nature07669.

Steinbrecht, W., and Coauthors, 2009: Ozone and temperature trends in the upper stratosphere at five stations of the network for the detection of atmospheric composition change. *Int. J. Remote Sens.,* in press.

Stolarski, R. S., and S. Frith, 2006: Search for evidence of trend slow-down in the long-term TOMS/SBUV total ozone data record: The importance of instrument drift uncertainty and fingerprint detection. *Atmos. Chem. Phys.,* **6,** 4057–4065.

Strahler, A., D. Muchoney, J. Borak, M. Friedl, S. Gopal, E. Lambin, and A. Moody, 1999: MODIS land cover and land-cover change. MODIS land cover product ATBD version 5, 59 pp. [Available online at http://modis.gsfc.nasa.gov/data/atbd/atbd_mod12.pdf.]

Svoboda, M., and Coauthors, 2002: The Drought Monitor. *Bull. Amer. Meteor. Soc.,* **83,** 1181–1190.

Takahashi, T., and Coauthors, 2009: Climatological mean and decadal change in surface ocean pCO_2, and net sea-air CO_2 flux over the global oceans. *Deep-Sea Res. II*, **56,** 554–557, doi:10.1016/j.dsr2.2008.12.009.

Talley, L. D., 2008: Freshwater transport estimates and the global overturning circulation: Shallow, deep and throughflow components. *Progr. Oceanogr.,* **78,** 257–303, doi:10.1016/j.pocean.2008.05.001.

Tans, P. P., I. Y. Fung, and T. Takahashi, 1990: Observational constraints on the global atmospheric CO_2 budget. *Science,* **247,** 1431–1439, doi:10.1126/science.247.4949.1431.

Tape, K., M. Sturm, and C. Racine, 2006: The evidence for shrub expansion in Northern Alaska and the Pan-Arctic. *Global Change Biol.,* **12,** 686–702.

Tedesco, M., X. Fettweis, M. van den Broeke, R. van de Wal, and P. Smeets, 2008: Extreme snowmelt in northern Greenland during summer 2008. *Eos, Trans. Amer. Geophys. Union*, **89,** 391, 10.1029/2008EO410004.

Thomas, H., A. E. Friederike Prowe, I. D. Lima, S. C. Doney, R. Wanninkhof, R. J. Greatbach, U. Schuster, and A. Corbiere, 2008: Changes in the North Atlantic Oscillation influence CO_2 uptake in the North Atlantic over the past two decades. *Global Biogeochem. Cycles,* **22,** GB4027, doi:10.1029/2007GB003167.

Thompson, D. W. J., J. J. Kennedy, J. M. Wallace, and P. D. Jones, 2008: A large discontinuity in the mid-twentieth century in observed global-mean surface temperature. *Nature,* **453,** 646–649.

Thorne, P. W., D. E. Parker, J. R. Christy, and C. A. Mears, 2005a: Uncertainties in climate trends: Lessons from upper-air temperature records. *Bull. Amer. Meteor. Soc.,* **86,** 1437–1442.

——, ——, S. F. B. Tett, P. D. Jones, M. McCarthy, H. Coleman, and P. Brohan, 2005b: Revisiting radiosonde upper air temperatures from 1958 to 2002. *J. Geophys. Res.,* **110,** D18105, doi:10.1029/2004JD005753.

Trenberth, K. E., J. Fasullo, and L. Smith, 2005: Trends and variability in column-integrated atmospheric water vapor. *Climate Dyn.,* **24,** 741–758.

——, and Coauthors, 2007: Observations: Surface and atmospheric climate change. *Climate Change 2007: The Physical Science Basis,* S. Solomon et al., Eds., Cambridge University Press, 235–335.

Trigo R. M., I. M. Trigo, C. C. DaCamara, and T. J. Osborn, 2004: Winter blocking episodes in the European-Atlantic sector: Climate impacts and associated physical mechanisms in the Reanalysis. *Climate Dyn.,* **23,** 17–28.

Tucker, C. J., D. Slayback, J. Pinzon, S. O. Los, R. B. Myneni, and M. G. Taylor, 2001: Higher northern latitude Normalized Difference Vegetation Index and growing season trends from 1982 to 1999. *Int. J. Biometeor.,* **45,** 184–190.

Våge, K., and Coauthors, 2009: Surprising return of deep convection to the subpolar North Atlantic Ocean in winter 2007–2008. *Nat. Geosci.,* **2,** 67–72, doi:10.1038/ngeo382.

van den Broeke, M., W. J. van de Berg, and E. van Meijgaard, 2006: Snowfall in coastal West Antarctica much greater than previously assumed. *Geophys. Res. Lett.,* **33,** L02505, doi:10.1029/2005GL025239.

van der Werf, G. R., J. T. Randerson, L. Giglio, G. J. Collatz, P. S. Kasibhatla, and A. F. Arellano, 2006: Interannual variability in global biomass burning emissions from 1997 to 2004. *Atmos. Chem. Phys.,* **6,** 3423–3441.

van de Wal, R. S. W., W. Greuell, M. R. van den Broeke, C. H. Reijmer, and J. Oerlemans, 2006: Surface mass-balance observations and automatic weather station data along a transect near Kangerlussuaq, West Greenland. *Ann. Glaciol.,* **42,** 311–316.

Vaughan D. G., and Coauthors, 2003: Recent rapid regional climate warming on the Antarctic Peninsula. *Climatic Change,* **60,** 243–274.

Vautard, R., P. Yiou, and G. J. van Oldenborgh, 2009: Decline of fog, mist and haze in Europe over the past 30 years. *Nat. Geosci.,* **2,** 115–119.

Vecchi, G. A., K. L. Swanson, and B. J. Soden, 2008: Climate Change: Whither hurricane activity? *Science,* **322,** 687–689, doi:10.1126/science.1164396.

Verbyla, D., 2008: The greening and browning of Alaska based on 1982–2003 satellite data. *Global Ecol. Biogeogr.,* **17,** 547–555.

Vose, R. S., R. L. Schmoyer, P. M. Steurer, T. C. Peterson, R. Heim, T. R. Karl, and J. Eischeid, 1992: The Global Historical Climatology Network: Long-term monthly temperature, precipitation, sea level pressure, and station pressure data. ORNL/CDIAC-53, NDP-041. [Available online at http://cdiac.esd.ornl.gov/epubs/ndp/ndp041/ndp041.html.]

Waliser, D. E., and C. Gautier, 1993: A satellite-derived climatology of the ITCZ. *J. Climate,* **6,** 2162–2174.

Walker, D. A., and Coauthors, 2008: Arctic patterned-ground ecosystems: A synthesis of field studies and models along a North American Arctic Transect. *J. Geophys. Res.,* **113,** G03S01, doi:10.1029/2007JG000504.

Wallace, D. W. R., 1995: Monitoring global ocean carbon inventories. Ocean Observing System Development Panel Background Rep. 5, 54 pp.

Wallace, J. M., Y. Zhang, and J. A. Renwick, 1995: Dynamic contribution to hemispheric mean temperature trends. *Science,* **270,** 780–783.

Wang, B., and J. C. L. Chan, 2002: How strong ENSO events affect tropical storm activity over the western North Pacific. *J. Climate,* **15,** 1643–1658.

Wang, J., L. Zhang, A. Dai, T. Van Hove, and J. Van Baelen, 2007: A near-global, 8-year, 2-hourly atmospheric precipitable water dataset from ground-based GPS measurements. *J. Geophys. Res.,* **112,** D11107, 10.1029/2006JD007529.

Wang, L., C. Derksen, and R. Brown, 2008a: Detection of Pan-Arctic terrestrial snowmelt from QuikSCAT, 2000 – 2005. *Remote Sens. Environ.,* **112,** 3794–3805.

Wang, L., and Coauthors, 2008b: Characteristics of the extreme low-temperature, heavy snowstorm and freezing disasters in January 2008 in China. *Meteor. Monthly,* **34**, 95–100.

Waugh, D. W., L. Oman, S. R. Kawa, R. S. Stolarski, S. Pawson, A. R. Douglass, P. A. Newman, and J. E. Nielsen, 2009: Impacts of climate change on stratospheric ozone recovery**.** *Geophys. Res. Lett.,* **36,** L03805, doi:10.1029/2008GL036223.

Weber, M., S. Dhomse, F. Wittrock, A. Richter, B.-M. Sinnhuber, and J. P. Burrows, 2003: Dynamical control of NH and SH winter/spring total ozone from GOME observations in 1995–2002. *Geophys. Res. Lett.,* **30,** 1853, doi:10.1029/2002GL016799.

——, L. N. Lamsal, M. Coldewey-Egbers, K. Bramstedt, and J. P. Burrows, 2005: Pole-to-pole validation of GOME WFDOAS total ozone with groundbased data. *Atmos. Chem. Phys.,* **5,** 1341–1355.

——, ——, and J. P. Burrows, 2007: Improved SCIAMACHY WFDOAS total ozone retrieval: Steps towards homogenising long-term total ozone datasets from GOME, SCIAMACHY, and GOME2. *Proc. Envisat Symp. 2007,* ESA SP-636, Montreux, Switzerland, European Space Agency, 5 pp. [Available online at http://envisat.esa.int/envisatsymposium/proceedings/posters/3P4/463281we.pdf.]

Wentz, F. J., 1997: A well-calibrated ocean algorithm for Special Sensor Microwave/Imager. *J. Geophys. Res.,* **102** (C4), 8703–8718.

——, L. Ricciardulli, K. A. Hilburn, and C. A. Mears, 2007: How much more rain will global warming bring? *Science,* **317,** 233–235.

WGMS, 2007: *Glacier Mass Balance Bulletin No. 9* (2004-2005). World Glacier Monitoring Service, 100 pp.

——, 2008: Global glacier changes: Facts and figures. UNEP-World Glacier Monitoring Service, Zurich, Switzerland, 88 pp.

Whitney, L. D., and J. S. Hobgood, 1997: The relationship between sea surface temperatures and maximum intensities of tropical cyclones in the eastern North Pacific Ocean. *J. Climate,* **10,** 2921–2930.

Wielicki, B. A., and Coauthors, 1998: Clouds and the Earth's Radiant Energy System (CERES): Algorithm overview. *IEEE Trans. Geosci. Remote Sens.,* **36,** 1127–1141.

Wijffels, S. E., R. W. Schmitt, H. L. Bryden, and A. Stigebrandt, 1992: Freshwater transport by the ocean. *J. Phys. Oceanogr.,* **22,** 155–162.

——, J. Willis, C. M. Domingues, P. Barker, N. J. White, A. Gronell, K. Ridgway, and J. A. Church, 2008: Changing expendable bathythermograph fall rates and their impact on estimates of thermosteric sea level rise *J. Climate,* **21,** 5657–5672.

Wild, M., and Coauthors, 2005: From dimming to brightening: Decadal changes in solar radiation at earth's surface. *Science,* **308,** 847–850.

Willis, J., D. Roemmich, and B. Cornuelle, 2004: Interannual variability in upper-ocean heat content, temperature and thermosteric expansion on global scales. *J. Geophys. Res.,* **109,** C12036, doi:10.1029/2003JC002260.

——, D. P. Chambers, and R. S. Nerem, 2008: Assessing the globally averaged sea level budget on seasonal and interannual timescales. *J. Geophys. Res.,* **113,** C06015, doi:10.1029/2007JC004517.

WMO, 2008: The Year of Tropical Convection. *Proc. Seventh Session of the Int. Steering Committee for THORPEX*, WMO CAS/ICSC-7/DOC5.2.1, Geneva, Switzerland, World Meteorological Organization, 2 pp. [Available online at www.wmo.int/pages/prog/arep/wwrp/new/documents/doc5_2_1_yotc.pdf.]

Wohltmann, I., R. Lehmann, M. Rex, D. Brunner, and J. A. Mäder, 2007: A process-oriented regression model for column ozone. *J. Geophys. Res.,* **112,** D12304, doi:10.1029/2006JD007573.

Wong, T., B. A. Wielicki, R. B. Lee III, G. L. Smith, K. A. Bush, and J. K. Willis, 2006: Reexamination of the observed decadal variability of the earth radiation budget using altitude-corrected ERBE/ERBS nonscanner WFOV data. *J. Climate,* **19,** 4028–4040.

Woodgate, R. A., K. Aagaard, and T. J. Weingartner, 2006: Interannual changes in the Bering Strait fluxes of volume, heat and freshwater between 1991 and 2004. *Geophys. Res. Lett.*, **33**, L15609, doi:10.1029/2006GL026931.

World Glacier Monitoring Service, 2009: Glacier mass balance data 2006 and 2007. [Available online at www.wgms.ch/mbb/mbb10/sum07.html.]

Wu, B., J. Wang, and J. E. Walsh, 2006: Dipole anomaly in the winter Arctic atmosphere and its association with sea ice motion. *J. Climate,* **19,** 210–225.

Wunsch, C., 2008: Mass and volume transport variability in an eddy-filled ocean. *Nat. Geosci.,* **1,** 165–168, doi:10.1038/ngeo126.

——, and P. Heimbach, 2006: Estimated decadal changes in the North Atlantic meridional overturning circulation and heat flux 1993–2004. *J. Phys. Oceanogr.,* **36,** 2012–2024.

Xie, P., and P. A. Arkin, 1997: Global precipitation: A 17-year monthly analysis based on gauge observations, satellite estimates, and numerical model outputs. *Bull. Amer. Meteor. Soc.,* **78,** 2539–2558.

Xue, Y., T. M. Smith, and R. W. Reynolds, 2003: Interdecadal changes of 30-yr SST normals during 1871–2000. *J. Climate,* **16,** 1601–1612.

Yang, E. S., D. M. Cunnold, M. J. Newchurch, and R. J. Salawitch, 2005: Change in ozone trends at southern high latitudes. *Geophys. Res. Lett.,* **32,** L12812, doi:10.1029/2004GL022296.

Yang, X. Y., R. X. Huang, and D. X. Wang, 2007: Decadal changes of wind stress over the Southern Ocean associated with Antarctic ozone depletion. *J. Climate,* **20,** 3395–3410.

Yashayaev, I., and J. W. Loder, 2009: Enhanced production of Labrador Sea Water in 2008. *Geophys. Res. Lett.,* **36,** L01606, doi:10.1029/2008GL036162.

Yu, L., X. Jin, and R. A. Weller, 2008a: Multidecade global flux datasets from the Objectively Analyzed Air-sea Fluxes (OAFlux) Project: Latent and sensible heat fluxes, ocean evaporation, and related surface meteorological variables. Woods Hole Oceanographic Institution, OAFlux Project Tech. Rep. OA-2008-01, 64 pp.

Zebiak, S. E., 1989: Oceanic heat content variability and El Niño cycles. *J. Phys. Oceanogr.,* **19,** 475–486.

Zhang, C., 2005: Madden-Julian Oscillation. *Rev. Geophys.,* **43,** RG2003, doi:10.1029/2004RG000158.

——, and J. Gottschalck, 2002: SST anomalies of ENSO and the Madden–Julian oscillation in the equatorial Pacific. *J. Climate,* **15,** 2429–2445.

Zhang, R., 2008: Coherent surface-subsurface fingerprint of the Atlantic meridional overturning circulation. *Geophys. Res. Lett.,* **35,** L20705, doi:10.1029/2008GL035463.

Zhang, X., and Coauthors, 2005: Trends in Middle East climate extreme indices from 1950 to 2003. *J. Geophys. Res.,* **110,** D22104, doi:10.1029/2005JD006181.

Zimov, S., E. A. G. Schuur, and F. S. Chapin, 2006: Permafrost and the global carbon budget. *Science,* **312,** 1612–1613.

Zou, C.-Z., M. Gao, and M. Goldberg, 2009: Error structure and atmospheric temperature trends in observations from the Microwave Sounding Unit. *J. Climate*, **22,** 1661–1681.

Zwally, H. J., M. B. Giovinetto, J. Li, H. G. Cornejo, M. A. Beckley, A. C. Brenner, J. Saba, and Y. Donghui, 2005: Mass changes of the Greenland and Antarctic ice sheets and shelves and contributions to sea-level rise: 1992–2002. *J. Glaciol.,* **51,** 509–527.

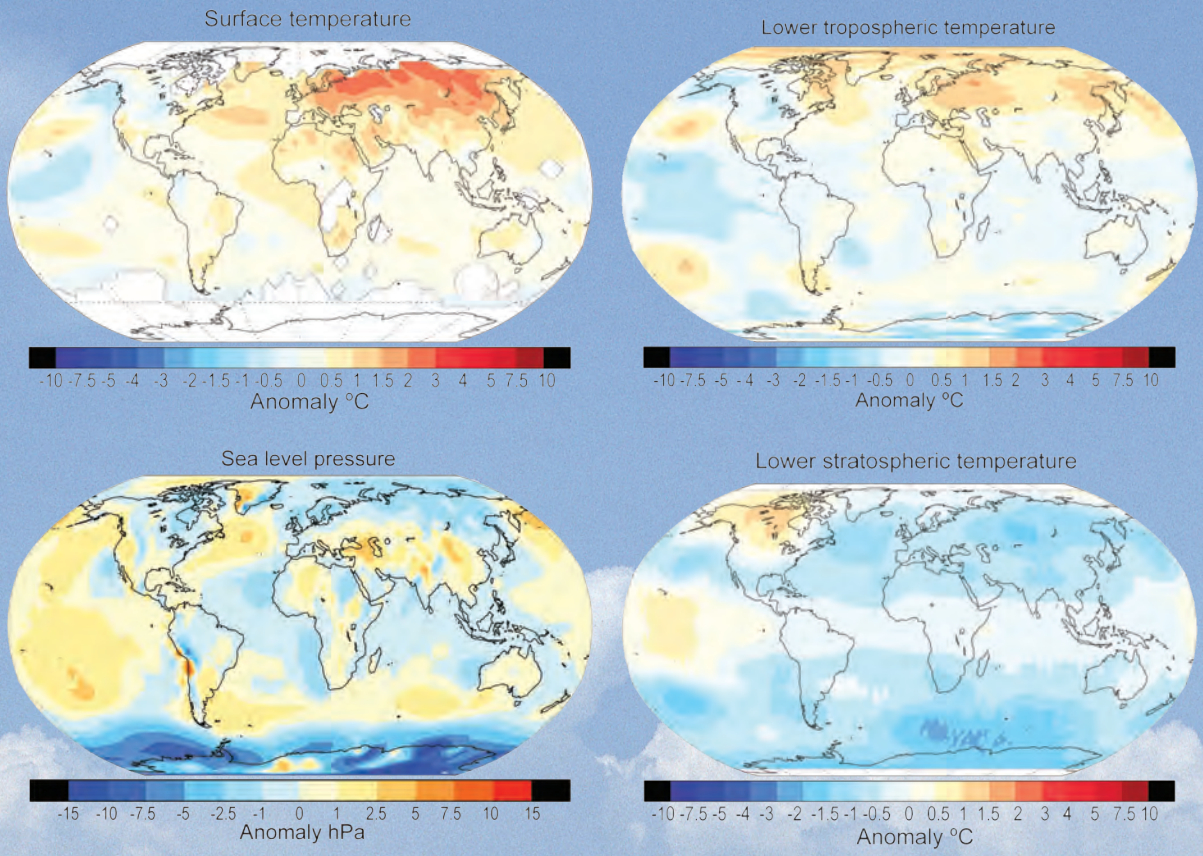

Libraries: Please file with the *Bulletin of the American Meteorological Society*, Vol. 90, Issue 8